UNIVERSITY OF SOUTHAMPTON

FACULTY OF ENGINEERING AND THE ENVIRONMENT

Aerodynamics and Flight Mechanics Group

Volume 1 of 1

Helicopter power transmission : Changing the paradigm

by

Frank BUYSSCHAERT

Thesis for the degree of Doctor of Philosophy

April 2015

UNIVERSITY OF SOUTHAMPTON

ABSTRACT

FACULTY OF ENGINEERING AND THE ENVIRONMENT

Aerodynamics and Flight Mechanics

Thesis for the degree of Doctor of Philosophy

HELICOPTER POWER TRANSMISSION : CHANGING THE PARADIGM

by Frank BUYSSCHAERT

In the conventional helicopter, the transmission and powerplant systems are the major production and operator direct operating cost drivers. Additionally, they are related to helicopter safety and reliability concerns and impose performance boundaries. As a consequence, they need to be addressed.

Adapting the transmission and powerplant systems with the introduction of more electric technologies, which are reported to be more reliable and cost friendly, involves a gross weight penalty, which cannot be accepted from a performance viewpoint. The implementation of liquid hydrogen, with the objective to introduce a sustainable energy carrier and free cold source for the high temperature superconductive devices driving the tail rotor, appears unattractive, from either a weight or a exploitation standpoint. Biodiesel could be an alternative to Avgas driven configurations, but at the moment, it has questionable chemical characteristics and is therefore discarded. Conceptual alternatives to the conventional helicopter explored in an attempt to verify their ability to overcome the stated performance, safety and cost aspects, are subjected to the same problems, the Turbine Driven Rotor (TDR) helicopter configuration excepted. The TDR helicopter drives a coaxial rotor configuration by means of a rotor embedded Ljungström turbine, omitting the need for a mechanical transmission system.

Three TDR helicopter thermodynamic cycles are proposed. The piston engine powered TDR cycle shows to be of interest for the low weight class helicopters. The turbofan powered TDR cycle is preferred in the mid and high weight categories, benefitting from its configurational simplicity. The more complex turboshaft powered TDR cycle requires a heat exchanger, is heavier and thus not recommended.

With respect to the Ljungström turbine, the loss models of Soderberg and Ainley and Mathieson used to establish its geometry and performance characteristics are generally acceptable and appear coherent, while a deviation angle correction is developed to cope with the radial outflow configuration of the turbine. Similarly, loss models for the internal leakage and disk friction are proposed. However, these models could not be substantiated by means of experiments.
A design methodology to implement the Ljungström turbine in the helicopter rotor head is presented and allows adjusting the thermodynamic cycle characteristics such as to maximise the performance gain with respect to the conventional helicopter. For nominal operating conditions, ISA SLS, a VLR-class TDR helicopter shows to bear a performance gain of 10% over a conventional helicopter when equipped with an Avgas engine and 14% when a Diesel engine is used. Hereby, the cycle pressure ratio remained low, i.e. approximately 1.25, allowing a turbine polytropic efficiency of 87%. An identical study with a NH-90-class TDR helicopter proved to offer a performance potential of 50% at a cycle pressure ratio around 1.6 and a turbine polytropic efficiency of 90%. In all cases, the gas temperature at the inlet of Ljungström turbine remained below the rotor bearing temperature limit of 400 K.

–TERMS OF A NON-DISCLOSURE AGREEMENT MAY APPLY–

Contents

List of Figures

List of Tables

Declaration of authorship

I, Frank Buysschaert, declare that the thesis **Helicopter power transmission : Changing the paradigm** and the work presented therein are my own and has been generated by me as the result of my own original research.

I confirm that :

1. This work was done wholly or mainly while in candidature for a research degree at this University;
2. Where any part of this thesis has previously been submitted for a degree or any other qualification at this University or any other institution, this has been clearly stated;
3. Where I have consulted the published work of others, this is always clearly attributed;
4. Where I have quoted from the work of others, the source is always given. With the exception of such quotations, this thesis is entirely my own work;
5. I have acknowledged all main sources of help;
6. Where the thesis is based on work done by myself jointly with others, I have made clear exactly what was done by others and what I have contributed myself;
7. Parts of this work have been published in :
    - Nine-month report
    - Transfer thesis
    - F. Buysschaert, S. Newman, S. Walker, H. Antoine, and P. Hendrick, *The TDR helicopter concept : Design and integration of the Ljungström turbine,* 41st European Rotorcraft Forum, Munich, Germany, September, 2015.
    - F. Buysschaert, S. Newman, S. Walker, H. Antoine, and P. Hendrick, *The turbine driven rotor concept, a new vision for helicopter propulsion,* 40th European Rotorcraft Forum, Southampton, United Kingdom, September, 2014.
    - F. Buysschaert, S. Newman, S. Walker, H. Antoine, and P. Hendrick, *The Ljungström turbine for aeronautical applications,* 5th European Conference for Aeronautics and Space Sciences, Munich, Germany, July, 2013.
    - F. Buysschaert, P. Hendrick, S. Newman, *Conventional helicopters : an adaptiveness study for more electric and alternative propulsion technologies.* Institution of Mechanical Engineers, Part G : Journal of Aerospace Engineering, November 16th, 2011. (DOI 10.1177/0954410011417948) – Institution of Mechanical Engineers' Aerospace Division William Sweet Smith prize 2013.
    - F. Buysschaert, P. Hendrick, S. Newman, *Conventional helicopters and their adaptiveness for more electric and alternative transmission technologies,* 36th European Rotorcraft Forum, Paris, France, September 7-9, 2010.

Signed : .....

Date : 14th of April 2015

Aknowledgements

"To reach a port, we must sail – sail, not tie at anchor – sail, not drift."

Franklin D. Roosevelt*

I was privileged to have Simon Newman as my supervisor and mentor. I owe him my sincerest gratitude for taking me under his wings and sharing his views. His advice has been most valuable (and sometimes also went beyond the topic of this dissertation to include insights on the whereabouts of Queen Victoria in public buildings).

I also wish to thank Scott Walker, my second supervisor, for his invaluable support and guidance. There were many moments when I got lost in the maze of my research and when he helped me find the right path.

Since graduation in 2001, Patrick Hendrick has supported my endeavours. He has allowed me to orient my career and undertake the research that I am now able to present. It is an understatement to say that this is much appreciated. Thanks again, Patrick.

I am also indebted to Hubert Antoine, without whom I would not have been able to accomplish this work. I truly hope that my work can contribute to the further development and success of the TDR helicopter concept.

The Université Libre de Bruxelles merits credit for the financial and intellectual support it has provided. Gérard Degrez, Bernard Leduc, Alessandro Parente and my fellow colleagues of the Aero-Thermo-Mechanics Group (and students) : thanks!

I must also express my gratitude to Ron Barrett, of the University of Kansas, for enabling me to start this quest.

AgustaWestland, The Boeing Company, NASA, Vitalii Dudnik, Denis Mosolov, Joachim Kurzke, Frank Jørgensen, Young June Moon, SAGE Publications, Hubert Antoine and the Belgian Defence/DG Com are recognised for granting permission to use of their proprietary material in this dissertation.

I would like to acknowledge Geert, Matt, Dieter, Ingrid, Renaat, Dries, Didier (please forgive me if I forgot someone) for their support and interesting discussions. Tack så mycket!

*Unless stated otherwise, the quotations that introduce the chapters in this study have been selected from http://www.azquotes.com.

Also the many canines of the animal shelter deserve a pat on the back, for their warmth, playfulness and being man's best friend, while giving me time to think and forget.

Finally, and most importantly, my parents Marnix and Marie-Christine, my sister Heidi and Isis, thank you so much for your invaluable support and empathy. You were my life raft. I owe you more than anyone else!

Outline and objectives

Helicopters play an irreplaceable role in present-day society. Their impact on our quality of life may be regarded as substantial, directly or indirectly. Therefore, continuous efforts are made to improve its safety, performance and cost. ***The first objective*** *of the work at hand is to uncover the technical components in a conventional helicopter that compromise these aspects and propose alternatives.* This discussion is developed as follows :

→ The first chapter aims at exposing those technical systems in a *conventional* helicopter that contribute most to the degradation of safety, performance and cost.

→ The second chapter proposes and assesses technical alternatives for direct implementation in a conventional helicopter, in an attempt to address the aspects of concern found in the first chapter.

→ The third chapter discusses conceptual alternatives to the conventional helicopter and proposes the TDR helicopter concept as a viable solution. This helicopter concept uses a *Ljungström turbine* to drive the rotors.

Having selected the TDR helicopter concept as a potential answer to the first objective, ***the second objective*** *aims at the development of a sound theoretical basis to examine its qualities as an alternative to the conventional helicopter during nominal operation.* Since the implementation of a Ljungström turbine in a helicopter platform was never undertaken, ***the third objective*** *is establishing a performance and geometry model of the Ljungström turbine integrated in a helicopter rotor head.* As a result :

→ The fourth chapter develops and discusses three TDR helicopter thermodynamic cycles and uncovers the major cycle variables. The need to evaluate the impact of the cycle characteristics on the performance of the Ljungström turbine, and vice versa, appears necessary.

→ The fifth chapter develops the governing equations necessary to examine the Ljungström turbine performance characteristics.

→ The sixth chapter proposes loss models applicable to the Ljungström turbine.

→ The seventh chapter develops a model to establish the performance characteristics and geometry of the Ljungström turbine.

→ The eighth chapter combines the conditioning cycles with the Ljungström turbine performance model by means of two case studies.

Note that due to the various challenges and the multiple objectives involved, the structure of this thesis may deviate slightly from the traditional format; yet an attempt was made to present a coherent account integrating the various aspects of the research. In order to improve its readability, a nomenclature list has been included at the end of each chapter, with the exception of the third chapter, where it was found unnecessary.

Chapter 1

The conventional helicopter : Anamnesis

> *"Not until nearly four years after the first airplane flight (in 1903) did some helicopters lift their pilots off the ground. These attempts achieved only short, tricky, and badly controlled flights. Most of them ended in failure. Their cinema records look today like the best slapstick comedy ever made. Subsequent improvement was slow."*
>
> Jacob Shapiro in *The Helicopter (1958)*

It takes courage when birds leave their nest for the first time, stretching their wings and taking the first steps towards the frontiers of familiarity. Each and everyone of them takes the risk of whirling down and end in a misadventure. The difference between helicopter pioneering and birds lays within the fact that most birds are anatomically fit to fly, while human-mind-conceived contraptions are not. The records of men that sacrificed their life are a bitter testimony of how difficult it is to achieve vertical flight and the lack of profound knowledge of the physical problem and its consequences, overshadowed by the craving of success and the ability to fly. But it would be immoral not to praise the bravery of these pioneers, as it allowed vertical flight to evolve to the helicopters known today, which play an invaluable role in modern society. The evolution the helicopter underwent, is historic. The result however, could be reflected by the word *anamnesis*. It echoes the inventory of mishaps and difficulties related to vertical flight, but also questions the capability of man to find the solution that yields the best capable vertical lift-off platform[i]. Indeed, contemporary knowledge, political and financial burdens all influence the final result, effectively working as "a natural selection of the fittest".
After the Second World War, the helicopter morphology became more or less fixed, probably by the industrialisation and mass-production of the most successful configurations.

[i] In his Meno dialogue, Plato argues that the answer to the *paradox of inquiry* lies with the innate knowledge of man, which only needs to be recalled to find the solution to a problem. Therefore he uses the Greek word *Anamnesis* – Samet (2008). The paradox of inquiry states that the solution to a problem of which the nature is not known, can only be accepted when the perception of the nature of the problem is correct. But since the nature of the problem is à priori unknown, how can one be sure the solution is correct ?

But even today engineers still try to overcome major issues related to reliability, safety, performance and cost. In the country of the blind, the one-eyed man is king, a conclusion drawn by many researchers as several new concepts arise and battle for survival. However, if a new concept must survive, it has to overcome the weaknesses of the dominant morphology, while exhibiting a superior fitness for the job.
Finding the major technical weaknesses of the current conventional helicopters will be the subject of this chapter, examining accident data, cost parameters as well as important performance constraints. The result of this assessment will serve as the basis for the next chapter, in which alternative configurations will be sought with the main objective to improve the competitiveness of the conventional helicopter.

1.1 The conventional helicopter configuration

Evaluating new concepts requires a standard for comparison. Adopting the conventional helicopter as the reference is natural, but the perception of the term *conventional* still needs a proper definition. In Western countries, helicopters typically have a single main rotor with tail rotor or similar (Fig.1.1), with the exception of the tandem configuration, which is mainly used for heavy transport (Fig.1.2(a)). Eastern countries however, mostly develop and produce helicopters with coaxially placed rotors (Fig.1.2(b)). The interpretation of what helicopter configuration is "conventional" therefore has a strong geographic dependence. The conventional helicopter discussed in this work is the western configuration. It will be seen though that the conclusions drawn from the subsequent conventional helicopter assessment will also apply to its eastern counterpart.

Even though the general morphology of a conventional helicopter is invariant, it can be subcategorised. The sub-configurations depend on the design requirements on the one hand and are also subjected to technical improvements over time on the other. These effects work on the external shape of the conventional helicopter as well as on the internal configuration. A short survey of the most noteworthy configurations is given next.

1.1.1 External configurations

Important elements contributing to the external configuration are the fuselage, undercarriage, tail boom and tail rotor. The stated mission requirements influence strongly the external configuration of a conventional helicopter.

With regard to the fuselage, helicopters made for executive transport normally exhibit the better cruise speeds and require streamlined bodies (Fig.1.3(a)), whereas cargo-oriented transport helicopters demand a maximum stowage, causing its shape to become more angular, i.e. functional (Fig.1.3(c)). If it must float on water in case of an emergency, the fuselage must work as a hull (Fig.1.3(b)), or in other cases inflatable bags are installed in

FIGURE 1.1. Conventional helicopter configuration (AW GrandNew), AgustaWestland (2015).

the sponsons, which make part of the fuselage (Fig.1.3(d)). The sponsons can also contain fuel tanks and or a part of the retractable landing gear.

For the undercarriage, two options exist : skids or wheels (Fig.1.4). Prouty (2007) explains that skids should be preferred when the helicopter lands on soft ground. Also the skids function as a parking brake omitting the problem of rolling away when put on inclined surfaces. The disadvantage is ground handling. Moving the helicopter from the hangar to the apron requires in most cases special equipment and approaching the take-off zone can only be done by air taxiing. As a result, wheels are typically selected for the undercarriage of the larger and heavier helicopters. Besides the ease of ground handling by ground crew, wheels offer also the advantage of ground taxiing, which reduces the downwash during the manoeuvre considerably decreasing the risk of "placer mining"[ii], compromised visibility and the blowing-away of objects along the taxi trajectory. Retractable wheels should only be considered when speed is important, while the impact resistance against a hard landing or crash is reduced.

Three anti-torque devices are commonly used on conventional helicopters : the tail rotor, the fan-in-tail or fenestron and the fan-in-boom or NOTAR[iii] (Fig.1.5). Most conventional helicopters use the tail rotor, as shown in Fig.1.5(a). Though, it comes in different configurations with for example a variable number of tail rotor blades, angle of the rotational axis with respect to the longitudinal plane of the rotorcraft and rotor position with respect

[ii] A term adopted from Prouty (2002) indicating the potential of the rotor downwash to dig out soil underneath the helicopter.

[iii] NO Tail Rotor; NOTAR is a trademark of MD Helicopters, now the Boeing Company.

(a) Tandem helicopter configuration (AgustaWestland ICH-47F), AgustaWestland (2015).

(b) Coaxial helicopter configuration (Kamov Ka-226), Denis Mosolov.

FIGURE 1.2. Non-conventional helicopter configurations.

(a) Smooth fuselage (Eurocopter AS365-N3), Patrick Penna, Eurocopter.

(b) Hull shaped fuselage of the Westland SeaKing Mk48, Belgian Defence/DG COM.

(c) Angular fuselage (NH Industries NH90), AgustaWestland (2015).

(d) Sponsons on the Sikorsky CH-53E Super Stallion, Sikorsky.

FIGURE 1.3. Major fuselage configurations.

(a) Skid undercarriage (AW109 Trekker), AgustaWestland (2015).

(b) Semi-retractable-wheel undercarriage (AW139M), AgustaWestland (2015).

Figure 1.4. Helicopter undercarriage configurations.

to the vertical stabiliser. Regardless of the selected configuration, the working method remains similar and an aerodynamic force is mainly used to compensate the reaction torque exerted on the fuselage by the main gearbox. The problem with the tail rotor is its vulnerability, noise production and being a potential danger to anything near. The fan-in-tail reduces these issues partially as it consists of a shrouded rotor with more, smaller and faster turning blades placed in front of a stator (Fig.1.5(b)). The power consumption of the ducted fan configuration could be lower than that of the tail rotor configuration when considering the same diameter (Newman (2003)), but the fan is normally smaller. The consequence of embedding a rotor in the tail is a large vertical tail, which brings along a mass penalty. A large vertical fin on the other hand, takes over the function of the fan progressively with increasing flight speed, which is advantageous, and offers in some cases the ability to perform a controlled landing in case of a fan failure. The fan-in-boom or NOTAR tackles the problems of vulnerability and noise. The NOTAR system is a patented anti-torque system of MD Helicopters (now the Boeing Company), which produces an aerodynamic force along the helicopter tail boom (Fig.1.5(c)), mainly via circulation control (Coandă effect) and the vertical tailplanes[iv], and partially thanks to an orientable jet near the tail boom extremity (Fig.1.5(d)). A frequently reported disadvantage of the system concerns a slow response to yaw inputs by the pilot, as reported by Sampatacos et al. (1983), but they also highlighted that test pilots claimed better handling qualities.

1.1.2 Internal configurations

When looking underneath the skin of a conventional helicopter, it is possible to distinguish "perpetual" components : engine(s), gearboxes, shafts, fuel tanks, cabin and cargo stowage, and a structure that holds the components. The relationship between these

[iv] This depends on the flight conditions.

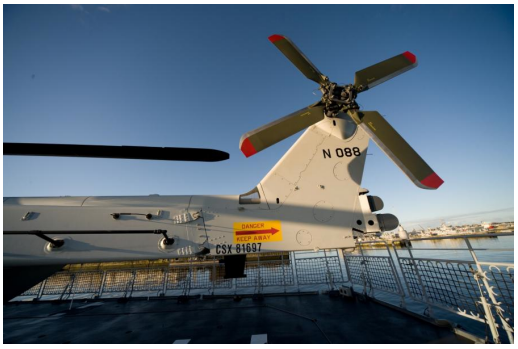

(a) Tail rotor (NHI NH90 MFH), Belgian Defence/DG COM.

(b) Fan-in-tail (EC-135 EMS), Olivier Balmain, Eurocopter.

(c) Tail boom with air slots (MD-900), Terence Rayee, ULB.

(d) Orientable jet thruster (MD-900), Terence Rayee, ULB.

FIGURE 1.5. Conventional helicopter anti-torque system configurations.

components and their spatial distribution form the internal configuration of the helicopter. With time, the components were optimised, replaced, and some were positioned elsewhere in the helicopter all to exhibit a better performance per unit of mass and an improved reliability (Fig.1.6). Important improvements consisted of the implementation of new lightweight materials such as composites, high power density turboshaft engines and better materials for the gearbox components.

In general, internal combustion engine(s) provide(s) power to the rotors via multiple reduction stages (Fig.1.7). In many cases, a first reduction takes place in the engine, after which a larger reduction occurs in the main gearbox of the helicopter. Multiple shafts can leave the main gearbox. Most noteworthy are the shaft to the main rotor and the shaft driving the tail rotor system. Both rotors are limited in rotational velocity due to rotor blade Mach number constraints – Prouty (2002). Depending on the mutual position between the main gearbox and the tail rotor, several shafts and intermediate angle-and-or-speed-changing gearboxes can be required. For a given power, increasing the rotational speed of the shafts reduces the torque and consequently the amount of material used. However, unstable phenomena such as resonance and torsion buckling limit the maximum rotational speed, such as depicted by Dyess (1991) and Welborn (1967). Hence, instead of one long shaft, several shaft-segments supported by bearings and dampers will be found.
Besides the main gearbox, the tail gearbox deserves attention too. In many cases, it concerns a bevel gearbox with an output shaft nearly perpendicular to the input shaft. Unlike the main gearbox, the tail gearbox is much more exposed to vibrations, dirt and risks for shocks – for example when the tail hook hits the ground during flare – and has no similar oil-cooling provisions.

The ensemble of gearboxes and shafts with concurring accessories such as the oil system and shaft suspensions is defined as the transmission system. The powerplant, consisting of the internal combustion engine with accessories, together with the fuel and transmission systems forms the propulsion system. Fig.1.7 shows a schematic overview of a conventional helicopter propulsion system (the fuel system excepted[v]). Note the presence of a cooling system used to evacuate the heat produced inside the gearbox by friction losses. The necessity of an intermediate gearbox in this helicopter is required by the positioning of the tail rotor on the fuselage. However, an intermediate gearbox is not always found in a conventional helicopter.

[v] When using the term *propulsion system* in this thesis, one refers generally to the powerplant and the drive subsystems as the fuel subsystem is of lesser importance from either a weight or cost perspective. This may be proven by the model of Beltramo & Morris (1980), adopted in Appendix A.

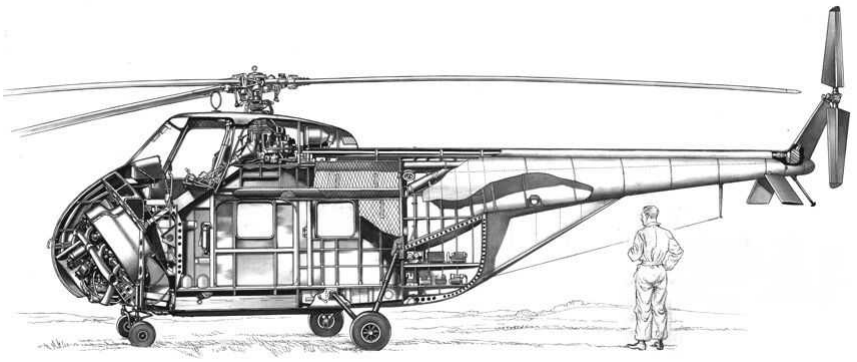

(a) Sikorsky S-55 Whirlwind. The helicopter has a radial piston engine mounted in the nose and the pilots sit on top of the passenger cabin. Note the diagonally placed shaft between the engine in the nose and the main gearbox installed behind the pilots.

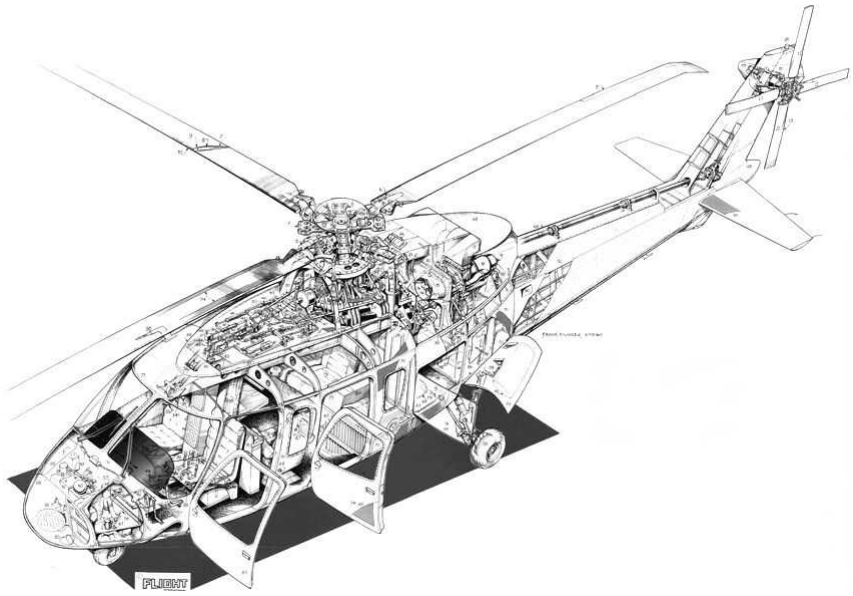

(b) Sikorsky S-76. Multiple turboshaft engines provide mechanical power and the transmission system is much more compact. This allows almost all propulsion system components to be placed above the cabin, which increases the useful volume of the rotorcraft.

FIGURE 1.6. Conventional helicopter internal configurations, evolution with time - Adopted from FlightGlobal (2015).

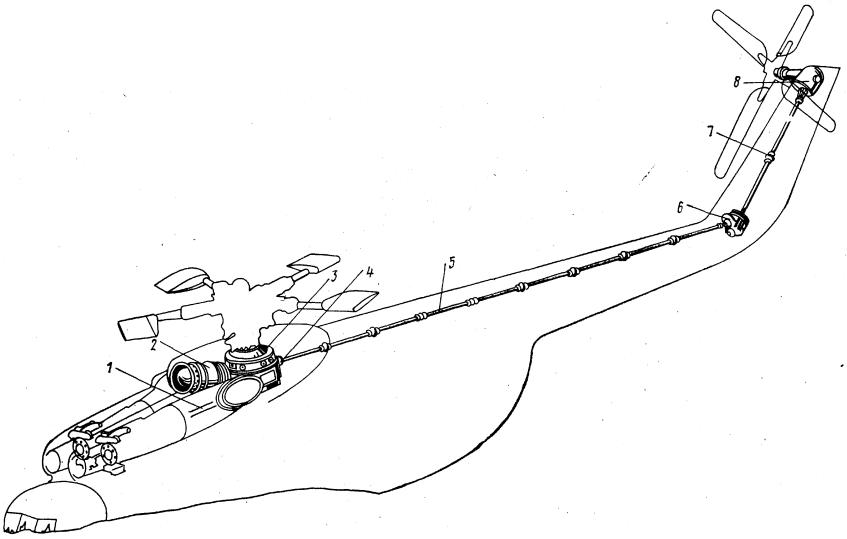

Figure 1.7. Sketch of the Mil Mi-6 propulsion system.
1. Engine drive shaft; 2. Oil cooling fan drive shaft; 3. Main gearbox; 4. Main rotor brake; 5. Tail boom shaft; 6. Intermediate gearbox; 7. Tail rotor shaft; 8. Tail rotor gearbox
Adopted from Bushmarin et al. (1983).

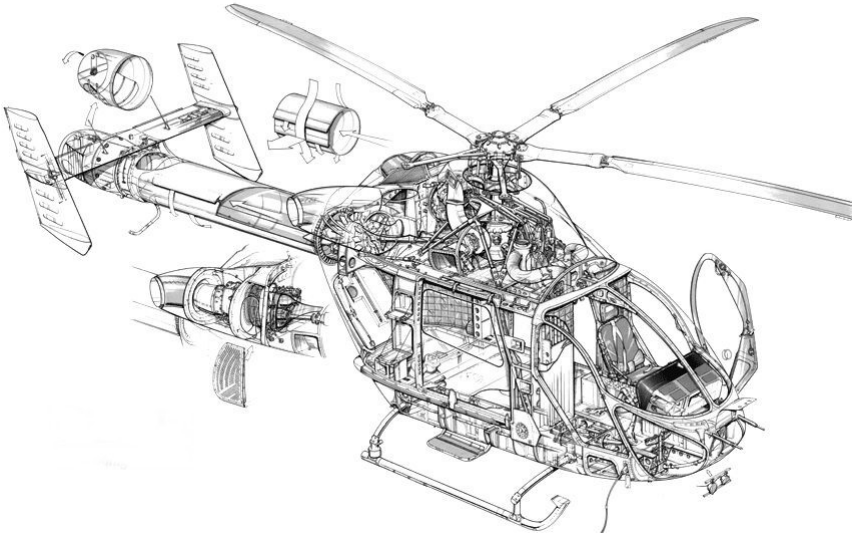

Figure 1.8. The internal architecture of the MD-900 with NOTAR. Note the absence of a tail boom shaft and the presence of a fan in the tail root, required to generate the compressed air flow. The size of the transmission system is clearly reduced with respect to the helicopters with tail rotor. Adopted from FlightGlobal (2015).

A noteworthy alternative to the internal configuration depicted so far comes from the NOTAR system (Fig.1.8). In that particular case, the main gearbox drives – albeit via an additional reduction – a variable pitch fan placed near the entry of the hollow tail boom. The tail boom shaft does not appear in this configuration, only air at a slight over-pressure flowing through slots in the tail boom and jet thruster. The jet thruster pod is mounted on a collar bearing and is turned mechanically via a cable. Although not visible on the picture, pilot inputs also change the pitch of the blades of the fan, which in turn varies the air mass flow through the tail boom in order to guarantee sustained control.

1.1.3 Concluding notes

The conventional helicopter layout can be subdivided into an external and an internal configuration. After assessing the possible morphologies, it is clear that in general and for a given timeframe, similar components can be found in the conventional helicopter bearing a similar degree of importance in the system, regardless its subcategory. The subsequent performance, reliability and cost examinations can therefore be generalised to the definition of the conventional helicopter, without expecting a major loss in accuracy.

1.2 Conventional helicopter costs

1.2.1 Introduction and objectives

An important cost parameter to either the manufacturer or the helicopter operator is the helicopter Life Cycle Cost or *LCC*. It is the total cost from purchase to retirement and serves according to Jenkinson et al. (1999) and Burns (1994) as a yardstick for the financial competitiveness of rotorcraft. It can be subdivided into (Fig.1.9) :

→ Research cost

→ Development, test and evaluation (DT&E) cost

→ Production/Acquisition cost. The manufacturer production cost with a fair profit margin is mainly the acquisition cost of the operator. Depending on the type of operator (commercial or governmental), several factors can impact the cost distribution. Whereas the research and DT&E cost can be borne by the government in case of a military project, it must still be paid by the client (airliner) in case the aircraft is developed entirely by means of public funding. However, if the commercial product is a spin-off of a governmental sponsored project, it affects *LCC* of the commercial product strongly.

→ Operating and maintenance cost

→ Disposal cost

The objective of the intended cost study is to analyse the financial "fitness" of a component in a conventional helicopter from a technical point of view. Then, the cost effectiveness of a system is reflected most reliably by the recurring costs of the manufacturer C_{RM} and the Direct Operating Costs *DOC* of the operator (Fig.1.9). Indeed, Sostilio (1997) notes that the non-recurring costs of the manufacturer, under which the research and DT&E costs fall, may be well below usual if it concerns a spin-off product, which leads to an unreliable basis for comparison[vi]. Liebeck et al. (1995) on the other hand explain that helicopter manufacturers evaluate the impact of the use of different technology levels in a platform by means of *DOC*. Alvarez (1974) confirms this by stating that even though the operator's Indirect Operating Costs *IOC* are substantial, they do not relate to the helicopter from a technical viewpoint. Hence, it is reasonable to examine C_{RM} and *DOC* only in order to retrieve the cost driving (physical) elements in a conventional helicopter.

1.2.2 Then-year vs. Now-year

Before discussing the recurring production & assembly costs of the manufacturer and the direct operating cost of the operator, it must be noted that the cost of a product is

[vi] For example, the Sikorsky S-92 was derived from the H-60 Black Hawk, of which the latter's development costs are borne by tax payers.

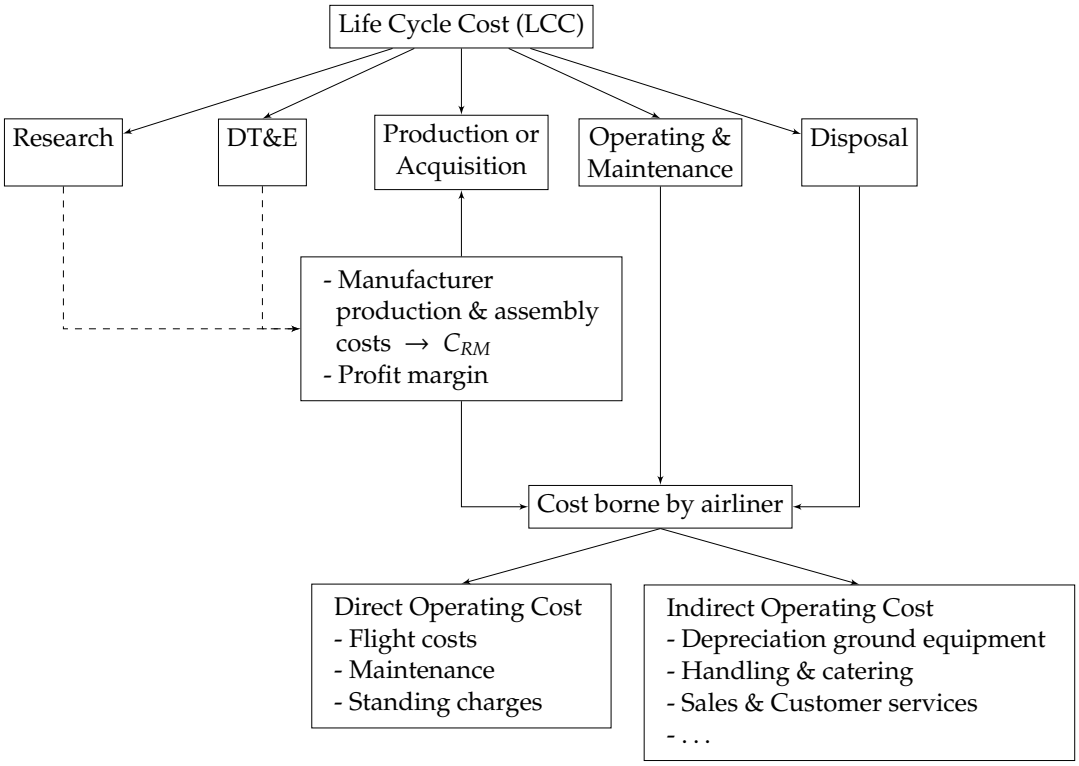

Figure 1.9. Life Cycle Cost breakdown – Raymer (1992), Nicolai & Carichner (2010) and Berrittella et al. (2009).

influenced by deflation or inflation. For example, the cost of a product in the past (*then-year*) must be corrected to the contemporary financial standards (*now-year*), if it is meant to serve as a basis of comparison in present-day terms. In the aircraft industry, the consumer price index *CPI* is generally used for this purpose, as reported by for example Burns (1994) and Raymer (1992). It varies with time and is presented in Fig.1.10. As a result, if the absolute cost calculated by a model in *then-year* needs to be expressed in *now-year*, it only needs to be corrected by introduction of a *CPI*-correction factor k_{CPI}, which is expressed as follows :

$$k_{CPI} = \frac{\text{Cost } \textit{now-year}}{\text{Cost } \textit{then-year}} \tag{1.1}$$

1.2.3 Manufacturer recurring production and assembly costs C_{RM}

With regard to the estimation of the recurring production and assembly costs, several cost models exist. The most detailed models are aircraft company owned and not available in the public domain. However, for the purpose of this study, it is sufficient to rely on somewhat less accurate models, which are usually established in light of government funded studies – for example Large et al. (1976). Unfortunately, most cost models target the

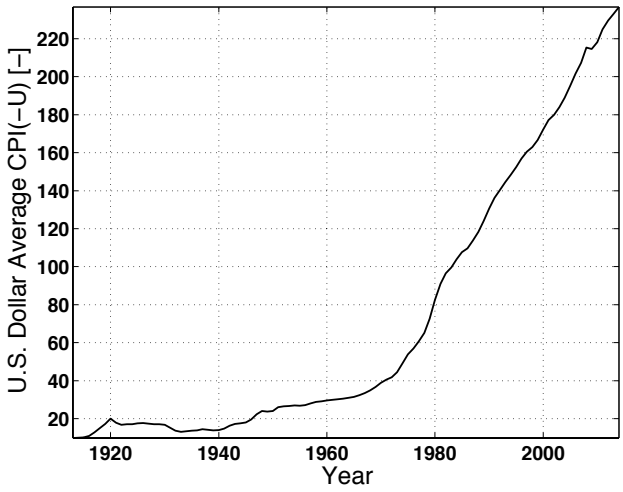

FIGURE 1.10. U.S. Dollar Average Consumer Price Index evolution issued by the Bureau of Labor Statistics, U.S. Department of Labor.

aeroplane niche, which makes finding a reasonably complete cost model for conventional helicopters cumbersome. The cost model established by Beltramo & Morris (1980) specifically targets the helicopter manufacturing recurring production and assembly costs, and was found to be sufficiently complete for the study at hand. As a consequence, it is used to investigate C_{RM}.

The model of Beltramo & Morris (1980) covers the recurring production costs C_{RP}, which include the costs of the raw materials from which the prime components are made, the fabrication procedures (labour), and tooling and production engineering. The larger components acquired via sub-contractors also fall under this category. Also, the model yields values for the recurring assembly costs C_{RA} related to the assembly phase, which starts as soon as two prime components are put together and incorporates all other technical actions that lead to the final product, such as minor and major assemblies, paint jobs, quality control, cleaning, sealing and testing.
The cost calculated by Beltramo & Morris (1980) is mainly based on the relationship between cost and weight of a certain component and its production volume Q, since all production processes are susceptible to a learning curve, which causes a decline in cost with each produced unit. With regard to the influence of weight, the helicopter is subdivided in multiple component groups (Table 1.1[vii]), for each of which the empty weight[viii] $W_{E,i}$ is determined. The index i stands for the group number. $W_{E,i}$ then serves to estimate the group recurring production cost $C_{RP,i}$, where $W_{E,i}$ is approximated via inter alia the helicopter design gross weight W_g. Thereupon, the cost model calculates C_{RA} via $C_{RP,i}$. Note however that even though C_{RP} and thus C_{RA} vary generally commensurate with

[vii] The used classification is also recommended by the Society of Allied Weight Engineers R.P.8.

[viii] Although referred to as "weight" by convention, the term will normally represent a mass. The same is true for gross weight.

mass, the advantage of a low weight component can be deceptive in terms of total cost as it may cause higher development costs, such as described by the work of Turner (1986). However, this effect has been neglected in the model. The model of Beltramo & Morris (1980) is explained further in Appendix A.

Table 1.1. Helicopter mass and recurring cost group subdivision as used in the model of Beltramo & Morris (1980).

Group name	**Group number**
Production costs	
Wing system	1
Main rotor system	2
Tail system	3
Body system	4
Alighting gear system (undercarriage)	5
Nacelle system	6
Propulsion system	7
Flight controls system	8
Auxiliary power system	9
Instruments system	10
Hydraulic system	11
Pneumatic system	12
Electrical system	13
Avionics system	14
Furnishings & equipment system	15
Air conditioning system	16
Anti-icing system	17
Load & handling system	18
Assembly costs	
In-house assembly	19

For some systems, amongst which the body system group (4), parameters different from the empty weight are required to find C_{RP}, such as the wetted surface of the body volume. In order to reduce the amount of independent variables in the cost model, the author of this work found it sensible to make all component groups a function of gross weight. Therefore the necessary "transformation" correlations were established using data from an extensive survey performed by this author (Appendix H) and from the work of Beltramo & Morris (1980). This discussion and the model proposed by Beltramo & Morris (1980) with modifications are adopted in Appendix A. Here it is sufficient to note that the

manufacturer recurring production and assembly cost is obtained by (Eq.A.53) :

$$C_{RM} = k_{CPI} \left(\sum_{k=1}^{18} C_{RP,k} + C_{RA} \right)$$

where k represents the group number and k_{CPI} the factor addressing inflation (Eq.1.1). The best way to evaluate the cost driving elements is by presenting the relative share of each group on the total balance for a range of helicopter design gross weights and production volumes. The result of this parametric study is plotted in Fig.1.11.

From Fig.1.11 it is clear that regardless of gross weight, *the propulsion system and assembly costs are responsible for the largest part of* C_{RM}. When Q increases, a decrease in assembly costs is observed, which amplifies the relative importance of the propulsion system. However, this rise is also due to the lesser susceptibility of the propulsion system for the learning effect (higher complexity). For the larger gross weights, the significance of the body and rotor groups becomes more prominent, but they do not attain the same level of importance as the propulsion system. Note the slight increase of the propulsion system cost for the heaviest gross weight configuration, where, following Table A.2, the impact of installing a third engine becomes visible. The cost of the additional engine influences the recurring cost only slightly because less powerful engines are installed.
Obviously, C_{RM} reveals that the most complex components in a conventional helicopter, i.e. the engine and transmission systems (propulsion system), are the highest recurring production and assembly cost drivers. The rotor and body systems are indeed less complex, but still form a substantial part of the contemporary conventional helicopter, which their noteworthy relative contribution to C_{RM} proves. The other component groups are fairly "common" and, from a weight and cost perspective, not substantial. Finally note that since the study is based on a relative cost study, the impact of *CPI* is eliminated.

1.2.4 Operator Direct Operating Costs

The operator direct operating cost *DOC* is composed of several elements, which are reflected in Table 1.2. Earlier, it was stated that helicopter manufacturers use *DOC* to compare various technology levels. Indeed, the technology level has a significant impact on the standing charges, maintenance and fuel cost. Ideally, from a technical point of view, the helicopter should be unbreakable, consume no fuel and evidently answer to the client's performance requirements. More maintenance and increased fuel consumption means that the system uses inadequate technologies or applies it inappropriately. However, this can also reveal that contemporary state-of-the-art technology is not ripe for application in a system.

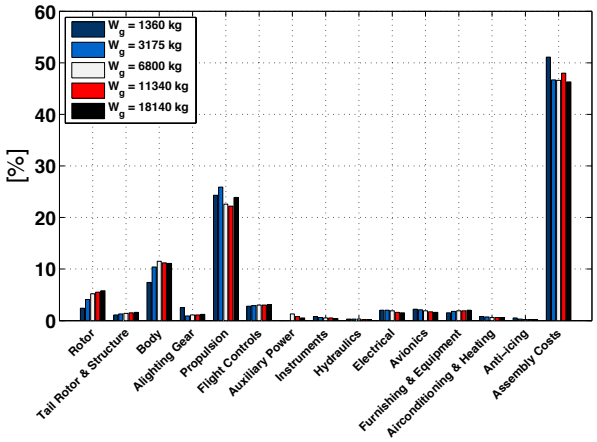

(a) Production volume Q=10

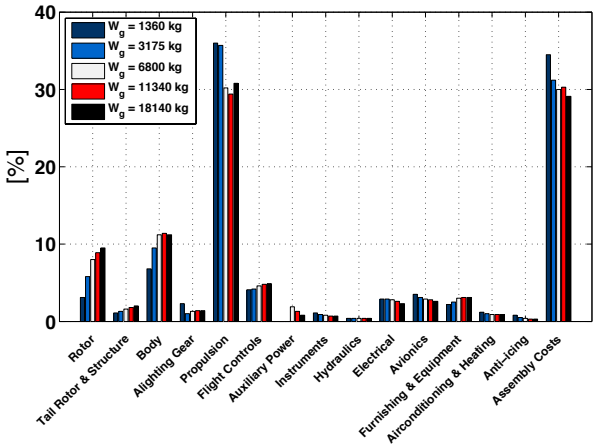

(b) Production volume Q=100

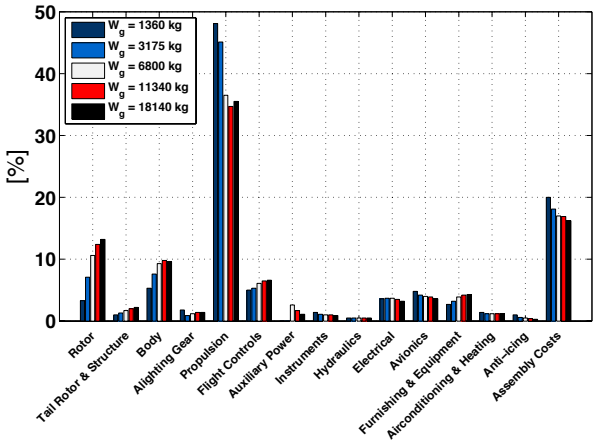

(c) Production volume Q=1000

FIGURE 1.11. Relative C_{RM} of the discussed helicopter component groups.

Two important systems have been identified as *DOC* drivers : the engine and the transmission system. Cale (1979) states that 50% of the *DOC* is linked to the engine, including fuel cost, while Million (1978) identified the engine and transmission systems as the major maintenance cost drivers, i.e. up to 62% in total, where vibrations appeared to play an important role. *Thus it appears that the propulsion system is not only expensive to produce (C_{RM}), but also costly to operate.*

Table 1.2. Direct operating costs – Jenkinson et al. (1999).

Standing charges	Insurance, interest charges, depreciation, leasing
Maintenance	Airframe, engine related, spares, overhead
Flight costs	Fuel, oil, crew, airport fees

1.3 Conventional helicopter accident facts

Safety has always been of utmost importance in commercial aviation. This applies also to the helicopter, which flies under FAR Part 135 "On-demand" regulations. Unfortunately, accidents[ix] still occur. In light of the conventional helicopter assessment, it is interesting to examine which factors play a significant role in the chain of events leading to an accident and what technical components are affected first. These initial technical failures are also called *first occurrences*. For this purpose, the author studied the accident reports of National Transportation and Safety Board (NTSB) of the last decade[x] and European Aviation Safety Agency (EASA) documentation[xi]. The following observations were then made :

→ The average helicopter accident rate is 15.1 per million of flight hours. 18% of these accidents are fatal.

→ The region (Fig.1.12) and type of operation (Fig.1.13) have an important influence on the average accident rate.

When studying the first occurrences, 50% of these could be associated with loss of control and the engine(s). Assessment of the impact of the flight phase on the first occurrences shows that 61% of the first occurrences takes place during the most intensive parts of

[ix] An accident is defined as an occurrence taking place somewhere between boarding and disembarking of an aircraft where any person suffers serious injury or death or where the aircraft receives substantial damage. An accident is the result of a sequence of events, which have occurred since the *first occurrence* of a failure or malfunction. This event is seen from a pure technical viewpoint and in many cases does not disclose the cause that led to the first occurrence, such as bad piloting. However, it gives a good indication of those elements that compromise safe helicopter operations.

[x] NTSB Annual Review of Aircraft Accident Data (1998-2005).

[xi] EASA Annual Safety Review (2005-2007).

flight, i.e. take-off, climb, approach, landing and manoeuvring, and finally hover, where *engine(s) and controls are loaded significantly* (Fig.1.14). Majumdar et al. (2009) confirms this analysis, while stressing *the susceptibility to failure of the transmission system during the intensive flight phases*. Also, it is remarkable that aeroplanes flying under the same regulations as the helicopter have a 10% lower engine failure rate than helicopters where the bulk of these aeroplanes use piston engines. Since piston engines are generally perceived as less reliable than turboshaft engines, of which the latter principally drive the helicopters falling under this certification category, and since the higher accident rate of helicopters with respect to fixed-wing (up to 7 times), it is sensible to accept that the increased accident rate is implicitly caused by the conventional helicopter concept (for example by the higher work load of the pilot) and explicitly as a result of the heavier loaded technical components of which engine, transmission and flight controls appear to be most liable to failure. Note that the above discussion involves the first occurrences. In most cases, these technical failures are preceded by human (piloting) errors. Again, this may prove the existence of a conceptual issue.

1.4 Conventional helicopter performance limitations

A well performing helicopter is one capable of fulfilling the requirements for which it was designed. However, a product can be well performing in its own niche, but score inadequately compared to other products designed under other requirements. For example, an aircraft may be more productive than a helicopter thanks to its speed, but it can only be operated from airports. Generally, conceptual and mechanical limitations introduce performance constraints, which is especially true for the helicopter configurations we know today.

1.4.1 Conceptual boundaries

One of the most noteworthy conceptual barriers to which helicopters are exposed, is limited speed, which is inherently associated with horizontally placed rotors. Nonetheless, research persistently pursues new ways to enhance the speed envelope of the helicopter and more importantly, according to Leishman (2007) and Shapiro (1958), its productivity, even though increasing speed may result in significant operating costs. Solutions coping with this issue generally rely on technical interventions, of which the following were already undertaken :

→ a better understanding of rotor blade aerodynamics, for example BERP[xii] – Leishman (2002)

→ the introduction of conceptual modifications such as compounding (Lockheed AH-56 Cheyenne) – Prouty (2007)

[xii] British Experimental Rotor Programme

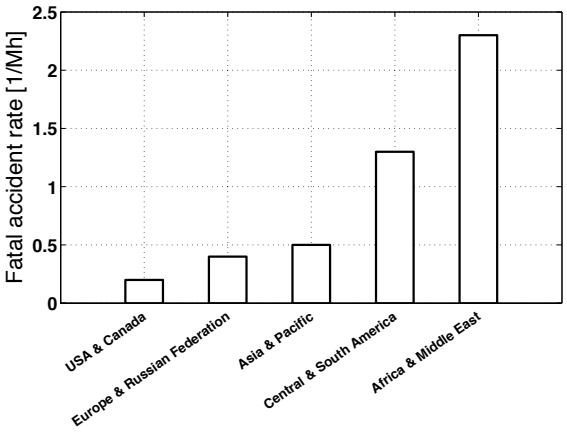

FIGURE 1.12. Impact of geographic location of operations on accident rate per million of flight hours (based on NTSB and EASA data).

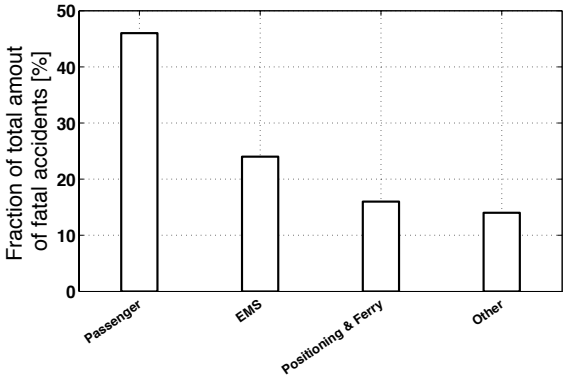

FIGURE 1.13. Impact of operation type on accident rate per million of flight hours (based on NTSB and EASA data).

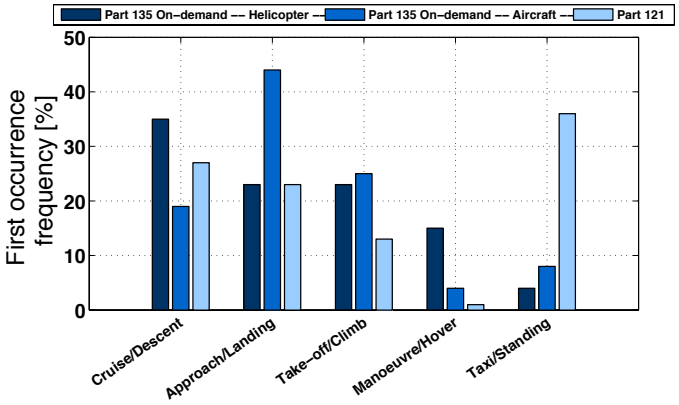

FIGURE 1.14. Influence of flight phase on first occurrence (based on NTSB and EASA data).

→ the implementation of other propulsion techniques such as tip-jet and outboard-engine driven rotorcraft (Fairey Rotodyne) – Gibbings (2009)

→ the installation of coaxial rigid rotor variants (Sikorsky S-69 and X-2) – Prouty (2007)

→ use of variable speed rotors (Boeing A160T) – DARPA (2008)

To this day, none of the above – the improved rotor blade aerodynamics excepted – has shown to be a successful solution for the conventional helicopter problems or is used on a large scale.

1.4.2 Mechanical performance boundaries

Other performance boundaries are due to mechanical (and thermal) limitations. Most important here are the powerplant and drive subsystems forming the most important part of the propulsion system, which already passed the cost and safety review, and where they showed concern. These subsystems are typically flat rated[xiii] while designed for maximum power densities, which is not unusual as the propulsion group represents about 20% of the total gross weight[xiv], making it the heaviest system in the helicopter (see Beltramo & Morris (1980)). According to Krantz (1994), *the transmission system performance strongly impacts the helicopter performance, while needing continuous improvements in the domain of safety, reliability, efficiency, vibrations and acoustic noise*. Krantz & Handschuh (1990) report that this is especially true for the main gearbox. Hereby, maximum efficiency must be strived for as the temperature regulating devices in the gearbox, such as heat exchangers, have a non-negligible impact on the rotorcraft empty weight. As a consequence, several gearbox technologies emerge(d) in an attempt to cope with the previously mentioned issues, such as the multi-stage planetary or epicyclic gears as discussed by Krantz & Handschuh (1990)), self-aligning bearingless planetary gears presented in the works of Folenta & Lebo (1988) and Folenta (1983), high contact ratio gears as reported by Henry (1995) and split-torque transmissions splitting the power load-path over multiple gears without the use of any epicyclic gear stages resulting in an improved reliability, weight and gearbox efficiency, as presented in the works of Rashidi & Krantz (1992) and White (1985). Nevertheless, they are neither exempted from flat rating, nor from the cost and safety records discussed previously.

1.5 Conclusions

In the previously conducted discussions, the configuration of a conventional helicopter was determined, while the physical components in the latter that drive cost, compromise reliability/safety and limit the performance were exposed. The evaluation showed that the propulsion system, mainly composed of the engine and the transmission (sub)systems, is

[xiii] i.e. limited in power output.
[xiv] Weight is an important parameter affecting performance.

of concern. In fact, it is not a surprise that these (sub)systems appear as crucial. Indeed, since the propulsion system was already reported to be the heaviest part in the conventional helicopter, the engine and transmission have to be designed for a maximum power density, i.e. a high power transmission per unit of mass, in a vibrating environment. Inevitably, with the inherent mechanical complexity of these systems, this causes a substantial impact on the component cost, as indicated in the manufacturer recurring cost survey and regardless of fuel cost, with only a minimal allowance to handle the system improperly, which is reflected in the accident rates and the performance flat rating. The selection of the conventional helicopter configuration can be clearly associated with the aforementioned issues. Note that these conclusions may be extrapolated to most other helicopter configurations, such as the coaxial-rotor and the tandem helicopter, as they rely on similar components in comparable operating conditions. In the next chapter, alternative technologies will be examined and assessed for their aptness to be integrated in the conventional helicopter, in an attempt to cope with the stated issues.

1.6 Nomenclature

Please note that the units listed below apply unless stated otherwise.

Abbreviations and substance formulae

C	Cost	[US $]
$CPI(-U)$	Consumer price index (-user)	[-]
DARPA	Defence advanced research project agency	
DOC	Direct operating cost	[US $]
DT&E	Design, testing and evaluation	
EASA	European aviation safety agency	
FAR	Federal aviation regulations	
IOC	Indirect operating cost	[US $]
k_{CPI}	CPI-based cost correction term	[-]
LCC	Life cycle cost	[US $]
NOTAR	No tail rotor	
NTSB	National transportation safety board	
Q	Production volume	[-]
W_E	Helicopter empty weight/mass	[kg]
W_g	Helicopter (design) gross weight/mass	[kg]

Subscripts and superscripts

RM	Recurring manufacturer/ing
RP	Recurring production
RA	Recurring assembly
TE	Trailing edge

Chapter 2

The conventional helicopter : implementation of alternative technologies

"If there is no struggle, there is no progress"

Frederick Douglass – *Cabrera et al. (2013)*

2.1 Introduction

In the previous chapter, the engine and transmission systems appeared to compromise the conventional helicopter cost, reliability/safety and performance most. This chapter proposes and investigates alternatives for these systems and examines whether they are mature for implementation in the conventional helicopter or if the conventional helicopter is a suitable platform to introduce these technologies. First, alternatives will be proposed for the main gearbox, without interfering in the selection of the powerplant. Subsequently, other propulsion systems will be assessed, combining various powerplant systems and energy carriers. Lastly, the most competitive combinations emerging from that assessment will be implemented in a conventional helicopter environment and their "fitness" examined on a conceptual level.

The assessed alternatives will mostly include electric technologies. According to Rekik et al. (2008), electrical locomotion is continuously gaining importance in the transportation sector, where one strives for the best results with regard to cost, performance and reliability. These characteristics are critical in the conventional helicopter and the pursuit of their optimisation is in line with the stated objectives. Hence, several (new) "electric" technologies and their integrability in a conventional helicopter platform will be studied such as magnetic gears, switched reluctance (SR) and permanent magnet (PM) motors, high-temperature-superconductive (HTS) devices, battery and PEM fuel cell systems, and

compared with non-electric configurations.

2.2 Transmission alternatives

2.2.1 Hydrostatic worm gear transmission

A remarkable alternative to the conventional main gearbox configurations discussed in Section 1.4.2 is the hydrostatic worm-gearing, as explained by Chaiko (1990) and Sun & Yuan (1995). Here, each engine is connected to a worm gear, which in turn drives a common centre gear connected to the main rotor. Thanks to an oil film squeezed between worm and centre gear, the impact of the high relative velocity between the intermeshing planes can be largely reduced. Chaiko (1990) states that the configuration allows reduction ratios over 100 with an efficiency beyond 99% while saving 59% in weight over a conventional architecture. In addition, he mentions lower maintenance costs, longer service life and a reduced noise production. Table 2.1 gives a general survey of the system developed for a helicopter with a gross weight of 31 metric tons with 3 engines producing 4000 kW each. The reason why this technology has not found its way

Table 2.1. Hydrostatic worm gearbox characteristics – Chaiko (1990).

Mass†	1151 kg
Mass-weighed power density†	10.4 kW/kg
Volume-weighed power density‡	0.22 kW/cm^3
Efficiency	99.14%
Pump oil pressure	350 bar
Oil flow	39 L/min

† Complete gearbox including sumps and pumps.

‡ Volume of 3 worms with bearings and worm gear only.

to the helicopter industry is not known. Since at the moment the literature does not oppose against the use of the worm gear technology in a helicopter, it will be adopted in the assessment study, which is conducted later in this chapter.

2.2.2 Magnetic gears

Unlike the conventional gearboxes using intermeshing gears, magnetic gearboxes use magnetic forces to transmit mechanical power in addition to achieving a speed reduction, without any physical contact between input and output shafts. An industrial solution became feasible thanks to the use of powerful rare-earth magnets such as $SmCo_5$[i] and NdFeB[ii]. With respect to the mechanical gearboxes, Atallah (2004) and Nagrial et al. (2007) mention the magnetic gearboxes to have the following advantages :

[i] Samarium-Cobalt

[ii] Neodymium-Iron-Boron

→ lower acoustic noise

→ less vibrations

→ improved reliability

→ lower maintenance

→ ease of manufacturing

→ inherent protection against overload (protecting the expensive powerplant against over-torquing or overheating)

→ robustness

→ no physical contact between input and output shafts

From the perspective of a helicopter, these characteristics appear most attractive. Early magnetic gearbox architectures resemble the mechanical counterparts significantly, with, for example, spur, spiral, bevel and worm configurations. Their specific torque-densities ρ_τ however remained poor (Table 2.2), where the specific torque-density is defined as the amount of (output) torque the gearbox can transfer per unit of volume $V_{mag.GB}$:

$$\rho_\tau \triangleq \frac{\tau}{V_{mag.GB}} \tag{2.1}$$

Newer designs were noticeably improved, with the concentric magnetic gear, magnetic planetary gear, cycloid permanent magnet gear (Fig.2.1) and magnetic harmonic gear (Table 2.2). The downside of these technologies is weight and the current level of acquired reduction ratios, possibly requiring multiple stages.

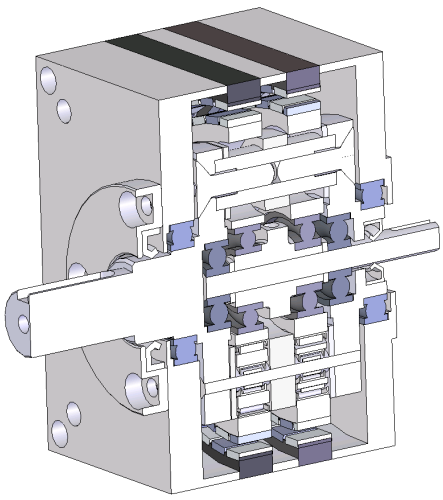

Figure 2.1. An example of a cycloid permanent magnet gear – Jørgensen et al. (2008).

A benchmark for the magnetic torque transfer capabilities is, according to Rasmussen et al. (2005), the torque coupler, which performs no reduction. Current cycloid permanent magnet gearbox prototypes exhibit the largest torque-potential, but it is still half as much as the torque coupler. Also, the efficiency of this type of gearbox turns out to be lower than those observed with a mechanical transmission (up to 7%, Table 2.2). Nevertheless, in case of a single-stage configuration, the reported reduction ratios are well within reach of the required reduction ratio of the helicopter main gearbox for the lower gross weights, which is confirmed by comparing the values indicated in Table 2.2 and Fig.2.2. Note that the required reduction ratio i is :

$$i = \frac{N_E}{N_{MR}} \tag{2.2}$$

N_{MR} is the rotational speed of the main rotor, while N_E the rotational speed of the output shaft of the engine. If the rotor blade tip speed is known as well as the rotor tip radius R_{tip}, then Eq.2.2 can be written as :

$$i = \frac{2\pi R_{tip}}{v_{tip}} N_E \tag{2.3}$$

Table 2.2. Characteristics of magnetic gearing devices.

Type	ρ_τ **[kNm/m^3]***	**Reduction**	**Efficiency**† [%]
Magnetic worm (MWM) Huang et al. (2008)	0.1	33:1	-
Spiral magnetic gear (SMG) Huang et al. (2008)	1.7	3:1	-
Concentric magnetic gear (CMG) Rasmussen et al. (2005)	92	5.5:1	96
Magnetic planetary gear (MPG) Huang et al. (2008)	97.3	3:1	-
Cycloid permanent magnet gear (CYMG) Joergensen et al. (2006)	183	21:1	92-94
Magnetic harmonic gear (MHG) Rens et al. (2007)	110	20+:1‡	-
Torque coupler (MTC) Rasmussen et al. (2005)	400	1:1	-
Conventional mechanical gearbox Folenta (1983)	600-3000⋆	Fig.2.2	>97

* Observed torque density ruling on output shaft.

† Best efficiency (near maximum torque)

‡ Possibility of two stages resulting in a reduction of 860:1 and more.

⋆ Based on magnetic gearbox material density ρ_m=8000 kg/m^3 – Rasmussen et al. (2005)

It will be shown in Section 8.3.2 that R_{tip} is a function of helicopter gross weight (Eq.8.30). For the work at hand and based on the survey data reflected in Fig.2.3, v_{tip} is considered independent of helicopter gross weight and equal to 215 m/s. Even though the selection of v_{tip} will rely on the (design) speed and altitude requirements of a helicopter (Mach number and drag related), the assumption of a constant value for v_{tip} is found reasonable. Finally, an examination of N_E of the contemporary turboshaft engines showed that mainly two rotational speeds are commonly found (Fig.2.4). For turboshafts with maximum take-off power (*MTOP*) at sea level standard day conditions below 1 MW, the average N_E was found to be 6139 RPM. Otherwise above 1 MW, N_E is 21686 RPM on average. The installed *MTOP* is also a function of helicopter gross weight (see Appendix A). With this information, the required reduction i is determinable.

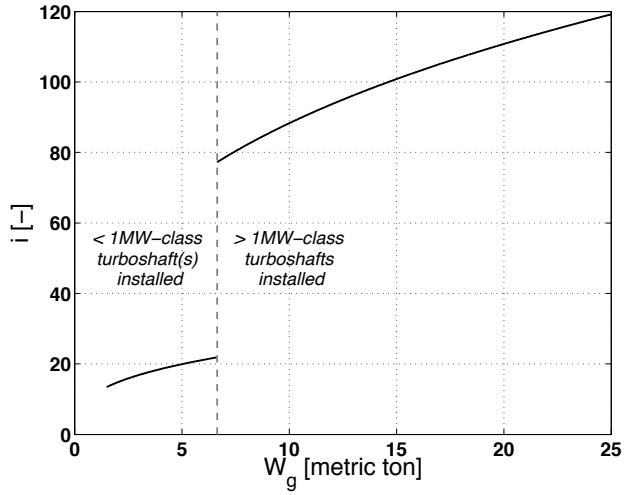

FIGURE 2.2. Total reduction i between (turboshaft) engine output and main rotor shaft.

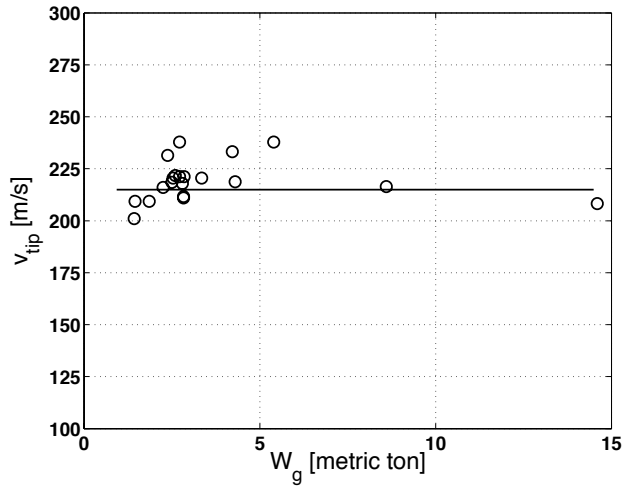

FIGURE 2.3. Main rotor tip speed as a function of gross weight – Appendix H.

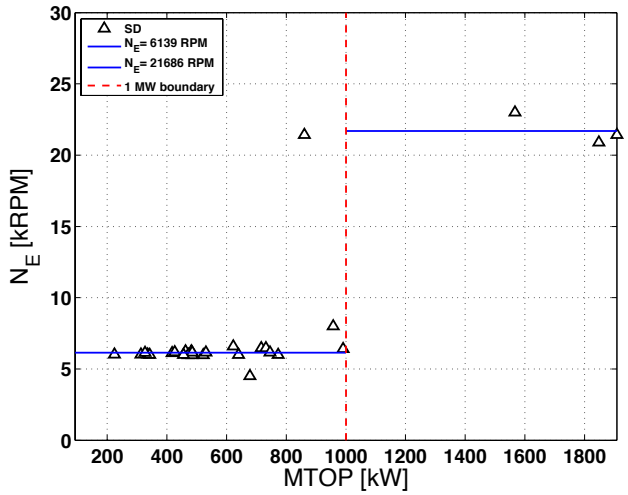

Figure 2.4. Turboshaft output shaft rotational speed as a function of engine maximum take-off power regime, ISA SLS – Appendix H.

Since the magnetic gearboxes have the potential to cover the range of required helicopter main gearbox reduction ratios, it is sensible to monitor the feasibility of a magnetic gearbox on a helicopter and more specifically with the objective to replace the conventional main gearbox. For conceptual purposes, a good verification parameter is the relative importance of the magnetic gearbox weight with respect to the conventional helicopter gross weight W_g, as it impacts the required engine power installed in the helicopter and thus fuel consumption. The maximum transmitted torque is here estimated by :

$$\tau = \frac{H_{pe}\, R_{tip}}{v_{tip}} \tag{2.4}$$

where H_{pe} the installed engine power in the helicopter. For its calculation, the reader is referred to Appendix A. The volume of the required magnetic gearbox can then be calculated via the torque density (Eq.2.1) :

$$V_{mag.GB} = \frac{\tau}{\rho_\tau} \tag{2.5}$$

Applying the average density of the contemporary magnetic gearboxes as discussed by Rasmussen et al. (2005), i.e. $\rho_m = 8000\,\mathrm{kg/m^3}$, the weight fractions of the above-mentioned magnetic gearbox types with respect to helicopter gross weight are retrieved :

$$\frac{W_{mag.GB}}{W_g} = \frac{H_{pe}\, R_{tip}}{v_{tip}\, W_g}\, \frac{\rho_m}{\rho_\tau} \tag{2.6}$$

Whereas the mechanical gearboxes represent only about 10% of the gross weight (Appendix A), the magnetic gearboxes turn out to be heavy (Fig.2.5). For the lower segment of gross weights, the lower power requirements and the smaller blade radius result in lower

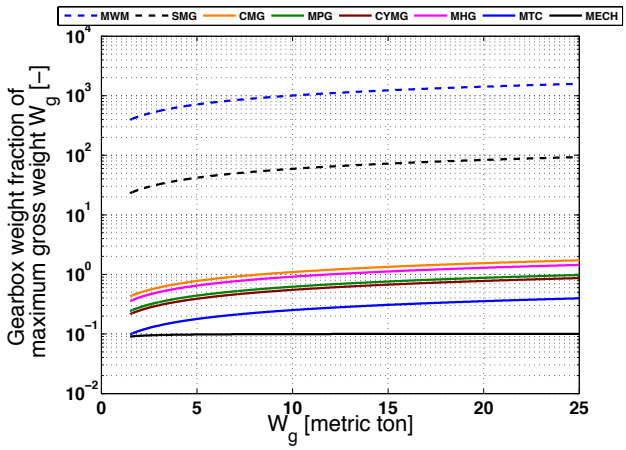

FIGURE 2.5. MGB mass survey for several magnetic gearbox technologies.

torque on the shaft, which eventually leads to lower magnetic gearbox weights. The mass of the lightest and thus best configuration, i.e. the cycloid permanent magnet gear, ranges from twice to tenfold the mass of the mechanical gearboxes installed, which is already considered as too heavy. Thus, it appears currently unwise to analyse these magnetic gearboxes in a helicopter-integrated environment as most of these systems have a mass in the same order of magnitude of the unmodified helicopter. It must be noted however that the stated performance characteristics were adopted from small-scale magnetic gearbox prototypes. Hence, torque density improvements are still achievable. Research should also further optimise gearbox efficiency and examine the maximum reduction ratios per stage. Finally note that magnets should be kept at operating temperatures below 300°C at all times to avoid demagnetisation – MMPA (2009).

2.3 Propulsion system alternatives

This section will examine relevant mechanical power sources and energy carriers that could offer an alternative for the current propulsion system standard, which is based on the turboshaft with kerosene derivatives as the energy carrier. Hereby, more sustainable (greener) solutions will also be introduced. The discussion starts with a survey of several energy carriers (fuels) after which the conversion elements (motors) are studied. Then, a sensible combination of energy carrier and conversion element will be proposed and evaluated. Subsequently, the high temperature superconductive (HTS) devices used in a few of these combinations will be explored. Finally, a more detailed examination of the installation of the most promising combinations of the aforementioned systems in a conventional helicopter will complete this section.

2.3.1 Available energy carriers

An energy carrier delivers the energy to drive an engine or motor. The energy carrier must be stored aboard the aircraft, where volume and weight need to be minimised. Compared to the electro-chemical energy carriers, the fossil fuels (kerosene, Avgas, (bio-)diesel) perform well when observing the mass-weighed energy density $\rho_{E,m}$ and the volume-weighed energy density $\rho_{E,V}$ (Table 2.3). However, liquid hydrogen (LH_2) – which is categorised under the more sustainable fuels – has a $\rho_{E,m}$ which is about three times larger but exhibits a noticeable fourfold lower $\rho_{E,V}$ compared to kerosene.
Electrical power carriers, such as Lithium-Sulphur (LiS) batteries, still lack performance compared to chemical fuels, while being constrained by the limited mass-weighed power density $\rho_{P,m}$ (Table 2.3). Indeed, for the lower range of required endurance, more batteries will need to be installed just to deliver the required power level, causing an excess of endurance. This is explained as follows. If P_{req} and T_{req} are the required power and required endurance respectively, and, E_{req} and E_{mi} respectively denoting the required energy and minimum installed energy, then :

$$E_{req} = P_{req}\, T_{req} \tag{2.7}$$

$$m_{mi} = \frac{P_{req}}{\rho_{P,m}} \tag{2.8}$$

$$E_{mi} = m_{mi}\, \rho_{E,m} \tag{2.9}$$

$$\epsilon_E \triangleq \frac{E_{req}}{E_{mi}} = \frac{\rho_{P,m}\, T_{req}}{\rho_{E,m}} \tag{2.10}$$

with m_{mi} the minimum installed mass to deliver the required power and ϵ_E the energy carrier efficiency. ϵ_E larger than unity ($E_{req} > E_{mi}$) is not realistic since then, the required mass of batteries to yield the demanded power is no longer critical and an excess mass of batteries no longer mandatory. At that point, for a given power, the amount of required energy carrier depends solely on its mass-weighed energy density and the required endurance. The required endurance for which ϵ_E becomes unity is defined as the compensated endurance T_{ce}. Fig.2.6 shows the ratio of excess mass to energy-weighed required mass m_{ex}/m_{req} becoming zero at the compensated endurance. Note that :

$$E_{req} = m_{req}\, \rho_{E,m} \tag{2.11}$$

$$\frac{m_{ex}}{m_{req}} = \frac{1}{\epsilon_E} - 1 \tag{2.12}$$

The AEROPAK^{TM}, a fuel cell with an energy cartridge, clearly shows a less efficient tendency with respect to the LiS batteries ($T_{ce,AEROPAK} > T_{ce,LiS}$). Chemical energy carriers do not have this issue, hence always having ϵ_E of unity.

TABLE 2.3. Energy carrier performance.

Type	$\rho_{E,m}$ [MJ/kg]	$\rho_{E,V}$ [MJ/L]	$\rho_{P,m}$ [kW/kg]	ρ [kg/m^3]
Chemical				
Kerosene (LHV*)	43.2	34.7	-	804
– AIR BP (2000)				
Avgas 100 LL (LHV*)	43.7	31.3	-	715
– AIR BP (2000)				
Bio-diesel (LHV)	38.8	27.3	-	880†
– Knothe (2008)				
Hydrogen (LHV*)	120	8.51‡	-	71‡
– EERE&NIST				
Electro-chemical				
Lithium Sulphur battery	1.26	1.26	0.2	1.064
– Akridge & Mikhaylik (2005)				
Vanadium Boride air cell‡‡	-	18	-	-
– Licht (2008)				
AEROPAK^{TM}‡‡	1.62	0.89	0.1	548
– Horizon Energy Systems (2009)				

* Lower Heating Value : 288.15K, 1 atm. † Average density according to DIN EN 14214.

‡ Saturated liquid state : 20 K, 1 bar. ‡‡ Irreversible process, requires partial replacement.

2.3.2 Sustainable energy carriers

The fossil fuel depletion and the greenhouse issues set many researchers en route to find an alternative or sustainable well-performing energy carrier. At the present time, there is no consensus of what is the better solution. While some reject hydrogen as the future energy carrier such as Bossel (2005), or believe that the helicopter market will continue using carbon-based bio-fuels in a sustainable environment as, for example, stated in Leishman (2007), others examine(d) the feasibility of implementing hydrogen in aircraft such as Brewer et al. (1978) and Verstraete (2009). Hydrogen can be produced in many ways : from oil via steam-reforming (Bastien & Handler (2006)) or via electrolysis. Although Bossel (2006) proves that delivering hydrogen alone to the end user consumes about three times the power it is meant to generate eventually, the cryogenic storage of hydrogen could provide opportunities using more electric high temperature superconductive devices (HTS), which will be discussed later on.

For safety reasons, only liquid hydrogen (LH_2) allows the installation of a significant amount of energy in a fuel tank for airborne applications. Gaseous hydrogen would require high pressure storage, eventually leading to a heavy tank and explosion risks.

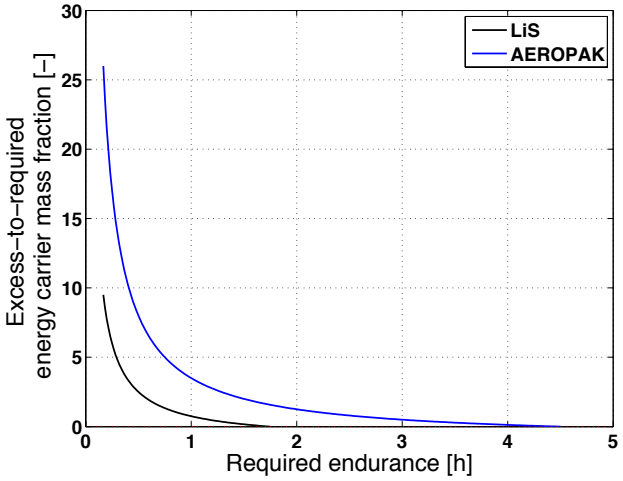

FIGURE 2.6. Excess mass requirements as a function of endurance.

Other storage methodologies, such as hybrid (chemical) storage and use of solid or slush hydrogen, were reported by Verstraete et al. (2010) to be unattractive from either a tank weight/volume or energy conversion efficiency perspective. To estimate the mass of a liquid hydrogen fuel tank, the gravimetric efficiency ϵ_g is defined as – Verstraete et al. (2010) :

$$\epsilon_g = \frac{m_{LH_2}}{m_{LH_2} + m_{ft}} \tag{2.13}$$

where m_{LH_2} and m_{ft} represent respectively the initial mass of liquid hydrogen in the tank and the mass of the fuel tank. For typical helicopter applications, a gravimetric efficiency of 25% can be expected, as shown by extrapolation of the data for regional jets given in Verstraete & Hendrick (2008) and Verstraete et al. (2010). Therefrom the optimum maximum or critical operating pressure in a multilayer insulated tank was derived to be approximately 8 bar, keeping 3% ullage to avoid the pressure relief valve to become inoperative, i.e. the valve does not come into contact with the liquid hydrogen fraction. Since the liquid hydrogen will expand and increase in both pressure and temperature due to heat entering the tank during flight, the tank cannot be filled completely during refuelling. When filled at approximately 1 bar[iii], which yields the largest tank thermal capacity, and respecting the maximum tank pressure of 8 bar, only 75% of the volume is available if 3% ullage is required at the maximum operating pressure (Fig.2.7, Verstraete & Hendrick (2008) & Verstraete et al. (2010)). For all calculations, para-hydrogen was selected, as suggested by Barron (1985).

[iii] A slight overpressure should be preferred in order to avoid air to enter the tank, of which most chemical components would congeal at the temperatures of liquid hydrogen, which compromises safety.

Table 2.4. Energy conversion elements.

Type	$\rho_{P,m}$ [kW/kg]	η_{th} [%]
Chemical to Mechanical		
Turboshaft (TS)*	4.2	25
Diesel piston engine (DPE)	1.31	41†
– Michael Zoche Antriebstechnik (2007)		
Piston engine (Avgas)	1.0	27
– Optimal Aircraft Design Software (2008)		
Electrical to Mechanical		
Switched reluctance motor (SR)‡	2.2⋆	80. . . 95◇
Permanent magnet motor (PM)**	2.6 ⋆⋆	88.4◇◇
HTS motor	>10△	94. . . 98□
Chemical to Electrical		
PEM fuel cell	1.0△△	57□□

† 225g/kWh with LHV bio-diesel - Michael Zoche Antriebstechnik (2007)
‡ Rotational speed of 15000 RPM, Krishnan et al. (2003) ; 10000 RPM Jack et al. (1996) and Uematsu & Wallace (1995).
⋆ Krishnan et al. (2003), Jack et al. (1996) and Uematsu & Wallace (1995)
* Average value taken from survey
** Rotational speed of 10000 RPM
△△ Berton et al. (2003)
□ Kwon et al. (2007)
□□ Serenus (2009)
◇ Kachapornkul et al. (2007)
△ Masson & Luongo (2007)
⋆⋆ Jack et al. (1996)
◇◇ Chan & Chau (1996)

Finally, it is interesting to report the contemporary vision on the use of bio-diesel by means of an example. While a Federal Aviation Administration (FAA) sponsored study advises against the use of bio-diesel and its blends because of its chemical instability over time and congealing problems at the lower temperatures – Hileman et al. (2009), the Boeing Company invests in bio-diesel research (green diesel) in collaboration with the FAA – Boeing (2014). Clearly, the discussion on what the better bio-fuel is and whether bio-diesel is a worthy aviation fuel, has not come to a conclusion yet. For the time being, bio-diesel is adopted in the subsequent energy carrier study, but it should remembered that its safe use has, for now, not been confirmed.

2.3.3 Energy conversion elements

Table 2.4 summarises important energy conversion elements that have à priori a reasonable potential to be installed in a helicopter platform. Here, for the conventional helicopter, the rotors are considered to be driven mechanically. This means that at least a mechanical power source must be installed and that the necessary energy conversion has to be provided (for example, hydrogen to fuel cell to electric motor). In this study, three types of energy conversion elements are distinguished. Firstly, the internal combustion

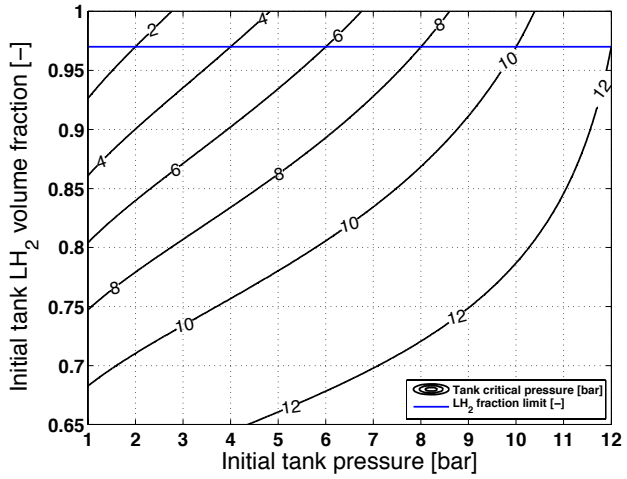

Figure 2.7. Tank filling fraction using saturated liquid hydrogen. Recreated from Verstraete & Hendrick (2008).

engines, i.e. turboshaft, spark ignition (Avgas) and Diesel engines. Secondly, the electric motors of which the most important are the switched reluctance motor (SR) and permanent magnet motor (PM). Thirdly, the electrochemical energy converters such as the fuel cell. Only the proton exchange membrane fuel cell will be examined[iv] since it works with hydrogen, which is one of the fuel carriers examined in this work.

The best choice between a SR- or PM-synchronous motor for aeronautical applications remains rather unclear. While Krishnan et al. (2003) concluded that the SR-motor is the best choice for implementation in aircraft due to its robustness and fault tolerance with respect to other electrical motors amongst which the PM-motor, Bennett & Jack (2004) argued against the mediocre volume-weighed power density of the SR-motor and advocated the use of a PM-motor, since it stresses less the bearings in case of a fault leading to radial imbalance forces. According to Mecrow et al. (1999), the bearings are the weakest components in electric motors, causing 51% of malfunctions in industrial machines and up to 95% in military applications. But Choi & Siebert (2006) solved these problems by suspending the rotor of the SR-motor magnetically, making bearings obsolete and thus improving Mean Time Between Failure (MTBF). Mecrow et al. (1999) suggests introducing multiple redundant phases in a PM-motor in order to increase MTBF. Indeed, according to Klung & Griggs (2004), better redundancy levels can be achieved for a system when redundant sub-systems are installed instead of doubling the system. Based on this discussion and for the alternative system integration and assessment study, which will be performed at the end of this chapter (Section 2.3.6), the heavier but more robust and simpler SR-motor was elected. Though, this does not mean that the PM-motor should be excluded from any future consideration.

[iv] Here, the AEROPAK^{TM} is considered as a hybrid battery.

Note the existence of another high power density electric motor, i.e. the high temperature superconductive (HTS) motor. It will be explained more thoroughly during the discussion of the HTS devices.

2.3.4 Energy carrier and conversion element combinations

Several configurations with energy carrier and conversion elements can be made. Table 2.5 presents the examined configurations, which will now be investigated qualitatively. Discarding the effects of helicopter mass reduction with time on the required power due to fuel burning, the total mass of energy carrier and conversion elements m_{pfs} is calculated by :

$$m_{pfs} = m_{cv} + m_{ec} \tag{2.14}$$

where m_{cv} and m_{ec} are respectively the mass of the energy conversion element and energy carrier. Defining η_{th} as the efficiency of the conversion element and $P_{m,req}$ the required mechanical power, m_{pfs} then is, using Eqs.2.7-2.12 :

$$m_{pfs} = P_{m,req}\left(\frac{1}{\rho_{P,m_{cv}}} + \frac{T_{req}}{\eta_{th}\ \rho_{E,m_{ec}}}\left[1 + \left(\frac{1}{\epsilon_E} - 1\right)_{\epsilon_E<1}\right]\right) \tag{2.15}$$

The last term between brackets in Eq.2.15 only appears when ϵ_E is less than unity. A parametric study on m_{pfs} is subsequently conducted, with the required endurance and mechanical power as independent variables. The performance of a configuration is regarded to improve when for a given mechanical power and m_{pfs}, an increase in endurance is established.

Fig.2.8 (configurations 1-5) shows that a turboshaft operating with kerosene is a logical choice for the propulsion of a helicopter offering the lightest *and* simplest configuration, while a bio-diesel-piston-engine-combination emerges as a good alternative for the Avgas-piston-engine configuration, but it is also likely to satisfy the low-power turboshaft niche which has a 25% lower $\rho_{P,m}$ than the one indicated in Table 2.4. The use of bio-diesel in a turboshaft shows no advantage over the kerosene fuelled turboshaft as it suffers from a decreased energy density. Interestingly, a combination of liquid hydrogen and a turboshaft, appears to offer the lowest m_{pfs}. However, the increased fuel tank weight and volume has not been taken into account. This problem will be studied in a subsequent section and will be shown to result in a noticeable rise of the helicopter gross weight.

Considering the more-electric configurations 6-9 (Fig.2.9), m_{pfs} turns out to be much larger and thus less attractive for helicopter propulsion. However, for the longer endurances, a PEM fuel cell might become interesting, but once more, one must be careful with the interpretation of the results as liquid hydrogen has a significant impact on tank weight and volume, and thus also on helicopter gross weight. The effects of T_{ce} are again clearly visible for LiS and AEROPAK^{TM} energy carriers via the slope discontinuity, while

Table 2.5. Examined carrier-conversion-element configurations.

1	Kerosene + Turboshaft (TS)
2	Avgas 100LL + Piston engine (PE)
3	Bio-diesel + Diesel piston engine (DPE)
4	Bio-diesel + Turboshaft (TS)
5	LH_2 + Turboshaft (TS)
6	LiS + Switched reluctance motor (SR)
7	AEROPAK^{TM} + Switched reluctance motor (SR)
8	LiS + Permanent magnet motor (PM)
9	LH_2 + PEM fuel cell + Switched reluctance motor (SR)

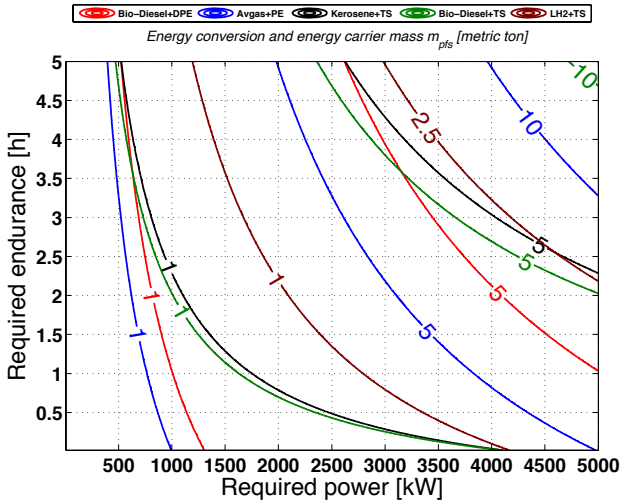

Figure 2.8. Mass of energy carrier and conversion elements using internal combustion engines. For abbreviations, see Table 2.5.

the difference in m_{pfs} using a SR- or a PM-synchronous motor remains minimum.

2.3.5 High Temperature Superconductive (HTS) devices

The introduction of high temperature superconductive[v] materials such as BSCCO (Bismuth-Strontium-Calcium-Copper-Oxide) and YBCO (Yttrium-Barium-Copper-Oxide), having a critical temperature T_c[vi] near 100 K, opened doors to achieve high mass- and volume-weighed power densities for electric motors and generators (Table 2.4 & Figs.2.11-2.14). The impact of HTS materials on the power generating market is regarded as substantial : Sheahen et al. (2002) predicts that the technology will be implemented in 75% of the motor

[v] Not to be confused with cryogenic, which represents those machines operating at low temperatures but still above the critical temperature, below which the superconductive characteristics of a material appears. Cryogenic machines benefit from the lower Ohmic losses due to the lower operating temperatures and still use common electric materials such as aluminium and copper – Brown et al. (2005).

[vi] Above this temperature, the HTS material loses its superconductive characteristics.

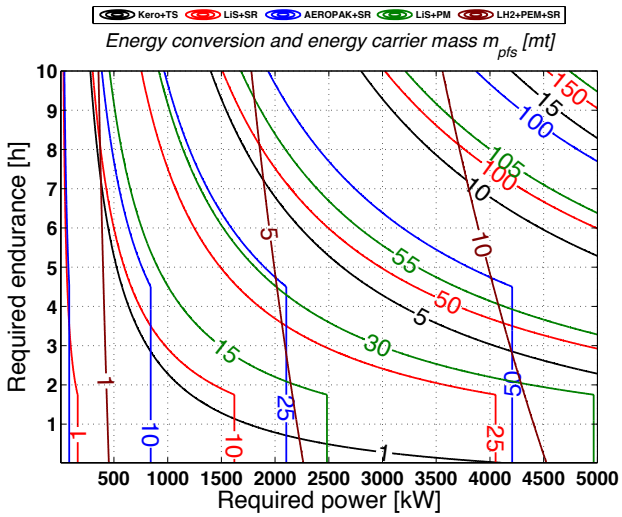

FIGURE 2.9. Mass of energy carrier and conversion elements using more-electric solutions. For abbreviations, see Table 2.5.

and 80% of the transformer market, while Lewis & Müller (2007) report that the cost of HTS materials will become about five times lower than copper[vii]. The importance of the HTS materials can again be emphasised knowing that Siemens (Nerowski et al. (2004)) and General Electric (Sivasubramaniam et al. (2009)) investigate the integration of HTS technologies in their motors and generators, while it is already installed in some ship propulsion systems as described by Woodruff et al. (2005). Masson et al. (2005) examined the implementation of HTS technology in a Cessna 172 giving encouraging results, while the United States Air Force (USAF) developed and tested a multimegawatt electric power system using HTS technologies – Sivasubramaniam et al. (2009). Therefore, it would be interesting to examine to what extent the helicopter could profit from this technology too.

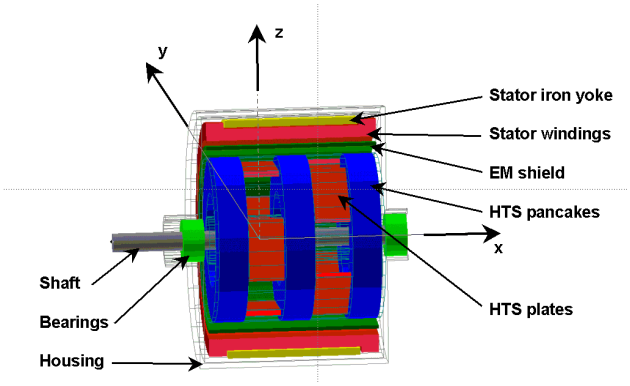

FIGURE 2.10. HTS motor using flux-trapping. Courtesy of Masson et al.

[vii] Based on Linz wire.

HTS devices achieve their high performance thanks to the high magnetic field produced in the superconductive field windings. Various architectures exist, some use the homopolar configuration such as Kwon et al. (2007), others are more exotic using flux trapping as shown in the work of Masson et al. (2007) (Fig.2.10), a technique that specifically uses the diamagnetic characteristic of superconductive materials[viii].

In this study, two ways are proposed to cool the HTS materials : via a cryocooler or via liquid hydrogen stored in the helicopter fuel tank. For both configurations, the HTS motor mass- and volume-weighed power densities, respectively $\rho_{P,m}$ and $\rho_{P,V}$, follow in Figs.2.11-2.14, using data of Masson et al. (2005), Masson & Luongo (2007) and Radebaugh (2009). The derivation of these characteristics is adopted in Appendix B.

For the higher range of rotational speeds, the HTS motor performs better than state-of-the-art turboshafts, except for low power outputs. Though, it is not worthwhile to drive the main rotor with a HTS motor directly, since the main rotor turns at rotational velocities of one order of magnitude lower than 3000 RPM. This would lower the HTS motor mass-weighed power density by one order of magnitude too (Appendix B), i.e. around 1 kW/kg (Fig.2.11 & Fig.2.13) while still needing to be fed electrically with, for example, a high-speed HTS generator[ix] driven by a turboshaft. Also, the mass-weighed power density advantage of a mechanical gearbox makes this configuration unattractive, which is in the order of 4-5 kW/kg – Folenta (1983). However, the HTS devices may be interesting to drive the tail rotor directly, removing a major part of the mechanical transmission system. This is studied in the next section. Note that the selection of 6000 RPM and 20000 RPM in Figs.2.11-2.14 correspond to the typical output shaft speeds of turboshaft engines (Fig.2.4).

[viii] See for example Frankel (1979)

[ix] A HTS generator has already been developed and tested successfully for the United States Air Force – Sivasubramaniam et al. (2009).

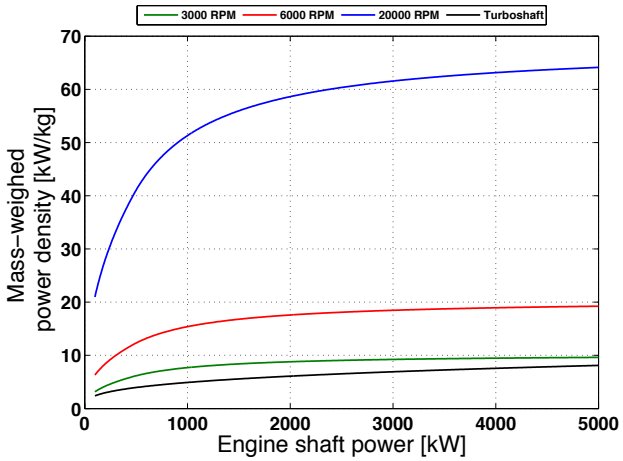

FIGURE 2.11. HTS motor $\rho_{P,m}$ (20 K).

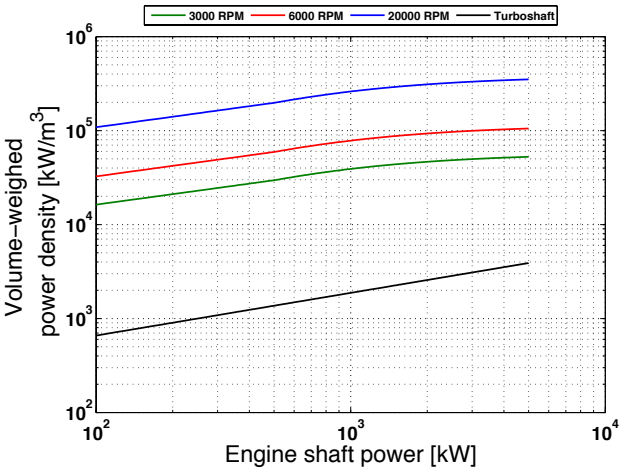

FIGURE 2.12. HTS motor $\rho_{P,V}$ (20 K).

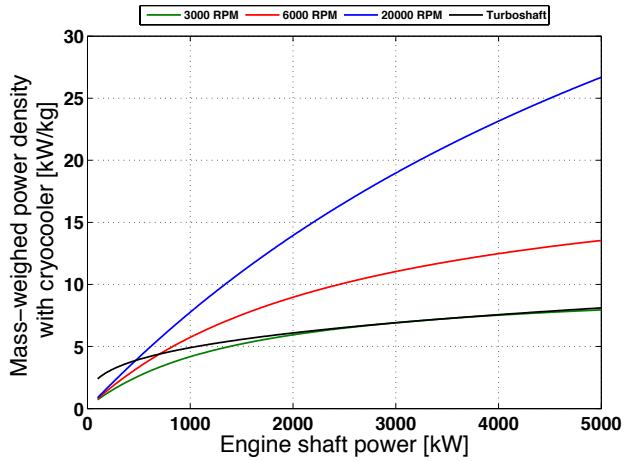

FIGURE 2.13. HTS motor with cryocooler $\rho_{P,m}$ (20 K).

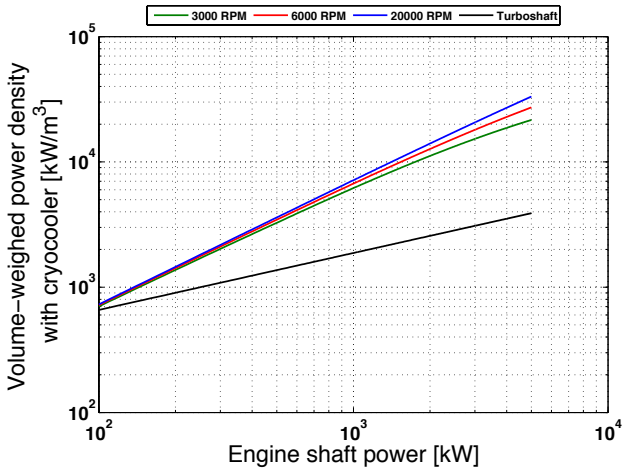

FIGURE 2.14. HTS motor with cryocooler $\rho_{P,V}$ (20 K).

2.3.6 Alternative system integration and assessment

The results of the previous studies are not very optimistic when it comes to replacing the engine and transmission system with better alternatives. Indeed, if one wants to retain the level of performance, weight must not differ largely and even if a better efficiency could be achieved, there is currently no factual guarantee/evidence that reliability or operating costs will/would improve. Nevertheless, the configuration using an electric motor fed by a HTS generator to drive the tail rotor, which in fact removes a part of the transmission system, deserves further attention. Indeed, the power demanded from the powerplant to drive the tail rotor is significantly lower than the one required for the main rotor and since the transmission system weight is substantial, the possibility of a gross weight reduction by replacing a part of the transmission by an electrical alternative should therefore be examined. Additionally, the use of liquid hydrogen appeared attractive, but the impact of the tank mass on the empty weight of the platform has not yet been assessed.

Seven configurations of which four using more electric devices will now be examined in a conventional helicopter environment (Table 2.6 and Fig.2.15). Three configurations use liquid hydrogen as the energy carrier. The electric devices aim specifically at removing the tail rotor part of the transmission system, viz. the tail boom shaft with dampers and bearings, and the tail gearbox(es). Then, the tail rotor is driven directly via an electric motor and fed by a HTS generator mounted close to the engine(s).

The modelling of the implementation of new technologies in the conventional helicopter is governed by the methodology described in Fig.2.16. The objective is to examine the induced gross weight variation for a given endurance and number of occupants. The lightest configuration should then be preferred as it offers the best fuel economy (cost) or has the potential to increase the borne payload. The followed philosophy in Fig.2.16 is now discussed.

First, a crew and passenger number N_{cp} is selected. This is the first independent variable in the assessment study. Besides determining the weight of the additional payload W_{pay}, it yields a first estimation of the gross weight $W_{g,ini}$ of the studied helicopter configuration. Indeed, its gross weight can differ from the conventional helicopter gross weight by the introduction/removal of system components and the selection of a fuel type and quantity. Because gross weight affects all components in the helicopter, it has to be calculated iteratively (outermost loop in Fig.2.16). A survey performed by the author shows that N_{cp} correlates well with the conventional helicopter gross weight :

$$W_{g(,ini)} = 6.0461\, N_{cp}^2 + 300.18\, N_{cp} \tag{2.16}$$

The foregoing equation is shown in Fig.2.17 and is used to establish the initial gross weight of the studied helicopter configuration. The gross weight of the helicopter can be

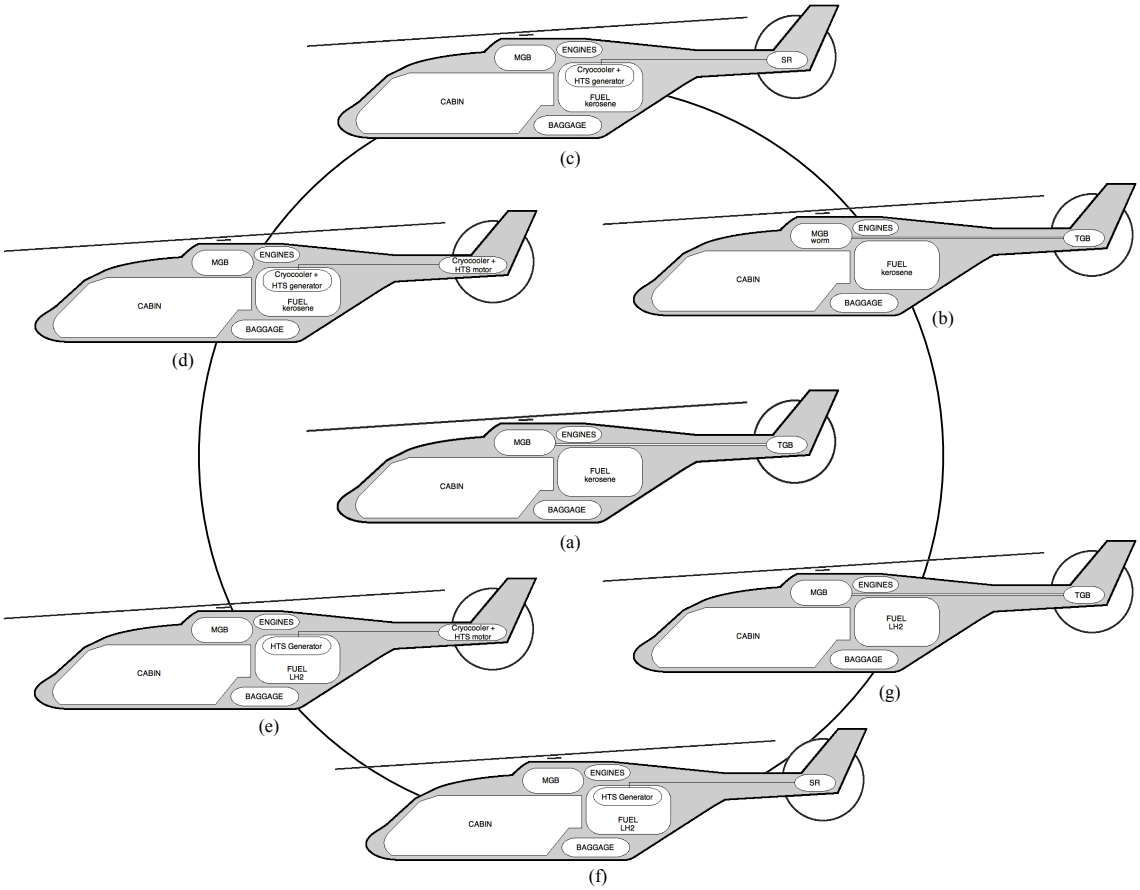

FIGURE 2.15. The examined configurations.

TABLE 2.6. Configuration overview.

Nr.	Fuel	Worm gearing	TR driver	HTS generator	Abbrev. Fig. 2.22
(a)	Kerosene	no	Turboshaft	no	K
(b)	Kerosene	yes	Turboshaft	no	K/W
(c)	Kerosene	no	SR	yes+CrC	K/HgSR
(d)	Kerosene	no	HTS motor + CrC	yes+CrC	K/HgHm
(e)	LH_2	no	HTS motor + CrC	yes	LH_2/HgHm
(f)	LH_2	no	SR	yes	LH_2/HgSR
(g)	LH_2	no	Turboshaft	no	LH_2

CrC = Cryocooler installed

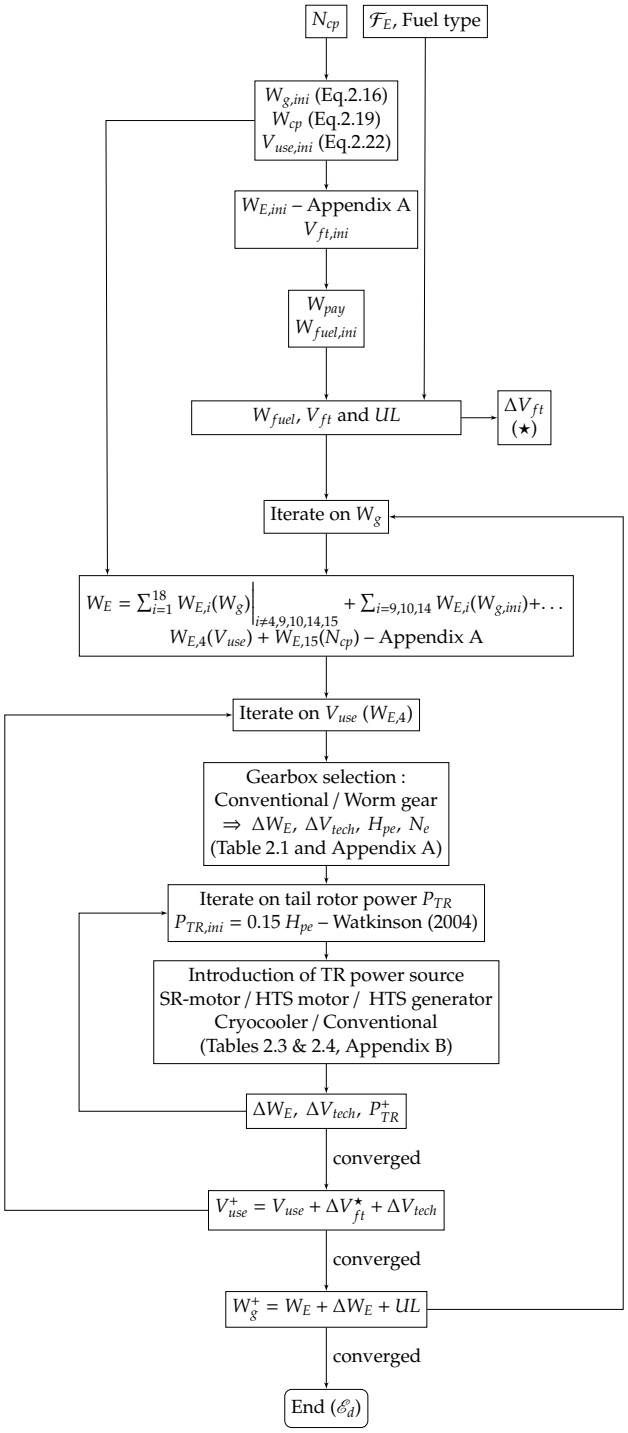

FIGURE 2.16. New technology integration procedure.

subdivided into an empty weight W_E and a useful load UL fraction. Following the typical convention as suggested by Landers et al. (2001) and AIAA (2003) :

$$W_g = W_E + UL \tag{2.17}$$

$$UL = W_{cp} + W_{fuel} + W_{pay} \tag{2.18}$$

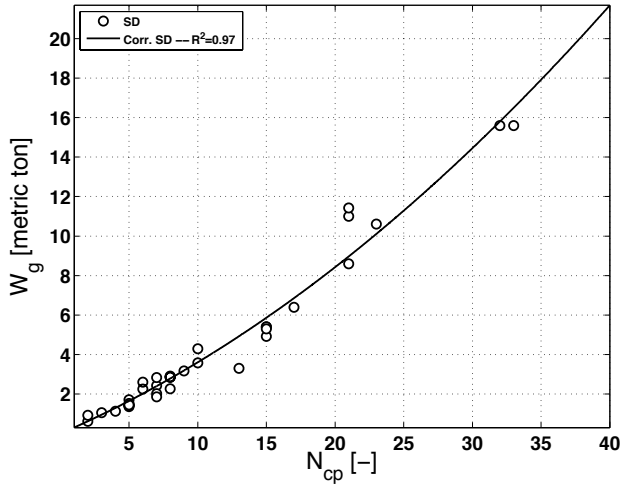

Figure 2.17. Conventional helicopter gross weight as a function of crew and passenger count N_{cp} – Appendix H.

The useful load represents the summed weight of crew and passengers W_{cp}, payload W_{pay} and fuel W_{fuel}. Note that :

$$W_{cp} = N_{cp}\, W_p \tag{2.19}$$

W_p represents the weight of one person and equals 77 kg as indicated by EASA CS-27/29. Hence, the impact of the new technologies on the helicopter can be written as :

$$\Delta W_g = \Delta W_E + \Delta UL \tag{2.20}$$

The model has not only to consider the crew and passenger count, but must also reflect the influence of flight endurance on gross weight. In the model, the endurance is adopted most conveniently by varying the amount of fuel carried in the helicopter. To study this effect, a second independent variable is introduced, viz. the stored energy fraction $\mathcal{F}_E$, which is :

$$\mathcal{F}_E \triangleq \frac{E_{fuel}}{E_{fuel,ini}} \tag{2.21}$$

where $E_{fuel,ini}$ is the carried reference energy of the conventional helicopter at $W_{g,ini}$, and E_{fuel} the selected internally stored energy in the examined helicopter. N_{cp}, $\mathcal{F}_E$ and the selected fuel type now allow the useful load to be found along with the required fuel tank volume V_{ft} of the examined helicopter configuration.

The gross weight and empty weight of a helicopter are implicitly related, i.e. changing the empty weight of one component will affect the gross weight and in turn the empty weight of most other components in the helicopter. A weight variation also impacts the required

engine power H_{pe} and consequently the (specific) fuel consumption, which becomes clear studying the weight estimation relationships of the model of Beltramo & Morris (1980). These are adopted in Appendix A. Obviously, this mathematical problem cannot be solved analytically, which explains the outermost loop in Fig.2.16. For the *conventional* components inside the helicopter, the model of Beltramo & Morris (1980) is used to estimate their contribution to empty weight (Table 1.1). Most of them can be considered a function of the ruling gross weight W_g, with the exception of component groups 4, 9, 10, 14 and 15. The instruments and avionics weight groups (10 & 14) will be more dependent on range, while cabin amenities (15) depend principally on N_{cp}. The auxiliary power system weight group (9) is assumed to depend on $W_{g,ini}$ only. Also, the body-weight group (4) should be treated differently. According to Beltramo & Morris (1980), the mass of the helicopter structure depends on its *wetted surface*. The wetted surface encapsulates a certain volume, which might change substantially with the implementation of new technologies, for example by the placement of the much larger liquid hydrogen tank. It is therefore sensible to relate the body mass to a useful volume V_{use} :

$$V_{use,ini} = V_{MGB} + V_{Eng} + V_{ft} + V_{cab} + V_{lug} \tag{2.22}$$

$$V_{use} = V_{use,ini} + \sum_i \Delta V_{tech,i} + \Delta V_{ft} \tag{2.23}$$

where V_{MGB}, V_{Eng}, V_{ft}, V_{cab} and V_{lug} are respectively the volume of the main gearbox, the engines, the fuel tank, the cabin and the luggage compartment. For these volumes, correlations were established and implemented in the model, based on survey data (Figs.2.18-2.21 and Appendix A) :

$$V_{MGB} = 901.16 \cdot 10^{-9}\ W_g^{1.6220} \qquad [\mathrm{m}^3][\mathrm{kg}] \tag{2.24}$$

$$V_{Eng} = 0.0184\ N_e \left(\frac{MTOP}{N_e}\right)^{0.4712} \qquad [\mathrm{m}^3][\text{-}][\mathrm{kW}] \tag{2.25}$$

$$V_{ft} = 0.000244\ W_g - 0.024737 \qquad [\mathrm{m}^3][\mathrm{kg}] \tag{2.26}$$

$$V_{cab} = 51.85 \cdot 10^{-9}\ W_g^2 + 0.0011075\ W_g \qquad [\mathrm{m}^3][\mathrm{kg}] \tag{2.27}$$

$$V_{lug} = 0.0002568\ W_g \qquad [\mathrm{m}^3][\mathrm{kg}] \tag{2.28}$$

$MTOP$ and N_e are respectively the engine maximum take-off power at ISA SLS and number of engines installed. Correlations for these parameters are given in Appendix A. Since all volume correlations are functions of gross weight, it is possible to approximate the body empty weight $W_{E,4}$ by retrieving the gross weight for the required useful volume (inverse function) and introducing it into the body empty weight correlation of Beltramo & Morris (1980) (Appendix A). This requires an iterative approach (middle loop in Fig.2.16). With respect to Eq.2.23, it is sensible that gross weight impacts the installed power requirement H_{pe}, the number of engines N_e, and consequently the required engine volume. Similarly, the volume of the main gearbox changes with the power requirement and with

the selected type of gearbox (conventional or worm). The integration of other technologies also affect V_{use} and thus $W_{E,4}$ by adding a certain system volume inside the fuselage. All this is accounted for by ΔV_{tech}, of which the calculation is based on the component volume-weighed power densities. Once determined, a new value for $W_{E,4}$ can be retrieved and a new estimation of the gross weight made, including the additional empty weight corrections, which incorporate the weight influence of the installation of new technologies (ΔW_E).

Driving the tail rotor electrically can increase the tail rotor power required from the engine (P_{TR}), since an electrical efficiency needs to be accounted for. The efficiency is a function of the type of installed electric device. The change in required tail rotor power is captured by the innermost loop indicated in Fig.2.16. An iterative approach is required to allow for a power dependent electrical efficiency.

The endurance $\mathscr{E}_d$ can now be calculated, while assuming a constant *SFC* and power demand over time :

$$\mathscr{E}_d = \frac{E_{fuel,ini}\,\mathcal{F}_E}{LHV}\,\frac{1}{SFC\,H_{pe}} \tag{2.29}$$

where *SFC* the engine specific fuel consumption.

Finally note that, with regard to the use of liquid hydrogen, the model uses the design recommendations stated in Section 2.3.2. The working temperature of the HTS devices was the temperature of saturated liquid hydrogen at 1.2 bar (21 K – Stewart & Roder (1964)), or, in case a cryocooler is used, 20 K. The effects of a varying operating pressure during flight were not accounted for.

The results of the parametric study conducted on the configurations (a)-(g) in Table 2.6 are shown in Fig.2.22 for an arbitrarily chosen endurance of 2 hours. The conclusions drawn however, are generally applicable to other values of $\mathscr{E}_d$, and these are consequently not adopted in this work.

Note that near the N_e-transition zone, multiple solutions are possible for a given N_{cp} and configuration. This result originates from the fact that an increase in fuel weight ($\mathcal{F}_E$), and thus gross weight, requires more power to airlift the helicopter. In case a certain power requirement is exceeded, an additional engine is installed by the model (Appendix A). Near the transition zone, the specific fuel consumption of the configuration with the highest engine number will be more important (lower power category engine). It leads to a higher fuel demand for an imposed endurance, which explains the possibility of a non-unique solution.

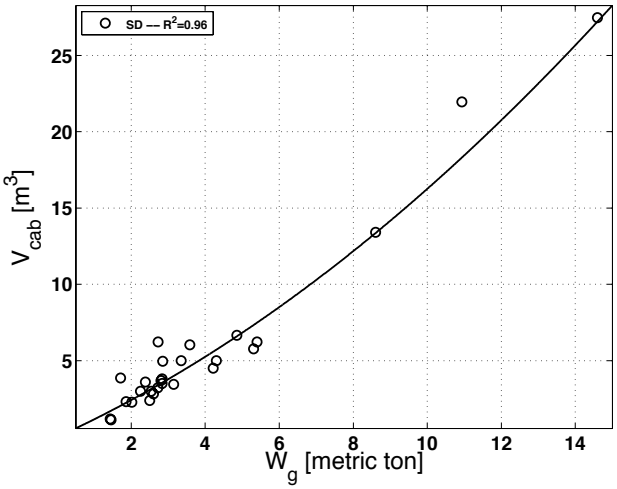

FIGURE 2.18. Cabin volume V_{cab} as a function of gross weight – Appendix H.

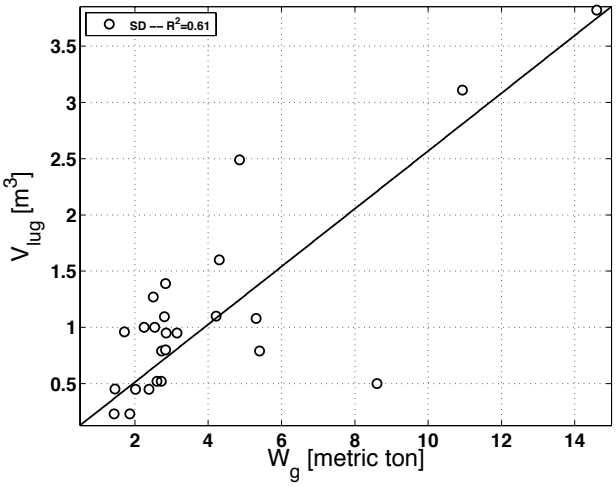

FIGURE 2.19. Storage (luggage) volume V_{lug} as a function of gross weight – Appendix H.

At this point, the weight influence factor $m_{\Delta c}$ is introduced, which depends on the considered configuration (i) and is defined as the relative weight increase with respect to the conventional configuration, viz. (a) :

$$m_{\Delta c} = \left.\frac{W_{g,(i)} - W_{g,(a)}}{W_{g,(a)}}\right|_{\mathscr{E}_d} \quad [\%] \tag{2.30}$$

Configuration (a) serves as the benchmark. The worm-gear configuration reduces the helicopter gross weight with approximately 13%, which applies to all N_{cp}, which is mainly due to the decreased gearbox weight. Unfortunately, the more-electric solutions all involve a gross weight penalty. Configuration (c) uses a turboshaft-driven HTS generator to power the tail rotor via a SR-motor. Since the energy carrier is kerosene, a cryocooler must cool down the generator to its nominal temperature, which is 20 K in the consid-

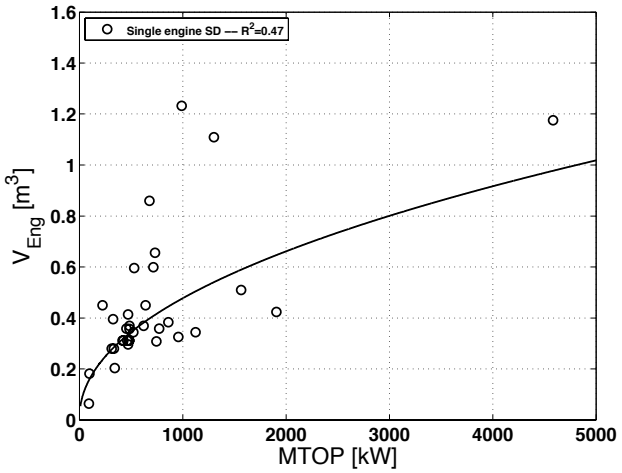

FIGURE 2.20. Engine volume V_{Eng} as a function of installed maximum take-off power (ISA SLS). Appendix H.

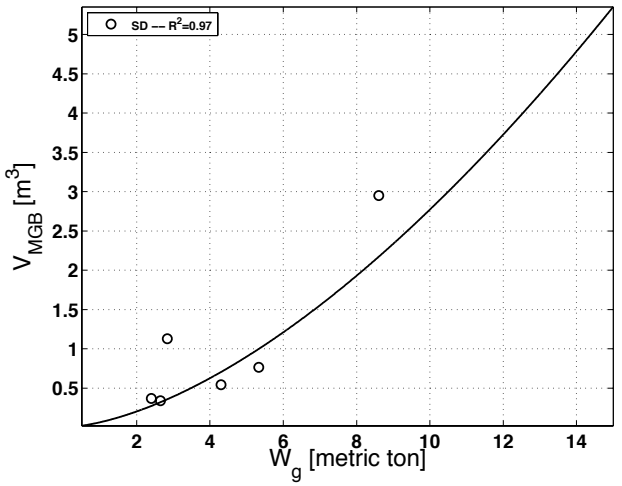

FIGURE 2.21. Transmission volume V_{MGB} as a function of gross weight – Appendix H.

ered case. For an increasing gross weight, $m_{\Delta c}$ lays between 15 - 5%. Interestingly, the helicopter configuration (d) using a HTS motor to drive the tail rotor and fed by a HTS generator, while both refrigerated with cryocoolers at 20 K, claims the third place with $m_{\Delta c}$ between 30. . . 6%. The tendency of $m_{\Delta c}$ to decrease with gross weight in both cases (c) and (d) can be explained by the fact that a heavier helicopter needs more tail rotor power, delivered electrically by a HTS generator. The more powerful the generator, the higher the mass- and volume-weighed power density (as is the case with the HTS motor, see Figs. 2.13-2.14), leading to a lower impact on gross weight. This phenomenon affects the lower power class mostly. Note that configuration (d) is about twice as sensitive to this characteristic as configuration (c) since it uses also a HTS device to drive the tail rotor. It is important to note that the effect of the installation of an electric motor (c) and a cryocooler

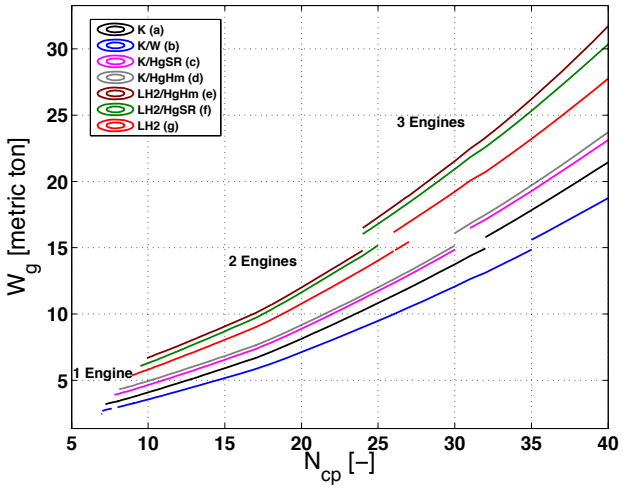

FIGURE 2.22. Configuration evaluation, 2h endurance (See Table 2.6).

(d) in the tail will have a negative influence on the position of the helicopter centre of gravity. This issue should merit significant attention and could be coped with by moving the main rotor aft, or in the worst case requires the introduction of "dead weight" in the nose of the helicopter, not to mention the requirement of a stronger tail structure. The weight increase could therefore still be too optimistic.

Liquid hydrogen as a fuel carrier (g), in contrast with what one expected earlier in Figure 2.8, raises gross weight up to 50% for the smaller helicopters and up to 25% when it concerns the larger ones ($\mathscr{E}_d$ of 2h). This is explained by the significant weight impact of the fuel tank and the increase of structural weight required to store the low-density liquid hydrogen. For larger $\mathscr{E}_d$, the negative impact of the tank weight and volume requirements persists also in the heavier gross weight class, raising its effect to approximately 50%. As seen with configurations (c) and (d), comparing (e) and (f) shows the slightly better characteristics of the SR-motor driven tail rotor. Even though liquid hydrogen now cools the HTS generator, the absence of the cryocooler has no significant impact on the gross weight results.

Before concluding the discussion, three important issues need to be emphasised.

First, the SR-motor mass-weighed power density expounded in Table 2.4 counts for a rotational speed around 10000 RPM. The tail rotor does not normally turn at this speed. It is therefore possible that the SR-motor power-density should be reviewed, making the HTS motor configurations more attractive.

A second important notice is the need for a HTS generator when driving an electric motor, for the current calculations assumed to be operating at 10000 RPM. Indeed, conventional

generators are bulky and heavy and would increase the helicopter gross weight significantly. However, a major drawback of the HTS devices is the cooling time, as discussed by Wen et al. (2009) (about 2 K/h). A fast and safe cooling method should need to be sought for in order to enhance the helicopters operability. Lastly, the HTS motors were all considered to turn at 3000 RPM, meaning that for the larger helicopters, the gross weight is estimated on the optimistic side (lower tail rotor speed).

Thirdly, in the above discussion, endurance was always used as the performance benchmark. However, it should be noted that in the present context, endurance is related to an amount of energy installed in the helicopter and an engine specific fuel consumption at a given power demand. The latter depend on the selected engine regime, the atmospheric conditions and the time-dependent gross weight, which are functions of (the position in) the flight/mission profile. These are, in the conducted assessment, unknown. Hence, it is important that the reader observes the endurance stated in this work in abstraction from the definitions found in aircraft design textbooks. For the same reason, it is not sensible to develop a range performance yardstick in the actual context, as flight speed is not considered here explicitly.

2.4 Conclusions

The proposed technological alternatives to replace or upgrade the conventional helicopter gearbox or propulsion system in an attempt to cope with the latter's cost, reliability and performance concerns, appear not to be sufficiently adequate to fulfil this role. Mainly because of an important weight penalty, or technology that has not matured sufficiently for implementation in a helicopter platform. A summary of the most important facts follows next.

The magnetic gearbox offers several advantages over the mechanical gearbox, but at this time, it appears too heavy for implementation in helicopters. Nevertheless, the potential of this technology should not be discarded and its evolution followed.

Several combinations of energy carriers and converters were proposed to replace (part of) the conventional helicopter propulsion system, including batteries, a fuel cell, PM- and SR-motors. Unfortunately, the implementation of these technologies drive the helicopter gross weight to unacceptable levels. The conventional combination of kerosene and a turboshaft engine proved to be the most weight efficient solution. For the lower power class helicopter, a Diesel engine using bio-diesel is attractive when compared to the Avgas engine configuration because it appears to be lighter, but the use of bio-diesel (green Diesel) is not recommended yet, since it is reported to be chemically unstable while subjected to congealing problems at the lower temperatures.

The use of liquid hydrogen increases the helicopter gross weight substantially by the increased weight and volume of the fuel tank for a given energy level. As a result, liquid hydrogen as an energy carrier in a helicopter configuration is found uneconomical, while its employability relies on the available infrastructure, and it does not offer a solution to the cost/safety/performance concerns stated for the conventional helicopters. However, it is a free coolant when used in combination with HTS devices.

Driving the tail rotor by means of electric devices, including the use of a HTS generator and motor, involves a helicopter gross weight penalty and the HTS device cooling time might be problematic. Even though electric devices are reported to be reliable, the previously stated aspects make their use in a helicopter platform currently unattractive.

Worm gearing was stated to be promising, but the lack of interest by the helicopter industry in this concept will have its reasons. Since the system generating the oil film is quite complex, it might be problematic from a reliability point of view, but it has not been possible to substantiate this hypothesis.

The main conclusion is that currently no alternatives exist to replace the helicopter transmission or propulsion system, without adding substantial weight, which impacts fuel cost and consequently operating costs negatively. In addition, the examined solutions do not circumvent the conceptual difficulties the conventional helicopter encounters : less (fuel) efficient than aircraft, limited in forward speed and a source of vibrations, the latter causing an important rise in *DOC* due to the increased maintenance costs. Note also that the same conclusions may be extrapolated to tandem and coaxial rotor variants, where the same powerplant types and mechanical transmission technologies are used. Therefore, it would be most interesting to examine what other helicopter concepts could offer, bearing the conclusions of the previous study in mind.

2.5 Nomenclature

Please note that the units listed below apply unless stated otherwise.

Abbreviations and substance formulae

BSCCO	Bismuth-Strontium-Calcium-Copper-Oxide	
CMG	Concentric Magnetic Gear	
CrC	With cryocooler	
CYMG	Cycloid Permanent Magnetic Gear	
DPE	Diesel piston engine	
E	Energy	[J]
$\mathscr{E}_d$	Simplified endurance	[h]
EERE	Energy Efficiency and Renewable Energy	
$\mathcal{F}_E$	Stored energy fraction	[-]
FAA	Federal Aviation Administration	
FC	Fuel cell	
H_2	Hydrogen	
Hg	HTS generator installed	
Hm	HTS motor installed	
H_{pe}	Total installed power	[W]
HTS	High Temperature Superconductive	
i	Main gearbox reduction ratio	[-]
ICE	Internal combustion engine	
ISA	International Standard Atmosphere	
K	Kerosene	
LH_2	Liquid Hydrogen	
LHV	Lower heating value	[MJ/kg]
LiS	Lithium Sulphur	
m	Mass	[kg]
$m_{\Delta c}$	Weight influence factor	[-]
MECH	MECHanical drive system	
MGB	Main GearBox	
MHG	Magnetic Harmonic Gear	
MPG	Magnetic Planetary Gear	
MTC	Magnetic Torque Coupler	
$MTOP$	Maximum Take-Off Power	[W]
MWM	Magnetic WorM	
N	Number of	[-]

N_E	Engine output shaft rotational speed	[1/s]
N_{MR}	Main rotor rotational speed	[1/s]
NdFeB	Neodymium-Iron-Boron	
NIST	National Institute of Standards and Technology	
p	Pressure	[Pa]
P	Power	[W]
PEM	Proton exchange membrane	
PM	Permanent magnet motor	
R	Range	[NM]
R_{tip}	Rotor tip radius	[m]
RPM	Revolutions Per Minute	[1/min]
S	Surface	[m^2]
SD	Survey data	
SFC	Cycle specific fuel consumption	[g/kWh]
SMG	Spiral Magnetic Gear	
SLS	Sea Level Static	
$SmCo_5$	Samarium-Cobalt	
SR	Switched Reluctance Motor	
T	Temperature or time	[K] or [s]
T_{ce}	Compensated endurance	[s]
TS	Turboshaft	
UL	Useful load	[kg]
USAF	United States Air Force	
v_{tip}	Rotor blade tip speed	[m/s]†
V	Volume	[m^3]
W	Mass or weight	[kg or N]
W_E	Helicopter empty weight/mass	[kg]
W_g	Helicopter (design) gross weight/mass	[kg]
WW	World War	
YBCO	Yttrium-Barium-Copper-Oxide	
ε_g	Gravimetric efficiency	[-]
ρ	Material density	[kg/m^3]
ρ_m	Magnetic gearbox material density	[kg/m^3]
$\rho_{P,m}$	Mass-weighed power density	[kW/kg]
$\rho_{P,V}$	Volume-weighed power density	[kW/m^3]
$\rho_{Pe,m}$	Mass-weighed electric power density	[kW/kg]
$\rho_{Pe,V}$	Volume-weighed electric power density	[kW/m^3]

ρ_τ	Torque density	[Nm/m^3]
τ	Torque	[Nm]
Ω	Rotational velocity	[rad/s]

Subscripts and superscripts

c	Critical
cab	Cabin
cp	Crew and passengers
Cryo	Cryocooler
cv	Conversion elements
e	Engine
E	Energy carrier, engine or empty weight related
ec	Energy carrier
ep	Engine to powerplant
ex	Excess, exhaust gasses
ext	External
f	Fuel
ft	Fuel tank
g	Generator or combustion gasses
HTS	High Temperature Superconductive
ini	Initial
kero	Kerosene
liq	Liquid
lug	Luggage
m	Motor or mass-weighed
M	Mechanical, transmission
mag.GB	Magnetic gearbox related
mi	Minimum installed
MGB	Main GearBox
MR	Main rotor
pay	Payload
pfs	Energy carrier and conversion elements
sat	Saturated
req	Required
TR	Tail rotor
tech	New technologies related
use	Usable

v	Volume-weighed
vap	Vapour

Chapter 3

The event horizon : alternative concepts

"A pessimist sees the difficulty in every opportunity. An optimist sees the opportunity in every difficulty."

Sir Winston Churchill

3.1 Introduction

Finding solutions that cope with the conceptual issues of conventional helicopters is nowadays an important research topic for most helicopter manufacturers. Especially the limited performance envelope appears to get much attention, where the confined maximum forward speed pushes the designers to important conceptual changes. Today, the conceptual alternatives to the conventional helicopter can be mainly categorised into :

→ Compound (hybrid) helicopters

→ Tilt-rotor helicopters

→ Reaction-force-driven-rotor helicopters

→ Exotic VTOL aircraft

The strengths and weaknesses of some of the previously mentioned concepts will be discussed, and evaluated from the transmission and powerplant (propulsion) system viewpoint established during the previous chapters. This chapter concludes with the introduction of the turbine driven rotor (TDR) helicopter concept, which will constitute the basis of the subsequent studies performed in light of this thesis.

3.2 Compound helicopters

In the work at hand, compound helicopters include all helicopters that rely on additional thrust and or lift producing devices, which improve the flight envelope. Contemporary examples of such helicopters are the Sikorsky X-2 and Airbus Helicopters X^3 technology demonstrators (Fig.3.1). Even though they represent distinctive configurations, both address the imposed speed boundaries caused by (a) horizontally placed rotor(s).

Indeed, in forward flight and increasing flight speed, the (average) air velocity over the advancing and retreating rotor blades evolves towards respectively a higher and a lower value. In order to continue flight, the aerodynamic loads between the advancing and retreating side must be balanced, which requires a lower angle of attack setting for the advancing blade and a higher angle of attack setting for the retreating blade. Mainly two phenomena hinder a high forward speed : retreating blade stall and blade compressibility issues. With increasing flight speed, the retreating blade will have to be positioned at higher angles of attack due to the decreased flow speed and the emergence of a reverse flow region, until at a certain point, the blade or a part of it stalls. The advancing blade on the other hand will experience performance losses due to compressibility effects even with a decreasing angle of attack setting : one notes an increase in vibration, a tendency for a nose down moment of the blade putting more stress on the control rods and a significant rise in drag (drag divergence). Additionally, the increased flight speed causes a parasite drag growth, requiring an even higher rotor loading, which is detrimental to the aerodynamic performance. As a result, conventional helicopters encounter a forward speed boundary – Leishman (2007).

The solution Sikorsky proposes to cope with the forward speed limit, and forming an integral part of the X-2 demonstrator, is based on the experience gained from the *Advancing Blade Concept* (ABC), which was studied in the past. The concept uses two closely stacked rigid contra-rotating rotors. Thanks to this, the rotor disk loading can be reduced allowing a lower angle of attack setting, which is beneficial at the higher speeds. The fact that the rotors are contra-rotating enables the asymmetric load of the rotors caused by forward flight to cancel each other mostly. Note that the increased (parasite) drag due to the higher forward speed must also be compensated, but thanks to the coaxial rotor layout, a larger thrust potential is available with respect to the single rotor concept. Additionally, the installation of externally mounted propulsion devices such as a pusher propeller seen on the X-2, further alleviates the rotor by vouching for the increased parasite drag of the platform.
The X^3 is confronted with the same issues, but approaches them differently – Nelms (2012). Here the single main rotor load is decreased with forward flight speed and the helicopter lift production is taken over by the small horizontal wings, of which the lift production is also positively influenced by the propeller wash. The propulsive force is

(a) Sikorsky X-2 technology demonstrator, Ashish Bagai.

(b) Eurocopter X^3 technology demonstrator, Anthony Pecchi.

FIGURE 3.1. Compound helicopters.

accounted for by the turboprop engines with propellers.

It must be noted however that the mechanical transmission system, and the control system, in both demonstrators is complex, larger and thus heavier. Hence, it is questionable whether this concept will tackle the reliability and cost issues that were expounded earlier in this work, and these aspects should be weighed against the gain in performance.

3.3 Tilt-rotor helicopters

The major advantage of the tilt-rotors is the increased maximum flight speed, while no longer subjected to the physical limitations of a horizontally placed rotor. The Boeing V-22 Osprey and AgustaWestland AW609 are good examples of the contemporary military and commercially available tilt-rotors (Fig.3.2). Even though their capabilities have been proven useful, Leishman (2007) correctly questions their cost effectiveness and autorotative capabilities in case of an engine failure. Also, the inclination of the engines and the high propeller/rotor disk loading pose important technical challenges from both a structural and a propulsive system viewpoint. From the previous chapters, it was seen that the most highly loaded and complex components are particularly targeted by cost, safety and performance (weight) concerns. From this global perspective, the tilt-rotor cannot be seen as the better solution for the conventional helicopter.

3.4 Reaction-force-driven-rotor helicopters

This concept mainly aims at avoiding the use of the complex transmission system found in a conventional helicopter. Here, the rotor is generally driven by ducting a flow of cold or hot pressurised air toward the blade tips (pressure jet system), or by feeding small engines installed in the blade tips with fuel (tip engine system). In the former case, nozzles

(a) Boeing V-22 Osprey, The Boeing Company.

(b) AW609, AgustaWestland (2015).

FIGURE 3.2. Tilt-rotor helicopters.

with or without reheat expand the air or combustion gases in order to produce thrust. In the latter case, only the tip-mounted ramjets generate thrust[i]. The developed force then provides the necessary torque making the rotor turn. This misleadingly "simple" technology was already known by Heron of Alexandria, where he described a contraption of dancing figures in his book *Pneumatica*. A priori, this principle is indeed quite elementary and therefore many tip-jet-driven rotor helicopters were developed in the past, such as the Fairey Rotodyne or the Sud-Ouest Djinn, but even today, new exotic concepts emerge such as the Boeing X-50A Dragonfly, which uses a tip-jet driven rotor. This unmanned aerial vehicle converts to an aeroplane at the higher speeds while stopping its rotor and using it as a wing.

The advantage of tip-jet-driven rotors is the absence of a (heavy) transmission system, allowing a higher useful load fraction. But generally, this advantage is outweighed by the usually excessive noise production and the higher fuel consumption, which can amount to ten times as much as the one found in a conventional helicopter – Watkinson (2004) and Prouty (2007). Prouty (2007) mentions that when tip engines are used, the rotor drag may be increased significantly. Consequently, the autorotative performance is deteriorated substantially. In addition, he reports that of all tip-jet-driven systems, the pressure jet system is the quietest in operation, but this advantage is overshadowed by the frictional and concurring pressure losses in the airflow pumped through the ducts inside the rotor blades. These losses are accountable for the destruction of most of the power gained by the omission of the complex transmission system.

The reaction-force-driven-rotor helicopter can be used in a compound configuration, as was the case with the Fairey Rotodyne (Gibbings (2009)), but the main objection against the exploitation of this concept is, even if the increased propulsion losses would be discarded,

[i]Note that the Hiller Aircraft Company Inc. proposed the installation of a turbojet on each rotor blade tip – Nichols (1964). However, this kind of solution gives rise to gyroscopic problems, requiring, for example, twin balanced spools.

noise. Noise regulations are increasingly stringent. As a consequence, the noise issue could constrain the operating area of such an aircraft. This cannot be accepted.

3.5 Exotic VTOL aircraft

The "exotic" category contains all other helicopter configurations, which are neither conventional helicopters, nor fall under the above discussed configurations. Examples are the cyclogyro (Boirum (2009)) and the NASA puffin electric tailsitter (Moore (2010)). Mostly, exotic VTOL aircraft are crossbreeds between conventional helicopters and aeroplanes. Another interesting concept is proposed by Schroijen (2009), who proposes to use the Coandă effect over wings, which produces lift during hover (Fig.3.3).
Nevertheless, the fact that concepts are tagged by the word exotic, means that their "fitness" has not been proven (yet), while the other discussed concepts have earned their spurs (deserved or not) by claiming their own niche in the helicopter world.
Even though resembling the external configuration of a conventional helicopter, the TDR helicopter concept discussed in the subsequent section could currently be classified as an exotic helicopter type, but it will be addressed separately as it is part of the study conducted in this thesis.

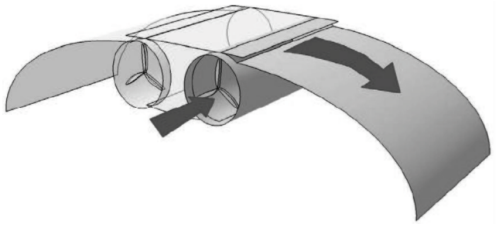

Figure 3.3. Coanda-type MAV concept - Adopted from Schroijen (2009).

3.6 The TDR helicopter concept

The previously studied non-exotic conceptual alternatives to the conventional helicopter have type-specific performance advantages over the conventional helicopter, but there are concessions to make, such as the increased complexity and cost, which the designer and the operator must be willing to accept. Also, an ineffectual attempt was made in the previous chapter to *upgrade* the most performance restrictive components of the conventional helicopter, while Leishman (2007) shows that for the conventional helicopter concept, no further dramatic improvements in performance is currently to be expected, since as good as all technological advances are, they only contribute to the optimisation of the platform. It thus appears designers are confronted with a stalemate, as there is no general improvement available, i.e. increase the performance envelope *and* at a lower cost *and* an increased reliability.

There is however, a possible alternative, which has been proposed recently by the Belgian company Sagita S.A., named the *Turbine Driven Rotor* concept (TDR). It is a helicopter combining the benefits of coaxially contra-rotating rigid rotors (ABC-concept) with the absence of a transmission system and tail rotor (reaction-force-driven rotor), without revolutionising the conventional helicopter layout (Fig.3.4). Sagita suggests driving rigid contra-rotating coaxial rotors by means of an air-driven low pressure *Ljungström* turbine integrated in the helicopter rotor head. Driving coaxial rotors directly by a turbine or radial engine was already patented/undertaken by respectively Ramme in 1968 (Ramme (1968)) and Wagner in 1960 (Rotocar III, Polte (2006)). The concept of Ramme was highly complex, using nozzles installed in the rotor head to achieve yaw control, and probably never left the drawing board. The concept of Wagner integrated a 51 kW-strong radial engine in the rotor head, which is not ideal, neither from an operating perspective (vibrations, dirt, drag), nor from a performance/weight perspective in case larger helicopters are envisaged, and was abandoned due to lack of funding. Note that the low pressure Ljungström turbine does not have the noise problems of the reaction-force-driven rotor concepts as the technique relies on a much lower gas expansion ratio.

Figure 3.4. The TDR concept, Hubert Antoine.

The rotor embedded Ljungström turbine (RELT) in the TDR configuration has no stator vanes and consists of two turbine halves (Fig.3.5 & Fig.3.6) on which multiple blade rows are installed. Each turbine half is suspended by bearings on a static rotor mast and drives a rotor. The turbine halves, and thus the rotors, turn in opposed senses. The only mechanical forces transmitted from the turbine to the fuselage are the friction forces in the bearings. Yaw control is achieved via circulation control over the helicopter tail boom at low flight speeds and by a vertical empennage at the higher flight speeds, as discussed by Runge et al. (2013)[ii]. The air expanding through the RELT is delivered by a

[ii] 2D/3D URANS simulations were undertaken using NUMECA's FINE/Open software suite, but it appeared not possible to capture the flow separation points on the tail boom adequately, nor derive acceptable

thermodynamic (*conditioning*) cycle. In the example given in Fig.3.4, the cycle is based on a piston engine, which sucks in air via a compressor, and of which the exhaust gases are mixed with bypass air prior to entering the turbine.

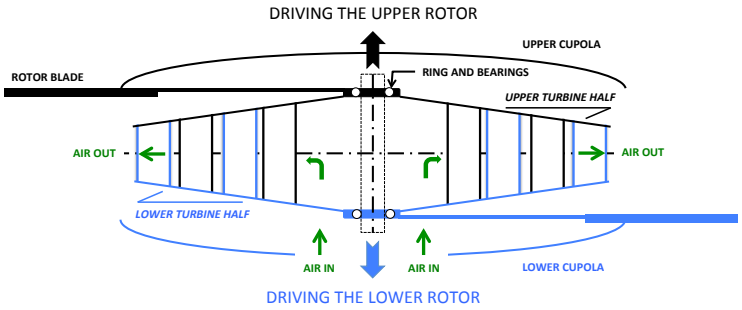

FIGURE 3.5. The rotor embedded Ljungström turbine (RELT) - Vertical plane.

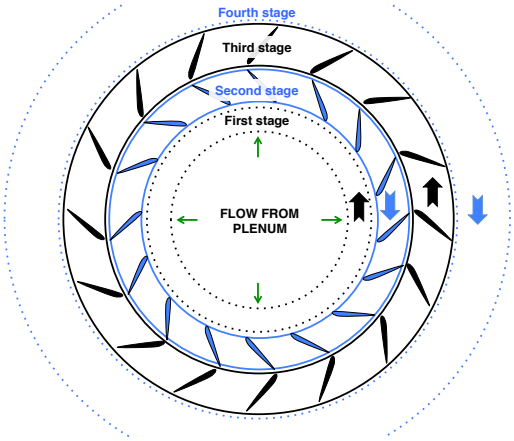

FIGURE 3.6. The rotor embedded Ljungström turbine (RELT) - Horizontal plane.

Historically, it is interesting to discuss this cycle more in detail via a sketch made by the inventor of the concept, Hubert Antoine, adopted in Fig.3.7. First, air is admitted in a plenum (5), i.e. a pressurised and airtight vessel in the helicopter, after being pressurised by a compressor (4) driven by an internal combustion engine (1). Behind the compressor, the airflow path is split. A part of the air is sucked into the piston engine, while the remainder of the air bypasses the engine to be subsequently mixed with the exhaust gases of the engine. Then the air leaves the plenum via ducting (6) and enters the Ljungström turbine, with halves (23) and (24), which are directly connected to the their respective rotor (14) and (15). The turbine consequently discharges the air into the atmosphere. The turbine halves are suspended around a fixed shaft (7), which is connected to the body structure (3). Note that (23) and (24) represent the turbine halves with fairing, i.e. the cupolae.
In February 2010, proof of concept was successfully delivered by Sagita by means of a

force coefficients, as was proven by means of wind tunnel tests. The simulations were consequently adopted in a new research framework and excluded from consideration in this disseration.

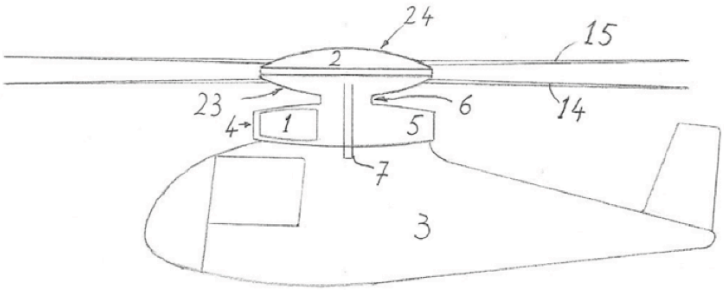

FIGURE 3.7. The TDR concept explained, Antoine et al. (2009).

FIGURE 3.8. TDR scale model demonstrator, Hubert Antoine.

TDR scale model, after being tested extensively in the wind tunnel facilities of the University of Liège (Fig.3.8). The scale model uses an electrically driven fan to generate the air flux necessary for the turbine. However, a profound theoretical study underpinning the major design parameters was not yet conducted, and several conditioning cycles remained to be explored. Since the TDR concept has the potential to contribute positively to the helicopter conceptual and propulsion system limitations discussed previously, and since the capabilities of the concept still need to be assessed thoroughly, the following objectives are stated for the remainder this thesis[iii] :

→ Evaluate the existing piston engine powered TDR cycle proposed by Sagita (Chapter 4).

→ Propose and evaluate other conditioning cycles (Chapter 4).

→ Examine the Ljungström turbine performance characteristics and develop its geometry with the objective to be implemented in a helicopter rotor head (Chapters 5 - 7).

→ Match the turbine and cycle characteristics for nominal operating conditions and

[iii] These concur with the second and third objectives stated at the beginning of this document.

compare the TDR performance characteristics with those of the conventional helicopter (Chapter 8).

From the study performed in Chapter 2 for conventional helicopters, only internal combustion engines emerged as weight and energy efficient mechanical power sources. Based on these results, it is decided to focus initially on three conditioning cycles :

→ Reciprocating engine powered, using Avgas and Diesel piston engines.

→ Turboshaft engine powered, evaluating the potential of implementing the most commonly used helicopter engine in the TDR concept.

→ Turbofan engine powered, offering the potential of compounding and enhancing the helicopter speed envelope if required.

Some components in the conditioning cycles will not be examined, because their characteristics are well known in the literature, or not required to be known in detail as off-design calculations are not adopted in this thesis. Such is the case for the compressor, the plenum, ducting and the internal combustion engines.

Basic design methodologies for the Ljungström turbine were only found in the works of Stodola (1922) and Houberechts (1972), but these authors focus on using steam as working fluid[iv] of which the characteristics differ substantially from air. Also, the proposed performance models were found inadequately elaborated and/or detailed to develop design recommendations to implement a Ljungström turbine in the rotor head of a helicopter and to establish its off-design characteristics. This work therefore examines loss models eligible for the RELT based on contemporary loss models available in the turbine domain, and develops a methodology enabling the designer to establish a turbine geometry for integration in the TDR helicopter.

Finally note that the omission of the transmission system offers the TDR helicopter concept, according to Chapter 1, an important cost, safety and performance advantage. For example, the gearbox flat rating boundary is removed and the risk of engine overtorquing is reduced. However, the required engine power and potential weight gain still needs consideration, which will be examined lastly.

[iv] The development and use of the Ljungström turbine goes back to the beginning of the 20th century as an answer to the steam-leakage plagued and bulky steam turbine plants – Van Loenen Martinet (1915), Van Zoest (1935), STAL (1927) and STAL (1939). The result was a dramatic reduction in plant size and steam losses, and thus and improved cycle efficiency. After the Second World War, the Ljungström turbine fell in disuse. Probably by the increased efforts of the industry to develop efficient axial turbines for the aeropropulsion market. According to Peng (2008), the advantages of the Ljungström turbine became outweighed by its manufacturing cost.

Chapter 4

TDR Cycle study

"There cannot be a greater mistake than that of looking superciliously upon practical applications of science. The life and soul of science is its practical application."

Lord Kelvin

This chapter describes practical configurations to drive the Ljungström turbine embedded in the centre of the coaxial rotors. A general cycle will be studied from which simplified cycles will be derived and evaluated for three types of internal combustion engines, viz. the piston engine, the turboshaft and the turbofan. The chapter concludes with a comparison between the simplified cycles. The impact of bleed air to assure directional control at low speeds is neglected in the subsequent study, since its magnitude is currently unknown.

4.1 Driving the Rotor Embedded Ljungström turbine

The rotor embedded Ljungström turbine (RELT) delivers power to the coaxial rotors while expanding air/combustion gases at a mass flow rate of $\dot{m}_t$ over the turbine stages. Usually, the heat losses in this process can be neglected, which allows the expansion to be characterised as adiabatic. The power delivered by the turbine to the rotors, denoted as P_T^*, is quantified by general thermodynamics for an open system in steady state :

$$P_T^* = \dot{m}_t \left(h_{t,in} - h_{t,out}\right) \tag{4.1}$$

h_t is the specific total enthalpy. When considering perfect gases, the above equation can be transformed into :

$$P_T^* = \dot{m}_t C_p T_{t,in} \left[1 - \left(\frac{1}{\pi_T}\right)^{\frac{\gamma-1}{\gamma}\cdot\eta_{p,T}}\right] \tag{4.2}$$

where,

→ C_p = Specific heat at constant pressure of the expanding gases [J/kgK]

→ π_T = Total expansion ratio over the RELT [-]

→ $T_{t,in}$ = Total temperature of the gases entering the RELT, or *LTIT* [K]

→ γ = Ratio of specific heats [-]

→ $\eta_{p,T}$ = Turbine polytropic efficiency [-]

Note the use of total components for the enthalpy and temperature, while the polytropic efficiency is preferred over the isentropic efficiency when evaluating the "goodness" of a turbine or compressor, since it is a better yardstick to reflect the efficiency of the used technology – Walsh & Fletcher (2004).
Two important issues need to be highlighted when studying Eq.4.2. Firstly, as with every turbine, there exists a maximum gas inlet temperature. For turbines in conventional gas turbines used for civil aviation applications, the latest technology allows turbine inlet temperatures up to 1850 K. This temperature range is not achievable with the RELT. Its maximum inlet temperature is essentially limited by the maximum operating temperature of the bearings inside the rotor head, not by the mechanical stresses working on it. For bearings lubricated with grease, the turbine inlet temperature of the RELT is limited to the order of magnitude of 400 K (see for example the bearing product information provided by Timken). If an oil circuit with temperature monitoring were to be installed, higher inlet temperatures could be achieved, though penalising simplicity and reliability. Secondly, an increase in mass flow through and expansion ratio over the RELT results in a rise of delivered power. This requires the careful selection of (a) compressor(s) to feed the RELT, since the compressor mass flow, pressure ratio and efficiency are interrelated, as depicted by for example Lewis (1996).

4.2 The general cycle

Eq.4.2 shows that expanding hot and pressurised air over a turbine adiabatically, generates mechanical power. Delivering hot pressurised air efficiently is an important design criterion. Several ways exist to achieve the required objective. Presenting the complete cycle by a black-box, which is now referred to as the general cycle, allows determining some cycle design guidelines, which favour high cycle thermal efficiencies.

Observe the general cycle represented on Fig.4.1. The cycle comprises an open thermodynamic system working under steady state conditions, where energy enters and leaves the control volume per unit time under various forms, notably via enthalpy flows $\dot{H}$, heat flows $\dot{Q}$ and mechanical power P_T^*. From the conceptual setup, it is known that the RELT is the only component in the cycle that delivers mechanical power to the load, i.e. rotors, which are placed outside the boundaries of the general cycle. It has no mechanical

connection with any component in the cycle. Thus, the sole purpose of all the other components in the general cycle is the conditioning and delivery of a certain enthalpy flow to the RELT.
Since a mass flow needs to flow through the RELT, it is necessary to install a compressor in the system. Where and how is at this point not important. However, it requires a mechanical power source. For this purpose, the choice will be restricted to internal combustion engines (ICE), of which the superior suitability to provide mechanical power on an airborne platform such as the conventional helicopter was proven earlier. This work will consider the following three types of internal combustion engines :

→ Piston engine (Avgas, Diesel)

→ Turboshaft (kerosene)

→ Turbofan[i] (kerosene)

Hence, three cycles may be established, each using one type of the above discussed internal combustion engines. The detailed discussion about the integration of one or more of one type of engines in the cycle, is addressed in the subsequent sections. However, in spite of its simplicity, the general cycle already enables establishing important indications about how the engines should be integrated in the cycle in order to improve efficiency. For this purpose, assume that (Fig.4.1) :

→ $\dot{H}_{t,in}$ = Enthalpic flow of the gases entering the system

→ $\dot{H}_{t,out}$ = Enthalpic flow of the gases expanding through the RELT to the atmosphere

→ $\dot{H}_{t,ex}$ = Enthalpic flow of gases leaving the system, but not via the RELT (for example bleed air, ICE exhaust gases, etc.)

→ $\dot{Q}_F$ = Heat flow "entering" the system by the combustion of fuel in the ICE

→ $\dot{Q}_{PC}$ = Heat added to the system by an additional heat source (for example post-combustion)

→ $\dot{Q}_C$ = Heat extracted from the system (losses, heat-exchangers, etc.)

Applying the first law of thermodynamics, one finds for P_T^* :

$$P_T^* = (\dot{H}_{t,in} + \dot{Q}_F + \dot{Q}_{PC}) - (\dot{H}_{t,out} + \dot{H}_{t,ex} + \dot{Q}_C) \tag{4.3}$$

If a given heat flux $\dot{Q}_F$ enters the system, maximum power availability will be observed when the negative right term is minimised. Since the RELT must deliver power, $\dot{H}_{t,out}$ cannot be zero[ii]. However, all energetic losses, represented in the cycle by $\dot{H}_{t,ex}$ and $\dot{Q}_C$

[i] Note that the fan of the turbofan is a low pressure ratio compressor which is an integral part of the engine.
[ii] That would imply zero mass flow passing through the turbine.

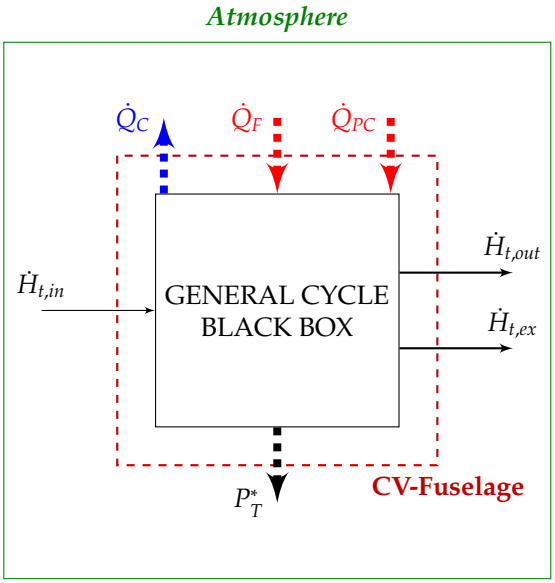

FIGURE 4.1. The general cycle.

should be removed. This means that the exhaust gases of the internal combustion engine should preferably be kept inside the system and "recycled" by the RELT. This is a very important conclusion, which will be pursued when developing the RELT-driving cycles. Additionally, the system should be well insulated in order to reduce the heat losses to the environment. Insulation is however, not an absolute necessity, since the gases flow through the system quickly and as a result, the heat losses are considered to be of negligible importance.

If one seeks a maximum efficiency for the cycle, one should optimise the thermal effectiveness of the system ϵ_{th} :

$$\epsilon_{th} = \frac{P_T^*}{\dot{Q}_F + \dot{Q}_{PC}} \tag{4.4}$$

Eq.4.4 explains that the heat input by combustion of fuel to obtain a given P_T^*-level should be kept as low as possible. Now substituting Eq.4.3 in the above equation gives :

$$\epsilon_{th} = \frac{(\dot{H}_{t,in} + \dot{Q}_F + \dot{Q}_{PC}) - (\dot{H}_{t,out} + \dot{H}_{t,ex} + \dot{Q}_C)}{\dot{Q}_F + \dot{Q}_{PC}} \tag{4.5}$$

Again, it is clear that the system should minimise its losses (avoid $\dot{H}_{t,ex}$ and $\dot{Q}_C$). Next, three cycles will be formulated and studied in detail, i.e. one cycle per type of engine.

4.3 Piston engine powered TDR cycle

4.3.1 Introduction to the piston engine

The piston engine (PE) is a low cost, low specific fuel consumption and low weight solution to deliver mechanical power in the lower power class range, i.e. around 300 kW and below (Torenbeek & Wittenberg (2009)). Several types of piston engines exist. The bulk of the piston engines used for aircraft propulsion are the Avgas-fed spark ignition engines (SPI). These are mainly – if not all – four-stroke engines, however, low-power EURO-95 (E95) fuelled two-stroke engines recently found their way to the VLR[iii]-market and became a promising cost-efficient solution for small aircraft. The Diesel engine is another technology that is gradually gaining importance in the piston engine market under the impetus of the greener technology requirements. Similar to the spark ignition engine, four- and two-stroke Diesel configurations are currently offered. Table 4.1 summarises some important performance characteristics concerning the above mentioned engine types.

Table 4.1. General piston engine characteristics : Maximum (continuous) power setting ISA SLS (Bosch (2007) and survey by author – Appendix H).

Type	**intake**†	**strokes**	**fuel admin.**	SPV **[kW/L]**	SPP **[kW/kg]**	SFC_{PE} **[g/kWh]**
SPI Avgas	atm.	4	carburetor injection	20 . . . 26	0.8 . . . 1.2	250 . . . 400
SPI Avgas	turbo	4	injection	21 . . . 27	0.8 . . . 1.3	250 . . . 400
SPI E95	atm.	2	injection	70 . . . 80	1.3 . . . 1.7	350 . . . 600
Diesel	turbo	4	injection	50 . . . 65	0.7 . . . 1.0	220 . . . 320
Diesel	turbo	2	injection	39 . . . 42	0.95 . . . 1.34	220 . . . 320

RPM range : 2400-2800 min^{-1} except for SPI E95 : 5200-6000 min^{-1}

†conditioning of air near intake manifold : atm. = atmospherically aspirated – turbo = turbocharger.

An important engine variable is the fuel-to-air ratio FAR, which is a function of engine regime, fuel and type, and represents the amount of fuel injected per unit of air admitted in the engine :

$$FAR = \frac{\dot{m}_{fuel}}{\dot{m}_{air}} \tag{4.6}$$

For a combustion process, a stoichiometric fuel-to-air ratio, i.e. FAR_{st}, can be determined. Usually, the fuel-to-air ratio differs from the stoichiometric one and the difference is

[iii] Very Light Rotorcraft ; Maximum gross weight is lower than 600 kg.

Table 4.2. FAR selected for cycle calculations. Maximum (continuous) regime (Bosch (2007)).

Engine type	ϕ **[-]**	$FAR_{st}[-]$	FAR **[-]**
Spark ignition engine (avgas)	1.5	1:14.7	1:9.8
Diesel engine (diesel)	0.7	1:14.5	1:20.7

reflected by the equivalence ratio ϕ (Table 4.2) :

$$\phi = \frac{FAR}{FAR_{st}} \tag{4.7}$$

For spark ignition engines, best efficiency is obtained for ϕ close to unity. Best performance on the other hand is achieved at values for ϕ up to 1.8 – Taylor (1985a). This concurs with an incomplete combustion, but increases the power output due to the higher mass contained in the cylinders. The current cycle calculations will use a conservative value for the equivalence ratio ϕ at maximum performance, viz. ϕ=1.5. For Diesel engines however, ϕ at maximum performance is close to 0.7 – Taylor (1985b). Even though lower than the stoichiometric limit, higher ϕ will lead to incomplete combustion and an unacceptable amount of smoke production. Note that for the cycle study one selects the piston engine on its maximum power output[iv]. This assures the smallest engine for the application, while bearing in mind that with an increase in helicopter horizontal speed, the power requirement of the rotors will initially drop by the decrease in induced power (power bucket), as described by for example Prouty (2002). This will lead to a lower ϕ, more specifically closer to unity in case of spark ignition engines, and results in better efficiency in forward flight.

The combustion process in the engine releases heat, which is quantified by the fuel mass flow $\dot{m}_f$ and the fuel lower heating value (LHV) – assuming the water produced during the combustion remains under gaseous form. Table 4.3 reflects the lower heating value for the most important aviation fuels. Note that the combustion process is not perfect. Since there is an important excess of air for the Diesel engine, the combustion efficiency η_{CC} will be assumed to be close to unity. For the spark ignition engines however, maximum performance is achieved while injecting more fuel than stoichiometrically possible. This means that a part of the fuel will not release heat, since it cannot react with oxygen and it needs to be accounted for in the energy balance. If the heat released by combustion is $\dot{Q}_F$, then :

$$\dot{Q}_F = \dot{m}_f \, \eta_{CC} \, LHV \tag{4.8}$$

[iv] This is typically also the maximum continuous regime.

or in case of an ideal stoichiometric combustion process :

$$\dot{Q}_F = \dot{m}_{f,st}\, LHV \tag{4.9}$$

An estimation of the combustion efficiency then follows from the substitution of Eq.4.9 in Eq.4.8, while neglecting the impact of the incomplete combustion on the lower heating value :

$$\eta_{CC} = \frac{1}{\phi} \tag{4.10}$$

The foregoing equation will be used in the simplified cycle calculations using spark ignition engines. With regard to the Diesel engine, the large excess air suggests a high combustion efficiency. For the subsequent considerations with the Diesel engine, it is assumed that – Jacques (2004b)

$$\eta_{CC} = 0.99 \tag{4.11}$$

Table 4.3. Fuel lower heating values (288.15 K).

Fuel type	*LHV* **[MJ/kg]**	**ref.**
Kerosene	43.2	AIR BP (2000)
Diesel	42.5	Bosch (2007)
Avgas	43.7	AIR BP (2000)

4.3.2 Piston engine powered TDR cycle set-up

The thermodynamic cycle wherein one piston engine drives the RELT is shown in Figs. 4.2 and 4.4. Air enters the system, which is an air-tight compartment in the fuselage (plenum), in which the pressure is increased by the compressor (C). A part of the air leaving the compressor, i.e. the primary flow $\dot{m}_p$, provides the piston engine with the correct amount of fresh air. In the piston engine, fuel is injected at a rate $\dot{m}_f$. The piston engine produces mechanical power necessary to drive the compressor and compensates any losses or power requirements of auxiliaries. Between the compressor and the piston engine, a reduction might be necessary. For this purpose, a gearbox (GBX) is placed between both components. The exhaust gases leave the piston engine and enter the mixer (MIX), where they are mixed with the remaining flow of the compressor, i.e. the secondary flow $\dot{m}_s$. Note that the engine is placed in the pressurised plenum. This operating condition is acceptable for a piston engine thanks to its robustness. It is assumed not to be the case for gas turbines. The shut-off-valve (SOV) disconnects the engine exhaust gas

path from the RELT, in case of an engine failure.

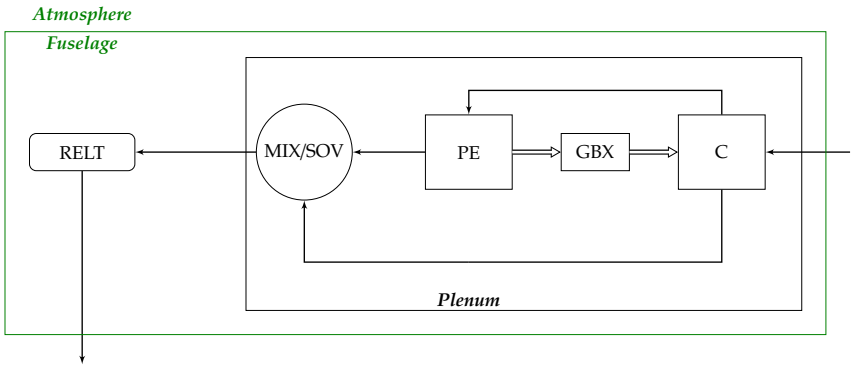

FIGURE 4.2. PE powered TDR cycle basics.

The piston engine powered TDR cycle will now be analysed using simplified laws of thermodynamics enabling a better understanding of its performance characteristics. Important performance and design parameters will be the specific fuel consumption *SFC*, the coefficient of performance *COP*, the bypass-ratio *BPR* and the limiting conditions to which the cycle is susceptible. These parameters are discussed next.

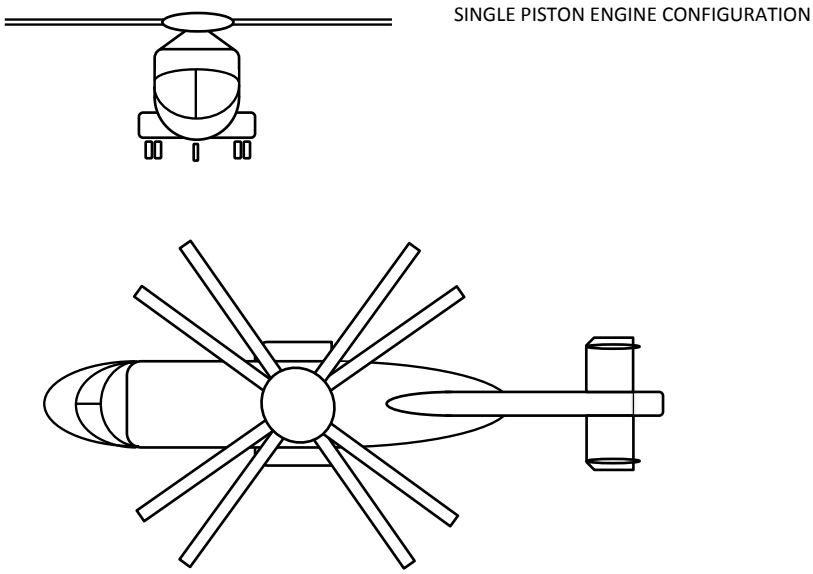

FIGURE 4.3. PE powered TDR helicopter (Illustrative purposes only).

4.3.3 Cycle study : Simplified theory

Cycle mass flows and power output

The power P_T^* delivered by the RELT can be found applying the first law of thermodynamics over the control volume $CV1$ (Fig.4.4) :

$$P_T^* = \dot{m}_t(h_{t45} - h_{t5}) \tag{4.12}$$

or also,

$$P_T^* = \dot{m}_t C_{pg}(T_{t45} - T_{t5}) \tag{4.13}$$

where,

→ $\dot{m}_t$ = Mass flow of combustion gases passing through the RELT [kg/s]

→ h_{t45} = Specific total enthalpy of the gases entering the RELT [J/kg]

→ h_{t5} = Specific total enthalpy of the gases leaving the RELT [J/kg]

→ C_{pg} = Specific heat at constant pressure of the combustion gases [J/kgK]

→ T_{t45} = Total temperature at RELT inlet ($LTIT$) [K]

→ T_{t5} = Total temperature at RELT outlet [K]

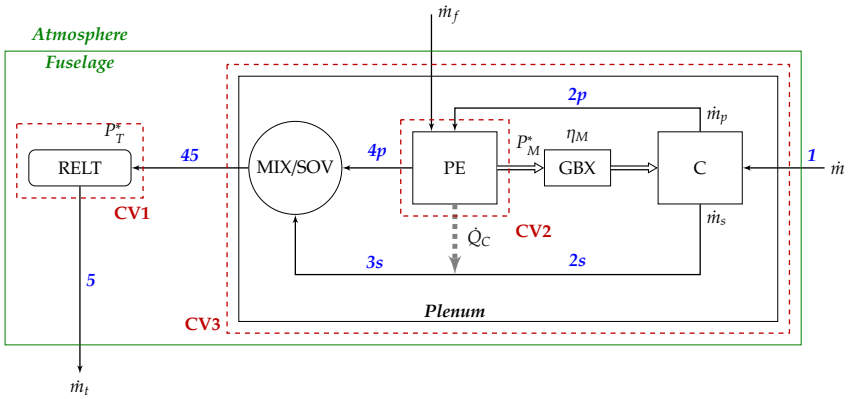

FIGURE 4.4. PE powered TDR cycle setup.

The temperature drop over the RELT depends on the realised expansion ratio and the efficiency at which this process takes place. For an adiabatic evolution (Eq.4.2) :

$$P_T^* = \dot{m}_t C_{pg} T_{t45}\left[1 - \left(\frac{1}{\pi_T}\right)^{\frac{\gamma_g - 1}{\gamma_g} \cdot \eta_{p,T}}\right] \tag{4.14}$$

where,

→ π_T = Total expansion ratio over the RELT [-]

→ γ_g = Ratio of specific heats for combustion gases [-]

→ $\eta_{p,T}$ = RELT polytropic efficiency [-]

A correct determination of π_T is only possible when having a detailed thermodynamic model of the RELT. For the current preliminary performance study, this level of detail is not required and it is assumed tacitly that the total compression ratio π_C of the compressor C equals the expansion ratio π_T over the RELT. Then, the mass flow $\dot{m}_t$ can be found for a given π_C, $LTIT$ and P_T^* by rewriting Eq.4.14 :

$$\dot{m}_t = \frac{P_T^*}{C_{pg} T_{t45} \left[1 - \left(\frac{1}{\pi_C} \right)^{\frac{\gamma_g - 1}{\gamma_g} \cdot \eta_{p,T}} \right]} \tag{4.15}$$

where π_C can now be denoted as the *cycle pressure ratio*. The fuel mass flow $\dot{m}_f$ on the other hand is calculable using control volume $CV3$ (Fig.4.4). Applying the first law and rearranging terms :

$$\dot{m}_f = \frac{(\dot{m} + \dot{m}_f) C_{pg} T_{t45} - \dot{m} C_p T_{t1}}{\eta_{CC} LHV} \tag{4.16}$$

where,

→ C_p the specific heat at constant pressure for air [J/kgK]

→ $\dot{m}$ = the mass flow of air entering the compressor [kg/s]

→ η_{CC} = the combustion efficiency [-]

Recall that the heat produced by burning fuel $\dot{Q}_F$ can be quantified using Eq.4.8 :

$$\dot{Q}_F = \eta_{CC} \dot{m}_f LHV$$

Usually $\dot{m}_f$ is a negligible quantity with respect to $\dot{m}$, yielding :

$$\dot{m}_t \approxeq \dot{m} \tag{4.17}$$

$$\dot{m}_f \approxeq \frac{\dot{m}(C_{pg} T_{t45} - C_p T_{t1})}{\eta_{CC} LHV} \tag{4.18}$$

The primary mass flow $\dot{m}_p$ follows from the definition of fuel-to-air ratio (Eq.4.6), which is assumed to be a constant for a given operating regime (see Table 4.2) :

$$\dot{m}_p = \frac{\dot{m}_f}{FAR} \tag{4.19}$$

Introducing Eq.4.19 in Eq.4.18, one obtains for $\dot{m}_p$:

$$\dot{m}_p = \frac{\dot{m}(C_{pg}T_{t45} - C_pT_{t1})}{\eta_{CC}LHV\ FAR} \tag{4.20}$$

Conservation of mass delivers the secondary mass flow $\dot{m}_s$:

$$\dot{m}_s = \dot{m}\left(1 - \frac{\dot{m}_p}{\dot{m}}\right) \tag{4.21}$$

Substituting Eq.4.20 in Eq.4.21 :

$$\dot{m}_s = \dot{m}\left(1 - \frac{C_{pg}T_{t45} - C_pT_{t1}}{\eta_{CC}LHV\ FAR}\right) \tag{4.22}$$

An important cycle design parameter is the bypass-ratio *BPR*, which is :

$$BPR \triangleq \frac{\dot{m}_s}{\dot{m}_p} \tag{4.23}$$

This factor influences the dimensions of the plenum, the mixer and tubing. Replacing $\dot{m}_p$ and $\dot{m}_s$ with their values found in respectively Eqs. 4.20 and 4.22 :

$$BPR = \frac{\eta_{CC}LHV\ FAR}{C_{pg}T_{t45} - C_pT_{t1}} - 1 \tag{4.24}$$

The above equation shows that for a fixed engine regime (*FAR*), *BPR* depends only on *LTIT* (T_{t45}) and the atmospheric temperature T_a, which is assumed equal to T_{t1}. This assumption is acceptable when the velocity of the aircraft remains below Mach 0.3, thus where the ram effects remain minor, which is true for the bulk of the contemporary helicopters. The tendency of a decrease in *BPR* with an increase of *LTIT* can be explained by the fact that a higher *LTIT* needs more fuel to heat up the gases per unit $\dot{m}$ (Eq.4.16). Consequently, since under the current evaluation criteria the fuel-to-air ratio is a constant, the piston engine is forced to ingest more $\dot{m}_p$ per unit $\dot{m}$ (Eq.4.20). The impact of the lower heating value on *BPR*, i.e. using Avgas or Diesel, remains minor because of the small difference between both values. However, the fuel-to-air ratio of a Diesel engine at maximum performance is significantly lower while its combustion efficiency higher than the one of spark ignition engines using Avgas because of the important difference in equivalence ratio ϕ (Table 4.2). Consequently, the Diesel engine will consume more primary air causing a lower *BPR* than observed with spark ignition engines, as shown in Fig.4.5.

At this point, it is interesting to introduce the non-dimensional *RELT* inlet temperature $\frac{T_{t45}}{T_{t1}}$, which is an important parameter when determining the performance of the cycle.

Introducing this variable in Eq.4.24 :

$$BPR = \frac{\eta_{CC} LHV\ FAR}{C_p T_{t1}\left(\frac{C_{pg}}{C_p}\frac{T_{t45}}{T_{t1}} - 1\right)} - 1 \tag{4.25}$$

Here, the effect of a variable atmosphere (T_{t1}) on the bypass ratio becomes clear, but it will be examined separately and discussed later in Section 4.3.5. Note that selecting a bypass ratio alone is not sufficient to fix a value for P_T^*, since it has no authority on π_C. In reality, for a given bypass ratio, an operating range will be offered, depending on the specific fuel consumption of the piston engine (see also Table 4.1). A more detailed examination of the operating domain of the cycle follows at the end of this section.

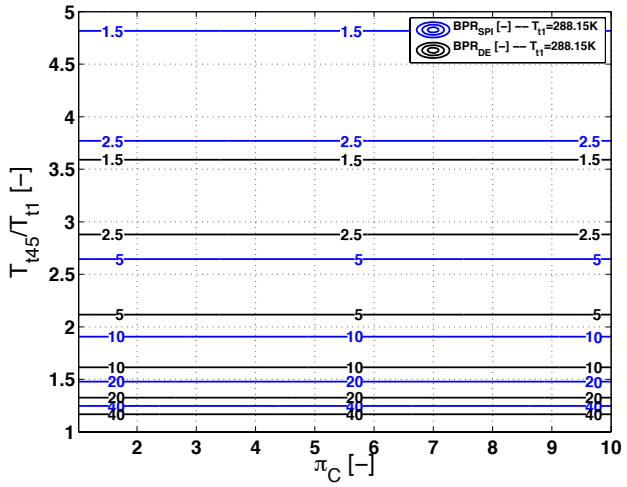

Figure 4.5. Bypass ratio as a function of $\frac{T_{t45}}{T_{t1}}$, ISA SLS, no losses (except combustion related). Note that π_C has no influence on *BPR*.

Cycle specific fuel consumption

The specific fuel consumption *SFC* of the cycle is defined as :

$$SFC \triangleq \frac{\dot{m}_f}{P_T^*} \tag{4.26}$$

Multiplying numerator and denominator by $\dot{m}$ and using Eq.4.18 and Eq.4.15, where in the latter it is assumed that $\dot{m}_t \cong \dot{m}$:

$$SFC = \frac{1 - \frac{C_p}{C_{pg}}\frac{T_{t1}}{T_{t45}}}{\eta_{CC} LHV\left[1 - \left(\frac{1}{\pi_C}\right)^{\frac{\gamma_g - 1}{\gamma_g}\cdot\eta_{p,T}}\right]} \tag{4.27}$$

In the above equation, the non-dimensional RELT inlet temperature $\frac{T_{t45}}{T_{t1}}$ and cycle pressure ratio π_C appear. To attain the best possible specific fuel consumption, the cycle pressure ratio should be selected high, as it increases the turbine power density $P_T^*/\dot{m}$. The turbine power density increases also for an increase in $\frac{T_{t45}}{T_{t1}}$, but this beneficial impact is outweighed by the higher fuel flow fraction, which causes a more influential *SFC*. $\frac{T_{t45}}{T_{t1}}$ should therefore be selected as low as possible. Fig.4.6 reflects the cycle *SFC* for respectively Avgas and Diesel. The difference in cycle specific fuel consumption between both engine types is due to the substantially lower combustion efficiency of the spark ignition engine when operated at maximum power regime.

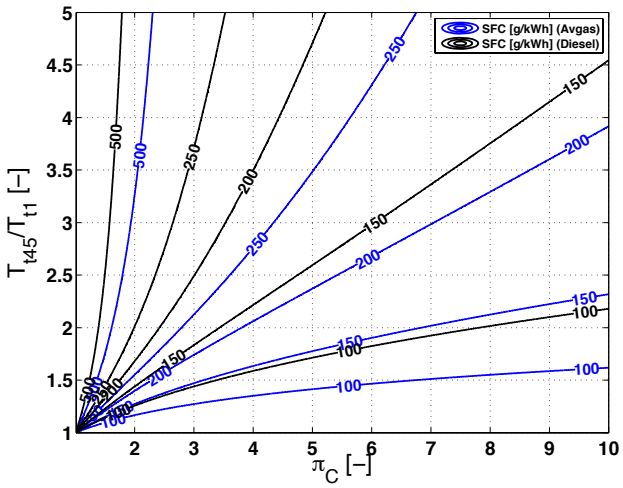

FIGURE 4.6. Specific fuel consumption as a function of $\frac{T_{t45}}{T_{t1}}$ and π_C, ISA SLS, no losses (except combustion related).

Cycle coefficient of performance

The power necessary to compress the air flow $\dot{m}$ can be found according to the first law of thermodynamics, assuming once more an adiabatic evolution :

$$P_C = \dot{m}\,(h_{t2} - h_{t1}) \tag{4.28}$$

$$P_C = \dot{m}\,C_p(T_{t2} - T_{t1}) \tag{4.29}$$

For a given compressor polytropic efficiency, the above equation can be rewritten as :

$$P_C = \dot{m}\,C_p T_{t1}\left(\pi_C^{\frac{\gamma-1}{\gamma}\frac{1}{\eta_{p,C}}} - 1\right) \tag{4.30}$$

The piston engine must deliver this power P_C, increased with the mechanical losses in the interconnecting drive train (for example gearbox(es), bearings, etc.) and the power consumed by auxiliaries (pumps, generators, etc.). The mechanical efficiency η_M represents

these losses :

$$P_M^* = \frac{P_C}{\eta_M} \tag{4.31}$$

Since there is no mechanical link between the piston engine and the RELT, it is incorrect to consider P_M^* equal to P_T^*. A performance yardstick to quantify the difference between both is the coefficient of performance *COP*, which is defined as :

$$COP = \frac{P_T^*}{P_M^*} \tag{4.32}$$

A high coefficient of performance should be strived for as it reflects the capability of the cycle to transfer the mechanical power delivered by the internal combustion engine to the helicopter rotors. Substituting Eq.4.14 and Eq.4.30 into Eq.4.32 :

$$COP = \eta_M \frac{C_{pg}}{C_p} \frac{T_{t45}}{T_{t1}} f_{COP}(\pi_C) \tag{4.33}$$

where the function $f_{COP}(\pi_C)$ is :

$$f_{COP}(\pi_C) = \frac{1 - \left(\frac{1}{\pi_C}\right)^{\frac{\gamma_g - 1}{\gamma_g}\eta_{p,T}}}{\pi_C^{\frac{\gamma-1}{\gamma}\frac{1}{\eta_{p,C}}} - 1} \tag{4.34}$$

For fixed polytropic efficiencies, this is a decreasing function with π_C. Again, note that *COP* relies on the non-dimensional variables $\frac{T_{t45}}{T_{t1}}$ and π_C. Fig.4.7 shows the evolution of *COP* as a function of these two parameters[v]. Clearly *COP* improves with an increase in $\frac{T_{t45}}{T_{t1}}$ and with decreasing π_C. The former because of the higher turbine power density $P_T^*/\dot{m}$, the latter due to the required compressor power, which becomes less important than the power delivered by the turbine. The optimum operating point will thus be a compromise between *COP* and *SFC*.

Note the potential to have a *COP* larger than unity exists. The recovery of the piston engine exhaust gases in the cycle allows this effect to take place. Comparing this with the conventional helicopter, one would retrieve paradoxically a "mechanical efficiency" higher than unity.

[v]The difference between the coefficient of performances of the Avgas en the Diesel engine powered TDR cycles is due to simplified calculation of C_{pg}, which is slightly higher for the Diesel engine.

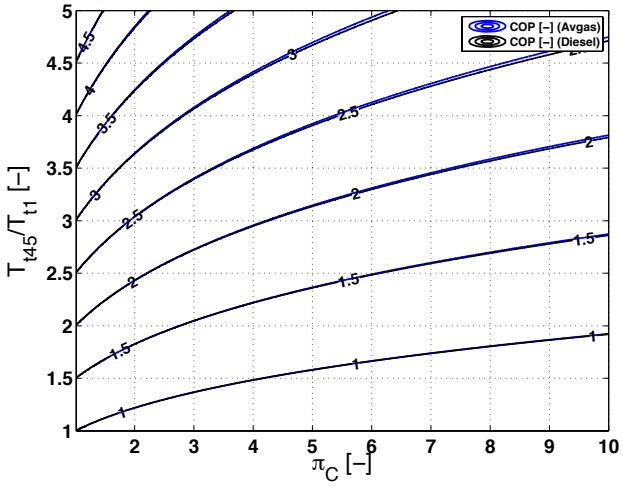

Figure 4.7. Coefficient of performance as a function of $\frac{T_{t45}}{T_{t1}}$ and π_C, ISA SLS, no losses (except combustion losses).

Relation between *SFC* and *COP*

Relying on the definitions of cycle specific fuel consumption (Eq.4.26) and coefficient of performance (Eq.4.32), it is possible to write :

$$COP \cdot SFC = \frac{P_T^*}{P_M^*} \cdot \frac{\dot{m}_f}{P_T^*} = \frac{\dot{m}_f}{P_M^*} \tag{4.35}$$

The right term in the foregoing equation is the specific fuel consumption of the internal combustion engine, or :

$$COP = \frac{SFC_{PE}}{SFC} \tag{4.36}$$

This equation is very useful. It reveals that the cycle will be at least as fuel efficient as the installed internal combustion engine when $COP \geq 1$. As a consequence, *COP* presents also how good the engine specific fuel consumption is transferred to the cycle.

Compressor and turbine polytropic efficiencies

A high turbine polytropic efficiency results in a better cycle specific fuel consumption (Eq.4.27) and coefficient of performance (Eq.4.33 and Eq.4.34). This is normal as it influences the RELT power output directly and only. For a given P_T^*, it will influence the required mass flow. In case the efficiency decreases, the cycle will have to process a higher mass flow for a given $\frac{T_{t45}}{T_{t1}}$ and π_C. Besides the increased size of the system, a more powerful and thus more fuel consuming engine will need to be installed.

The compressor polytropic efficiency is not always explicitly present in the above stated

equations, making the detection of its influence on the cycle parameters less straightforward. While an increase in compressor polytropic efficiency yields a better coefficient of performance, it appears to have no influence at all on the cycle specific fuel consumption, bypass ratio or mass flow. However, this is quite misleading as it does impact the required characteristics of the installed piston engine. Indeed, in case the compressor efficiency drops for a given $\frac{T_{t45}}{T_{t1}}$ and π_C, the engine will have to deliver more power per unit mass flow (Eq.4.30) to produce the same pressure ratio. At the same time, the turbine inlet temperature is not allowed to change ($\frac{T_{t45}}{T_{t1}} = C^t$). As a consequence, the specific fuel consumption of the piston engine SFC_{PE} has to decrease because the fuel flow fraction does not change (Eq.4.18), or, in other words, a more efficient piston engine will need to be installed. The relationship between *SFC* and *COP* was already discussed via Eq.4.36. The benefits of this increase in piston engine efficiency by the lower SFC_{PE} is in fact completely destroyed by the reduced compressor polytropic efficiency (lower *COP*). Clearly, an as high as possible compressor efficiency should therefore be strived for.

Mechanical efficiency

A similar discussion can be conducted to explain the effect of the mechanical efficiency η_M on the cycle parameters.

Effect of pre-compression

According to Taylor (1985b), the available power P^*_M of a piston engine is mainly a function of and commensurate with air density. In the examined cycle, the compressor feeds the piston engine and works as a turbocharger. Consequently :

$$P^*_M \approxeq \frac{\rho_{t2}}{\rho_a} P^*_{M,a} \tag{4.37}$$

or, neglecting the compressibility effects ($\rho_{ta} \approxeq \rho_a$) :

$$P^*_M = \frac{\rho_{t2}}{\rho_{t1}} \frac{p_{t1}}{p_{ta}} P^*_{M,a} \tag{4.38}$$

where,

- $\rightarrow$ $P^*_{M,a}$ = PE available power under atmospheric conditions [W]
- $\rightarrow$ ρ_{ta} = (Atmospheric) air density [kg/m^3]
- $\rightarrow$ ρ_{t1} = Total density of air entering the compressor [kg/m^3]
- $\rightarrow$ ρ_{t2} = Total density of air leaving the compressor [kg/m^3]

Defining the ram recovery *RR* as a measure for the inlet losses and ram effects :

$$RR \triangleq \frac{p_{t1}}{p_{ta}} \leq 1 \tag{4.39}$$

After substitution of Eq.4.39 in Eq.4.38 :

$$P^*_M = RR \frac{\rho_{t2}}{\rho_{t1}} P^*_{M,a} \tag{4.40}$$

The density ratio $\frac{\rho_{t2}}{\rho_{t1}}$ can be quantified as :

$$\frac{\rho_{t2}}{\rho_{t1}} = \pi_C^{\frac{1-\gamma}{\gamma}\frac{1}{\eta_{p,C}}+1} \tag{4.41}$$

Introducing Eq.4.41 in Eq.4.40 yields :

$$P^*_M = PCF\, P^*_{M,a} \tag{4.42}$$

defining *PCF* as the pre-compression factor :

$$PCF \triangleq RR\, \pi_C^{\frac{1-\gamma}{\gamma}\frac{1}{\eta_{p,C}}+1} \tag{4.43}$$

Fig.4.8 clearly shows that for an adiabatic compression and a given $P^*_{M,a}$, P^*_M will increase almost linearly with π_C. The fact that the piston engine inlet temperature $T_{t2(p)}$ increases simultaneously with π_C does not necessarily compromise the engine's operational domain. The cylinder head temperature may remain well within specifications as the combustion process is intermittent, thus less susceptible to the higher combustion temperatures. Nevertheless, a good temperature monitoring will be indispensable and will undoubtedly impose boundaries on the maximum value of π_C. In Chapter 8, the cycle pressure ratio will be shown to be low. Consequently, it is reasonable to expect that the integration of an unmodified piston engine is then feasible. Also note that the crankshaft must withstand the higher torque delivered by the engine.

Because of pre-compression, selecting a piston engine based on P^*_M is à priori not advisable, because in general $PCF > 1$ and consequently $P^*_M > P^*_{M,a}$. Indeed, $P^*_{M,a}$ should be the selection criterion for a piston engine, which is readily provided by the engine manufacturer for standard day sea level conditions. Hence, thanks to pre-compression, a lighter engine can be installed.
If P^*_T is known to the designer, an equivalent coefficient of performance (ECOP) should be used to select the required piston engine, i.e. :

$$ECOP \triangleq \frac{P^*_T}{P^*_{M,a}} = PCF \cdot COP \tag{4.44}$$

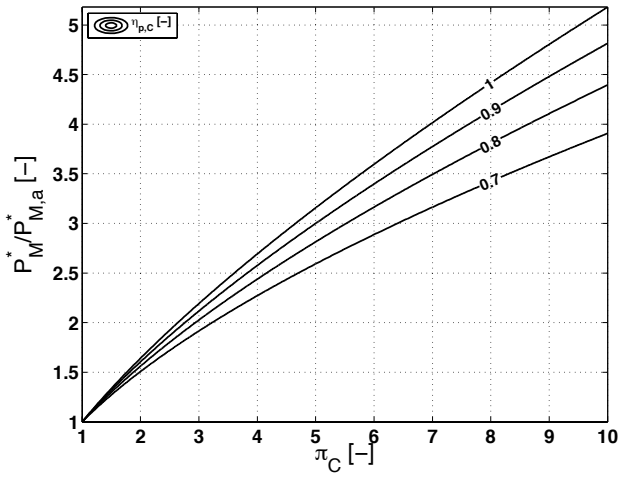

FIGURE 4.8. Influence of π_C and $\eta_{p,C}$ on PE power output.

4.3.4 Cycle operating boundaries

The cycle of which the major performance parameters were examined in the previous section, has not yet been evaluated on its pertinence. Indeed, some boundaries will be imposed by thermodynamical constraints or by operational limitations from components placed in the cycle, such as the piston engine. This is examined next.

Cycle Carnot effectiveness

From a thermodynamic point of view, the cycle effectiveness can never be larger than the cycle effectiveness of Carnot. The cycle effectiveness of Carnot applies to reversible closed cycles only. However, even though investigating an open system, one could imagine the recovery of the gases escaping the RELT and reintroducing them in the system after being brought to the initial state. Since the fuel mass flow is low with respect to the mass flow passing through the studied system, the impact of the combustion process on the gas composition may be seen as minor. Hence, the open system can be closed by simply connecting the outlet of the RELT with the inlet of the compressor via a heat exchanger. Indeed, this is necessary. The Kelvin-Planck law states that no net work can be delivered by a cycle using heat from a single heat reservoir. In the open system, heat is only extracted from the fictitious heat reservoir representing the combustion process at a temperature T_H. As a consequence, the excess thermal power that needs to be evacuated from the system, leaves via the enthalpic flux. In the fictitious heat exchanger, this thermal power is yielded to the surroundings, which is the atmosphere at temperature T_L. As a consequence, the cycle effectiveness must obey the following relation :

$$\epsilon_{th} \leq 1 - \frac{T_L}{T_H} = \epsilon_{Carnot} \tag{4.45}$$

and,

$$\epsilon_{th} = \frac{P^*_T}{\dot{Q}_F} \tag{4.46}$$

where,

→ ϵ_{th} = Cycle thermal effectiveness [-]

→ T_L = Temperature of the cold heat source [K]

→ T_H = Temperature of the hot heat source [K]

For the subsequent boundary calculations, Eq.4.46 will be substituted in Eq.4.45, but this implies a simplification that needs to be exposed prior to continuing the discussions. The Carnot effectiveness applies to all *closed* reversible cycles. Heat is hereby exchanged isothermally between the boundaries of the cycle and the heat sources. When closing an open system and the Carnot effectiveness is strived for, it must also be completely reversible. Since the exhaust gases are usually not at the same temperature of the environment even though at the same pressure, they can only be restored reversibly to the initial state temperature by a sequence of two thermodynamic evolutions. First, an isentropic expansion or compression is required to convert the outlet temperature to the initial state temperature. Second, an isothermal heat exchange brings the gases to the initial pressure, as could be shown on a T-s diagram, commonly used in thermodynamic textbooks. With these two processes, work is involved. Denoting this work as P_R, then it is only possible to achieve the Carnot effectiveness in the reversible closed system, if the open cycle and the system closing the open cycle are reversible. In other words :

$$\frac{P^*_{T,rev} + P_R}{\dot{Q}_F} = \epsilon_{Carnot} \tag{4.47}$$

In the real process however, the work potential of the exhaust gases is not recovered and results in pure entropy production, or $P_R = 0$. As a consequence, $\epsilon_{th} < \epsilon_{Carnot}$. Hence, calculating the cycle boundaries by imposing $\epsilon_{th} = \epsilon_{Carnot}$ is not very accurate since it implicitly uses an irreversible method to restore the exhaust gases, i.e. a heat exhanger, wherein no work is generated or absorbed. This issue can be coped with by establishing the exergy balance over the open system – Çengel & Boles (2006). However, when applied to the discussed thermodynamic cycles, the solution can become too involved for the purpose it serves and analytical solutions not always possible. Since the operating boundaries of the components used in the cycle will be shown to be most critical, the cycle Carnot boundary criteria can be relaxed. As a consequence, to find the cycle boundaries, it will be assumed that :

$$\epsilon_{th} \cong \epsilon_{Carnot} \tag{4.48}$$

With respect to the lower bound temperature T_L, it is equal to the atmospheric temperature T_a. The choice of the temperature of the hot heat source on the other hand, is not evident. Considering the maximum temperature to be the adiabatic flame temperature, i.e. around 2500 K (Torenbeek & Wittenberg (2009)), the maximum cycle efficiency should be lower than 0.885 at sea level ISA conditions. This is still a high value, but it allows removing the thermodynamically impossible solutions from the evaluated performance domain.

Piston engine cycle limitations

Besides the interaction of the cycle with the atmosphere, the heat balance between the piston engine and the plenum in which it is installed, needs examination. Since a simplified thermodynamical representation of the piston engine cycle is adopted in the system, its operating domain must be traced too.
From the control volume $CV2$ in Fig.4.4, it is possible to understand the power balance in effect over the piston engine. Heat enters the piston engine cycle from the combustion of fuel ($\dot{Q}_F$ via $\dot{m}_f$) and delivers mechanical power to the surroundings P^*_M, i.e. the plenum, while a part of the thermal energy is lost via the piston engine cooling system ($\dot{Q}_C$) and another part via the enthalpy leaving the engine by the exhaust gases. The thermal efficiency of the cycle can again be calculated by closing the open system in $CV2$ by means of a fictitious heat exchanger, which brings the gases back to the initial state via a fictitious heat flux $\dot{Q}_2$ (not indicated on $CV2$). Since the piston engine works in the plenum, the initial state is represented by the outlet conditions of the compressor. In case the pressure losses are neglected and the speed of the flow considered low, it is then possible to write for the cycle effectiveness :

$$\epsilon_{th,PE} = \frac{P^*_M}{\dot{Q}_F} = \frac{\dot{Q}_F - \dot{Q}_C - \dot{Q}_2}{\dot{Q}_F} \cong 1 - \left[\frac{\dot{Q}_C + \dot{m}_p\, C_p(T_{t4p} - T_{t2})}{\dot{Q}_F}\right] \tag{4.49}$$

The cooling heat flux $\dot{Q}_C$ can be presented as a fraction of the heat introduced in the system. Defining the cooling fraction x_c :

$$x_c \triangleq \frac{\dot{Q}_C}{\dot{Q}_F} \tag{4.50}$$

Substitution of the previous equation in Eq.4.49 and imposing again the piston engine cycle Carnot effectiveness, which implies the simplification discussed in the previous section, yields :

$$\epsilon_{th,PE} = 1 - \left[x_c + \frac{\dot{m}_p\, C_p(T_{t4p} - T_{t2})}{\dot{Q}_F}\right] \leq 1 - \frac{T_{t2}}{T_H} \tag{4.51}$$

T_H is once more considered to be the adiabatic flame temperature, for which the value of 2500 K is adopted. Elaborating the foregoing equation results in a minimum piston

engine exhaust gas temperature $T_{t4p_{BD}}$ required for the cycle to be physically possible :

$$T_{t4p} \geq T_{t4p_{BD}} = \left(\frac{T_{t2}}{T_H} - x_c\right)\frac{\dot{Q}_F}{\dot{m}_p\, C_p} + T_{t2} \tag{4.52}$$

The piston engine exhaust gas temperature T_{t4p} can be estimated by applying the first law on control volume $CV2$, while neglecting the fuel mass flow :

$$\dot{m}_p C_p T_{t2} + \dot{Q}_F - P_M^* - \dot{m}_p C_{pg} T_{t4p} - \dot{Q}_C = 0 \tag{4.53}$$

and,

$$T_{t2} = T_{t1}\pi_C^{\frac{\gamma-1}{\gamma}\frac{1}{\eta_{p,C}}} \tag{4.54}$$

then after substitution of Eq.4.8 and Eq.4.54 in Eq.4.53 and rearranging terms, its is found that :

$$T_{t4p} = \frac{C_p}{C_{pg}} T_{t1}\left[\pi_C^{\frac{\gamma-1}{\gamma}\frac{1}{\eta_{p,C}}}\left(1 - \frac{1+BPR}{\eta_M}\right) + \frac{1+BPR}{\eta_M}\right] + \frac{(1-x_c)\eta_{CC} LHV \cdot FAR}{C_{pg}} \tag{4.55}$$

At the same time, $T_{t4p_{BD}}$ can be expressed as a cycle pressure ratio limitation. Starting from Eq.4.49 and the definition of the cycle Carnot effectiveness, it is possible to write :

$$1 - \frac{P_M^*}{\dot{Q}_F} \geq \frac{T_{t2}}{T_H} \tag{4.56}$$

Substitution of Eq.4.8, Eq.4.30 and Eq.4.54 in this equation and rearranging terms gives :

$$\pi_C \leq \pi_{C_{BD}} = \frac{\left[1 + \frac{(1+BPR)\; C_p T_{t1}}{\eta_M\; \eta_{CC}\; FAR\; LHV}\right]^{\frac{\gamma}{\gamma-1}\eta_{p,C}}}{\left[\frac{(1+BPR)\; C_p T_{t1}}{\eta_M\; \eta_{CC}\; FAR\; LHV} + \frac{T_{t1}}{T_H}\right]^{\frac{\gamma}{\gamma-1}\eta_{p,C}}} \tag{4.57}$$

$\pi_{C_{BD}}$ is only a function of $\frac{T_{t45}}{T_{t1}}$ and T_{t1} (Eq.4.25). The other values are considered to be constant for the selected operating regime.

Taylor (1985b) estimates the cooling fraction and is usually found in the order of magnitude of 35%. The heat released by the radiator $\dot{Q}_C$ is absorbed by the secondary flow before entering the mixer. Note that there exists a maximum heat transfer $\dot{Q}_C$ allowable between the piston engine and the secondary flow. The walls of the piston engine (radiator) and the secondary flow work as a heat exchanger. The magnitude of the exchanged heat depends on the maximum temperature gradient in effect over the heat exchanger and the flow/material conditions on both sides. However, since the used value for the cooling fraction is realistic, this limiting condition is not further studied.

Available power boundary

The available power $P^*_{M,a}$ at sea level (standard day) for a piston engine ranges between 50 kW to 300 kW. For higher power requirements in aviation, the piston engine is replaced with a turboshaft, since it has a better power density – Torenbeek & Wittenberg (2009). Note however that pre-compression now extends the operating domain of the piston engine. Nevertheless, the market offers a limited range of piston engine solutions, which in turn restricts the usability of the examined cycle.

Piston engine SFC boundaries

Neglecting the effects of pressure on the fuel distribution and combustion processes, Taylor (1985b) explains that for a given engine regime SFC_{PE} remains fairly insensitive to pressure and temperature variations, so that it may be considered as constant. Recall that (Eq.4.35) :

$$SFC_{PE} = \frac{\dot{m}_f}{P^*_M} \tag{4.58}$$

For Diesel engines, Taylor (1985b) notes that the operational domain may be reduced at lower pressures due to a compromised combustion process, more specifically imposed by the smoke limit. Fortunately, this issue is postponed thanks to the pre-compression process.

Seen that SFC_{PE} is pressure and temperature independent, it is reasonable to expect the pre-compression process to have a negligible impact on this parameter too. As a consequence SFC_{PE} in the cycle will be set equal to the value given for the selected engine regime at standard day conditions, sea level.

However, SFC_{PE} in the cycle still depends on the selected piston engine, as highlighted in Table 4.1. The cycle is indeed delimited by the variety of SFC_{PE} found within the available piston engine population for the required power P^*_M. Once a piston engine is selected, SFC_{PE} is fixed in the cycle and the cycle pressure becomes dependent on the selected non-dimensional turbine inlet temperature, or vice versa. Proof is given by substituting Eq.4.58 and Eq.4.18 in Eq.4.30. Rearranging terms yields :

$$\pi_C = \left(\eta_M \frac{\frac{C_{pg}}{C_p}\frac{T_{t45}}{T_{t1}} - 1}{SFC_{PE}\eta_{CC}LHV} + 1\right)^{\frac{\gamma\eta_{p,C}}{\gamma-1}} \tag{4.59}$$

For a given SFC_{PE}, π_C becomes indeed completely dependent on $\frac{T_{t45}}{T_{t1}}$.

LTIT boundary

The maximum allowable $LTIT$ depends on the maximum operating temperature of the bearings. Especially when using grease lubrication, $LTIT$ should not exceed 400 K.

4.3.5 Effect of the atmospheric pressure and temperature

The nominal cycle operating conditions depend on the imposed design flight conditions. The previous theoretic developments showed the importance of the non-dimensional turbine inlet temperature $\frac{T_{t45}}{T_{t1}}$. The cycle characteristics will thus depend on the selected turbine inlet temperature (T_{t45}) at nominal operation and the selected altitude (T_{t1}). The evolution of atmospheric pressure p_a and temperature T_a with altitude is standardised in aviation and is adopted in the International Standard Atmosphere (ISA). At sea level static (SLS), the standard pressure is 1 atm and the standard temperature 288.15 K. These values are often used to reduce p_a and T_a to non-dimensional values :

$$\theta_a = \frac{T_a}{288.15\ \text{K}} \qquad [\text{-}] \tag{4.60}$$

$$\delta_a = \frac{p_a}{101325\ \text{Pa}} \qquad [\text{-}] \tag{4.61}$$

Additionally, a non-dimensional density is defined :

$$\sigma_a = \frac{\rho_a}{1.225} \tag{4.62}$$

Without major loss in accuracy one may prove that for the considered inlet conditions – AIAA (2003) and Cumpsty (2000) :

$$\theta_a \cong \theta_{t1} = \frac{T_{t1}}{288.15} \tag{4.63}$$

$$RR\ \delta_a \cong \delta_{t1} = \frac{p_{t1}}{101325} \tag{4.64}$$

$$RR\ \sigma_a \cong \sigma_{t1} = \frac{\rho_{t1}}{1.225} \tag{4.65}$$

These parameters are useful to study the influence of a variable atmosphere on the performance characteristics of the cycle. Note also that :

$$\sigma_{t1} = \frac{\delta_{t1}}{\theta_{t1}} \tag{4.66}$$

In the subsequent analysis, the impact of a changing atmosphere on the most important cycle parameters is examined, using sea level conditions as datum and imposing a fixed value for the cycle independent non-dimensional parameters $\frac{T_{t45}}{T_{t1}}$ and π_C. Finally, it will be proven that the cycle operating condition at sea level cannot be extrapolated to other atmospherical conditions, without changing one of the independent cycle parameters.

Piston engine power output

As explained earlier when discussing the pre-compression, the power output of the piston engine is a function of air density near the intake manifold :

$$P^*_{M,a,corr} = \frac{P^*_{M,a}}{\sigma_{ta}} \tag{4.67}$$

where the suffix "corr" stands for the corrected value of the examined parameter, i.e. the value found at ISA SLS, when operated under invariable non-dimensional (engine) cycle conditions, amongst which the cycle pressure ratio and the non-dimensional RELT inlet temperatur. $P^*_{M,a,corr}$ is usually given by the piston engine manufacturer. From Eq.4.67, the effect of air density on the engine power output is observed easily. A decrease in air density will result in a proportional deterioration of engine power. The same reasoning applies with pre-compression (Eq.4.37 and π_C is constant) :

$$P^*_{M,corr} = \frac{P^*_M}{\sigma_{t1}} \tag{4.68}$$

Piston engine specific fuel consumption

As explained during the discussion of the piston engine SFC boundaries in Section 4.3.4, SFC_{PE} remains fairly insensitive to temperature and pressure variations. Consequently, this yields an immediate result for the corrected SFC_{PE} :

$$SFC_{PE,corr} = SFC_{PE} = SFC_{PE,a} \tag{4.69}$$

Bypass ratio

Recalling Eq.4.25 :

$$BPR = \frac{\eta_{CC} LHV \cdot FAR}{C_p T_{t1}\left(\frac{C_{pg}}{C_p}\frac{T_{t45}}{T_{t1}} - 1\right)} - 1$$

Substitution of the non-dimensional temperature θ_{t1} into the above equation and after some manipulation :

$$\frac{BPR + 1}{BPR_{corr} + 1} = \frac{1}{\theta_{t1}} \tag{4.70}$$

or,

$$BPR_{corr} = (BPR + 1)\theta_{t1} - 1 \tag{4.71}$$

Eq.4.71 has been plotted in Fig.4.9. From this graph it is clear that for a given $\frac{T_{t45}}{T_{t1}}$ and being given a certain BPR_{corr}, BPR is inversely proportional to the atmospheric temperature.

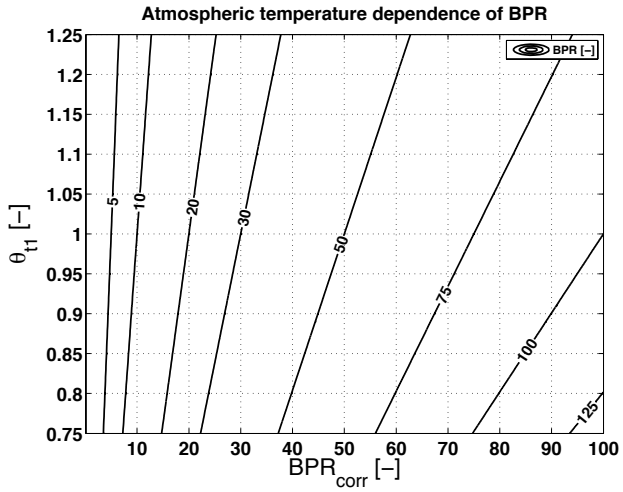

FIGURE 4.9. Impact of atmospheric temperature on BPR for fixed $\frac{T_{t45}}{T_{t1}}$, no losses.

Cycle specific fuel consumption and coefficient of performance

Examination of Eq.4.27 and Eq.4.33 shows SFC and COP to be independent of atmospheric temperature and pressure variations in case a fixed π_C and $\frac{T_{t45}}{T_{t1}}$ are selected. As a consequence :

$$COP_{corr} = COP \tag{4.72}$$

$$SFC_{corr} = SFC \tag{4.73}$$

Primary mass flow and fuel flow

The fuel mass flow $\dot{m}_f$ is commensurate with air density since :

$$\dot{m}_f = SFC_{PE}\, P^*_M \tag{4.74}$$

or,

$$\dot{m}_f = \sigma_{t1} SFC_{PE,corr}\, P^*_{M,corr} \tag{4.75}$$

Hence, the corrected fuel mass flow becomes :

$$\dot{m}_{f,corr} = \frac{\dot{m}_f}{\sigma_{t1}} \tag{4.76}$$

Since the equivalence ratio ϕ remains invariable for a selected engine regime, FAR is constant also, which yields for the primary mass flow $\dot{m}_p$:

$$\dot{m}_{p,corr} = \frac{\dot{m}_p}{\sigma_{t1}} \tag{4.77}$$

Cycle total mass flow

The total mass flow $\dot{m}$ passing through the turbine, and compressor when neglecting the impact of the fuel mass flow, is according to Eq.4.18 and after rearranging terms :

$$\dot{m} = \frac{SFC_{PE} LHV \eta_{CC}}{C_p \left(\frac{C_{pg}}{C_p} \frac{T_{t45}}{T_{t1}} - 1 \right)} \frac{P^*_M}{T_{t1}} \tag{4.78}$$

Introducing the non-dimensional atmospheric variables gives :

$$\dot{m} = \frac{\delta_{t1}}{\theta^2_{t1}} \frac{SFC_{PE,corr} LHV \eta_{CC}}{C_p \left(\frac{C_{pg}}{C_p} \frac{T_{t45}}{T_{t1}} - 1 \right)} \frac{P^*_{M,corr}}{288.15} \tag{4.79}$$

The corrected total mass flow then becomes :

$$\dot{m}_{corr} = \frac{\dot{m} \theta^2_{t1}}{\delta_{t1}} = \frac{\dot{m} \theta_{t1}}{\sigma_{t1}} \tag{4.80}$$

Clearly, $\dot{m}$ is much more sensitive to atmospheric temperature variations than $\dot{m}_p$ and $\dot{m}_f$. The latter mass flows depend directly and only on the power delivered by the engine, which is density dependent (σ_{t1}). $\dot{m}$ on the other hand relies on the required temperature increase established in the cycle, i.e. $T_{t45} - T_{t1}$, and the fuel mass flow, as explained by Eq.4.18. An increase in atmospheric temperature will decrease the power output of the engine and thus $\dot{m}_f$ via σ_{t1} (Eq.4.68 and Eq.4.76), which in turn reduces the heat input by the combustion process. As a consequence, this effect must be compensated by a reduction in $\dot{m}$ (σ_{t1} term in Eq.4.80).
At the same time, for a constant non-dimensional inlet temperature $\frac{T_{t45}}{T_{t1}}$, the interval $T_{t45} - T_{t1}$ must *increase*. Then, the only manner to attain the required turbine inlet temperature is by decreasing $\dot{m}$ even more via θ_{t1} (Eq.4.80). Note that this effect was already uncovered by the bypass ratio θ_{t1} dependency discussed earlier. Both effects combined, explains the higher sensitivity of $\dot{m}$ to atmospheric temperature fluctuations, which results in the quadratic behaviour of $\dot{m}$ with θ_{t1}.

Until now, only the influence of δ_{t1} and θ_{t1} on the more important cycle parameters was studied, while assuming constant $\frac{T_{t45}}{T_{t1}}$ and π_C, which are seen as independent variables. However, when submitting the complete cycle to a new atmospheric condition, it is no longer possible to operate the cycle under the same operating conditions. The reason originates from the difference between the corrected total mass flow $\dot{m}_{corr}$ (Eq.4.80) and the corrected mass flow found for a compressor or fan, which is used to determine its pressure and efficiency characteristics, and defined as $\dot{m}_{C,corr}$, – Cumpsty (2000) :

$$\dot{m}_{C,corr} = \frac{\dot{m} \sqrt{\theta_{t1}}}{\delta_{t1}} \tag{4.81}$$

Both corrected flows are based on $\dot{m}$ and must remain identical, regardless the atmospheric conditions, if a constant cycle/compressor pressure ratio and compressor efficiency is required. Since :

$$P_{C,corr} = \frac{P_C}{\delta_{t1}\sqrt{\theta_{t1}}} \tag{4.82}$$

$$P^*_{M,corr} = \frac{P^*_M \delta_{t1}}{\theta_{t1}} \tag{4.83}$$

and,

$$P_C = P^*_M \eta_M \tag{4.84}$$

it is found for all but one operating point :

$$P_{C,corr} \neq P^*_{M,corr} \eta_M \tag{4.85}$$

In other words, a simple extrapolation of the cycle performance characteristics observed under ISA SLS using δ_{t1} and θ_{t1} to estimate the performance parameters at other atmospheric conditions is not allowed, unless variable compressor characteristics are taken into account.

4.3.6 Parametric cycle study

The cycle performance is now evaluated parametrically using the non-dimensional input variables π_C and $\frac{T_{t45}}{T_{t1}}$. The impact of the other cycle parameters such as the efficiencies and atmospheric conditions on the cycle performance was already discussed qualitatively in the previous sections, and will not be repeated here. The study assesses two cycle configurations, viz. one with a 4-stroke Avgas engine and one with a 2-stroke Diesel engine. These engines will be used in Chapter 8, where the Ljungström turbine characteristics are integrated in the cycle study. In the current discussion, the turbine efficiency is considered invariable. The other cycle parameters are reflected in Table 4.4.

The results are shown in Fig.4.10 and Fig.4.11, representing the non-dimensional cycle performance characteristics of respectively the Avgas and the Diesel powered cycles at ISA SLS.
The cycle boundaries are indicated on the graphs, where the grey lines represent the range of SFC_{PE} wherein a solution is possible and the red (full) line the maximum cycle pressure ratio $\pi_{C_{BD}}$ for a given inlet temperature (Eq.4.57). For reasons of readability, the cycle Carnot limitation is not plotted. In all considered cases, it is less stringent than the piston engine cycle limitation represented via $\pi_{C_{BD}}$.
Since the cycle is examined at ISA SLS conditions, it is possible to indicate the *LTIT* limit of 400 K on the graph (dashed red line). Note that the position of this boundary on the

graph depends on the atmospheric temperature.

Table 4.4. Cycle variable value summary.

Variable		note
$\eta_{p,T}$	0.87 [-]	Chapter 8
$\eta_{p,C}$	0.90 [-]	Van den Braembussche (2013)
$\eta_{CC,SPI}$	0.67 [-]	Eq.4.10
$\eta_{CC,Diesel}$	0.99 [-]	Eq.4.11
η_M	0.98 [-]	assumed
γ	1.40 [-]	air
γ_g	1.33 . . . 1.4 [-]	interpolation between air and combustion gases
R_g	287.05 [J/kgK]	specific gas constant air and combustion gases
x_c	0.35 [-]	Taylor (1985b)
RR	0.99 [-]	assumed

For both the Avgas and Diesel engine powered TDR cycles, Fig.4.10 and Fig.4.11 confirm the behaviour of the assessed cycle parameters, which were defined and discussed while developing the simplified theory. It is recalled and substantiated by the figures that *COP* improves when a lower π_C and higher $\frac{T_{t45}}{T_{t1}}$ is selected, while the opposite is true for *SFC*. However, the figures clearly show that the ability to choose π_C and $\frac{T_{t45}}{T_{t1}}$ freely is deceptive. Indeed, once a piston engine is selected, SFC_{PE} is fixed. The selection of the engine and its SFC_{PE} may depend entirely on the availability of an engine to provide the cycle with the required mechanical power P^*_M. Then, $\frac{T_{t45}}{T_{t1}}$ becomes of function of π_C, as was already demonstrated by Eq.4.59. When this restriction is introduced, the figures reveal that *COP* and *SFC* improve with an increase in cycle pressure ratio. As a consequence, an as high as possible turbine inlet temperature should be strived for.
Unfortunately, the turbine inlet temperature is confined to the maximum operating temperature of the rotor bearings. Fig.4.10 and Fig.4.11 then clearly show that the cycle pressure ratio is well below 2 for both engine types. From a practical point of view, this is encouraging as it limits the pre-compression, which decreases the weight of the pressurised plenum on the one hand, and makes the use of a unmodified off-the-shelf piston engine more plausible. From a performance point of view, *COP* is lower than unity but still higher than 90%. This means that the cycle will produce less power in the turbine than what is generated mechanically by the piston engine and consume more fuel. Nevertheless, the power dissipation in the tail rotor and transmission system in the conventional helicopter is not longer present in the TDR helicopter. A lower *COP* is therefore not necessarily an indication that the cycle is outperformed by the conventional helicopter. This is a discussion performed in Chapter 8, where it will be shown not to be the case.

Comparing the Avgas and the Diesel engine powered configurations, it is possible to observe that the Diesel engine powered TDR cycle works in a narrower SFC_{PE} operating domain for a given $\frac{T_{t45}}{T_{t1}}$ than the Avgas engine powered TDR cycle, which guarantees neither the same π_C nor COP in the cycle. The following questions may then be formulated in case the turbine generates in each cycle an identical amount of power at a fixed non-dimensional turbine inlet temperature $\frac{T_{t45}}{T_{t1}}$:

1. Which cycle is the most fuel efficient ?
2. Which cycle requires the highest $P^*_{M,a}$ and thus has the heaviest engine ?

The difference in fuel consumption between the Diesel and the spark ignition engine for a given P^*_T can be expressed in relative terms, i.e. :

$$\frac{\dot{m}_{f,D}}{\dot{m}_{f,A}} = \frac{SFC_{PE,D}P^*_{M,D}}{SFC_{PE,A}P^*_{M,A}} \tag{4.86}$$

where the suffixes D and A represent respectively the Diesel and Avgas (spark ignition) piston engine. Introducing the definition of COP (Eq.4.36) and keeping P^*_T constant :

$$\frac{\dot{m}_{f,D}}{\dot{m}_{f,A}} = \frac{SFC_{PE,D}COP_A}{SFC_{PE,A}COP_D} \tag{4.87}$$

Substituting Eq.4.33 and imposing a constant $\frac{T_{t45}}{T_{t1}}$ for both engine types :

$$\frac{\dot{m}_{f,D}}{\dot{m}_{f,A}} = \frac{SFC_{PE,D}}{f_{COP,D}}\frac{f_{COP,A}}{SFC_{PE,A}} \tag{4.88}$$

Although $\frac{f_{COP}}{SFC_{PE}}$ is a function of π_C, it was proven earlier that π_C becomes a pure function of $\frac{T_{t45}}{T_{t1}}$ when a fixed value for SFC_{PE} is imposed (Eq.4.59). Consequently, the same conclusion applies on $\frac{f_{COP}}{SFC_{PE}}$. Fig.4.12 shows $\frac{f_{COP}}{SFC_{PE}}$ and f_{COP} as a function of $\frac{T_{t45}}{T_{t1}}$ and SFC_{PE} for both engine types, while assuming unity for the values of the polytropic efficiencies $\eta_{p,C}$ and $\eta_{p,T}$[vi]. Clearly, when $SFC_{PE,D} \leq SFC_{PE,A}$, $\frac{f_{COP,D}}{SFC_{PE,D}} > \frac{f_{COP,A}}{SFC_{PE,A}}$. If $LTIT$ and P^*_T are imposed, the more efficient engine, in this case *the Diesel engine, always consumes less fuel*. This answers the first question.

Since f_{COP} is a declining function with π_C, Fig.4.12 then shows that for a given SFC_{PE}, the Diesel engine powered TDR cycle will operate at a lower π_C[vii]. Earlier, it was discussed that the coefficient of performance of the cycle improves with reduced π_C. Consequently the Diesel powered cycle produces more turbine power per unit of mechanical power delivered by the engine[viii]. However, this mechanical power P^*_M is a function of pre-

[vi] Even if other values are taken for the polytropic efficiencies, the conclusions will remain identical.

[vii] Another approach to prove this might be via Eq.4.59, which shows that a decrease in η_{CC} results in a higher π_C for a given SFC_{PE}. Indeed, since $\dot{m}_f$ increases, the engine will generate more power, which is entirely compensated by the higher required cycle pressure ratio.

[viii] Note that since P^*_T is constant, $P^*_{M,A} > P^*_{M,D}$ since $COP_D > COP_A$.

compression and the installed power $P_{M,a}$. The difference in installed power now is :

$$\frac{P^*_{M,a,D}}{P^*_{M,a,A}} = \frac{PCF_A}{PCF_D}\frac{COP_A}{COP_D} = \frac{PCF_A}{PCF_D}\frac{f_{COP,A}}{f_{COP,D}} \tag{4.89}$$

or (Eq.4.44),

$$\frac{P^*_{M,a,D}}{P^*_{M,a,A}} = \frac{ECOP_A}{ECOP_D} \tag{4.90}$$

Eq.4.90 is shown in Fig.4.13. If both engines have similar SFC_{PE}, the Diesel engine powered TDR cycle will have a lower π_C (see f_{COP}) and therefore a higher coefficient of performance but a smaller pre-compression factor than the Avgas engine powered TDR cycle. The combined result causes the Diesel engine to have a lower *ECOP* for the same turbine power output. Consequently, *a more powerful and heavier Diesel engine is demanded*, which answers the second question. Though, it was proven earlier via Eq.4.88 that this does not necessarily occurs with a higher fuel consumption. At this point, the piston engine specific power density (*SPP*) – thus engine mass – as indicated in Table 4.1 becomes important. For a given P^*_T, the designer will have to find the best combination between a low SFC_{PE}, where the diesel piston engine has the advantage, and the specific power density, where the Avgas piston engine has the potential to perform better.

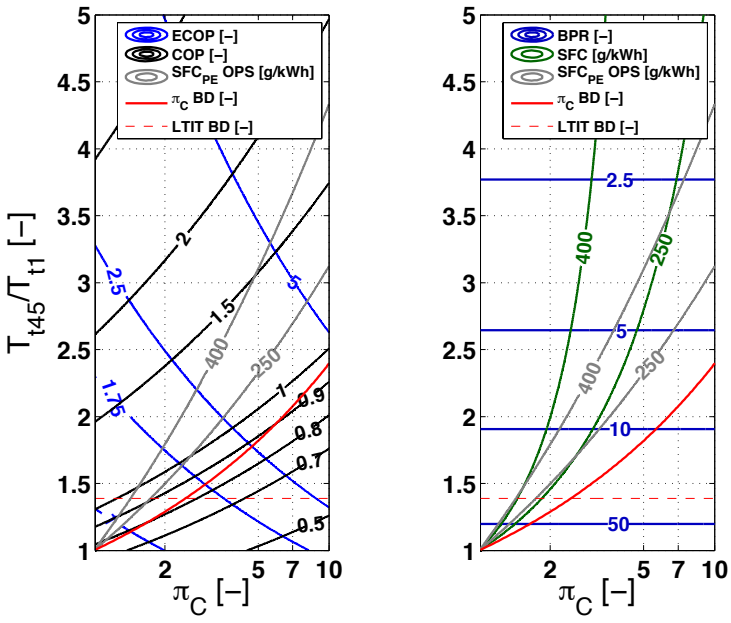

FIGURE 4.10. Avgas engine powered TDR cycle characteristics, conditions Table 4.4, ISA SLS.

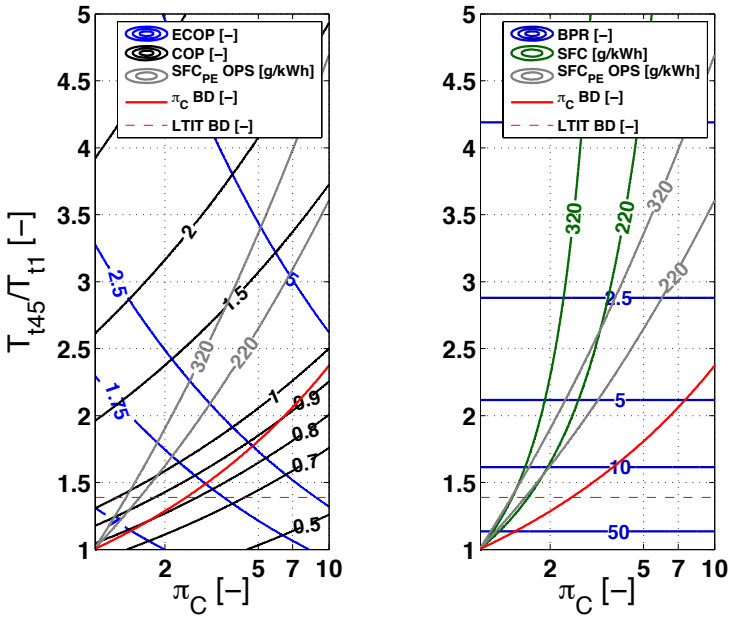

FIGURE 4.11. Diesel engine powered TDR cycle characteristics, conditions Table 4.4, ISA SLS.

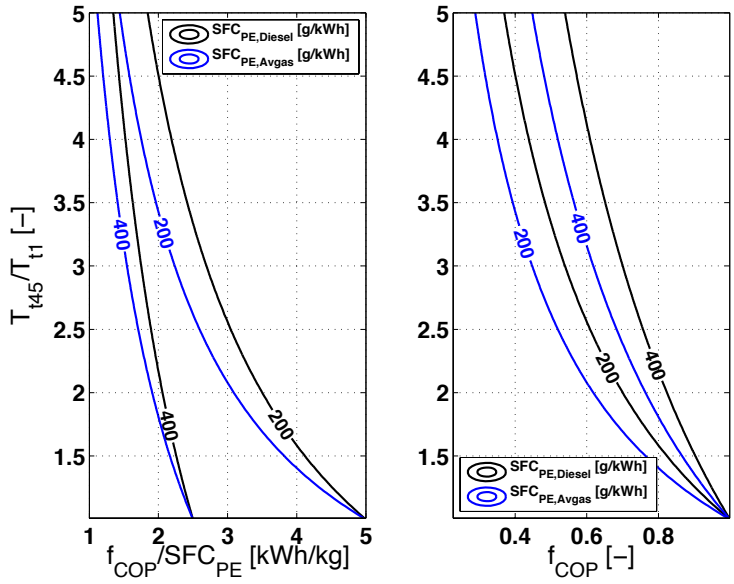

FIGURE 4.12. $\frac{f_{COP}}{SFC_{PE}}$ and f_{COP} as a function of $\frac{T_{t45}}{T_{t1}}$ and SFC_{PE} ($\eta_{p,C} = \eta_{p,T} = 1$).

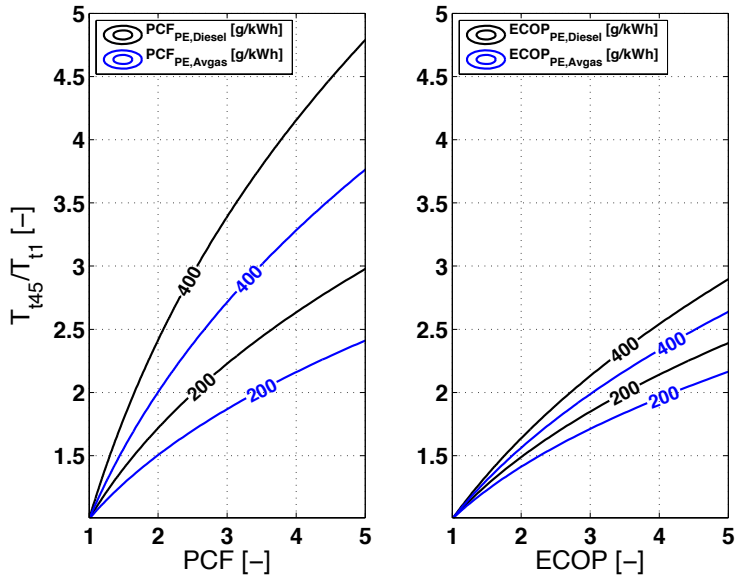

FIGURE 4.13. *PCF* and *ECOP* as a function of $\frac{T_{t45}}{T_{t1}}$ and SFC_{PE} ($\eta_{p,C} = \eta_{p,T} = 1$).

4.4 Turboshaft engine powered TDR cycle

4.4.1 Introduction to the turboshaft engine

The turboshaft engine (TS) is a gas turbine designed to deliver mechanical power at a superior power-to-weight ratio than the piston engine for the larger power demands (typically larger than 300 kW – Torenbeek & Wittenberg (2009)). It allowed the development of high performing and/or large helicopters. Besides a higher power-to-weight ratio, the turboshaft vibrates less and is more reliable than a piston engine in the considered power category. In aviation, most turboshafts turn on kerosene. This type of fuel is less flammable than Avgas and also cheaper. Table 4.5 reflects some typical characteristics of the turboshaft engine. The discussion of the turboshaft powered TDR cycle follows next.

Table 4.5. General turboshaft characteristics : Maximum continuous power setting.

fuel type		kerosene based derivatives
LHV [MJ/kg] kerosene	43.2	AIR BP (2000)
SPP [kW/kg]	2.2 . . . 8.0	survey by author – Appendix H
SFC_{TS} [g/kWh]	270 . . . 450	survey by author – Appendix H

4.4.2 Turboshaft engine powered TDR cycle set-up

Figure 4.14 shows the cycle wherein a turboshaft (TS) drives a compressor (C), which provides the RELT with pressurised air. In between the RELT and the compressor, a heat exchanger (HEX) and a shut-off valve (SOV) are included, the latter protecting the RELT in case of an engine or a compressor failure. The heat exchanger recovers a part of the thermal energy of the exhaust gases leaving the turboshaft. If desirable, gearboxes may allow the turboshaft to be located away from the compressor air inlet for practical reasons and/or enable a rotational velocity reduction between the output shaft of the turboshaft and the drive shaft of the compressor. From the general cycle it was learned that it is advantageous to recover as much heat as possible in the system in order to improve its performance. In the piston engine powered TDR cycle, thermal energy was recovered by mixing the exhaust gases with the secondary flow leaving the compressor. However, this requires the engine to work in a pressurised environment (i.e. in the plenum), which is prohibited in case of a turboshaft. This is the reason for the installation of the heat exchanger. The turboshaft is indeed less robust than the piston engine and is designed to work under atmospheric conditions, i.e. moderate pressures and temperatures which are not much higher than those observed on a standard day at sea level, not to say below. This means that if a significant temperature rise exists due to the pre-compression process, the

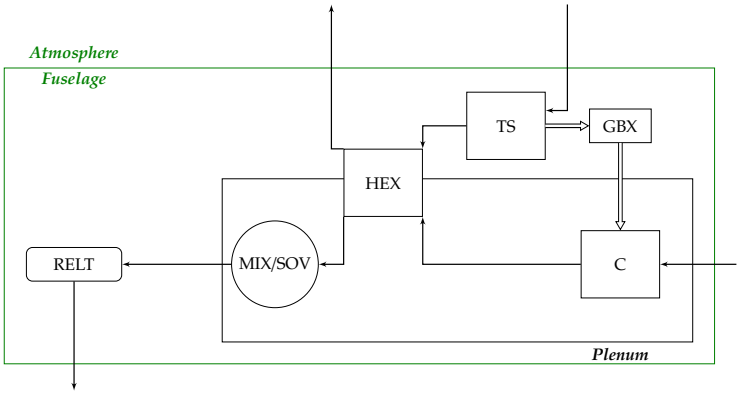

FIGURE 4.14. TS powered TDR cycle - one engine, basics.

air should need to be conditioned before entering the turboshaft by means of, for example, an additional heat exchanger[ix] in front of the turboshaft inlet, at least, if a maximum power output is pursued – Buysschaert & Hendrick (2004). Also, a pressure rise increases the mechanical power on the shafts connecting the engine compressors with their respective turbines. In order to maintain the required safety margins while pursuing the maximum potential of the engine, design interventions seem unavoidable of which the costs are assumed unacceptable. Unless the TDR helicopter concept breaches the monopoly of the conventional helicopter, it seems currently more reasonable to let the turboshaft operate in an environment for which it was designed. An additional advantage of this layout is that a second (or third) engine may be added in the cycle, without compromising safety when one engine fails. Indeed, the engines are physically disconnected from the RELT. The SOV now serves to disengage the inoperative part in case of an engine or compressor failure, guaranteeing the overpressure in the plenum.

4.4.3 Cycle study : Simplified theory

Cycle power output

The power delivered by RELT to the rotors P_T^* is quantified by an adiabatic expansion of which the total pressure expansion over the turbine π_T is assumed to be equal to the compressor total pressure ratio π_C. This combined with the first law of thermodynamics and applied on control volume $CV1$, the following relation is established (Fig.4.16) :

$$P_T^* = \dot{m} C_p T_{t45} \left[1 - \left(\frac{1}{\pi_C} \right)^{\frac{\gamma-1}{\gamma} \eta_{p,T}} \right] \tag{4.91}$$

Note that γ and C_p of air are used since no combustion gases pass through the RELT. Likewise, $\dot{m}_t = \dot{m}$.

[ix] This corresponds with the introduction of $\dot{Q}_C$ in the general cycle, which results in a reduction of the cycle's performance potential.

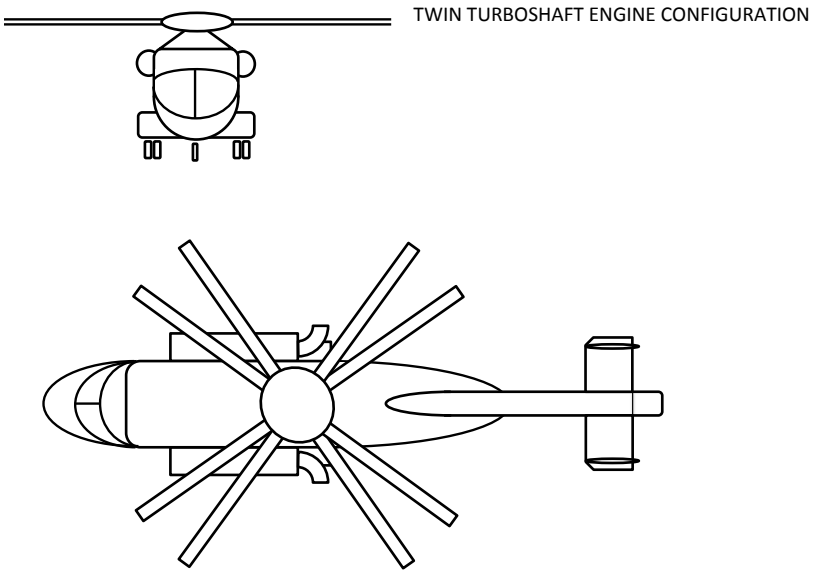

FIGURE 4.15. Twin-TS powered TDR helicopter (Illustrative purposes only).

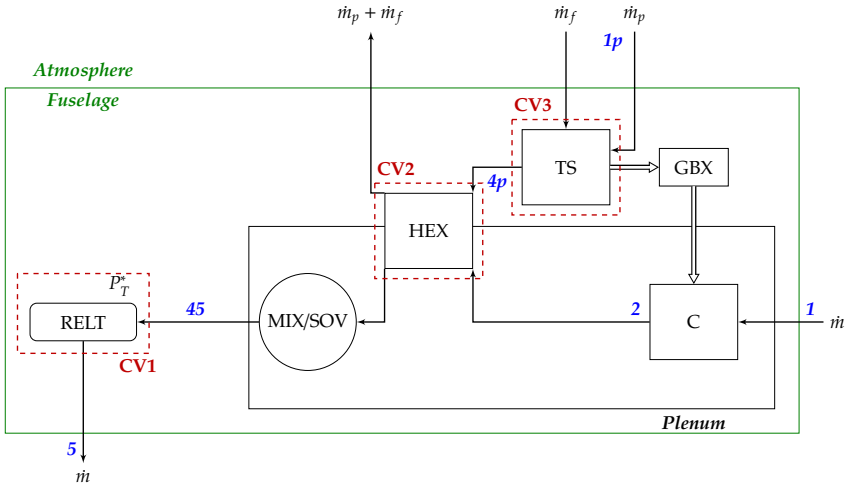

FIGURE 4.16. TS powered TDR cycle setup.

Cycle specific fuel consumption

The cycle specific fuel consumption is defined as :

$$SFC \triangleq \frac{\dot{m}_f}{P_T^*} \tag{4.92}$$

Table 4.6. Turboshaft specific fuel consumption $SFC^{\star}_{TS}$.

$SFC_{TS} = a\ {P^*_M}^{-b}$ [g/kWh][kW]	a	b	
Maximum take-off rating ISA SLS	970.5	0.161	(Eq.8.27)
Maximum continuous rating ISA SLS	1093.1	0.179	(Fig.4.17)

⋆ Values for a single turboshaft.

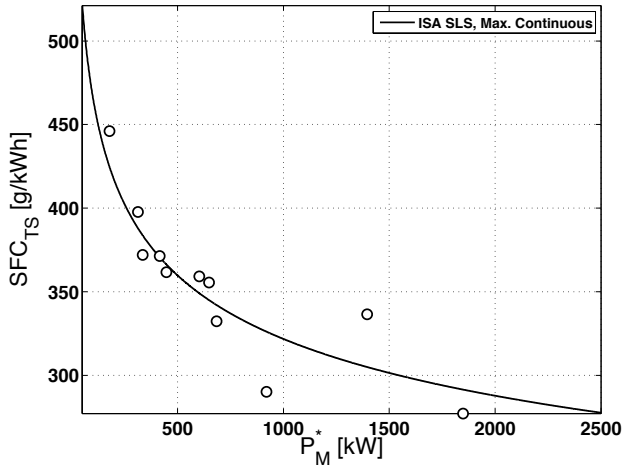

Figure 4.17. SFC_{TS} as a function of turboshaft engine power P^*_M at maximum continuous regime, ISA SLS (Author survey).

The specific fuel consumption of the engine SFC_{TS} is :

$$SFC_{TS} \triangleq \frac{\dot{m}_f}{P^*_M} \tag{4.93}$$

A survey performed by the author (Appendix H) shows that SFC_{TS} is a decreasing function of P^*_M approximated by :

$$SFC_{TS} = a\ {P^*_M}^{-b} \tag{4.94}$$

Values for a and b are summarised in Table 4.6[x]. Substituting Eq.4.91 and Eq.4.93 in Eq.4.92 :

$$SFC = \frac{SFC_{TS} P^*_M}{\dot{m} C_p T_{t45} \left[1 - \left(\frac{1}{\pi_C}\right)^{\frac{\gamma-1}{\gamma}\eta_{p,T}}\right]} \tag{4.95}$$

[x]In Chapter 8 it will be shown that establishing a similar correlation for piston engines is discouraged due to the low correlation of the data. However, here, and similar to the piston engine, the correlation helps determining the turboshaft SFC_{TS} operating range.

If the mechanical transmission efficiency is η_M, the delivered power is also :

$$P_M^* = \frac{\dot{m} C_p T_{t1} (\pi_C^{\frac{\gamma-1}{\gamma}\frac{1}{\eta_{p,C}}} - 1)}{\eta_M} \tag{4.96}$$

Finally, introducing Eq.4.96 in Eq.4.95 :

$$SFC = SFC_{TS} \cdot \frac{f_{SFC}(\pi_C)}{\eta_M \frac{T_{t45}}{T_{t1}}} \tag{4.97}$$

where,

$$f_{SFC}(\pi_C) = \frac{\pi_C^{\frac{\gamma-1}{\gamma}\frac{1}{\eta_{p,C}}} - 1}{1 - \left(\frac{1}{\pi_C}\right)^{\frac{\gamma-1}{\gamma}\eta_{p,T}}} = \frac{1}{f_{COP}(\pi_C)} \tag{4.98}$$

which is an increasing function with π_C (Fig.4.18). Again two non-dimensional performance parameters appear : $\frac{T_{t45}}{T_{t1}}$ and π_C. From Eq.4.98, one may deduce that the cycle *SFC* improves when a low π_C, a high *LTIT* and/or low T_{t1} is selected. *SFC* increases by selecting higher π_C because the specific power requirement of the compressor grows faster than the specific power output of the RELT at the same inlet temperature (i.e. $f_{SFC}(\pi_C)$). If $\frac{T_{t45}}{T_{t1}}$ in Eq.4.97 increases solely, *SFC* will improve by the increased turbine power density (Eq.4.91).

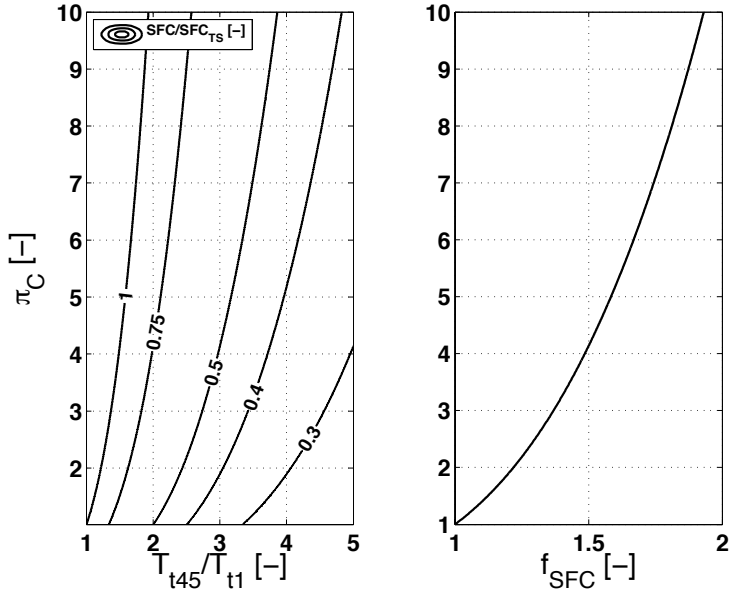

Figure 4.18. Relative cycle *SFC* and f_{SFC}-function – no losses (except TS).

Effects of multiple engines

The effect of multiple engines on the performance of the cycle can be introduced in the above considerations by imposing the following modifications :

→ for the mechanical power delivered by the engines in the cycle P^*_M :

$$P^*_M = N_e \cdot P^*_{M,1-TS} \tag{4.99}$$

→ for the function calculating the specific fuel consumption as a function of P^*_M :

$$SFC_{TS}(P^*_M) = SFC_{1-TS}\left(\frac{P^*_M}{N_e}\right) \tag{4.100}$$

→ for the specific power density function of the engine, $SPP \triangleq \frac{P^*_M}{m_{TS}}$, with m_{TS} the mass of the engine :

$$SPP_{TS}(P^*_M) = SPP_{1-TS}\left(\frac{P^*_M}{N_e}\right) \tag{4.101}$$

Cycle coefficient of performance

The definition of *COP* is identical to the one used for the piston engine powered TDR cycle. For convenience, Eq.4.32 is retaken :

$$COP = \frac{P^*_T}{P^*_M}$$

Substituting Eq.4.91 and Eq.4.96 into Eq.4.32, one finds :

$$COP = \eta_M \frac{T_{t45}}{T_{t1}} f_{COP}(\pi_C) \tag{4.102}$$

where the function $f_{COP}(\pi_C)$ is equal to Eq.4.34 (except that γ_g is replaced with γ) :

$$f_{COP}(\pi_C) = \frac{1 - \left(\frac{1}{\pi_C}\right)^{\frac{\gamma-1}{\gamma}\eta_{p,T}}}{\pi_C^{\frac{\gamma-1}{\gamma}\frac{1}{\eta_{p,C}}} - 1}$$

Again, f_{COP} is a decreasing function with π_C. Note the reappearance of the non-dimensional variables $\frac{T_{t45}}{T_{t1}}$ and π_C. *COP* improves when selecting a low π_C and high *LTIT* or low T_{t1} for the same reasons explained during the cycle *SFC* discussion. Fig.4.19 confirms the discussed behaviour. Finally, note that a similar simple relation between

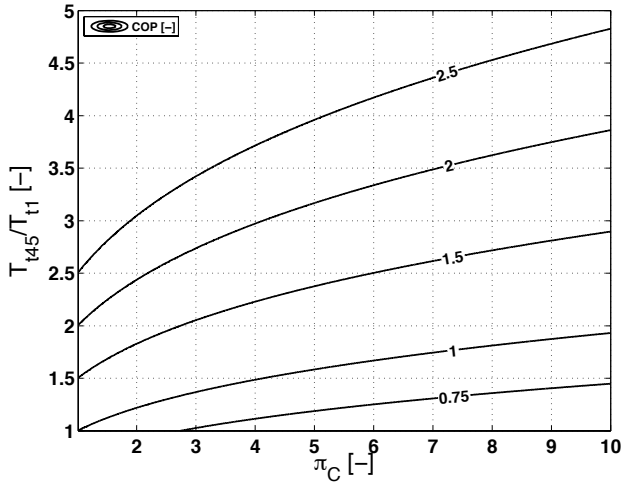

FIGURE 4.19. Cycle *COP* as a function of π_C and $\frac{T_{t45}}{T_{t1}}$ – no losses (except TS).

COP and *SFC* exists as found in Eq.4.36 :

$$COP = \frac{SFC_{TS}}{SFC} \tag{4.103}$$

A *COP* larger than unity means a cycle which is more fuel efficient than the installed turboshaft, while producing more turbine power than generated by the turboshaft.

Cycle mass flows

Three mass flows are defined in the system :

→ mass flow of air passing through the pressurised system, or secondary flow : $\dot{m}$=$\dot{m}_t$

→ mass flow of air entering the turboshaft, or primary flow : $\dot{m}_p$

→ fuel mass flow feeding the turboshaft : $\dot{m}_f$

They are all related to each other via the turboshaft characteristics. Firstly, for a given P^*_M, SFC_{TS} is found (Eq.4.94) and consequently $\dot{m}_f$. Then, the fuel-to-air ratio of the turboshaft allows retrieving $\dot{m}_p$ via $\dot{m}_f$:

$$\dot{m}_p = \frac{\dot{m}_f}{FAR} \tag{4.104}$$

Even though *FAR* is a function of the selected engine regime, it is practical to use a fixed value for *FAR* for the simplified cycle calculations. For the calculations at hand, as suggested by Jacques (2004b), *FAR* is set to 1:60. As a result, the secondary flow is

(Eq.4.96) :

$$\dot{m} = \frac{\eta_M P_M^*}{C_p T_{t1}(\pi_C^{\frac{\gamma-1}{\gamma}\frac{1}{\eta_{p,C}}} - 1)} \tag{4.105}$$

Although trivial, Eq.4.105 allows the calculation of $\dot{m}$ for a given P_M^*, π_C and temperature T_{t1}. $\dot{m}_f$ and $\dot{m}_p$ depend also on P_M^* (Eq.4.93 and Eq.4.104), which proves the interrelationship between the mass flows. Next, one defines the bypass ratio BPR as :

$$BPR = \frac{\dot{m}}{\dot{m}_p} \tag{4.106}$$

Substituting Eq.4.93 in Eq.4.104 gives :

$$\dot{m}_p = \frac{SFC_{TS} P_M^*}{FAR} \tag{4.107}$$

Introducing this result with Eq.4.105 in Eq.4.106, one finds for BPR :

$$BPR = \frac{\eta_M FAR}{SFC_{TS} C_p T_{t1}(\pi_C^{\frac{\gamma-1}{\gamma}\frac{1}{\eta_{p,C}}} - 1)} \tag{4.108}$$

BPR decreases by an increase in π_C and T_{t1}, and becomes higher when installing more P_M^*. Indeed, for a given P_M^* and thus $\dot{m}_f$ and $\dot{m}_p$, increasing π_C or T_{t1} will require more work per unit mass in the compressor. Since P_M^* is fixed, $\dot{m}$ must be smaller and thus BPR too. An increase in P_M^* on the other hand at constant π_C, results in a lower SFC_{TS} (Eq.4.94), which reduces the primary air fraction proportionally. BPR thus increases. Fig.4.20 shows the foregoing discussion for two power settings. Note that the highest power setting represents the lowest value of SFC_{TS} (Eq.4.94).

Ram recovery

If inlet losses are present, they need to be accounted for. This can be done by introducing them in the non-dimensional inlet variables δ_{t1} and θ_{t1}, in an identical way as done in Section 4.3.5. If the flow is adiabatic, θ_{t1} will not be influenced. Only the pressure losses then have an important effect on the total pressure of the flow. Defining the ram recovery RR as :

$$RR \triangleq \frac{p_{t1}}{p_{ta}} \tag{4.109}$$

where p_{ta} typifies the total pressure of the atmosphere, then δ_{t1} is determined as follows :

$$\delta_{t1} = RR \cdot \delta_{ta} \tag{4.110}$$

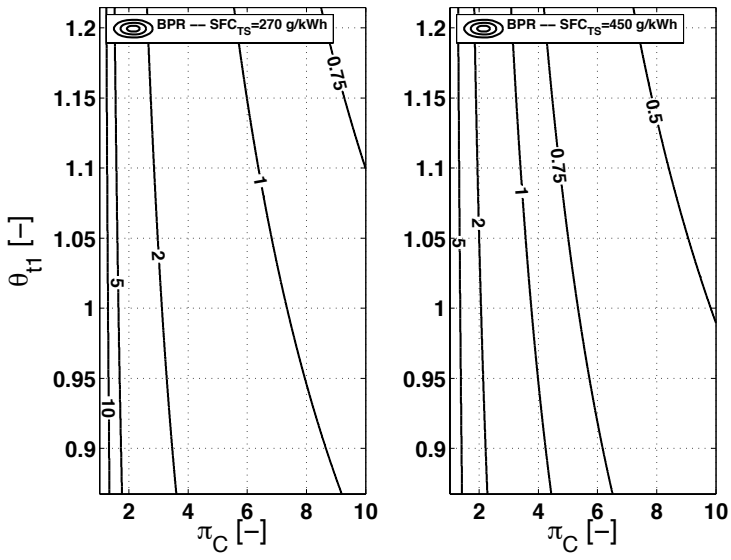

Figure 4.20. Cycle *BPR* as a function of π_C, SFC_{TS} and dimensionless inlet temperature $\theta_{t1} = \frac{T_{t1}}{288.15}$ – no losses.

Heat exchanger

The heat exchanger permits the recovery of a part of the thermal energy leaving the turboshaft. The recoverable amount of heat depends on the temperature difference between the primary and secondary flow, but also on the heat exchanger's effectiveness ϵ_H. ϵ_H is function of the geometry of the heat exchanger, the materials used and the ratio of heat capacities between the interacting flows. Moran & Shapiro (2004) defines ϵ_H as :

$$\epsilon_H = \frac{\dot{Q}_{ex}}{\dot{Q}_{\Delta T_{max}}} \tag{4.111}$$

where,

→ $\dot{Q}_{ex}$ = exchanged thermal energy between primary and secondary flow, positive when heat enters the secondary flow.

→ $\dot{Q}_{\Delta T_{max}}$ = maximum exchangeable thermal energy between primary and secondary flow, always positive.

$\dot{Q}_{ex}$ and $\dot{Q}_{\Delta T_{max}}$ are represented respectively by the Eqs. 4.112 and 4.113 :

$$\dot{Q}_{ex} = \dot{m}\, C_p(T_{t45} - T_{t2}) \tag{4.112}$$

$$\dot{Q}_{\Delta T_{max}} = \min\Big\{\dot{m}_p C_{pg}(T_{t4p} - T_{t2})\ ;\ \dot{m}\, C_p(T_{t4p} - T_{t2})\Big\} \tag{4.113}$$

4.4.4 Cycle operating boundaries

HEX inlet temperature constraints

The purpose of the heat exchanger is to transfer thermal energy from the primary flow into the secondary flow, not vice versa. This process only takes place when : $T_{t4p} \geq T_{t2}$. Via the first law applied on control volume $CV3$ (Fig.4.16) and after some manipulation, one may find the exhaust gas temperature T_{t4p} to be :

$$T_{t4p} = \frac{C_p}{C_{pg}} T_{t1} + \frac{FAR}{C_{pg}} \left(\eta_{CC} LHV - \frac{1}{SFC_{TS}} \right) \tag{4.114}$$

Here, the turboshaft is considered to be an adiabatic system, i.e. no heat is exchanged with its surroundings. Since $\dot{m}$ passes through the engine rapidly, it is reasonable to accept this assumption. Imposing the above-mentioned process constraint and substitution of Eq.4.54 in Eq.4.114 :

$$\pi_C \leq \left[\frac{C_p}{C_{pg}} + \frac{FAR}{T_{t1} C_{pg}} \left(\eta_{CC} LHV - \frac{1}{SFC_{TS}} \right) \right]^{\frac{\eta_{p,C} \cdot \gamma}{\gamma - 1}} \triangleq \pi_{C,L1} \tag{4.115}$$

The heat recovery requirement in the secondary flow thus sets limits to π_C, and depends mainly on SFC_{TS} and T_{t1} (Fig.4.21). The more efficient the engine, the lower T_{t4p} for a given power output and as a consequence, the operable π_C-domain gets reduced. Unfortunately, this also sets limits to the maximum attainable $LTIT$-value.

HEX effectiveness constraints

The effectiveness of a HEX cannot be larger than unity. This means that (Eq.4.111) :

$$\dot{Q}_{ex} \leq \dot{Q}_{\Delta T_{max}} \tag{4.116}$$

The minimum in Eq.4.113 can be related to a specific operating condition. This is easily observed when dividing both terms with $\dot{m}_p \, C_{pg}$ and rearranging :

$$BPR \leq \frac{C_{pg}}{C_p} \triangleq BPR_{L2} \qquad \Rightarrow \qquad \dot{Q}_{\Delta T_{max}} = \dot{m} \, C_p (T_{t4p} - T_{t2}) \quad \textit{Secondary flow restricted} \tag{4.117}$$

$$BPR > \frac{C_{pg}}{C_p} \triangleq BPR_{L2} \qquad \Rightarrow \qquad \dot{Q}_{\Delta T_{max}} = \dot{m}_p \, C_{pg} (T_{t4p} - T_{t2}) \quad \textit{Primary flow restricted} \tag{4.118}$$

For $BPR \leq BPR_{L2}$, substituting Eq.4.117 in Eq.4.116 gives the following trivial boundary:

$$T_{t4p} \geq T_{t45} \tag{4.119}$$

or,

$$T_{t45} \leq \frac{C_p}{C_{pg}} T_{t1} + \frac{FAR}{C_{pg}} \left(\eta_{CC} LHV - \frac{1}{SFC_{TS}} \right) \tag{4.120}$$

In its non-dimensional form :

$$\frac{T_{t45}}{T_{t1}} \leq \frac{C_p}{C_{pg}} + \frac{FAR}{C_{pg} T_{t1}} \left(\eta_{CC} LHV - \frac{1}{SFC_{TS}} \right) \triangleq \left[\frac{T_{t45}}{T_{t1}} \right]_{L2,1} \tag{4.121}$$

This sets an upper boundary to the maximum temperature one can establish for *LTIT* (Fig.4.21).

If $BPR > BPR_{L2}$, the affected π_C-domain is found after substitution of Eq.4.108 in Eq.4.118 :

$$\pi_C \leq \left(\frac{\eta_M FAR}{SFC_{TS} T_{t1} C_{pg}} + 1 \right)^{\frac{\gamma \eta_{p,C}}{\gamma - 1}} \triangleq \pi_{C,L2} \tag{4.122}$$

For π_C lower than $\pi_{C,L2}$, $\frac{T_{t45}}{T_{t1}}$ can never reach the value of $\frac{T_{t4p}}{T_{t1}}$ because the caloric capacity of the secondary mass flow is more important than the one of the primary mass flow. Imposing unity for ϵ_H, a boundary for *LTIT* may be established. In its non-dimensional form, i.e. $\frac{T_{t45}}{T_{t1}}$, the boundary is :

$$\frac{T_{t45}}{T_{t1}} \leq \left(1 - \frac{C_{pg}}{C_p} \frac{1}{BPR} \right) \pi_C^{\frac{\gamma - 1}{\gamma \eta_{p,C}}} + \frac{1}{BPR} \left[1 + \frac{FAR}{C_p T_{t1}} (\eta_{CC} LHV - \frac{1}{SFC_{TS}}) \right] \triangleq \left[\frac{T_{t45}}{T_{t1}} \right]_{L2,2} \tag{4.123}$$

This boundary results from the substitution of Eq.4.112, Eq.4.118 and Eq.4.114 in Eq.4.111. It is indicated in Fig.4.21.

HEX secondary flow limitations

Since heat has to enter the secondary flow, the following condition must apply :

$$T_{t45} \geq T_{t2} \tag{4.124}$$

Substitution of Eq.4.54 gives again a boundary for π_C (Fig.4.21) :

$$\pi_C \leq \left(\frac{T_{t45}}{T_{t1}} \right)^{\frac{\gamma \eta_{p,C}}{\gamma - 1}} \triangleq \pi_{C,L3} \tag{4.125}$$

Cycle and turboshaft operating boundaries

First, the turboshaft operating boundaries are discussed. From *CV*3 in Fig 4.4 it is clear that the open system the turboshaft represents, can be converted to a closed system by returning the exhaust gases to the inlet of the turboshaft via a heat exchanger, which has to remove heat from the cycle (Kelvin-Planck law). This fictitious heat removal $\dot{Q}_C$ can be

shown to be :

$$\dot{Q}_C = \dot{m}_p \, (h_{t4p} - h_{t1}) \tag{4.126}$$

Adopting again the simplifications related to the use of the Carnot effectiveness to establish the cycle boundaries (Section 4.3.4), and based on its definition, one may retrieve the following requirement for the turboshaft exhaust gas temperature :

$$T_{t4p} \geq T_{t1}\left(\frac{FAR \, \eta_{CC} \, LHV}{C_{pg} T_H} + \frac{C_{pg}}{C_p}\right) \tag{4.127}$$

T_H corresponds to the maximum temperature in the combustion chamber of the turboshaft. For contemporary civil gas turbines, this temperature limit is according to Jacques (2004b) near 1850 K. As a consequence, $T_{t4p} > T_{t1}$. A more practical approach to the problem is to examine with which SFC_{TF} this boundary concurs. Applying once more the definition of the Carnot effectiveness :

$$\frac{P^*_M}{\dot{Q}_F} = \frac{P^*_M}{\dot{m}_f \, \eta_{CC} \, LHV} \leq \epsilon_{Carnot} \quad \Rightarrow \quad SFC_{TS} \geq \frac{1}{\left(1 - \frac{T_{t1}}{T_H}\right) \eta_{CC} \, LHV} = SFC_{TS_{Carnot}} \tag{4.128}$$

With the values indicated in Table 4.7, $SFC_{TS_{Carnot}} \cong$ 100 g/kWh. This is well below the examined range.

Second, the complete cycle must be evaluated. Writing the thermal effectiveness of the cycle and comparing it to the one of Carnot :

$$\frac{P^*_T}{\dot{Q}_F} = \frac{COP}{SFC_{TS} \, \eta_{CC} \, LHV} \leq 1 - \frac{T_{t1}}{T_H} \tag{4.129}$$

The foregoing equation yields a maximum for the cycle coefficient of performance, viz. :

$$COP \leq \eta_{CC} \, LHV \, SFC_{TS}\left(1 - \frac{T_{t1}}{T_H}\right) = COP_{Carnot} \tag{4.130}$$

Using the data in Table 4.7, the most restrictive value for COP_{Carnot} may be found to be approximately 2.8. This condition will be never attained because the boundaries set by the heat exchanger are more stringent. This will become clear when discussing the parametric cycle study.

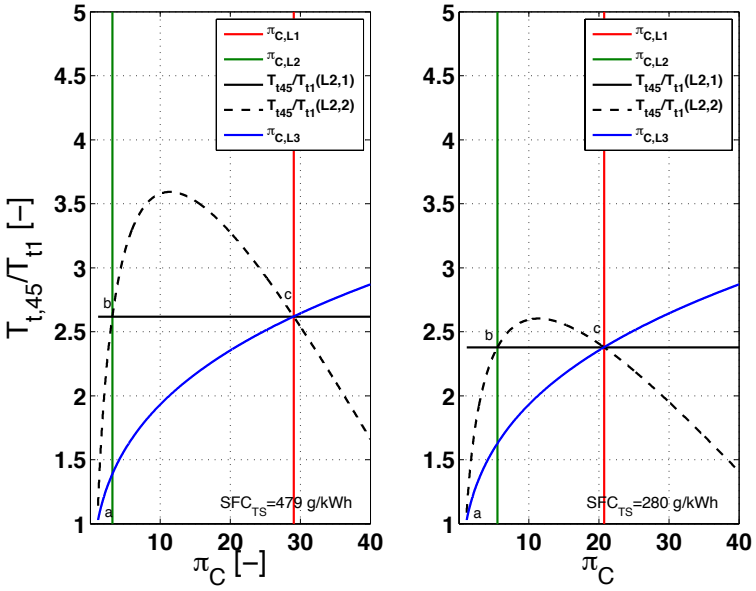

FIGURE 4.21. Cycle operating boundaries, ISA SLS. Maximum continuous regime – no losses (except TS).

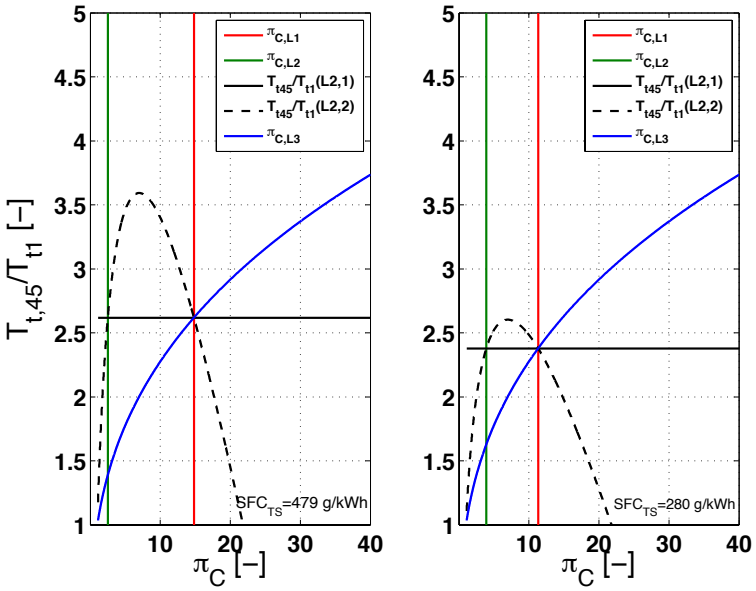

FIGURE 4.22. Cycle operating boundaries, ISA SLS. Maximum continuous regime – $\eta_{p,C} = 0.8$, otherwise no losses (except TS).

The discussed cycle boundaries uncover clearly that the cycle will be mainly restricted by the heat exchange conditions (Fig.4.21). Firstly, π_C may not be larger than $\pi_{C,L1}$ (red line), which keeps T_{t2} below T_{t4p}. So any solution must be sought on the left-hand side of the red line on the figure. Also, π_C must be lower than $\pi_{C,L3}$ (blue line). Otherwise,

T_{t2} would be larger than $LTIT$, which is prohibited (the goal is to extract heat from the exhaust gases). All relevant solutions are found above this line. Additionally, there are boundaries imposed on $\frac{T_{t45}}{T_{t1}}$. For all π_C higher than $\pi_{C,L2}$ (vertical green line), $\frac{T_{t45}}{T_{t1}}$ must remain lower than $\left[\frac{T_{t45}}{T_{t1}}\right]_{L2,1}$ ($T_{t45} < T_{t4p}$). The full black line represents this boundary. Useable solutions will be found below this line. Though, if π_C is lower than $\pi_{C,L2}$, $\frac{T_{t45}}{T_{t1}}$ must be kept beneath the $\left[\frac{T_{t45}}{T_{t1}}\right]_{L2,2}$ constraint ($\epsilon_H = 1$), which appears on the figure as the dashed black line. Eventually, a quasi-triangular operating domain (a-b-c) remains at the designer's disposal. Also, the more efficient the turboshaft (low SFC_{TE}), the smaller the available operating domain (a-b-c) becomes. Indeed, it is reasonable to expect a lower T_{t4p} if a more efficient engine delivers a given P_M^*, thus causing the operating domain to be smaller. Note that in case the cycle operating domain would turn out to be insufficiently large, one could consider installing a multi-engine configuration, since this increases SFC_{TS} for a given P_M^*. COP_{Carnot} has not been plotted on the figures as it is situated well above the a-b-c operating domain.

4.4.5 Note on efficiencies

Mechanical efficiency

Consider a turboshaft producing a constant power P_M^* at SFC_{TS}. Similar to the piston engine, a decrease in η_M causes a drop in secondary mass flow for a given π_C and affects BPR proportionally (Eq.4.108). If in addition one assumes a constant $\frac{T_{t45}}{T_{t1}}$, COP too will vary commensurate with η_M. Since the turboshaft is completely decoupled from the secondary mass flow, SFC must consequently have an inverse proportional dependency on η_M, which is clearly shown in Eq.4.97. Note that if $BPR > BPR_{L2}$ (Eq.4.118 and Eq.4.122), the required ϵ_H becomes also a function of η_M ($\eta_H \propto \eta_M$). The reduction in secondary mass flow resulting from a drop in η_M would cause an increase in $\frac{T_{t45}}{T_{t1}}$ for a given heat exchanger heat flux dominated by the primary flow. In case a constant $\frac{T_{t45}}{T_{t1}}$ is required, less heat must be exchanged, which can only be achieved with a lower ϵ_H.

Turbine and compressor efficiencies

The turbine polytropic efficiency only impacts COP and SFC. It should be as high as possible. The compressor polytropic efficiency on the other hand has a substantial impact on the position of the cycle boundaries, as indicated in Fig.4.22. Compared to Fig.4.21, the operating domain is squeezed to the left and significantly reduced. Decreasing $\eta_{p,C}$ with 20 per cent cuts the π_C-domain by a factor of two.

4.4.6 Effect of the atmospheric pressure and temperature

During the previous discussions, T_{t1} was seen as a completely independent but constant variable. The next paragraphs study the influence of a variable atmosphere and thus inlet

conditions, i.e. T_{t1} and p_{t1}[xi], on the complete cycle with as independent variables the non-dimensional RELT inlet temperature $\frac{T_{t45}}{T_{t1}}$ and compression ratio π_C. The influence of the temperatures and pressures on the cycle characteristics will again be expressed by means of their deviation with respect to the standard day conditions, i.e. 288.15 K and 1 atm – AIAA (2003). This is established using the corrected non-dimensional atmospheric temperature and pressure. Their definitions follow from the same reference :

$$\theta_{t1} = \frac{T_{t1}}{288.15} \tag{4.131}$$

$$\delta_{t1} = \frac{p_{t1}}{101325} \tag{4.132}$$

The reference standard day conditions are then indicated by the *"corr"* suffix, as was done earlier during the piston engine powered TDR cycle study.

Turboshaft corrected performance

From AIAA (2003), for a constant non-dimensional turboshaft turbine inlet temperature $\frac{TIT}{T_{t1}}$, overall compression ratio π_{ov}, inlet Mach number M_a and geometry, the influence of the atmospheric temperature and pressure on the following turboshaft performance characteristics is found :

$$P^*_{M,corr} = \frac{P^*_M}{\delta_{t1}\sqrt{\theta_{t1}}} \tag{4.133}$$

$$SFC_{TS,corr} = SFC_{TS} \tag{4.134}$$

$$\dot{m}_{p,corr} = \frac{\dot{m}_p\sqrt{\theta_{t1}}}{\delta_{t1}} \tag{4.135}$$

$$\dot{m}_{f,corr} = \frac{\dot{m}_f}{\delta_{t1}\sqrt{\theta_{t1}}} \tag{4.136}$$

$$FAR_{corr} = \frac{\dot{m}_{f,corr}}{\dot{m}_{p,corr}} = \frac{FAR}{\theta_{t1}} \tag{4.137}$$

$$\tag{4.138}$$

Cycle coefficient of performance and RELT power output

Observing Eq.4.102, *COP* turns out to be independent of the atmospheric conditions for a fixed $\frac{T_{t45}}{T_{t1}}$ and π_C. Using the definition of *COP* (Eq.4.32) in Eq.4.133 leads to the conclusion that P^*_T is corrected in an identical way as P^*_M :

$$P_{T,corr} = \frac{P^*_T}{\delta_{t1}\sqrt{\theta_{t1}}} \tag{4.139}$$

This means that a high atmospheric temperature and high pressure influence the RELT power output positively. Note that there is still an upper limit imposed on the turbine

[xi] note that $p_{t1} = RR\, p_{ta}$.

inlet temperature of both the RELT and the turboshaft, so that the premise of a constant $\frac{T_{t45}}{T_{t1}}$ or $\frac{TIT}{T_{t1}}$ is not always achievable.

Cycle specific fuel consumption

Under the stated conditions, SFC is commensurate with SFC_{TS}, what follows clearly when observing Eq.4.97. Hence, using Eq.4.134, one obtains for the corrected value of SFC :

$$SFC_{corr} = SFC \tag{4.140}$$

Cycle bypass ratio

Eq.4.108 shows that the susceptibility of BPR to a variable atmosphere depends on the following combination of inlet-temperature-dependent parameters :

$$BPR \propto \frac{FAR}{SFC_{TS} T_{t1}} \tag{4.141}$$

Substitution of Eq.4.134, Eq.4.137 and Eq.4.131 in the foregoing equation yields :

$$BPR \propto \frac{FAR_{corr}\ \theta_{t1}}{SFC_{TS,corr}\ 288.15 \theta_{t1}} \tag{4.142}$$

which then leads to :

$$BPR_{corr} = BPR \tag{4.143}$$

In contradiction to what was found initially in Section 4.4.3, where an increase in T_{t1} showed to decrease BPR (Eq.4.108), it appears that – the total impact of T_{t1} on all cycle characteristics considered – BPR remains unaffected by a variation of atmospheric conditions. In the former case, T_{t1} does not impact the other cycle parameters, more specifically FAR, which explains the stated observation.

Cycle boundaries

Examining the operational boundaries described during the study of the heat exchanger, it can be concluded that all but $SFC_{TS_{Carnot}}$ and COP_{Carnot} are already written in a standardised form. The effect of an increase in atmospheric temperature will somewhat deteriorate $SFC_{TS_{Carnot}}$ and COP_{Carnot}, but the importance of these boundaries with respect to those imposed by the heat exchanger was already highlighted to be of no concern.
Hence, the operating domain of the turboshaft powered TDR cycle can be completely established for standardised atmospheric conditions, while the corrected variables allow extrapolation of the results to any (reasonable) given atmosphere wherein one chooses to operate. Unlike the piston engine powered TDR cycle, the mechanical power of each working element in the turboshaft powered TDR cycle is reduced by $\delta_{t1}\sqrt{\theta_{t1}}$. Hence, the

theory of corrected values can also be used to extrapolate the cycle performance characteristics to other atmospherical conditions for fixed non-dimensional cycle parameters.

4.4.7 Parametric cycle study

The cycle operating domain is now evaluated as a function of the non-dimensional parameters $\frac{T_{t45}}{T_{t1}}$ and π_C. Table 4.7 summarises the values of all relevant variables, which are considered fixed, with the exception of those studied parametrically. These parameters are reflected in Table 4.8. Note that the study applies to either a single or a multi-engine configuration as not the power P^*_M but SFC_{TS} is examined parametrically (see Eq.4.100). The assessed SFC_{TS} range is determined by the 100-2000 kW P^*_M-range typical of contemporary turboshaft engines (maximum continuous regime, ISA SLS – Table 4.6).

Table 4.7. Cycle fixed variable summary.

Variable	value	note
η_{CC}	0.99	Jacques (2004b)
η_M	0.98	assumed
$\eta_{p,C}[-]$	0.9	Van den Braembussche (2013)
$\eta_{p,T}[-]$	0.87	Chapter 8
γ	1.40	air, Jacques (2004b)
γ_g	1.33	combustion gases, Jacques (2004b)
R_g	287.05 J/kgK	specific gas constant, Jacques (2004b)
LHV	43.2 MJ/kg	Table 4.5
FAR	1:60	Jacques (2004b)
T_{ta}	288.15 K	ISA SLS
p_{ta}	1 atm	ISA SLS
RR	0.99	assumed

Table 4.8. Cycle parametric variable summary.

Variable	range
$P^*_{M,1TS}$ [kW]*	100 . . . 2000
$P^*_{M,2TS}$ [kW]*	200 . . . 4000
SFC_{TS} [g/kWh]*	280 . . . 479
$\frac{T_{t45}}{T_{t1}}$ [-]	1 . . . 5
π_C [-]	1 . . . 40

* Max. Continuous regime

The bypass ratio (Fig.4.23), coefficient of performance (Fig.4.24) and specific fuel consumption (Fig.4.25) of the cycle show the already known tendencies, discussed in the

previous sections. Here however, it is important to highlight the effect of the heat exchanger efficiency and the maximum *LTIT* (400 K).

Obeying the maximum *LTIT* limit, it is observed that the π_C-range is always lower than 3 and *BPR* larger than unity at ISA SLS. The low pressure ratio range decreases the structural weight of the plenum, which is beneficial. Unfortunately, this beneficial effect is compromised by the higher *BPR* concurring with a lower π_C, which increases the weight of the heat exchanger. A weight trade-off study in the available pressure range appears unavoidable, but is not conducted here.

For a given π_C, $\frac{T_{t45}}{T_{t1}}$ increases when ϵ_H improves. The consequence is a higher *COP* and lower *SFC*. Again, the system weight issue may be problematic as a higher ϵ_H will require a larger and heavier heat exchanger (Fig.4.26). The helicopter platform weight may hereby be affected negatively.
Note that if ϵ_H is fixed, *COP* peaks at BPR_{L2}, and offers also the best *SFC*. This phenomenon explains itself due to the fact that it concurs with the heat exchanger operating point of maximum heat transfer and maximum temperature rise. More thermal energy is thus transferred to the RELT and the power output peaks. Note also that the cycle with the highest (worst) SFC_{TS} offers the opportunity to achieve higher *COP* levels. This is due to the fact that the turboshaft exhaust gas temperature rises with increasing SFC_{TS}, enabling higher achievable *LTIT* and thus higher RELT specific power outputs.

With regard to *COP* in the usable operating domain, it ranges between $0.8 - 1$. The highest available *COP* near unity is found for the low power range turboshaft (100 kW) at the maximum heat exchanger efficiency, of which the specific fuel consumption is significantly higher than the one of a piston engine generating a similar power output. From a fuel flow perspective yielding an identical power output P_T^*, it can be shown that the piston engine powered TDR cycle outperforms the turboshaft driven cycle :

$$\frac{\dot{m}_{f,PE}}{\dot{m}_{f,TS}} = \frac{COP_{TS}\ SFC_{PE}}{COP_{PE}\ SFC_{TS}} \approxeq \frac{1 \cdot 400}{0.9 \cdot 479} < 1 \tag{4.144}$$

This added to the increased weight penalty by having to select a high heat exchanger efficiency, renders the turboshaft driven cycle less attractive for the low power output range.

Heat exchanger effectiveness considerations

At this point, the selection of ϵ_H remained quite arbitrary and the full range was used in the discussion of the cycle operating domain. Although the use of the higher range of ϵ_H may appear natural since it leads to better *COP* and *SFC*, it has an adverse impact on the system weight. Clearly, when $\eta_{p,C}$ and $\eta_{p,T}$ are high, one might be content with

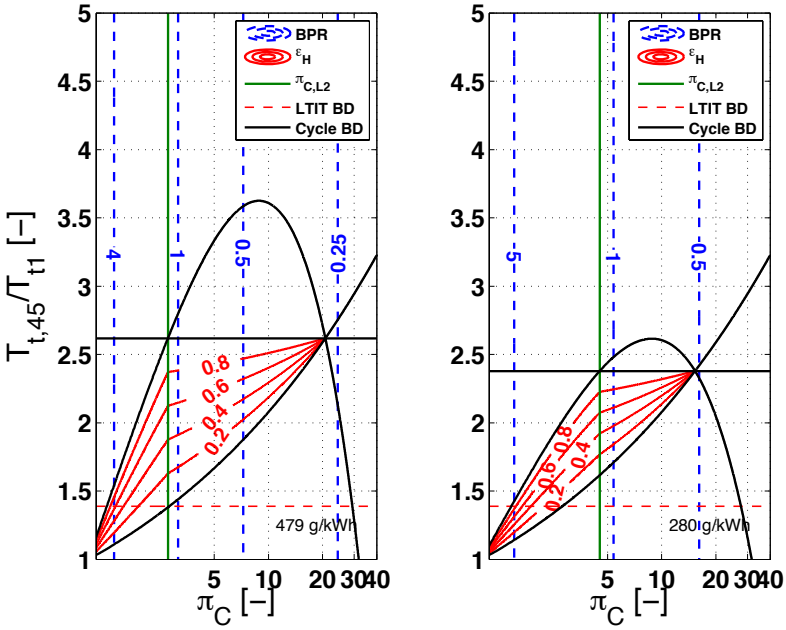

FIGURE 4.23. Cycle BPR, ISA SLS. Maximum continuous regime.

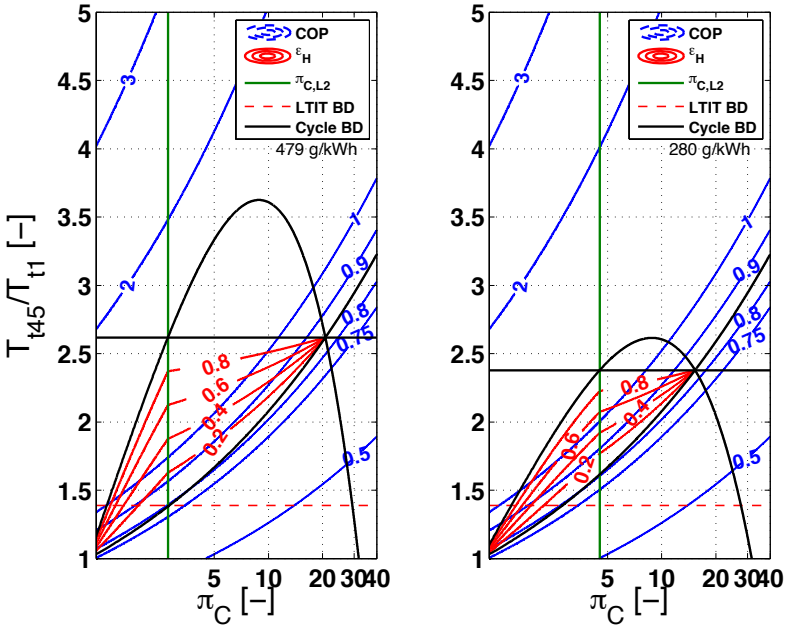

FIGURE 4.24. Cycle COP, ISA SLS. Maximum continuous regime.

the selection of a relatively low ϵ_H, which leads to a lower system mass and lower *COP*. Indeed, according to Privoznik (1968), who performed a study on the installation of a heat exchanger to recover a part of the thermal energy of the exhaust gases leaving the Allison T63 turboshaft engine, the mass of the propulsion system including the heat exchanger increases all but linearly with an increase in ϵ_H. From data given by Semple (1976), an

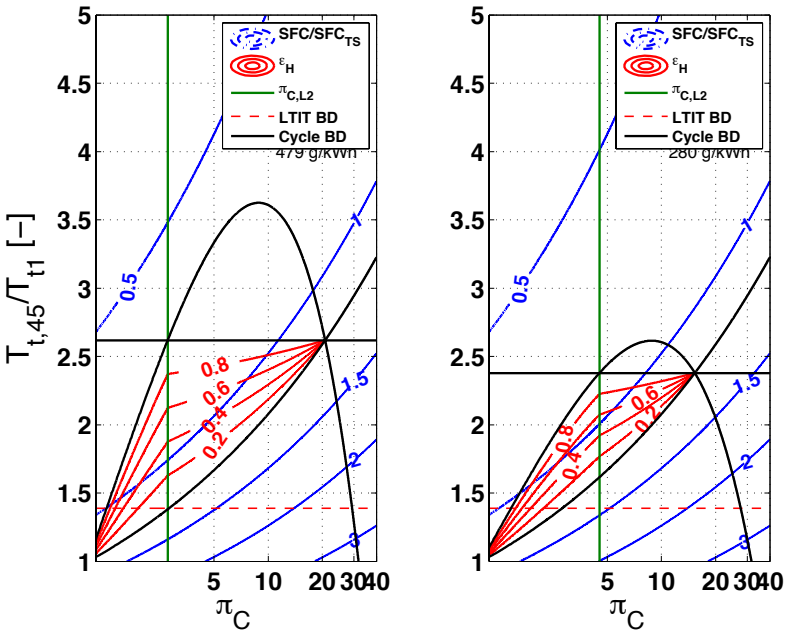

FIGURE 4.25. Cycle SFC, ISA SLS. Maximum continuous regime.

exponential growth with ϵ_H may be observed (Fig. 4.26). As a consequence, the empty weight and thus fuel weight that need to be supported will increase accordingly, resulting in a much less efficient system than what would be achieved with no heat exchanger at all.

The previously mentioned studies prove in fact that there exist an optimum ϵ_H, which is in the range of $0.65-0.7$ for turboshaft overall pressure ratios π_{ov} around $6-8$. The reason why these relatively low pressure ratios give best performance is due to the existence of the combined effect of better heat recovery at the higher exhaust gas temperatures, which concurs with the lower π_{ov} range, and better turboshaft efficiency at the higher range of π_{ov}. Note also the additional positive effect of a decreased engine compressor weight when a lower π_{ov} is selected.

In case of the turboshaft powered TDR cycle, the overall pressure ratio of the turboshaft is of lesser importance since it does not influence the cycle pressure ratio directly. However, BPR does affect the mass of the heat exchanger (m_{HEX}), a factor which was invariable in the studies of Privoznik (1968) and Semple (1976), where $BPR \cong 1$. If BPR increases, it is reasonable to expect that for a given turboshaft, m_{HEX} will rise substantially. As a matter of fact, for a constant gas velocity, the cross-sectional area and thus volume will need to increase not only due to a higher secondary mass flow, but also due to a decreased density stemming from the inverse relationship between BPR and π_C.

Finally, it is important to note that the above discussed heat exchangers were all shell-and-tube recuperators. The other important heat exchanger type is the regenerator, which contains one or more rotating porous disks P (Fig.4.27) through which heat is transferred from the hot gases flowing through a duct A_H to the cold gases passing through a duct

A_C. The hot and cold gases each flow in a separate duct at different pressures. The seals s (Fig.4.27) must in theory prevent any leakage between both flows. In reality, this appears a tedious task and leakages may become prohibitively large. Indeed, according to Beck & Wilson (1996), regenerators currently appear to be unattractive for application in helicopters because of the important leakage losses between disk and seals, even though their theoretical potential outperforms the one of recuperators (lower weight and cost). However, this leakage originates from the high pressure difference inside the turboshaft between the cold flow at π_{ov} and the hot flow near atmospheric pressure. If the pressure ratio π_C remains fairly low, i.e. well below π_{ov} which is around 8, there is à priori no reason to currently exclude the regenerator, except for its complexity.

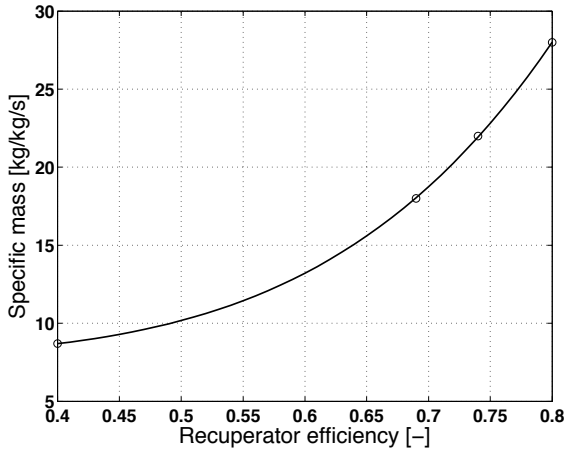

FIGURE 4.26. Recuperator specific mass $m_{HEX}/\dot{m}$, $BPR \cong 1$ – Semple (1976).

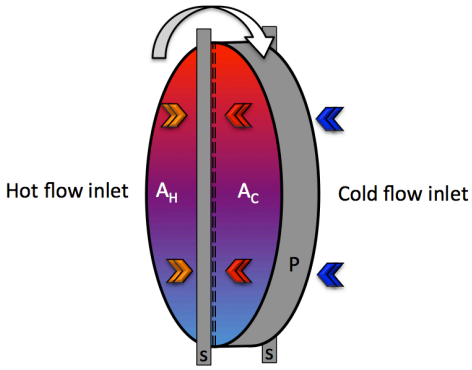

FIGURE 4.27. Simplified scheme of a regenerator.

4.5 Turbofan engine powered TDR cycle

4.5.1 Introduction to the turbofan engine

The early gas turbines installed on aeroplanes were turbojets, which produced thrust at a low propulsive efficiency. Indeed, the kinetic energy of the gases leaving this kind of engine remains high with respect to the propulsive power requirement. Unless high-speed propulsion is envisaged, it is advisable to use a more efficient propulsion system (see for example Walsh & Fletcher (2004)). The turbofan (TF – Fig.G.1) is one possible solution, which proves successful in aviation. This engine uses a low pressure compressor or fan driven by and placed in front of a core, effectively reducing the total kinetic energy of the expelled gases and consequently increasing the propulsive efficiency (Fig.4.28). Note that a bypass ratio for a turbofan BPR_{TF} is defined as the ratio of air passing through the fan alone to the air passing through the core, i.e. :

$$BPR_{TF} = \frac{\dot{m}_s}{\dot{m}_p} \tag{4.145}$$

Besides the imposed net thrust T_N, BPR_{TF} plays a major role in the design process of the engine. Indeed, the flight speed of the aircraft, for which the turbofan needs to be designed, impacts the selection of BPR_{TF} considerably. As explained by Cumpsty (2000), the dimensioning of the engine frontal area gains much importance when flight speed increases, because the frontal area impacts drag significantly. Hence, under these circumstances, BPR_{TF} must be lowered (lower fan diameter). Some characteristics of the turbofan engine are summarised in Table 4.9.

During the RELT-cycle examination with the turbofan, it will appear necessary to acquire good estimates of the engine specific thrust SPT and thrust specific fuel consumption $TSFC$. Correlations are now developed for both variables, and more specifically for take-off (T/O) conditions at ISA SLS, for which engine data is readily available (Appendix H).

Table 4.9. General turbofan characteristics for subsonic use – survey author (Appendix H).

T_N (ISA SLS) [kN]	2.5 . . . > 500
BPR_{TF} (ISA SLS)	4.5 . . . 12
$TSFC$ [g/daNh]	300 . . . > 450
fuel type	kerosene based derivatives
LHV [MJ/kg]	43.2

Specific thrust at maximum engine rating, ISA SLS

The specific thrust of a turbofan SPT is defined as, where $\dot{m}$ the mass flow entering the engine :

$$SPT = \frac{T_N}{\dot{m}} \tag{4.146}$$

It is reasonable to expect that for a given net thrust, SPT decreases by increasing the bypass ratio thanks to the reduced exhaust gas speed. Jacques (2004a) and data from a survey performed by the author (Fig.4.29) confirms this tendency. Assuming that SPT depends only on BPR_{TF} is incorrect, but in some extent acceptable for conceptual calculations, since it will reduce the total amount of independent variables. To assure a well founded correlation, a theoretical model was established based on momentum theory and is explained next.

Consider a control volume encapsulating the turbofan (Fig.4.28). Using the unidimensional momentum equation, while neglecting the static pressure rise in the nozzles of core and bypass in case of choking, as well as the fuel mass flow, one finds for SPT :

$$SPT = \frac{(v_8 - v_a) + BPR_{TF}(v_{18} - v_a)}{1 + BPR_{TF}} \tag{4.147}$$

and (Fig.4.28),

→ v_a = the speed of the aircraft

→ v_8 = the speed of the exhaust gases leaving the core section

→ v_{18} = the speed of the gases leaving the bypass section

Assuming v_a to be negligible with respect to the speed of the exhaust gases :

$$SPT = \frac{v_8 + BPR_{TF} \cdot v_{18}}{1 + BPR_{TF}} \tag{4.148}$$

The total power that needs to be delivered by the turbines in the turbofan $P_{T,tot}$ is the power absorbed by the compressors[xii] (fan,intermediate and high pressure stages) and is approximated by :

$$P_{T,tot} = \dot{m}_t C_{pF} \Delta T_F + \dot{m}_p C_{pC} \Delta T_C = \dot{m}_p C_{pT}(TIT - EGT) \tag{4.149}$$

with :

→ C_{pF} = average specific heat constant at constant pressure over fan

→ C_{pC} = average specific heat constant at constant pressure over all compressor stages except fan

[xii] The mechanical losses and the power absorbed by auxiliaries are neglected.

→ C_{pT} = average specific heat constant at constant pressure over all turbines

→ ΔT_i = total temperature variation over the component i (F=fan, C=compressors w/o fan)

→ TIT = high pressure turbine inlet temperature

→ EGT = exhaust gas temperature

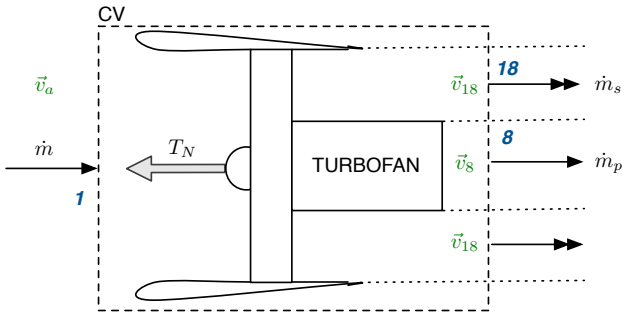

FIGURE 4.28. Control volume around turbofan engine.

v_8 is related to EGT via the Mach number at the outlet of the core nozzle M_8. Assuming the core jet velocity to be close to the speed of sound :

$$v_8 \cong \sqrt{\gamma R_g \left(\frac{EGT}{1 + \frac{\gamma - 1}{2} M_8^2} \right)} \tag{4.150}$$

Eq.4.150 can now be substituted in Eq.4.148. Eq.4.149 on the other hand may be used to replace EGT. In general, for state of the art engines designed to serve the same goal (for example maximum efficiency for commercial applications), TIT, ΔT_{fan} and ΔT_C are of the same order of magnitude, while M_8 is usually not larger than unity since it is highly unlikely to find convergent-divergent nozzles on commercial turbofans. Under these conditions, the difference between the total and static temperature is assumed to remain relatively small ($\leq 20\%$). Then, it is found that :

$$SPT \cong \frac{\sqrt{\gamma R_g \{TIT - [(1 + BPR_{TF})\Delta T_F + \Delta T_C]\}} + BPR_{TF} \cdot v_{18}}{1 + BPR_{TF}} \tag{4.151}$$

Or in simplified form :

$$SPT = \frac{\sqrt{c_1 - c_2(1 + BPR_{TF})} + c_3 \cdot BPR_{TF}}{(1 + BPR_{TF})} \tag{4.152}$$

The constants c_1-c_3 in Eq.4.152 are found via a best fit algorithm in MatLab, while using the data in Fig.4.29. Orders of magnitude for c_1-c_3 can be found via Eq.4.151. The results found via MatLab are summarised in Table 4.10. The orders of magnitude of the constants are within the acceptable range. Substitution of the values for c_1-c_3 in 4.152 gives :

TABLE 4.10. *SPT* best fit coefficients, T/O – ISA SLS.

Coefficient	Estimated order of magnitude	MatLab
c_1	$O(10^5)$	$5.489 \cdot 10^5$
c_2	$O(10^4)$	$1.996 \cdot 10^4$
c_3	$O(10^2)$	252.5

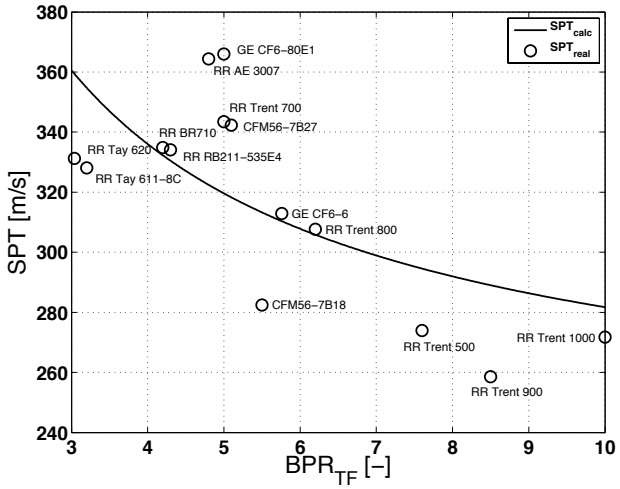

FIGURE 4.29. Turbofan specific thrust as a function of bypass-ratio. Take-off regime ISA SLS, Appendix H.

$$SPT = \frac{[5.489 \cdot 10^5 - 1.996 \cdot 10^4(1 + BPR_{TF})]^{\frac{1}{2}} + 252.5\, BPR_{TF}}{1 + BPR_{TF}} \quad \text{[m/s]} \tag{4.153}$$

This equation is presented in Fig.4.29. Note that the established correlation is based on important simplifications and that discrepancies are inevitable. Though, it explains the tendency of SPT with BPR_{TF} reasonably well at the maximum thrust setting (T/O ISA SLS) and suffices for the conceptual design purposes of the TDR cycle.

Thrust specific fuel consumption at maximum engine rating, ISA SLS

Cumpsty (2000) shows the thrust specific fuel consumption ($TSFC$) to be a decreasing function of BPR_{TF}. Here, it is substantiated by relating $TSFC$ to SPT. Starting from the definition of $TSFC$:

$$TSFC \triangleq \frac{\dot{m}_f}{T_N} \tag{4.154}$$

or :

$$TSFC = \frac{\dot{m}_f}{\dot{m}_p} \cdot \frac{\dot{m}_p}{\dot{m}} \cdot \frac{\dot{m}}{T_N} \approxeq \frac{FAR}{(1 + BPR)SPT} \tag{4.155}$$

Substitution of Eq.4.153 in Eq.4.155 yields :

$$TSFC = \frac{FAR}{[5.489 \cdot 10^5 - 1.996 \cdot 10^4(1 + BPR_{TF})]^{\frac{1}{2}} + 252.5\, BPR_{TF}} \tag{4.156}$$

Evaluation of the above formula confirms that $TSFC$ varies inversely with BPR_{TF} for ISA SLS, take-off regime (Fig.4.30). Cumpsty (2000) mentions another important variable that influences $TSFC$, but which does not explicitly appear in the above equations : the turbofan engine overall pressure ratio OPR. For minimum $TSFC$, OPR should be as high as reasonably possible[xiii]. For peak SPT, which is for example required for fighter aeroplanes, best OPR turns around 20. In fact, Cumpsty (2000) mentions the mutual dependency of OPR, BPR_{TF} and the fan pressure ratio π_F. He notes that optimising these parameters for the intended application is tedious. Now, note that for a given compressor inlet temperature and fixed TIT, increasing OPR will result in a lower fuel-to-air ratio. Though, in light of the conceptual study, it is sufficient to gain insight in the performance tendencies of an engine and its impact on the cycle wherein it operates[xiv]. Assuming that FAR remains a constant for the given maximum thrust regime, such as stated by Jacques (2004b) for simplified calculations, it appears that $TSFC$ becomes simply a function of BPR_{TF}. For high-bypass-ratio (HBPR) turbofans (high efficiency), Walsh & Fletcher (2004) indicates that π_F remains normally within the $[> 1 \ldots 1.9]$ interval. Since this corresponds to a moderate temperature rise of the gases before they enter the high pressure compressor stages, assuming a constant FAR is a priori reasonable. From survey data (Appendix H), an average FAR was established for maximum thrust conditions, viz. $FAR = 0.022$. According to Cumpsty (2000), this is an acceptable value. Hence :

$$TSFC = \frac{0.022}{[5.489 \cdot 10^5 - 1.996 \cdot 10^4(1 + BPR_{TF})]^{\frac{1}{2}} + 252.5 BPR_{TF}} \quad [\text{kg/Ns}] \tag{4.157}$$

Fig.4.30 visualises Eq.4.157. $TSFC$ will likely be underestimated for the higher range of BPR_{TF}.

4.5.2 Turbofan engine powered TDR cycle set-up

Previously, two cycles were discussed that drive the RELT by means of an integrated mechanical power source : a piston engine and a turboshaft. In that case, pursuing the best Ljungström turbine power output per unit of delivered mechanical power (COP) forced the designer to select an as low as possible pressure ratio, while managing high $LTIT$. However, there are limits to the usability of these cycles. Indeed, both aero-engine types have limited power-outputs. Also, when it comes to high power delivery, the turboshaft powered cycle would require large heat exchangers, since a low compression ratio increases the mass flow demand while still imposing low pressure losses.

[xiii] There are weight and dimensional constraints imposed on the engine. Increasing OPR requires the installation of more compressor stages, which leads to higher engine weight and larger dimensions.

[xiv] A more detailed turbofan model will be used in Chapter 8.

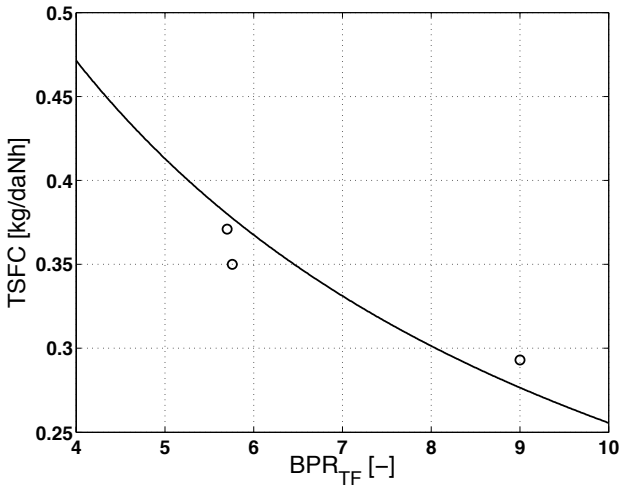

FIGURE 4.30. Turbofan *TSFC* estimation for maximum thrust regime (Take-off, ISA SLS). Appendix H.

A good compromise could then be the use of another type of gas turbine engine that essentially provides a high mass flow under low overpressure : the turbofan. Indeed, when the primary and secondary flow are mixed, the exhaust gas temperature remains acceptably low, while the fan provides the pressure rise to feed the RELT. The fact that the turbofan is designed to produce thrust appears particularly interesting in a compound configuration (Chapter 3). Then, at the higher flight speeds, the rotors and thus RELT can be alleviated by providing propulsive thrust via the turbofan.
The turbofan powered TDR cycle is shown in Fig.4.31. The presented cycle embeds two turbofans allowing symmetric thrust production. Again, a mixer merges the gases originating from both engines, while the shut-off-valve disconnects the gas path of a failing engine. The thrust valve (TV) opens gradually with the increasing demand of propulsive force. When no thrust is required, the valve remains closed.

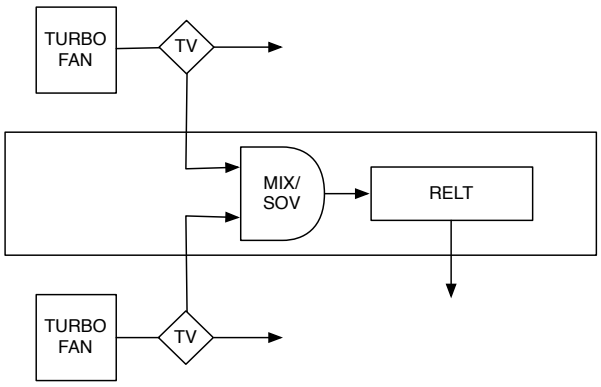

FIGURE 4.31. Turbofan powered TDR cycle.

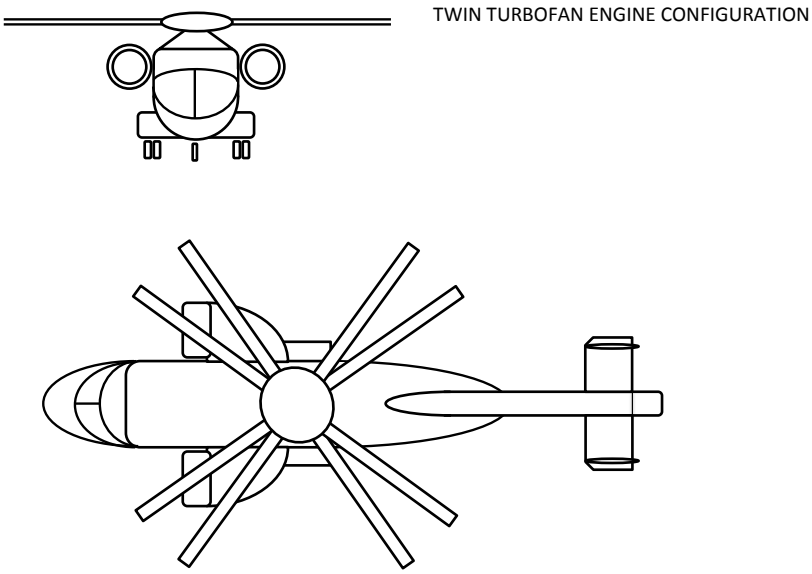

FIGURE 4.32. Twin-turbofan powered TDR helicopter (Illustrative purposes only).

4.5.3 Cycle study : Simplified theory

The nomenclature used for the thermodynamic study is shown in Fig.4.33. For terms of ease, only one turbofan is adopted in the scheme. Nevertheless, the theory provides all means to examine the cycle performance with multiple engines. The independent variables in the cycle differ from those used in the piston engine and turboshaft powered TDR cycles. Here, mainly π_F and BPR_{TF} are selected as independent parameters. The required net thrust then depends on the demanded RELT power. Results will be discussed at the end of this section.

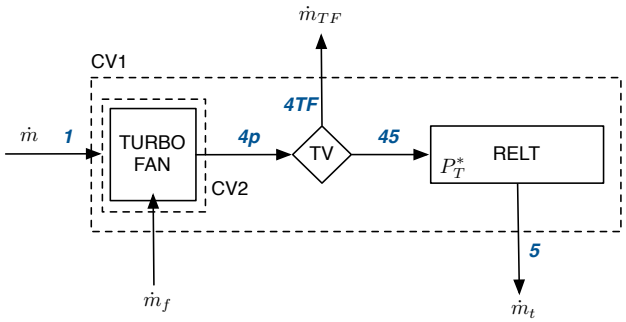

FIGURE 4.33. Turbofan powered TDR cycle setup.

RELT power output and mass flows

It is assumed again that the total expansion ratio over the RELT π_T equals the fan total pressure ratio π_F. This implicates equal total pressures of the gases leaving bypass and core. The effects of mixing will be shortly discussed in Chapter 8. For an adiabatic expansion over a turbine with polytropic efficiency $\eta_{p,T}$, the delivered power P_T^* is :

$$P_T^* = \dot{m}_t C_{pg} T_{t45} \left[1 - \left(\frac{1}{\pi_F} \right)^{\frac{(\gamma_g - 1)}{\gamma_g} \eta_{p,T}} \right] \tag{4.158}$$

where,

$\rightarrow$ $\dot{m}_t$ = mass flow passing through the RELT

$\rightarrow$ T_{t45} = RELT total inlet temperature ($LTIT$)

Note that the nozzle of the turbofan is now replaced by the adiabatic RELT and that the turbofan cycle is assumed not to be affected by this intervention. Even though the thrust of the unmodified engine will be used in subsequent examinations, it should however be regarded as the fictitious thrust the turbofan would generate when the flow in front of the RELT is expanded to the atmosphere via a fictitious nozzle. Even though in the TDR helicopter the turbofan produces a propulsive force, the latter is expected to be suppressed entirely by the upward deflection of the exhaust gases towards the RELT, unless a fraction of this flow is expanded horizontally through the thrust valve, in which case part of the propulsive thrust is recovered.

If a fraction $\dot{m}_{TF}$ of the total mass flow $\dot{m}$ is diverted to propel the aircraft, $\dot{m}_t$ will decrease (Fig.4.33). Defining the thrust factor τ_f as the amount of thrust taken from the total thrust T_{Nt} generated by all engines to produce a propulsion force T_P :

$$\tau_f = \frac{T_P}{T_{Nt}} \approxeq \frac{\dot{m}_{TF}}{\dot{m}} \tag{4.159}$$

then P_T^* is, using Eq.4.146 and Eq.4.159 in Eq.4.158 :

$$P_T^* = \frac{(1 - \tau_f) T_{Nt}}{SPT} C_{pg} \frac{T_{t45}}{T_{t1}} T_{t1} \left[1 - \left(\frac{1}{\pi_F} \right)^{\frac{(\gamma_g - 1)}{\gamma_g} \eta_{p,T}} \right] \tag{4.160}$$

Note that :

$$\dot{m}_t = \dot{m}(1 - \tau_f) \tag{4.161}$$

and (Eq.4.146) :

$$\dot{m} = N_e \frac{T_N}{SPT} = \frac{T_{Nt}}{SPT} \tag{4.162}$$

where N_e is the number of engines. The fuel mass flow $\dot{m}_f$ follows from T_{Nt} and $TSFC$:

$$\dot{m}_f = N_e \, TSFC \, T_N = TSFC \, T_{Nt} \tag{4.163}$$

Now, proof is delivered that the non-dimensional RELT inlet temperature $\frac{T_{t45}}{T_{t1}}$, which was earlier examined as independent variable, depends entirely on BPR_{TF} and FAR. Examining control volume $CV2$ and neglecting the fuel mass flow on the mass balance, the first law gives :

$$\dot{m} C_p T_{t1} + \dot{m}_f LHV \eta_{CC} = \dot{m} C_{pg} T_{t4p} \tag{4.164}$$

Discarding any thermal losses, it is known that $T_{t4p} = T_{t45}$. Consequently :

$$C_p T_{t1} + TSFC \, \frac{T_{Nt}}{\dot{m}} \, LHV \eta_{CC} = C_{pg} T_{t45} \tag{4.165}$$

Finally, after substitution of Eq.4.155 :

$$\frac{T_{t45}}{T_{t1}} = \frac{C_p}{C_{pg}} + \frac{FAR/T_{t1}}{C_{pg}(1 + BPR_{TF})} LHV \eta_{CC} \tag{4.166}$$

where $\frac{T_{t45}}{T_{t1}}$ is only a function of BPR_{TF} (Fig. 4.34). For the considered BPR_{TF} domain, $\frac{T_{t45}}{T_{t1}}$ remains fairly low and under ISA SLS conditions, $LTIT$ resides mostly within the temperature operating range for a RELT suspended on grease-lubricated bearings ($\leq$ 400 K). For a given fuel-to-air ratio, $\frac{T_{t45}}{T_{t1}}$ drops with an increase in BPR_{TF} as a lower air fraction passes through the core section of the engine. Consequently, a lower temperature of the mixture of primary and secondary gases is observed. Substitution of Eq.4.166 in Eq.4.160 then yields for the RELT power output P_T^* :

$$P_T^* = \frac{(1 - \tau_f) T_{Nt}}{SPT/T_{t1}} \left[C_p + \frac{FAR/T_{t1}}{(1 + BPR_{TF})} LHV \eta_{CC} \right] \cdot \left[1 - \left(\frac{1}{\pi_F} \right)^{\frac{(\gamma_g - 1)}{\gamma_g} \eta_{p,T}} \right] \tag{4.167}$$

At this stage, one can evaluate the influence of the independent variables in Eq.4.167 on P_T^*. In order to maximise the delivered turbine power, values for T_{Nt}, π_F and $\eta_{p,T}$ must be high. Although having a lesser effect on the power production than the aforementioned parameters, a low BPR_{TF} should then be preferred. Indeed, selecting a low BPR_{TF} causes an increase in $\frac{T_{t45}}{T_{t1}}$, which is more important than the accompanying rise in SPT (this corresponds to a decrease in $\dot{m}$ – Section 4.5.1). Fig.4.35 substantiates this, where PG is the power gain, which is the power produced per unit of thrust $\frac{P_T^*}{T_{Nt}}$ and is discussed next.

Cycle power gain and coefficient of performance

In contrast to engines producing mechanical power, a thrust producing engine such as a turbofan does not allow the straightforward definition of a coefficient of performance.

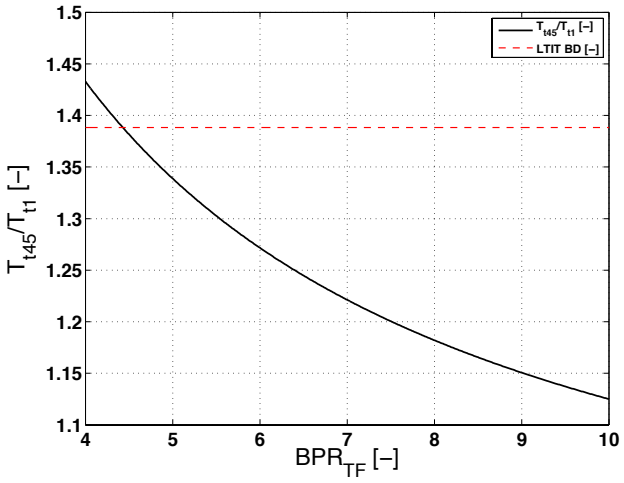

FIGURE 4.34. $\frac{T_{t45}}{T_{t1}}$ as a function of BPR_{TF} – Take-off regime.

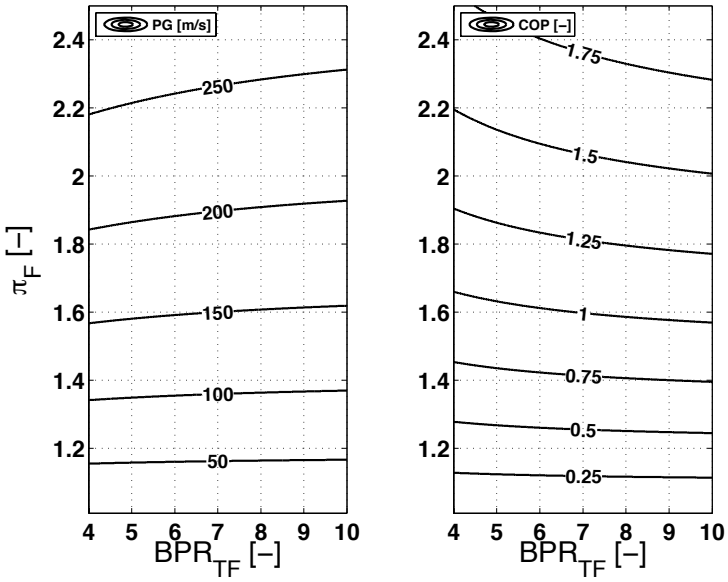

FIGURE 4.35. *PG* and *COP* as a function of BPR_{TF} and π_F, no losses (except TF), $\tau_f = 0$, T/O regime, ISA SLS.

A first yardstick for the efficiency of the thrust-to-power conversion is given by the power gain *PG*, which is nothing more than :

$$PG \triangleq \frac{P_T^*}{T_{Nt}} \tag{4.168}$$

Fig.4.35 already showed the effects of the independent variables BPR_{TF} and π_F on the power gain. A relation for the power gain is found easily by dividing Eq.4.160 by T_{Nt} :

$$PG = \frac{(1-\tau_f)}{SPT} C_{pg} \frac{T_{t45}}{T_{t1}} T_{t1} \left[1 - \left(\frac{1}{\pi_F} \right)^{\frac{(\gamma_g - 1)}{\gamma_g} \eta_{p,T}} \right] \tag{4.169}$$

or,

$$PG = \frac{(1-\tau_f)}{SPT/T_{t1}} \left[C_p + \frac{FAR/T_{t1}}{(1+BPR_{TF})} LHV \eta_{CC} \right] \cdot \left[1 - \left(\frac{1}{\pi_F} \right)^{\frac{(\gamma_g - 1)}{\gamma_g} \eta_{p,T}} \right] \tag{4.170}$$

Hence, the conclusions drawn for maximum turbine power output are also valid when aiming at maximising the power gain, viz. a need for high π_F, $\eta_{p,T}$, and low BPR_{TF}. Fig.4.35 shows that the power gain is mainly depending on π_F and much less on BPR_{TF} and accompanying $\frac{T_{t45}}{T_{t1}}$ variations. Since the turbofan net thrust ranges up to hundreds of kiloNewtons while the power gain is of the order of magnitude of 100, it becomes clear that important power levels can be achieved that lay well beyond the capability of any piston engine or turboshaft.

Unfortunately, the power gain does not reflect well how good the RELT recovers the total work performed by the turbofan on the gases per unit of time. This amount of work is the change in kinetic energy between inlet and outlet of the engine :

$$\dot{E}_k = \frac{1}{2} \left[\dot{m}_p \left(v_{j8}^2 - v_a^2 \right) + \dot{m}_s \left(v_{18}^2 - v_a^2 \right) \right] \tag{4.171}$$

Introducing an average exhaust gas speed $v_{j,av}$ and neglecting the airspeed v_a,

$$\dot{E}_k = \frac{1}{2} \dot{m} \, v_{j,av}^2 \tag{4.172}$$

By approximation, $v_{j,av}$ can be extracted from momentum theory (Fig. 4.28) :

$$v_{j,av} \approxeq \frac{T_{Nt}}{\dot{m}} = SPT \tag{4.173}$$

Defining now a new performance yardstick for the power-to-power conversion, denoted as coefficient of performance COP_{TF} :

$$COP_{TF} \triangleq \frac{P_T^*}{\dot{E}_k} \approxeq \frac{P_T^*}{\frac{1}{2} T_{Nt} \, SPT} = \frac{PG}{\frac{1}{2} SPT} \tag{4.174}$$

Substitution of Eq.4.167 in Eq.4.174 gives :

$$COP_{TF} \approxeq \frac{2(1-\tau_f)}{SPT^2/T_{t1}} C_{pg} \frac{T_{t45}}{T_{t1}} \left[1 - \left(\frac{1}{\pi_F} \right)^{\frac{(\gamma_g - 1)}{\gamma_g} \eta_{p,T}} \right] \tag{4.175}$$

or,

$$COP_{TF} = \frac{2(1-\tau_f)}{SPT^2/T_{t1}}\left[C_p + \frac{FAR/T_{t1}}{(1+BPR_{TF})}LHV\eta_{CC}\right]\cdot\left[1-\left(\frac{1}{\pi_F}\right)^{\frac{(\gamma_g-1)}{\gamma_g}\eta_{p,T}}\right] \tag{4.176}$$

The results are plotted in Fig.4.35. Therefrom one learns that COP_{TF} increases by selecting higher π_F and BPR_{TF}. The increase in COP_{TF} with BPR_{TF} was to be expected due to the quadratic influence of SPT, or, said differently, the decrease of the kinetic energy with rising BPR_{TF}.

Cycle specific fuel consumption

The cycle specific fuel consumption is identical to those defined for the previous cycles and is repeated here for matters of readability :

$$SFC \triangleq \frac{\dot{m}_f}{P_T^*} = \frac{TSFC}{PG} \tag{4.177}$$

Introducing Eq.4.163, Eq.4.155 and Eq.4.167 in the foregoing equation results in :

$$SFC = \frac{FAR/T_{t1}}{(1-\tau_f)(1+BPR_{TF})\left(C_p + \frac{FAR/T_{t1}}{(1+BPR_{TF})}LHV\eta_{CC}\right)\left(1-\left[\frac{1}{\pi_F}\right]^{\frac{\gamma_g-1}{\gamma_g}\eta_{p,T}}\right)} \tag{4.178}$$

SFC decreases unambiguously by an increase in BPR_{TF} and π_F. Evidently, decreasing the polytropic turbine efficiency deteriorates SFC. When the cycle needs to provide the system with a propulsive force, $\dot{m}_t$ drops while the injected amount of fuel remains unaltered. SFC will thus be sacrificed[xv]. Eq.4.178 is plotted in Fig.4.36 for maximum thrust settings at sea level, ISA atmosphere. Note that SFC of this cycle is in the same range of the ones found for the piston engine and turboshaft powered TDR cycles. Best efficiency is clearly obtained with high bypass ratio turbofan engines.

4.5.4 Cycle boundaries

Since the turbofan powered TDR cycle is an open system with no heat fluxes leaving the system, it is possible to close the open system by installing a fictitious heat exchanger, which brings the exhaust gases back to the initial state. Similar to Eq.4.128 in Section 4.4.4, it is possible to retrieve an approximation for the cycle Carnot specific fuel consumption SFC_{Carnot} :

$$\frac{P_T^*}{\dot{Q}_F} \leq \epsilon_{Carnot} \quad \Rightarrow \quad SFC \geq \frac{1}{\eta_{CC}LHV\left(1-\frac{T_{t1}}{T_H}\right)} = SFC_{Carnot} \tag{4.179}$$

[xv]If the flight speed v_a becomes important, a better way to define COP_{TF} and PG is then obtained by replacing the numerator in their respective definitions by $P_T^* + T_P\, v_a$, as the propulsive power yielded by the cycle $T_P\, v_a$ is also useful.

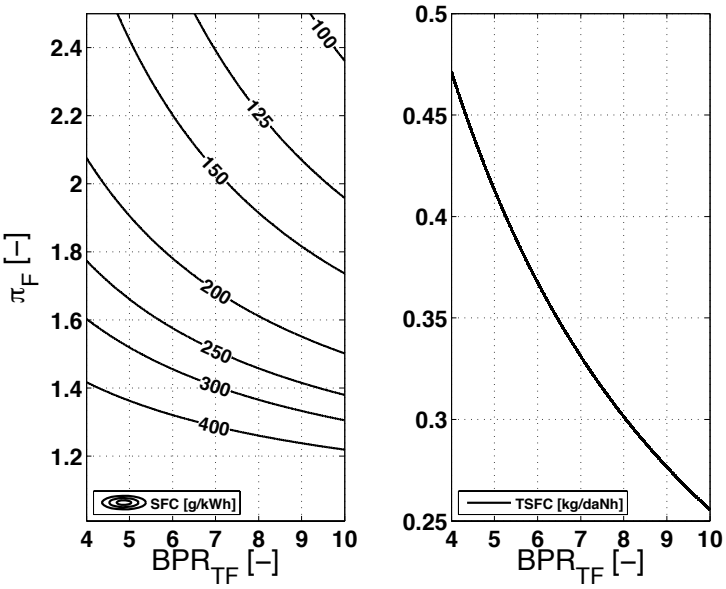

FIGURE 4.36. *SFC* and *TSFC* as a function of BPR_{TF} and π_F, no losses, $\tau_f = 0$, Take-off regime, ISA SLS.

From Jacques (2004b) and Table 4.9 : $T_H \cong 1850$ K, $\eta_{CC} \cong 0.99$ and $LHV = 43.2$ MJ/kg, which yields for ISA SLS conditions :

$$SFC_{Carnot} \cong 100 \text{ g/kWh} \tag{4.180}$$

With colder temperatures, this limit is further reduced, but has to be borne in mind.

4.5.5 Effect of the atmospheric pressure and temperature

One relies once more on the theory of corrected variables when examining the influence of variable atmospheric conditions on the performance parameters of the cycle. This technique however, may only be used when imposing fixed values for turbofan $\frac{TIT}{T_{t1}}$, flight Mach number, compressor pressure ratios and geometry (exhaust nozzle areas). The corrected performance parameters are the performance parameters one would observe on a standard day at sea level, thus at 288.15 K and 1 atm. For a turbofan it is found that, using AIAA (2003) :

$$T_{N,corr} = \frac{T_N}{\delta_{t1}} \tag{4.181}$$

$$TSFC_{corr} = \frac{TSFC}{\sqrt{\theta_{t1}}} \tag{4.182}$$

$$\dot{m}_{corr} = \frac{\dot{m}\sqrt{\theta_{t1}}}{\delta_{t1}} \tag{4.183}$$

$$\dot{m}_f = \frac{\dot{m}_f}{\delta_{t1}\sqrt{\theta_{t1}}} \tag{4.184}$$

From these equations, the corrected terms for FAR, SPT and BPR_{TF} are found :

$$FAR_{corr} = \frac{FAR}{\theta_{t1}} \tag{4.185}$$

$$SPT_{corr} = \frac{SPT}{\sqrt{\theta_{t1}}} \tag{4.186}$$

$$BPR_{TF,corr} = BPR_{TF} \tag{4.187}$$

Under the stated operating conditions, the corrected variables indicate that the colder the atmosphere, the lower the FAR and SPT will be. However, BPR_{TF} remains unaffected since primary and secondary mass flows undergo the same variation.

Substitution of the corrected variables in Eq.4.167, P_T^* then becomes :

$$P_{T,corr}^* = \frac{P_T^*}{\delta_{t1}\sqrt{\theta_{t1}}} \tag{4.188}$$

$$\tag{4.189}$$

Likewise, PG and COP_{TF} are found :

$$PG_{corr} = \frac{PG}{\sqrt{\theta_{t1}}} \tag{4.190}$$

$$COP_{TF,corr} = COP_{TF} \tag{4.191}$$

$$SFC_{corr} = SFC \tag{4.192}$$

The RELT power output will decrease when the atmospheric temperature and pressure drops. While PG deteriorates under colder atmospheric conditions, neither COP_{TF} nor SFC change under any temperature or pressure fluctuation. Nevertheless, the efficiency parameters of the cycle still depend on the evolution of the *required* P_T^* as a function of atmospheric conditions, viz. by the coaxial rotors. If more P_T^* is required, the turbofan thrust setting will have to be modified. Consequently, the performance characteristics of the cycle will have to be examined for a different corrected power setting. A model of the helicopter with coaxial rotors will allow the determination of the RELT power requirement. This work is examined in Chapter 8.

4.5.6 Notes on the parametric cycle study

Under the stated simplifications on which the above theory was established, a turbofan with high bypass and fan pressure ratio should be selected since it has a beneficial impact on SFC, $TSFC$ and COP_{TF}. Even though an increase in bypass ratio has been proven to affect the power gain negatively, it was observed that this effect remains minor.

The previous study assessed the performance characteristics of the cycle for the turbofan

operating at take-off regime under ISA SLS conditions, for which the engine manufacturer provides data. In case other operating regimes are required, a more detailed turbofan model will have to be established.

The results rely on an estimation of *SPT* and *TSFC*, for which correlations were derived. In Chapter 8, where a RELT will be designed for a specific application, a more involved calculation procedure will be used to establish the aforementioned variables.

4.6 Case study : cycle comparison

The performance characteristics of the piston engine, the turboshaft and the turbofan powered TDR cycles are now compared, using the realistic component parameters given in Table 4.11. The choice of the compressor and Ljungström turbine polytropic efficiencies differ slightly from those used previously during the piston engine and turboshaft powered TDR cycle studies – since based on other references – where now a more conservative value for the compressor efficiency is selected and an improved efficiency for the RELT. Note that the study where the Ljungström turbine efficiency is related to the cycle characteristics is part of Chapter 8.
The discussed cycles have their respective internal combustion engines working at the maximum operating regime. The engine parameters that will be examined parametrically are indicated in Table 4.12. The results of the comparative study are presented in Tables 4.13-4.18. There, the selected governing parameter to calculate the cycle performance will be indicated by the $\star$-symbol. Besides the parametric study on the engine parameters, variable cycle *LTIT* and atmospheric conditions will be assessed as well. Note that an *LTIT* higher than the limit of 400 K will be examined too in order to evaluate the performance capability of the cycles beyond the currently adopted temperature limit.
The impact of the variable atmosphere on the cycle performance is evaluated at two different altitudes, i.e. ISA sea level and ISA 10,000 ft. Since the new operating conditions are established using the procedures explained previously for a varying temperature and pressure, it is possible that some components in the cycle will need to be adapted in order to achieve the imposed cycle conditions, notably the compressor in the piston engine powered TDR cycle. However, this is acceptable since here, the cycles are evaluated from a design point perspective.
First, the results of each cycle will be analysed separately, after which the operating characteristics of the RELT cycles are compared for ISA SLS conditions.

4.6.1 Piston engines : Avgas (SPI) and Diesel

Tables 4.13-4.16 once more confirm the observations made during the previous sections. The most important differences between the Avgas and Diesel engine powered TDR cycles for a given *LTIT* and T_{t1} are (Tables 4.13-4.16) :

Table 4.11. Case study cycle component characteristics.

Variable	value	note
RR	0.98	assumed
η_M	0.98	assumed
$\eta_{p,C}$	0.86	Walsh & Fletcher (2004)
$\eta_{p,T}$	0.91	Houberechts (1972)
η_{CC} (GT)	0.99	Jacques (2004b)
η_{CC} (PE)	Eq.4.10 or Eq.4.11	Section 4.3.1
ϵ_H (TS)	0.80	Beck & Wilson (1996)

→ *BPR* Diesel < *BPR* Avgas, mainly because *FAR* Diesel < *FAR* Avgas

→ π_C Diesel < π_C Avgas as a result of η_{CC} Diesel > η_{CC} Avgas

→ P_T^* Diesel < P_T^* Avgas for same $P_{M,a}^*$ (lower pre-compression), but $\dot{m}_f$ Diesel is lower

→ *COP* Diesel is always slightly better than *COP* Avgas (π_C-effect)

Tables 4.13-4.16 present the results for RELT inlet temperatures of 400 K and 800 K. At 800 K, the pre-compression becomes significant, causing P_M^* to become excessively large (more than threefold the installed power at ISA SLS). Unless important changes are made to the piston engine (mechanical and thermal resistance), P_M^* has to be flat-rated. Though, the potential of a piston engine in the considered platform is noticeable. *COP* remains close to unity in all cases, but the gain increases by factors up to 1.5 for the higher *LTIT*. The range of use of the piston engine in a helicopter platform is consequently extended. Since *COP* is close to unity, *SFC* of the cycle has about the same magnitude of SFC_{PE}.

The effect of increasing altitude for a fixed *LTIT* improves the cycle performance parameters thanks to the higher $\frac{T_{t45}}{T_{t1}}$-fraction. However, the effect of decreasing pressure causes

Table 4.12. ICE operating range.

Engine	governing variable	range
All PE	$P_{M,a,corr}^*$ [kW]	50 . . . 300
Avgas SPI PE	SFC_{PE} [g/kWh]	250 . . . 400
Diesel PE	SFC_{PE} [g/kWh]	220 . . . 320
TS	$P_{M,a,corr}^*$ [kW]	100 . . . 2000
TF	$T_{Nt}[kN]$	2.5 . . . 500
	π_F [-]	1.7. . . 1.9
	τ_f [-]	0.0 . . . 0.5

a reduction of P^*_M and therefore P^*_T. If $\frac{T_{t45}}{T_{t1}}$ is kept constant, the higher altitude has almost no effect on the major cycle performance characteristics. The lower atmospheric pressure results again in a reduced P^*_T.

4.6.2 Turboshaft engine

The disadvantage of the cycle with a turboshaft engine is the limited heat recovery, even though ϵ_H is 80%, and the impossibility of the turboshaft to work in a pressurised environment (no pre-compression). Because of this, $\frac{T_{t45}}{T_{t1}}$ cannot attain the higher levels available in the piston engine powered TDR cycle. However, note that *COP* remains fairly close to unity, as indicated in Table 4.17. There, the higher range of *LTIT* (i.e. >400 K) corresponds to the optimum *BPR* selection with the lowest *SFC*, which is BPR_{L2}. *SFC* remains relatively close to SFC_{TS}, which proves that the cycle remains relatively competitive with respect to the conventional layout using a turboshaft. If a multi-engine layout is demanded, as discussed during the theory, one only needs to modify the values indicated in the Table appropriately (see ‡). For similar levels of *LTIT*, the fuel efficiency competitiveness between the piston engine and the turboshaft powered TDR cycles will depend entirely on the fuel efficiency and mass impact of the installed power source, where for the lower power class, the piston engine has the advantage.

The main impact of a change in altitude is the lower power output and reduced mass flows. Following the theory expounded in Section 4.4.6, the non-dimensional cycle parameters indicated in Table 4.17 remain invariable.

4.6.3 Turbofan engine

This cycle is most remarkable since it not only provides mechanical power to the rotors, but it can also produce propulsive thrust. Table 4.18 shows the results for a thrust factor interval $\tau_f = [0\ ;\ 0.5]$.

The calculations evaluated the cycle performance for a range of T_{Nt}, BPR_{TF} and π_F. The bypass ratio with value of 4.41 produces the RELT inlet temperature of 400 K, which allows a basis for comparison with the other cycles. The highest temperature of 800 K is not achievable with the turbofan powered TDR cycle because of the mixing of primary and secondary flows. Instead, the bypass ratio has been increased to 8, which offers a wider view on the cycle performance characteristics.

For the conditions where the thrust factor $\tau_f = 0$, the cycle exhibits power gains well above 100. The higher fan pressure ratios yield the better cycle performance when it comes to the coefficient of performance and cycle specific fuel consumption. The impact of selecting a higher bypass ratio is especially beneficial to the specific fuel consumption, while the power gain decreases by less than 5%. Similar observations can be made at the

higher altitude.

The potential to deliver high RELT power is possible with the turbofan powered TDR cycle. However, the high power setting comes at a price : the mass flow is probably undesirably high. Since the mass flow must pass through the RELT at a low expansion ratio, its size may become prohibitive because of a too important increase in rotor parasite drag (see Chapter 8).

Note that an increase in τ_f causes an important inversely proportional deterioration of the cycle power gain and specific fuel consumption. However, the specific fuel consumption remains acceptable with respect to the other cycles and it should not be forgotten that the RELT may be unloaded because the rotors require less thrust. Indeed, the delivered propulsive power should not be disregarded. An equivalent *SFC* could then be proposed, for example :

$$SFC_{eq} = \frac{\dot{m}_f}{P^*_T + T_P \, v_a} \tag{4.193}$$

However, for as long as v_a is significantly small, $SFC_{eq} \cong SFC$. The continuation of this study is not in the scope of the work at hand.

The impact of altitude reduces the power gain and thrust, yielding a lower RELT power output, as calculated in Section 4.5.5.

4.6.4 Cycles compared at ISA SLS

Table 4.19 summarises the important cycle characteristics when operating at ISA SLS and the maximum allowable RELT inlet temperature of 400 K. Firstly, the bypass ratio of any gas turbine powered cycle is lower than those required in the piston engine powered TDR cycles. The reason is the reduced fuel-to-air ratio for gas turbine engines causing a higher primary airflow fraction for a given $\frac{T_{t45}}{T_{t1}}$. Secondly, all RELT cycle pressure ratios remain below 2. This is structurally interesting when it comes to minimising the mass of the system (ducting, plenum, compressor, etc.). Thirdly, the *SFC* of the turbofan powered TDR cycle appears to perform best, especially bearing in mind that a selection of $BPR_{TF} > 4.41$ would be most natural yielding lower *SFC* and *LTIT*. Though, the Diesel piston engine powered TDR cycle deserves attention too since it is a low-cost and robust solution. Thanks to the pre-compression, it may perform well at higher altitudes thanks to the postponed smoke-limit. Fourthly, the turbofan cycle allows alleviating the rotors by taking over the thrust production. It is less probable that a similar capability could be offered by the other cycles due to the lower available mass flow rate. Finally, the power domain of the piston engine and turbofan powered TDR cycles tend to overlap, which makes the use of the turboshaft powered TDR cycle less attractive due to its increased

complexity and invoked weight penalty due to the installation of (a) heat exchanger(s).

4.7 Conclusions

Three TDR cycles have been proposed and examined, of which the piston engine and turbofan powered cycles offer the highest performance potential in respectively the low helicopter power class and the mid to high power class. The turboshaft powered cycle was found unattractive because of the involved weight penalty and increased complexity. The Ljungström turbine, and more specifically the polytropic efficiency, was considered to be insensitive to the cycle characteristics – the expansion ratio excepted – which implicates an important simplification. As a consequence, a Ljungström turbine performance model must be developed in order to match the cycle operating conditions such that the highest power gain is attained over the conventional helicopter. The Ljungström turbine characteristics are studied in the subsequent chapters.

Table 4.13. SPI (Avgas) powered TDR cycle performance characteristics.

	ISA SLS (288.15K, 1 atm)								**ISA 10,000 ft (264.34K, 0.688 atm)**							
$LTIT^{\star}$ [K]	400				800				400				800			
$\frac{T_{t45}}{T_{t1}}$ [-]	1.39				2.78				1.49				2.98			
BPR [-]	24.8				4.53				21.0				4.34			
$SFC_{PE}{}^{\star}$ [g/kWh]	250		400		250		400		250		400		250		400	
π_C [-]	1.72		1.42		6.93		3.85		1.92		1.53		8.06		4.31	
COP [-]	0.910		0.960		1.20		1.43		0.94		1.01		1.23		1.48	
PCF [-]	1.41		1.24		3.57		2.41		1.52		1.30		3.95		2.6	
$ECOP$ [-]	1.28		1.19		4.28		3.45		1.42		1.31		4.86		3.85	
SFC [g/kWh]	275		415		208		279		266		397		203		269	
$P^{*}_{M,a,corr}$ [kW]	50	300	50	300	50	300	50	300	50	300	50	300	50	300	50	300
P^{*}_{M} [kW]	70	422	62.0	372	178	1071	121	723	55.9	336	48.1	288	146	875	96.0	576
P^{*}_{T} [kW]	64.0	384	59.0	357	214	1285	172	1034	52.6	315	48.5	291	179	1076	142	852
$\dot{m}_t$ [kg/s]	1.24	7.42	1.74	10.4	0.672	4.03	0.726	4.36	0.834	5.03	1.15	6.91	0.53	3.18	0.558	3.35
$\dot{m}_p$ [kg/s]	0.0479	0.287	0.067	0.405	0.121	0.729	0.131	0.788	0.0380	0.298	0.0523	0.314	0.0992	0.595	0.105	0.627
$\dot{m}_s$ [kg/s]	1.189	7.13	1.67	10.0	0.550	3.30	0.595	3.57	0.799	4.80	1.10	6.59	0.431	2.58	0.459	2.72
$\dot{m}_f$ [g/s]	4.89	29.3	6.88	41.3	12.4	74.4	13.4	80.4	3.88	23.3	5.34	32.0	10.1	60.7	10.7	64.0

Table 4.14. SPI (Avgas) powered TDR cycle performance characteristics (Ct'd).

	ISA 10,000 ft (264.34K, 0.688 atm)							
$LTIT$ [K]	373				746			
$\frac{T_{t45}}{T_{t1}}^{\star}$ [-]	1.39				2.78			
BPR [-]	26.7				4.92			
$SFC_{PE}^{\star}$ [g/kWh]	250		400		250		400	
π_C [-]	1.70		1.41		6.86		3.82	
COP [-]	0.911		0.963		1.20		1.44	
PCF [-]	1.40		1.23		3.55		2.40	
$ECOP$ [-]	1.27		1.18		4.26		3.46	
SFC [g/kWh]	274		415		208		279	
$P^{*}_{M,a,corr}$ [kW]	50	300	50	300	50	300	50	300
P^{*}_{M} [kW]	51.6	309	45.5	273	131	786	88.6	531
P^{*}_{T} [kW]	47.0	282	43.8	263	157	943	127	765
$\dot{m}_t$ [kg/s]	0.972	5.83	1.37	8.24	0.527	3.16	0.571	3.43
$\dot{m}_p$ [kg/s]	0.0351	0.211	0.0496	0.297	0.0891	0.535	0.0964	0.579
$\dot{m}_s$ [kg/s]	0.937	5.62	1.32	7.94	0.438	2.63	0.474	2.85
$\dot{m}_f$ [g/s]	3.58	21.5	5.03	30.3	9.09	54.5	9.84	59.0

Table 4.15. Diesel engine powered TDR cycle performance characteristics.

	ISA SLS (288.15K, 1 atm)								**ISA 10,000 ft (264.34K, 0.688 atm)**							
$LTIT^{\star}$ [K]	400				800				400				800			
$\frac{T_{t45}}{T_{t1}}$ [-]	1.39				2.78				1.49				2.98			
BPR [-]	16.5				2.82				13.9				2.69			
$SFC_{PE}{}^{\star}$ [g/kWh]	220		320		220		320		220		320		220		320	
π_C [-]	1.54		1.35		5.12		3.36		1.69		1.45		5.92		3.76	
COP [-]	0.939		0.975		1.32		1.49		0.978		1.02		1.35		1.55	
PCF [-]	1.31		1.20		2.92		220		1.39		1.26		3.20		2.37	
$ECOP$ [-]	1.23		1.17		3.85		3.28		1.36		1.29		4.34		3.68	
SFC [g/kWh]	234		328		167		214		225		313		162		206	
$P^{*}_{M,a,corr}$ [kW]	50	300	50	300	50	300	50	300	50	300	50	300	50	300	50	300
P^{*}_{M} [kW]	65.4	392	59.9	359	146	875	110	660	51.4	308	46.4	278	119	712	87.6	526
P^{*}_{T} [kW]	61.4	368	58.4	350	192	1155	164	984	50.2	301	47.3	284	160	961	136	815
$\dot{m}_t$ [kg/s]	1.45	8.69	1.93	11.6	0.705	4.23	0.774	4.65	0.969	5.81	1.27	7.63	0.554	3.23	0.595	3.57
$\dot{m}_p$ [kg/s]	0.0828	0.497	0.110	0.661	0.185	1.11	0.203	1.22	0.0650	0.390	0.0854	0.512	0.150	0.901	0.161	0.968
$\dot{m}_s$ [kg/s]	1.37	8.19	1.82	10.9	0.521	3.12	0.572	3.43	0.904	5.42	1.19	7.12	0.405	2.42	0.434	2.60
$\dot{m}_f$ [g/s]	4.00	24.0	5.32	31.9	8.91	53.5	9.78	58.7	3.14	18.8	4.12	24.7	7.25	43.5	7.79	46.7

Table 4.16. Diesel engine powered TDR cycle performance characteristics (Ct'd).

	ISA SLS (288.15K, 1 atm)	
$LTIT^{\star}$ [K]	400	
$\frac{T_{t45}}{T_{t1}}$ [-]	1.39	
BPR [-]	16.5	
$SFC_{PE}{}^{\star}$ [g/kWh]	250	
π_C [-]	1.46	
COP [-]	0.953	
PCF [-]	1.26	
$ECOP$ [-]	1.20	
SFC [g/kWh]	262	
$P^*_{M,a,corr}$ [kW]	50	300
P^*_M [kW]	63.1	379
P^*_T [kW]	60.1	361
$\dot{m}_t$ [kg/s]	1.59	9.53
$\dot{m}_p$ [kg/s]	0.0968	0.545
$\dot{m}_s$ [kg/s]	1.50	8.98
$\dot{m}_f$ [g/s]	4.38	26.3

Table 4.17. TS powered TDR cycle performance characteristics - single engine configuration.

	ISA SLS (288.15K, 1 atm)				**ISA 10,000 ft (268.34K, 0.688 atm)**					
$LTIT$[K]	400*		683	643	400*		636	598	373	
$\frac{T_{t45}}{T_{t1}}$ [-]	1.39		2.37	2.23	1.49		2.37	2.23	1.39*	
$P^*_{M,a,corr}{}^{\star\ddagger}$ [kW]	100	2000	100	2000	100	2000	100	2000	100	2000
$P^*_M{}^\ddagger$ [kW]	98.0	1960	98.0	1960	65.0	1301	65.0	1301	65.0	1301
SFC_{TS} [g/kWh]	463	287	463	287	463	287	463	287	643	287
BPR [-]	4.81	4.75	1.15* $^\diamond$	1.15* $^\diamond$	3.71	3.68	1.15* $^\diamond$	1.15* $^\diamond$	4.81	4.75
π_C [-]	1.30	1.52	2.64	4.22	1.40	1.70	2.65	4.22	1.30	1.52
COP [-]	0.986	0.941	1.36	1.11	1.03	0.976	1.36	1.11	0.986	0.941
SFC [g/kWh]	471	305	340	258	448	294	339	258	471	305
$P^*_T{}^\ddagger$ [kW]	96.6	1844	133	2176	67.0	1270	88.4	1444	64.1	1224
$\dot{m}_t{}^\ddagger$ [kg/s]	3.64	44.5	0.870	10.8	2.00	24.6	0.619	7.69	2.59	31.7
$\dot{m}_p{}^\ddagger$ [kg/s]	0.756	9.38	0.756	9.38	0.539	6.68	0.539	6.68	0.539	6.68
$\dot{m}_f{}^\ddagger$ [g/s]	12.6	156	12.6	156	8.36	104	8.36	104	8.36	104

‡ Multiply by N_e when installing N_e engines.
$\diamond$ $BPR = BPR_{L2}$, i.e. SFC_{min}

Table 4.18. TF powered TDR cycle performance characteristics - single engine configuration.

	ISA SLS (288.15K, 1 atm)								**ISA 10,000 ft (268.34K, 0.688 atm)**							
$LTIT$ [K]	400*				341				373				317			
$\frac{T_{t45}}{T_{t1}}$ [-]	1.39				1.182				1.39*				1.182			
BPR [-]	4.41				8*				4.41				8*			
$TSFC$ [kg/daNh]	0.446				0.301				0.430				0.291			
SPT [m/s]	329				292				317				282			
$\pi_F{}^\star$ [-]	1.7		1.9		1.7		1.9		1.7		1.9		1.7		1.9	
$T_{Nt,corr}{}^\ddagger$[kN]	2.5	500	2.5	500	2.5	500	2.5	500	2.5	500	2.5	500	2.5	500	2.5	500
$T_{Nt}{}^{\star\ddagger}$[kN]	2.45	490	2.45	490	2.45	490	2.45	490	1.68	337	1.68	337	1.68	337	1.68	337
$\dot{m}_f{}^\ddagger$ [kg/s]	0.0303	6.06	0.303	6.06	0.0205	4.10	0.0205	4.10	0.0201	4.02	0.0201	4.02	0.136	2.72	0.0136	2.72
τ_f=0.0																
PG [m/s]	159		190		152		182		154		184		147		176	
COP_{TF} [-]	0.969		1.16		1.04		1.25		0.969		1.16		1.04		1.25	
SFC [g/kWh]	280		234		198		166		280		234		198		166	
$P_T^{*\ddagger}$ [MW]	0.390	78.0	0.466	93.2	0.373	74.7	0.446	89.2	0.259	51.8	0.309	61.7	0.248	49.5	0.296	59.2
$\dot{m}_t{}^\ddagger$ [kg/s]	7.46	1491	7.46	1491	8.39	1678	8.39	1678	5.31	1063	5.31	1063	5.98	1196	5.98	1196
$T_P{}^\ddagger$ [kN]	0	0	0	0	0	0	0	0	0	0	0	0	0	0	0	0
τ_f=0.5																
PG [m/s]	79.6		95.1		76.2		91.0		76.8		91.8		73.5		87.8	
COP_{TF} [-]	0.485		0.579		0.522		0.624		0.485		0.579		0.522		0.624	
SFC [g/kWh]	560		468		396		331		560		468		396		331	
$P_T^{*\ddagger}$ [MW]	0.195	39.0	0.233	46.6	0.187	37.3	0.22	44.6	0.129	25.9	0.155	30.9	0.124	24.8	0.148	29.6
$\dot{m}_t{}^\ddagger$ [kg/s]	3.73	746	3.73	746	4.20	839	4.20	839	2.66	531	2.66	531	2.99	598	2.99	598
$T_P{}^\ddagger$ [kN]	1.225	245	1.225	245	1.225	245	1.225	245	0.842	168	0.842	168	0.842	168	0.842	168

‡ Multiply by N_e when installing N_e engines.

Table 4.19. Cycle comparison – ISA SLS, *LTIT*=400 K.

	SPI	**Diesel PE**	**TS**	**TF**	**TF**
ops. var. ⋆	SFC_{PE}	SFC_{PE}	$P_{M,a,corr}$	π_F	π_F
	250 . . . 400 g/kWh	220 . . . 320 g/kWh	100. . . 2000kW	1.7 . . . 1.9	1.7 . . . 1.9
				τ_f=0.0	τ_f=0.5
				T_{Nt}=2.5 . . . 500kN	
BPR [-]	24.8	16.5	4.81 . . . 4.75	4.41	4.41
$\pi_{C/F}$ [-]	1.72. . . 1.42	1.54. . . 1.35	1.30. . . 1.52	1.7. . . 1.9	1.7. . . 1.9
SFC [g/kWh]	275. . . 415	234. . . 328	471. . . 305	280. . . 234	560. . . 468
$COP_{(TF)}$ [-]	0.910. . . 0.960	0.939. . . 0.975	0.986 . . . 0.941	0.969. . . 1.16	0.485. . . 0.579
ECOP [-]	1.28 . . . 1.19	1.23 . . . 1.17	-	-	-
PG [m/s]	-	-	-	159 . . . 190	79.6 . . . 95.1
P^*_T [kW]	59 . . . 384	58.4 . . . 368	100 . . . 2000	390 . . . 93200	195 . . . 46600

• Note : the indicated range of values for one variable of a given engine type does not necessarily match with the ones stated for another for the same engine.
• The above-mentioned values are for single-engine configurations.

4.8 Nomenclature

Please note that the units listed below apply unless stated otherwise.

Abbreviations and substance formulae

BPR	Cycle bypass ratio	[-]
BPR_{TF}	Turbofan bypass ratio	[-]
C	Compressor	
C_p	Specific heat at constant pressure	[J/kgK]
COP	Coefficient of performance	[-]
COP_{TF}	Turbofan powered TDR cycle coefficient of performance	[-]
CV	Control volume	
$ECOP$	Equivalent coefficient of performance	[-]
EGT	Turbofan exhaust gas temperature	[K]
E95	Euro-95 fuel	
FAR	Fuel-to-air ratio	[-]
GBX	Gearbox	
h_t	Specific total enthalpy	[J/kg]
$\dot{H}_t$	Total enthalpy flux	[W]
HBPR	High bypass ratio	
HEX	Heat exchanger	
ISA	International Standard Atmosphere	
LHV	Fuel lower heating value	[J/kg]
$LTIT$	Ljungström turbine inlet temperature	[K]
$\dot{m}$	Mass flow rate	[kg/s]
$\dot{m}_f$	Fuel mass flow rate	[kg/s]
$\dot{m}_p$	Primary mass flow rate	[kg/s]
$\dot{m}_s$	Secondary mass flow rate	[kg/s]
$\dot{m}_t$	Turbine mass flow rate	[kg/s]
$\dot{m}_{TF}$	Mass flow bled to produce propulsive thrust	[kg/s]
M	Mach number	[-]
MIX	Mixing chamber	
N_e	Number of installed engines	[-]
$\mathcal{O}(x)$	Order of magnitude 10^x	[-]
OPR	Turbofan overall pressure ratio	[-]
p	Static pressure	[Pa]
p_t	Total pressure	[Pa]
P	Power	[W]

P^*_M	Delivered internal combustion engine power	[W]
P^*_T	Delivered turbine power	[W]
PCF	Pre-compression factor	[-]
PE	Piston engine	
PG	Power gain	[-]
$\dot{Q}$	Heat flow	[W]
$\dot{Q}_C$	(Cooling) Heat loss to environment	[W]
$\dot{Q}_F$	Heat added by the combustion process	[W]
R_g	Specific gas constant	[J/kgK]
RELT	Rotor-embedded Ljungström turbine	
RR	Ram recovery	[-]
SFC	Cycle specific fuel consumption	[kg/Ws]
SFC_{PE}	Piston engine specific fuel consumption	[kg/Ws]
SFC_{TS}	Turboshaft engine specific fuel consumption	[kg/Ws]
SLS	Sea Level Static	
SOV	Shut-off valve	
SPI	Spark ignition engine	
SPP	Specific power density, mass weighed	[kW/kg]
SPT	Turbofan specific thrust	[Ns/kg]
SPV	Specific power density, volume weighed	[kW/L]
T_N	Turbofan maximum take-off (net) thrust	[N]
T_{Nt}	Installed maximum take-off (net) thrust	[N]
T_P	Propulsive thrust	[N]
T_t	Total temperature	[K]
TDR	Turbine driven rotor	
TF	Turbofan	
TIT	Turbofan turbine inlet temperature	[K]
T/O	Take-off	
TS	Turboshaft	
$TSFC$	Thrust specific fuel consumption	[kg/Ns]
v	Absolute flow speed	[m/s]
$v_{j,av}$	Turbofan exhaust gas average speed (full expansion)	[m/s]
VLR	Very light rotorcraft	
x_c	Cooling fraction	[-]
γ	Isentropic exponent	[-]
δ	Non-dimensional pressure	[-]
δ_t	Non-dimensional total pressure	[-]

ΔT_C	Temperature increase over intermediate and high pressure compressor	[K]
ΔT_F	Temperature increase over fan	[K]
ΔT_{max}	Maximum temperature drop over heat exchanger	[K]
ϵ_{Carnot}	Carnot effectiveness	[-]
ϵ_H	Heat exchanger efficiency	[-]
ϵ_{th}	Cycle thermal effectiveness (efficiency)	[-]
η_{CC}	Combustion efficiency	[-]
η_M	Mechanical transmission efficiency	[-]
$\eta_{p,C}$	Compressor polytropic efficiency	[-]
$\eta_{p,T}$	Turbine total-to-total polytropic efficiency	[-]
θ	Non-dimensional temperature	[-]
θ_t	Non-dimensional total temperature	[-]
π_C	Cycle/Compressor pressure ratio	[-]
π_F	Turbofan fan pressure ratio	[-]
π_{ov}	Turboshaft overall pressure ratio	[-]
π_T	Turbine total-to-total expansion ratio	[-]
ρ	Density	[kg/m^3]
σ	Non-dimensional density	[-]
σ_t	Non-dimensional total density	[-]
τ_f	Thrust factor	[-]
ϕ	Equivalence ratio	[-]

Subscripts and superscripts

a	Atmosphere
A	Avgas engine related
C	Compressor related
$Carnot$	Related to the Carnot effectiveness boundary
$corr$	Corrected
D	Diesel engine related
ex	Exhaust gases
f	Fuel related
F	Fuel or fan related
g	Exhaust gas related
H	High temperature heat source
in	Inlet
L	Low temperature heat source
$L1$	Heat exchanger $T_{t2} \leq T_{t4p}$ limit
$L2$	Heat exchanger $\dot{Q}_{ex} \leq \dot{Q}_{\Delta T_{max}}$ limit

$L3$	Heat exchanger $T_{t2} \leq T_{t45}$ limit
M	Mechanical power, engine related
M, a	Installed mechanical power, engine related
out	Outlet
p	Primary flow related
PC	Post combustion
PE	Piston engine
s	Secondary flow related
st	Stoichiometric
t	RELT related or total component
TF	Turbofan
TS	Turboshaft
1	Compressor/Cycle inlet
18	Turbofan (fictitious) secondary flow outlet conditions
2	Compressor outlet
$2p$	Engine inlet
$2s$	Bypass inlet
$3s$	Secondary flow, mixer inlet
$4p$	Engine exhaust
45	RELT inlet
8	Turbofan (fictitious) primary flow outlet conditions

Chapter 5

Ljungström turbine governing parameters and equations

"There is nothing more practical than a good theory."

Immanuel Kant – *Demir et al. (2014)*

The goal of this chapter is to provide the key elements required to establish a Ljungström turbine performance model. First, the assumptions, definitions and conventions used will be highlighted. Then, the governing parameters and equations will be discussed, which allow the linking of the thermodynamic, fluid mechanic and geometric properties related to the turbine. Finally, some pertinent efficiency definitions will be discussed, as a prologue to the subsequent chapter dealing with the various losses in the turbine.

5.1 Conventions

5.1.1 Gases

The gases used in the model are considered to be ideal gases. This means that the perfect gas law is applicable, i.e. – Çengel & Cimbala (2010) :

$$p = \rho R_g T \tag{5.1}$$

Also, it implies that the specific heats C_p and C_v are temperature dependent. Walsh & Fletcher (2004) mention that a reasonably accurate prediction i.e. within 1% of the correct result may be achieved by performing the calculations assuming a constant value for C_p and C_v, which are determined for the average temperature over the examined process for the given gas.

5.1.2 Primary and secondary crown

With regard to the Ljungström turbine, the definition of a *crown* may be a matter of discussion. In French, *couronne* means crown, but it is also used to designate a single turbine stage. The author of this work regards crown as *the assembly of a single turbine disk with blades and rims*[i] (Fig.5.1). The primary crown (C1) has the first stage and all other odd numbered stages, while the secondary crown (C2) has the second stage and all the even numbered stages (Fig.5.2).

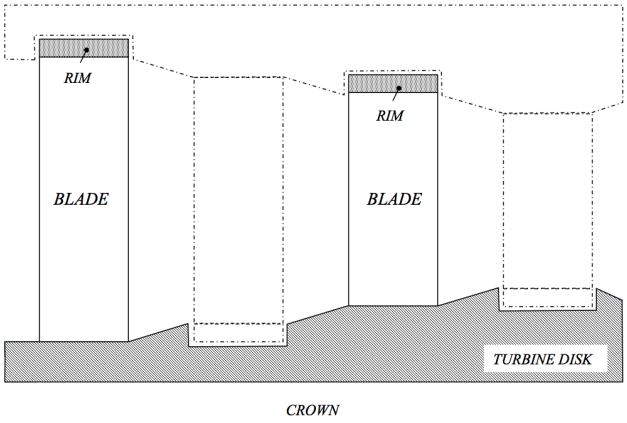

FIGURE 5.1. Ljungström turbine : definition of crown.

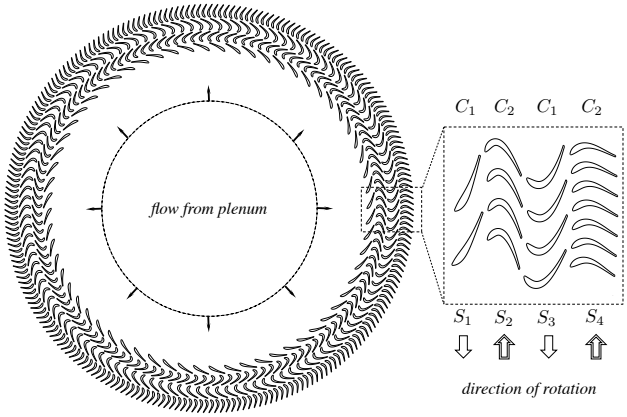

FIGURE 5.2. Ljungström turbine crown and stage numbering.

5.1.3 Planar uniform flow

For the modelling of the Ljungström turbine, a planar flow is assumed, i.e. axial flow components are considered negligible. The stream surfaces are consequently considered to lie in radial planes. As a result, velocity vectors will have only radial and tangential speed components. Three dimensional flow effects due to the presence of endwalls are

[i] Like the Saint Edward's crown, where the outer ring is connected to the centre.

adopted in the endwall losses. An additional simplification is to adopt the uniform flow condition in each section.

5.1.4 Flow angle reference system

In the literature, the angles of the flow with respect to the blade are expressed following generally two reference systems :

1. aligned with the rotational velocity vector $\vec{u}$ (e.g. Aungier (2006)).
2. perpendicular to the rotational velocity vector $\vec{u}$ (e.g. Lewis (1996), Dixon (2005)).

The author of this work follows the second convention, adopting the *radial* direction as the zero-angle reference. In contrast to what is found in the literature, the sign convention of vector angles will always follow the right-handed cartesian coordinate system regardless whether it concerns an inlet or an outlet. As a consequence, the sign of the angles are positive in the first quadrant and negative in the fourth quadrant. The angle conventions are indicated clearly in Fig.5.3.

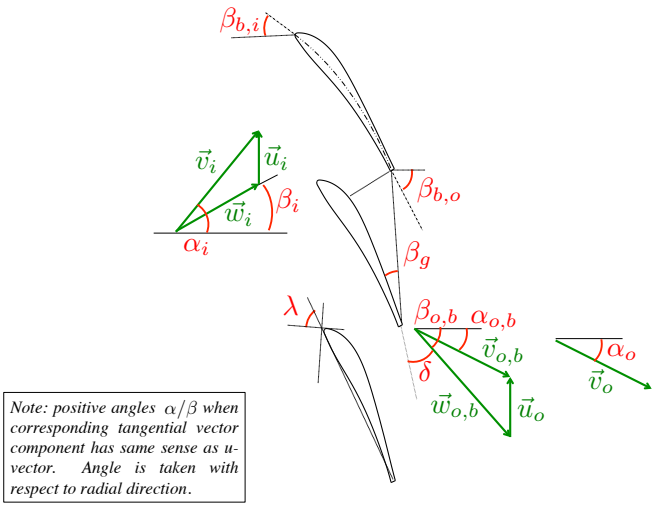

Figure 5.3. Angle and -sign convention used in a Ljungström turbine stage.

5.2 Geometric parameters

5.2.1 Suffixation

→ The suffix *i* will stand for the inlet of the turbine stage or turbine, unless explicitly stated otherwise.

→ The suffix *o* represents the outlet of the turbine stage or turbine.

→ The suffix o, b is designated to the properties as they leave the blade cascade, i.e. prior to mixing with the leakage mass flow and addition of disk friction loss effects.

→ Note that a suffix i, b will not be defined as it is assumed reasonable to consider the inlet conditions in front of the blade i, b and the stage i as equal.

→ The suffix j will stand for any stage or section in the turbine, unless stated otherwise.

5.2.2 Cascade related geometric parameters

The Ljungström turbine is a centrifugal turbine made of several stages. Each stage forms a rotating circular cascade (Fig.5.4). The flow enters the cascade at radius R_i and leaves it at radius R_o. The blade passage is the canal formed between the pressure side of one blade and the suction side of the subsequent blade. The inlet passage length t_i is the arc length between the leading edge of subsequent blades. The outlet passage length t_o is the arc length between the trailing edges of subsequent blades. The pitch angle Π_p is then defined as :

$$\Pi_p = \frac{t_j}{R_j} \tag{5.2}$$

where j stands for either the inlet section i or the outlet section o. The pitch of the stage s is the (linear) distance between the trailing edges of subsequent blades. If Π_p is small, it is found that :

$$s \approxeq t_o \tag{5.3}$$

5.2.3 Blade related geometric parameters

The chord c of the blade is indicated in Fig.5.4 and is the straight line connecting the leading edge with the trailing edge. The projection of c on the radial reference is c_a. Fig.5.4 also highlights the minimum section or throat of the blade passage o. Note that the position and size of o depends on the selected blade profile. The gauging angle β_g is by definition – Aungier (2006) :

$$\beta_g \triangleq \operatorname{asin}\left(\frac{o}{s}\right) \tag{5.4}$$

The height of the blade near the inlet is H_{bi}. The height of the blade may change throughout the passage. The blade height near the outlet of the stage then is H_{bo}. Consequently, the height of the blade is defined as the arithmetic mean of the previously stated, viz. (Fig.5.5) :

$$H_b \triangleq \frac{H_{bi} + H_{bo}}{2} \tag{5.5}$$

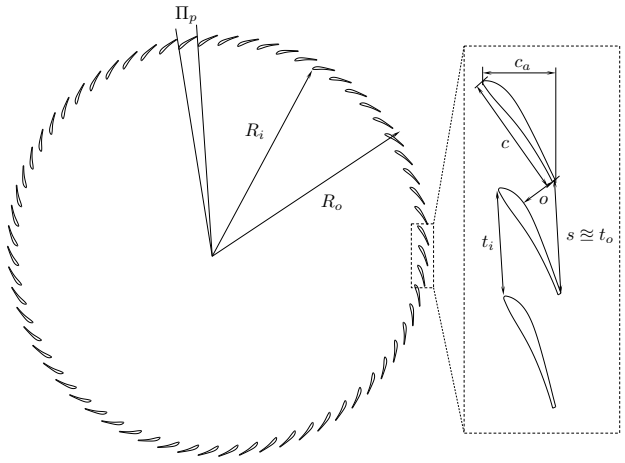

FIGURE 5.4. Geometric parameters defined for a Ljungström turbine stage.

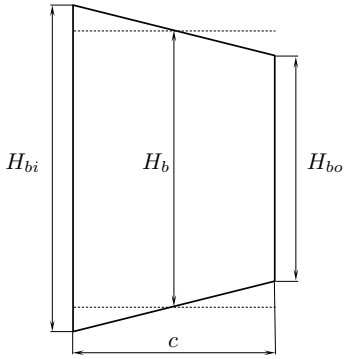

FIGURE 5.5. Blade height definitions for a Ljungström turbine stage.

and,

$$\overline{B} \triangleq \frac{H_{bo}}{H_{bi}} \tag{5.6}$$

An additional important geometric parameter is the blade aspect ratio $\mathcal{AR}$:

$$\mathcal{AR} \triangleq \frac{H_b}{c} \tag{5.7}$$

Some loss models require the projected aspect ratio $\mathcal{AR}_a$:

$$\mathcal{AR}_a \triangleq \frac{H_b}{c_a} \tag{5.8}$$

Finally it is essential to note that the outlet-to-inlet radius ratio R_o/R_i is a fundamental variable when studying the performance characteristics of a Ljungström turbine stage and that it impacts $\overline{B}$ significantly.

5.2.4 Interstage space related geometric parameters

The height of the space between two subsequent blade rows may also vary. If ${}^{j}H_{bo}$ is the outlet blade height of stage S_j and ${}^{j+1}H_{bi}$ the inlet blade height of stage S_{j+1}, then the following geometric parameter may be defined (Fig.5.6) :

$${}^{j}\overline{H} = \frac{{}^{j+1}H_{bi}}{{}^{j}H_{bo}} \tag{5.9}$$

The radial distance between two subsequent stages is Δ_{is}.

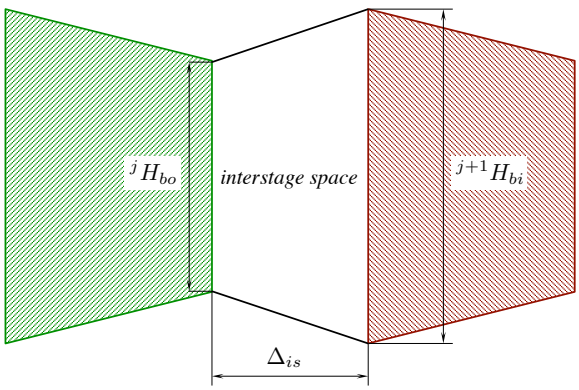

Figure 5.6. Interstage space height evolution between Ljungström turbine stages (for illustrative purposes only).

5.3 Duty parameters

5.3.1 Flow coefficient

The flow coefficient represents the non-dimensional radial flow speed at a given position in the turbine. It is defined as :

$$\phi_j \triangleq \frac{v_{R_j}}{u_j} \tag{5.10}$$

where v_{R_j} and u_j the radial speed and the rotational speed respectively in j. It must be noted that in the axial turbine theory, ϕ is considered to be constant. This is an important simplification of the theory, unless adopted as a design criterion. For the Ljungström turbine, the author prefers to avoid this simplification, especially since the effects of an increase in radius are à priori unknown, while imposing important design restrictions at this point would appear not sensible. Hence, because of the compressibility of the gases and the possible change in inlet i and outlet o areas, the flow coefficients at the inlet and the outlet can be smaller than, equal to or larger than each other :

$$\phi_i \lesseqgtr \phi_o \tag{5.11}$$

5.3.2 Work coefficient

The work coefficient ψ is the non-dimensional specific total enthalpy drop over the turbine blade passage in a stage :

$$\psi \triangleq \frac{h_{ti} - h_{to,b}}{u_i^2} \tag{5.12}$$

h_{ti} and $h_{to,b}$ are respectively the specific total enthalpy at the inlet of the stage and the specific total enthalpy at the outlet of the blade passage, i.e. before adding the enthalpy increment due to leakage and friction losses.

5.3.3 Reaction degree

The reaction degree $\hat{R}$ will appear important in the blade geometry selection process. It is the ratio of the reactive power and the total power delivered by the turbine blades in a stage :

$$\hat{R} \triangleq \frac{P_R}{P_{st,b}} \tag{5.13}$$

5.3.4 Non-dimensional inlet specific total enthalpy

The non-dimensional specific total enthalpy at the inlet $\hat{\theta}$ is by definition :

$$\hat{\theta} \triangleq \frac{h_{ti}}{u_i^2} \tag{5.14}$$

It represents not only the total temperature at the inlet of a turbine stage, but contains also additional information about the rotational velocity of the stage. Indeed, if a stage total inlet temperature T_{ti} is given and for a given inlet radius R_i :

$$\hat{\theta} \propto \frac{T_{ti}}{N^2} \tag{5.15}$$

where N the angular (rotational) velocity of the particular turbine stage. Rewriting the above equation leads to the typical expression of the reduced angular velocity of a turbine stage :

$$\frac{N}{\sqrt{T_{ti}}} \propto \frac{1}{\sqrt{\hat{\theta}}} \tag{5.16}$$

5.3.5 Turbine slip factor

The angular velocity of the primary and secondary crowns may differ since they are not mechanically connected. Designating the primary crown as the reference, one defines the turbine slip factor as :

$$S_\Omega \triangleq \left| \frac{\Omega_{C2}}{\Omega_{C1}} \right| \tag{5.17}$$

where Ω_{C1} and Ω_{C2} are respectively the angular velocity of the primary and the secondary crown.

5.4 Stage governing equations

5.4.1 Conservation of mass

The Ljungström turbine is on open system in which mass is conserved. Hence, it is possible to write for the system and each subsystem (continuity equation) :

$$\sum_{in} \dot{m} - \sum_{out} \dot{m} = 0 \tag{5.18}$$

5.4.2 First law

The Ljungström turbine is an open system, where any kind of heat exchange with the environment is neglected (adiabatic). The inlet and outlet of the turbine are in the same

horizontal plane and as a consequence there is no change in potential energy. It is assumed that there are no leakage losses between the inlet and outlet of the system. Hence, the mass flows entering and leaving the system are identical ($\dot{m}$). From the first law of thermodynamics, the power delivered by the surroundings on the system $\dot{W}$ then is :

$$\dot{W} = \dot{m}(h_{to} - h_{ti}) \tag{5.19}$$

Note that $\dot{W}$ is negative when power is delivered by the system to the surroundings. Applying the above formula on the blade passage of a stage, where $P_{st,b}$ the power delivered by the blades and in that particular case positive by convention :

$$P_{st,b} = \dot{m}_b(h_{ti} - h_{to,b}) \tag{5.20}$$

Note that the conditions at the outlet of the stage o will differ from the conditions at the outlet of the blades o, b by the presence of leakage and friction losses, as will be proven in a subsequent section.

5.4.3 Euler-Rateau

If the power delivered by the blades of a turbine stage on crown Cj *to* the surroundings is $P_{st,b}$ at an angular velocity Ω_{Cj}, then a torque is exerted on the flow, which may be expressed by the change in angular momentum. From Çengel & Cimbala (2010) it is proven that :

$$\frac{P_{st,b}}{|\Omega_{Cj}|} = \left(\sum \vec{R} \times \dot{m}_b \vec{v}\right)_i - \left(\sum \vec{R} \times \dot{m}_b \vec{v}\right)_{o,b} \tag{5.21}$$

where $\dot{m}_b$ the mass flow passing through the blade passages. $\vec{v}$ is the absolute speed of the flow and $\vec{R}$ the radius vector originating from the centre of the turbine. Further analysis of Eq.5.21 yields :

$$P_{st,b} = \dot{m}_b|\Omega_{Cj}|(R_i v_{i_u} - R_o v_{o,b_u}) \tag{5.22}$$

or,

$$P_{st,b} = \dot{m}_b(u_i v_{i_u} - u_o v_{o,b_u}) \tag{5.23}$$

which is the equation of Euler-Rateau. Note that the suffix u stands for the tangential component of the absolute speed v (Fig.5.3). Substituting Eq.5.20 in Eq.5.23 gives :

$$h_{ti} - h_{to,b} = u_i v_{i_u} - u_o v_{o,b_u} \tag{5.24}$$

5.4.4 Rothalpy

The definition of the specific total enthalpy is – Çengel & Cimbala (2010) :

$$h_t = h + \frac{v^2}{2} \tag{5.25}$$

Since planar flow is adopted, the above equation may be rewritten as (Fig.5.3) :

$$h_t = h + \frac{v_R^2}{2} + \frac{v_u^2}{2} = h + \frac{w_R^2}{2} + \frac{(u + w_u)^2}{2} \tag{5.26}$$

$$h_t = h + \frac{w^2}{2} + \frac{u^2}{2} + uw_u \tag{5.27}$$

Defining the specific relative total enthalpy as :

$$h_{tr} \triangleq h + \frac{w^2}{2} \tag{5.28}$$

and introducing the former in Eq.5.27 :

$$h_t = h_{tr} + \frac{u^2}{2} + uw_u \tag{5.29}$$

Substitution of this result in Eq.5.24 and simplifying the terms results in the following expression :

$$\mathcal{R} \triangleq h_{tri} - \frac{u_i^2}{2} = h_{tro,b} - \frac{u_o^2}{2} \tag{5.30}$$

where $\mathcal{R}$ is defined as the rothalpy of the rotor. It is constant throughout the turbine blade passage. An interesting consequence then is :

$$h_{tro,b} = h_{tri} - \frac{u_i^2}{2}\left[1 - \left(\frac{R_o}{R_i}\right)^2\right] \tag{5.31}$$

which will be of use in Section 5.4.7.

5.4.5 Active and reactive stage power

It is instructive to analyse the specific total enthalpy drop over the blades of the turbine stage using the rothalpy equation. Recalling Eq.5.25 and Eq.5.28 and substitution of these formulae in Eq.5.30 results in :

$$h_{ti} - h_{to,b} = \left(\frac{v_i^2 - v_{o,b}^2}{2}\right) + \left(\frac{w_{o,b}^2 - w_i^2}{2} - \frac{u_o^2 - u_i^2}{2}\right) \tag{5.32}$$

The active stage power is now defined as :

$$P_A \triangleq \dot{m}_b \left(\frac{v_i^2 - v_{o,b}^2}{2} \right) \tag{5.33}$$

while the reactive stage power is :

$$P_R \triangleq \dot{m}_b \left(\frac{w_{o,b}^2 - w_i^2}{2} - \frac{u_o^2 - u_i^2}{2} \right) \tag{5.34}$$

and,

$$P_{st,b} = P_A + P_R \tag{5.35}$$

The reaction degree $\hat{R}$ can now be rewritten as (Eq.5.13) :

$$\hat{R} = \frac{P_{st,b} - P_A}{P_{st,b}} = 1 - \frac{P_A}{P_{st,b}} \tag{5.36}$$

5.4.6 Blade inlet conditions

The absolute inlet flow angle α_i is considered to be known for each stage. Indeed, the gases enter the turbine radially ($\alpha_i = 0$) after leaving the plenum. For any other stage, a downstream marching turbine calculation procedure will allow the inlet conditions to be known from the analysis of the previous stage. A similar condition is also true for the total temperature T_{ti} and total pressure p_{ti} in front of each turbine stage. If the mass flow $\dot{m}_b$ entering the blade passages of the stage is :

$$\dot{m}_b = \rho_i A_i v_{i_R} \tag{5.37}$$

and the inlet section,

$$A_i = 2\pi R_i H_{bi} \tag{5.38}$$

while replacing ρ_i with p_i and T_i in Eq.5.37 using Eq.5.1 and substituting – Çengel & Cimbala (2010) :

$$T_{ti} = T_i \left(1 + \frac{\gamma - 1}{2} M_i^2 \right) \tag{5.39}$$

$$p_{ti} = p_i \left(1 + \frac{\gamma - 1}{2} M_i^2 \right)^{\frac{\gamma}{\gamma - 1}} \tag{5.40}$$

results in the following equation for mass flow :

$$\dot{m}_b = \frac{p_{ti}}{\sqrt{T_{ti}}} \sqrt{\frac{\gamma}{R_g}} \, A_i \, \Theta_i \, \cos \alpha_i \tag{5.41}$$

where,

$$\Theta_i = M_i \left(1 + \frac{\gamma - 1}{2} M_i^2\right)^{-\frac{1}{2}\frac{(\gamma+1)}{(\gamma-1)}} \tag{5.42}$$

Hence, Θ_i can be found via $\dot{m}_b$ and the total pressure and temperature, which allows calculating M_i, p_i, T_i and thus v_i :

$$v_i = M_i \, a_i \tag{5.43}$$

$$v_i = M_i \sqrt{\gamma R_g T_i} \tag{5.44}$$

From Ω_{Cj} and R_i, the rotational speed is retrieved :

$$u_i = \Omega_{Cj} R_i \tag{5.45}$$

The velocity triangle of the flow near the inlet of the blades is consequently determinable (Fig.5.7). It is found that :

$$v_{i_R} = v_i \, \cos\alpha_i \tag{5.46}$$

$$v_{i_u} = v_i \, \sin\alpha_i \tag{5.47}$$

$$w_{i_u} = v_{i_u} - u_i \tag{5.48}$$

$$w_{i_R} = v_{i_R} \tag{5.49}$$

$$w_i = \sqrt{w_{i_R}^2 + w_{i_u}^2} \tag{5.50}$$

$$\beta_i = \text{atan}\left(\frac{w_{i_u}}{w_{i_R}}\right) \tag{5.51}$$

The non-dimensional velocity triangle is established easily by dividing all terms with u_i. Everything can now be rewritten non-dimensionally using the flow coefficient ϕ_i (Fig.5.7). The non-dimensional velocity vector components now become :

$$\frac{v_{i_R}}{u_i} = \frac{w_{i_R}}{u_i} = \phi_i \tag{5.52}$$

$$\frac{v_{i_u}}{u_i} = \phi_i \, \tan\alpha_i \tag{5.53}$$

$$\frac{v_i}{u_i} = \phi_i \sqrt{1 + \tan^2\alpha_i} = \phi_i \sec\alpha_i \tag{5.54}$$

$$\frac{w_{i_u}}{u_i} = \phi_i \, \tan\alpha_i - 1 \tag{5.55}$$

$$\frac{w_i}{u_i} = \sqrt{\phi_i^2(1 + \tan^2\alpha_i) - 2\phi_i \tan\alpha_i + 1} \tag{5.56}$$

$$\beta_i = \text{atan}\left(\frac{\phi_i \, \tan\alpha_i - 1}{\phi_i}\right) \tag{5.57}$$

The following intensive properties may then be derived :

$$T_{tri} = T_i + \frac{w_i^2}{2C_p} \tag{5.58}$$

which is the relative total temperature and,

$$p_{tri} = p_i \cdot \left(\frac{T_{tri}}{T_i}\right)^{\frac{\gamma}{\gamma-1}} \tag{5.59}$$

which is the relative total pressure.

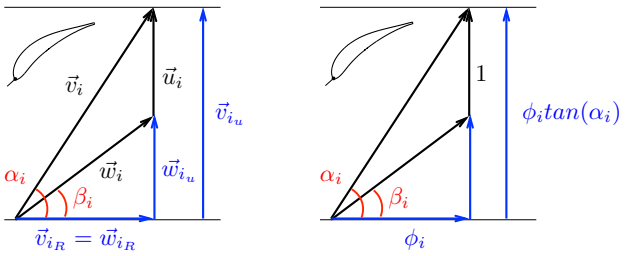

Figure 5.7. Blade inlet velocity triangle.

5.4.7 Blade outlet conditions

To establish the blade outlet velocity triangle, it would appear necessary to know the deflection of the flow over the blade. However, the flow deflection is à priori unknown to the designer. Fortunately, the required deflection can be determined by using some of the previously discussed non-dimensional parameters.

For example, the blade outlet absolute velocity is determinable imposing a certain ψ and $\hat{R}$, of which the importance will become clear when discussing the turbine stage design procedure topic expounded in Chapter 7. Substituting Eq.5.12, Eq.5.20 and Eq.5.33 in Eq.5.36 gives the absolute outlet velocity :

$$v_{o,b} = \sqrt{v_i^2 + 2(\hat{R} - 1)\psi u_i^2} \tag{5.60}$$

The importance of the reaction degree $\hat{R}$ can be observed clearly:

$$\hat{R} < 1 \quad \Rightarrow v_{o,b} < v_i \tag{5.61}$$

$$\hat{R} = 1 \quad \Rightarrow v_{o,b} = v_i \tag{5.62}$$

$$\hat{R} > 1 \quad \Rightarrow v_{o,b} > v_i \tag{5.63}$$

$\hat{R} = 1$ will ensure that the absolute speed at the inlet and the outlet of the blades of the turbine stage remains identical. $\hat{R} > 1$ is interesting when the inlet speed is low, e.g. near the inlet of the first stage. Then, the speed components in the next stage become larger

and a higher work output and a decreased profile loss are possible. Note that the effect of $\hat{R}$ is intensified by the work coefficient. Also, by the definition of $\hat{R}$, the lower it becomes, the less the flow will accelerate in the blade passage (decreased reactive power). $v_{o,b}$ can also be expressed non-dimensionally, dividing by the outlet rotational speed u_o :

$$\frac{v_{o,b}}{u_o} = \frac{R_i}{R_o}\sqrt{\phi_i^2(1+\tan^2\alpha_i) + 2(\hat{R}-1)\psi} \tag{5.64}$$

Note that :

$$\frac{u_o}{u_i} = \frac{R_o}{R_i} \tag{5.65}$$

The tangential component of the absolute speed v_{o_u} is found via Eq.5.12 and Eq.5.24 :

$$v_{o,b_u} = \frac{R_i}{R_o}(v_{i_u} - \psi u_i) \tag{5.66}$$

or, in its non-dimensional form :

$$\frac{v_{o,b_u}}{u_o} = \left(\frac{R_i}{R_o}\right)^2(\phi_i\ \tan\alpha_i - \psi) \tag{5.67}$$

The radial speed component v_{o_R} can then be found easily (Fig.5.8) :

$$v_{o,b_R} = \sqrt{v_{o,b}^2 - v_{o,b_u}^2} \tag{5.68}$$

In non-dimensional form :

$$\frac{v_{o,b_R}}{u_o} = \frac{R_i}{R_o}\sqrt{\phi_i^2\left(1+\tan^2\alpha_i\left[1-\left(\frac{R_i}{R_o}\right)^2\right]\right) + 2\psi\left[\hat{R}-1+\left(\frac{R_i}{R_o}\right)^2\phi_i\ \tan\alpha_i\right] - \left(\frac{R_i}{R_o}\psi\right)^2} \tag{5.69}$$

The outlet relative flow velocity $w_{o,b}$ can be established as follows (Fig.5.8) :

$$w_{o,b_R} = v_{o,b_R} \tag{5.70}$$

$$w_{o,b_u} = v_{o,b_u} - u_o \tag{5.71}$$

$$w_{o,b} = \sqrt{w_{o,b_R}^2 + w_{o,b_u}^2} \tag{5.72}$$

In non-dimensional form :

$$\frac{w_{o,b_R}}{u_o} = \frac{v_{o,b_R}}{u_o} = \phi_o \tag{5.73}$$

$$\frac{w_{o,b_u}}{u_o} = \left(\frac{R_i}{R_o}\right)^2(\phi_i\ \tan\alpha_i - \psi) - 1 \tag{5.74}$$

$$\frac{w_{o,b}}{u_o} = \sqrt{\phi_o^2 + \left[\left(\frac{R_i}{R_o}\right)^2(\phi_i\ \tan\alpha_i - \psi) - 1\right]^2} = \phi_o\sqrt{1+\tan^2\beta_{o,b}} \tag{5.75}$$

The absolute and relative outlet angles, respectively α_o and $\beta_{o,b}$:

$$\alpha_o = \text{atan}\left(\frac{v_{o,b_u}}{v_{o,b_R}}\right) \tag{5.76}$$

$$\beta_{o,b} = \text{atan}\left(\frac{w_{o,b_u}}{w_{o,b_R}}\right) = \text{atan}\left(\frac{\phi_o \ \tan\alpha_{o,b} - 1}{\phi_o}\right) \tag{5.77}$$

The foregoing equations provide the blade outlet velocity triangle. As a result of this, the

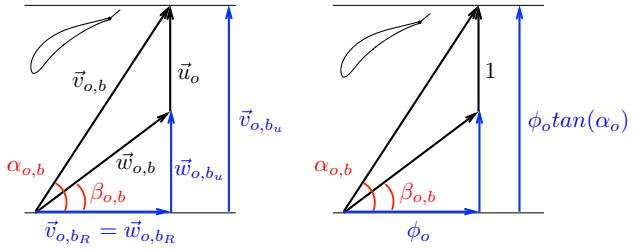

FIGURE 5.8. Blade outlet velocity triangle.

intensive properties at the outlet of the blades can be retrieved. The outlet specific total enthalpy is :

$$h_{to,b} = h_{ti} + u_i^2 \psi \tag{5.78}$$

The total-to-total expansion ratio over the blades of a turbine stage π_{Tb} can be found if the losses in the blade passage are quantified. At this point in the discussion, it is sufficient to represent these losses by the total-to-total polytropic efficiency $\eta_{p,Tb}$. Consequently, the total-to-total expansion ratio is – Çengel & Cimbala (2010) :

$$\pi_{Tb} \triangleq \frac{p_{ti}}{p_{to,b}} = \left(\frac{h_{ti}}{h_{to,b}}\right)^{\frac{\gamma}{\gamma-1}\frac{1}{\eta_{p,Tb}}} \tag{5.79}$$

or, using the non-dimensional parameters ψ and $\hat{\theta}$ (Eq.5.12 and Eq.5.14) in Eq.5.79 :

$$\pi_{Tb} = \left(1 - \frac{\psi}{\hat{\theta}}\right)^{\frac{\gamma}{1-\gamma}\frac{1}{\eta_{p,Tb}}} \tag{5.80}$$

The blade outlet total pressure $p_{to,b}$ can then be calculated. The static temperature at the outlet of the blades $T_{o,b}$ is calculable via the definition of the specific total enthalpy (Eq.5.25) :

$$T_{o,b} = T_{to,b} - \frac{v_{o,b}^2}{2C_p} \tag{5.81}$$

noting that :

$$T_{to,b} = \frac{h_{to,b}}{C_p} \tag{5.82}$$

The static pressure is then found using – Çengel & Cimbala (2010) :

$$p_{o,b} = p_{to,b}\left(\frac{T_{o,b}}{T_{to,b}}\right)^{\frac{\gamma}{\gamma-1}} \tag{5.83}$$

The flow absolute Mach number near the outlet of the blades $M_{o,b}$ finally is :

$$M_{o,b} = \frac{v_{o,b}}{a_{o,b}} = \frac{v_{o,b}}{\sqrt{\gamma R_g T_{o,b}}} \tag{5.84}$$

and $a_{o,b}$ the speed of sound in the gases expelled from the blade passages. Finally, the relative total temperature $T_{tro,b}$ and relative total pressure $p_{tro,b}$ can also be obtained by analogy with Eq.5.58 & Eq.5.59, and introduction of Eq.5.31 :

$$T_{tro,b} = T_{o,b} + \frac{w_{o,b}^2}{2C_p} = T_{tri} - \frac{u_i^2}{2\,C_p}\left[1 - \left(\frac{R_o}{R_i}\right)^2\right] \tag{5.85}$$

$$p_{tro,b} = p_{o,b}\left(\frac{T_{tro,b}}{T_{o,b}}\right)^{\frac{\gamma}{\gamma-1}} \tag{5.86}$$

Note that the blade passage outlet flow area $A_{o,b}$ can be calculated since :

$$A_{o,b} = \frac{\dot{m}_b}{\rho_{o,b} v_{o,b_R}} \tag{5.87}$$

and consequently :

$$H_{bo} = \frac{A_{o,b}}{2\pi R_o} \tag{5.88}$$

5.4.8 Deviation angle

The assumption of shock-free flow[ii] near the outlet of the turbine stage is not usually met. Consequently, *for a given geometry with angle* $\beta_{b,o}$, the outflow relative angle near the blade $\beta_{o,b}$ will need to be determined (Fig.5.3). Fortunately, the estimation of $\beta_{o,b}$ in a turbine is generally straightforward, especially when the flow deflection $(\beta_i - \beta_{o,b})$ is reasonably high – Schobeiri (2005). The model of Ainley & Mathieson (1955) and adapted by Aungier (2006) will be used for this purpose because it is complete and easily adopted in a computer model. It permits the determination of the deviation angle δ, which is the deviation with respect to the gauging angle β_g (Fig.5.3). Recalling the definition of β_g

[ii] Shock-free flow is a flow of which the relative speed is tangential to the blade camber line – Lewis (1996).

(Eq.5.4) :

$$\beta_g \triangleq \text{asin}\left(\frac{o}{s}\right)$$

Then, by definition :

$$\beta_{o,b} \triangleq \beta_g + \delta - \frac{\pi}{2} \tag{5.89}$$

Since the deviation angle model is developed for axial turbines – the model of Ainley & Mathieson (1955) being established for rectilinear turbine cascades – some corrections to cope with the radial Ljungström turbine need to be implemented. Indeed, in an axial turbine the stream surfaces principally move on a cylinders of constant radius and through a blade passage of constant pitch t_{AX}. This is no longer the case in a radial turbine, i.e. $t_o \neq t_i$ and $R_o \neq R_i$ (Fig.5.4). Corrections to the deviation angle δ are now proposed, before exploring the deviation model of Aungier (2006), in which the former will be adopted. At this stage, it is sufficient to pose :

$$\delta = f(\delta_{AM}, \Delta\delta_{\Pi_p}, \Delta\delta_{sl}) \tag{5.90}$$

where δ_{AM} the deviation angle proposed by Aungier (2006) and based on Ainley and Mathieson, for subsonic and supersonic flow conditions, $\Delta\delta_{\Pi_p}$ the deviation correction required due to the divergence of the blade passages Π_p and $\Delta\delta_{sl}$ the imposed deviation correction to include the slip vortex inside the blade passages.

Pitch angle deviation correction $\Delta\delta_{\Pi_p}$

Referring to Fig.5.4, where the pitch angle Π_p is :

$$\Pi_p = \frac{2\pi}{Z} = \frac{t_i}{R_i} = \frac{t_o}{R_o} \tag{5.91}$$

and Z the number of blades. In the axial turbine, $\Pi_p = 0$ because the flow is mainly axial. The additional diffusion in the Ljungström turbine due to the radially oriented flow is consequently not adopted in Aungier's model. Here, the author suggests the deviation rule of Constant, discussed in the work of Horlock & Denton (2005), to take this diffusion into account :

$$\delta = m\ \theta_c \left(\frac{t_o}{c}\right)^n \tag{5.92}$$

where θ_c is the blade camber, while m and n are constants. The deviation correction $\Delta\delta_{\Pi_p}$ is now proposed to be approximated by taking the first derivative of Constant's equation

and putting $\Pi_p = \Delta\theta_c$:

$$\Delta\delta_{\Pi_p} = m\left(\frac{t_o}{c}\right)^n \Pi_p = m\left(\frac{R_o}{c}\right)^n \Pi_p^{n+1} \tag{5.93}$$

using for $n = 0.5$ and $m = 0.19$, as reported by Dixon (2005) and Horlock & Denton (2005). Note that the value for $\Delta\delta_{\Pi_p}$ is positive, which is in agreement with flow diffusion and the orientation of angle δ as shown in Fig.5.3. The impact of $\Delta\delta_{\Pi_p}$ is shown graphically in Fig.5.9.

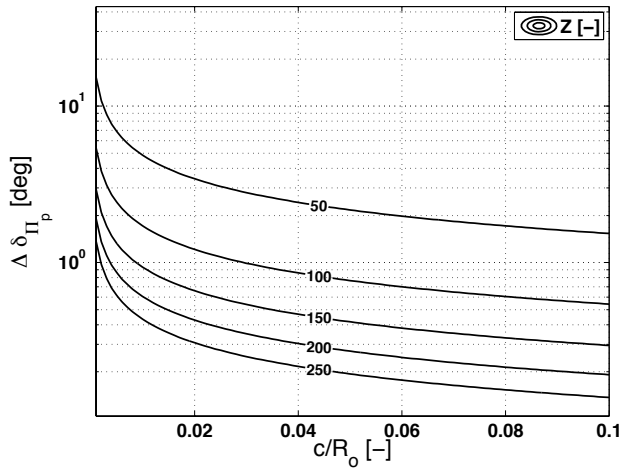

FIGURE 5.9. Ljungström turbine $\Delta\delta_{\Pi_p}$.

Slip speed deviation correction $\Delta\delta_{sl}$

In contrast to the axial turbines, the flow in the radial plane of the rotor of radial turbomachines is majorly affected by the rotating motion of the blade passages. Indeed, considering irrotational flow to enter the rotor, Helmholtz and Kelvin laws explain the inception of a vortex in each of the rotating blade passages, opposed to the rotor angular velocity Ω_C, and deflecting the flow near the rotor outlet – Anderson, Jr. (2001). This vortex affects the power delivered to or by the gases. In this study, the effect of the vortex is introduced to the flow deviation model by adding a corrective term defined as $\Delta\delta_{sl}$, where :

$$\Delta\delta_{sl} = \beta_{o,b_s} - \beta_{b,o} \tag{5.94}$$

β_{o,b_s} is the relative flow angle near the rotor outlet with slip vortex.

Stodola (1922) was the first to introduce a methodology to quantify this slip phenomenon in centrifugal compressors, calculating a slip speed $v_{o,b_{us}}$ that needs to be subtracted from the undisturbed outlet tangential speed component v^{∞}_{o,b_u} (Fig.5.10). Over time, other slip models were developed. Dixon (2005) mentions, most noteworthy, the slip models

of Busemann, Busemann-Wiesner and Stanitz. Busemann derived an exact model for the slip velocity considering an impeller with radial logarithmic spiral blades through which the mass flow is zero, while assuming an incompressible and frictionless flow – Van den Braembussche (2013). Even though this analysis does not always yield accurate results, as mentioned by Memardezfouli & Nourbakhsh (2009), it predicts the slip velocity in compressors reasonably well, even outside the theoretical boundaries for which it was conceived – Ferguson (1968). Wiesner successfully simplified the complex model of Busemann providing empirical correlations. This model is therefore called the Busemann-Wiesner slip model. Interestingly, the compressor slip models have also found their way

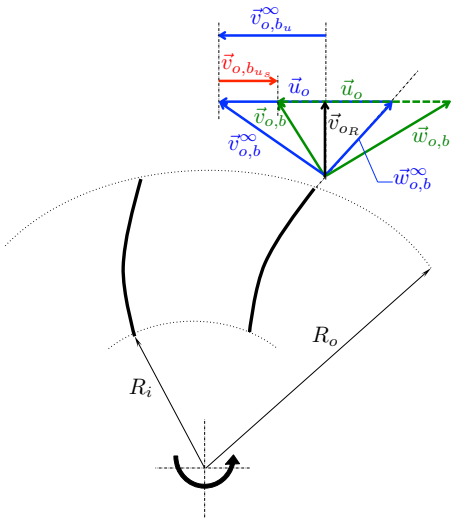

FIGURE 5.10. Impact of slip model on outlet velocity triangle.

into radial *inflow* turbine design to calculate the optimum inflow angle, as discussed by Aungier (2006) and Dixon (2005), but Moustapha et al. (2003) warned that they should be used wisely since the flow characteristics through the turbine and compressor rotor are completely different. However, since the Ljungström turbine is a *centrifugal* turbine, it appears consequently reasonable to introduce a compressor slip velocity correction to the rotor outlet flow in order to correct the flow deviation δ with an angle $\Delta\delta_{sl}$. For this purpose, the Busemann-Wiesner slip velocity is selected, and adapted for the relevant angle and sign conventions as indicated in Fig.5.3. Assuming the stream surfaces to be perpendicular to the rotation axis :

$$v_{o,b_{us}} = \frac{u_o \sqrt{\cos \beta_{b,o}}}{Z^{0.7}} \tag{5.95}$$

where $u_o = \Omega_C R_o$ and Z the stage blade number. Note that $v_{o,b_{us}}$ is only a function of blade outlet geometry and the blade number. This means that the influence of the flow angle near the blade inlet seems to be negligible. However, Eq.5.95 is limited to :

$$\epsilon = \frac{R_i}{R_o} \leq \exp\left(\frac{-8.16 \cos \beta_{b,o}}{Z}\right) = \epsilon_{LIM} \tag{5.96}$$

For $\epsilon > \epsilon_{LIM}$ Van den Braembussche (2013) and Dixon (2005) give :

$$v_{o,b_{us}} = u_o\left\{1 - \left[1 - \frac{u_o\sqrt{\cos\beta_{b,o}}}{Z^{0.7}}\right]\left[1 - \left(\frac{\epsilon - \epsilon_{LIM}}{1 - \epsilon_{LIM}}\right)^3\right]\right\} \tag{5.97}$$

The above equation shows that in case $\epsilon > \epsilon_{LIM}$, the magnitude of the slip speed $v_{o,b_{us}}$ increases significantly and tends to u_o. An identical conclusion may be drawn when Z is low. It needs to be emphasised though, that in the case of a turbine, the use of the Busemann-Wiesner slip model has neither been substantiated experimentally nor numerically. Therefore the author believes that for current purposes, it is more prudent to let the slip model predict moderate values for $v_{o,b_{us}}$ using Eq.5.95 only. Indeed, since $v_{o,b_{us}}$ is negative, it will increase the stage work output of the turbine. The validity of this model may then be investigated by checking whether the used number of turbine blades Z is near or higher than a critical blade number Z_{sl}, where :

$$Z \geq \frac{-8.16\ \cos\beta_{b,o}}{\ln(\epsilon)} = Z_{sl} \tag{5.98}$$

Using the velocity triangle at the blade outlet one may obtain for $\Delta\delta_{sl}$:

$$\Delta\delta_{sl} = \text{atan}\left(\tan\beta_{b,o} - \frac{v_{o,b_{us}}}{w_{o,b_R}}\right) - \beta_{b,o} \tag{5.99}$$

Note that $\Delta\delta_{sl}$ is negative since it must be opposed to u_o. It appears that in contrast to compressors, the slip speed will contribute to a higher power output of the turbine. Introducing the flow coefficient ϕ_o one finds (Fig.5.11) :

$$\Delta\delta_{sl} = \text{atan}\left(\tan\beta_{b,o} - \frac{1}{\phi_o}\frac{\sqrt{\cos\beta_{b,o}}}{Z^{0.7}}\right) - \beta_{b,o} \tag{5.100}$$

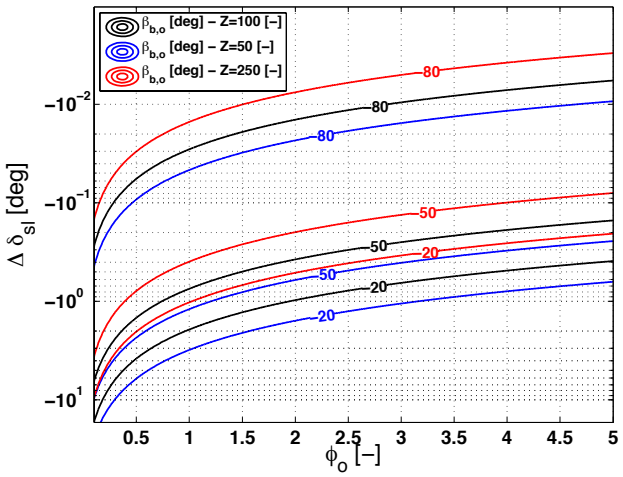

FIGURE 5.11. Ljungström turbine $\Delta\delta_{sl}$.

Deviation angle for axial turbines δ_{AM}

The deviation angle for the axial turbine serves as the basis to calculate the deviation angle for the Ljungström turbine. The subsonic outlet flow deviation angle correlation proposed by Aungier (2006) is :

$$\delta_{AM} = \delta_0 = \text{asin}\left\{\left(\frac{o}{t_o}\right)\left[1 + \left(1 - \frac{o}{t_o}\right)\left(\frac{2\beta_g}{\pi}\right)^2\right]\right\} - \beta_g \qquad M_{ro,b} \leq 0.5 \tag{5.101}$$

$$\delta_{AM} = \delta_0 \left(1 - 10 f_M^3 + 15 f_M^4 - 6 f_M^5\right) \quad \text{and} \quad f_M = 2M_{ro,b} - 1 \qquad 0.5 < M_{ro,b} \leq 1 \tag{5.102}$$

where $M_{ro,b}$ the relative outlet Mach number near the blade outlet. For $M_{ro,b} \leq 0.5$, the deviation angle δ_0 is only a function of cascade geometry. Note that if the blade trailing edge thickness is negligible, it is found that :

$$\frac{o}{t_{AX}} = \frac{o}{s} = \sin(\beta_g) \tag{5.103}$$

Under sonic conditions, i.e. $M_{ro,b} = 1$, a unidimensional sonic flow in the throat section o is considered. Assuming the throat in the blade passage to be close to the trailing edge of the blade, one may then indeed approximate the relative outlet flow angle reasonably by setting $\delta = 0$. Aungier (2006) proposes Eq.5.102 to interpolate in case $0.5 \leq M_{ro,b} \leq 1$. The difference with the model of Ainley & Mathieson (1955) is that the latter interpolates linearly. Aungier (2006) preferred using a smooth transition of δ near the sonic flow condition (Eq.5.102), because it provides better convergence during the iterative calculation process.

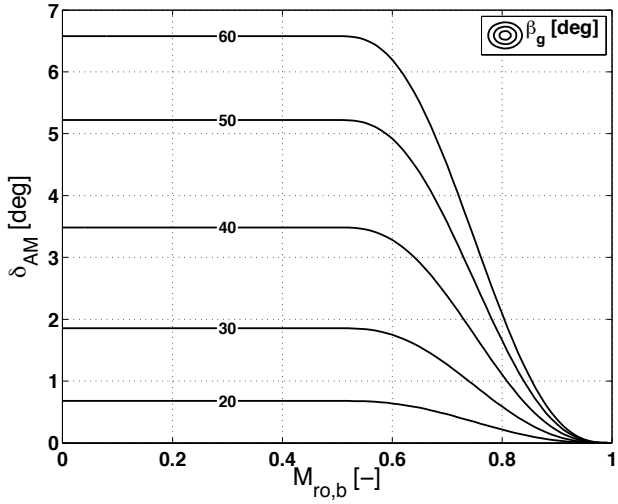

FIGURE 5.12. Subsonic flow δ_{AM} – Aungier (2006).

For supersonic flows Aungier (2006) adopts the model of Ainley & Mathieson (1955)

integrally :

$$\delta_{AM} = \text{asin}\left[\left(\frac{o}{t_o}\right)\left(\frac{\rho_* w_*}{\rho_{o,b} w_{o,b}}\right)\right] - \beta_g \qquad M_{ro,b} > 1 \qquad (5.104)$$

where ρ_* and w_* are respectively the density and the relative speed in the throat o under saturated conditions, while $\rho_{o,b}$ and $w_{o,b}$ are respectively the density and the relative speed at the blade outlet. The calculation of δ for supersonic flows relies on the conservation of mass. Even though more complex models exist using expansion waves, the above model gives satisfactory results – Horlock (1966). Note that this model for supersonic flows implicitly takes the effects of $\Delta\delta_{\Pi_p}$ and $\Delta\delta_{sl}$ into account. The implementation of the aforementioned deviations in a Ljungström turbine deviation angle model is treated next.

Ljungström turbine blade passage deviation angle model

For subsonic flows with $M_{ro,b} \leq 0.5$, it is proposed to calculate the deviation angle δ by simple superposition :

$$\delta_0 = \text{asin}\left\{\left(\frac{o}{t_o}\right)\left[1 + \left(1 - \frac{o}{t_o}\right)\left(\frac{2\beta_g}{\pi}\right)^2\right]\right\} - \beta_g \qquad \text{(Eq.5.101)}$$

$$\delta = \delta_0^* = \delta_0 + \Delta\delta_{\Pi_p} + \Delta\delta_{sl} \qquad M_{ro,b} \leq 0.5 \qquad (5.105)$$

For high subsonic and sonic flows, the following reasoning is adopted. The previous discussion provided the deviation flow angle δ for supersonic flows based on conservation of mass. Because of this, $\Delta\delta_{\Pi_p}$ and $\Delta\delta_{sl}$ cannot be explicitly modelled in that domain, but consequently, the statement that $\delta = 0$ for $M_{ro,b} = 1$ should stand. As a matter of fact, discontinuities in δ with $M_{ro,b}$ should not occur in order to avoid convergence problems. However, it is reasonable to accept that $\Delta\delta_{\Pi_p}$ and $\Delta\delta_{sl}$ take near zero values when $M_{ro,b}$ approaches unity. This is explained next.

Observing Fig.5.12 it is seen that δ_{AM} becomes zero regardless the value of β_g. This phenomenon is likely to be explained by the favourable effect of the higher speeds on the blade boundary layer, causing the flow to better adhere to the blade surface. Provided that sufficient blades are installed, $\Delta\delta_{\Pi_p}$ will remain small enough such that the above mentioned beneficial effect will still persist. Consequently formulating that $\Delta\delta_{\Pi_p} \to 0$ for $M_{ro,b} \to 1$ is acceptable.

The effect of the slip vortex on the deviation angle $\Delta\delta_{sl}$ is not cancelled in supersonic flow conditions. However, in order to avoid convergence problems during the calculation process, δ should ideally tend to zero approaching the choking condition from the subsonic side, which requires the effect of $\Delta\delta_{sl}$ to be neglected. Fortunately, observing Fig.5.11, increasing $M_{ro,b}$ and thus ϕ_o, decreases $\Delta\delta_{sl}$. In case Z is relatively high – which is the

case in a Ljungström turbine – $\Delta\delta_{sl}$ becomes very small near choking and consequently approves the use of $\Delta\delta_{sl} \rightarrow 0$ for $M_{ro,b} \rightarrow 1$.

Based on the previous discussion, it now appears reasonable to define the subsonic deviation model as :

$$\delta = \delta_0^* \left(1 - 10 f_M^3 + 15 f_M^4 - 6 f_M^5\right) \quad \text{and} \quad f_M = 2M_{ro,b} - 1 \qquad 0.5 < M_{ro,b} \leq 1 \qquad (5.106)$$

Note that the interpolation function of Aungier (2006) is again used to dampen the $\Delta\delta_{\Pi_p}$ and $\Delta\delta_{sl}$ functions when approaching the choking limit.

Since in a rotor-embedded Ljungström turbine the pressure drop over each stage will be low and supersonic expansion rather unrealistic, the deviation angle δ for $M_{ro,b} > 1$ is not further developed here and is discussed in Appendix C.

An example of the evolution of δ with β_g and $M_{ro,b}$ is given in Fig.5.13

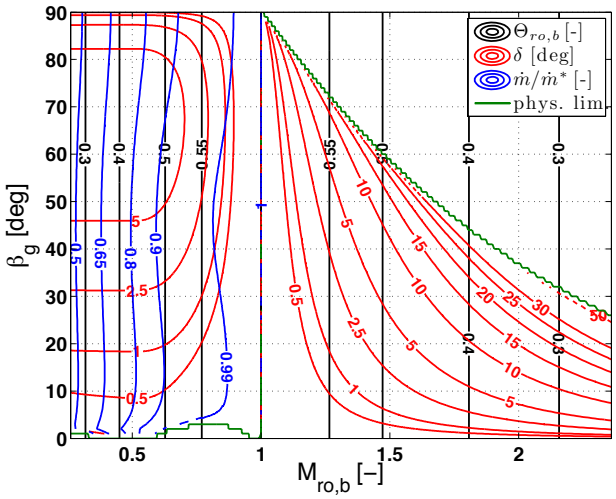

FIGURE 5.13. Deviation angle δ : example of a single Ljungström turbine stage – $M_{tu,o} = 0.085$ (see Appendix C).

5.4.9 Note on the application of the deviation angle

The previous considerations were based on the assumption that $\beta_{b,o}$ is known. The followed logic is then applicable for a given geometry on which, for example, off-design performance calculations are performed. However, during the design process, $\beta_{o,b}$ will be established first, based on the required performance criteria. Evidently, $\beta_{b,o}$ and thus the blade outlet geometry then follow from the above-stated δ-calculations.

5.4.10 Deflection angle

The deflection angle ϵ is the deflection the flow undergoes when expanding through the blade passage. By definition :

$$\epsilon \triangleq \beta_{o,b} - \beta_i \tag{5.107}$$

5.4.11 Inlet incidence angle correction

While the outlet deviation is widely discussed in the literature, no similar studies were found analysing the impact of the presence of the blade pressure field on the upstream flow angle. Even though an inlet incidence correction angle is conceivable – including the effects of slip speed in the blade passage – it is tacitly neglected in this study.

5.4.12 Impact of interstage space

The flow in the interstage spaces is subjected to diffusion. This process causes losses, of which the importance increases with the degree of required diffusion, as indicated by Aungier (2000). For this work, the diffusion process will be considered isentropic, while nonetheless acknowledging the impact this simplification will have on the accuracy of the model. As a consequence, the inlet conditions of stage S_{j+1} can be obtained from the outlet conditions of stage S_j. Using the conservation of angular momentum – Van den Braembussche (2013) :

$${}^{j+1}(v_{i_u} R_i) = {}^{j}(v_{o_u} R_o) \tag{5.108}$$

v_{o_u} is the tangential component of the stage outlet absolute velocity. Conservation of mass provides a correction for the radial component of the absolute speed – Van den Braembussche (2013) :

$${}^{j+1}v_{i_R} = \frac{{}^{j}(v_{o_R} \rho_o R_o H_{bo})}{{}^{j+1}(\rho_i R_i H_{bi})} \tag{5.109}$$

The inlet conditions of stage S_{j+1} must be established iteratively. Indeed, because a compressible flow is considered, ρ_i depends on the absolute speed, which is yet to be established. The iterative procedure on stage S_{j+1} may be closed in the following way :

$$v_i = \sqrt{v_{i_R}^2 + v_{i_u}^2} \tag{5.110}$$

$$T_i = T_{ti} - \frac{v_i^2}{2C_p} \tag{5.111}$$

$$p_i = p_{ti}\left(\frac{T_i}{T_{ti}}\right)^{\frac{\gamma}{\gamma-1}} \tag{5.112}$$

$$\rho_i^+ = \frac{p_i}{R_g T_i} \tag{5.113}$$

The new value of ρ_i (Eq.5.113) is then reintroduced in Eq.5.109 until convergence is obtained. Note that ${}^{j+1}T_{ti} = {}^{j}T_{to}$ and, because of the isentropic evolution, ${}^{j+1}p_{ti} = {}^{j}p_{to}$

5.4.13 Turbine power output

Each crown of the Ljungström turbine drives a shaft or in the case of the TDR-concept, a rotor. The power delivered by each crown, while neglecting any mechanical losses in the bearings is :

$$P_{C1} = \sum_{j=1}^{S_n/2} \dot{m}(h_{ti} - h_{to})_{S_{2j-1}} \tag{5.114}$$

$$P_{C2} = \sum_{j=1}^{S_n/2} \dot{m}(h_{ti} - h_{to})_{S_{2j}} \tag{5.115}$$

and S_n the amount of stages in the Ljungström turbine. In Section 6.5.1, it will be shown however, that the above formulae or not entirely correct because there is a small exchange of power between crowns due to viscous effects.

5.5 Note on efficiency

The efficiency of the turbine influences the fuel consumption in the thermodynamic cycle. For a given power output, the efficiency should be as high as reasonably possible in order to keep the helicopter fuel weight fraction low. Several efficiencies may be used in case of an adiabatic environment. Most noteworthy are the isentropic efficiencies and polytropic efficiencies. Their definition follows next.

5.5.1 Isentropic efficiency

There are several loss mechanisms working in the turbine. A qualitative and quantitative study of these losses will be conducted in Chapter 6. The methodology used to implement the losses will depend on the used loss model. For now, it is sufficient to represent the losses on a temperature-entropy (T-s) diagram (Fig.5.14). The expansion of the gases in the turbine will cause a total pressure drop and an entropy rise. Because the turbine is considered to be adiabatic, the entropy rise will be solely caused by entropy production (pure losses), as may be proven by the second law of thermodynamics for an open system.

Two efficiencies are frequently found in turbine literature. In general, the turbine total-to-total isentropic efficiency $\eta_{is,T}$ is used to represent the losses. The efficiency compares the actual specific total enthalpy drop over the turbine (stage) with the one obtained during

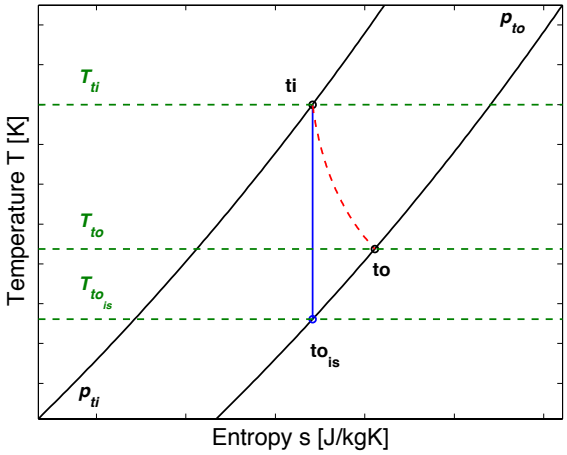

FIGURE 5.14. Basic loss representation in a Ljungström turbine stage.

an isentropic expansion, i.e. – Dixon (2005) :

$$\eta_{is,T} \triangleq \frac{h_{ti} - h_{to}}{h_{ti} - h_{to_{is}}} \tag{5.116}$$

where,

$$h_{to_{is}} = h_{ti}\left(\frac{1}{\pi_T}\right)^{\frac{\gamma-1}{\gamma}} \tag{5.117}$$

$$T_{to_{is}} = \frac{h_{to_{is}}}{C_p} \tag{5.118}$$

The flow kinetic energy is hereby implicitly present and remains part of the usable energy. In case of the last stage however, the outlet kinetic energy is of no use and lost. As a consequence, it is generally recommended to subtract the outlet kinetic energy from the denominator – Dixon (2005), which is the second efficiency, namely the total-to-static isentropic efficiency :

$$\eta_{is,T_{ts}} \triangleq \frac{h_{ti} - h_{to}}{h_{ti} - h_{o_{is}}} \tag{5.119}$$

and,

$$h_{o_{is}} = h_{to_{is}} - \frac{v_{o_{is}}^2}{2} = h_{ti}\left(\frac{p_o}{p_{ti}}\right)^{\frac{\gamma-1}{\gamma}} \tag{5.120}$$

$$T_{o_{is}} = \frac{h_{o_{is}}}{C_p} \tag{5.121}$$

5.5.2 Polytropic efficiency

The slight divergence of the isobars in the T-s diagram (Fig.5.15) is the cause of an important issue related to the appreciation of the isentropic efficiency. As explained by

Dixon (2005) and Aungier (2006), if the expansion ratio π_T increases by, for example, installing two identical turbine stages with similar isentropic efficiencies $\eta_{is,T_{12}}$ and $\eta_{is,T_{23}}$ (Fig.5.16), then the isentropic efficiency $\eta_{is,T_{13}}$ of the complete expansion process will rise. This phenomenon may be perceived as misleading to the designer, especially when one focusses on the aerodynamic quality of the flow. In light of this, the polytropic efficiency $\eta_{p,T}$ is defined, which copes with this problem. It is also known as the *small stage efficiency*. Following Dixon (2005) :

$$\eta_{p,T} \triangleq \frac{dh_t}{dh_{t_{is}}} \tag{5.122}$$

$$\eta_{p,T} = \left(\frac{\gamma-1}{\gamma}\right)\frac{\ln(p_{to}/p_{ti})}{\ln(h_{to}/h_{ti})} = \left(\frac{\gamma-1}{\gamma}\right)\frac{\ln(p_{to}/p_{ti})}{\ln(T_{to}/T_{ti})} \tag{5.123}$$

or in the more useful form,

$$\frac{h_{to}}{h_{ti}} = \frac{T_{to}}{T_{ti}} = \left(\frac{p_{to}}{p_{ti}}\right)^{\frac{(\gamma-1)}{\gamma}\eta_{p,T}} \tag{5.124}$$

Note for example that in Eq.5.80, the use of the polytropic turbine efficiency was already used to find the turbine pressure ratio. The above-mentioned efficiencies are applicable to all adiabatic evolutions in the turbine (either stage or complete turbine).

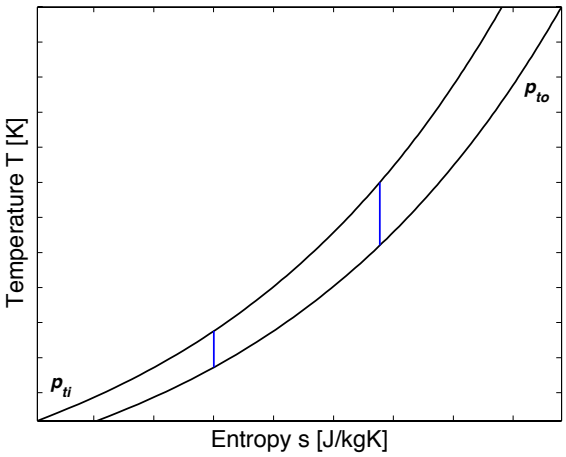

FIGURE 5.15. Isobar divergence in T-s diagram.

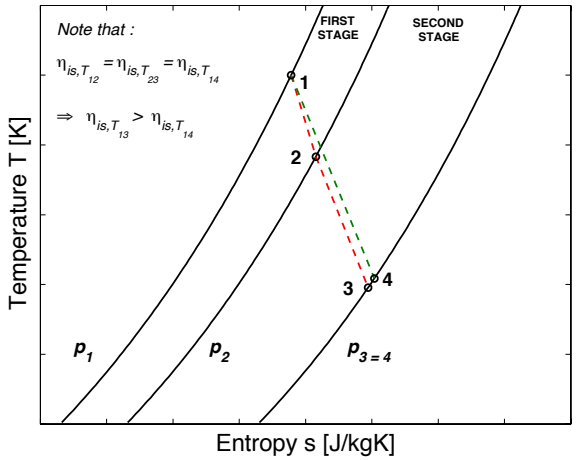

FIGURE 5.16. Impact of turbine expansion ratio on isentropic efficiency, illustrated by means of a two-stage turbine.

5.6 Nomenclature

Please note that the units listed below apply unless stated otherwise.

Abbreviations and substance formulae

A	Flow area	[m^2]
AR	Blade aspect ratio	[-]
AR_a	Blade projected aspect ratio	[-]
$\overline{B}$	Blade height ratio	[-]
c	Blade chord	[m]
c_a	Radial blade chord	[m]
$C1$	First crown	
$C2$	Second crown	
C_p	Specific heat at constant pressure	[J/kgK]
C_v	Specific heat at constant volume	[J/kgK]
$\overline{H}$	Interstage space height ratio	[-]
h	Specific enthalpy	[J/kg]
h_t	Specific total enthalpy	[J/kg]
h_{tr}	Specific relative total enthalpy	[J/kg]
H_b	Blade height	[m]
m	Constant's rule constant	[-]
$\dot{m}$	Mass flow rate	[kg/s]
M	Absolute Mach number	[-]
M_r	Relative Mach number	[-]
n	Constant's rule constant	[-]
N	Rotational/Angular speed	[rad/s]
o	Blade passage throat	[m]
p	Static pressure	[Pa]
p_t	Total pressure	[Pa]
p_{tr}	Relative total pressure	[Pa]
P	Power	[W]
P_A	Active power	[W]
P_R	Reactive power	[W]
P_{st}	Delivered stage power on crown	[W]
$P_{st,b}$	Delivered power by blade cascade	[W]
R	Radius	[m]
$\mathcal{R}$	Rothalpy	[J/kg]

$\hat{R}$	Reaction degree	[-]
R_i	Turbine (stage) inlet radius	[m]
R_g	Specific gas constant	[J/kgK]
R_o	Turbine (stage) outlet radius	[m]
s	Stage pitch	[m]
S	Stage	
S_n	Turbine stage number	[-]
S_Ω	Turbine slip factor	[-]
t	Passage length	[m]
T	Static temperature	[K]
T_t	Total temperature	[K]
T_{tr}	Relative total temperature	[K]
u	Rotational velocity	[m/s]
v	Absolute speed	[m/s]
$v_{o,b_{us}}$	Slip speed correction	[m/s]
w	Relative speed	[m/s]
Z	Stage blade number	[-]
α	Absolute flow angle	[rad]
β	Relative flow angle	[rad]
β_b	Camberline angle	[rad]
β_g	Gauging angle	[rad]
β_{o,b_s}	Relative flow angle near the rotor outlet with slip vortex	[rad]
γ	Isentropic exponent	[-]
δ	Stage flow deviation angle	[rad]
δ_{AM}	Axial turbine stage deviation angle	[rad]
δ_{sl}	Deviation angle correction due to slip vortex	[rad]
δ_{Π_p}	Deviation angle correction due to pitch angle	[rad]
Δ_{is}	Interstage space radial distance	[m]
ϵ	Flow deflection or R_i/R_o	[rad] or [-]
$\eta_{is,T}$	Turbine total-to-total isentropic efficiency	[-]
$\eta_{is,T_{ts}}$	Turbine total-to-static isentropic efficiency	[-]
$\eta_{is,Tb}$	Blade passage total-to-total isentropic efficiency	[-]
$\eta_{is,Ts}$	Stage isentropic total-to-total efficiency	[-]
$\eta_{p,T}$	Turbine total-to-total polytropic efficiency	[-]
$\eta_{p,Tb}$	Blade total-to-total passage polytropic efficiency	[-]
$\eta_{p,Ts}$	Stage total-to-total polytropic efficiency	[-]
$\hat{\theta}$	Non-dimensional inlet specific total enthalpy	[-]

Θ	Non-dimensional mass flow	[-]
π_T	Turbine total-to-total expansion ratio	[-]
π_{Tb}	Blade passage total-to-total expansion ratio	[-]
π_{Ts}	Stage total-to-total expansion ratio	[-]
Π_p	Pitch angle	[rad]
ρ	Density	[kg/m^3]
ϕ	Flow coefficient	[-]
ψ	Work coefficient	[-]

Subscripts and superscripts

AX	Axial turbine
b	Blade or blade passage related
$C1$	First crown
$C2$	Second crown
i	Inlet
j	Related to position j
o	Outlet
o, b	At outlet of a blade passage
r	Relative
R	Radial component
t	Total component
u	Tangential component
θ	Tangential component
∞	Infinite amount of blades
$*$	Saturated flow conditions

Chapter 6

Ljungström turbine loss modelling

"Although to penetrate into the intimate mysteries of nature and thence to learn the true causes of phenomena is not allowed to us, nevertheless it can happen that a certain fictive hypothesis may suffice for explaining many phenomena."

Leonhard Euler

In this chapter, the most prominent losses found in the Ljungström turbine will be discussed. Since no Ljungström turbine loss models were found in the literature, a similarity study with the axial turbine will be performed, which aims at evaluating the viability of using axial turbine loss models in the Ljungström turbine. Finally, the used loss models for turbine design and off-design calculations are proposed and discussed briefly.

6.1 Blade passage losses

Blade passage losses are those losses emerging in the flow due to the presence of blades. Based on the losses found in the literature for turbines in general, the following are found to be predominant :

1. Profile losses, emerging from the friction and pressure drag around the blades
2. Secondary losses, generated in the boundary layers of the stage endwalls
3. Supersonic expansion losses, due to shockwave losses near the trailing edge of the blades

A more detailed discussion of the above-mentioned losses follows now.

6.1.1 Blade passage loss categorisation

Profile losses

Blade profile losses are produced by the friction of the flow over each blade and the pressure losses emerging from viscous effects and a finite blade thickness. Depending

on the loss model employed, profile losses might not incorporate the trailing edge losses, which need then to be incorporated separately. Various parameters influence the profile loss, such as the blade profile, compressibility effects, the flow deflection, the blade surface condition and the flow incidence angle, as will be included in the loss models described in the subsequent sections. Generally, the profile losses prove to be the largest share of the observed losses.

Secondary losses

The secondary losses are caused by secondary flows which, even though finding their origin in viscous effects by the presence of an endwall, are in general inviscid phenomena – Denton (1993). Two important flow mechanisms may be distinguished, namely;
The first source of secondary flow is near the leading edge of the blade and close to the endwall. Outside the boundary layer of the endwall, the total pressure on the blade leading edge is determined by the free-stream velocity. In the boundary layer of the endwall however, the stagnation pressure is lower. Therefore a spanwise pressure gradient exists near the leading edge of the blade resulting in a flow towards the endwall, which will work as a flow source in a plane close to and parallel with the endwall. Consequently a region of reverse flow is invoked, which causes a three-dimensional flow separation of the endwall boundary layer near the blade leading edge as well as the inception of a horseshoe vortex (Fig.6.1) – Acharya et al. (2006). One leg of the horshoe vortex follows the suction side of the blade (H_s), the other follows initially the pressure side of the blade (H_p) – see Fig.6.2.

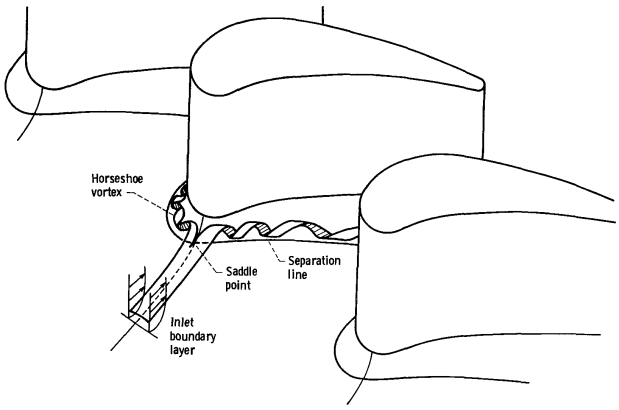

FIGURE 6.1. Formation of the horseshoe vortex – Gaugler & Russell (1982).

The second major source of secondary flows is the cross passage pressure gradient. The blade passage being formed by the pressure side of one blade and the suction side of the subsequent blade, clearly shows the existence of a pressure gradient, which causes the inception of a transverse flow along the endwall boundary (Fig.6.2). This will not only cause the pressure leg of the horseshoe vortex to convect to the suction side of the subsequent blade, but will also strengthen it. When reaching the suction side, it will react

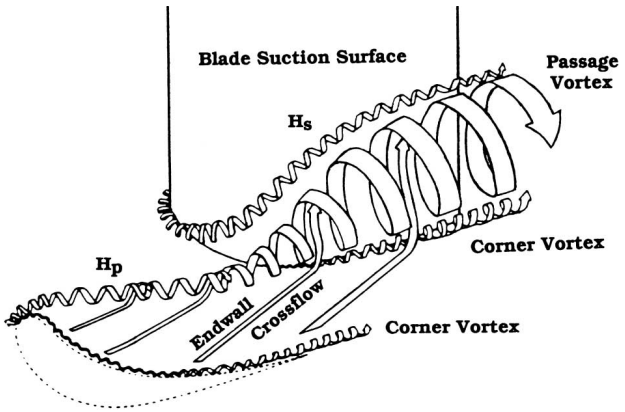

FIGURE 6.2. Secondary losses in a axial turbine blade passage – Moon & Koh (2001), used with permission.

with the suction leg of the horseshoe vortex, which has a sense of rotation opposed to the former, and form the passage vortex. The discussed vortices will also provoke other vortical elements, such as the corner and wall vortices – Acharya et al. (2006).

The kinetic energy of the secondary flows is not recoverable, as reported by Kumar & Govardhan (2011). It is diffused downstream the blade passage and is eventually dissipated to heat. Currently, there are no accurate secondary loss models that are generally applicable. According to Denton (1993), most *macroscopic* models are based on empirical observations and have no sound physical background. It is important to highlight that the secondary losses are approximately inversely proportional to the blade aspect ratio $\mathit{Æ}$.

Supersonic expansion losses

Supersonic expansion losses originate from shockwaves formed in the supersonic outlet of the blade passage. However, they prove not to be of importance in the RELT, as Mach numbers are subsonic and low. It will therefore be excluded from further consideration.

6.1.2 Concluding notes on the blade passage losses

The level of accuracy of the loss predictions will depend on the complexity of the selected loss model. Before tackling the discussion of the different loss models, the aptness of the available loss models needs examination. Because the Ljungström turbine is made of large-radius circular cascades, it is sensible to analyse in what degree it differs from the axial turbine, the losses of the latter frequently modelled by means of rectilinear cascades.

6.1.3 Axial turbine loss model aptness study : similarity study

In order for the axial turbine blade loss model to be applicable, which is essentially based on the flow in rectilinear cascades, similarity between the flow in a rectilinear cascade

and the flow in the Ljungström turbine, i.e. a circular cascade, should be proven. This condition is obtained when the inlet and outlet properties remain identical between both turbine types. Note that for this similarity study, no abstraction is made between the outlet conditions at the blade o, b and at the turbine stage o, which is acceptable for the subsequent order-of-magnitude-based analysis.

With regard to the inlet conditions of the rectangular and circular cascades, complete similarity is possible while imposing identical inlet intensive and extensive fluid properties, blade profiles, inlet blade geometries and stagger angles, and inlet velocity triangles (Fig.5.3 and Fig.5.4) :

$$t_{AX} = t_i = 2\pi R_i \quad H_{b_{AX}} = H_{bi} = C^t \quad \alpha_{i_{AX}} = \alpha_i \quad \lambda_{AX} = \lambda \tag{6.1}$$

$$T_{ti_{AX}} = T_{ti} \quad p_{ti_{AX}} = p_{ti} \quad v_{i_{AX}} = v_i \quad u_{AX} = u_i = \Omega_C R_i \tag{6.2}$$

where the suffix AX stands for the axial turbine, the suffix i and o respectively the inlet and the outlet of the circular cascade, t the blade pitch, H_b the blade height, λ the stagger angle, T_t the total temperature, p_t the total pressure, v the absolute speed, u the rotational velocity, Ω_C the angular velocity and R the radius. Evidently, for this similarity study, the inlet conditions of the Ljungström turbine are taken to be equal to the inlet conditions of the axial turbine.
In case c is denoted as the blade chord, c_a as the axial projection of c in the axial turbine but also the radial projection of c in the Ljungström turbine, and considering the Ljungström turbine to fulfill the following realistic requirements :

$$\frac{c}{R_j} = \frac{1}{\cos\lambda}\frac{c_a}{R_j} = O(-2) \tag{6.3}$$

$$\frac{t_j}{c} = \cos\lambda\,\frac{t_j}{c_a} = O(0) \tag{6.4}$$

then one may find for the pitch angle Π_p (Eq.5.91) :

$$\Pi_p = \frac{t_j}{R_j} = \frac{t_j}{c}\frac{c}{R_j} = O(-2) \tag{6.5}$$

Note again that the suffix j stands for either the inlet section i or the outlet section o. The blade number Z should then be at least :

$$Z = \frac{2\pi}{\Pi_p} = O(2) \tag{6.6}$$

Considering the difference in pitch, it is found that :

$$\frac{t_o - t_i}{t_i} = \frac{\Pi_p \, (R_o - R_i)}{t_i} = \Pi_p \left(\frac{c_a}{t_i}\right) = O(-2) \quad \Rightarrow \quad t_o \cong t_i = t_{AX} \tag{6.7}$$

while it is reasonable to expect that (Eq.6.4) :

$$\frac{c_a}{t_i} = O(0) \tag{6.8}$$

Consequently the following conclusion may be drawn for the passage outlet area :

$$\frac{A_o}{A_i} \cong \left(\frac{R_i + c_a}{R_i}\right) = 1 + \frac{c_a}{R_i} \cong 1 \quad \Rightarrow \quad A_o \cong A_i = A_{AX} \tag{6.9}$$

Since $t_o \cong t_i$ it is reasonable to expect that $o \cong o_{AX}$, which leads to equal gauging angles $\beta_g \cong \beta_{g_{AX}}$. Note that blade blockage effects are neglected since the trailing edge thickness of the blades is significantly smaller than the blade pitch, and thus $s \cong t_o$ (Fig.5.4).
In the rotor, the centrifugal and Coriolis inertial forces work in the radial plane. In the axial turbine, this plane is generally perpendicular to the stream surfaces. The radial plane and the stream surfaces, however, are parallel in the Ljungström turbine. The consequence of this is not captured by the axial turbine model, even though a slip speed correction is introduced. Only a quantitative study, such as experimental testing, will allow an examination of their importance and to what extent they cause the predicted losses to deviate from reality. Therefore, their impact on the flow losses is currently tacitly neglected. From an energetic perspective on the other hand, one may show that under the previously stated conditions (Eq.6.3 and Eq.6.4), the effect of the inertial forces remains negligible. Proof is delivered by the low change in relative total enthalpy by means of the conservation of rothalpy $\mathcal{R}$ (Eq.5.30) in turbine rotors :

$$\mathcal{R} \triangleq h_{tr,j} - \frac{u_j^2}{2} = h_{tR,j} - \frac{(\Omega_C R_j)^2}{2} = C^t \tag{6.10}$$

Note that in case of an axial turbine $h_{tr} = C^t$. The effect of changing radius should therefore have a minimum impact on h_{tro} :

$$\frac{\partial h_{tr}}{\partial R} = \Omega_C^2 \, R \cong \frac{\Delta h_{tr}}{\Delta R} \quad \Rightarrow \quad \frac{\Delta h_{tr}}{h_{tri}} \cong \frac{\Omega_C^2 R_i}{h_{tri}} \Delta R = \frac{\Omega_C^2 R_i}{h_{tri}} c_a \tag{6.11}$$

For helicopters $\Omega_C = O(1)$ because of rotor tip speed limitations, as mentioned by Prouty (2002), and $R_o = O(0)$ is a conservative value necessary to minimise rotor hub drag. Because $R_o/R_i \cong 1$, the inlet radius $R_i = O(0)$. The order of magnitude for h_{tr} can be found from its definition :

$$h_{tr} = h + \frac{w^2}{2} = O(5) \tag{6.12}$$

while assuming an ideal gas for which $h = C_p T = \mathcal{O}(5)$. Eq.6.11 then yields :

$$\frac{\Delta h_{tr}}{h_{tri}} \cong \frac{\mathcal{O}(2)\,\mathcal{O}(0)}{\mathcal{O}(5)}\mathcal{O}(-2) = \mathcal{O}(-5) \quad \Rightarrow \quad h_{tro} \cong h_{tri} = h_{tr_{AX}} \tag{6.13}$$

and thus :

$$\frac{\Delta T_{tr}}{T_{tri}} \cong \mathcal{O}(-5) \quad \Rightarrow \quad T_{tro} \cong T_{tri} = T_{tr_{AX}} \tag{6.14}$$

Consequently, the effect of the radial forces on the total relative enthalpy and temperature are clearly negligible. A similar conclusion applies to the relative total pressure :

$$p_{tr} \cong p_{ti}\left(\frac{T_{tr}}{T_{ti}}\right)^{\frac{\gamma}{\gamma-1}} \tag{6.15}$$

$$\frac{\partial p_{tr}}{\partial R} = \frac{\partial p_{tr}}{\partial T_{tr}}\frac{\partial T_{tr}}{\partial R} = \left(\frac{\gamma}{\gamma-1}\frac{p_{ti}}{T_{ti}^{\frac{\gamma}{\gamma-1}}}T_{tr}^{\frac{1}{\gamma-1}}\right)\cdot\left(\frac{\Omega_C^2 R}{C_p}\right) = \mathcal{O}(2) \tag{6.16}$$

The relative change in total relative pressure then is :

$$\frac{\Delta p_{tr}}{p_{ti}} = \frac{\partial p_{tr}}{\partial R}\frac{c_a}{R_i}\frac{R_i}{p_{ti}} = \mathcal{O}(-5) \quad \Rightarrow \quad p_{tro} \cong p_{tri} = p_{tr_{AX}} \tag{6.17}$$

With regard to the velocity triangle at the blade outlet, the following is found for the rotational velocity :

$$\frac{\Delta u}{u_i} = \frac{R_i + c_a}{R_i} = 1 + \frac{c_a}{R_i} = 1 + \mathcal{O}(-2) \approx 1 \quad \Rightarrow \quad u_o \cong u_i = u_{AX} \tag{6.18}$$

It can be shown using the conservation of mass that the relative speed $w_o = f(\dot{m}, A_o, p_{tro}, T_{tro}, \beta_o)$ (Appendix C). All parameters have been shown to be more or less constant, except β_o, which is treated next. The impact of the radial turbine configuration on the relative outlet flow angle may be represented by : $\Delta\beta_o = \Delta\delta_{\Pi_p} + \Delta\delta_{sl}$. The discussion of these quantities was already conducted in Section 5.4.8. Observing Figs. 5.11 & 5.10, and the values they represent for $\Delta\delta_{\Pi_p}$ and $\Delta\delta_{sl}$, it appears that $\Delta\beta_o$ for the Ljungström turbine configuration is quite low (around $\mathcal{O}(-2)$) :

$$\frac{\Delta\beta_o}{\beta_{o_{AX}}} = \frac{\Delta\delta_{\Pi_p} + \Delta\delta_{sl}}{\beta_{o_{AX}}} \cong \frac{\mathcal{O}(-2)}{\mathcal{O}(0)} = \mathcal{O}(-2) \quad \Rightarrow \quad \beta_o \cong \beta_{o_{AX}} \tag{6.19}$$

Hence, one may state that $w_o \cong w_{o_{AX}}$. The velocities w_o, u_o and β_o fix the velocity triangle at the outlet of the turbine and thus $v_o \cong v_{o_{AX}}$. This leads to the following observation, while assuming a perfect gas and the total-to-static conversion formulae as described by

Çengel & Cimbala (2010) :

$$T_o = T_{tro} - \frac{w_o^2}{2C_p} \quad \Rightarrow \quad T_o \approxeq T_{o_{AX}} \tag{6.20}$$

$$p_o = p_{tro}\left(\frac{T_o}{T_{tro}}\right)^{\frac{\gamma}{\gamma-1}} \quad \Rightarrow \quad p_o \approxeq p_{o_{AX}} \tag{6.21}$$

$$\rho_o = \frac{p_o}{R_g\, T_o} \quad \Rightarrow \quad \rho_o \approxeq \rho_{o_{AX}} \tag{6.22}$$

$$T_{to} = T_o + \frac{v_o^2}{2C_p} \quad \Rightarrow \quad T_{to} \approxeq T_{to_{AX}} \tag{6.23}$$

$$p_{to} = p_o\left(\frac{T_{to}}{T_o}\right)^{\frac{\gamma}{\gamma-1}} \quad \Rightarrow \quad p_{to} \approxeq p_{to_{AX}} \tag{6.24}$$

Finally, this means that other important similarity parameters over the turbine will also be conserved, such as Reynolds number Re_c and Mach numbers M_j. Except for the fact that the radial forces influence the flow differently, of which the total impact on the flow behaviour is currently not quantitatively known, most flow parameters meet the similarity requirements. Conclusion : *it appears at this stage reasonable to apply an axial turbine loss model on the Ljungström turbine to examine its performance*.

6.1.4 Axial turbine blade loss model discussion and selection

Three empirical axial turbine models are currently widely adopted, starting with the early but concise model of Soderberg adopted in the work of e.g. Horlock (1966), the model of Ainley & Mathieson (1955) – which has been upgraded several times over time, as mentioned by Aungier (2006) and Moustapha et al. (2003) – and the model of Craig & Cox (1970-1971).

Gradually, the flow phenomena in turbines were better documented and analysed and there is nowadays a tendency to implement losses as entropy production in the thermodynamic models instead of using a loss model that provides a (non-dimensional) pressure loss. The entropy production approach is advocated by e.g. Denton (1993) and Wilson (1987). Although powerful, it requires a detailed analysis of the flow in the turbine, which is not in the scope of the currently used *macroscopic* interpretation. Hence, only the models of Ainley & Mathieson (1955) and Craig & Cox (1970-1971) answer to this criterion. Horlock (1966) indicates that the model of Soderberg (1949) is less accurate to determine the losses over a wide range of operating regimes (deviations up to 3%). However, it demands much less information and is consequently much quicker to obtain a

first estimate of the losses, which is convenient when performing a design point analysis, when examining a wide range of geometries. For the off-design performance calculations used to establish the turbine performance map, the models of Ainley & Mathieson (1955) and Craig & Cox (1970-1971) should be considered solely.
The models of Ainley & Mathieson (1955) and Craig & Cox (1970-1971) were compared by Lozza (1982). He indicated that these are applicable for optimisation of turbines based on a good design standard, but that the difference in loss prediction between both models is sometimes significant. Also, he stressed that the discussed loss components in each model are not interchangeable. Since the model of Ainley & Mathieson (1955) requires less input data than Craig & Cox (1970-1971)'s model, because it enables also the calculation of the deviation angle, and thanks to the modifications made by Aungier (2006) removing some of the issues discussed by Lozza such as an excessive estimation of the secondary losses at low blade aspect ratios AR_a, the model of Ainley & Mathieson (1955) modified by Aungier (2006) was adopted for the Ljungström turbine stage blade loss evaluation. However, it requires detailed information of the stage configuration, which is initially unknown. Therefore, the performance evaluation using this model will be preceded by a design-point study using the less demanding but still reasonably accurate model of Soderberg.

6.1.5 Model of Soderberg

Introduction

The model of Soderberg (1949) is, even though dated, still frequently mentioned as a good tool to get reasonably accurate predictions for the profile and secondary losses in a turbine stage – Horlock (1966) and Dixon (2005). Horlock (1966) indicates that Soderberg's model performs reasonably well over a substantial range of blade aspect ratios and Reynolds numbers for the optimum blade-pitch-to-chord ratio[i]. He indicates however that the model does neither involve the influence of reaction degree $\hat{R}$, nor the impact of blade geometry. The latter shortcoming, in combination with a relatively accurate loss prediction, makes this model extremely attractive to perform pre-design calculations, where the designer has initially no view on the required blade geometry at all. Soderberg's model describes the profile losses, the secondary losses and applies a Reynolds correction for flow conditions with Reynolds number different from the reference, which was used to establish the model. These effects are now explained in the subsequent sections.

[i]Soderberg relied on the model of Zweifel (1945) for this purpose.

Profile and secondary losses under reference conditions : ζ_1

The profile losses and secondary losses under reference conditions, i.e. $Re = 10^5$ and $\text{Æ}R_a = 3$ are – Dixon (2005) :

$$\zeta_1 = 0.04 + 0.06\left(\frac{\epsilon}{1.74533}\right)^2 \quad [\text{-}][\text{rad}] \tag{6.25}$$

Note that the losses depend only on the flow deflection $\epsilon = \beta_i - \beta_{o,b}$.

Profile and secondary losses allowing non-reference $\text{Æ}R_a$ **:** ζ_2

Soderberg proposes to correct ζ_1 in case $\text{Æ}R_a \neq 3$ as follows :

$$\zeta_2 = (1 + \zeta_1)\left(0.975 + \frac{0.075}{\text{Æ}R_a}\right) - 1 \tag{6.26}$$

Profile and secondary losses allowing non-reference Re **:** ζ_3

In case Re of the flow passing over the blade differs from the reference $Re = 10^5$, a correction needs to be introduced. The blade losses then become :

$$\zeta_3 = \left(\frac{10^5}{Re}\right)^{0.25} \zeta_2 \tag{6.27}$$

while Re is defined as – Shaw (1966) :

$$Re \triangleq \frac{\rho_{o,b} w_{o,b} D_h}{\mu_{o,b}} \tag{6.28}$$

and the hydraulic diameter D_h – Shaw (1966) :

$$D_h \triangleq \frac{2\, s\, H_{bo} \cos\beta_{o,b}}{s \cos\beta_{o,b} + H_{bo}} \tag{6.29}$$

The implementation of ζ_3 in the stage governing equations is discussed next.

Implementation into the stage governing equations

The model of Soderberg provides a specific total enthalpy loss, which is in case of a rotor – Lewis (1996) :

$$h_{tL} = \zeta_3 \frac{w_{o,b}^2}{2} \tag{6.30}$$

and,

$$h_{tL} = h_{to,b} - h_{to,b_{is}} \tag{6.31}$$

From this point on, all other variables are derivable, such as the stage expansion ratio π_{Ts} and efficiencies (see also Fig.5.14 and Section 5.5). The more detailed discussion of the implementation of Soderberg's model into the governing equations follows in Chapter 7, where the Ljungström turbine design procedure is developed, and in which Soderberg's loss model plays a vital role.

6.1.6 Model of Ainley and Mathieson

Introduction

The model of Ainley & Mathieson (1955), as presented and corrected by Aungier (2006), will be used to quantify the losses in the *off-design turbine model, where all relevant turbine dimensions are known*. In contrast to the model of Soderberg, it allows the separate determination of the impact of compressibility effects, a detailed examination of blade roughness and Reynolds number effects, an $\mathcal{AR}$-based secondary loss estimation, but most importantly, it enables the quantification of non-shock-free flow losses necessary to establish off-design performance characteristics. However, it requires well determined geometrical characteristics which can only be known if a (pre)design analysis is conducted, wherein the (initial) blade profile is established.

The model distinguishes the blade profile loss Y_p, the secondary loss Y_s, the trailing edge loss Y_{TE} and the supersonic expansion losses Y_{EX}. Because the blades are always shrouded (Fig.6.7), the blade clearance losses were not taken into account. The gap between shroud and turbine disk will, however, be studied in the subsequent disk friction section. The non-dimensional pressure loss Y is defined by Ainley & Mathieson (1955) as :

$$Y = \frac{p_{tro,b_{ID}} - p_{tro,b}}{p_{tro,b} - p_{o,b}} = \sum_j Y_j = Y_p + Y_s + Y_{TE} + Y_{EX} \tag{6.32}$$

where $p_{o,b}$ the static pressure, $p_{tro,b}$ the relative total pressure and $p_{tro,b_{ID}}$ the relative total pressure obtained without losses at the outlet of the blade passage, i.e. :

$$p_{tro,b_{ID}} = p_{tri}\left(\frac{T_{tro,b}}{T_{tri}}\right)^{\frac{\gamma}{\gamma-1}} \tag{6.33}$$

The correlations used by the model of Ainley & Mathieson (1955) and modified by Aungier (2006) are found in Appendix D, since they are too involved to be summarised in the present context. The following sections will discuss the above-mentioned losses briefly.

Profile loss coefficient Y_p

The blade profile loss is based on loss data in nozzle and impulse cascades established by experiments done by Ainley & Mathieson (1955), and modified to take blade passage geometrical, incidence, roughness, compressibility and designer experience effects into

account.

Secondary losses Y_s

The model of Ainley & Mathieson (1955) has been revised and updated by several authors with time. With regard to the secondary losses, credit must be given to Dunham & Came (1970) and Kacker & Okapuu (1982) whose work improved the estimation of the secondary losses, which was specifically developed to be implemented in the model of Ainley & Mathieson (1955). The resulting model, and modified by Aungier (2006), is used by this author for the off-design calculations. The correlations for these losses are covered in Appendix D. Again, it is important to highlight that the secondary losses are approximately inversely proportional to the blade aspect ratio $\mathcal{AR}$:

$$Y_s \propto \frac{1}{\mathcal{AR}} \tag{6.34}$$

In case of the RELT, $\mathcal{AR}$ should be chosen high enough in order to avoid the secondary losses to become predominant.

Trailing edge losses Y_{TE}

The trailing edge loss coefficient proposed by Aungier (2006) is based on the abrupt expansion of the flow in the outlet due to finite blade trailing edge. They are not included in the profile losses.

Supersonic expansion losses Y_{EX}

When the flow leaves the blade at supersonic speeds, the effect of shock losses must be accounted for. However, since the flow through the blade passages will remain subsonic in case of the RELT, Y_{EX} will remain zero.

Implementation into the stage governing equations

Recalling Eq.6.32,

$$Y = \frac{p_{tro,b_{ID}} - p_{tro,b}}{p_{tro,b} - p_{o,b}} = \sum_j Y_j = Y_p + Y_s + Y_{TE} + Y_{EX}$$

and Eq.6.33,

$$p_{tro,b_{ID}} = p_{tri}\left(\frac{T_{tro,b}}{T_{tri}}\right)^{\frac{\gamma}{\gamma-1}}$$

Y is related to the relative total pressure loss in a blade passage, considering a constant value for $T_{tro,b}$. Fig.6.3 reveals how to implement the Y-loss mechanism in the stage

governing equations[ii]. Y causes a horizontal shift on the T-s diagram $(tro, b_{ID} - tro, b)$, which concurs with an entropy increase at constant total relative temperature. From this shift, $p_{tro,b}$ can be calculated, which allows the outlet velocity triangle and intensive properties to be established. However $p_{o,b}$ and $p_{tro,b}$ are unknown for as long as Y is not determined, while Y in turn depends on the former. As a consequence, an iterative calculation procedure is required, of which a simplified representation is given in Fig.6.4. The iterative procedure to calculate $\beta_{o,b}$, which is part of the Y calculations, is adopted in Fig.6.5. The iterative calculations start by posing $p_{tro,b} = p_{tro,b_{ID}}$ and finding a first value for Y. This value is then used to calculate $p^{+}_{tro,b}$, which is then applied to retrieve a new value for Y. The iteration ends when the error drops below a certain threshold.
Note that $\dot{m}^{*}_{o}$ represents the choking mass flow rate, as discussed in Appendix C. In case $\dot{m}_b > \dot{m}^{*}_{o}$, there exists no physical solution for the value of $\dot{m}_b$.

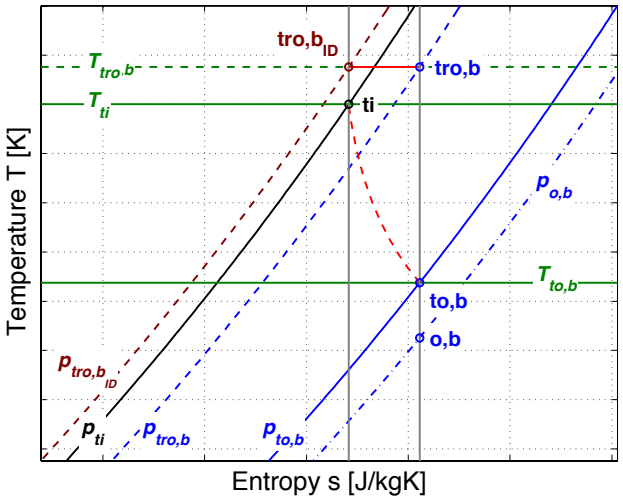

FIGURE 6.3. Representation of Y-loss coefficient on a T-s diagram.

[ii]Note that the inlet and outlet variables used in Fig.6.3 are already explained in Section 5.4.6 and Section 5.4.7 and will not be repeated here.

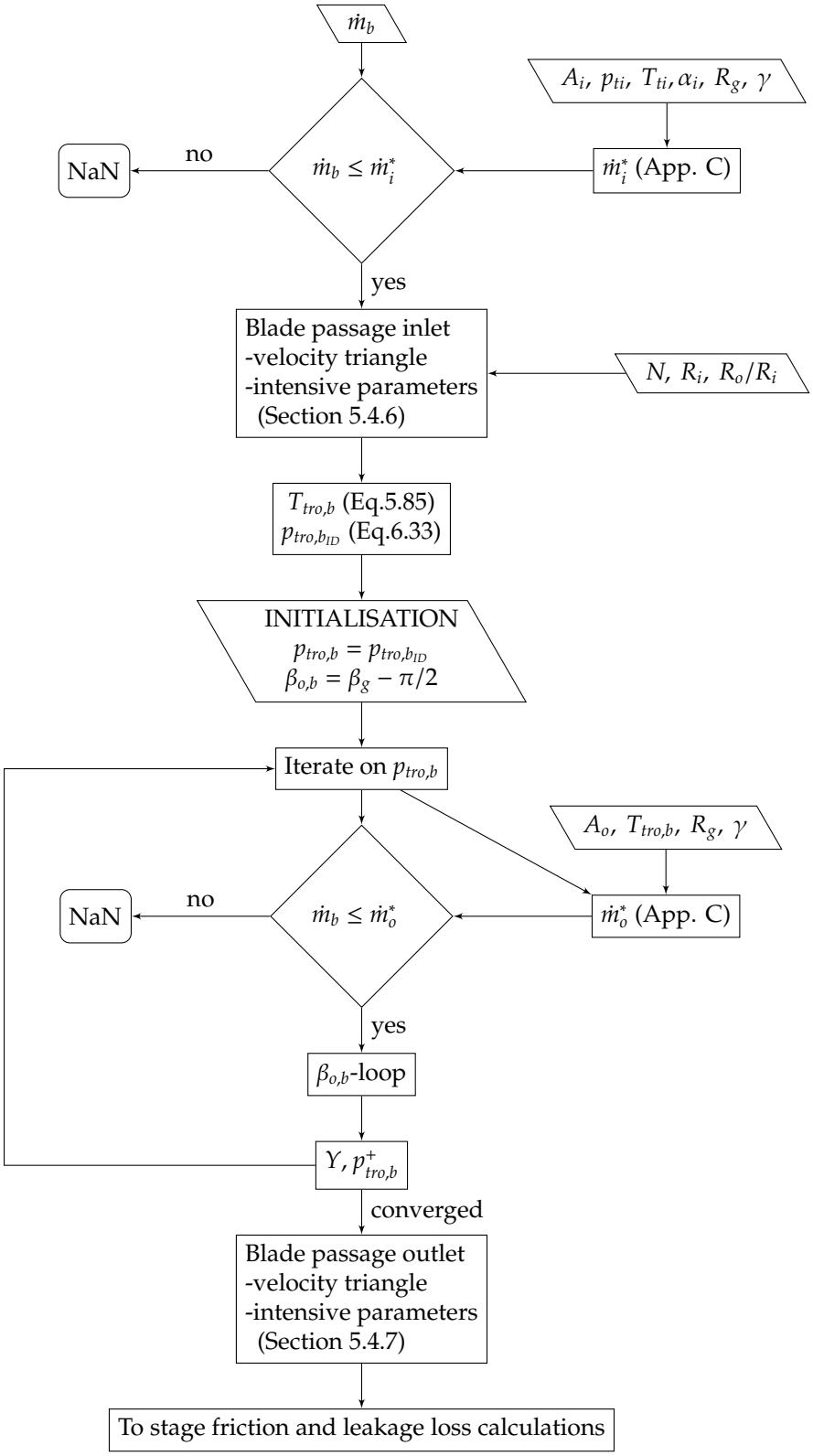

FIGURE 6.4. Iteration procedure to find blade passage outlet conditions for a given geometry.

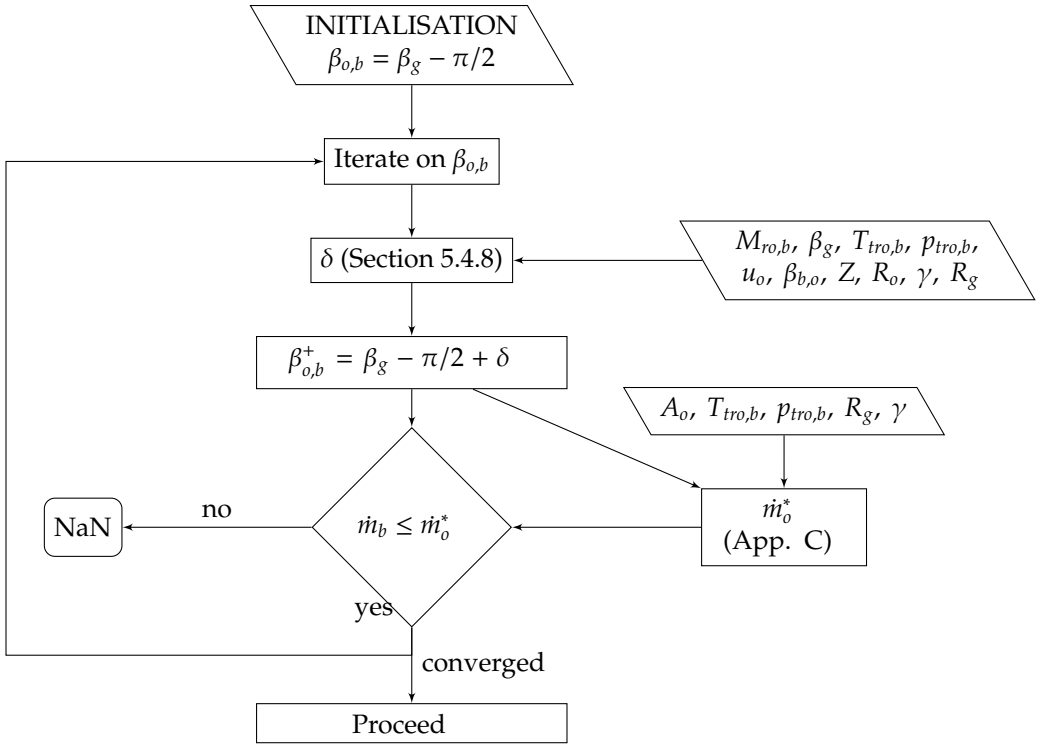

FIGURE 6.5. Iteration procedure to find $\beta_{o,b}$.

6.1.7 Endwall fences

In case the turbine stage design study imposes a low $\mathcal{AR}$-blade, high secondary losses may be expected. A possible technical solution to overcome this issue partially, is by using endwall fences (Fig.6.6). Endwall fences are reported to drastically reduce the secondary losses. Indeed, Moon & Koh (2001) mention an extensive list of experimental work, amongst which Kawai et al. (1989), Chung et al. (1991) and Lee (1997), and highlight that an endwall fence positioned halfway along the blade passage with a height of 1/3 of the inlet boundary thickness, has the potential to reduce the secondary losses by 20%. Indeed, the endwall fence hinders the crossflow and the migration of the pressure leg of the horseshoe vortex to the suction side of the subsequent blade. This reduces the vortex strength and hence, the secondary losses.
In case the installation of endwall fences appears advisable by the presence of an important amount of secondary losses, then it is proposed to reduce Y_s by 20%, i.e. :

$$Y_{s_{new}} = K_{EWF} Y_s \quad \text{Ainley and Mathieson} \tag{6.35}$$

where K_{EWF} is defined as the secondary loss attenuation factor K_{EWF}. The following values for K_{EWF} may then be applied :

$$K_{EWF} = 0.8 \quad \text{(with endwall fences)} \tag{6.36}$$

Otherwise,

$$K_{EWF} = 1 \quad \text{(without endwall fences)} \tag{6.37}$$

Note that this correction should only be applied to the model of Ainley and Mathieson. Indeed, Soderberg's model does not differentiate primary and secondary losses in his model, making the introduction of K_{EWF} impossible. As a consequence, the impact on the turbine efficiency by installing endwall fences will only become clear when examining the off-design performance characteristics of the geometry established with Soderberg's model. In that case however, even though a decrease in losses will influence the velocity triangles and cause the flow to become non-shock-free at nominal operation, it is reasonable to expect an increase of the total turbine efficiency by installing endwall fences.

6.2 Stage disk friction loss

Besides the blade passage losses obtained from the modified axial turbine loss model of Ainley and Mathieson, and which specifically deals with the flow through the rotating circular cascade, disk friction losses still need to be accounted for. In this work, the *disk friction loss* is the general term used for friction losses between the annular rim joining

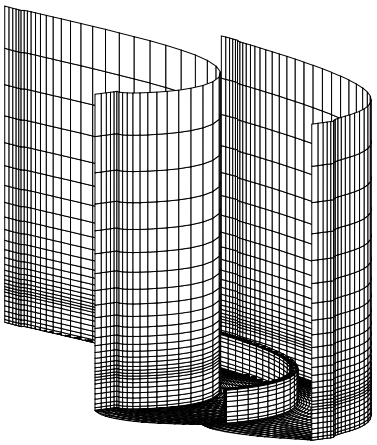

FIGURE 6.6. Secondary loss abatement by installing endwall fences – Moon & Koh (2001).

the blade tips of a stage and the surface of the disk of the opposing turbine half in which it revolves (Fig.6.7). Following the strategy of Aungier (2006), the disk friction loss will be reintroduced in the flow as a total enthalpy increment. Note however that the disk friction loss model proposed by Aungier (2006) for an axial turbine was found not suitable for the Ljungström turbine because losses of two interacting rotors have to be examined. As a consequence, an alternative to this model is developed next.

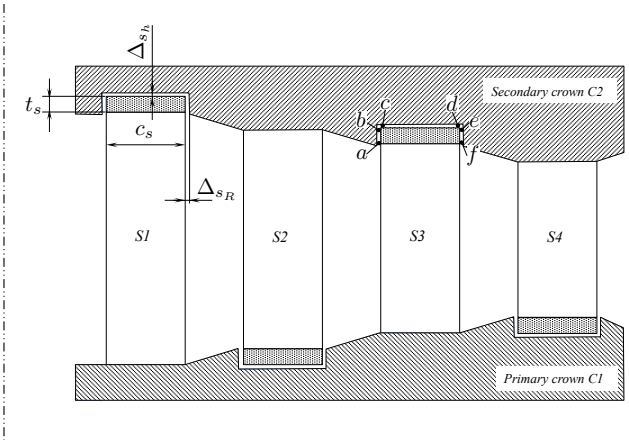

FIGURE 6.7. Cross-sectional view on a four-stage Ljungström turbine layout with radial respectively axial play Δ_{s_R} and Δ_{s_h}.

Observing Fig.6.7, two distinct friction loss types may be noted. Firstly, one has a *Taylor-Couette* viscous flow between sections $a-b$ and $e-f$. This flow is mainly characterized by the viscous shear forces in the gap between two coaxially placed rotating cylinders. In section $c-d$, a *torsional Couette* flow is found, which is typically represented as the viscous flow between a revolving disk and a shroud placed at close distance. The subsequent paragraphs discuss these losses more in detail from which a disk friction loss model will be derived.

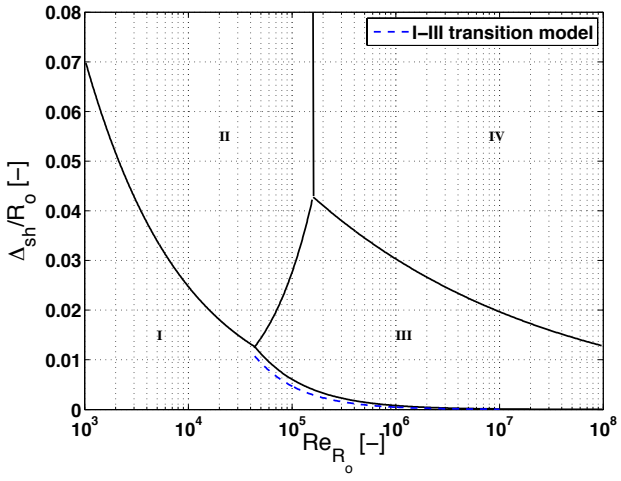

FIGURE 6.8. Four torsional Couette flow regimes adopted from Haddadi & Poncet (2008), and I-III transition model.

6.2.1 Torsional Couette flow loss

Haddadi & Poncet (2008) mention the work of Daily & Nece (1960) as having been groundbreaking in the domain of torsional Couette flow. They indicate that it is still widely adopted in the literature when modelling this kind of flow. Daily and Nece examined this flow type theoretically and via experiments for a revolving flat disk suspended between two static sidewalls. The distance between the sidewalls and the disk could be varied, which was necessary to study the impact of the gap width on the boundary layer development. Daily & Nece (1960) reveal four flow regimes :

→ Regime 1 : laminar flow between disk and sidewalls, the boundary layers of shroud and disk are merged

→ Regime 2 : laminar flow between disk and sidewalls, the boundary layers of shroud and disk remain separated

→ Regime 3 : turbulent flow between disk and sidewalls, the boundary layers of shroud and disk are merged

→ Regime 4 : turbulent flow between disk and sidewalls, the boundary layers of shroud and disk remain separated

Fig.6.8 reflects the four flow regimes as a function of Reynolds number Re_{R_o} and non-dimensional axial gap width Δ_{s_h}/R_o, where :

$$Re_{R_o} = \frac{\rho \omega R_o^2}{\mu} \tag{6.38}$$

while R_o the outer radius of the rotating disk, ω the disk angular velocity and Δ_{s_h} the gap width, as indicated on Fig.6.7. What the Ljungström turbine concerns, $Re_{R_0} = O(6 \text{ à } 7)$

since :

$$Re_{R_o} = \frac{\rho\omega R_o^2}{\mu} = \frac{\rho\omega(R_o/c)^2}{\mu}c^2 = \frac{O(0)\,O(1\ à\ 2)\,O(4)}{O(-5)}\,O(-4) = O(6\ à\ 7) \tag{6.39}$$

where c the blade chord. The selection of the non-dimensional gap width $\Delta s_h/R_o$ is a design parameter and should be chosen wisely. It should be taken large enough to allow for deflections under mechanical and, in a lesser extent, thermal loads, such that good functioning is guaranteed, i.e. collision between opposing components is avoided. Since, from a material point of view, the temperature at nominal regime in a rotor-embedded Ljungström turbine configuration is low, the required space for thermal expansion can remain low. Similarly, important deformations of the disk because of bending forces are not expected. A small axial gap is also significant from a weight perspective. A large value of $\Delta s_h/R_o$ will cause the opposing disk to become thicker and thus heavier. Indeed, transferring the delivered stage torque to the rotors requires a minimum disk thickness in order to satisfy material strength constraints. To this thickness the axial gap width Δ_{s_h} needs to be added. Nevertheless, the choice of an as-small-as-possible Δ_{s_h}/R_o turns out not to be a correct choice either. To explain this, the model of Daily & Nece (1960) needs further examination. Here, it is sufficient to accept that, for the time being, $\Delta_{s_h}/R_o = O(-3)$. This condition will be relaxed a small amount afterwards, but that will form part of the subsequent discussion.

Observing Fig.6.8, and adopting the assumption that $\Delta_{s_h}/R_o = O(-3)$, while $Re_{R_o} = O(6\,à\,7)$ (Eq.6.39), the torsional Couette flow will generally be of type III. In case Δ_{s_h}/R_o is extremely small, or during startup i.e. at low rotational velocities, type I flow is also possible. In the latter situation, transition from type I to type III flow at some point is apparent. The torsional Couette wall friction torque $\mathcal{T}_{TOC}$ exerted by the fluid on the rim or the opposing disk depends on the flow type, and is usually expressed by the general formula – Goulburn & Wilson (1975):

$$\mathcal{T}_{TOC} = k_\tau \frac{1}{2}\rho\omega^2\, R_o^5 \tag{6.40}$$

with ρ the density of the fluid and k_τ the torque coefficient given by the functions of Daily and Nece, as cited by Goulburn & Wilson (1975) :

$$k_{\tau,I_{DN}} = \frac{2\pi}{(\Delta_{s_h}/R_o)\,Re_{R_o}} \qquad \textit{Regime I} \tag{6.41}$$

$$k_{\tau,III_{DN}} = \frac{0.0622}{(\Delta_{s_h}/R_o)^{\frac{1}{4}} Re_{R_o}^{\frac{1}{4}}} \qquad \textit{Regime III} \tag{6.42}$$

Here, it is important to note that the torque coefficients were derived for a revolving disk with *two* exposed sides. The turbine rim has only *one* wetted side. The torque coefficients therefore need to be halved. As a consequence, the torque coefficients for either the rim

or the disk in the Ljungström turbine become :

$$k_{\tau,I} = \frac{\pi}{(\Delta_{s_h}/R_o)\, Re_{R_o}} \qquad \textit{Regime I} \tag{6.43}$$

$$k_{\tau,III} = \frac{0.0311}{(\Delta_{s_h}/R_o)^{\frac{1}{4}} Re_{R_o}^{\frac{1}{4}}} \qquad \textit{Regime III} \tag{6.44}$$

In case transition occurs from type I to III or vice versa, the author proposes to model the process by assuming $k_{\tau,I} = k_{\tau,III}$ at the critical point, yielding :

$$\frac{\Delta_{s_h}}{R_o} = \left(\frac{\pi}{0.0311}\right)^{\frac{4}{3}} Re_{R_o} \tag{6.45}$$

This will avoid a discontinuous evolution of $k_\tau = f(\Delta_{s_h}/R_o, Re_{R_o})$, which improves convergence of the calculations. The considered I-III transition model is indicated in Fig.6.8 and proves satisfactory.
It needs to be highlighted again that the Ljungström turbine setup is not identical to the experiment of Daily and Nece, which must be accounted for in the determination of ω. By considering a relative frame of motion fixed either to the rim or opposing disk, this issue is dealt with. ω in Eq.6.40 then is :

$$\omega = |{}^R\Omega_C| + |{}^D\Omega_C| \tag{6.46}$$

where ${}^R\Omega_C$ and ${}^D\Omega_C$ are the angular velocities of respectively the blade rim and the turbine disk.
Another important adjustment to Eq.6.40 must yield a correction term to account for the important inlet radius size in the Ljungström turbine. In contrast to the setup of Daily and Nece, not a full disk with negligible hub dimensions is subjected to friction, but only a part of a disk, viz. zone $c - d$ between radii R_i and R_o. To cope with this, it is proposed to subtract the friction torque of the non-existing part of the disk by considering a fictitious revolving disk with radius R_i operating under the same conditions, including Re_{R_0}. Eq.6.40 then becomes :

$$\mathcal{T}_{TOC} = k_\tau \frac{1}{2} \rho \omega^2 \, (R_o^5 - R_i^5) \tag{6.47}$$

At this point, it is interesting to discuss the selection of the axial gap width Δ_{s_h}. In case an optimum turbine performance is sought, the data provided by Daily and Nece appears useful. Plotting k_τ as a function of Δ_{s_h}/R_o and Re_{R_o}, shows the existence of a friction minimum (Fig.6.9). This torque friction *bucket* is situated around $\Delta_{s_h}/R_o = 0.025$. Then, based on Fig.6.8, one observes that flow type II and IV are also possible. For these flow types, Goulburn & Wilson (1975) mention that only graphical data exists to estimate the friction torque. However, plotting Eq.6.43 and Eq.6.44 for respectively flow type I and III on Fig.6.9 (blue lines), which is repeated in Fig.6.10, clearly shows that these

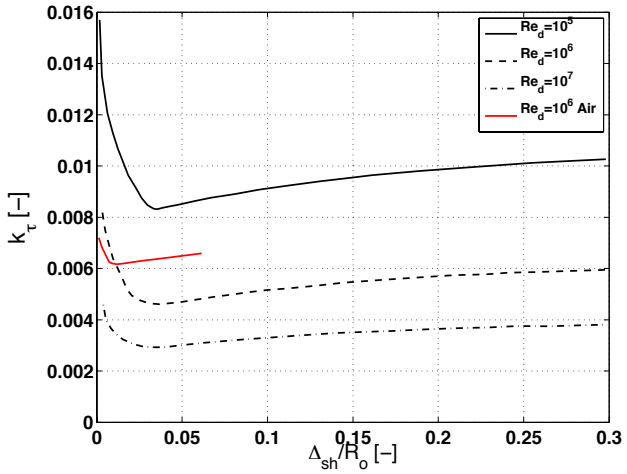

FIGURE 6.9. Torsional Couette flow with liquids and air as compressible substance – adopted from Goulburn & Wilson (1975).

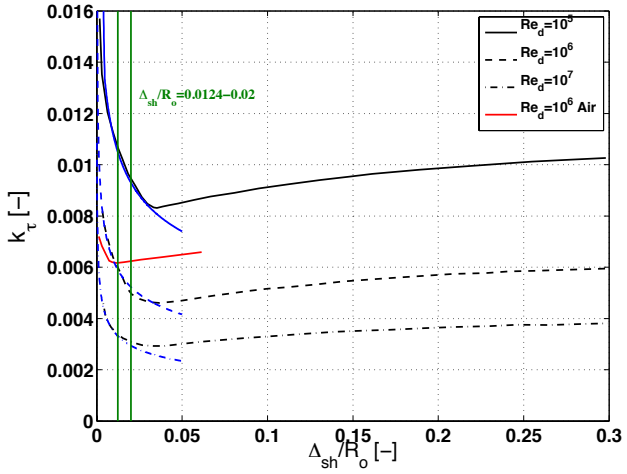

FIGURE 6.10. Torsional Couette flow with air as compressible substance, I-III transition model and suggested design range – adopted from Goulburn & Wilson (1975).

expressions remain reasonably valid (deviation less than 10%), until say $\Delta_{s_h}/R_o \approxeq 0.03$. This explains the initial choice of $\Delta_{s_h}/R_o = O(-3)$, which allowed the I-III transition model to be developed without the need to consider types II and IV flows. The existence of a friction minimum also highlights that, besides the weight penalty, large axial gaps do not necessarily contribute to a lower loss. The designer should therefore opt for an axial gap width near the friction torque bucket. It is important to note that Daily and Nece used liquids to develop the torque models. Goulburn & Wilson (1975) examined a torsional Couette flow with air and found that the model of Daily and Nece is only sufficiently accurate for non-dimensional gap widths $\Delta_{s_h}/R_o \leq 0.0124$. This because the friction torque bucket for air was found by Goulburn & Wilson (1975) to be near $\Delta_{s_h}/R_o \approxeq 0.0124$. For higher values of Δ_{s_h}/R_o, k_τ breaks away from the model of Daily and Nece. Fig.6.9 reveals this clearly. Since Goulburn & Wilson (1975) proved this for $Re_{R_o} = 10^6$ only, *the author of*

this work prefers to retain the model of Daily and Nece, noting a good design rule for Δ_{s_h}/R_o to be situated between 0.0124 and 0.02 (Fig.6.10). This is close to both minima stated by Goulburn & Wilson (1975) and Daily & Nece (1960), while not too high on the steep side of the torque friction bucket, which causes a significant increase in friction torque when further reducing the axial gap width. From this discussion it is now clear that $\Delta s_h/R_o = O(-3)$ may be relaxed a little, viz. $\Delta_{s_h}/R_o = O(-2\,\grave{a} - 3)$, even though type I and III flow are used to model the torsional Couette losses.

6.2.2 Taylor-Couette flow loss

Taylor-Couette flow is found between two closely coaxially placed cylinders turning at different angular speeds. This is the case for sections $a-b$ and $e-f$ (Fig.6.7). The flow characteristics are complex because of the possibility of instabilities in the flow. In case these instabilities occur in the flow, the friction torque no longer increases linearly with rotational speed – Dou et al. (2008). The work of Dou et al. (2008) also highlights that when $\Delta_{s_R} << R_i$, which is the case for the Ljungström turbine, the onset of these instabilities becomes difficult to predict[iii] using the currently available and reasonably simple models. Then they propose to estimate the wall friction by planar Couette flow. Following Çengel & Cimbala (2010), the cylindrical surface may locally be seen as a flat plate for which the wall shear stress is :

$$\tau_w = \mu \frac{\partial u}{\partial y} \tag{6.48}$$

and u the velocity of the flow parallel to the plate and y the vertical distance from the flat plate. Denoting ξ the component to which the smallest radius R_ξ applies (either rim or disk), and η the component to which the largest radius R_η applies (either disk or rim), Eq.6.48 becomes :

$$\tau_w = \mu \frac{|^{\xi}\Omega_C R_\xi| + |^{\eta}\Omega_C R_\eta|}{R_\eta - R_\xi} = \mu \frac{|^{\xi}\Omega_C R_\xi| + |^{\eta}\Omega_C R_\eta|}{\Delta_{s_R}} \tag{6.49}$$

The shear stress is identical for both components. The friction moment exerted on each component is then reflected by the following relations :

$$\mathcal{T}_{TAC_\xi} = R_\xi \int_A \tau_w \, dA = 2\pi\mu \left(\frac{|^{\xi}\Omega_C R_\xi| + |^{\eta}\Omega_C R_\eta|}{\Delta_{s_R}} \right) R_\xi^2 \, t_s \tag{6.50}$$

$$\mathcal{T}_{TAC_\eta} = R_\eta \int_A \tau_w \, dA = 2\pi\mu \left(\frac{|^{\xi}\Omega_C R_\xi| + |^{\eta}\Omega_C R_\eta|}{\Delta_{s_R}} \right) R_\eta^2 \, t_s \tag{6.51}$$

[iii] Usually the Taylor number $Ta \triangleq \frac{{}^{i}\Omega_C{}^2 R_i^2 \Delta_{s_R}^3}{\nu^2 R_j}$ is used for this purpose, with the critical value $Ta_c = 1708$ – Dou et al. (2008).

where t_s the rim height (Fig.6.7). Since $R_\xi \approx R_\eta$, the above equations may be replaced by :

$$\mathcal{T}_{TAC} \cong 2\pi\mu \left(\frac{\omega}{\Delta_{s_R}}\right) R^3 \, t_s \tag{6.52}$$

where R is the stage inlet radius R_i in case of section $a-b$, or the stage outlet radius R_o in case of section $e-f$. Consequently, since each Ljungström turbine stage has two zones with Taylor-Couette flow ($a-b$ and $e-f$). Their contribution to the friction torque now yields :

$$\mathcal{T}_{TAC} = 2\pi\mu \left(\frac{\omega}{\Delta_{s_R}}\right) (R_i^3 + R_o^3) \, t_s \tag{6.53}$$

The simplified theory using planar Couette flow shows that the friction torque by Taylor-Couette flows are inversely proportional to the gap width Δ_{s_R}. A larger gap would appear to reduce the friction losses. Although this is sensible, a larger gap also increases the leakage flow. This loss has a detrimental impact on the stage efficiency since not all mass flow is expanded through the blade stages. The leakage loss should therefore be minimised, while the gap width "optimised". An optimisation study of this kind is not considered in the work at hand.

6.2.3 Stage disk friction loss

Eqs. 6.47 and 6.53 show that the frictional torque on the annular rim and the opposing disk are identical. The disk friction torque on rim or disk then is :

$$\mathcal{T}_{DF} = \mathcal{T}_{TOC} + \mathcal{T}_{TAC} = k_\tau \frac{1}{2} \rho\omega^2 \, (R_o^5 - R_i^5) + 2\pi\mu \left(\frac{\omega}{\Delta_{s_R}}\right) (R_i^3 + R_o^3) \, t_s \tag{6.54}$$

6.3 Leakage mass flow

Over the gap formed between points a and f the stage pressure drop is in effect. As a consequence, a leakage mass flow $\dot{m}_{LL}$ will arise. This loss needs to be quantified. The model that will be developed for that purpose is based on see-through labyrinth seals. Even though this implies various simplifications, under which neglecting the complex behaviour of the Couette flows, it is the opinion of the author that it is currently the best time-efficient and accessible approach available.

6.3.1 See-through labyrinth seal leakage mass flow modelling

An example of a see-through labyrinth seal is shown in Fig.6.11. The goal of a labyrinth seal is to minimise $\dot{m}_{LL}$ by restriction of the flow via the vena contracta in the gap Δ_s near each seal strip, and by partially dissipating the kinetic energy in the cavity directly behind it. In addition, the higher the number of seal strips N_{ss}, the more the leakage mass flow is reduced. Several models exist in the literature to model $\dot{m}_{LL}$ – Woo (2011), but the

empirical model of Neumann (1964) will be adopted here, as given by e.g. Malvano et al. (2001) and Eser & Kazakia (1995), since frequently used.

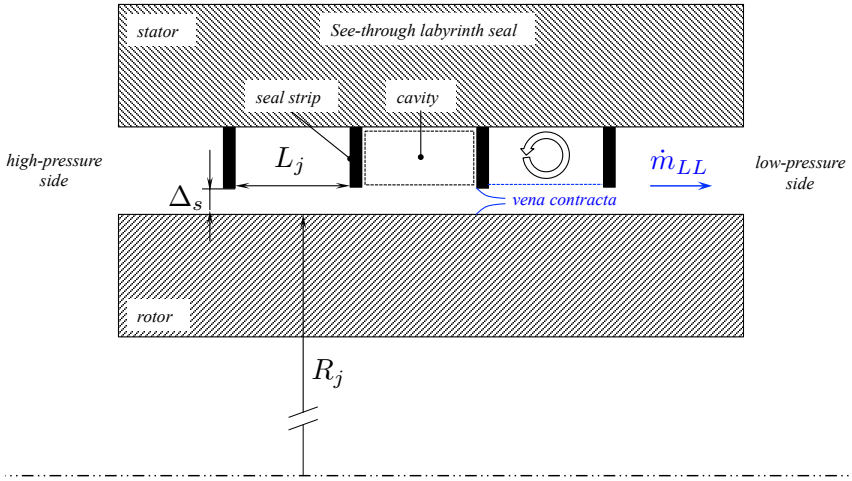

FIGURE 6.11. See-through labyrinth seal with seal strips fixed on the stator.

Neumann considers an isothermal flow passing through the labyrinth seal, which behaves like a perfect gas, while assuming the pressure drop over each seal strip to remain minor[iv]. Additionally, he assumes the pressure of the expanding jet to rule also in the cavity trapped between two strip seals with length L_j (Fig.6.11). It is important to note that the model of Neumann calculates the mass flow per seal strip, requiring an iterative approach to find the leakage loss over the labyrinth seal. Neumann's loss equation given for a seal strip j in the labyrinth is :

$$\dot{m}_{LL_j} = \mu_{vc_j}\, \mu_{kco_j}\, A_{LL_j} \sqrt{\frac{p_{j-1}^2 - p_j^2}{R_g T}} \tag{6.55}$$

where μ_{vc_j} the contraction coefficient, μ_{kco_j} the kinetic carry-over coefficient and A_{LL_j} the area between seal strip tip j and the opposing surface. A_{LL_j} is for $\Delta_s << R_j$ (Fig.6.11) :

$$A_{LL_j} \cong 2\pi R_j \Delta_s \tag{6.56}$$

p_j is the pressure behind seal strip j and R_g the specific gas constant. p_{j-1} represents the pressure in front of the seal strip j, thus of the preceding cavity. T concurs with the temperature at the inlet of the labyrinth seal and remains, following Neumann's model, constant throughout the seal. A sensible value for T, even though it involves an approximation, is the turbine stage total inlet temperature T_{ti}. Similarly, a reasonable

[iv] This condition is due to the simplifications introduced to the first law of thermodynamics, which served as the basis for Neumann's loss formula – Hodkinson (1939).

value for the seal inlet pressure is the turbine stage total inlet pressure p_{ti}. Hence :

$$T_{ti} = T = T_j = \ldots = T_{N_{ss}} \tag{6.57}$$

$$p_{t_i} = p_0 \tag{6.58}$$

where N_{ss} is the number of seal strips. The expansion over the labyrinth seal is such that the outlet pressure of the last seal $p_{N_{ss}}$ equals the turbine outlet pressure p_{to}, again relying on the assumption that the total pressure may be used. Because the mass flow through each seal strip is identical in steady state conditions :

$$\dot{m}_{LL} = \dot{m}_{LL_j} \ldots = \dot{m}_{LL_{N_{ss}}} \tag{6.59}$$

Malvano et al. (2001) and Eser & Dereli (2007) use for the contraction coefficient μ_{vc} Chaplygin's empirical model :

$$\mu_{vc} = \frac{\pi}{\pi + 2 - 5S_j + 2S_j^2} \quad < 1 \tag{6.60}$$

$$S_j = \left(\frac{p_j}{p_{j-1}}\right)^{\frac{\gamma-1}{\gamma}} - 1 \tag{6.61}$$

while for the kinetic carry-over coefficient μ_{kco}, they propose the approximation of Neumann (1964) :

$$\mu_{kco} = 1 \quad \text{for} \quad j = 1 \tag{6.62}$$

$$\mu_{kco} = \sqrt{\frac{N_{ss}}{(1 - J_j)N_{ss} + J_j}} \quad \text{for} \quad \forall j \neq 1 \tag{6.63}$$

$$J_j = 1 - (1 + 16.6\ \Delta_{s_j}/L_j)^{-2} \tag{6.64}$$

The contraction coefficient μ_{vc} is necessary to account for the presence of the vena contracta between the seal strip and the opposing surface (Fig.6.11). The kinetic carry-over coefficient μ_{kco} corrects for the kinetic energy which was not dissipated in the preceding cavity before entering the subsequent seal strip. Ideally, the kinetic energy increase due to the expansion over the seal strip is fully dissipated in the cavity, concurring with a μ_{kco} of unity. This is generally not the case and $\mu_{kco} > 1$. Essentially, a higher inlet speed near the seal strip will reduce the accompanying achievable pressure drop for a given $\dot{m}_{LL}$. Note that $\mu_{kco} = 1$ is always valid for the first seal strip ($j = 1$) because the flow speed near the entry is considered to be negligible[v]. Observing Eqs.6.62-6.64, the impact of the ratio of seal gap width Δ_s and cavity length L_j becomes clear. Large cavity lengths L_j allow better dissipation of the kinetic energy in the cavity, leading to values of μ_{kco} closer

[v] Malvano et al. (2001) and Eser & Kazakia (1995) do not mention this condition, while Scharrer (1987) and Hodkinson (1939) do. It is not clear what the reason for this is, but it could be due to the presence of an inlet cavity prior to the first seal strip, which indeed causes kinetic carry-over to occur.

to unity. But this condition is unfortunately not always feasible, nor desirable because it would require a more complicated seal geometry or make the labyrinth seal too large. Finally, it is important to note that Neumann's model for μ_{kco} gives the asymptotic value $\mu_{kco} \rightarrow \sqrt{N_{ss}}$ for large Δ_s/L_j, which is in line with the findings of Hodkinson (1939).
Before developing the calculation procedure for $\dot{m}_{LL}$, Malvano et al. (2001) and Eser & Dereli (2007) indicate the possibility of the choking of *the last seal strip*. The choking process limits the mass flow passing through the gap. The mass flow per unit area during saturation can be derived easily and is described by the following formula[vi] – Çengel & Cimbala (2010) :

$$\frac{\dot{m}^*_{LL}}{A_{LL_{N_{ss}}}} = p_t \sqrt{\frac{\gamma}{R_g T_t}} \left(\frac{\gamma+1}{2}\right)^{-\frac{(\gamma+1)}{2(\gamma-1)}} \tag{6.65}$$

Eser & Kazakia (1995) propose to use this equation, multiplied by μ_{vc} and μ_{kco} to find the mass flow through the choked seal strip[vii] :

$$\frac{\dot{m}^*_{LL}}{A_{LL_{N_{ss}}}} = \mu_{vc}\mu_{kco}\, p_t \sqrt{\frac{\gamma}{R_g T_t}} \left(\frac{\gamma+1}{2}\right)^{-\frac{(\gamma+1)}{2(\gamma-1)}} \tag{6.66}$$

The calculation technique of Scharrer (1987) is followed to calculate $\dot{m}_{LL}$. First, an estimation of the pressure drop over each seal strip is made, for example $\Delta_p = (p_{ti} - p_{to})/N_{ss}$. This delivers the pressure in the cavity in front of the last seal strip :

$$p_{N_{ss}-1} = p_{to} + \Delta_p \tag{6.67}$$

Thanks to this estimation of the pressure drop, it is possible to examine whether the flow is choked or not and make a first estimation of $\dot{m}_{LL}$, viz. :

$$\frac{p_{N_{ss}-1}}{p_{to}} < \pi^*_n \quad \rightarrow \quad \text{adapted : Eq.6.55} \tag{6.68}$$

$$\frac{p_{N_{ss}-1}}{p_{to}} \geq \pi^*_n \quad \rightarrow \quad \text{choked : Eq.6.66} \tag{6.69}$$

where,

$$\pi^*_n = \left(\frac{\gamma+1}{2}\right)^{\frac{\gamma}{\gamma+1}} \tag{6.70}$$

Then a backward marching calculation procedure is performed calculating consecutively the pressure of the preceding stages up to the pressure in front of the first seal strip p_0 (Fig.6.12). In case $p_0 < p_{ti}$, Δ_p over the last stage, and thus $\dot{m}_{LL}$, must be increased. If

[vi] In literature, the mass flow saturation formula is sometimes called Fliegner's model, after the name of the person who first derived it.

[vii] The exponent indicated in Eser & Kazakia (1995) was $-\gamma/(\gamma-1)$ instead of $-(\gamma+1)/[2(\gamma-1)]$, which is not in line with the theory of Fliegner. This is believed to be erroneous.

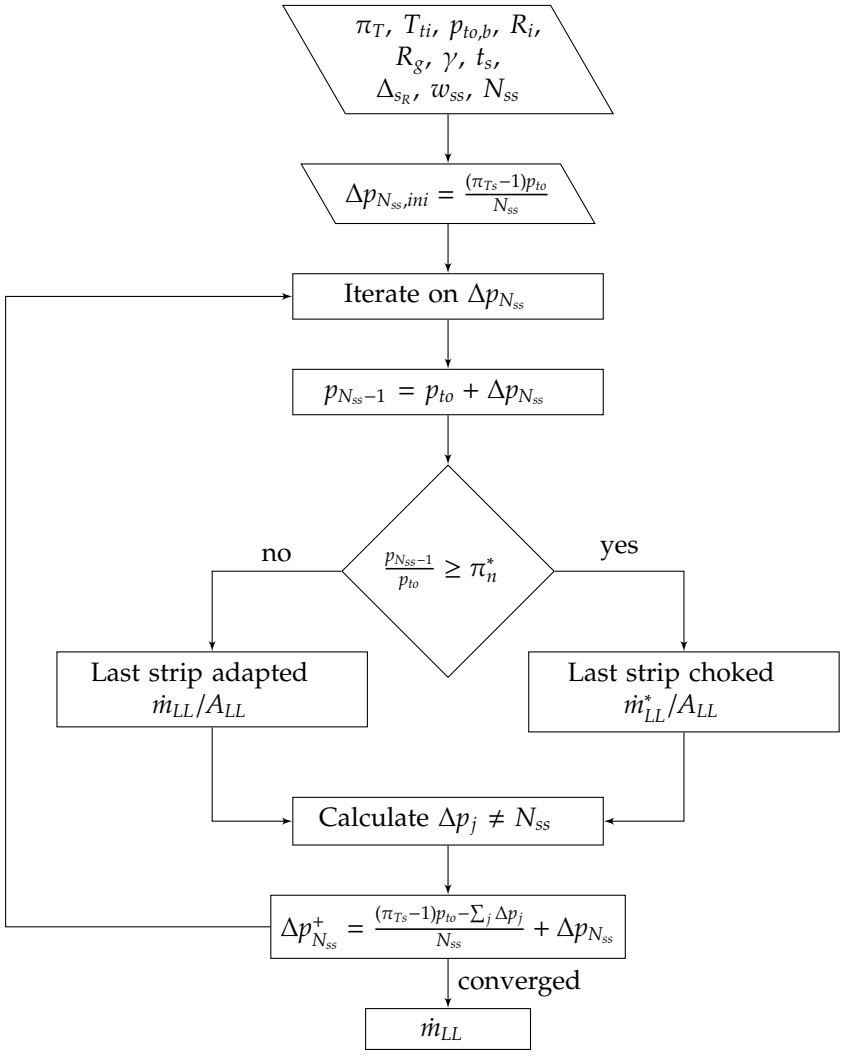

FIGURE 6.12. Iteration procedure to find $\dot{m}_{LL}$.

$p_0 > p_{ti}$, Δ_p over the last stage and $\dot{m}_{LL}$ will have to be reduced. The iteration procedure lasts until $p_0 \cong p_{ti}$.

It is important to note that a discrepancy was detected when calculating the mass flow with Eq.6.55 and Eq.6.66. Indeed, when :

$$\frac{p_{N_{ss}-1}}{p_{to}} = \pi_n^* \tag{6.71}$$

both equations do not overlap. Proof is given when equating Eq.6.55 and Eq.6.66 for this condition, which yields :

$$\frac{\dot{m}^*_{LL\ Eq.6.55}}{\dot{m}^*_{LL\ Eq.6.66}} = \left(\frac{\gamma+1}{2}\right)^{\frac{\gamma+1}{2(\gamma-1)}} \sqrt{\frac{1}{\gamma}\left[1-\left(\frac{1}{\pi_n^*}\right)^2\right]} \tag{6.72}$$

or,

$$\frac{\dot{m}^*_{LL\ Eq.6.55}}{\dot{m}^*_{LL\ Eq.6.66}} \triangleq \mu_{cor} \approxeq 1.24 \quad \text{with } \gamma = 1.4 \tag{6.73}$$

This issue needs to be coped with because the predicted sudden drop in mass flow is not physical. A conservative choice for the efficiency is then to multiply Eq.6.66 with μ_{cor}, even though expecting a reduction in accuracy. As a consequence, the following expression must replace Eq.6.66 :

$$\frac{\dot{m}^*_{LL}}{A_{LL_{N_{ss}}}} = \mu_{cor}\mu_{vc}\mu_{kco}p_t\sqrt{\frac{\gamma}{R_g T_t}}\left(\frac{\gamma+1}{2}\right)^{-\frac{(\gamma+1)}{2(\gamma-1)}} \tag{6.74}$$

Using MATLAB, leakage mass flow characteristics were obtained using the above theory for, for example, $\Delta_s/L = 0.0584$. The results are shown in Fig.6.13. Note that an increase in N_{ss} reduces $\dot{m}_{LL}$, but that the benefits of selecting a higher number of seal strips are limited, since the leakage mass flow does not drop off proportionally. Also, for the lower N_{ss}, the change in slope of $\dot{m}_{LL}$ due to choking can be observed clearly. The onset of choking is indicated by the $p_{N_{ss}-1}/p_{to} = \pi^*_n$-line in red. Fig.6.14 highlights the effects of choking in the last seal strip and $\mu_{kco_{j=1}} = 1$ in the first seal strip for labyrinth seal with 15 seal strips and a turbine stage pressure ratio of 7.

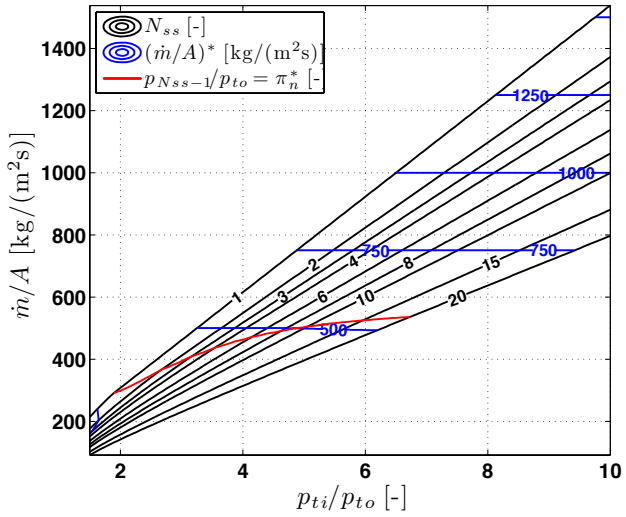

Figure 6.13. See-through labyrinth seal characteristics, impact N_{ss} – $\Delta_s/L = 0.0584$ and $p_{to} = 1$ bar.

6.3.2 Leakage mass flow in the Ljungström turbine – plane rim

Based on the theory expounded in the previous section for the see-through labyrinth seal, a approximate model can be derived for $\dot{m}_{LL}$ in the Ljungström turbine. For this purpose, the geometry of the cavity between the rim and opposing disk (Fig.6.7) is described, as

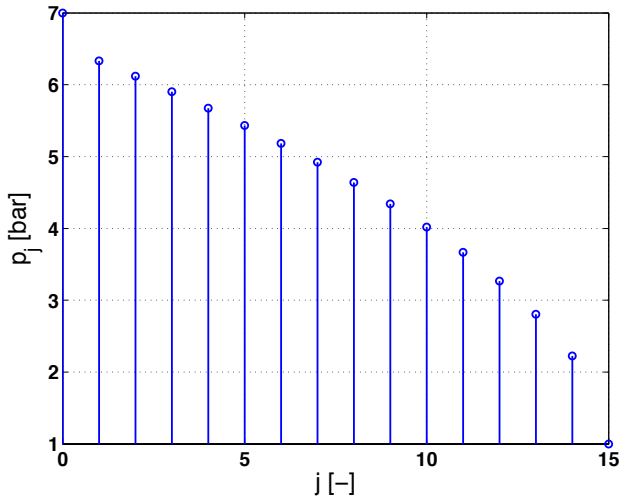

FIGURE 6.14. See-through labyrinth seal characteristics, pressure drop evolution for $p_{ti}/p_{to} = 7$, $p_{to} = 1$ bar and $\Delta_s/L = 0.0584$.

shown in Fig.6.15. This unfolded view resembles a see-through labyrinth seal with two wide seal strips ($N_{ss} = 2$). According to Denton (1993), and for the considered configuration, the width of the seal strip is not too important since the pressure reduction process in the seal strip is mainly an inviscid process, while the viscous pressure losses remain minor. Recall that as stated before, the gap width Δ_{s_R} near the inlet and outlet will be assumed identical.

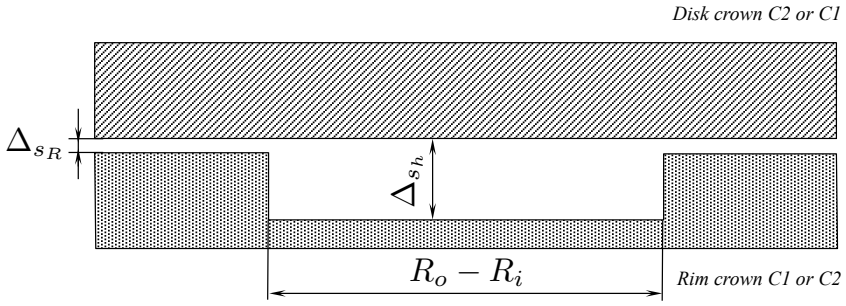

FIGURE 6.15. Stage gap, unfolded view.

A major difference between the current configuration and the usual labyrinth seal configuration is that the inlet and the outlet lie in the radial plane instead of on a cylinder of fixed radius. This causes the flow to diverge between inlet and outlet areas, respectively A_i and A_o. Nonetheless, the effect may be found negligible since :

$$A_i \approxeq 2\pi R_i \Delta_{s_R} \tag{6.75}$$

$$A_o \approxeq 2\pi R_o \Delta_{s_R} \tag{6.76}$$

$$\frac{A_o}{A_i} = \frac{R_o}{R_i} = \frac{R_i + c_s}{R_i} = 1 + \frac{c_s}{R_i} \tag{6.77}$$

and the study of orders of magnitude shows :

$$\frac{c_s}{R_i} = O(-2) \Rightarrow \frac{A_o}{A_i} \cong 1 \quad \text{or} \quad A_o \cong A_i \tag{6.78}$$

The see-through labyrinth seal approximation is therefore reasonable. Although the real flow conditions will force the flow to bend twice over right angles, the bending-effect on the mass flow will be assumed negligible. Note that $c_s \cong c_a$ (Fig.6.7). The author would also like to draw the reader's attention on the fact that only an estimation of the leakage mass flow is attempted, and it is considered that the Couette flows have no effect on the leakage mass flow calculation.

Referring to the geometric design conditions imposed by the torsional Couette flow to minimise friction losses (Section 6.2.1), it was shown that : $\Delta_{s_h}/R_o = O(-2)$. Relying on the fact that for the rotor-embedded Ljungström turbine $R_o = O(0)$, Δ_{s_h} will then have to be in the order of centimeters, i.e. $O(-2)$. The axial gap Δ_{s_h} will consequently not function adequately as a seal to limit $\dot{m}_{LL}$, but will behave more like a cavity between two gaps $a - b$ and $e - f$. As a consequence, the latter will have to provide sufficient sealing functionality. The order of magnitude for Δ_s in see-through labyrinth seals is typically around $O(-4)$, as found in the works of Hodkinson (1939) and Jia & Liu (2013). Consequently, a reasonable design value is : $\Delta_{s_R} = O(-4)$. The kinetic carry-over effect may now be quantified knowing that :

$$L_{cav} = R_o - R_i = c_s = O(-2) \tag{6.79}$$

$$\frac{\Delta_{s_R}}{L_{cav}} = \frac{O(-4)}{O(-2)} = O(-2) \tag{6.80}$$

$$J_j = 1 - (1 + 16.6\, O(-2))^{-2} \cong 0 \quad \text{(Eq.6.64)} \tag{6.81}$$

Hence, after substitution of $J_j \cong 0$ in Eq.6.63, one may find the kinetic carry-over coefficient for the second seal strip[viii] :

$$\mu_{kco} \cong 1 \tag{6.82}$$

Finally, it is possible to rewrite Eq.6.55 and Eq.6.74 for the Ljungström turbine with the configuration proposed in Fig.6.15 ($N_{ss} = 2$) :

$$\frac{\dot{m}_{LL}}{A_i} = \mu_{vc_j} \sqrt{\frac{p_{j-1}^2 - p_j^2}{R_g T}} \tag{6.83}$$

$$\frac{\dot{m}^*_{LL}}{A_i} = \mu_{cor}\mu_{vc}\, p_t \sqrt{\frac{\gamma}{R_g T_t}} \left(\frac{\gamma+1}{2}\right)^{-\frac{(\gamma+1)}{2(\gamma-1)}} \tag{6.84}$$

[viii] Recall that for the first seal strip $\mu_{kco} = 1$.

After multiplying with A_i :

$$\dot{m}_{LL} = 2\pi R_i \Delta_{s_R}\ \mu_{vc_j} \sqrt{\frac{p_{j-1}^2 - p_j^2}{R_g T}} \tag{6.85}$$

$$\dot{m}^*_{LL} = 2\pi R_i \Delta_{s_R}\ \mu_{cor}\mu_{vc}\ p_t \sqrt{\frac{\gamma}{R_g T_t}} \left(\frac{\gamma+1}{2}\right)^{-\frac{(\gamma+1)}{2(\gamma-1)}} \tag{6.86}$$

Note that for as long as the condition $\Delta_{s_R}/L_{cav} << 1$ is met, there is only a proportional effect of Δ_{s_R} on $\dot{m}_{LL}$. This leakage loss model can now be adopted in a higher order loss model of the Ljungström turbine.

Fig.6.16 shows an example of the leakage losses through a Ljungström turbine stage for several expansion ratios with $p_{to} = 1$ bar. At this stage, it is important to note that the indicated values for $\dot{m}_{LL}$ are only meaningful when compared to the mass flow passing through the blade cascade $\dot{m}_b$. Fig.6.16 reveals that it is also interesting to examine the installation of more seal strips in the Ljungström turbine ($N_{ss} > 2$). A minor increase in N_{ss} appears to reduce $\dot{m}_{LL}$ significantly, and thus deserves further attention. Consequently, the Taylor-Couette friction losses will have to be revisited.

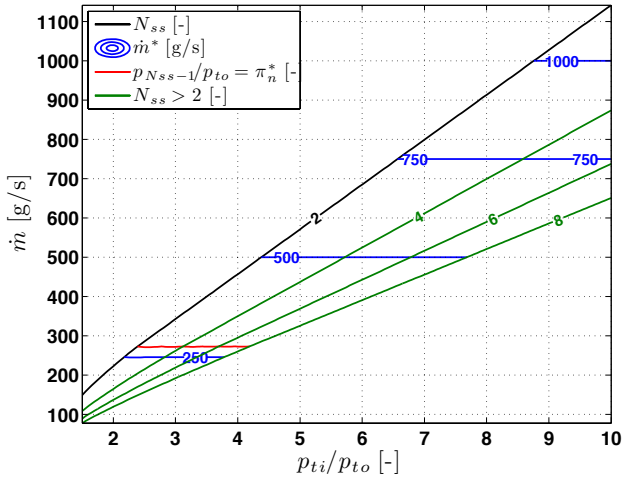

Figure 6.16. Leakage losses for a Ljungström turbine stage expanding to $p_{to} = 1$ bar. $R_i = 0.497$ m and $\Delta_{s_R} = 0.3$ mm.

6.3.3 Leakage mass flow in the Ljungström turbine – notched rim

From Fig.6.16 it was noted that even a minor increase in seal strips has a beneficial impact on the leakage losses. However, the seal strips have to be introduced in a confined space with limited flexibility on their dimensions. Moreover, because of the turbine layout, additional seal strips should only be put on faces $a - b$ and $e - f$ (Fig.6.7). Putting seal strips on face $c - d$ would require more material to be removed, which is less economic, while making them more prone to wear since more susceptible to disk vibrations. Taking the previous considerations into account and the requirement of a minimum seal strip

thickness, limits the usable amount of seal strips.
Fig.6.17 shows a notched rim configuration for $N_{ss} = 4$ and $N_{ss} = 6$. Note that a symmetric layout will be used, i.e. N_{ss} is always an even number. The fact that the rim thickness t_s is limited (Fig.6.7), deteriorates the positive influence of increasing N_{ss}. Indeed, considering Fig.6.17 :

$$L_j = \frac{t_s - \frac{N_{ss}}{2} w_{ss}}{\frac{N_{ss}}{2} - 1} \quad \forall j \neq \left[0, \frac{N_{ss}}{2}\right] \tag{6.87}$$

where w_{ss} the seal strip width, L_0 the entry cavity which is not considered here, and $L_{N_{ss}/2}$ the cavity near $c - d$ and treated in a similar way as discussed with the plain rim configuration (L_{cav}). Hence, an increase in N_{ss} will clearly result in higher values for Δ_{s_R}/L_j (Fig.6.17). Eq.6.64 consequently shows that for a fixed t_s, the kinetic carry-over μ_{kco_j} will increase and thus destroys the advantages of a high number of seal strips. From the preceding considerations, it appears sensible to expect an optimum N_{ss}. This will be proven with an example of which the relevant turbine stage geometry parameters are given in Table 6.1. The results of the leakage model calculations are reflected in Fig.6.18. Indeed, an optimum N_{ss} is found. $N_{ss} = 6$ yields the lowest leakage mass flow, while the loss increases again when $N_{ss} \geq 8$. Also, compared to Fig.6.16 where $\mu_{kco_j} = 1$ everywhere, the plot reveals that the benefits of more seal strips is reduced significantly because of the rim width limitation.
From an engineering perspective, $N_{ss} = 4$ deserves attention. Indeed, the leakage mass flow is found to be about the same as the one obtained for $N_{ss} = 6$, but the former configuration is less demanding to manufacture and will also allow more freedom to the manufacturer to find an appropriate seal strip width w_{ss}, while not impeding Δ_{s_R}/L_j too much. Therefore, $N_{ss} = 4$ should appear as the most sensible choice to the designer, offering a leakage mass flow improvement of roughly 20% over the plain rim configuration. Note that the optimum N_{ss} is still a function of rim width t_s and seal strip width w_{ss}, but neither of both are expected to differ much from their respective values indicated in Table 6.1.

Table 6.1. Example of a Ljungström turbine seal strip configuration.

Stage inlet radius R_i	497 mm
Rim thickness t_s	20 mm
Seal strip width w_{ss}	2 mm
Seal strip gap width Δ_{s_R}	0.3 mm
p_{to}	1 bar
T_{ti}	288 K
fluid	air

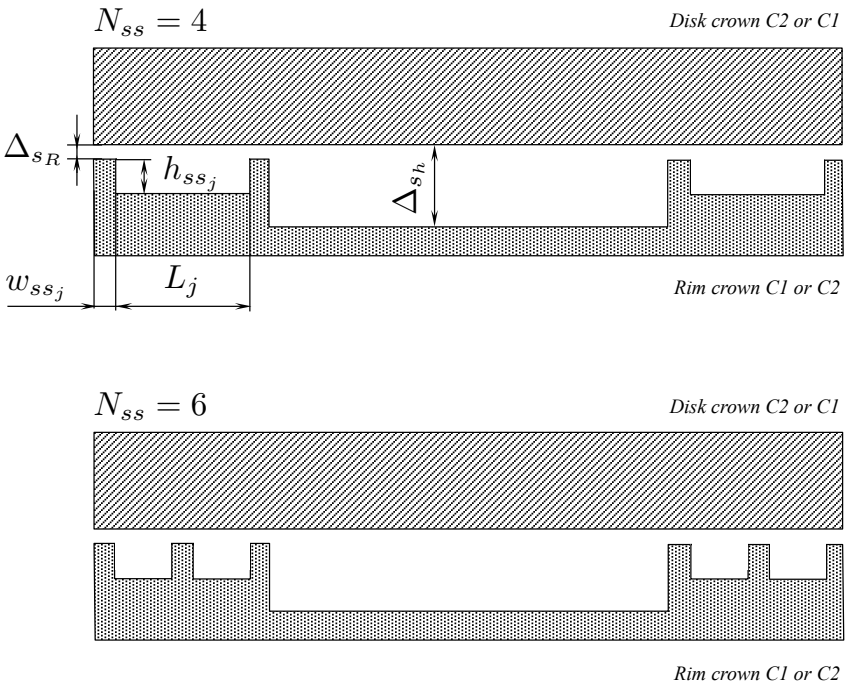

FIGURE 6.17. Notched rim – $N_{ss} = 4$ and $N_{ss} = 6$.

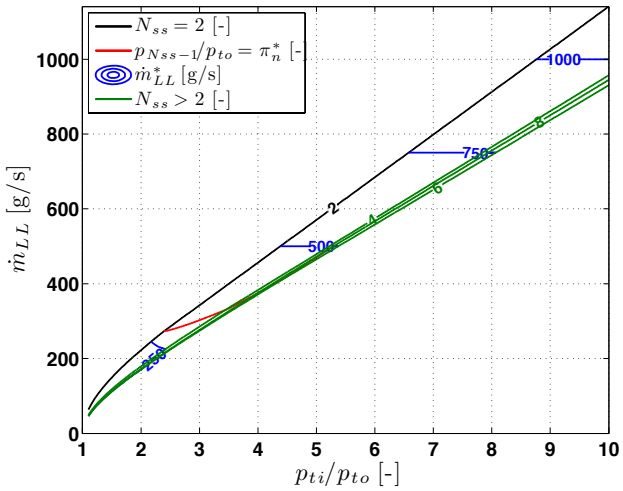

FIGURE 6.18. Leakage losses for the Ljungström turbine stage configuration in Table 6.1.

6.4 Disk friction losses with labyrinth seal

The previous section indicated that the use of a see-through labyrinth seal on the rim faces $a - b$ and $e - f$ results in a significant drop in leakage mass flow. As a consequence, it is also necessary to review the formula for friction torque, viz. Eq.6.52 and thus Eq.6.54, because the flow in the cavities cannot be modelled by the simplified Taylor-Couette flow. Indeed, Scharrer (1987) and Eser & Dereli (2007) explain that the flow in the cavities is turbulent and that its shear forces on the walls should approximated by considering each cavity as a duct in which the flow circulates. Scharrer (1987) calculates the shear forces

in see-through labyrinth seals using a two-control-volume model, where the cavity is subdivided into a jet domain and a recirculation domain. Even though this approach was mentioned to give accurate results, the single control volume method described by Eser & Dereli (2007) will serve as the basis to estimate the friction torque because it is more practical to implement and more time efficient, while still being reported to give good results.

Following Eser & Dereli (2007), the shear stresses $\tau_{w,cav}$ on the cavity walls are determined by seeking the value for the friction loss coefficient f_w, and more specifically, by using the implicit equation of *Colebrook-White* given in the work of the former :

$$\frac{1}{\sqrt{f_w}} = -2.0 \log_{10}\left(\frac{\epsilon_f/D_h}{3.7} + \frac{2.51}{Re_{D_h}\sqrt{f_w}}\right) \tag{6.88}$$

and the shear stress on the walls of the cavity, as reported by Eser & Dereli (2007) :

$$\tau_{w,cav} = \frac{1}{2}\rho_t v_{cav}^2 f_w \tag{6.89}$$

where ϵ_f/D_h the relative roughness of the duct material, D_h the hydraulic diameter of the duct, Re_{D_h} the Reynolds number based on the hydraulic diameter, ρ_t the stagnation density near the turbine stage inlet and v_{cav} the velocity of the fluid in the cavity. Since only the circumferential component of the shear stress is of interest, which results in friction torque, it is reasonable to use only the circumferential component $v_{\theta,cav}$ of v_{cav} in Eq.6.89. $v_{\theta,cav}$ is then estimated using the same strategy as discussed with the Tayler-Couette flows, but now averaged between rim and opposing disk :

$$v_{\theta,cav} \cong \left(\frac{|^R\Omega_C| + |^D\Omega_C|}{2}\right) R = \frac{1}{2}\omega R \tag{6.90}$$

where $R = R_i$ for section $a-b$ and $R = R_o$ for section $e-f$.
A more pragmatic approach to calculate f_w is achieved using the explicit equation of Haaland, as reported by Çengel & Cimbala (2010), which avoids the required iterative procedure to find f_w using the Colebrook-White equation, while resulting in only a minor loss in accuracy :

$$\frac{1}{\sqrt{f_w}} = -1.8 \log_{10}\left[\frac{6.9}{Re_{D_h}} + \left(\frac{\epsilon_f/D_h}{3.7}\right)^{1.11}\right] \tag{6.91}$$

Following Fig.6.17, the hydraulic diameter D_h is :

$$D_h = 2L_j \frac{h_{ss} + \Delta_{s_R}}{h_{ss} + L_j} \tag{6.92}$$

The friction torque due to the seal strip cavity may then be quantified. On the rim, near

the stage inlet side $a-b$:

$$ {}^{R}\mathcal{T}_{CAV_i} \cong 2\pi R_i^2 \left(\frac{N_{ss}}{2}-1\right)\left(2h_{ss}+L_j\right)\tau_{w,cav_i} \tag{6.93} $$

and on the rim, near the stage outlet side $e-f$:

$$ {}^{R}\mathcal{T}_{CAV_o} \cong 2\pi R_o^2 \left(\frac{N_{ss}}{2}-1\right)\left(2h_{ss}+L_j\right)\tau_{w,cav_o} \tag{6.94} $$

With respect to the disk, one finds in a similar way for the stage inlet side $a-b$:

$$ {}^{D}\mathcal{T}_{CAV_i} = 2\pi R_i^2 L_j \left(\frac{N_{ss}}{2}-1\right)\tau_{w,cav_i} \tag{6.95} $$

and on the disk, near the stage outlet side $e-f$:

$$ {}^{D}\mathcal{T}_{CAV_o} = 2\pi R_o^2 L_j \left(\frac{N_{ss}}{2}-1\right)\tau_{w,cav_o} \tag{6.96} $$

The total contribution of the seal cavities to the disk friction torque is :

$$ {}^{R}\mathcal{T}_{CAV} = {}^{R}\mathcal{T}_{CAV_i} + {}^{R}\mathcal{T}_{CAV_o} \tag{6.97} $$

$$ {}^{D}\mathcal{T}_{CAV} = {}^{D}\mathcal{T}_{CAV_i} + {}^{D}\mathcal{T}_{CAV_o} \tag{6.98} $$

Taylor-Couette flow is assumed to remain in effect between the faces that constitute the seal strips. Therefore Eq.6.53 must be rewritten as :

$$ \mathcal{T}_{TAC} = 2\pi\mu \left(\frac{\omega}{\Delta_{s_R}}\right)(R_i^3 + R_o^3)\left(\frac{N_{ss} w_{ss}}{2}\right) \tag{6.99} $$

The disk friction losses on the rim then are :

$$ {}^{R}\mathcal{T}_{DF} = \mathcal{T}_{TOC} + \mathcal{T}_{TAC} + {}^{R}\mathcal{T}_{CAV} \tag{6.100} $$

and on the opposing disk :

$$ {}^{D}\mathcal{T}_{DF} = \mathcal{T}_{TOC} + \mathcal{T}_{TAC} + {}^{D}\mathcal{T}_{CAV} \tag{6.101} $$

Note that the friction torque on the disk and on the rim are no longer identical. The mechanical power dissipated because of disk friction losses on the rim side are:

$$ {}^{R}P_{DF} = {}^{R}\Omega_C {}^{R}\mathcal{T}_{DF} \tag{6.102} $$

while on the opposing disk side :

$$ {}^{D}P_{DF} = {}^{D}\Omega_C {}^{D}\mathcal{T}_{DF} \tag{6.103} $$

Finally, it is important to highlight that the use of see-through labyrinth seals will introduce a rim torsion moment and likely an axial force because the pressure drop over each seal is not identical. However, the study of this effect is not in the scope of this work and will be part of future research.

6.5 Introduction of disk friction and leakage losses into the stage governing equations

6.5.1 Impact on outlet specific total enthalpy and turbine power balance

Consider the control volume shown in Fig.6.19 (dashed lines), which is made of the volume through which flow passes in the turbine stage and tangent to the turbine blades, rim and opposing disk. $P_{st,b}$ is the mechanical power delivered to the blades by the gases passing through the blade passage, ${}^{D}P_{DF}$ and ${}^{R}P_{DF}$ the mechanical power introduced in the control volume by, respectively, the opposing disk and the blade rim but completely dissipated in the control volume by viscous effects. h_{ti} and h_{to} are respectively the specific total enthalpy of the gases entering and exiting the stage. For a given mass flow $\dot{m}$ passing through the control volume, the first law then yields :

$$P_{st,b} = \dot{m}(h_{ti} - h_{to}) + {}^{D}P_{DF} + {}^{R}P_{DF} \tag{6.104}$$

For the performance calculations, it is important to identify h_{to}. A first step to the solution

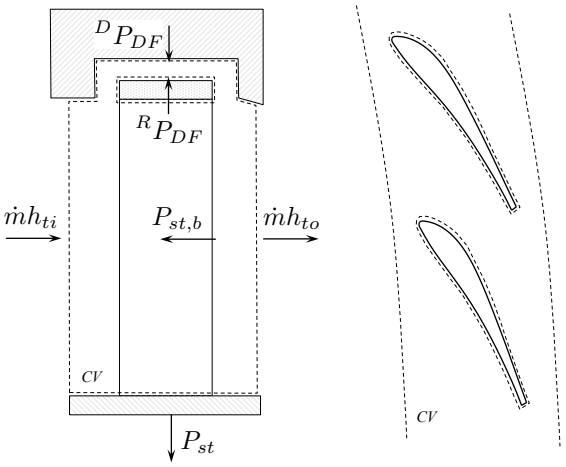

FIGURE 6.19. Single stage power balance.

is introducing another expression for $P_{st,b}$:

$$P_{st,b} = \dot{m}_b(h_{ti} - h_{to,b}) \tag{6.105}$$

where $h_{to,b}$ the specific total enthalpy of the gases leaving the blade passage and which is obtained from the blade velocity triangles and passage loss models. $\dot{m}_b$ is the mass flow

passing through the blade passages only, i.e. :

$$\dot{m} = \dot{m}_b + \dot{m}_{LL} \tag{6.106}$$

and consequently after substitution of Eq.6.106 in Eq.6.105 :

$$P_{st,b} = \dot{m}(h_{ti} - h_{to,b}) - \dot{m}_{LL}(h_{ti} - h_{to,b}) \tag{6.107}$$

Equating Eq.6.107 and Eq.6.104 gives :

$$\dot{m}(h_{ti} - h_{to}) = \dot{m}(h_{ti} - h_{to,b}) - \dot{m}_{LL}(h_{ti} - h_{to,b}) - {}^{D}P_{DF} - {}^{R}P_{DF} \tag{6.108}$$

or,

$$h_{ti} - h_{to} = (h_{ti} - h_{to,b}) - \frac{\dot{m}_{LL}}{\dot{m}}(h_{ti} - h_{to,b}) - \frac{{}^{D}P_{DF}}{\dot{m}} - \frac{{}^{R}P_{DF}}{\dot{m}} \tag{6.109}$$

and leads to the corrected value for the total specific enthalpy at the outlet of the turbine stage :

$$h_{to} = h_{to,b} + \Delta h_{t,LL} + {}^{D}\Delta h_{t,DF} + {}^{R}\Delta h_{t,DF} \tag{6.110}$$

where the previously mentioned corrective terms are expressed as :

$$\Delta h_{t,LL} = \frac{\dot{m}_{LL}}{\dot{m}}(h_{ti} - h_{to,b}) \tag{6.111}$$

$${}^{D}\Delta h_{t,DF} = \frac{{}^{D}P_{DF}}{\dot{m}} \tag{6.112}$$

$${}^{R}\Delta h_{t,DF} = \frac{{}^{R}P_{DF}}{\dot{m}} \tag{6.113}$$

The stage mechanical power output P_{st} can be calculated applying the power balance over the blade (Fig.6.19) :

$$P_{st} = P_{st,b} - {}^{R}P_{DF} \tag{6.114}$$

Introducing Eq.6.104 and Eq.6.112 in Eq.6.114 results in :

$$P_{st} = \dot{m}(h_{ti} - h_{to} + {}^{D}\Delta h_{t,DF}) \tag{6.115}$$

Another form of P_{st} can be found by substituting Eq.6.110 in Eq.6.115 :

$$P_{st} = \dot{m}(h_{ti} - h_{to,b} - \Delta h_{t,LL} - {}^{R}\Delta h_{t,DF}) \tag{6.116}$$

Note that P_{st} is the mechanical power contribution of the stage to the crown of which it is an integral part. However, the part of the crown working as opposing disk destroys part

of the delivered useful power P_{st} by viscous losses, and this needs to be accounted for. If S_n is the number of stages, then :

$$P_{C1} = \sum_{j=1}^{S_n/2} P_{st_{(2j-1)}} - \sum_{j=1}^{S_n/2} {}^{D}P_{DF_{(2j)}} \tag{6.117}$$

$$P_{C2} = \sum_{j=1}^{S_n/2} P_{st_{(2j)}} - \sum_{j=1}^{S_n/2} {}^{D}P_{DF_{(2j-1)}} \tag{6.118}$$

Note that the crowns influence each other's power output via the opposing disk viscous losses, an effect which was not accounted for in Eqs.5.114 and 5.115.

6.5.2 Impact on stage total outlet pressure

It is important to investigate what the impact is of the mixing process of $\dot{m}_b$ and $\dot{m}_{LL}$ on the total pressure. This can be done thanks to the second law of thermodynamics which states that for an open system in steady state :

$$\sum_{out} \dot{m}(s - s_{ref}) - \sum_{in} \dot{m}(s - s_{ref}) = \sum \frac{\dot{Q}}{T_B} + \Sigma_i \tag{6.119}$$

where s the specific entropy, s_{ref} the reference entropy[ix], $\dot{Q}$ the heat passing through the boundaries of the open system at temperature T_B and Σ_i the entropy production inside the system. It is reasonable to assume that the mixing process is adiabatic and isobaric, i.e. :

$$p_{o,b} = p_{LL} = p_o \tag{6.120}$$

$$\sum \frac{\dot{Q}}{T_B} = 0 \tag{6.121}$$

where p_{LL} the static pressure of the leakage flow behind the last seal strip, $p_{o,b}$ the static pressure of the gases expelled by the blade cascade and p_o the static pressure of the gases leaving the stage after mixing. For a perfect gas, the entropy can be calculated for a given pressure and temperature after developing Gibbs' equation – Çengel & Boles (2006) :

$$s - s_{ref} = C_p \ \ln\left(\frac{T}{T_{ref}}\right) - R_g \ \ln\left(\frac{p}{p_{ref}}\right) = C_p \ \ln\left(\frac{T_t}{T_{ref}}\right) - R_g \ \ln\left(\frac{p_t}{p_{ref}}\right) \tag{6.122}$$

Note that Eq.6.122 is applicable to both static and total components of a perfect gas. Using Eq.6.119 for the mixing process and imposing the value of $s_{ref} = 0$:

$$\Sigma_i = \dot{m}s_o - \dot{m}_b s_b - \dot{m}_{LL} s_{LL} \tag{6.123}$$

[ix]Since the mixing process does not change the chemical composition of the gases, s_{ref} can be given a constant value such as *zero* and will drop out of the equations.

Substituting the definition of entropy for a perfect gas (Eq.6.122) and developing the static terms for an isobaric process (Eq.6.120) yields :

$$\Sigma_i = \dot{m}\, C_p \left[\ln\left(\frac{T_o}{T_{ref}}\right) - \frac{\dot{m}_b}{\dot{m}}\ \ln\left(\frac{T_{o,b}}{T_{ref}}\right) - \frac{\dot{m}_{LL}}{\dot{m}}\ \ln\left(\frac{T_{LL}}{T_{ref}}\right)\right] \tag{6.124}$$

The total components on the other hand give for Σ_i (Eq.6.122) :

$$\begin{aligned}\Sigma_i = \dot{m}\, C_p \left[\ln\left(\frac{T_{to}}{T_{ref}}\right) - \frac{\dot{m}_b}{\dot{m}}\ \ln\left(\frac{T_{to,b}}{T_{ref}}\right) - \frac{\dot{m}_{LL}}{\dot{m}}\ \ln\left(\frac{T_{t,LL}}{T_{ref}}\right)\right] - \dots \\ \dot{m}\, R_g \left[\ln\left(\frac{p_{to}}{p_{ref}}\right) - \frac{\dot{m}_b}{\dot{m}}\ \ln\left(\frac{p_{to,b}}{p_{ref}}\right) - \frac{\dot{m}_{LL}}{\dot{m}}\ \ln\left(\frac{p_{t,LL}}{p_{ref}}\right)\right]\end{aligned} \tag{6.125}$$

Note that :

$$1 = \frac{\dot{m}_{LL}}{\dot{m}} + \frac{\dot{m}_b}{\dot{m}} \tag{6.126}$$

Equating Eq.6.124 and Eq.6.125 results in :

$$\begin{aligned}\dot{m}\, C_p \left[\ln\left(\frac{T_{to}}{T_o}\right) - \frac{\dot{m}_b}{\dot{m}}\ \ln\left(\frac{T_{to,b}}{T_{o,b}}\right) - \frac{\dot{m}_{LL}}{\dot{m}}\ \ln\left(\frac{T_{t,LL}}{T_{LL}}\right)\right] - \dots \\ \dot{m}\, R_g \left[\ln\left(\frac{p_{to}}{p_{ref}}\right) - \frac{\dot{m}_b}{\dot{m}}\ \ln\left(\frac{p_{to,b}}{p_{ref}}\right) - \frac{\dot{m}_{LL}}{\dot{m}}\ \ln\left(\frac{p_{t,LL}}{p_{ref}}\right)\right] = 0\end{aligned} \tag{6.127}$$

For perfect gases, Çengel & Boles (2006) :

$$\frac{T_t}{T} = 1 + \left(\frac{\gamma - 1}{2}\right) M^2 \tag{6.128}$$

As an approximation, it is reasonable to assume that the Mach number M of the gases entering and leaving the system (mixing process) are approximately the same or :

$$\frac{T_{to}}{T_o} \approxeq \frac{T_{to,b}}{T_{o,b}} \approxeq \frac{T_{t,LL}}{T_{LL}} \tag{6.129}$$

Then, Eq.6.127 may be further reduced to :

$$\ln\left(\frac{p_{to}}{p_{ref}}\right) = \frac{\dot{m}_b}{\dot{m}}\ \ln\left(\frac{p_{to,b}}{p_{ref}}\right) + \frac{\dot{m}_{LL}}{\dot{m}}\ \ln\left(\frac{p_{t,LL}}{p_{ref}}\right) \tag{6.130}$$

If one further states that the total pressure of the leakage mass flow is in the same order of magnitude of the total pressure of the gases leaving the blade cascade :

$$p_{t,LL} \approxeq p_{to,b} \tag{6.131}$$

then Eq.6.130 and Eq.6.126 reveal that :

$$p_{to} \cong p_{to,b} \tag{6.132}$$

and thus, what the total-to-total expansion ratios concern of the stage π_{Ts} and blade cascade π_{Tb} :

$$\pi_{Ts} \cong \pi_{Tb} \tag{6.133}$$

6.5.3 Impact of disk friction and leakage losses on cascade outlet velocity triangle

The absolute speed of the gases leaving the cascade $\vec{v}_o$ is influenced by the disc friction losses and leakage mass flow. Examining $\vec{v}_o$ in the radial plane yields the following components :

$$\vec{v}_o = v_{o_R}\ \vec{1}_R + v_{o_u}\ \vec{1}_\theta \tag{6.134}$$

The impact on the tangential component v_{o_u} is found by applying the angular momentum equation, which is for a steady stage regime given by – Çengel & Cimbala (2010) :

$$\sum_j \vec{M}_j = \left(\sum \vec{R} \times \dot{m}\vec{v}\right)_o - \left(\sum \vec{R} \times \dot{m}\vec{v}\right)_i \tag{6.135}$$

where the left term is the sum of the moments *acting on the control volume* and positive when in the same sense as the unit vectors of the right-handed orthogonal coordinate system, such as indicated in Fig.6.20. The right terms in Eq.6.135 represent the flux of angular momenta respectively exiting and entering the control volume. Applying Eq.6.135 on the turbine stage, more specifically on the previously defined control volume retaken in Fig.6.20, results in :

$$-\mathcal{T}_{st,b} + {}^{R}\mathcal{T}_{DF} - {}^{D}\mathcal{T}_{DF} = \dot{m}(R_o v_{o_u} - R_i v_{i_u}) \tag{6.136}$$

Note that the flow is considered to be purely two dimensional (no speed component in the axial plane). $\mathcal{T}_{st,b}$ is the torque delivered by the blade cascade to the concurring stage disk. Because in Eq.6.135 the moments *on* the system are required, a minus sign needs to be added to $\mathcal{T}_{st,b}$ in Eq.6.136. Similarly, the sense of the ${}^{R}\mathcal{T}_{DF}$ and ${}^{D}\mathcal{T}_{DF}$ torque vectors can be found by examining the shear forces on the affected control volume faces. Another way to express $-\mathcal{T}_{st,b}$ is by applying Eq.6.135 over the blade cascade only, yielding :

$$-\mathcal{T}_{st,b} = \dot{m}_b(R_o v_{o_u,b} - R_i v_{i_u}) \tag{6.137}$$

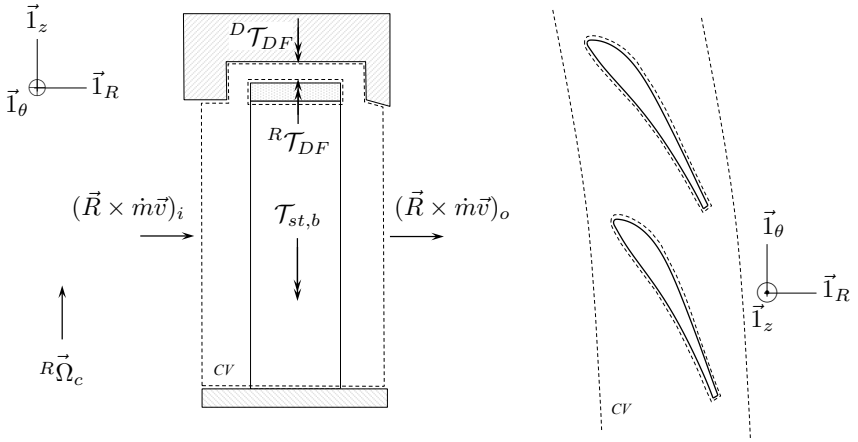

FIGURE 6.20. Single stage torque balance.

Substituting Eq.6.137 and Eq.6.106 in Eq.6.136 and rearranging terms gives :

$$v_{o_u} = v_{o_u,b} + \frac{{}^R\mathcal{T}_{DF} - {}^D\mathcal{T}_{DF} - \dot{m}_{LL}(R_o v_{o_u,b} - R_i v_{i_u})}{\dot{m}\, R_o} \tag{6.138}$$

where $v_{o_u,b}$ represents the tangential component of the absolute speed of the gases leaving the blade cascade. When there are no disk friction or leakage losses, $v_{o_u} = v_{o_u,b}$. Examining Eq.6.138 clearly shows that, since it was previously shown that ${}^R\mathcal{T}_{DF} \cong {}^D\mathcal{T}_{DF}$, the leakage losses decrease the magnitude of v_{o_u} ($v_{o_u} \leq v_{i_u}$ for a turbine).
The consequences of disk friction and leakage losses on the absolute speed $\vec{v}_o$ can now be developed fully. For this purpose, the continuity equation, the perfect gas law and total-to-static conversion equations are used in an iterative procedure. This procedure is explained next.
Using an estimation of the static temperature in the outlet T_o (taking $T_{o,b}$ for this purpose is most appropriate), a new value for the static outlet pressure may be found considering the total-to-static conversion law for a perfect gas :

$$p_o = p_{to}\left(\frac{T_o}{T_{to}}\right)^{\frac{\gamma}{\gamma-1}} \tag{6.139}$$

Note that the total components follow from the previous theoretical discussions and are invariant in the iterative process. From p_o and T_o it is possible to find the density ρ_o using the perfect gas law :

$$\rho_o = \frac{p_o}{R_g T_o} \tag{6.140}$$

The continuity equation then allows to find a value for the radial component of the absolute speed v_{o_R}, viz. :

$$v_{o_R} = \frac{\dot{m}}{\rho_o \, A_o} \tag{6.141}$$

Calculating the norm of the absolute speed vector $\vec{v_o}$:

$$v_o = \sqrt{v_{o_u}^2 + v_{o_R}^2} \tag{6.142}$$

allows to establish a new estimation for T_o via the total-to-static conversion equation for perfect gases :

$$T_o^+ = T_{to} - \frac{v_o^2}{2C_p} \tag{6.143}$$

When converged, the new stage absolute speed outlet angle may be obtained :

$$\alpha_o = \text{atan}\left(\frac{v_{o_u}}{v_{o_R}}\right) \tag{6.144}$$

The logic and integration of the friction and leakage losses is highlighted in Fig.6.21.

6.5.4 T-s diagram

The impact of the leakage and friction losses on the intensive properties is shown in Fig.6.22. If the blade passage losses are represented according to the model of Ainley & Mathieson (1955), as indicated in Section 6.1.6, it is possible to continue the discussion based on the analysis which was already established for Fig.6.3. The major difference here is that the expansion process over the complete stage is examined ($ti - to$) and not over the blade passage only ($ti - to, b$). The entropy rise caused by the leakage and friction losses discussed earlier is now introduced considering an isobaric process on the outlet total pressure, as proven in Section 6.5.2. The consequence of these losses is indicated in Fig.6.22 by the red line extending between to, b and to. As expected, the total temperature increases, resulting in a reduced stage turbine power output.

6.6 Turbine stage interstage space losses

As already indicated in Section 5.4.12, the flow in the interstage space is considered to be isentropic. As a consequence, the friction losses will be neglected. Since the flow is subsonic, the diverging interstage space will cause the static pressure to increase slightly, while total temperature and total pressure are conserved.

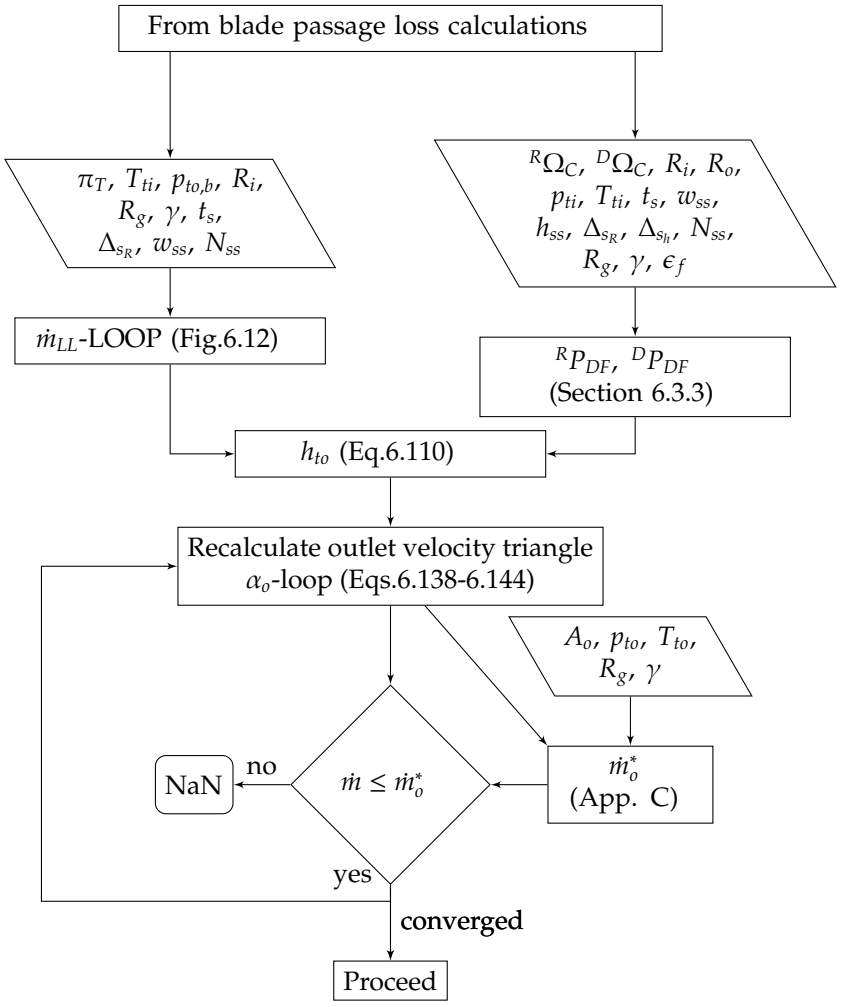

FIGURE 6.21. Iteration procedure to find the stage leakage and friction losses, and impact on α_o.

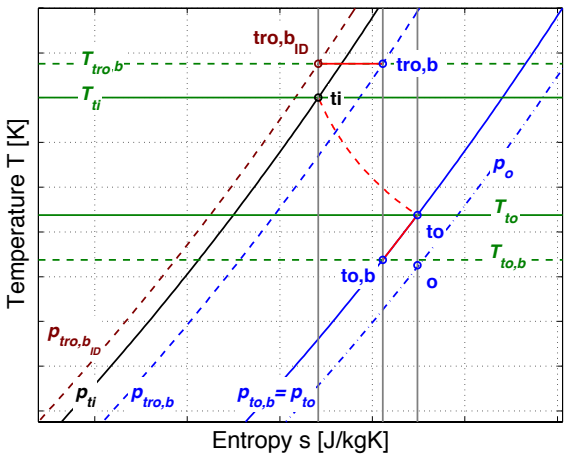

FIGURE 6.22. Introduction of friction and leakage losses.

6.7 Performance calculation

The performance calculation of a stage is performed by integrating the blade passage losses, the friction losses and the leakage losses. The flowchart in Fig.6.23 represents this logic. A sequence of these loops, i.e. one for each stage, yields the turbine performance. Note that in case the leakage mass flow $\dot{m}_{LL}$ appears to be small, the loop on $\dot{m}_b$ may be neglected, offering a significant gain in calculation time. The isentropic and polytropic efficiencies are now calculable (Section 5.5).

6.8 Conclusion

This chapter justified the use of axial turbine loss models to estimate the losses in the Ljungström
turbine. These models use geometric and flow intensive properties. The latter can be established by the governing equations described in Chapter 5. With this information, the performance of a Ljungström turbine is calculable. However, it is the designer's task to develop a turbine geometry, which complies with the imposed performance requirements. This discussion is conducted in the next chapter.

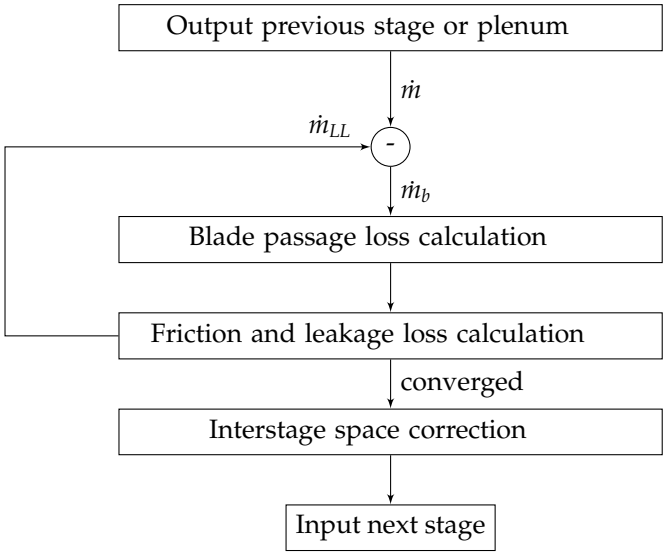

FIGURE 6.23. Iteration procedure to calculate the stage losses.

6.9 Nomenclature

Please note that the units listed below apply unless stated otherwise.

Abbreviations and substance formulae

A	Flow area	[m^2]
AR	Blade aspect ratio	[-]
AR_a	Blade projected aspect ratio	[-]
c	Blade chord	[m]
c_a	Radial blade chord	[m]
C_p	Specific heat at constant pressure	[J/kgK]
D_h	Hydraulic diameter	[m]
h	Specific enthalpy	[J/kg]
h_t	Specific total enthalpy	[J/kg]
f_w	Friction loss coefficient	[-]
h_{tL}	Specific total enthalpy loss	[J/kg]
h_{tr}	Specific relative total enthalpy	[J/kg]
h_{ss}	Seal strip height	[m]
H_b	Blade height	[m]
k_{tau}	Torque coefficient	[-]
K	Correction factor	[-]
$L_{(j)}$	Labyrinth seal cavity length	[m]
$\dot{m}$	Mass flow rate	[kg/s]
M	Moment	[Nm]
N	Rotational/Angular speed	[rad/s]
N_{ss}	Number of seal strips	[-]
o	Blade passage throat	[m]
p	Static pressure	[Pa]
p_t	Total pressure	[Pa]
p_{tr}	Relative total pressure	[Pa]
P	Power	[W]
P_{st}	Delivered stage power on crown	[W]
$P_{st,b}$	Delivered power by blade cascade	[W]
$\dot{Q}$	Heat flow	[W]
R	Radius	[m]
$\mathcal{R}$	Rothalpy	[J/kg]
R_g	Specific gas constant	[J/kgK]
R_i	Turbine (stage) inlet radius	[m]

R_o	Turbine (stage) outlet radius	[m]
Re	Reynolds number	[-]
s	Stage pitch or specific entropy	[m] of [J/kgK]
S_n	Turbine stage number	[-]
S_Ω	Turbine slip factor	[-]
t	Passage length	[m]
t_s	Rim thickness	[m]
T	Static temperature	[K]
T_t	Total temperature	[K]
T_{tr}	Relative total temperature	[K]
$\mathcal{T}$	Torque	[Nm]
Ta	Taylor number	[-]
u	Rotational velocity	[m/s]
v	Absolute speed	[m/s]
w_{ss}	Seal strip width	[m]
Y	Non-dimensional relative total pressure loss	[-]
w	Relative speed	[m/s]
Z	Stage blade number	[-]
α	Absolute flow angle	[rad]
β	Relative flow angle	[rad]
β_b	Camberline angle	[rad]
β_g	Gauging angle	[rad]
γ	Isentropic exponent	[-]
δ_{sl}	Deviation angle correction due to slip vortex	[rad]
δ_{Π_p}	Deviation angle correction due to pitch angle	[rad]
Δ_s	See-through labyrinth seal, strip clearance	[m]
Δ_{s_h}	Axial gap clearance	[m]
Δ_{s_R}	Radial gap clearance	[m]
ϵ	Flow deflection or R_i/R_o	[rad] or [-]
ζ_1	Soderberg loss coefficient, standard conditions	[-]
ζ_2	Soderberg loss coefficient, non-reference $Æ_a$	[-]
ζ_3	Soderberg loss coefficient, non-reference Re	[-]
λ	Blade stagger angle	[rad]
μ	Dynamic viscosity	[Pa s]
μ_{cor}	Flow correction coefficient	[-]
μ_{kco}	Kinetic carry-over coefficient	[-]
μ_{vc}	Flow contraction coefficient	[-]

π_n^*	Critical pressure ratio	[-]
π_{Tb}	Blade passage total-to-total expansion ratio	[-]
π_{Ts}	Stage total-to-total expansion ratio	[-]
Π_p	Pitch angle	[rad]
ρ	Density	[kg/m^3]
$\dot{\Sigma}_i$	Entropy production	[W]
τ_w	Wall shear stress	[Pa]
ω	Angular velocity	[rad/s]
Ω	Crown angular velocity	[rad/s]

Subscripts and superscripts

AX	Axial turbine
b	Blade or blade passage related
B	Control volume boundary
C	Crown related
$C1$	First crown
$C2$	Second crown
cav	Labyrinth cavity
CAV	Labyrinth seal cavity related
D	Opposing disk
DF	Disk friction
DN	Daily and Nece model
EWF	Endwall fence
EX	Supersonic expansion
i	Inlet
j	Related to position j
LL	Leakage loss
o	Outlet
o,b	At outlet of a blade passage
p	Profile related
R	Radial component
R	Rim
ref	Reference
s	Secondary flow
ss	Seal strip
t	Total component
TAC	Taylor-Couette
TE	Trailing edge

TOC	Torsional Couette
u	Tangential component
θ	Tangential component
$*$	Saturated flow conditions
$+$	New result after one iteration

Chapter 7

Preliminary Ljungström turbine design

"Everything should be made as simple as possible, but not simpler."

Albert Einstein – *Einstein et al. (2010)*

Designing the Ljungström turbine relying on the governing parameters and formulae stated in Chapter 5 and the loss models discussed in Chapter 6 is the goal of this chapter. In order to limit the freedom of design, criteria will be imposed. As a direct consequence of this, important relationships between duty and geometric parameters will emerge, which will eventually lead to the geometry of a Ljungström turbine seeking as high as possible efficiency for the demanded power output. The chapter concludes with the discussion of some off-design characteristics.

7.1 Nominal operating point design

The nominal operating point is the working point at which the turbine delivers the required power at the required pressure ratio imposed by TDR-cycle considerations, with high as reasonably possible efficiency.

7.1.1 Design criteria

The variation of performance of a Ljungström turbine may be represented by a physical function f for which one may write :

$$f(\mathcal{D}, \mathcal{G}, \mathcal{Y}) = 0 \tag{7.1}$$

where, as discussed in Chapters 5 and 6 :

→ $\mathcal{D}$ the duty parameters : $\phi_{i/o}$, ψ, $\hat{\theta}$, $\hat{R}$, $\eta_{p,T}$, Θ_i, S_Ω, ...

→ $\mathcal{G}$ the geometric parameters : R_o/R_i, $\overline{B}$, $\overline{H}$, Π_p, Δ_{is}/c_a, $\mathcal{G}_{blade}$, ϵ, λ, $\mathit{Æ}$, ...

$\rightarrow$ $\mathcal{Y}$ the thermo-fluid-mechanical parameters : γ, Re, $M_{i/o}$, ...

The governing equations relate some of the stated parameters, but other closing equations still need to be chosen by the designer. Besides the design recommendations stemming from studies performed in the subsequent sections, design criteria will already be imposed for determining the nominal operating point in order to prevent a design being achieved by chance. They are reviewed next.

Velocity triangles

For each stage, the flow inlet and outlet velocity triangles need to be established. Fig.7.1 shows that the inlet velocity triangle of one stage is determined by the outlet velocity triangle of the previous stage.

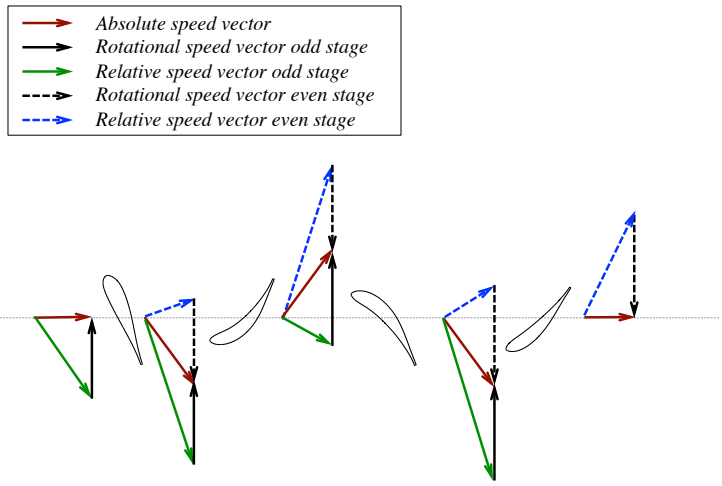

FIGURE 7.1. Velocity triangle dependence for a multi-stage Ljungström turbine.

The inflow of the gases near the first stage is purely radial ${}^{1}\alpha_i = 0$ because the flow emerges from the centre of the turbine, which is connected to the pressurised plenum inside the helicopter fuselage. This is a design parameter. Note that the superscript 1 in ${}^{1}\alpha_i$ stands for the first stage.

In order to maximise the total-to-static efficiency of the turbine, it is advisable to remove any tangential speed component at the outlet of the last stage. As a consequence, ${}^{L}\alpha_o = 0$ will be imposed. Note that the superscript L in ${}^{L}\alpha_o$ stands for the last stage.

The model of Soderberg showed the importance of flow deflection on the blade losses. The higher the value of ϵ the more blade losses arise. Hence, it is sensible to distribute ϵ evenly over all middle stages, i.e. all stages between the first and the last stage, or :

$$^{M}\epsilon = C^{t} \tag{7.2}$$

where the superscript M stands for the middle stages. Building further upon this reasoning, it is practical to keep the inlet angles identical in front of each middle stage, i.e. :

$$^{2}\alpha_i = {}^{M}\alpha_i = \ldots = {}^{L-1}\alpha_i \tag{7.3}$$

As a direct consequence – the effect of the interstage space will be discussed later – the outlet angle of one stage must equal the inlet angle of the subsequent stage :

$$^{1}\alpha_o = -{}^{M}\alpha_i = {}^{M}\alpha_o \tag{7.4}$$

Note that the minus sign appears because the positive angle reference must be respected, which depends on the sense of the local rotational velocity. Another direct consequence is :

$$^{L}\alpha_i = -{}^{M}\alpha_o \tag{7.5}$$

If for all middle stages a general conservation of the velocity triangle respectively at the inlet and at the outlet is imposed, which is a sensible choice given the constant ${}^{M}\epsilon$ and since $(-{}^{M}\alpha_i) = {}^{M}\alpha_o$, then, evidently, it is found that (Fig.5.7 and Fig.5.8) :

$$^{M}\beta_i = C^t = {}^{M}\beta_{o,b} + {}^{M}\epsilon \tag{7.6}$$

$$^{M}\beta_{o,b} = C^t \tag{7.7}$$

If finally the velocity triangle at the outlet of the first stage is set equal to the outlet velocity triangle of the middle stages, and if the inlet velocity triangle of the last stage is put equal to the inlet velocity triangle of the middle stages, it is possible to conclude observing Fig.5.7 and Fig.5.8 :

$$^{M}\phi_i = C^t = {}^{L}\phi_i \tag{7.8}$$

$$^{M}\phi_o = C^t = {}^{1}\phi_o \tag{7.9}$$

Rewriting Eq.5.57 and Eq.5.77 leads to the following important equations :

$$\phi_i = \frac{1}{\tan\alpha_i - \tan\beta_i} \tag{7.10}$$

$$\phi_o = \frac{1}{\tan\alpha_{o,b} - \tan\beta_{o,b}} \tag{7.11}$$

When applied to the first stage they become :

$$ {}^{1}\phi_i = \frac{-1}{\tan {}^{1}\beta_i} \tag{7.12} $$

$$ {}^{1}\phi_o = \frac{1}{\tan {}^{1}\alpha_{o,b} - \tan {}^{1}\beta_{o,b}} = {}^{M}\phi_o \tag{7.13} $$

When applied to the middle stages :

$$ {}^{M}\phi_i = \frac{1}{\tan {}^{M}\alpha_i - \tan {}^{M}\beta_i} \tag{7.14} $$

$$ {}^{M}\phi_o = \frac{1}{\tan {}^{M}\alpha_{o,b} - \tan {}^{M}\beta_{o,b}} = \frac{-1}{\tan {}^{M}\alpha_i + \tan ({}^{M}\beta_i - {}^{M}\epsilon)} \tag{7.15} $$

And to the last stage :

$$ {}^{L}\phi_i = \frac{1}{\tan {}^{L}\alpha_i - \tan {}^{L}\beta_i} = {}^{M}\phi_i \tag{7.16} $$

$$ {}^{L}\phi_o = \frac{-1}{\tan {}^{L}\beta_{o,b}} = \frac{-1}{\tan ({}^{L}\beta_i - {}^{L}\epsilon)} \tag{7.17} $$

These equations will prove useful when establishing the (conceptual) performance model.

Turbine slip factor

For nominal operation, it is reasonable to impose equal magnitudes to the rotational velocity of each crown ($\Omega_{C1} = \Omega_{C2}$). Hence, the design turbine slip factor $S_\Omega = 1$.

Interstage space coefficient

The interstage spacing Δ_{is} is the distance between the outlet and the inlet of two subsequent stages. Moustapha et al. (2003) discuss that this length should not be too high in order to reduce the friction losses, but not too low either to avoid high cycle fatigue resulting from the impingement of the wake of the previous stage on the blades of the subsequent stage. They propose the following design rule for Δ_{is} :

$$ \frac{\Delta_{is}}{c_a} = 0.2 \ldots 0.35 \triangleq \hat{c} \tag{7.18} $$

(Fig.5.5). $\hat{c}$ is the interstage space coefficient. For this work, the design criterion that $\hat{c}$ remains identical for all stages is imposed.

Interstage space free vortex

Even though friction effects in the interstage space are reported to have an important impact on the selection of $\hat{c}$, as discussed above, this work will adopt isentropic flow in the interstage space (Section 6.6). The hypothesis consequently allows a free vortex to be

imposed, which applies to flows on which no moments are exerted. From Eq.6.135 :

$$^{j}|R_o v_{o_u}| = {}^{j+1}|R_i v_{i_u}| \tag{7.19}$$

The absolute values must be taken since in the interstage space, there is no change of the angle reference system.

Interstage space density change

Since no work is performed in the interstage space and since the interstage space will remain relatively small, density changes in the interstage space will be neglected, i.e. :

$$^{j}\rho_o = {}^{j+1}\rho_i \tag{7.20}$$

Diffusor

Behind the last stage of the turbine, a diffuser is installed to expel the gases to the atmosphere. The effect of the diffuser will be neglected, considering the size of the diffuser to be minimal such that $^{L}p_o = p_a$, where p_a the atmospheric pressure.

Impact of leakage mass flow and disk friction losses

As discussed in Chapter 6, leakage losses arise in the Ljungström turbine. However, they will appear reasonably small (less than 1%). The impact of this loss on the blade geometry will consequently be neglected.

Impact of disk friction losses on stage outlet density change

An additional simplification performed is assuming that the impact of the disk friction losses on the outlet density is low enough such that :

$$^{j}\rho_{o,b} = {}^{j+1}\rho_i \tag{7.21}$$

This is a reasonable assumption, for as long as the impact of the disk friction losses on the stage efficiency remains relatively low ($T_{to,b} \approxeq T_{to}$).

Since it is reasonable to expect that $^{R}\mathcal{T}_{DF} \approxeq {}^{D}\mathcal{T}_{DF}$ under the conditions that $h_{ss} << L_j$ and $\dot{m}_{LL} << \dot{m}$, the impact of the disk friction losses and leakage losses on α_o appear negligible (Eq.6.138). Therefore, the design procedure will adopt :

$$^{j}\alpha_o \approxeq {}^{j}\alpha_{o,b} \tag{7.22}$$

The impact of these losses on the outlet specific total enthalpy will, however, not be neglected.

7.1.2 Inlet conditions

Determined by the TDR-cycle optimum

The inlet conditions in front of the RELT are imposed by the TDR cycle and internal combustion engine operating point. The turbine design point should match the design point conditions of the compressor or fan, where the compressor delivers a certain mass flow $\dot{m}$ at a total pressure p_{t2}. Neglecting the pressure losses in the ducts and plenum, the following formula can be applied :

$$^{1}p_{ti} = p_{t2} = RR\ p_{ta}\ \pi_C \tag{7.23}$$

where π_C the total-to-total cycle pressure ratio, RR the inlet losses and p_{ta} the total pressure near the inlet of the compressor or fan. The turbine expansion ratio is :

$$\pi_T = \frac{^{1}p_{ti}}{^{L}p_{to}} \tag{7.24}$$

If the turbine flow outlet Mach number is low, it is reasonable to state :

$$^{L}p_{to} \cong {}^{L}p_o = p_a \tag{7.25}$$

As helicopter flight speeds are small ($p_{ta} \cong p_a$), it is consequently found that :

$$\pi_T \cong \frac{RR p_{ta} \pi_C}{^{L}p_a} \cong RR\ \pi_C \tag{7.26}$$

Note that π_T is a total-to-total expansion ratio. Each turbine stage contributes to the total expansion of the gases, i.e. :

$$\pi_T = \Pi_j {}^{j}\pi_{Ts} \tag{7.27}$$

where ${}^{j}\pi_{Ts}$ represents the total expansion ratio realised in stage j. The inlet temperature $^{1}T_{ti}$ will depend on the cycle operating conditions, as discussed in Chapter 4. A method to find the optimum conditions will be developed in Chapter 8. At this point, it is sufficient to consider $^{1}T_{ti}$ as input variable and thus known by the designer. The non-dimensional turbine inlet specific total enthalpy $^{1}\hat{\theta}$ can be found when a value for $^{1}u_i$ is imposed. This value will be determined later, during the aerodynamic and disk friction loss trade-off study.

Determined by the required turbine power

The RELT is designed to deliver a power $P_T^* = P_{C1} + P_{C2}$ to the rotors. From the first law of thermodynamics (Eq.5.19), it is possible to retrieve the required mass flow $\dot{m}$, to which the blade height H_b is related, if a certain specific total enthalpy drop between inlet and

outlet ${}^1h_{ti} - {}^Lh_{to}$ is imposed :

$$\dot{m} = \frac{P_T^*}{{}^1h_{ti} - {}^Lh_{to}} = \frac{P_T^*}{{}^1h_{ti}\left[1 - \left(\frac{1}{\pi_T}\right)^{\frac{\gamma-1}{\gamma}\eta_{p,T}}\right]} \triangleq \frac{P_T^*}{\psi_T {}^1u_i^2} \tag{7.28}$$

and ψ_T the effective work coefficient over the complete turbine. The selected enthalpy drop depends on the majorly TDR-cycle dependent conditions ${}^1h_{ti}$ and π_T, but also on the turbine polytropic efficiency $\eta_{p,T}$. Here, it is also instructive to equate the denominator of the third term with the denominator of the fourth term, which yields an equation similar to Eq.5.80, but now for the complete turbine :

$$\psi_T = {}^1\hat{\theta}\left(1 - \pi_T^{\frac{1-\gamma}{\gamma}\eta_{p,T}}\right) \tag{7.29}$$

Now, the independent duty parameters may be retrieved, as will be discussed next.

7.1.3 Design parameter selection

With regard to the power output, non-dimensionalising the governing equation of Euler-Rateau (Eq.5.24) and substitution of Eq.5.53, Eq.5.73 and Eq.5.76 in the former yields for the stage work coefficient ψ :

$$\psi = \frac{v_{i_u}}{u_i} - \left(\frac{u_o}{u_i}\right)^2 \frac{v_{o,b_u}}{u_o} \tag{7.30}$$

$$\psi = \phi_i \tan\alpha_i - \left(\frac{R_o}{R_i}\right)^2 \phi_o \tan\alpha_{o,b} \tag{7.31}$$

Consequently, one observes that ${}^j\psi = f({}^j\phi_i, {}^j\phi_o, {}^j\alpha_i, {}^j\alpha_{o,b}, R_o/R_i)$. Note again that ψ does not take the disk friction and leakage mass flow losses into consideration. To account for these losses, ψ_S is defined as the *effective* work coefficient over a stage, in which the previously mentioned losses are adopted, viz. :

$$\psi_S = \frac{h_{ti} - h_{to}}{u_i^2} = \psi - \frac{h_{to} - h_{to,b}}{u_i^2} \tag{7.32}$$

Note that $\psi_S < \psi$ and $\psi_S = f(\psi, \zeta_{FL})$, denoting ζ_{FL} the impact of the disk friction and leakage losses in the stage. In addition, it is possible to reflect the work coefficient of each stage ψ_S in the turbine work coefficient ψ_T as the mass flow through each stage remains identical :

$${}^1h_{ti} - {}^Lh_{to} = \sum_j {}^j(h_{ti} - h_{to}) = \sum_j {}^j(u_i^2 \psi_S) \tag{7.33}$$

Dividing by ${}^1u_i^2$ yields :

$$\psi_T = \sum_j \left(\frac{{}^j u_i}{{}^1 u_i}\right)^2 {}^j\psi_S \tag{7.34}$$

or,

$$\psi_T = \sum_j \left(\frac{{}^j u_i}{{}^1 u_i}\right)^2 {}^j f(\psi, \zeta_{FL}) \tag{7.35}$$

From Chapter 6 and using the model of Soderberg, it becomes clear that the aerodynamic losses here defined as ζ_A depend on $\zeta_3 = f(\epsilon, \mathit{AR}_a, Re)$ and $w_o/u_o = f(\phi_o, \beta_{o,b})$. If the inlet velocity triangle is known as well as $\beta_{o,b}$, it is possible to calculate ϵ (Sections 5.4.6 and 5.4.7). As a consequence (for each stage) :

$$\zeta_A = f(\phi_i, \phi_o, \alpha_i, \alpha_{o,b}, \mathit{AR}_a, Re) \tag{7.36}$$

The efficiency of the turbine may then be expressed as $\eta_{p,T} = f({}^j\zeta_A, {}^j\zeta_{FL}, {}^j\psi)$. The design of the turbine greatly depends on finding an optimum nominal efficiency in order to provide good TDR-cycle performance characteristics.

The impact of the above equations is significant as it shows that the following duty, geometric and thermo-fluid-mechanical parameters need examination for each stage :

1. ${}^j\phi_i$: the inlet flow coefficient
2. ${}^j\phi_o$: the outlet flow coefficient
3. ${}^j\alpha_i$: the flow inlet absolute angle
4. ${}^j\alpha_{o,b}$: the flow outlet absolute angle
5. ${}^j\mathit{AR}_a$: the blade projected aspect ratio
6. ${}^jRe$: the flow Reynolds number
7. ${}^j\zeta_{FL}$: the disk friction and leakage losses
8. ${}^j\frac{R_o}{R_i}$: the outlet-to-inlet radius ratio

Clearly, it is not practical to select each variable independently. Fortunately, the earlier stated design criteria already reduce the amount of freedom, as will the introduction of the governing equations. These are discussed next, prior to tackling the detailed turbine design procedure.

7.1.4 Stage matching

Stage matching is the action where subsequent stages are configured in such a way that continuous flow characteristics are insured while obeying the imposed design rules. Of specific interest is the relationship between the flow coefficient at the outlet of one stage and the flow coefficient at the inlet of a subsequent stage. From conservation of mass :

$$^{j}(\rho_o v_{o_R} A_o) = {}^{j+1}(\rho_i v_{i_R} A_i) \tag{7.37}$$

or in non-dimensional form using Eq.5.9, Eq.7.20, and since $S_\Omega = 1$:

$$^{j}\phi_o = {}^{j}\overline{H} \left(\frac{^{j+1}R_i}{^{j}R_o} \right)^2 {}^{j+1}\phi_i \tag{7.38}$$

Observing Fig.5.6, it is found that :

$$^{j}\Delta_{is} = {}^{j+1}R_i - {}^{j}R_o \tag{7.39}$$

Substitution of Eq.7.39 in Eq.7.38 yields :

$$^{j}\phi_o = {}^{j}\overline{H} \left(1 + \frac{^{j}\Delta_{is}}{^{j}R_o} \right)^2 {}^{j+1}\phi_i \tag{7.40}$$

Defining $\hat{i}$ as :

$$\hat{i} = \left(1 + \frac{\Delta_{is}}{R_o} \right)^2 \tag{7.41}$$

results in the following stage matching equation :

$$^{j+1}\phi_i = {}^{j}\left(\frac{\phi_o}{\hat{i}\,\overline{H}} \right) \tag{7.42}$$

The interstage damping $^{M}\chi$ is defined as :

$$^{M}\chi \triangleq \hat{i}\,\overline{H} \tag{7.43}$$

and as a result :

$$^{j}(^{M}\chi) = \frac{^{j}\phi_o}{^{j+1}\phi_i} \tag{7.44}$$

Some important conclusions can be made using Eq.7.44. For this purpose, observe Fig.7.2. The design criteria impose $^{M}\phi_i = C^t$ (Eq.7.8) and $^{M}\phi_o = C^t$ (Eq.7.9). As a result :

$$^{j+1}(^{M}\phi_i) = {}^{j}(^{M}\phi_i) \tag{7.45}$$

$$^{j+1}(^{M}\phi_o) = {}^{j}(^{M}\phi_o) \tag{7.46}$$

Consequently :

$$^{j}(^{M}\chi) = {}^{M}\chi \tag{7.47}$$

$$^{M}\phi_o = {}^{M}\chi \, {}^{M}\phi_i \tag{7.48}$$

Hence : *the interstage space parameters not only determine the flow transition in the interstage space, but also impose the evolution of the flow coefficient in the middle stage blade cascades, the outlet flow coefficient of the first stage and the inlet flow coefficient of the last stage.* $^{M}\chi$ is therefore an important design parameter.

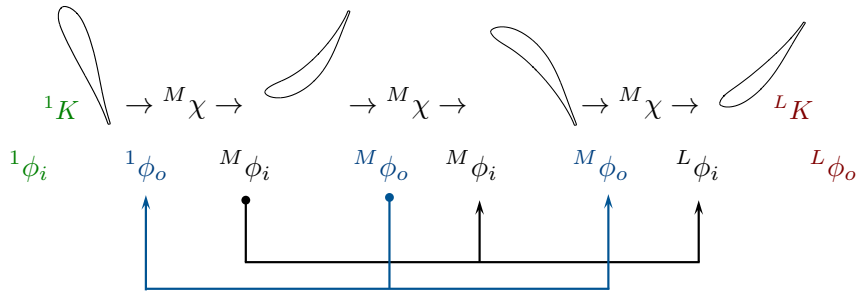

FIGURE 7.2. Ljungström turbine stage matching.

Note that $^{M}\chi$ does not relate $^{1}\phi_i$ to $^{1}\phi_o = {}^{M}\phi_o$ and $^{L}\phi_o$ to $^{L}\phi_i = {}^{M}\phi_i$. This dependency remains the designer's choice. By definition ^{1}K and ^{L}K are design parameters obeying the following relations :

$$^{1}\phi_i \triangleq {}^{1}K \, {}^{1}\phi_o = {}^{1}K \, {}^{M}\chi \, {}^{M}\phi_i \tag{7.49}$$

$$^{L}\phi_o \triangleq {}^{L}K \, {}^{L}\phi_i = {}^{L}K \, {}^{M}\phi_i \tag{7.50}$$

The interstage space height evolution $^{j}\overline{H}$ follows from the existence of the free vortex between all stages. The design criteria impose that :

$$^{j}|\alpha_o| = {}^{j+1}|\alpha_i| \tag{7.51}$$

$$^{j}|R_o v_{o_u}| = {}^{j+1}|R_i v_{i_u}| \quad \text{(Eq.7.19)}$$

Note again that in the interstage space the angle reference system remains conserved causing the need for absolute values. Developing the tangent of both terms in Eq.7.51 and introduction of the conservation of mass equation gives :

$$^{j}\left|\frac{v_{o_u}\rho_o A_o}{\dot{m}}\right| = {}^{j+1}\left|\frac{v_{i_u}\rho_i A_i}{\dot{m}}\right| \tag{7.52}$$

or,

$$^{j}(|v_{o_u}R_o|\rho_o H_{bo}) = {}^{j+1}(|v_{i_u}R_i|\rho_i H_{bi}) \tag{7.53}$$

According to Eq.7.19, the terms in absolute value vanish, which finally gives for $\overline{H}$:

$$^{j}\overline{H} = \frac{^{j}\rho_o}{^{j+1}\rho_i} \cong 1 \tag{7.54}$$

Since in the interstage $^{j}\rho_o \cong {}^{j+1}\rho_i$ (Eq.7.20), a $\overline{H}$ of unity must consequently to be imposed on *any* interstage space geometry. Note that $\overline{H}$ is a geometric design parameter.

Finally, the interstage space geometry will be proven to fix the turbine stage outlet-to-inlet radius ratio R_o/R_i. For this purpose, Eq.7.41 is examined more in detail. Substitution of Eq.7.18 and Eq.7.39 in Eq.7.41 yields :

$$\hat{\imath} = \left[1 + \left(1 - \frac{R_i}{R_o}\right)\hat{c}\right]^2 \tag{7.55}$$

In this equation, R_o/R_i clearly emerges. Since $^{M}\chi$ was selected as a design parameter, it is interesting to include Eq.7.43 in to the above relation. Rearranging terms then leads to :

$$^{j}\left(\frac{R_o}{R_i}\right) = {}^{j}\left(\frac{\hat{c}}{\hat{c} - \sqrt{\frac{^{M}\chi}{\overline{H}}} + 1}\right) \tag{7.56}$$

Since $\overline{H} = 1$ as imposed by the free vortex flow, since the design criteria impose $^{j}\hat{c} = \hat{c} = C^t$, since $^{M}\chi$ is in effect over all stages, it is found that $R_o/R_i = C^t$ for all stages :

$$\frac{R_o}{R_i} = \frac{\hat{c}}{\hat{c} - \sqrt{^{M}\chi} + 1} \tag{7.57}$$

This is a remarkable result, where $^{M}\chi$ allows the designer to modify R_o/R_i such to achieve best performance characteristics.

7.1.5 Flow deflection

The flow deflection ϵ can be written as a function of the selected design parameters ϕ_i, α_i and ^{1}K, $^{M}\chi$ or ^{L}K. The study establishing the ϵ-functions is treated next.

First stage

Recalling Eq.7.49 :

$$^{1}\phi_i \triangleq {}^{1}K\,{}^{1}\phi_o$$

Substitution of Eq.7.12 and Eq.7.13 in the above yields :

$$^{1}K \tan {}^{1}\beta_i = -\tan {}^{1}\alpha_o + \tan({}^{1}\beta_i - {}^{1}\epsilon) \tag{7.58}$$

Using the mathematical identity (applicable to any stage) – Abramowitz & Stegun (1972) :

$$\tan(\beta_i - \epsilon) = \frac{\tan\beta_i - \tan\epsilon}{1 + \tan\beta_i \tan\epsilon} \tag{7.59}$$

and substitution of Eq.5.57 (applicable to any stage), which is :

$$\tan\beta_i = \frac{\phi_i \ \tan\alpha_i - 1}{\phi_i}$$

leads to the following deflection angle law for the first stage, where ${}^1\alpha_o = -{}^M\alpha_i$:

$$\tan({}^1\epsilon) = \frac{(\tan {}^M\alpha_i \ {}^1\phi_i + {}^1K - 1) \ {}^1\phi_i}{{}^1\phi_i{}^2 + \tan {}^M\alpha_i \ {}^1\phi_i + {}^1K} \tag{7.60}$$

or (Eq.7.49) :

$$\tan({}^1\epsilon) = \frac{(\tan {}^M\alpha_i \ {}^1K \ {}^M\chi \ {}^M\phi_i + {}^1K - 1) \ {}^1K \ {}^M\chi \ {}^M\phi_i}{({}^1K \ {}^M\chi \ {}^M\phi_i)^2 + \tan {}^M\alpha_i \ {}^1K \ {}^M\chi \ {}^M\phi_i + {}^1K} \tag{7.61}$$

With the exception of ${}^1K$, the deflection of the first stage depends completely on the characteristics of the middle stages, i.e. : ${}^1\epsilon = f({}^M\phi_i, \ {}^M\alpha_i, \ {}^1K, \ {}^M\chi)$.

Middle stages

The deflection of the middle stages ${}^M\epsilon$ may be retrieved in a similar way as the one discussed for the first stage. Introducing Eq.7.14 and Eq.7.15 in Eq.7.48 :

$$\frac{{}^M\chi}{\tan {}^M\alpha_i - \tan {}^M\beta_i} = \frac{-1}{\tan {}^M\alpha_i + \tan({}^M\beta_i - {}^M\epsilon)} \tag{7.62}$$

Using the tangent identity (Eq.7.59), substitution of Eq.5.57 and solving for ${}^M\epsilon$ yields :

$$\tan({}^M\epsilon) = \frac{\{[2\tan({}^M\alpha_i){}^M\phi_i - 1] \ {}^M\chi + 1\} \ {}^M\phi_i}{[{}^M\phi_i + \tan({}^M\alpha_i) - \tan^2({}^M\alpha_i){}^M\phi_i] \ {}^M\chi {}^M\phi_i - \tan({}^M\alpha_i){}^M\phi_i + 1} \tag{7.63}$$

From the above equation it is concluded that : ${}^M\epsilon = f({}^M\phi_i, \ {}^M\alpha_i, \ {}^M\chi)$.

Last stage

The deflection of the last stage is found by substituting Eq.7.16 and Eq.7.17 in Eq.7.50 and solving for ${}^L\epsilon$ using the same procedure as discussed with the other stages :

$$\frac{{}^LK}{\tan {}^L\alpha_i} = \frac{1}{-\tan({}^L\beta_i - {}^L\epsilon)} \tag{7.64}$$

from which the following equation results :

$$\tan({}^{L}\epsilon) = \frac{[{}^{L}K \tan({}^{M}\alpha_i){}^{L}\phi_i - {}^{L}K + 1]\ {}^{L}\phi_i}{-\tan({}^{M}\alpha_i){}^{L}\phi_i + {}^{L}K{}^{L}\phi_i{}^{2} + 1} \tag{7.65}$$

and since ${}^{L}\phi_i = {}^{M}\phi_i$,

$$\tan({}^{L}\epsilon) = \frac{[{}^{L}K \tan({}^{M}\alpha_i){}^{M}\phi_i - {}^{L}K + 1]\ {}^{M}\phi_i}{-\tan({}^{M}\alpha_i){}^{M}\phi_i + {}^{L}K{}^{M}\phi_i{}^{2} + 1} \tag{7.66}$$

As a conclusion : ${}^{L}\epsilon = f({}^{M}\phi_i,\ {}^{M}\alpha_i,\ {}^{L}K)$.

7.1.6 Blade passage work coefficient

Eq.7.31 allows finding the work coefficient for each stage type. They are derived next.

First stage

In the first stage, ${}^{1}\alpha_i = 0$ and ${}^{1}\alpha_o = -{}^{M}\alpha_i$. The work coefficient of the first stage consequently is :

$${}^{1}\psi = \left(\frac{R_o}{R_i}\right)^2 {}^{1}\phi_o \tan({}^{M}\alpha_i) \tag{7.67}$$

or,

$${}^{1}\psi = \left(\frac{R_o}{R_i}\right)^2 {}^{M}\chi\, {}^{M}\phi_i \tan({}^{M}\alpha_i) \tag{7.68}$$

Since $R_o/R_i = f({}^{M}\chi,\ \hat{c})$ (Eq.7.57) it is found that ${}^{1}\psi = f({}^{M}\phi_i,\ {}^{M}\alpha_i,\ {}^{M}\chi,\ \hat{c})$.

Middle stages

Relying again on Eq.7.31 and ${}^{M}\alpha_o = -{}^{M}\alpha_i$:

$${}^{M}\psi = {}^{M}\phi_i \tan({}^{M}\alpha_i) - \left(\frac{R_o}{R_i}\right)^2 {}^{M}\phi_o \tan({}^{M}\alpha_o) \tag{7.69}$$

$${}^{M}\psi = {}^{M}\phi_i \tan({}^{M}\alpha_i)\left[1 + {}^{M}\chi\left(\frac{R_o}{R_i}\right)^2\right] \tag{7.70}$$

and thus ${}^{M}\psi = f({}^{M}\phi_i,\ {}^{M}\alpha_i,\ {}^{M}\chi,\ \hat{c})$.

Last stage

In a same manner, ${}^{L}\psi$ is obtained where ${}^{L}\alpha_o = 0$:

$${}^{L}\psi = {}^{L}\phi_i \tan({}^{L}\alpha_i) = {}^{M}\phi_i \tan({}^{M}\alpha_i) \tag{7.71}$$

As a result ${}^{L}\psi = f({}^{M}\phi_i,\ {}^{M}\alpha_i,\ {}^{M}\chi,\ \hat{c})$.

7.1.7 Blade passage static density variation

In contrast to the density change in the interstage space, the density change $\rho_{o,b}/\rho_i$ in the blade cascade must be accounted for. Here, the density ratio is modelled by means of non-dimensional parameters. The result will allow deriving an important closing equation between ψ and ϕ_i (Section 7.1.9). Considering an ideal gas, it is possible to write – Çengel & Boles (2006) :

$$\frac{\rho_{o,b}}{\rho_i} = \frac{\rho_{to,b}}{\rho_{ti}}\left(\frac{1+\frac{\gamma-1}{2}M_i^2}{1+\frac{\gamma-1}{2}M_{o,b}^2}\right)^{\frac{1}{\gamma-1}} \tag{7.72}$$

$$\frac{\rho_{o,b}}{\rho_i} = \left(\frac{p_{to,b}T_{ti}}{p_{ti}T_{to,b}}\right)\left(\frac{1+\frac{\gamma-1}{2}M_i^2}{1+\frac{\gamma-1}{2}M_{o,b}^2}\right)^{\frac{1}{\gamma-1}} \tag{7.73}$$

Substitution of Eq.5.124 and development of terms yields :

$$\frac{\rho_{o,b}}{\rho_i} = m\left[1-\left(\frac{h_{ti}-h_{to,b}}{h_{ti}}\right)\right]^k \tag{7.74}$$

with the following definitions for m and k :

$$m = \left(\frac{1+\frac{\gamma-1}{2}M_i^2}{1+\frac{\gamma-1}{2}M_{o,b}^2}\right)^{\frac{1}{\gamma-1}} \tag{7.75}$$

$$k = \frac{(1-\eta_{p,Tb})\gamma\ +\ \eta_{p,Tb}}{(\gamma-1)\eta_{p,Tb}} \tag{7.76}$$

$\eta_{p,Tb}$ is the blade passage total-to-total polytropic efficiency considering only the blade passage losses and thus $k = f(\zeta_A)$ or $k = f({}^{M}\phi_i,\ {}^{M}\alpha_i,\ {}^{M}\chi,\ \hat{c},\ \text{Æ}_a,\ Re)$ (Eq.7.36). Note that the Mach numbers can be written as a function of the design parameters. With respect to the inlet Mach number M_i, it is possible to write, starting from Eq.5.44 :

$$M_i = \frac{v_i}{\sqrt{\gamma R_g T_i}} = \frac{v_{i_R}/u_i}{\cos\alpha_i}\sqrt{\frac{u_i^2}{\gamma R_g\left(T_{ti}-\frac{v_i^2}{2C_p}\right)}} \tag{7.77}$$

From Çengel & Boles (2006) :

$$C_p = \left(\frac{\gamma}{\gamma-1}\right)R_g \tag{7.78}$$

Applying this formula to the former and introduction of the non-dimensional parameters, provides the required equation for M_i :

$$M_i = \frac{\phi_i}{\sqrt{(\gamma-1)(\hat{\theta}\cos^2\alpha_i - \phi_i^2/2)}} \tag{7.79}$$

In a similar way, $M_{o,b}$ may be found :

$$M_{o,b} = \frac{\phi_o}{\sqrt{(\gamma-1)\left[\left(\frac{R_i}{R_o}\right)^2(\hat{\theta}-\psi)\cos^2\alpha_o - \phi_o^2/2\right]}} \tag{7.80}$$

using the relation :

$$\frac{h_{to,b}}{u_o^2} = \left(\frac{R_i}{R_o}\right)^2(\hat{\theta}-\psi) \tag{7.81}$$

As a consequence, $m = f({}^M\phi_i,\ {}^M\alpha_i,\ {}^M\chi,\ \hat{c},\ {}^j\hat{\theta},\ [{}^1K \text{ or } {}^LK])$ can be calculated. Note that one may prove that :

$${}^{j+1}\hat{\theta} = {}^j\left(\frac{\hat{\theta}-\psi_S}{\hat{i}}\right) \tag{7.82}$$

and consequently ${}^{j+1}\hat{\theta} = f({}^M\phi_i,\ {}^M\alpha_i,\ {}^M\chi,\ \hat{c},\ {}^j\hat{\theta},\ {}^j\zeta_{FL})$. Finally, introducing Eq.5.12 and Eq.5.14 in Eq.7.74 :

$$\frac{\rho_{o,b}}{\rho_i} = m\left(1-\frac{\psi}{\hat{\theta}}\right)^k \tag{7.83}$$

7.1.8 Blade height evolution

While the free vortex condition in the interstage space allowed $\overline{H}$ to be unity, the imposition of the stage matching conditions will not necessarily lead to the same condition with regard to $\overline{B}$. Indeed, the increasing turbine radius and the decreasing density of the gases when progressing through the turbine, may in fact require the blade height to be modified in order to ensure the design criteria are met. Applying conservation of mass on the blade passage, the following relation can be retrieved for the blade height ratio $\overline{B}$ (Eq.5.6) :

$$\overline{B} = \frac{R_i}{R_o}\frac{\rho_i}{\rho_{o,b}}\frac{v_{i_R}}{u_i}\frac{u_o}{v_{o,b_R}}\frac{u_i}{u_o} = \left(\frac{R_i}{R_o}\right)^2\frac{\rho_i}{\rho_{o,b}}\frac{\phi_i}{\phi_o} \tag{7.84}$$

Substitution of Eq.7.83 in the above formula :

$$\overline{B} = \frac{\left(\frac{\phi_i}{\phi_o}\right)}{m\left(1 - \frac{\psi}{\hat{\theta}}\right)^k \left(\frac{R_o}{R_i}\right)^2} \tag{7.85}$$

The evolution of $\overline{B}$ is now examined in the following sections for each stage type.

First stage

The evolution of ${}^1\overline{B}$ is readily found by introduction of Eq.7.49 in Eq.7.85 :

$${}^1\overline{B} = \frac{{}^1K}{{}^1m\left(1 - \frac{{}^1\psi}{{}^1\hat{\theta}}\right)^{1k} \left(\frac{R_o}{R_i}\right)^2} \tag{7.86}$$

A more pragmatic approach would be the selection of ${}^1\overline{B}$ from which ${}^1K$ can be obtained. In the design procedure, this will be preferred approach. From a constructional viewpoint, it is indeed easier to keep the blade height constant and ${}^1\overline{B} = 1$ may consequently be adopted. Hence ${}^1\overline{B} = f({}^M\phi_i,\ {}^M\alpha_i,\ {}^M\chi,\ \hat{c},\ {}^1K,\ {}^1\hat{\theta},\ {}^1\text{Æ}_a,\ {}^1Re)$ or ${}^1K = f({}^M\phi_i,\ {}^M\alpha_i,\ {}^M\chi,\ \hat{c},\ {}^1\overline{B},\ {}^1\hat{\theta},\ {}^1\text{Æ}_a,\ {}^1Re)$.

Middle stages

Substitution of Eq.7.48 in Eq.7.85 :

$${}^j\overline{B} = \frac{1}{{}^jm\ {}^M\chi\left(1 - \frac{{}^M\psi}{{}^j\hat{\theta}}\right)^{jk} \left(\frac{R_o}{R_i}\right)^2} \tag{7.87}$$

Consequently it is found that ${}^j\overline{B} = f({}^M\phi_i,\ {}^M\alpha_i,\ {}^M\chi,\ \hat{c},\ {}^j\hat{\theta},\ {}^j\text{Æ}_a,\ {}^jRe)$

Last stage

Substitution of Eq.7.50 in Eq.7.85 :

$${}^L\overline{B} = \frac{1}{{}^Lm\ {}^LK\left(1 - \frac{{}^L\psi}{{}^L\hat{\theta}}\right)^{Lk} \left(\frac{R_o}{R_i}\right)^2} \tag{7.88}$$

As with the first stage, it is practical to impose ${}^L\overline{B} = 1$ for construction purposes. The above equation then allows retrieving a value for ${}^LK$. Hence ${}^L\overline{B} = f({}^M\phi_i,\ {}^M\alpha_i,\ {}^M\chi,\ \hat{c},\ {}^LK,\ {}^L\hat{\theta},\ {}^L\text{Æ}_a,\ {}^LRe)$ or ${}^LK = f({}^M\phi_i,\ {}^M\alpha_i,\ {}^M\chi,\ \hat{c},\ {}^L\overline{B},\ {}^L\hat{\theta},\ {}^L\text{Æ}_a,\ {}^LRe)$.

Note from the preceding discussion it is clear that $\overline{B} = 1$ is not guaranteed, except for the first and last stage, where the designer has an additional degree of freedom to match the design criteria. The impact of the geometry is also expounded via $Æ_a$ and Re. Since the geometry is à priori unknown, an iterative design approach will be inevitable.

7.1.9 $\phi_i - \psi$-function

Another way to relate the stage work coefficient to the stage inlet flow coefficient is by considering conservation of mass and a given blade height evolution. This function will appear particularly interesting during the iterative calculations used to establish the turbine geometry in Section 7.1.15. Recalling Eq.7.85 and solving for R_o/R_i yields :

$$\frac{R_o}{R_i} = \sqrt{\frac{\phi_i/\phi_o}{\overline{B}\, m \left(1 - \frac{\psi}{\hat{\theta}}\right)^k}} \tag{7.89}$$

Eq.7.31 also allows writing :

$$\frac{R_o}{R_i} = \sqrt{\frac{\psi - \phi_i \tan\alpha_i}{-\phi_o \tan\alpha_{o,b}}} \tag{7.90}$$

The design criteria impose $\alpha_{o,b} \cong \alpha_o$. Hence :

$$\frac{R_o}{R_i} = \sqrt{\frac{\psi - \phi_i \tan\alpha_i}{-\phi_o \tan\alpha_o}} \tag{7.91}$$

Substitution of Eq.7.89 in Eq.7.91 gives the following relation between ψ and ϕ_i, which is applicable to any blade passage :

$$\frac{\phi_i \tan\alpha_i}{\hat{\theta}} = \frac{\overline{B}\, m \left(1 - \frac{\psi}{\hat{\theta}}\right)^k}{\overline{B}\, m \left(1 - \frac{\psi}{\hat{\theta}}\right)^k - \frac{\tan\alpha_o}{\tan\alpha_i}} \frac{\psi}{\hat{\theta}} \tag{7.92}$$

or,

$$\frac{\phi_i \tan\alpha_i}{\hat{\theta}} = f\left(\frac{\psi}{\hat{\theta}}, m, k, \overline{B}\right) \tag{7.93}$$

7.1.10 Reaction degree

Horlock (1966) mentions the importance of the reaction degree in the selection of the blade profile. The reaction degree therefore deserves further examination. From Eq.5.60,

the following generally applicable formula is found :

$$\hat{R} = 1 - \frac{1}{2\psi}\left[\left(\frac{\phi_i}{\cos\alpha_i}\right)^2 - \left(\frac{\phi_o}{\cos\alpha_o}\frac{R_o}{R_i}\right)^2\right] \tag{7.94}$$

Since – Abramowitz & Stegun (1972) :

$$\frac{1}{\cos^2\alpha_i} = 1 + \tan^2\alpha_i = \sec^2\alpha_i \tag{7.95}$$

Eq.7.94 may also be rewritten in the following more practical form :

$$\hat{R} = 1 - \frac{\phi_i^2}{2\psi}\left[1 + \tan^2\alpha_i - (1 + \tan^2\alpha_o)\left(\frac{\phi_o}{\phi_i}\frac{R_o}{R_i}\right)^2\right] \tag{7.96}$$

First stage

Applying Eq.7.96 and Eq.7.68 on the first stage yields after simplification :

$${}^1\hat{R} = 1 - \frac{{}^M\chi\,{}^M\phi_i}{2\tan({}^M\alpha_i)}\left\{\left({}^1K\frac{R_i}{R_o}\right)^2 - [1 + \tan^2({}^M\alpha_i)]\right\} \tag{7.97}$$

with ${}^1\hat{R} = f({}^M\phi_i,\ {}^M\alpha_i,\ {}^1K,\ {}^M\chi,\ \hat{c})$.

Middle stages

Combining Eq.7.96 and Eq.7.70 and elaborating results in :

$${}^M\hat{R} = 1 - \frac{{}^M\phi_i}{2}\left[\frac{1 + \tan^2({}^M\alpha_i)}{\tan({}^M\alpha_i)}\right]\left[\frac{1 - \left({}^M\chi\frac{R_o}{R_i}\right)^2}{1 + {}^M\chi\left(\frac{R_o}{R_i}\right)^2}\right] \tag{7.98}$$

with ${}^M\hat{R} = f({}^M\phi_i,\ {}^M\alpha_i,\ {}^M\chi,\ \hat{c})$.

Last stages

The same procedure but now on the last stage with Eq.7.96 and Eq.7.70 yielding :

$${}^L\hat{R} = 1 + \frac{{}^M\phi_i}{2\tan({}^M\alpha_i)}\left\{\left({}^LK\frac{R_o}{R_i}\right)^2 - [1 + \tan^2({}^M\alpha_i)]\right\} \tag{7.99}$$

with ${}^L\hat{R} = f({}^M\phi_i,\ {}^M\alpha_i,\ {}^LK,\ {}^M\chi,\ \hat{c})$.

7.1.11 Conceptual performance model

Introduction

From the previous analysis, the non-dimensional turbine performance parameters Π_T appear to be governed by :

1. Turbine related design parameters : ${}^M\phi_i,\ {}^M\alpha_i,\ {}^M\chi,\ \hat{c},\ {}^1\hat{\theta},\ S_n$
2. Stage specific design parameters : $\mathit{\AA}_a,\ Re,\ \zeta_{FL},\ {}^1\overline{B},\ {}^L\overline{B}$

At this point, it is interesting to reflect on the optimum turbine efficiency design criterion. The calculation of the losses in a turbine stage were addressed in Chapter 6 and involved two steps. First, the blade passage losses were determined (ζ_A). Second, only when the flow conditions behind the blade passage were obtained, was it possible to superimpose the stage friction losses (ζ_{FL}). As a result, it is reasonable to expect that some stage flow characteristics can be related to a high stage aerodynamic efficiency without having to consider stage friction. This study is the subject of the conceptual performance model. The friction losses will be discussed and introduced later in a more detailed model, which will rely on the findings of this conceptual performance model. In addition, the conceptual performance model will allow the selection of appropriate blade profiles by studying the reaction degree.

Hypotheses

The conceptual performance model follows the design criteria of Section 7.1.1, but imposes in addition, following Eq.6.3 :

$$\frac{R_o}{R_i} \approxeq 1 \quad \text{(large radius with respect to blade chord)} \tag{7.100}$$

This hypothesis leads to Eq.7.57 and Eq.7.55 :

$$ {}^M\chi \approxeq 1 \Rightarrow {}^M\phi_i = {}^M\phi_o = {}^1\phi_o = {}^L\phi_i \tag{7.101}$$

$$ \hat{i} \approxeq 1 \tag{7.102}$$

Since in the Ljungström turbine it will appear that $\psi << \hat{\theta}$, it is reasonable to state :

$$\frac{\psi}{\hat{\theta}} \approxeq 0 \tag{7.103}$$

Because the flow absolute Mach numbers will show to be in the low subsonic range ($M \leq 0.3$) or of the same order of magnitude : $m \approxeq 1$. Eq.7.87 then leads to the following observation :

$$ {}^M\overline{B} \approxeq 1 \tag{7.104}$$

If in addition one imposes ${}^{1}\overline{B} = {}^{L}\overline{B} = 1$, which is in line with the foregoing equation and less costly from a construction viewpoint, it is found that (Eq.7.86 and Eq.7.88) :

$$ {}^{1}K \approxeq 1 \Rightarrow {}^{1}\phi_i = {}^{M}\phi_i \tag{7.105} $$

$$ {}^{L}K \approxeq 1 \Rightarrow {}^{L}\phi_o = {}^{M}\phi_i \tag{7.106} $$

Relying on the above simplifications, and considering $\mathcal{R}_a$ and Re to be more or less identical for all stages, it is found that the turbine non-dimensional performance parameters all become function of :

$$ \Pi_T = f({}^{M}\phi_i,\ {}^{M}\alpha_i,\ {}^{1}\hat{\theta},\ \mathcal{R}_a,\ Re,\ S_n) \tag{7.107} $$

The above parameters allow examining ζ_A for each stage and of the complete turbine. ${}^{M}\phi_i$ and ${}^{M}\alpha_i$ will act as independent variables, while a sensitivity study will be performed on $\mathcal{R}_a$, Re and S_n. Note that in the present context ${}^{j}\hat{\theta} = f({}^{M}\phi_i,\ {}^{M}\alpha_i,\ {}^{1}\hat{\theta},\ j)$. However, since the turbine inlet temperature is rather low (TDR-cycle observations) as well as the temperature drop and inlet rotational speed over each stage, ${}^{j}\hat{\theta}$ will not change much for each stage and will at this point be discarded from consideration, i.e. :

$$ {}^{j}\hat{\theta} \approxeq {}^{1}\hat{\theta} \tag{7.108} $$

Design ${}^{M}\alpha_i$

The performance parameter of interest is the turbine aerodynamic loss ζ_{AT}, which should be minimised. By definition (Eq.6.30), and using Eq.5.77 :

$$ \zeta_A \triangleq {}^{j}\left(\frac{h_{tL}}{u_o^2}\right) = \frac{1}{2}\zeta_3 \frac{w_{o,b}^2}{u_o^2} = \frac{1}{2}\zeta_3 \phi_o^2 \left(1 + \tan^2 \beta_{o,b}^2\right) \tag{7.109} $$

$$ \zeta_A = \frac{1}{2}\zeta_3 [\phi_o^2 (1 + \tan^2 \alpha_o) - 2\phi_o \tan \alpha_o + 1] \tag{7.110} $$

The turbine aerodynamic loss then is :

$$ \zeta_{AT} = \sum_j \frac{{}^{j}u_o{}^2}{{}^{1}u_o{}^2} {}^{j}\zeta_A \tag{7.111} $$

and can be further simplified to (Eq.7.100) :

$$ \zeta_{AT} = \sum_j {}^{j}\zeta_A = {}^{1}\zeta_A + (S_n - 2){}^{M}\zeta_A + {}^{L}\zeta_A \tag{7.112} $$

Note that ${}^{M}\zeta_A$ is identical for all middle stages, which is a direct consequence of the simplifications. As stated before, $\zeta_3 = f(\epsilon,\ \mathcal{R}_a,\ Re)$. Applying the hypotheses, the flow

deflection for each stage type is (Eq.7.61, Eq.7.63 and Eq.7.66) :

$$\tan({}^{1}\epsilon) = \frac{\tan({}^{M}\alpha_i)\ {}^{M}\phi_i{}^{2}}{{}^{M}\phi_i{}^{2} + \tan{}^{M}\alpha_i {}^{M}\phi_i + 1} \tag{7.113}$$

$$\tan({}^{M}\epsilon) = \frac{2\tan({}^{M}\alpha_i){}^{M}\phi_i{}^{2}}{[1 - \tan^2({}^{M}\alpha_i)]{}^{M}\phi_i{}^{2} + 1} \tag{7.114}$$

$$\tan({}^{L}\epsilon) = \frac{\tan({}^{M}\alpha_i){}^{M}\phi_i{}^{2}}{{}^{M}\phi_i{}^{2} - \tan({}^{M}\alpha_i){}^{M}\phi_i + 1} \tag{7.115}$$

The above set of equations allow a parametric study of ζ_{AT} to be established. Note however that a more pragmatic approach is to represent $\zeta_{A(T)}$ by means of an efficiency. Since ζ_{AT} represents the enthalpic losses, it can be easily adopted in the isentropic efficiency relation, which was already defined in Eq.5.116 :

$$\eta_{is,T} \triangleq \frac{h_{ti} - h_{to}}{h_{ti} - h_{to_{is}}}$$

Since ζ_{FL} is neglected ($h_{to,b} = h_{to}$), it is possible to write for a single stage :

$$\eta_{is,Ts} = \eta_{is,Tb} = \frac{1}{1 + \frac{h_{to,b} - h_{to,b_{is}}}{h_{ti} - h_{to,b}}} \tag{7.116}$$

$$\eta_{is,Ts} = \eta_{is,Tb} \approxeq \frac{1}{1 + \frac{\zeta_A}{\psi}} \tag{7.117}$$

or for the complete turbine,

$$\eta_{is,T} = \frac{1}{1 + \frac{\zeta_{AT}}{\psi_T}} \tag{7.118}$$

Note again that the conceptual model imposes $\psi_S = \psi$. Now, the values of ψ and ψ_T can be found easily. Using Eq.7.68, Eq.7.70 and Eq.7.71 :

$${}^{1}\psi = {}^{M}\phi_i \tan({}^{M}\alpha_i) \tag{7.119}$$

$${}^{M}\psi = 2 \cdot {}^{M}\phi_i \tan({}^{M}\alpha_i) \tag{7.120}$$

$${}^{L}\psi = {}^{M}\phi_i \tan({}^{M}\alpha_i) \tag{7.121}$$

An interesting observation is made comparing the above equations. Indeed, it is found that :

$${}^{1}\psi = {}^{L}\psi = \frac{{}^{M}\psi}{2} \tag{7.122}$$

Substitution of Eq.7.122 in Eq.7.34 then yields :

$$\psi_T = (S_n - 1)\,{}^M\psi \tag{7.123}$$

and as a consequence (Eq.7.118) :

$$\eta_{is,T} = \frac{1}{1 + \frac{\zeta_{AT}}{2(S_n-1)^M\phi_i \tan({}^M\alpha_i)}} \tag{7.124}$$

The result of the parametric study is reflected in Figs. 7.3-7.4. The sensitivity study range on $\mathcal{AR}_a$, Re and S_n is highlighted in Table 7.1. Note that the figures represent the middle-stage work coefficient ${}^M\psi$. This allows a better analysis of the turbine efficiency as a function of stage loading. Indeed, ψ_T depends on S_n (Eq.7.34), which renders the evaluation of the impact of S_n on stage level less obvious. Assessing Figs. 7.3-7.4, it is

TABLE 7.1. ζ_A sensitivity study range.

$\mathcal{AR}_a$	0.25, 5
Re/Re_{ref}	0.25, 2
S_n	4, 10

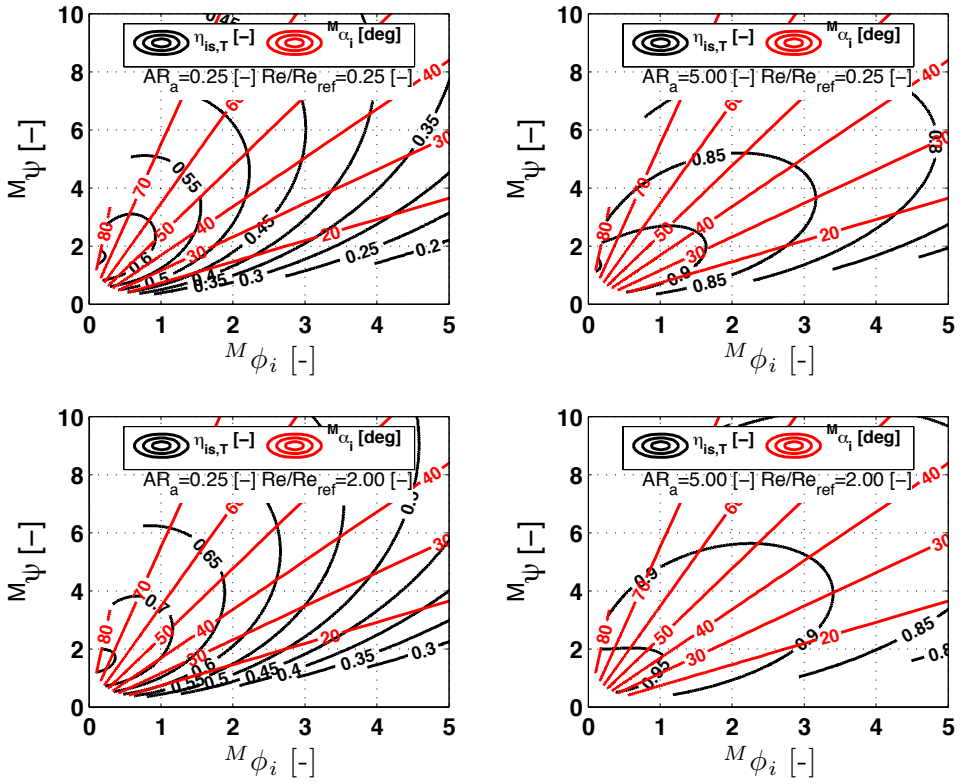

FIGURE 7.3. Ljungström turbine parametric design and sensitivity study : $S_n = 4$.

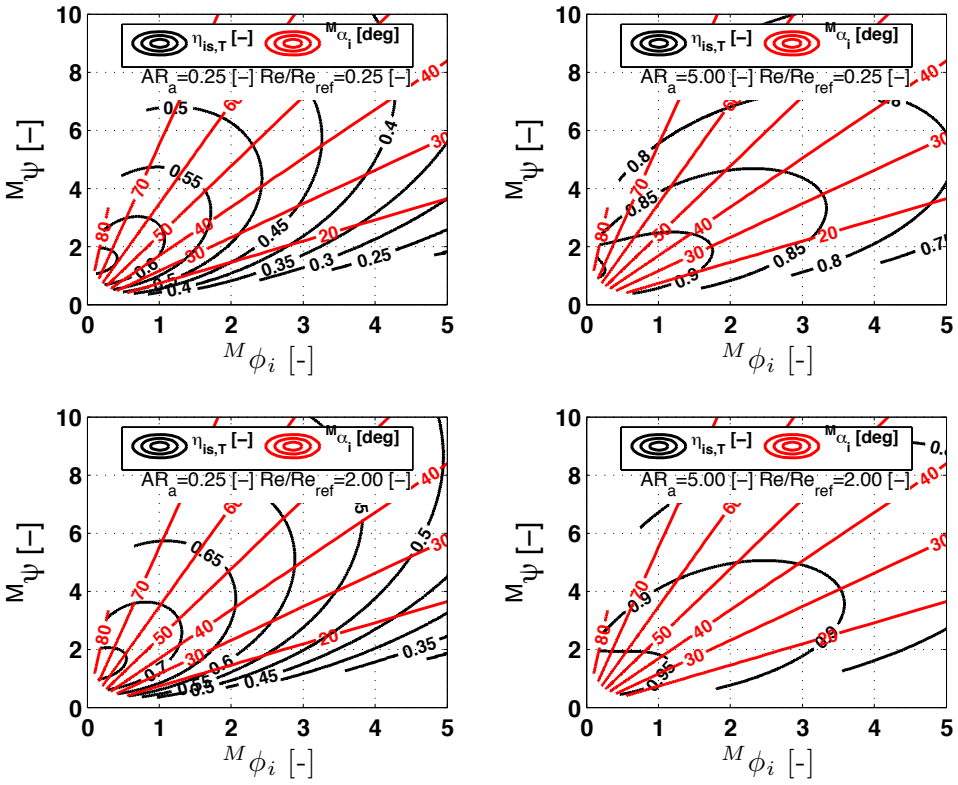

FIGURE 7.4. Ljungström turbine stage parametric design and sensitivity study : $S_n = 10$.

found that :

→ An increase in $\mathit{Æ}_a$ and Re/Re_{ref} improves the turbine efficiency $\eta_{is,T}$.

→ For a same stage loading, an increase in S_n impacts $\eta_{is,T}$ minimally, moving the optimum to slightly higher ${}^M\phi_i$. This is because the optimum ζ_A of the middle stages is found at higher ${}^M\phi_i$ than those for the first and last stage. More stages means that $\eta_{is,T}$ becomes biased towards the value observed for the middle stages, as more of them are installed. Fig.7.5 reveals this tendency, which is also found similar for other $\mathit{Æ}_a$, Re and S_n. This figure also explains the small decrease in efficiency with increasing turbine stage number, because the middle stages operate at higher flow deflections than the first and last stage and thus induce higher losses.

→ If $\eta_{is,T} \geq 0.85$ is sought in order to impose a reasonable value for the cycle efficiency, it is clear that ${}^M\psi \leq 10$ (see iso-efficiency lines). From Eq.5.80 and since $\psi_S < \psi$ (Eq.7.32), it is then found that the stage expansion ratio $\pi_{Ts} \leq 1.3$[i]. Under these circumstances it becomes apparent that each Ljungström turbine stage will work under adapted operation conditions with a significant margin with respect to the choking pressure ratio (Eq.6.70). Hence, it is safe to neglect any supersonic expansion losses in the turbine.

[i] A reasonable value for $\hat{\theta} \cong 155$, as proven later in Chapter 8.

→ A design range for ${}^{M}\alpha_i$ can be established. Observing the figures and biasing the optimum towards a slightly higher work coefficient in order to minimise the stage count, it is acceptable to select for the high $\mathit{Æ}_a$:

$$ {}^{M}\alpha_i \cong 40° \text{ à } 50° \tag{7.125} $$

while for the low $\mathit{Æ}_a$

$$ {}^{M}\alpha_i \cong 60° \text{ à } 65° \tag{7.126} $$

These values may be used as *design* ${}^{M}\alpha_i$.

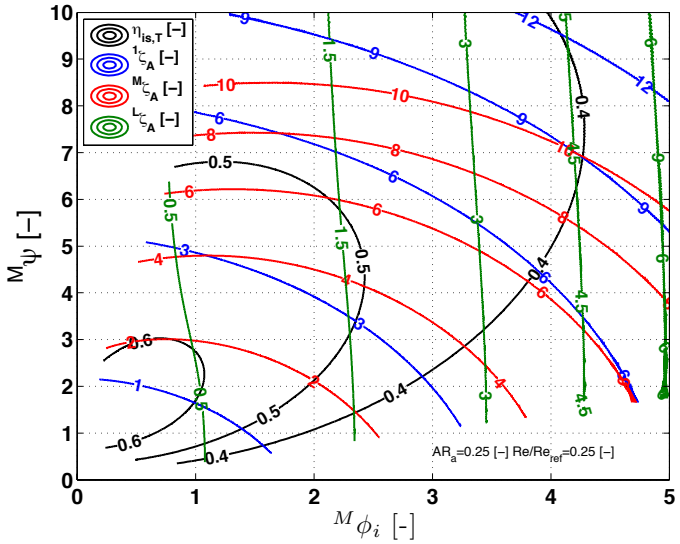

FIGURE 7.5. Ljungström turbine stage ζ_A behaviour, expounded using $S_n = 10$.

The foregoing *rules of thumb* for ${}^{M}\alpha_i$ allow to fix the required number of turbine stages for a given cycle pressure ratio π_C, here approximated by the turbine expansion ratio π_T. Indeed, recalling Eq.7.29 :

$$ \psi_T = {}^{1}\hat{\theta}\left(1 - \pi_T^{\frac{1-\gamma}{\gamma}\eta_{p,T}}\right) $$

yields the required ψ_T. Conceptual design plots such as Figs. 7.3-7.4 then lead to the determination of the maximum value for ${}^{M}\psi$, while imposing a target turbine efficiency. The turbine stage count S_n is consequently found using Eq.7.123. Finally, Eq.7.120 yields ${}^{M}\phi_i$ for the selected design ${}^{M}\alpha_i$.

${}^{M}\phi_i$ is necessary to calculate the blade height of the turbine blades (and reiterate on $\mathcal{R}_a$). The answer to this problem still needs examination since (Eq.7.28) :

$$\dot{m} = \frac{P_T}{\psi_T {}^{1}u_i^2}$$
$$H_{bi} = \frac{\dot{m}}{2\pi R_i \rho_i \phi_i u_i} \tag{7.127}$$

where the important dimensional design parameters u_i and R_i still need to be selected such that the turbine total efficiency remains high. Clearly, the impact of the disk friction and leakage losses ζ_{FL} therefore requires further analysis. This research is conducted after the important discussion on the stage reaction degree and some geometric considerations, which are treated next.

Reaction degree

The reaction degree was already studied in Section 7.1.10. Applying the conceptual model simplifications to the formulae established for $\hat{R}$ yields valuable design characteristics. From Eq.7.97, Eq.7.98 and Eq.7.99, it is found that :

$${}^{1}\hat{R} = 1 + \frac{{}^{M}\phi_i \ \tan({}^{M}\alpha_i)}{2} \quad > 1 \tag{7.128}$$
$${}^{M}\hat{R} = 1 \tag{7.129}$$
$${}^{L}\hat{R} = 1 - \frac{{}^{M}\phi_i \ \tan({}^{M}\alpha_i)}{2} \quad < 1 \tag{7.130}$$

Referring to Eq.5.60, the above equations clearly state that the absolute speed of the flow over the blade passage is increased in the first stage, conserved in the middle stages and decelerated in the last stage. This behaviour is particularly beneficial since the first stage will increase Re over the middle stages where the deflection is higher (see model of Soderberg), while kinetic energy is recuperated in the last stage before the gases are expelled to the atmosphere. In addition, all but the last stage have $\hat{R} \geq 1$. From this observation, it is possible to select the blade profile (family).

7.1.12 Geometry assessment

Blade profile selection and turbine geometry development

For turbines where the reaction degree is important (i.e. > 0.5), which is the case for most/all[ii] of the stages in the Ljungström turbine, Horlock (1966) recommends the use the A_3K_7 reaction blade profile, shown in Fig.7.6. In general, the thickness-to-camberline-length ratio t/l is 20% for this profile, but Dunavant & Erwin (1956) explains that t/l may

[ii] This will depend on ${}^{L}\hat{R}$. The current study however, will consider a high-reaction-degree profile for all stages.

be changed, using the following modification :

$$y_{bp} = y_{bp_{0.2}}\left(\frac{t/l}{0.20}\right) \tag{7.131}$$

$$R_{LE} = R_{LE_{0.2}}\left(\frac{t/l}{0.2}\right)^2 \tag{7.132}$$

where y_{bp} the y-coordinate and R_{LE} the leading edge radius of the base profile. The suffix 0.2 stands for the values applicable to the standard base profile ($t/l = 0.2$). For the trailing edge radius R_{TE}, no modifications were given in the literature, but the author of this work proposes the following correction :

$$R_{TE} = R_{TE_{0.2}}\left(\frac{t/l}{0.2}\right) \tag{7.133}$$

Note that most of the Ljungström turbine stages will have a high reaction degree. As a result, for this study a blade thickness-to-camberline-length ratio of 20% will be selected, as indicated by Horlock (1966).
The A_3K_7 base profile is now constructed by creating splines going through the non-dimensional profile data points given by Dunavant & Erwin (1956), while inspecting the blade surface for smoothness and assuring a smooth evolution between the splines and leading edge as well as trailing edge radii (Fig.7.7).

The *design* camber of the A_3K_7 blade is provided by NACA and is given for a *design* load coefficient C_{L0} producing a camberline deflection ϵ_b of approximately 41° (Fig.7.8). For other blade loadings, requiring a higher or a lower deflection ϵ_b, the camberline y-coordinate y_c may be corrected proportionally :

$$y_c = y_{c_{C_{L0}}} \frac{C_L}{C_{L0}} \tag{7.134}$$

The C_L values do not have to be known. What is important is that the y_c coordinate has to be increased or decreased such that the required deflection is met. Once the new camberline is established, the base profile is consequently wrapped around the camberline.

Clearly, the camberline deflection ϵ_b depends on the flow deflection $\epsilon = \beta_i - \beta_{b,o}$, which can only be determined when the stage relative flow angles β_i and $\beta_{o,b}$ are known. These may be obtained from the performance analysis, including the flow deviation δ. Then, the camberline deflection ϵ_b may be calculated :

$$\epsilon_b = \beta_{b,i} - \beta_{b,o} \approxeq \beta_i - \beta_{o,b} - \delta \tag{7.135}$$

Note that an induced flow correction to the inlet flow angle is not introduced in this work. This is because not much information was given about this phenomenon in the literature. It is also believed not to have an as important impact on the flow conditions

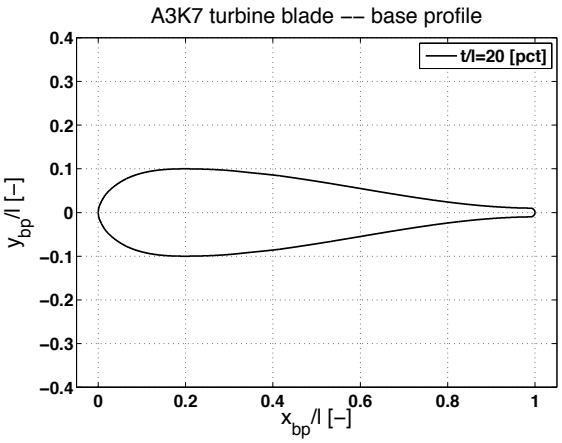

FIGURE 7.6. A_3K_7 turbine blade, base profile, standardised coordinates.

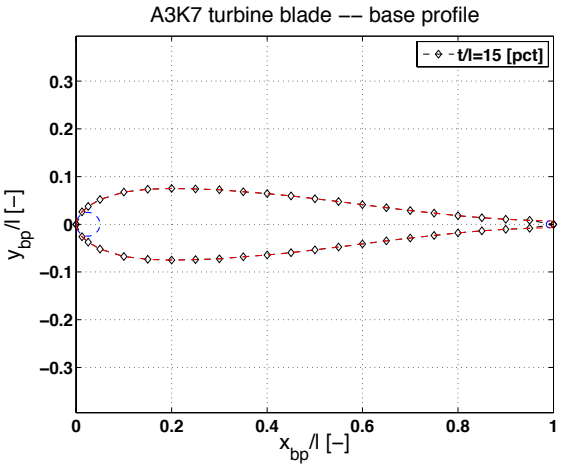

FIGURE 7.7. A_3K_7 turbine blade, base profile, standardised coordinates. Made using data of Dunavant & Erwin (1956).

as the deviation angle has on the outlet, even though impacting the flow losses to some extent. The evaluation of this will need to be undertaken in future research. The blade stagger angle λ can consequently be calculated. From Fig.5.3, where λ is indicated as positive, it is found that :

$$\lambda = \beta_{c,LE} - \beta_{b,i} \tag{7.136}$$

where $\beta_{c,LE}$ the angle of the camberline near the leading edge with radially positioned chord, while using the slope sign convention from a normal Cartesian coordinate system (e.g. positive on Fig.7.8). From a manufacturing viewpoint, putting the chord of the blade at an angle λ with respect to a radial line, will automatically assure that the design flow conditions are met. Note that λ is measured at the blade leading edge.

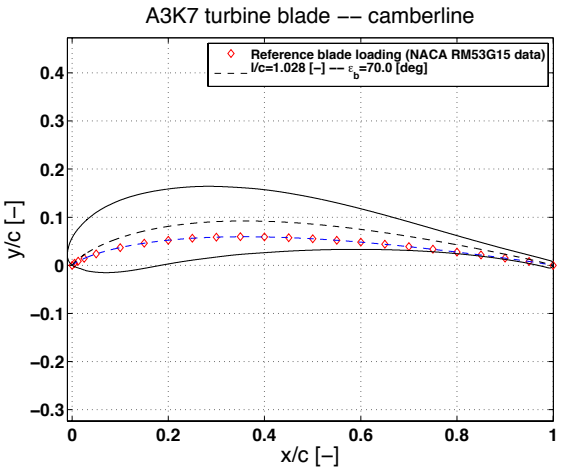

FIGURE 7.8. A_3K_7 turbine blade, $\epsilon_b = 70°$, standardised coordinates. Made using data of Dunavant & Erwin (1956).

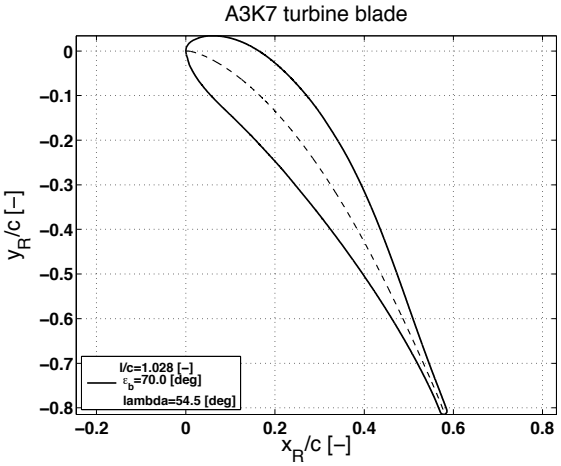

FIGURE 7.9. A_3K_7 turbine blade, $\beta_{b,i} = 0°$, $\epsilon_b = 70°$, standardised coordinates.

The new coordinates x_R and y_R may be calculated via a simple transformation :

$$\begin{pmatrix} x_R \\ y_R \end{pmatrix} = \begin{pmatrix} \cos\ \lambda & \sin\ \lambda \\ -\sin\ \lambda & \cos\ \lambda \end{pmatrix} \cdot \begin{pmatrix} x \\ y \end{pmatrix} \tag{7.137}$$

Since the flow deviation δ already takes the impact of the centrifugal turbine configuration into account, it is assumed that no other interventions to the geometry are required. In the case of the inlet radius R_i and chord c being known to the designer, it is possible to calculate the stage outlet radius R_o :

$$R_o = \sqrt{(R_i + \cos\lambda\ c)^2 + (\sin\lambda\ c)^2} \tag{7.138}$$

from which the radial component of the chord c_a may be retrieved :

$$c_a = R_o - R_i = \sqrt{(R_i + \cos\lambda\ c)^2 + (\sin\lambda\ c)^2} - R_i \tag{7.139}$$

c/R_i can be calculated via Eq.7.138. Since R_o/R_i is known by the selection of ${}^M\chi$ and $\hat{c}$, it is possible to write :

$$\frac{c}{R_i} = -\cos\lambda + \sqrt{\cos^2\lambda - \left[1 - \left(\frac{R_o}{R_i}\right)^2\right]} \tag{7.140}$$

While $R_o \to R_i$, it is clear that for any λ, $c/R_i \to 0$, which is in line with the findings of Eq.6.3. Note that R_i will follow from the design procedure explained in Section 7.1.14, allowing the determination of c.
Continuing the development of the circular cascade, the new coordinates now become after transformation :

$$\begin{pmatrix} x_C \\ y_C \end{pmatrix} = \begin{pmatrix} \cos\ \Pi & \sin\ \Pi \\ -\sin\ \Pi & \cos\ \Pi \end{pmatrix} \cdot \begin{pmatrix} x_R + R_i \\ y_R \end{pmatrix} \tag{7.141}$$

where $\Pi = [0, \Pi_p, \ldots 2\pi[$. An example of a Ljungström turbine stage is shown in Fig.7.10.

Gauging angle β_g

In the model of Ainley & Mathieson (1955), the gauging angle β_g appears of significant importance. In order to calculate β_g, the throat section o needs to be determined. The throat is the minimum section between two adjacent blades. In the theory presented by Aungier (2006) and applied by the author of this work, the throat is modelled by expecting it to extend between the trailing edge of one blade and the nearest point on the suction side of the subsequent blade, as indicated in Fig.5.3. Unfortunately, this condition is not always guaranteed when using an existing profile. Fig.7.11 clearly reveals this issue, where the throat is found upstream of the trailing edge. Nevertheless, in this work

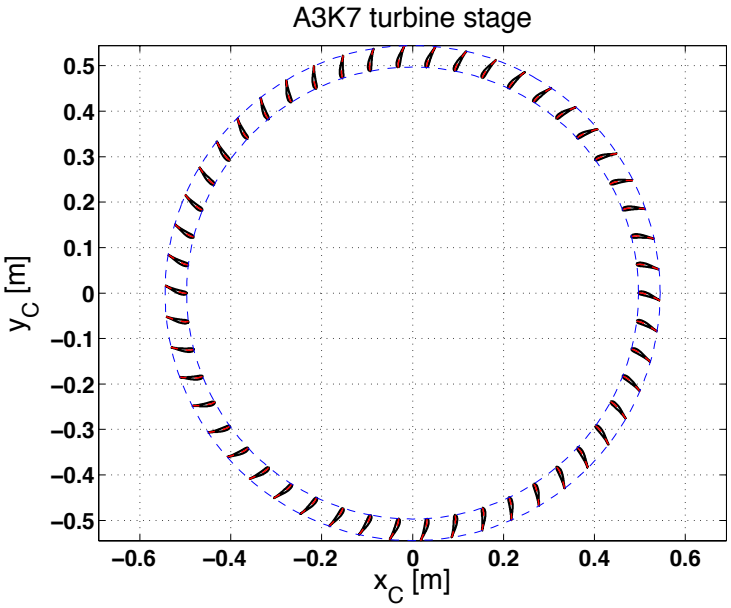

FIGURE 7.10. A_3K_7 turbine blade, $c = 50$ mm, $R_i = 497$ mm (For illustrative purposes only).

the *modelled* gauging angle will be used as proposed by Aungier (2006), even though it implies an error. This approximation however, is expected to remain reasonably valid when the real and modelled throat bear the same order of magnitude, while the flow in the blade passage stays subsonic. The discussed issue also invites the designer to utilise more involved geometry codes to assure a better correlation between theory and used geometry, using e.g. Bezier curves, but it is the authors opinion that for preliminary design purposes, it is not mandatory. The developed geometry can always be optimised in conjunction with CFD simulations. This research is not in the scope of this work.

Radius of curvature R_c

The radius of curvature of the suction side of a blade between throat and trailing edge is important to calculate the K_M loss factor in the model of Ainley & Mathieson (1955) (Appendix D). For this purpose, the radius of an arc drawn through three equally spaced points on the suction side of the blade between throat and trailing edge is calculated. The first point is near the throat, the second near the trailing edge and the third halfway the aforementioned points. The parameter equations of the lines perpendicular to the circle chords established via the three points give the center of the radius of curvature :

$$x_{ctr} = \frac{1}{2}(x_1 + x_2) + \frac{1}{2}\frac{(x_2 - x_3)(x_3 - x_1) + (y_2 - y_3)(y_3 - y_1)}{(x_2 - x_1)(y_3 - y_1) - (y_2 - y_1)(x_3 - x_1)}(y_2 - y_1) \tag{7.142}$$

$$y_{ctr} = \frac{1}{2}(y_1 + y_2) - \frac{1}{2}\frac{(x_2 - x_3)(x_3 - x_1) + (y_2 - y_3)(y_3 - y_1)}{(x_2 - x_1)(y_3 - y_1) - (y_2 - y_1)(x_3 - x_1)}(x_2 - x_1) \tag{7.143}$$

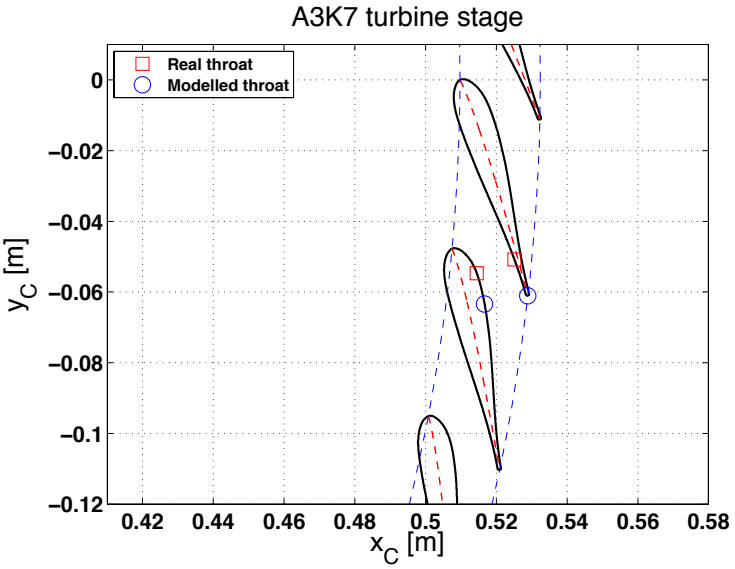

FIGURE 7.11. A_3K_7 turbine blade throat modelling – example.

The radius of curvature then is :

$$R_c = \sqrt{(x_1 - x_{ctr})^2 + (y_1 - y_{ctr})^2} \tag{7.144}$$

7.1.13 Impact of disk friction losses

The conceptual performance model focussed on minimising the aerodynamic loss ζ_{AT} and finding indicative values for ${}^{M}\alpha_i$. Here, the disk friction enthalpic losses ζ_{FL} are studied, based on the observations already made in Section 6.2.

Enthalpic loss ζ_{FL}

Similar to ζ_A, it is possible to define ζ_{FL} as an enthalpic loss :

$$\zeta_{FL} \triangleq \frac{\Delta h_{t_{FL}}}{u_o^2} \tag{7.145}$$

(7.146)

and (Eq.6.111, Eq.6.112 and Eq.6.113),

$$\Delta h_{t_{FL}} = \Delta h_{t,LL} + {}^{D}\Delta h_{t,DF} + {}^{R}\Delta h_{t,DF} \tag{7.147}$$

Since $S_\Omega = 1$ and the leakage losses are neglected ($h_{t,LL} \cong 0$), it is possible to obtain the disk friction losses produced over a stage. Recalling Eq.6.100 and Eq.6.101 :

$$\zeta_{FL} = \frac{({}^{R}\mathcal{T}_{DF} + {}^{D}\mathcal{T}_{DF})\,\Omega}{\dot{m}\,(\Omega R_o)^2} \tag{7.148}$$

where $\Omega = \Omega_{C1} = \Omega_{C2}$. If $h_{ss} << L_j$ and since $R_o/R_i \cong 1$, then it is possible to state that (Section 6.4) :

$$^{R}\mathcal{T}_{DF} \cong^{D} \mathcal{T}_{DF} \triangleq \mathcal{T}_{DF} \tag{7.149}$$

Consequently, for a single stage :

$$\zeta_{FL} = \frac{2\mathcal{T}_{DF}}{\dot{m}\,\Omega R_o^2} = \frac{2(\mathcal{T}_{TOC} + \mathcal{T}_{TAC} + \mathcal{T}_{CAV})}{\dot{m}\,\Omega R_o^2} = 2(\zeta_{FL_{TOC}} + \zeta_{FL_{TAC}} + \zeta_{FL_{CAV}}) \tag{7.150}$$

Eq.7.150 is now used to examine each component of the disk friction losses.

Torsional Couette

Recalling Eq.6.47 and Eq.6.46, and considering only type-I flow (Eq.6.43) for matters of simplicity, it is possible to write :

$$\mathcal{T}_{TOC} = \frac{\pi\mu}{\Delta_{s_h}}\Omega R_i^4 \left(\frac{R_i}{R_o}\right)\left[\left(\frac{R_o}{R_i}\right)^5 - 1\right] \tag{7.151}$$

Rewriting the above equation in terms of specific enthalpy loss by reduction as indicated in Eq.7.150 :

$$\zeta_{FL_{TOC}} = \frac{h_{t,TOC}}{u_o^2} = \left(\frac{\pi\mu}{\Delta_{s_h}}\frac{R_i^2}{\dot{m}}\right)\left(\frac{R_i}{R_o}\right)^3\left[\left(\frac{R_o}{R_i}\right)^5 - 1\right] \tag{7.152}$$

Note that even though $(\pi\mu\, R_i^2)/(\Delta_{s_h}\, \dot{m})$ is a non-dimensional term, it is decided not to use this coefficient as independent variable. Indeed, it does not appear in the other yet-to-be-discussed loss terms, while it is much more instructive to examine the impact of R_i and $\dot{m}$ on the friction losses. R_i and $\dot{m}$ are important design parameters, while found in all friction loss terms.
For a given seal strip geometry, the torsional Couette losses lead to the following enthalpic loss :

$$\zeta_{FL_{TOC}} \propto \left(R_i, \frac{R_o}{R_i}, \frac{1}{\dot{m}}\right) \quad \text{or} \quad \propto \left(R_i, {}^{M}\chi, \frac{1}{\hat{c}}, \frac{1}{\dot{m}}\right) \tag{7.153}$$

Taylor-Couette

Eq.6.52 represents the formula for $\mathcal{T}_{TAC}$. Writing this equation as an enthalpic loss, it is found that :

$$\zeta_{FL_{TAC}} = \frac{h_{t,TAC}}{u_o^2} = 2\pi\frac{\mu}{\dot{m}}\frac{N_{ss}w_{ss}}{\Delta_{s_R}}R_i\left(\frac{R_i}{R_o}\right)^2\left[1 + \left(\frac{R_o}{R_i}\right)^3\right] \tag{7.154}$$

Consequently :

$$\zeta_{FL_{TAC}} \propto \left(R_i, \frac{R_o}{R_i}, \frac{1}{\dot{m}}\right) \quad \text{or} \quad \propto \left(R_i, {}^{M}\chi, \frac{1}{\hat{c}}, \frac{1}{\dot{m}}\right) \tag{7.155}$$

Labyrinth seal cavity loss

Since $R_o \cong R_i$, it is possible to write that Eq.6.93 is approximately equal to Eq.6.94. The same is true for Eq.6.95 and Eq.6.96. Assuming again that $h_{ss} << L_j$ the following equation may be retrieved for either rim or disk including both the inlet and outlet face :

$$\mathcal{T}_{CAV} = 2\pi\left(\frac{N_{ss}}{2} - 1\right)L_j \rho f_w \Omega^2 R_i^4 \left(\frac{R_o}{R_i}\right)^4 \tag{7.156}$$

with (Eq.6.90 and Eq.6.89) :

$$\tau_{w,cav} = \frac{1}{2}\rho(\Omega R_o)^2 f_w \tag{7.157}$$

Eq.7.150 then yields :

$$\zeta_{FL_{CAV}} = \frac{h_{t,CAV}}{u_o^2} = 2\pi\left(\frac{N_{ss}}{2} - 1\right)L_j \rho f_w \frac{\Omega R_i^2}{\dot{m}}\left(\frac{R_o}{R_i}\right)^2 \tag{7.158}$$

From the above equation, it is observed that :

$$\zeta_{FL_{CAV}} \propto \left(R_i, \frac{R_o}{R_i}, \Omega, \frac{1}{\dot{m}}\right) \quad \text{or} \quad \propto \left(R_i, {}^{M}\chi, \frac{1}{\hat{c}}, \Omega, \frac{1}{\dot{m}}\right) \tag{7.159}$$

Discussion of results and optimum chord length

The previously obtained equations reveal that in order to minimise the friction losses, the following observations should be borne in mind :

1. Minimise the inlet radius R_i.
2. Minimise the radius ratio R_o/R_i i.e. minimise ${}^{M}\chi$ and maximise $\hat{c}$.
3. Minimise the turbine angular velocity Ω.
4. Maximise the mass flow $\dot{m}$ through the turbine.

As a consequence, $u_i = \Omega R_i$ should be as low as possible, while the radial blade chord c_a and thus chord c (Eq.7.139) should be minimised. From a manufacturing perspective, c should not be lower than c_{min} =2 cm – Antoine & Buysschaert (2014a).
Note however, that a low u_i reduces the deliverable stage power density $P_T^*/\dot{m}$ (Eq.7.28), while limits are imposed to ψ in order to keep the aerodynamic efficiency within an acceptable range. For a given power requirement P_T^*, this will increase $\dot{m}$ and as a result H_b and $\mathit{Æ}R_a$ (Eq.7.127). In as much as the aerodynamic efficiency benefits from a high $\mathit{Æ}R_a$, a

higher H_b impacts the frontal rotor hub area, which might be detrimental to the hub drag. If in addition the number of stages and the stage inlet conditions are imposed, which is a reasonable assumption, selecting a lower R_i and Ω to lower the disk friction losses, will increase the stage work coefficient and inlet flow coefficient (Section 7.1.11). The advantages of low viscous friction ζ_{FL} can consequently be outweighed by the increase in aerodynamic losses ζ_A. From this observation, one may conclude that it is sensible to expect an optimum working point. The trade-off study between the aerodynamic losses on the one hand (Section 7.1.11) and friction losses on the other (this section), is now examined.

7.1.14 Aerodynamic and disk friction losses : a trade-off study

It is important to note that this trade-off study is restricted to the turbine losses. The impact of the rotor hub drag increment due to the increase of the turbine blade height H_b on the helicopter performance is disregarded. Here also, as already discussed in the previous section, it is sensible to abandon a completely non-dimensional study. Indeed, R_i, Ω and $\dot{m}$ are required to quantify the disk friction losses and the non-dimensional parameter group they form in the ζ_{FL}-formulae, viz. Eq.7.152, Eq.7.154 and Eq.7.158, are neither identical, nor of substantial physical significance. The goal of this trade-off study is to establish design tendencies from which important design conclusions can be drawn.

Referring to Section 7.1.3, it was indicated that $\eta_{p,T} = f(\zeta_A, \zeta_{FL}, \psi, S_n)$. The introduction of ζ_{FL} adds several additional parameters that need to be accounted for if a general loss balance is to be examined. Since the rotational velocity u_i is an important parameter for both losses, it intuitive to choose Ω as the first independent variable, being the angular velocity of each rotor half. In the current framework, it is indeed sensible to expect restrictions on R_i while $u_i \propto \Omega$.
Relying on the results of the conceptual performance model in Section 7.1.11, it is possible to write for the aerodynamic losses :

$$^{M}\alpha_i = C^t \quad \Rightarrow \quad \zeta_A = f(^{M}\phi_i,\ \text{Æ}R_a,\ Re) \tag{7.160}$$

It is therefore reasonable to select $^{M}\phi_i$ as the second independent variable in the trade-off study. Note that the aerodynamic loss model used in the trade-off study is identical to the loss model explained in the conceptual performance model (Section 7.1.11), except for the approach to determine $\text{Æ}R_a$ and Re. Here, they will be estimated relying on the independent variables on the one hand, and the variables on which a sensitivity study will be performed on the other. The variables used in the sensitivity study are :

1. R_i : Finding a reasonable dimension for the inlet radius is paramount. It determines the size of all subsequent stages and thus also the evolution of the friction losses. Note also that R_i and Ω determine u_i, which is the term used to (non-)dimensionalise the turbine flow and power characteristics.

2. $\dot{m}$: The mass flow has an important impact on the aerodynamic and friction losses. While it is usually derived from P_T^*, it will be treated here as independent parameter.

3. R_o/R_i : The radius ratio should be selected as low as possible, as was already indicated in Section 7.1.13. Though, the impact on the total loss balance is still to be evaluated. Note that the interstage damping ${}^M\chi$ could also be used here, while the interstage space coefficient $\hat{c}$ is a constant, but it is less intuitive.

4. ${}^M\alpha_i$: The conceptual performance study showed that a limited ${}^M\alpha_i$ range is expected, depending on $Æ_a$ and Re. Its influence must be analysed.

5. π_T : It is interesting to introduce the turbine expansion ratio in the trade-off study, because it is approximately equal to the cycle pressure ratio, which will result from the cycle study. For the trade-off study at hand, the stage inlet temperature has been fixed (Table 7.2). Thanks to this intervention, either Ω or ${}^M\phi_i$ will lose its independency. The graphical solution of the "unidimensional" problem will be shown later by the "operating line".

6. S_n : The number of stages impact the required effective stage work coefficient ψ_S (Eq.7.123) and as a result also the aerodynamic performance. Note however, that the increasing ${}^jR_i$ for each stage is not adopted in this model, i.e. ${}^1R_i = {}^jR_i = C^t$.

The sensitivity study parameters and their respective range are summarised in Table 7.2

Model setup

A flowchart representing the calculation procedure is shown in Fig.7.12. The model calculates the losses in a similar way as the conceptual performance model, but here (Eq.7.150) :

$$\zeta_T = ({}^1\zeta_A + {}^1\zeta_{FL}) + (S_n - 2)({}^M\zeta_A + {}^M\zeta_{FL}) + ({}^L\zeta_A + {}^L\zeta_{FL}) \tag{7.161}$$

Modifying Eq.7.118 according to the above equation gives :

$$\eta_{is,T} = \frac{1}{1 + \frac{\zeta_T}{\psi_T}} \tag{7.162}$$

From the input variables, while currently assuming π_T to be a dependent variable, it is possible to calculate ψ_T using the following relation :

$$\psi_T \approxeq \sum_j {}^j\psi - \sum_j {}^j\zeta_{FL} \approxeq {}^1\hat{\theta}\left(1 - \pi_T^{\frac{1-\gamma}{\gamma}}\right) - \zeta_T \tag{7.163}$$

TABLE 7.2. $\zeta_A - \zeta_{FL}$ sensitivity study range.

π_T	1.25*, 2
R_i	0.3*, 0.6 m
$\dot{m}$	1*, 5 kg/s
S_n	4*, 10
R_o/R_i	1.03*, 1.1
${}^M\alpha_i$	50°*, 65°
T^*_{ti}	110 °C
N_{ss} (Section 6.3.3)	4
t^*_s	0.02 m
w^*_{ss}	0.002 m
h^*_{ss}	0.003 m
$\Delta^*_{s_R}$	0.0003 m
$\Delta^*_{s_h}$	0.01 m
ϵ^*_f	0.0005 m
ρ_e (Eq.7.166)	1.2 kg/m^3
μ_e (Eq.7.171)	$1.8 \cdot 10^{-5}$ Pa.s
$R_g = 287$ J/kgK	$\gamma = 1.4$ [-]

* : *Basis of comparison in sensitivity study.*

$*$: *Early estimations by Antoine & Buysschaert (2014b).*

which yields a value for π_T and $\eta_{is,T}$ (Eq.7.162). Using Eq.7.29, here recalled for reasons of clarity :

$$\psi_T = {}^1\hat{\theta}\left(1 - \pi_T^{\frac{1-\gamma}{\gamma}\eta_{p,T}}\right)$$

the polytropic turbine efficiency $\eta_{p,T}$ may be found as well. At this point and if the variables falling under the sensitivity study are known, the problem is two dimensional, i.e. a function of ${}^M\phi_i$ and Ω. However, since it is instructive to take the cycle pressure ratio into account, a value of π_T is imposed. As a result, ${}^M\phi_i$ and Ω become mutually dependent and the problem is rendered unidimensional. The relation between ${}^M\phi_i$ and Ω can consequently be approximated by (Eq.7.120, Eq.7.123 and Eq.7.163) :

$${}^M\phi_{i_{Ops}} \cong \frac{{}^1\hat{\theta}\left(1 - \pi_T^{\frac{1-\gamma}{\gamma}\eta_{p,T}}\right) + \sum_j {}^j\zeta_{FL}}{2(S_n - 1)\tan {}^M\alpha_i} \cong \frac{{}^1\hat{\theta}\left(1 - \pi_T^{\frac{1-\gamma}{\gamma}\eta_{p,T}}\right)}{2(S_n - 1)\tan {}^M\alpha_i} \tag{7.164}$$

where ${}^M\phi_{i_{Ops}} = f(\Omega)$[iii] the solution of the problem. It should be borne in mind that the use of the above equation implies that $u_i = {}^ju_i$ and hence $R_o/R_i = 1$. Indeed, the

[iii] A function of Ω via $\hat{\theta}$ in Eq.7.29.

sensitivity study will only examine the effects of a varying R_o/R_i on the losses ζ_{FL} and allows retrieving the appropriate range for ζ_A via $Æ_a$ and Re (see subsequent sections), while assuming $R_i = {}^jR_i$. As a consequence, ζ_{FL} will be on the optimistic side. Also ζ_{FL} will be considered low enough with respect to ψ_T, such that finding the optimum by the above simplifications stands. When this is not the case, the solution will yield a low turbine efficiency, which will then be discarded anyway.

$Æ_a$ correction

Thanks to the selection of the variables subjected to the sensitivity study, the blade projected aspect ratio can be determined, as well as the blade Reynolds number. The latter will be discussed in the subsequent section. These parameters are important to estimate the aerodynamic losses in the blade passage (Section 7.1.11).
A mass-flow-based equation for $Æ_a$ may be found by applying the continuity equation and replacing v_{i_R} by the definition of ϕ_i. The following simple relation then follows :

$$Æ_a = \frac{\dot{m}}{2\pi\rho_e\Omega R_i^3\left(\frac{R_o}{R_i} - 1\right)\phi_i} \tag{7.165}$$

Since π_T is rather low for the RELT, it is reasonable to adopt for each stage in the turbine (ISA sea level conditions) :

$$\rho_e = 1.2 \text{ kg/m}^3 \tag{7.166}$$

Re correction

Recalling Soderberg's model (Section 6.1.5), the following Re-correction needs to be performed (Eq.6.27) :

$$\zeta_3 = \left(\frac{10^5}{Re}\right)^{0.25}\zeta_2$$

where, Eq.6.28 and Eq.6.29 :

$$Re = \frac{\rho_{o,b}w_{o,b}D_h}{\mu_{o,b}}$$
$$D_h = \frac{2H_{bo}s\cos\beta_{o,b}}{s\cos\beta_{o,b} + H_{bo}}$$

Writing the blade pitch s as :

$$s = \left(\frac{s}{c_a}\right)c_a \tag{7.167}$$

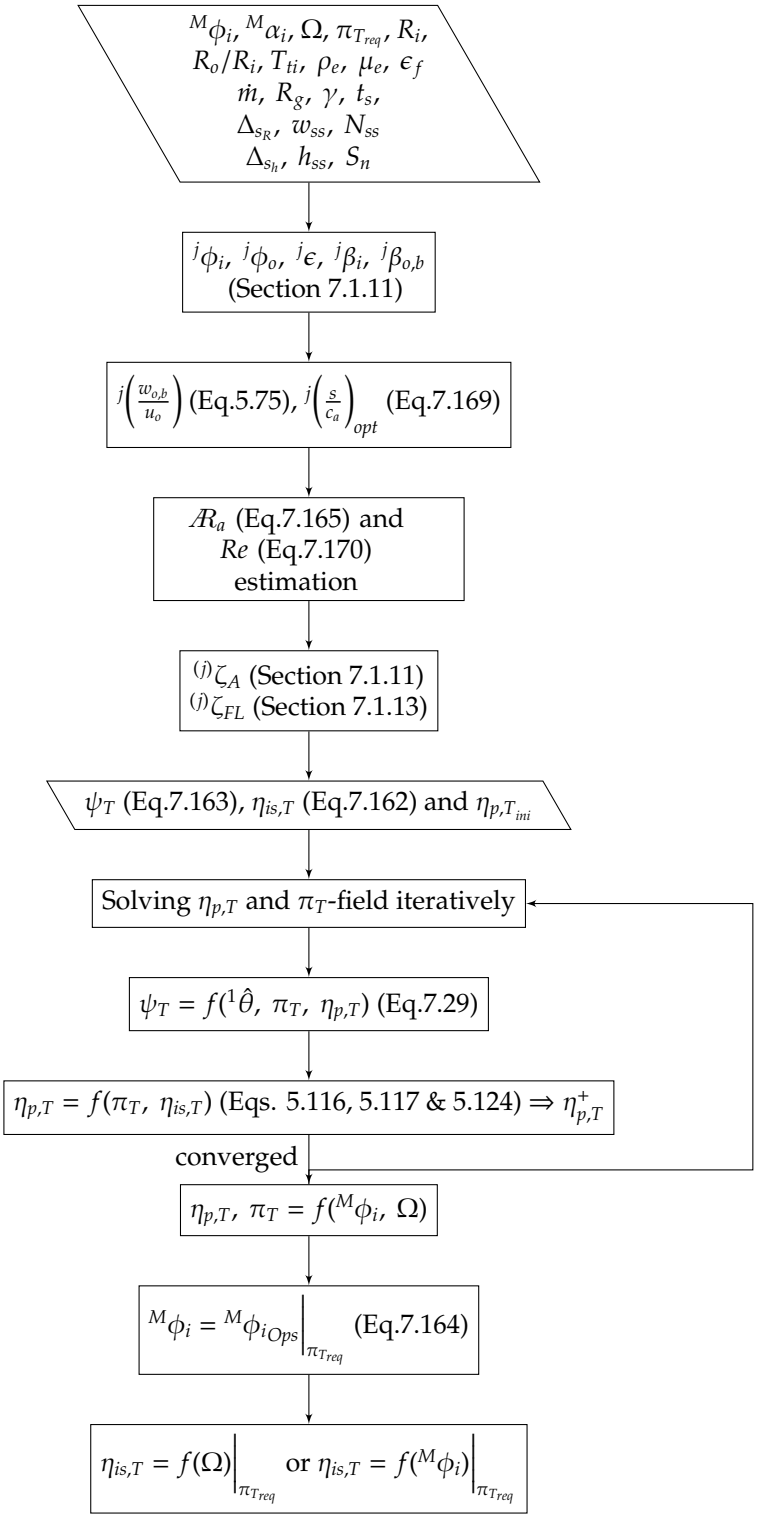

FIGURE 7.12. $\zeta_A - \zeta_{FL}$ trade-off model flowchart.

and substitution of above in Eq.6.29 while applying the definition of $\mathcal{R}_a$ (Eq.5.8) yields :

$$D_h = \frac{2(s/c_a)_{opt}\mathcal{R}_a(R_o - R_i)\cos\beta_{bo}}{(s/c_a)_{opt}\cos\beta_{o,b} + \mathcal{R}_a} \tag{7.168}$$

Since the optimum efficiency is the goal, the optimum pitch-to-chord ratio of Zweifel (1945) can be used, as mentioned by Shaw (1966) :

$$\left(\frac{s}{c_a}\right)_{opt} = \frac{0.425}{(\tan\beta_i - \tan\beta_{o,b})\cos^2\ \beta_{o,b}} \tag{7.169}$$

Substitution of Eq.7.169 in Eq.7.168, and subsequently in Eq.6.28 gives for the Reynolds fraction, after simplifying terms :

$$\frac{Re}{Re_{ref}} = \frac{2}{10^5}\,\frac{\rho_e}{\mu_e}\,\phi_o\,\frac{(s/c_a)_{opt}\,\text{Æ}_a\,R_i^2\left(\frac{R_o}{R_i}-1\right)\frac{R_o}{R_i}\Omega}{(s/c_a)_{opt}\cos\beta_{o,b} + \text{Æ}_a} \tag{7.170}$$

Again, since the temperature change over the complete turbine is rather low, a value for μ_e applicable to each turbine stage will be used, i.e. – Walsh & Fletcher (2004) :

$$\mu_e \approxeq 1.8 \cdot 10^{-5}\ \text{Pa.s} \tag{7.171}$$

The calculation of Æ_a and Re now allows estimating the aerodynamic losses for a specific operating condition.

Sensitivity study assessment

The sensitivity study is performed graphically using the data in Table 7.2 and compared with the base data indicated therein with a "$\star$". For matters of readability, only the graphical representation of the effect of π_T and R_i will be shown for the selected independent variables ${}^M\phi_i$ and Ω (Fig.7.13 – Fig.7.18). The impact of the other parameters in the sensitivity study will be discussed, but their graphical representation is presented in Appendix E.

Fig.7.13 & Fig.7.14 show the influence of the independent variables ${}^M\phi_i$ and Ω on $\eta_{is,T}$. The angular velocity Ω is for matters of convenience represented by N in revolutions per minute :

$$N = \frac{\Omega}{2\pi}60$$

The observed behaviour of $\eta_{is,T}$ can be better understood via Fig.7.15 & Fig.7.16, wherein the turbine aerodynamic enthalpic loss ζ_{AT} and disk friction enthalpic loss ζ_{FLT} are represented. Clearly, an increase in angular velocity N for a given ${}^M\phi_i$ and thus – following the previously adopted simplifications – ψ_T, always increases ζ_{AT} and ζ_{FLT} and will consequently reduce $\eta_{is,T}$. Analysis of Fig.7.17 & Fig.7.18 uncovers that ζ_{AT} is in fact penalised by the decreased Æ_a, regardless the positive impact of a higher N on the flow Reynolds number. Indeed, for a given ${}^M\phi_i$ and $\dot{m}$, selecting a higher N results in higher radial flow velocities, which explains the previously mentioned effect (Eq.7.165 & Eq.7.170).

A decrease in ${}^{M}\phi_i$ on the other hand, and thus ${}^{M}\psi$ (gray lines on the figures) and ψ_T, reduces ζ_{AT} for a given angular velocity because the increase in $\mathit{Æ}_a$ (Eq.7.165) and decrease in ϵ (Eqs. 7.113, 7.114 and 7.115) have a more substantial positive impact on the aerodynamic losses than the deteriorating effect caused by the decreasing Re (Eq.7.170, Fig.7.17). The fact that ζ_{FLT} then becomes more important than ζ_{AT} is considered to be partially the reason for the flattening of the iso-efficiency lines in Fig.7.13 & Fig.7.14. The tendency of an increasing Re for the very low ${}^{M}\phi_i$ further amplifies the previously mentioned phenomenon (significant drop in ζ_{AT}), which is due to the $\cos\beta_{o,b}$ effect in Eq.7.170, where $\beta_{o,b}$ becomes high due to the lower deflection. However, $\eta_{is,T}$ will eventually drop for the lower ${}^{M}\phi_i$ because then ψ_T goes to zero (Eq.7.162), while the losses for a non-zero rotational velocity, will not.

The decision to impose a turbine expansion ratio, makes the rotational velocity a function of ${}^{M}\phi_i$, as was already discussed earlier. For a fixed turbine configuration, it is consequently possible to show that, following Eq.7.164 :

$$ {}^{M}\phi_{i_{Ops}} \propto \frac{1}{N^2} \tag{7.172} $$

From the above examinations, it is then reasonable to expect an optimum efficiency due to the interaction of an initial tendency to increase the efficiency by selecting a low ${}^{M}\phi_i$, which – following Eq.7.172 – imposes a high rotational velocity, and where the latter condition yields a tendency to decrease the efficiency instead. This efficiency optimum appears clearly when plotting the valid operating conditions in Fig.7.13 and Fig.7.14. These operating conditions are indicated by a green line and further referred to as *operating line* (Eq.7.164). Fig.7.13 and Fig.7.14 then also reveal the existence of an optimum u_i ($u_{i,opt}$) for which $\eta_{is,T}$ is maximised. If maximum efficiency is strived for, then it is possible to select the values of ${}^{M}\phi_{i_{opt}}$ and N_{opt} at which the turbine should operate. Note however that N_{opt} appears to be rather high. Working at N_{opt} can consequently not be guaranteed since N is also limited by the maximum rotor blade tip speed v_{tip} and the imposed rotor radius R_{tip}. This discussion is conducted later. The impact of the other variables in the scope of the sensitivity study is summarised next.

Inlet radius R_i The impact of increasing R_i causes :

- → a general and significant reduction of $\eta_{is,T}$ along the operating line
- → a downward shift of the operating line because (Eq.7.164) : if ${}^{M}\phi_i = C^t \Rightarrow {}^{1}\hat{\theta} = C^t \Rightarrow u_i = C^t \Rightarrow N \searrow$; the decrease in $\eta_{is,T}$ amplifies this effect
- → in general, no significant impact on $u_{i,opt}$

Conclusion : R_i should be minimised.

Turbine expansion ratio π_T The impact of increasing π_T causes :

→ a general reduction of $\eta_{is,T}$ along the operating line

→ an upward shift of the operating line because (Eq.7.164) : if ${}^{M}\phi_i = C^t \Rightarrow {}^{1}\hat{\theta} \searrow \Rightarrow u_i \nearrow \Rightarrow N \nearrow$; the decrease in $\eta_{is,T}$ reduces this effect

→ an increase in $u_{i,opt}$

Conclusion : π_T should be minimised.

Mass flow $\dot{m}$ The impact of increasing $\dot{m}$ causes :

→ a general improvement of $\eta_{is,T}$ along the operating line

→ a slight upward shift of the operating line since (Eq.7.164) : if $\eta_{p,T} \nearrow \Rightarrow {}^{1}\hat{\theta} \searrow \Rightarrow N \nearrow$

→ an increase in $u_{i,opt}$

Conclusion : for maximum $\eta_{is,T}$ it is beneficial to increase $\dot{m}$. However, $u_{i,opt}$ is high.

Stage outlet-to-inlet radius ratio R_o/R_i An increase in R_o/R_i results in :

→ a general and important reduction in $\eta_{is,T}$ along the operating line

→ a slight downward shift of the operating line since (Eq.7.164) : if $\eta_{p,T} \searrow \Rightarrow {}^{1}\hat{\theta} \nearrow \Rightarrow N \searrow$

→ no significant changes of $u_{i,opt}$

Conclusion : R_o/R_i should be minimised.

Stage number S_n An increase in stages causes :

→ a general improvement of $\eta_{is,T}$ along the operating line

→ a downward shift of the operating line (Eq.7.164) : if ${}^{M}\phi_i = C^t \Rightarrow \psi_T \nearrow \Rightarrow {}^{1}\hat{\theta} \nearrow \Rightarrow N \searrow$

→ a decrease in $u_{i,opt}$

Conclusion : S_n should be maximised. However, this observation will appear to be only applicable when ${}^{j}R_i$ is significantly low.

Middle stage absolute inflow angle ${}^{M}\alpha_i$ Increasing ${}^{M}\alpha_i$ causes :

→ a slight improvement of $\eta_{is,T}$ along the operating line

→ a downward shift of the operating line (Eq.7.164) : if ${}^{M}\phi_i = C^t \Rightarrow \psi_T \nearrow \Rightarrow {}^{1}\hat{\theta} \nearrow \Rightarrow N \searrow$

→ no significant impact on $u_{i,opt}$

Conclusion : ${}^{M}\alpha_i$ should be taken around 65°

From the above considerations, the following observations and design recommendations may be established :

1. Coupling the aerodynamic losses with the friction losses showed the existence of an optimum rotational speed $u_{i,opt}$. This value should be strived for, but is constrained by the helicopter rotor design criteria. Also, its accuracy is constrained by the model simplifications. It is therefore an *indicative* value.

2. The trade-off study appears to encourage a high number of stages S_n. However, the impact of increasing ${}^{j}R_i$ for each stage has not been taken into account. The negative impact of large R_i has shown to be of concern (see also Section 7.1.13). A low R_i is therefore indispensable in case a large amount of stages is endeavoured in order to keep $\eta_{is,T}$ within acceptable terms.

3. The ${}^{M}\alpha_i$-range established with the conceptual performance model may be reduced to a single value around 65°, while relying on the earlier rules of thumb for the optimum ${}^{M}\alpha_i$ range in Section 7.1.11.

4. A good compromise for a required P_T^* would be a low π_T favouring a high $\dot{m}$ – of course, within the limits allowed by the TDR-cycle study, while selecting R_i as high as reasonably possible to keep N reasonably low and $\eta_{is,T}$ within acceptable standards. A high $\dot{m}$ (high power output) will be essential to obtain acceptable values for $\eta_{is,T}$, i.e. ≥ 0.8. Though, it should not be selected too high either in order to keep the blade height within the margins of a low rotor hub drag.

Table 7.3 reflects the range of $u_{i,opt}$ obtained during the sensitivity study. Clearly, $u_{i,opt}$ varies with the selected design criteria and most under the effects of π_T, $\dot{m}$ and S_n. It remains to answer the question as to whether $u_{i,opt}$ lies within the designer's reach. Indeed, the maximum usable $u_{i,max}$ depends on helicopter rotor design criteria. This study is performed next.

Table 7.3. $u_{i,opt}$-range from sensitivity study.

Sensitivity parameters		$u_{i,opt}$ **[m/s]**
base	$\pi_T = 1.25$	39
	$\pi_T = 2$	55 (±)
$\dot{m} = 5$ kg/s	$\pi_T = 1.25$	52
	$\pi_T = 2$	80
$R_o/R_i = 1.1$	$\pi_T = 1.25$	35 (±)
	$\pi_T = 2$	50 (±)
$S_n = 10$	$\pi_T = 1.25$	26
	$\pi_T = 2$	38 (±)
${}^{M}\alpha_i = 65°$	$\pi_T = 1.25$	36
	$\pi_T = 2$	54 (±)

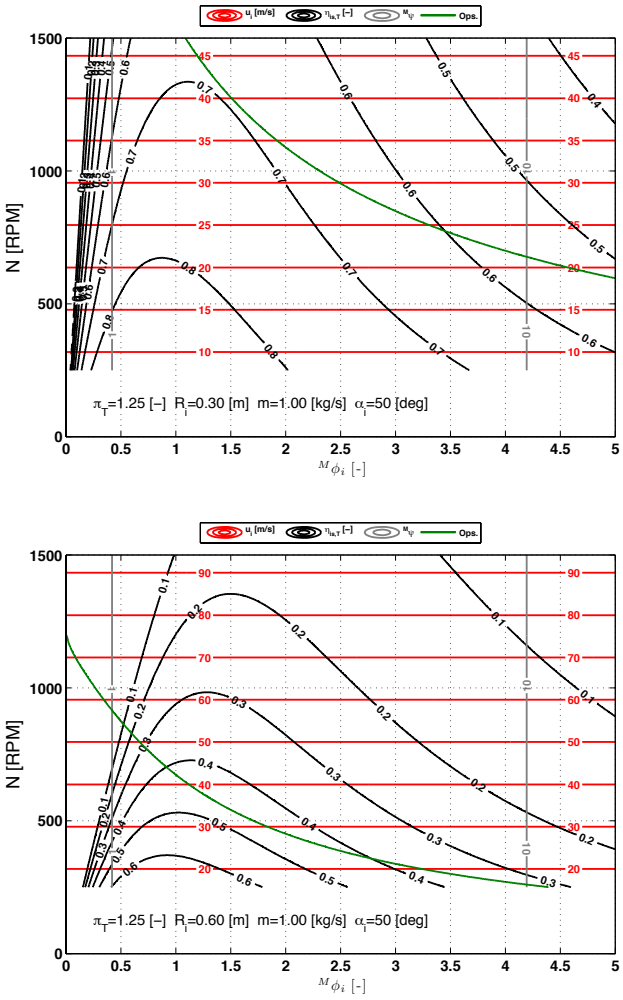

FIGURE 7.13. Sensitivity study on π_T and R_i - others are base parameters.

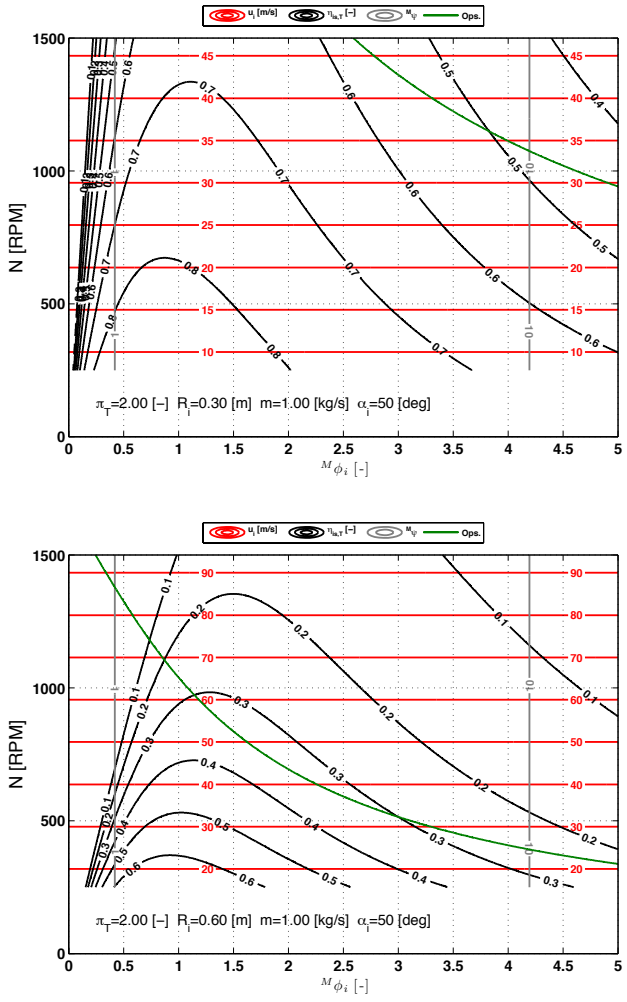

FIGURE 7.14. Sensitivity study on π_T and R_i continued - others are base parameters.

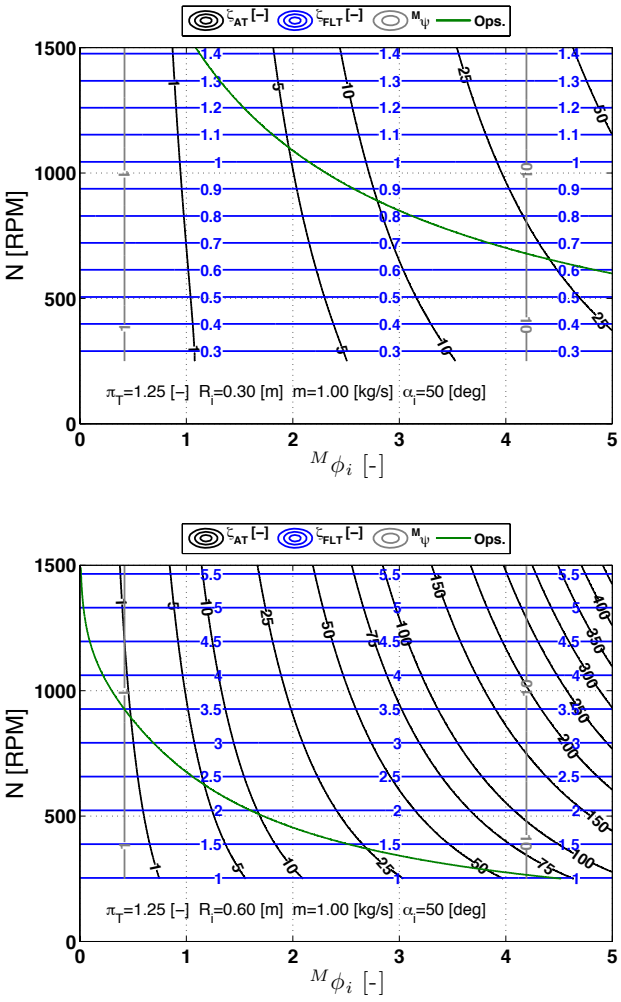

FIGURE 7.15. Sensitivity study on π_T and R_i - others are base parameters.

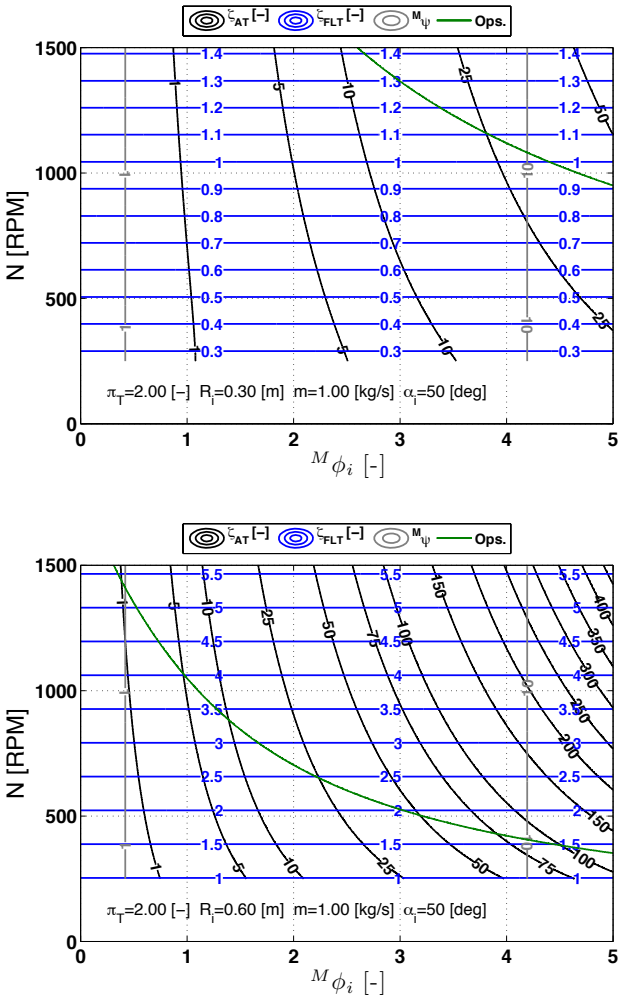

FIGURE 7.16. Sensitivity study on π_T and R_i continued - others are base parameters.

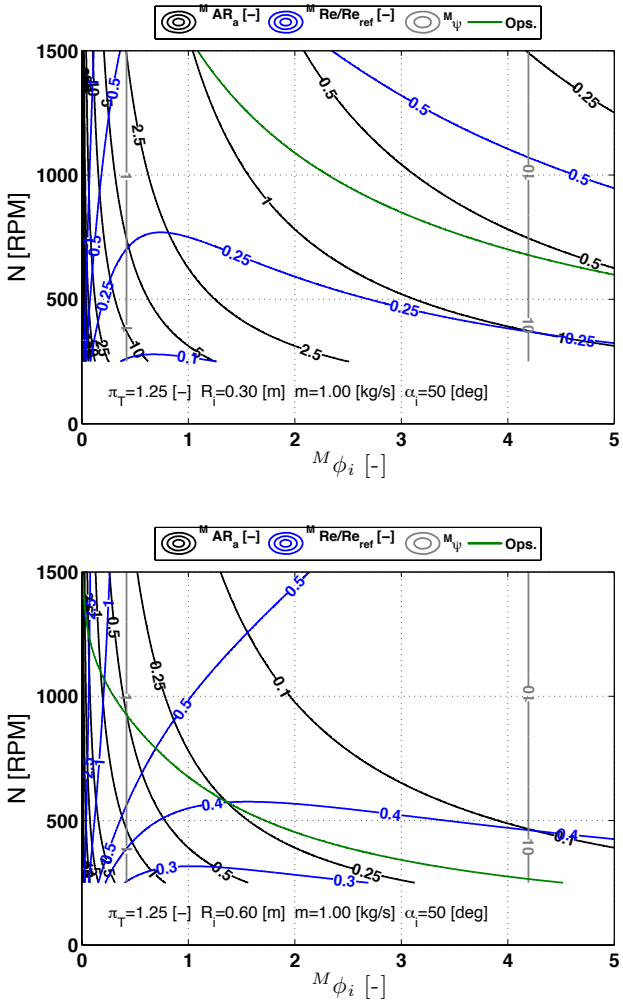

FIGURE 7.17. Sensitivity study on π_T and R_i - others are base parameters.

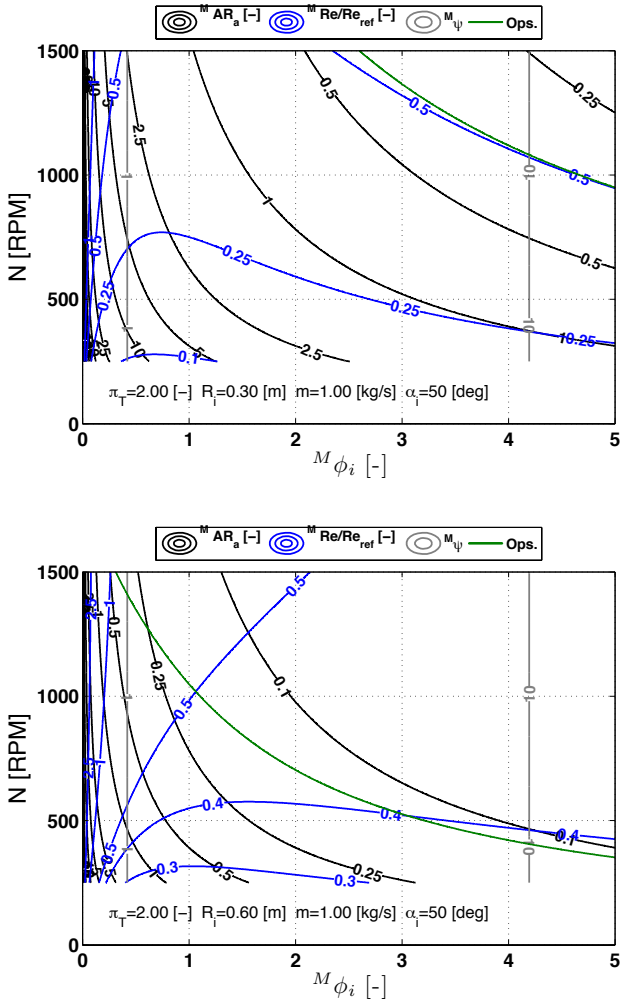

FIGURE 7.18. Sensitivity study on π_T and R_i continued- others are base parameters.

Maximum turbine inlet speed and specific inlet radius

From the previous discussions, the importance of ${}^1u_i$ became clear. Choosing ${}^1u_i$ high will allow more power to be extracted per turbine stage, but will not necessarily lead to the optimum configuration. In the case that $u_{i,opt}$ is high, it is not necessarily feasible.
In the loss trade-off study, values for $u_{i,opt}$ were found graphically by means of the operating line considering the turbine angular speed Ω as a function of ${}^M\phi_i$, which was most intuitive. At this point, it is interesting to focus the discussion on the integration of a Ljungström turbine in a helicopter rotor. Generally, the rotor angular speed is fixed, which is consequently imposed on the turbine. Then, modifying ${}^1u_i$ is only possible by changing ${}^1R_i$. While the trade-off study highlighted that the latter parameter should remain as low as possible, it is also subjected to an optimum in case Ω is kept constant instead. The reasoning to explain this optimum is similar to the one expounded in the previous section with varying Ω (${}^1u_i = \Omega\ {}^1R_i$). Graphical proof of this optimum will be shown later in Chapter 8. However, there are restrictions on the magnitude of ${}^1R_i$, and thus ${}^1R_{i,opt}$ and $u_{i,opt}$, because of helicopter rotor power concerns. This is discussed next, while a working range for ${}^1R_{i(,opt)}$ and $u_{i(,opt)}$ is established.

The turbine drives the helicopter rotors directly, of which the tip speed is limited. From the study in Section 2.2.2, the average tip speed of helicopter rotors is :

$$v_{tip} = 215 \text{ m/s} \tag{7.173}$$

or under ISA SLS conditions :

$$M_{tip} \approxeq 0.63$$

The inlet of the Ljungström turbine is positioned at ${}^1R_i$ and as a consequence :

$$\overline{r_i} \triangleq \frac{{}^1R_i}{R_{tip}} = \frac{{}^1u_i}{v_{tip}} \tag{7.174}$$

where $\overline{r_i}$ is defined as the turbine specific inlet radius. The higher $\overline{r_i}$ the larger the hub size with respect to the rotor disk area and consequently the more power is required to lift the helicopter (hover), while a larger frontal drag is expected during forward flight. Imposing a maximum $\overline{r_i}$ is therefore sensible. In this work $\overline{r}_{imax}$ is obtained by comparing the ideal power consumption of a rotor with and without hub in hover. The ideal power is calculated considering a uniform downwash below an actuator disk, which represents both rotors. Indeed, according to Stepniewski & Keys (1984) and Johnson (1994), coaxial rotor power calculations may be conducted using the single rotor theory in case the following condition is met (Fig.7.19) :

$$\Delta z_r \leq 0.1\ R_{tip} \tag{7.175}$$

The TDR rotor configuration meets this requirement. From the actuator disk theory, it is then found that for a rotor without hub[iv] ($R_H = 0$) – Johnson (1994) :

$$P_{i,nh} = \sqrt{\frac{W_g^3}{2\rho A_{R,nh}}} \tag{7.176}$$

and,

$$A_{R,nh} = \pi R_{tip}^2 \tag{7.177}$$

where $P_{i,nh}$ the induced rotor power without hub, W_g the helicopter gross weight, ρ the atmospheric density and $A_{R,nh}$ the rotor disk area of the rotor with no hub. Similarly, for the TDR helicopter with hub radius R_H, it is found that – Johnson (1994) :

$$P_i = \sqrt{\frac{W_g^3}{2\rho A_R}} \tag{7.178}$$

and,

$$A_R = \pi(R_{tip}^2 - R_H^2) \tag{7.179}$$

where P_i and A_R respectively the induced power and disk area of a rotor with hub. For a given helicopter weight and atmospheric density, the induced power difference between rotor with and without hub can be expressed as :

$$\frac{P_i}{P_{i,nh}} = \left[1 - \left(\frac{R_H}{R_{tip}}\right)^2\right]^{-1/2} = \left[1 - \left(\frac{{}^L R_o}{R_{tip}}\right)^2\right]^{-1/2} \tag{7.180}$$

It can be proven that using Eq.7.55, while knowing that $R_o/R_i = C^t$ (Eq.7.57) and $\hat{c} = C^t$ (Eq.7.55) for all stages :

$${}^L R_o = \hat{i}^{\frac{S_n - 1}{2}} \left(\frac{R_o}{R_i}\right)^{S_n} {}^1 R_i \tag{7.181}$$

Since $\hat{i} \cong 1$, it is possible to write after substitution of Eq.7.181 in Eq.7.180 and developing terms :

$$\frac{P_i}{P_{i,nh}} = \left\{1 - \left[\overline{r_i}\left(\frac{R_o}{R_i}\right)^{S_n}\right]^2\right\}^{-1/2} \tag{7.182}$$

Eq.7.182 is plotted in Fig.7.20. In case an induced power increase of 5 – 10% is tolerated

[iv] Rotor blade root cutout conditions will not be considered here. A rotor without hub then implicitly uses blades without root cutout.

due to the presence of a hub, then the design rule becomes :

$$\overline{r_i} = [0; 0.25 - 0.40] \tag{7.183}$$

An acceptable range for the turbine inlet radius ${}^1R_{i(,opt)}$ may then be determined by ${}^1R_i = \overline{r_i} R_{tip}$. The maximum allowable inlet rotational speed of the turbine then is :

$${}^1u_{i,max} = 0.25 - 0.4\, v_{tip} \tag{7.184}$$

Finally note the impact of the number of turbine stages (Eq.7.182). Logically, the more stages installed, the smaller R_o/R_i needs to be to attain the same hub size and thus induced power ratio.

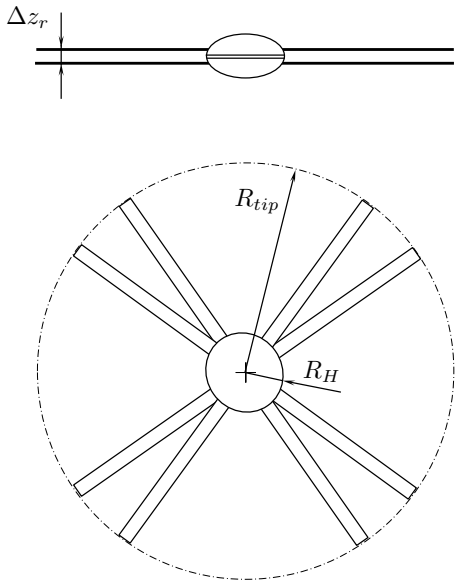

FIGURE 7.19. TDR rotor specifications.

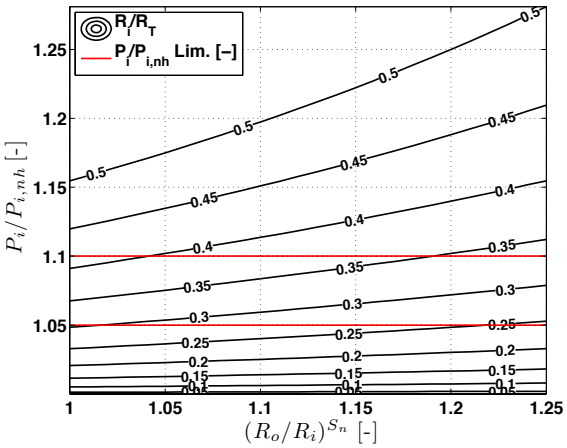

FIGURE 7.20. Effect of turbine specific inlet radius $\overline{r_i}$ and R_o/R_i on rotor induced power consumption.

7.1.15 Detailed design model

The design of the Ljungström turbine requires that the designer knows the following essential design specifications :

1. the power required by the coaxial rotor P_T^*
2. an estimation of the expansion ratio π_T required over the turbine, obtained from the TDR-cycle analysis
3. the turbine inlet temperature ${}^1T_{ti} = LTIT$, determined by the cycle study and limited by the maximum rotor bearing temperature
4. the rotor tip radius R_{tip} and rotor tip speed v_{tip}, imposing the turbine angular velocity

P_T^* is obtainable from an aerodynamic study of the helicopter rotor, where the helicopter performance characteristics play an important role. This study will not be conducted here. The procedures to be followed in order to obtain the turbine geometry are discussed in the subsequent sections.

Turbine design procedure

Here, a methodology is proposed to develop the geometry of a RELT for a given required rotor power and blade tip radius. The design procedure is essentially subdivided into three steps :

1. **Predesign** (Fig.7.21). This step couples the conceptual design theory with the $\zeta_A - \zeta_{FL}$ trade-off study to estimate the number of required stages S_n, the turbine inlet rotational speed u_i, the middle stage flow coefficient ${}^M\phi_i$ and providing an estimation of the turbine efficiency.
2. **Dimension and efficiency determination** (Fig.7.22). The results from the predesign step are introduced in the $D - \eta$ loop to obtain *near-target* design parameters for the turbine. Indeed, since the predesign step provides a rough estimation of the design parameters, the design targets will generally not be perfectly met using the detailed calculation procedures.
3. **Finetuning** (Fig.7.22). $\dot{m}$, ${}^M\phi_i$ and ${}^M\chi$ are slightly changed in order to meet the imposed power requirement P_T^* and ${}^Lp_o = p_a$.

A discussion of each step is now conducted.

Predesign

The predesign procedure is necessary to provide the designer with :

$\rightarrow$ the optimum specific inlet radius $\overline{r_i}$

→ the required flow coefficient ${}^{M}\phi_i$

→ the required amount of turbine stages

→ an order of magnitude for the attainable turbine efficiency $\eta_{p,T}$

The flowchart in Fig.7.21 highlights the calculation procedure leading to the above predesign requirements. First, the upper value for $\overline{r_i}$ is selected ($\overline{r_{imax}}$), based on the design recommendations of Eq.7.183. Since the angular speed of the turbine is identical to the angular speed of the concurring rotor half, it is possible to state that :

$$\Omega = \frac{v_{tip}}{R_{tip}} = \frac{{}^{j}u_i}{{}^{j}R_i} \tag{7.185}$$

Adopting a value for $\eta_{p,T}$ consequently allows retrieving a value for ψ_T. If a conservative value for ${}^{M}\psi$ is chosen (${}^{M}\psi_{tg}$), it is then possible to estimate the number of turbine stages S_n. Examining Fig.7.3 and Fig.7.4, it appears reasonable to select ${}^{M}\psi_{tg} \cong 1$ for this purpose. Since a maximum value for $\overline{r_i}$ is used initially, the model will start with the least possible number of stages and thus smallest turbine, which is interesting from a weight and cost perspective. In Section 7.1.14, it was found that ${}^{M}\alpha_i \cong 65°$ is generally acceptable, while $R_o/R_i \cong 1.03$ is assumed to be a good basis to perform the trade-off study, since as a rule $R_i >> c_a$. The trade-off model discussed in Section 7.1.14 is then used to find the optimum values for $\overline{r_i}$, ${}^{1}u_i$ and ${}^{M}\phi_i$. With the optimum values for ${}^{M}\phi_i$, $\overline{r_i}$ and ${}^{1}\hat{\theta}$, a new estimation for ${}^{M}\psi$ and ψ_T can be executed, which allows verifying the acceptability of the chosen initial value for S_n. The trade-off study delivers $\overline{r_{iopt}}$, which must be compared with the maximum allowable value $\overline{r_{imax}}$. In the case that $\overline{r_{iopt}} < \overline{r_{imax}}$, $\overline{r_{iopt}}$ can be retained. If $\overline{r_{iopt}} > \overline{r_{imax}}$ it is not possible to meet the optimum position, unless $\overline{r_i}$ is increased. Generally, increasing $\overline{r_i}$ should be discouraged because of the detrimental effects on the rotor induced power P_i (Eq.7.178). Finding a suitable predesign is essential and requires the predesign loop to be executed until a reasonable value for $\eta_{p,T}$ is achieved. For high-power turbines, the mass flow $\dot{m}$ will generally be high, as well as the efficiency. The blade height H_b might become an issue under these conditions, as will be discussed later. Modifying ${}^{M}\alpha_i$ may then appear necessary, sacrificing $\eta_{p,T}$ on the one hand and gaining a lower hub drag on the other.

Dimension and efficiency determination

Once the predesign loop is completed, it is possible to introduce the obtained values to a detailed design model, which calculates the aerodynamic and disk friction losses in detail using the theory expounded in Chapter 6 and the non-simplified theory derived at the beginning of Section 7.1. The flowchart in Fig.7.22 represents this calculation procedure ($D-\eta$ loop). First, a value for ${}^{M}\chi$ is adopted, which takes the impact of the radius change and interstage matching criteria into account. ${}^{M}\chi$ should be chosen as low as possible in order to obtain reasonable chord dimensions (a low ${}^{M}\chi$ results in a small blade chord

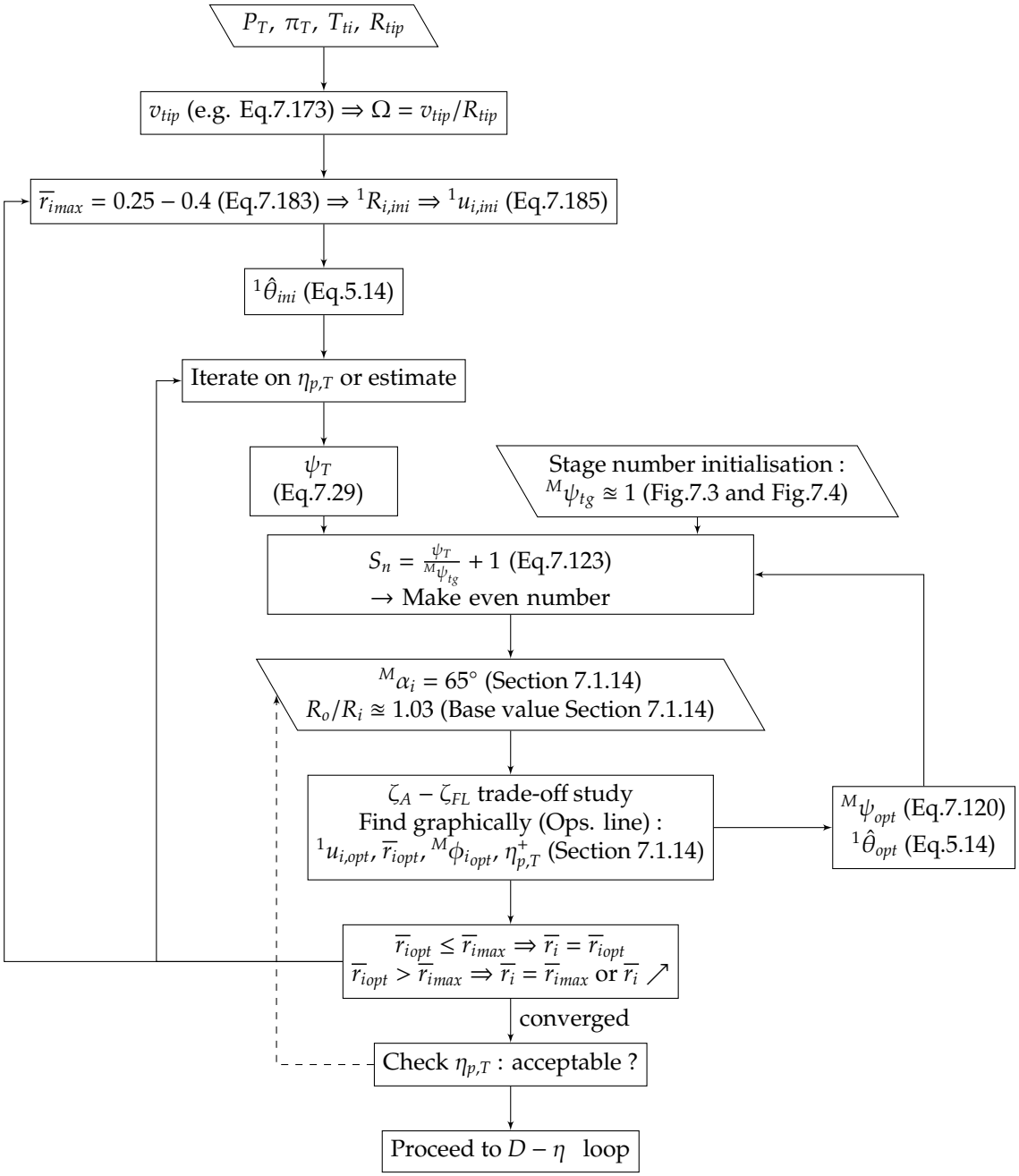

FIGURE 7.21. Predesign loop.

c) and thus low disk friction losses (Section 7.1.13). In case the obtained efficiency is not satisfactory, a lower ${}^M\chi$ may be selected, which decreases the impact of ζ_{FL}, while another stage count might appear considerable from either an aerodynamic viewpoint (lower/higher stage loading) or a disk friction viewpoint (lower/higher friction). Should S_n change, it will change ${}^M\phi_i$ substantially requiring the design process to go back to the predesign stage. In case the efficiency is found acceptable, the design process may continue to the finetuning procedure. If H_b is found to be too high with respect to the rotor blade radius, it is sensible to address the issue by modifying S_n, ${}^M\alpha_i$ or π_T. This

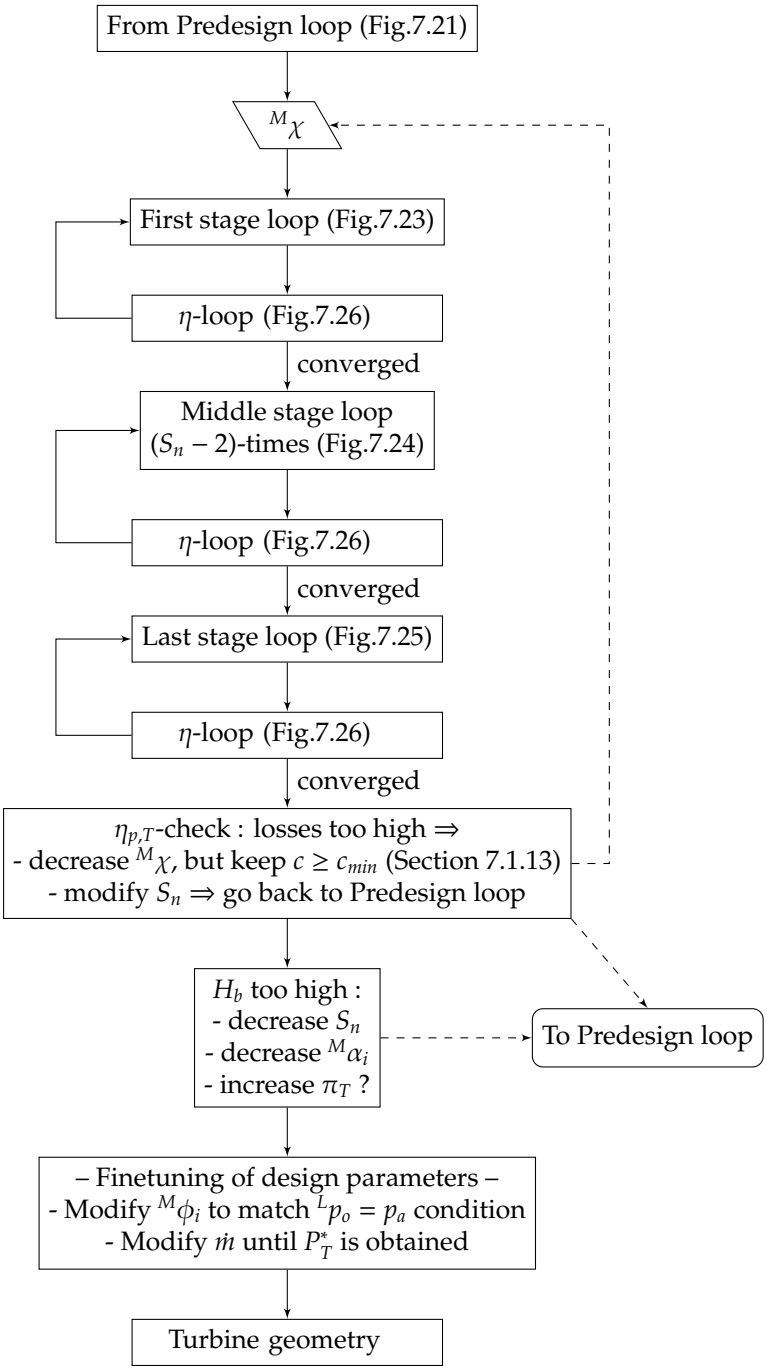

FIGURE 7.22. $D - \eta$ loop.

topic is discussed later. Prior to covering the last step in the design process (Finetuning), the *η-loop*, *First stage loop*, *Middle stage loop* and *Last stage loop* with concurring subloops, (Fig.7.22) will be discussed briefly.

The purpose of the first (Fig.7.23), middle (Fig.7.24) and last (Fig.7.25) stage loops is to calculate the required flow and geometric conditions of the concurring blade passage

type, necessary to satisfy the imposed design criteria, while considering a given blade passage polytropic efficiency ($\eta_{p,Tb}$). The blade passage polytropic efficiency as well as the stage polytropic efficiency, are subsequently established by the η-loop (Fig.7.26), of which the result is reintroduced in the first/middle/last stage loop until convergence is obtained. Note that the effect of the presence of disk friction losses is assumed to affect the total stage outlet temperature solely, a consequence from the discussion conducted in Section 6.5.2 and Section 7.1.1. As a result, the impact of the disk friction losses needs only to be introduced to $\hat{\theta}$ of the subsequent stage.

In the η-loop, the flow deflection δ is calculated by means of the δ-loop (Fig.7.27), enabling the definition of the geometric blade outlet angle $\beta_{b,o}$ and thus the geometry of the blade passage. The δ-loop is similar to the β-loop (Fig.6.5), but now the geometry is calculated from the required flow conditions.

The purpose of the flowcharts in Fig.7.22–Fig.7.27 is to serve as a comprehensive summary of the conducted calculations, performed in *MATLAB*. The abbreviations used in the flowcharts may be found in Chapter 5 and 6.
Finally, it is important to note that the author used the optimum blade pitch-to-chord $(s/c)_{opt}$ correlation proposed by Ainley & Mathieson (1955), and mentioned by Aungier (2006), to calculate the blade number Z (see Fig.7.27). It is discussed in Appendix F. The reason why the model of Ainley & Mathieson (1955) was preferred over the model of Zweifel (1945) for the detailed design procedure, is due to the fact that Aungier (2006) has found the former model to be more reliable and consistent than the latter. Also, in the η-loop, the designer acquires values for the leakage mass flow $\dot{m}_{LL}$ and the stage outflow angle α_o influenced by the losses (Section 6.5.3). Even though the effect of both on the outflow angles was neglected in the design procedure (Section 7.1.1), it is still important to substantiate the applicability of the adopted simplifications.

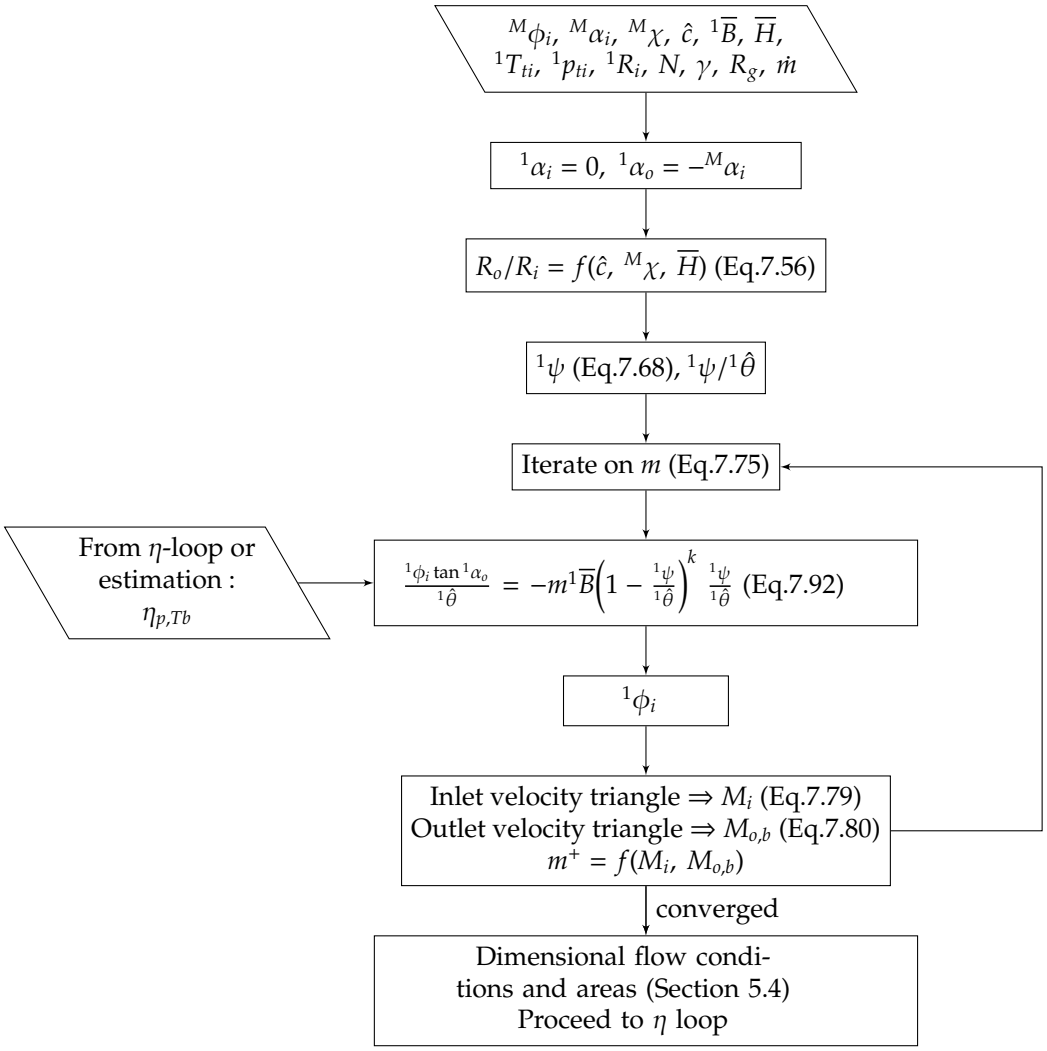

FIGURE 7.23. First stage loop.

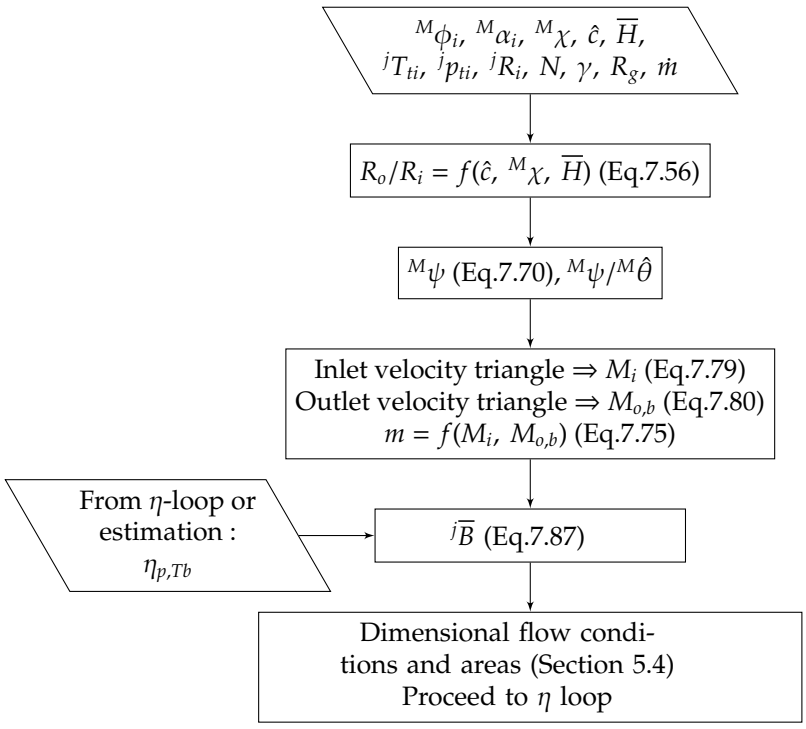

FIGURE 7.24. Middle stage loop.

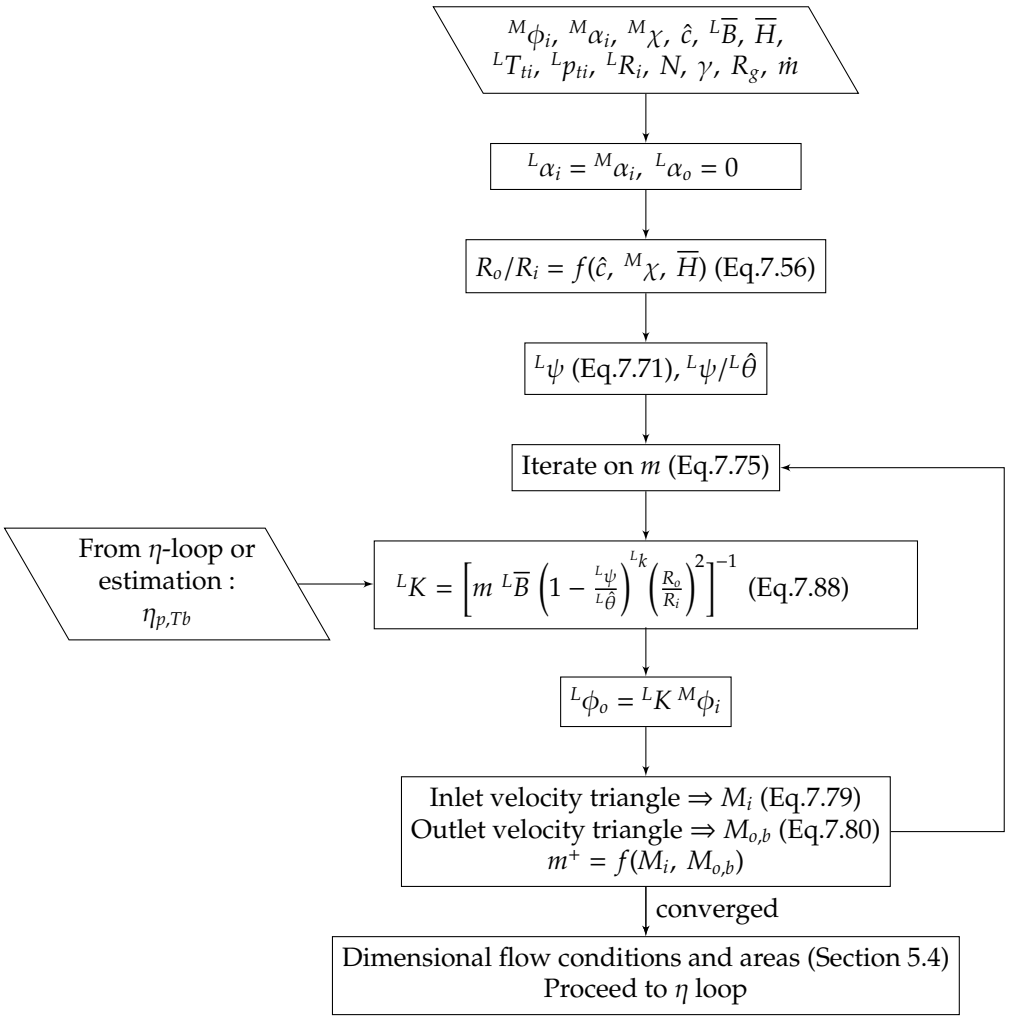

FIGURE 7.25. Last stage loop.

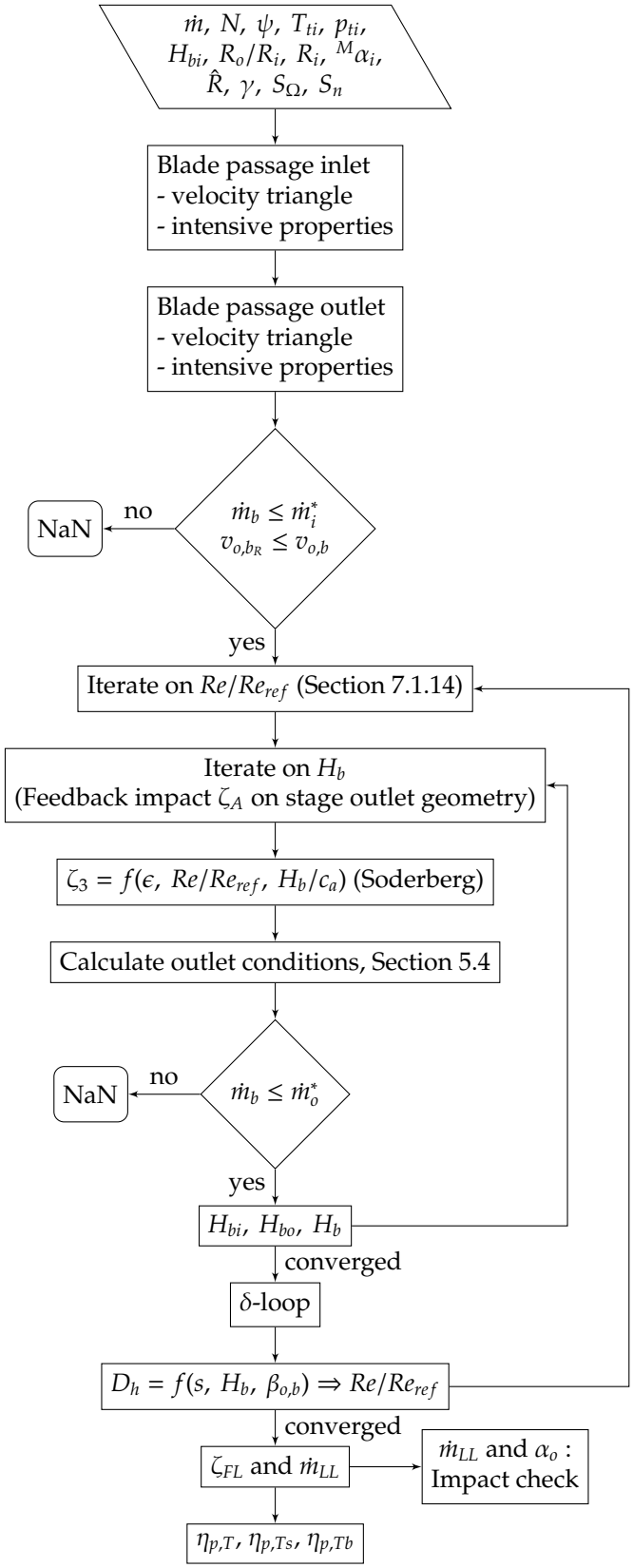

Figure 7.26. η-loop.

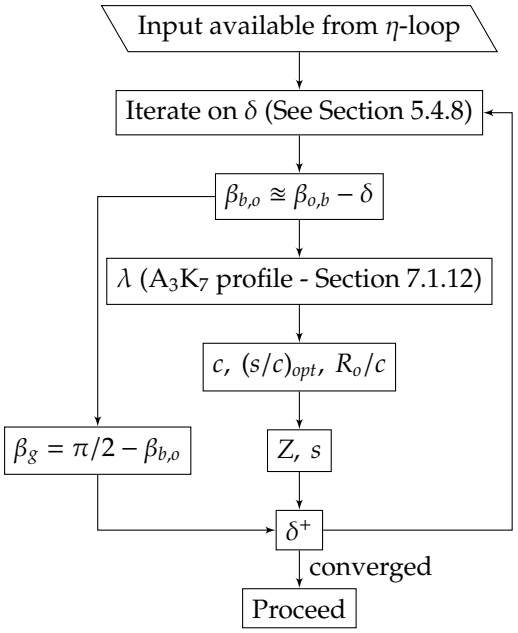

FIGURE 7.27. δ-loop.

Finetuning

The obtained turbine power P'^{*}_{T}-value resulting from the detailed loss calculations – the *prime* symbol ' indicating the calculated values by the model – differs usually from the required P^{*}_{T}. This is mainly due to the assumption that $\pi_T = \pi_C$ (Eq.7.26). Indeed, it is sensible that $\pi_T < \pi_C$ through the increased kinetic energy of the expelled gasses, i.e. ${}^{L}p_{to} > p_a$. Recalling Eq.7.28 :

$$P^{*}_{T} = \dot{m}\ {}^{1}(u_i^2\hat{\theta})\left[1 - \left(\frac{1}{\pi_T}\right)^{\frac{\gamma}{\gamma-1}\ \eta_{p,T}}\right]$$

The clear result of a lower π'_T is a decrease in P'^{*}_{T}. Additionally, since $\dot{m}$ is initially calculated via $\pi_T = \pi_C$, it will also be underrated, while ${}^{M}\phi_i$ overrated. As a consequence, ${}^{L}p'_o < p_a$. The Finetuning procedure accounts for this issue. First, ${}^{M}\phi_i$ is modified such that ${}^{L}p_o = p_a$. Indeed, increasing/decreasing ${}^{M}\phi_i$ will increase/decrease the stage loading ψ_T (Section 7.1.6). In a second phase, $\dot{m}$ is modified such that $P'^{*}_{T} = P^{*}_{T}$. Note that there exists a cross-coupling between $\dot{m}$ and ${}^{M}\phi_i$ (via π_T and $\eta_{p,T}$, Eq.7.28). However, the cross-coupling effect remains usually minor since the initial values for π'_T and $\eta'_{p,T}$ are near convergence. As a consequence and under the given circumstances, ${}^{M}\phi_i$ and $\dot{m}$ may be approached as independent variables. Once the design specifications are met, it is possible to establish the complete turbine geometry.

Blade height limitation

The height of the turbine blades may become problematic in case a high-power turbine is developed. Indeed, since the recommended TDR-cycle pressure ratio is low, a high mass flow will be required. Rewriting Eq.7.28 :

$$\dot{m} = \frac{P_T}{{}^{1}(u_i^2\hat{\theta})\left[1 - \left(\frac{1}{\pi_T}\right)^{\frac{\gamma}{\gamma-1}\ \eta_{p,T}}\right]} \tag{7.186}$$

where ${}^{1}u_i$ is limited by v_{tip} and $\overline{r}_i$, and ${}^{1}\hat{\theta}$ by the turbine inlet temperature restrictions, as highlighted during the cycle study. At this point it is interesting to examine what possibilities are offered to the designer to reduce H_b for a given $\dot{m}$. For this purpose, the inlet of a stage is considered. If the new condition is represented by the *prime* symbol ', then the conservation of mass yields :

$$R_i\ H_{bi}\ u_i\ \phi_i = R'_i\ H'_{bi}\ u'_i\ \phi'_i \tag{7.187}$$

while neglecting the effects of the velocity variation on ρ_i.

Further development of Eq.7.187 leads to :

$$\frac{H'_{bi}}{H_{bi}} = \left(\frac{\overline{r_i}}{\overline{r_i}'}\right)^2 \left(\frac{\Omega}{\Omega'}\right)\left(\frac{\phi_i}{\phi'_i}\right) \tag{7.188}$$

Note that decreasing $\overline{r_i}$ for a given ϕ_i, increases the blade height (H_{bi}). The above equation becomes very instructive to the designer when using Eq.7.29 for ψ_T and replacing ψ_T by ϕ_i using Eq.7.123 and e.g. Eq.7.120 from the conceptual performance model :

$$\frac{H'_{bi}}{H_{bi}} = \left(\frac{\Omega'}{\Omega}\right)\left(\frac{S'_n - 1}{S_n - 1}\right)\left(\frac{\tan {}^M\alpha_i{}'}{\tan {}^M\alpha_i}\right) \tag{7.189}$$

where it was considered that $\overline{r_i} = \overline{r_i}'$. Based on Eq.7.189, the following design manipulations leading to a lower blade height H_b are possible :

1. If R_{tip} is fixed, a lower rotor speed N should be strived for. This is because a lower rotational speed results in a higher stage loading ψ and consequently ϕ_i.

2. Ideally as low as possible stage number S_n should be selected. Similar to N, a reduction in S_n will increase the stage loading and consequently ϕ_i. Note that, strictly speaking, $S_n \geq 2$ (no middle stages), but that it is expected that in general $S_n \geq 4$ for the sake of efficiency.

3. Low values for ${}^M\alpha_i$ require ϕ_i to be higher to achieve the same stage loading. The optimum ${}^M\alpha_i$ was found to be close to 65°. However, a decrease in ${}^M\alpha_i$ is allowable for as long as $\eta_{p,T}$ meets the designer's objectives.

7.2 Off-design characteristics

The off-design characteristics of a Ljungström turbine are the performance characteristics of the turbine ruling at operating conditions other than the nominal regime for which it is designed. For example, when P_T^* changes or when a change in atmospheric conditions occurs, the turbine geometry is no longer the optimum configuration for the new operating regime.

Presenting the off-design performance is usually done by a *turbine map*, where the turbine efficiency and rotational velocity are plotted against turbine expansion ratio and a corrected mass flow, as exemplified by e.g. Cumpsty (2000), i.e. :

$$(\eta_{p,T},\ N_{corr}) = f(\dot{m}_{corr},\ \pi_T) \tag{7.190}$$

By definition, the corrected components are expressed as :

$$\dot{m}_{corr} = \frac{\dot{m}\ \sqrt{{}^{1}\theta_{ti}}}{{}^{1}\delta_{ti}} \tag{7.191}$$

$$N_{corr} = \frac{N}{\sqrt{{}^{1}\theta_{ti}}} \tag{7.192}$$

where,

$${}^{1}\delta_{ti} = \frac{{}^{1}p_{ti}}{101325} \tag{7.193}$$

$${}^{1}\theta_{ti} = \frac{{}^{1}T_{ti}}{288.15} \tag{7.194}$$

While corrected mass flow and turbine expansion ratio are sufficient to represent the off-design characteristics for a conventional turbine with a given geometry, it is not the case for the Ljungström turbine, where the turbine slip factor S_Ω still needs to be accounted for, viz. :

$$(\eta_{p,T},\ N_{corr}) = f(\dot{m}_{corr},\ \pi_T,\ S_\Omega) \tag{7.195}$$

Buysschaert et al. (2013) show that the impact of varying the slip factor on the output performance is mainly a power balance shift between turbine halves. This phenomenon will not be discussed in this work because the main objective focusses on the nominal operating performance where the cycle and turbine design characteristics are to be optimised and rotor angular speeds are identical ($S_\Omega = 1$).

The methodology to calculate the off-design characteristics was already revealed by the flow chart in Fig.6.23. The major difference with respect to the design calculation model is the use of the model of Ainley and Mathieson instead of Soderberg's model. An important difference between both models is that the model of Ainley and Mathieson allows capturing incidence variations for a given turbine blade geometry. This is not possible with Soderberg's model. The loss calculation procedure of the model of Ainley and Mathieson has already been expounded in Fig.6.4, while the correlations have been put in Appendix D. In the next chapter, the off-design characteristics of the proposed Ljungström turbines will be discussed briefly.

7.3 Note on mechanical stresses

In this work, the design of the turbine is limited to the aerodynamic study. The geometry evolving from the analysis still needs to be examined for its structural resistance against the forces exerted by the flow on the blades on the one hand, and the required thickness of the turbine disks to support these loads and transfer the generated torque to the rotors

at a minimum weight on the other. Since it is possible at this point to develop the blade passage geometry with labyrinth cavities, this examination could ideally be performed by coupling CFD calculations, which optimise the blade shape, with FEM software, allowing the verification of blade structural resistance and the dimensioning of disks and rims, while providing the designer a detailed global insight into the ruling physics.

7.4 Nomenclature

Please note that the units listed below apply unless stated otherwise.

Abbreviations and substance formulae

A	Flow area	[m^2]
A_R	Rotor disk area	[m^2]
AR	Blade aspect ratio	[-]
AR_a	Blade projected aspect ratio	[-]
$\overline{B}$	Blade height ratio	[-]
c	Blade chord	[m]
$\hat{c}$	Interstage space coefficient	[-]
c_a	Radial blade chord	[m]
C_L	Blade lift coefficient	[-]
C_{L0}	Blade reference lift coefficient	[-]
C_p	Specific heat at constant pressure	[J/kgK]
D_h	Hydraulic diameter	[m]
$\overline{H}$	Interstage space height ratio	[-]
h	Specific enthalpy	[J/kg]
h_t	Specific total enthalpy	[J/kg]
f_w	Friction loss coefficient	[-]
h_{tL}	Specific total enthalpy loss	[J/kg]
h_{ss}	Seal strip height	[m]
H_b	Blade height	[m]
k	Exponent	[-]
l	Camberline length	[m]
${}^{L}K$	Last stage flow acceleration factor	[-]
${}^{1}K$	First stage flow attenuation factor	[-]
K_M	Flow expansion loss factor	[-]
$L_{(j)}$	Labyrinth seal cavity length	[m]
$LTIT$	Ljungström turbine inlet temperature	[K]
m	Exponent	[-]
$\dot{m}$	Turbine mass flow rate	[kg/s]
$\dot{m}_{corr}$	Turbine corrected mass flow	[kg/s]
$\dot{m}_{LL}$	Leakage mass flow rate	[kg/s]
M	Absolute Mach number	[-]
M_r	Relative Mach number	[-]
N	Rotational/Angular speed	[rad/s]

N_{ss}	Number of seal strips	[-]
o	Blade passage throat	[m]
p	Static pressure	[Pa]
p_t	Total pressure	[Pa]
P_i	Rotor induced power	[W]
P_{st}	Delivered stage power on crown	[W]
$P_{st,b}$	Delivered power by blade cascade	[W]
P_T^*	Delivered turbine power	[W]
R	Radius	[m]
$\hat{R}$	Reaction degree	[-]
$\overline{r_i}$	Turbine specific inlet radius	[-]
R_c	Blade suction side radius of curvature	[m]
R_g	Specific gas constant	[J/kgK]
R_i	Turbine (stage) inlet radius	[m]
R_o	Turbine (stage) outlet radius	[m]
R_{tip}	Rotor blade tip radius	[m]
Re	Reynolds number	[-]
RELT	Rotor-embedded Ljungström turbine	
RR	Ram recovery	[-]
s	Stage pitch	[m]
S_n	Turbine stage number	[-]
S_Ω	Turbine slip factor	[-]
t	Blade thickness	[m]
t_s	Rim thickness	[m]
T	Static temperature	[K]
T_t	Total temperature	[K]
T_{tr}	Relative total temperature	[K]
$\mathcal{T}$	Torque	[Nm]
u	Rotational velocity	[m/s]
v	Absolute speed	[m/s]
w_{ss}	Seal strip width	[m]
w	Relative speed	[m/s]
y	Blade y-coordinate	[m]
x	Blade x-coordinate	[m]
α	Absolute flow angle	[rad]
β	Relative flow angle	[rad]
β_b	Camberline angle	[rad]

β_g	Gauging angle	[rad]
β_{o,b_s}	Relative flow angle near the rotor outlet with slip vortex	[rad]
γ	Isentropic exponent	[-]
δ	Stage flow deviation angle	[rad]
${}^1\delta_t$	Non-dimensional turbine total inlet pressure	[-]
Δ_{is}	Interstage space	[m]
Δ_{s_h}	Axial gap clearance	[m]
Δ_{s_R}	Radial gap clearance	[m]
$\Delta h_{t_{FL}}$	Stage specific enthalpic friction loss	[J/kg]
Δz_r	Axial rotor spacing	[m]
ϵ	Flow deflection or R_i/R_o	[rad] or [-]
ϵ_b	Blade camberline deflection	[rad] or [-]
ϵ_f	Blade roughness	[m]
ζ_A	Stage aerodynamic enthalpic loss coefficient	[-]
ζ_{AT}	Turbine aerodynamic enthalpic loss coefficient	[-]
ζ_{FL}	Stage friction enthalpic loss coefficient	[-]
ζ_T	Turbine total enthalpic loss coefficient	[-]
ζ_2	Soderberg loss coefficient, non-reference $Æ_a$	[-]
ζ_3	Soderberg loss coefficient, non-reference Re and $Æ_a$	[-]
$\eta_{is,T}$	Turbine total-to-total isentropic efficiency	[-]
$\eta_{is,Tb}$	Blade passage total-to-total isentropic efficiency	[-]
$\eta_{is,Ts}$	Stage isentropic total-to-total efficiency	[-]
$\eta_{p,T}$	Turbine total-to-total polytropic efficiency	[-]
$\eta_{p,Tb}$	Blade total-to-total passage polytropic efficiency	[-]
$\eta_{p,Ts}$	Stage total-to-total polytropic efficiency	[-]
$\hat{\theta}$	Non-dimensional inlet specific total enthalpy	[-]
Θ	Non-dimensional mass flow	[-]
${}^1\theta_t$	Non-dimensional turbine total inlet temperature	[-]
λ	Blade stagger angle	[rad]
μ	Dynamic viscosity	[Pa s]
π_T	Turbine total-to-total expansion ratio	[-]
π_{Tb}	Blade passage total-to-total expansion ratio	[-]
π_{Ts}	Stage total-to-total expansion ratio	[-]
Π	Blade pitch	[rad]
ρ	Density	[kg/m^3]
τ_w	Wall shear stress	[Pa]
ϕ	Flow coefficient	[-]

ψ	Stage work coefficient	[-]
ψ_S	Stage effective work coefficient	[-]
ψ_T	Turbine effective work coefficient	[-]
${}^{M}\chi$	Interstage damping	[-]
Ω	Crown angular velocity	[rad/s]

Subscripts and superscripts

a	Atmosphere
b	Blade or blade passage related
bp	Base profile
c	Camberline
C	Circular cascade coordinates
$C1$	First crown
$C2$	Second crown
cav	Labyrinth cavity
CAV	Labyrinth seal cavity related
D	Opposing disk
DF	Disk friction
e	Estimated
H	Hub
i	Inlet
is	Isentropic evolution
j	Related to position j
L	Last stage
LE	Leading edge
LL	Leakage loss
M	Middel stage
nh	No hub installed
o	Outlet
o,b	At outlet of a blade passage
Ops	Operating line
opt	Optimum
r	Relative
R	Radial component, Rim or Rectangular cascade coordinates
ref	Reference
t	Total component
tg	Target
TAC	Taylor-Couette

TE	Trailing edge
tip	Rotor tip related
TOC	Torsional Couette
u	Tangential component
1	First stage
+	New result after one iteration

Chapter 8

Case studies

"Allez en avant, la foi vous viendra"

Jean le Rond d'Alembert – *Schubring (2006)*

8.1 Introduction

In Chapter 4, the relation between cycle pressures and temperatures was examined, offering the possibility to find the best coefficient-of-performance-based cycle performance. During this study, the turbine (polytropic) efficiency was considered to be invariable.
Chapters 5, 6 and 7 gave insight into the design of a Ljungström turbine and the dependency of the turbine efficiency on flow and geometric parameters, amongst which the turbine expansion ratio π_T, which depends on the inlet pressure, and thus the cycle pressure ratio.
This chapter combines the acquired knowledge of the above-mentioned chapters. For this purpose, two TDR helicopters are studied and their performance compared with that of a conventional helicopter.

The first case concerns a VLR-class helicopter with a maximum take-off weight of 500 kg (Fig.8.1). Since this concerns a low-power category helicopter, the piston engine (PE) powered TDR helicopter configuration is selected.
The second case is a NH90-class helicopter with a maximum take-off weight around 10 metric tons and powered by a turbofan (TF) configuration.

The turboshaft powered TDR helicopter will not be considered here because it is more complex due to the need of a heat exchanger, while a *design range overlap* between the piston engine and turbofan TDR configurations is expected, possibly ruling out the use of the turboshaft in the contemporary known layout.

The study will be restricted to and oriented by the selection of the design point (DP) of

FIGURE 8.1. VLR-class TDR helicopter concept. Sagita S.A..

the TDR helicopter rotor embedded Ljungström turbine with concurring cycle settings under International Standard Atmosphere sea level conditions (ISA SLS). Under these atmospheric conditions, engine data is readily available. Because protecting the integrity of the Ljungström turbine is paramount, it is decided that the design point should be examined when the internal combustion engines are delivering their maximum power, which results in the maximum possible *LTIT*. The author acknowledges that it would be sensible to select the design point of the TDR helicopter such that it yields the best performance for a given flight profile. However, this requires a thorough insight into the off-design characteristics of the complete helicopter, which is not in the scope of the work at hand. As a consequence, the previously selected design point appears to be a sensible choice. Nevertheless, turbine off-design performance maps will be provided and discussed briefly.

Before examining both TDR helicopters, it is necessary to develop a methodology to compare the TDR helicopter with its conventional equivalent. This is made possible by the definition of the break-even coefficient of performance COP_{BE} and coefficient of performance margin COP_M.

8.2 Break-even coefficient of performance COP_{BE} and COP_M

8.2.1 Introduction

Developing a new helicopter concept is only useful when it performs at least better than the conventional helicopter. Without merits it is doomed to failure. From the safety and reliability viewpoint, the TDR helicopter merits credit since it has no longer a mechanical transmission, which was proven earlier to be of concern. However, fuel cost and performance envelope still need consideration. For this purpose, the break-even coefficient of performance COP_{BE} is defined. COP_{BE} is the minimum coefficient of performance a TDR helicopter should have to consume the same amount of fuel as the conventional equiva-

lent for a given flying time Δt_{flight}, including the power and weight changes invoked by the conceptual differences between both configurations. Consequently, denoting the fuel weight in the conventional helicopter and the TDR helicopter by respectively $W_{F,conv}$ and $W_{F,TDR}$:

$$W_{F,TDR} = W_{F,conv} \tag{8.1}$$

$$\dot{m}_{f,TDR}\Delta t_{flight} = \dot{m}_{f,conv}\Delta t_{flight} \tag{8.2}$$

and by the definition of COP_{BE},

$$\dot{m}_{f,TDR} = \dot{m}_{f,conv} \tag{8.3}$$

The definition of COP_{BE} depends on the power source. A relation for COP_{BE} will now be developed for both the piston engine and the turbofan powered TDR cycles.

8.2.2 Piston engine powered TDR cycle

From the definition of specific fuel consumption of an internal combustion engine (e.g. Eq.4.58) and using Eq.8.3 :

$$\frac{\dot{m}_{f,TDR}}{\dot{m}_{f,conv}} = \frac{SFC_{E,TDR}P^*_{M,TDR}}{SFC_{E,conv}P^*_{M,conv}} = 1 \tag{8.4}$$

where the suffix E stands for the characteristics of the installed internal combustion engine and P^*_M the mechanical power it delivers, as defined in Chapter 4. The power produced by the RELT and set on the coaxial rotors may now be introduced in the above equation via the definition of the coefficient of performance (Eq.4.32) :

$$1 = \frac{SFC_{E,TDR}(P^*_T/COP_{BE})}{SFC_{E,conv}P^*_{M,conv}} \tag{8.5}$$

wherein COP_{BE} represents the break-even coefficient of performance, or :

$$COP_{BE} = \frac{SFC_{E,TDR}}{SFC_{E,conv}}\frac{P^*_T}{P^*_{M,conv}} \tag{8.6}$$

From the survey performed by this author, it is possible to present the maximum installed take-off power[i] at ISA SLS conditions as a function of helicopter gross weight W_g (Fig.8.2). It is reasonable to expect that the power delivered at this engine setting is near to the maximum power absorbed by the rotors in the entire flight envelope for standard day conditions. Equating this power to $P^*_{M,conv}$ then yields the following power trend-line :

$$P^*_{M,conv} = f_{PMcv}(W_g) = 0.0680W_g^{1.1693} \quad \text{[kW][kg]} \tag{8.7}$$

[i] Also denoted as 5-minute power setting

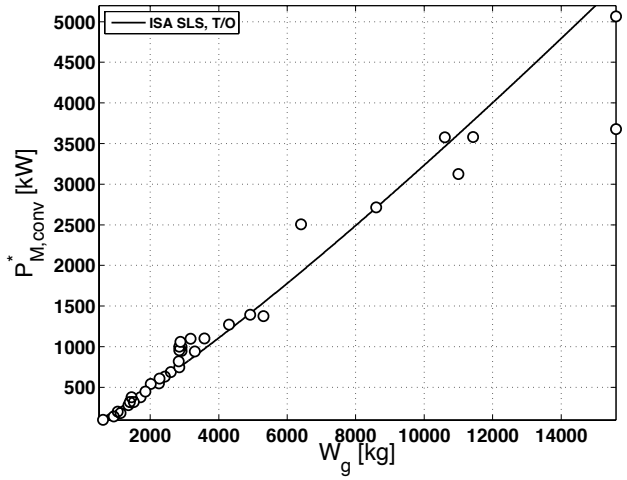

FIGURE 8.2. $P^*_{M,conv}$ as a function of conventional helicopter gross weight W_g – Author survey, Appendix H.

The required P^*_T remains to be calculated. For this purpose, the work of Coleman (1997) is instructive. He reports that the required rotor power of a helicopter with coaxial rotors is similar to the power absorbed by the main rotor of conventional helicopter with same rotor tip radius R_{tip} and disk loading DL, i.e. :

$$DL = \frac{W_g}{A_R} = C^t \Rightarrow P^*_{M,conv} = P^*_{M,coax} \tag{8.8}$$

where A_R the rotor disk area, already defined in Eq.7.179. However, in case of the TDR helicopter, it is not correct to state that $P^*_{M,conv} = P^*_T$ since the power absorbed in the tail rotor, the mechanical transmission losses and the induced power increase due to the larger hub radius R_H are not yet accounted for. Correction factors are now proposed to cope with these effects.

Johnson (1994) and Leishman (2002) provide yardsticks for the power consumed by the tail rotor and transmission system losses, which are summarised in Table 8.1. Starting from Eq.8.8, it is possible to write :

$$P^*_T = P^*_{M,conv} \cdot (1 - k_{TX} - k_{TR}) = f_{PMcv}(W_{g,conv}) \cdot (1 - k_{TX} - k_{TR}) \tag{8.9}$$

The possible empty weight changes ΔW_E due to the removal of the tail rotor, the mechanical transmission system and the installation of a Ljungström turbine, compressor etc., are function of the desired configuration. Since $W_{F,conv} = W_{F,TDR}$ (Eq.8.1), the change in empty weight is also the change in gross weight, where the gross weight has a direct impact on the required power (Fig.8.2). The required rotor and thus turbine power is then proposed to be estimated via Eq.8.7 using the newly estimated gross weight $W_{g,TDR}$,

Table 8.1. Conventional helicopter transmission and tail rotor power losses according to Johnson (1994) and Leishman (2002).

Transmission loss power fraction $k_{TX} = P_{TX}/P^*_{M,conv}$	0.04 . . . 0.09
Tail rotor power fraction $k_{TR} = P_{TR}/P^*_{M,conv}$	0.05 . . . 0.10

where :

$$W_{g,TDR} = W_{g,conv} + \Delta W_E \tag{8.10}$$

ΔW_E is negative in case of a weight reduction. Consequently :

$$P^*_T = f_{PMcv}(W_{g,TDR}) \cdot (1 - k_{TX} - k_{TR}) \tag{8.11}$$

Introducing Eq.8.11 in Eq.8.6 yields a new expression for COP_{BE} :

$$COP_{BE} = \frac{SFC_{E,TDR}}{SFC_{E,conv}} \frac{f_{PMcv}(W_{g,TDR}) \cdot (1 - k_{TX} - k_{TR})}{f_{PMcv}(W_{g,conv})} \tag{8.12}$$

Using the best-fit power-characteristic aW^b_g of Eq.8.7 in the previous relation with Eq.8.10 results in :

$$COP_{BE} = \frac{SFC_{E,TDR}}{SFC_{E,conv}} \left(1 + \frac{\Delta W_E}{W_{g,conv}}\right)^b (1 - k_{TX} - k_{TR}) \tag{8.13}$$

where $b = 1.1693$ and, by virtue of Eq.8.6 :

$$\frac{P^*_T}{P^*_{M,conv}} = \left(1 + \frac{\Delta W_E}{W_{g,conv}}\right)^b (1 - k_{TX} - k_{TR}) \tag{8.14}$$

When the hub size (R_H) becomes too important to neglect – a plausible condition in case of the TDR helicopter – it is proposed to correct the required turbine power by assuming that the power increase is proportional to the increase in induced power (Eqs.7.176 and 7.178) :

$$P^*_T \propto \left(\frac{P_i}{P_{i,nh}}\right) P^*_{M,conv} \tag{8.15}$$

or, using Eq.7.182 :

$$k_I \triangleq \frac{P^*_T}{P^*_{T,nh}} \cong \frac{P_i}{P_{i,nh}} = \left\{1 - \left[\overline{r}_i \left(\frac{R_o}{R_i}\right)^{S_n}\right]^2\right\}^{-1/2} \tag{8.16}$$

where $P^*_{T,nh}$ is the power required from the turbine when the hub dimensions are negligi-

ble. Introducing k_I into Eq.8.13 yields the general equation of COP_{BE}, useable for piston engine powered cycles :

$$COP_{BE} = \frac{SFC_{E,TDR}}{SFC_{E,conv}}\left(1 + \frac{\Delta W_E}{W_{g,conv}}\right)^b (1 - k_{TX} - k_{TR})\, k_I \tag{8.17}$$

and,

$$\frac{P^*_T}{P^*_{M,conv}} = \left(1 + \frac{\Delta W_E}{W_{g,conv}}\right)^b (1 - k_{TX} - k_{TR})\, k_I \tag{8.18}$$

which is generally applicable, i.e. not cycle type dependent. Note that the specific fuel consumption of the engines SFC_E is also function of the installed power. For these variables, information can be found in the literature. Since $P^*_{M,TDR}$ and $P^*_{M,conv}$ will not differ substantially, it is reasonable to assume that $SFC_{E,TDR} \approxeq SFC_{E,conv}$, causing the SFC_E terms to cancel each other in Eq.8.17.

8.2.3 Turbofan powered TDR cycle

COP_{BE} for a turbofan powered TDR cycle is derivable in a similar way as the one discussed previously with the piston engine. Since the TDR helicopter is compared with the conventional helicopter, the thrust factor τ_f is considered to be unity (Eq.4.159) and its impact on COP_{BE} is henceforth not further examined. Starting with Eq.8.1, but now introducing engine thrust T_N and thrust specific fuel consumption $TSFC$ at ISA SLS take-off conditions (Eq.4.154) yields :

$$\frac{\dot{m}_{f,TDR}}{\dot{m}_{f,conv}} = \frac{TSFC}{SFC_{E,conv}} \frac{T_N}{P^*_{M,conv}} = 1 \tag{8.19}$$

Substitution of the definition of cycle power gain PG (Eq.4.168) in the above equation allows determining the break-even power gain PG_{BE} :

$$PG_{BE} = \frac{TSFC}{SFC_{E,conv}} \frac{P^*_T}{P^*_{M,conv}} \tag{8.20}$$

Substitution of Eq.8.18 in Eq.8.20 gives the general equation of PG_{BE} :

$$PG_{BE} = \frac{TSFC}{SFC_{E,conv}}\left(1 + \frac{\Delta W_E}{W_{g,conv}}\right)^b (1 - k_{TX} - k_{TR})\, k_I \tag{8.21}$$

The turbofan engine is designed to deliver thrust and is not intended to drive a mechanical load. Chapter 4 addressed this issue by defining COP differently, using the delivered kinetic energy to the gases when expanded (fictitiously) to the atmosphere as datum with *zero flight speed*.

Recalling Eq.4.174 :

$$COP_{TF} \triangleq \frac{P_T^*}{\dot{E}_k}$$

where the kinetic energy change $\dot{E}_k$ and net thrust T_N are expressed as (Cumpsty (2000)) :

$$\dot{E}_k = (\dot{m} + \dot{m}_f)\frac{v_{j,av}^2}{2} \tag{8.22}$$

$$T_N = (\dot{m} + \dot{m}_f)v_{j,av} \tag{8.23}$$

and $v_{j,av}$ the (fictitious) average speed of the expelled combustion gases. Substitution of the above equations in Eq.4.174 :

$$COP_{TF} = \frac{2PG}{v_{j,av}} \tag{8.24}$$

Introduction of PG_{BE} in the above equation and writing $v_{j,av}$ as a function of SPT (Eq.4.146), i.e. :

$$v_{j,av} = \left(\frac{\dot{m}}{\dot{m} + \dot{m}_f}\right) SPT \tag{8.25}$$

finally results in an expression for COP_{BE} :

$$COP_{BE} = \frac{2}{SPT}\left(1 + \frac{FAR}{1 + BPR_{TF}}\right) PG_{BE} \tag{8.26}$$

where the fuel-to-air ratio (FAR) and the turbofan bypass ratio (BPR_{TF}) were already discussed in Section 4.5. $TSFC$ will be a function of the selected turbofan engine, where the engine overall pressure ratio (OPR) and turbine inlet temperature (TIT) play an important role. For more information about this, the reader is referred to the related literature, such as Walsh & Fletcher (2004) and Cumpsty (2000). Since the turbofan powered TDR cycle targets the higher helicopter weight class, it is then realistic to assume that the conventional helicopter equivalent will use a turboshaft as mechanical power source. A correlation for $SFC_{E,conv}$ may consequently be established relying on the data provided by the turboshaft engine manufacturers for the maximum take-off power regime (Fig.8.3). Again, a power relation is proposed to estimate $SFC_{E,conv}$ for any given $P^*_{M,conv}$, but note that the number of engines installed in the conventional helicopter N_e must be accounted for :

$$SFC_{E,conv} = 970.4962 \left(\frac{P^*_{M,conv}}{N_e}\right)^{-0.1608} \quad \text{[g/kWh][kW][-]} \tag{8.27}$$

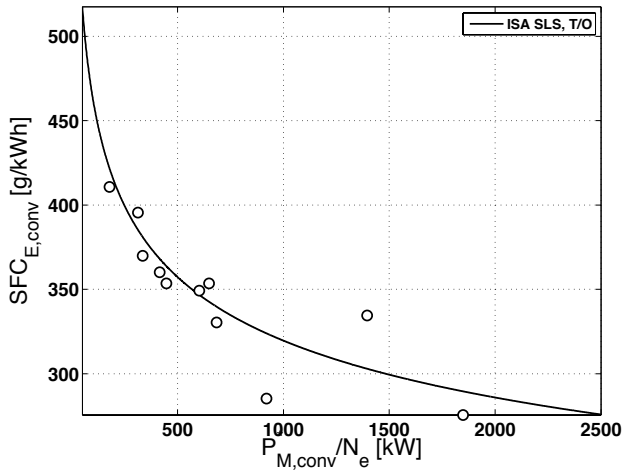

Figure 8.3. $SFC_{E,conv}$ as a function of turboshaft engine power $P^*_{M,conv}/N_e$ at maximum take-off regime, ISA SLS – Author survey, Appendix H.

8.2.4 *COP*-margin COP_M

The *COP*-margin COP_M is defined as :

$$COP_M \triangleq \frac{COP - COP_{BE}}{COP_{BE}} \tag{8.28}$$

During the design process, COP_M will be used as design metric where possible. The design point should be selected at the maximum available margin, offering the best performance potential over the conventional helicopter from either a fuel or an excess power capability viewpoint. The latter can indeed be obtained by installing, for example, more power in the TDR helicopter by the integration of a larger turbofan. This will increase the weight of the helicopter and indirectly the required fuel mass flow. Clearly, this kind of intervention enhances the performance envelope, but at the cost of COP_M. Note that from the above definition, COP_{BE} should be as low as possible.

8.3 PE-TDR cycle : VLR-class helicopter

8.3.1 Engine selection

The VLR-class helicopter is a lightweight and consequently low power class helicopter. From Fig.8.4 it is observed that the offered power range by the piston engines meets the designer's requirements amply. As already discussed in Section 4.3.1, several piston engine types exist. The 4-stroke (4-s) Avgas piston engine with atmospheric aspiration (ATM) and the 2-stroke (2-s) Diesel piston engine offer the best available SFC_{PE} and are consequently retained for the VLR TDR helicopter study (Fig.8.4), while they influence

COP_{BE} positively (Eq.8.17). Note that here :

$$SFC_{PE} = SFC_{E,conv} \tag{8.29}$$

From the scattered data in Fig.8.4 it is assumed that SFC_{PE} remains fairly constant *for the examined piston engine types*. For the study, the average values for SFC_{PE} can consequently be adopted from Fig.8.4. They are indicated in Table 8.2.

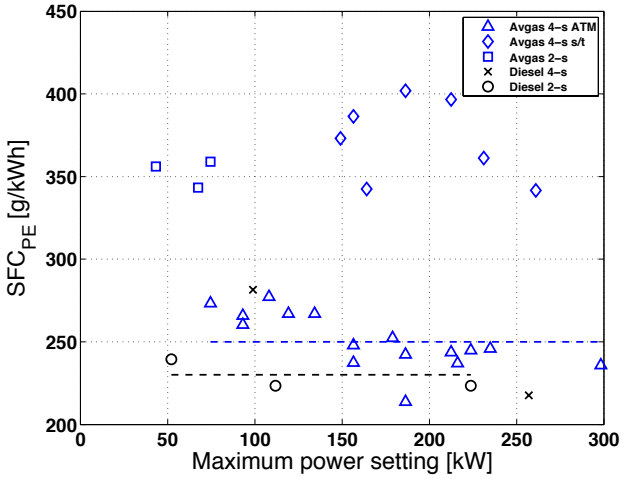

FIGURE 8.4. SFC_{PE} as a function of maximum available engine power $P^*_{M,conv}$ ISA SLS ; 4-s : 4-stroke, 2-s : 2-stroke, ATM : atmospheric induction, s/t : supercharged/turbocharged – Author survey, Appendix H.

TABLE 8.2. VLR-class TDR helicopter $SFC_{E,conv}$ – Author survey.

Avgas engine	$SFC_{E,conv}$ [g/kWh]	250
Diesel engine	$SFC_{E,conv}$ [g/kWh]	230

8.3.2 Rotor radius

Starting from the equal disk loading condition between the TDR helicopter and the conventional helicopter, it was decided to select the same rotor radius R_{tip} for the TDR helicopter as the one applicable to the conventional equivalent. Even though this decision could be questioned at this point due to $W_{g,TDR} \neq W_{g,conv}$, it will be shown later in Section 8.3.4 to be a conservative estimation. From the survey performed by this author, a correlation was established relating R_{tip} to the maximum gross weight of the conventional helicopter (Fig.8.5) :

$$R_{tip} = f_{Rt} = 0.4097\, W_{g,conv}^{0.3274} \quad [\text{m}][\text{kg}] \tag{8.30}$$

The tip radius then becomes for the VLR-class TDR helicopter :

$$R_{tip} \cong 3.2 \text{ [m]} \tag{8.31}$$

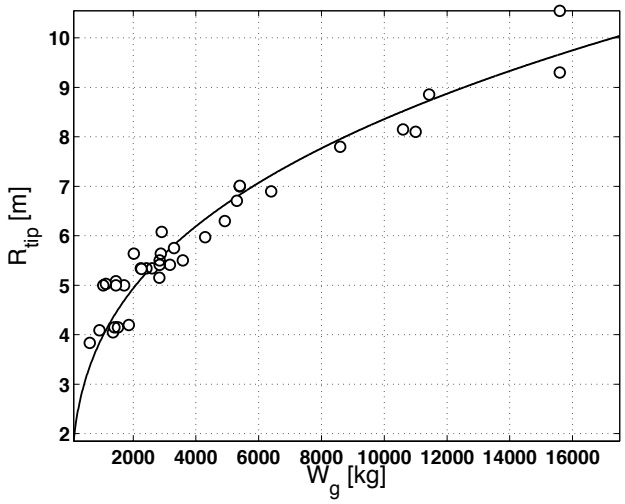

FIGURE 8.5. R_{tip} as a function of helicopter maximum gross weight W_g – Author survey, Appendix H.

8.3.3 Empty weight correction

Section 8.2.2 deduces the gross weight of the TDR helicopter based on the gross weight of the conventional equivalent and to which an empty weight correction factor is added (Eq.8.10). The empty weight correction is influenced by the removal of important systems installed in the conventional helicopter and the presence of new components, peculiar to the TDR helicopter. In case of the piston engine powered TDR helicopter, the most noteworthy weight variations are caused by :

→ The removal of the mechanical transmission system ($W_{E,7B}$).

→ The removal of the tail rotor ($W_{E,3A}$).

→ The rotor system using a coaxial rotor instead of a single rotor ($W_{E,2}$).

→ The installation of the RELT ($W_{E,T}$).

→ The installation of a compressor with diffuser ($W_{E,C}$).

The empty weight correction ΔW_E may then be expressed as :

$$\Delta W_E \cong W_{E,T} + W_{E,C} + \Delta W_{E,2} - W_{E,3A} - W_{E,7B} \tag{8.32}$$

The weight correlations for the tail rotor system $W_{E,3A}$ and mechanical transmission system $W_{E,7B}$ are function of W_g and were already discussed in Section 1.2 (see also

Appendix A, Eq.A.7 and Eq.A.25).
The rotor system weight variation $\Delta W_{E,2}$ can be established by considering that the rotors of the conventional helicopter and the TDR helicopter operate at the same C_T/σ_R, i.e. the ratio of rotor thrust coefficient C_T and rotor solidity σ_R, where :

$$C_T \triangleq \frac{W_g}{\rho A_R v_{tip}^2} \tag{8.33}$$

$$\sigma_R \triangleq \frac{N_b c_b}{\pi R_{tip}} \tag{8.34}$$

and v_{tip} the rotor blade tip speed, N_b the number of rotor blades and c_b the rotor blade chord. In other terms :

$$\left(\frac{C_T}{\sigma_R}\right)_{coax,1\ rotor} = \left(\frac{C_T}{\sigma_R}\right)_{conv} \tag{8.35}$$

Johnson (1994) indicates that C_T/σ_R represents the lift coefficient of the rotor blades. If the lift coefficient of each rotor blade is identical, it is sensible to expect similar drag figures, which is in line with the findings of Coleman (1997) adopted in the beginning of this chapter stating that for a constant effective disk loading : $P^*_{M,conv} = P^*_{M,coax}$ (Eq.8.8). Adopting the hypothesis that each rotor of the TDR helicopter produces an equal amount of thrust, and knowing that $R_{tip} = R_{tip,conv}$ while assuming $S_\Omega = 1$, it possible to write :

$$C_{T,coax,1\ rotor} = \frac{C_{T,conv}}{2} \tag{8.36}$$

and as a consequence :

$$\sigma_{R,coax,1\ rotor} = \frac{\sigma_{R,conv}}{2} \tag{8.37}$$

The above equation explains that the total blade area per rotor[ii] S_{pl} in the TDR configuration must be half of S_{pl} found on the conventional helicopter. The easiest way to achieve this practically is by splitting up the amount of blades N_b over each rotor evenly. However, it must be noted that this is not always possible notably for those conventional helicopter configurations with an uneven blade count or with less than four blades. Also, considering Eq.7.175, care must be taken that coaxial rotor blades remain stiff enough to prevent them from colliding. The aforementioned issues are not examined here.
Weight correlations for a rigid coaxial rotor head were not found and the author therefore adapted Eq.A.5 as follows, while relying on the above findings :

$$W_{E,2_{coax}} = 2\left[-194.685 + 12.164\left(\frac{S_{pl,conv}}{2}\right)\right] \quad [\text{lb}][\text{ft}^2] \tag{8.38}$$

[ii] Also referred to as blade planform surface area (Section 1.2).

where $S_{pl,conv}$ is calculated via Eq.A.4. $\Delta W_{E,2}$ then becomes :

$$\Delta W_{E,2} = W_{E,2_{coax}} - W_{E,2} \tag{8.39}$$

At the moment, no exact RELT ($W_{E,T}$) and compressor system ($W_{E,C}$) weight correlations are available. As a consequence, the author relies on weight fractions provided by Sagita S.A, which is currently developing the prototype of the Sherpa VLR-class helicopter. The weight fractions are therefore believed to be crude estimates. However, they are not evaluated against gross weight changes, which is a significant disadvantage when having to use these weight fractions in the heavier helicopter classes, as will be the case with the NH90-class TDR helicopter. Table 8.3 summarises the proposed weight fractions. The result of the weight study is presented in Fig.8.6 and Table 8.4. It highlights

Table 8.3. TDR helicopter turbine and compressor weight fractions.

$W_{E,T}/W_{g,conv}$ [-]	0.061
$W_{E,C}/W_{g,conv}$ [-]	0.013

Table 8.4. Helicopter maximum gross weight comparison.

VLR	**TDR**	**Conventional**
W_g [kg]	500	581

that the TDR helicopter benefits from a weight reduction with respect to the conventional equivalent. This is mainly due to the positive impact of the removal of the transmission system and the use of a coaxial rotor. The influence of the latter should be substantiated in future work, but it is not unreasonable to expect a slight drop in weight since each rotorhead only takes half of the bending moment exerted by the blades. Finally note that the introduction of the RELT and compressor introduces a weight increase of about 7% (as already indicated in Table 8.3), while the removal of the tail rotor system reduces the empty weight by no more than 1%. In case of the studied VLR helicopter with $W_{g,TDR} = 500$ kg, it was found that :

$$\frac{\Delta W_E}{W_{g,conv}} \cong -0.14 \tag{8.40}$$

8.3.4 Determination of COP_{BE}

Recalling Eq.8.17 and implementing the assumption that $SFC_{E,TDR} \cong SFC_{E,conv}$, which is a sensible assumption since for the VLR-class helicopter it is reasonable to expect that

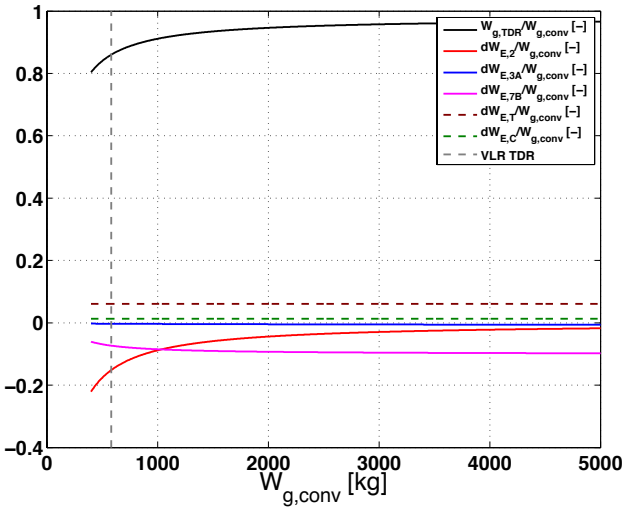

FIGURE 8.6. VLR TDR helicopter empty weight variation $\Delta W_E/W_{g,conv}$.

similar piston engines will be used, it is found that :

$$COP_{BE} \cong \frac{P^*_T}{P^*_{M,conv}} = \left(1 + \frac{\Delta W_E}{W_{g,conv}}\right)^b (1 - k_{TX} - k_{TR})\, k_I \tag{8.41}$$

In the previous sections, values for all unknown variables in Eq.8.41 were found, except for k_I. k_I represents the relative power increase caused by the reduction of A_R due to the existence of a larger rotor hub engendered by the presence of the RELT (Eq.8.16). Values for k_I must be calculated iteratively because the optimum turbine specific inlet radius $\overline{r_i}$ depends on the required power itself via the required mass flow.

However, calculations show that k_I remains rather low, i.e. around 1.02. In addition, it is considered reasonable to neglect k_I in most conditions, i.e. $k_I \cong 1$ because P^*_T is slightly overestimated by imposing the condition $R_{tip} = C^t$. Indeed, Eq.8.9 uses the function $f_{PMcv}(W_{g,TDR})$ to calculate P^*_T (Eq.8.7). This function is based on conventional helicopter data. When the gross weight of the conventional helicopter decreases, $P^*_{M,conv}$ is reduced, but it also causes a smaller $R_{tip,conv}$ (Eq.8.30), which is implicitly adopted in the power requirement function f_{PMcv}. By keeping the rotor radius constant (Section 8.3.2), the function $f_{PMcv}(W_{g,TDR})$ overestimates the required power as the TDR helicopter uses a larger rotor.

Even though it is difficult to acquire a clear view on the overrating of the required power by selecting a constant rotor radius, it is obvious that a small change in radius on the tip side of the rotor has a much more significant impact on the required rotor power than a small change in radius on the hub side. Therefore it is reasonable to expect that the TDR helicopter disk loading will be lower than the one observed for its conventional equivalent, even with a RELT installed[iii]. As a consequence, it is reasonable to state that P^*_T

[iii] The statement that the disk loading is lower for the TDR helicopter can be shown to be correct for the studied helicopters.

Table 8.5. Cycle specific independent variables.

	Avgas	**Diesel**
RR [-]	0.99	0.99
η_m [-]	0.98	0.98
$\eta_{p,C}$ [-]	0.90	0.90
η_{CC} [-]	0.99	0.67
SFC_{PE} [kg/kWh]	0.250	0.230
LHV [MJ/kg]	43.7	42.5
C_p [J/kgK]	1005	1005
C_{pg} [J/kgK]	1010	1012

is slightly overestimated by setting $R_{tip,TDR} = R_{tip,conv}$. Hence, it is assumed conservative to state $k_I \cong 1$, where the underrating of the required power by neglecting the size of the RELT in the hub is compensated by keeping the rotor radius constant for a lower (TDR helicopter) gross weight.
It is now possible to calculate the value of COP_{BE}. For both piston engine powered TDR helicopter cases, it is found that :

$$COP_{BE} \cong 0.721 \tag{8.42}$$

8.3.5 Determination of the cycle pressure ratio

The parametric study on the VLR TDR helicopter uses $LTIT$ as independent variable. From the cycle studies in Chapter 4, it was shown that for a given piston engine and SFC_{PE}, the cycle pressure ratio π_C becomes a pure function of $LTIT$. Indeed, recalling Eq.4.59 :

$$\pi_C = \left[1 + \frac{\eta_m}{\eta_{CC}\, LHV\, SFC_{PE}} \left(\frac{C_{pg} LTIT}{C_p T_{t1}} - 1\right)\right]^{\frac{\gamma}{\gamma-1}\eta_{p,C}} \tag{8.43}$$

The values for the cycle specific parameters in the above equation are detailed in Table 8.5, making it possible to find the cycle pressure ratio[iv] as a function of $LTIT$. The result is plotted in Fig.8.7. Note that the cycle pressure ratios are low, which causes low turbine expansion ratios and consequently contributes to better turbine efficiencies (Section 7.1.11). The parametrically studied inlet temperature conditions are indicated on Fig.8.7 by bullets. The corresponding pressure ratios are also found in Table 8.6.

[iv] This is considered equal to the compressor pressure ratio.

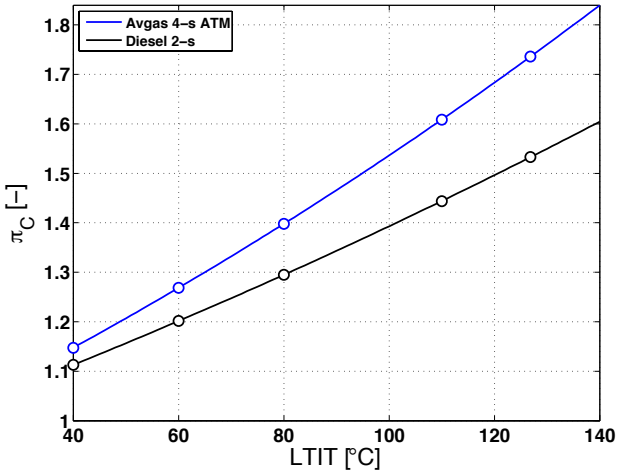

FIGURE 8.7. Avgas and Diesel cycle pressure ratio π_C as a function of selected *LTIT*.

TABLE 8.6. Turbine parametric input variables.

LTIT [°C]	**Avgas** π_C **[-]**	**Diesel** π_C **[-]**
126.85 (max. *LTIT*)	1.74	1.53
110	1.61	1.44
80	1.39	1.29
69	-	1.24⋆
60	1.26⋆	1.19
40	1.14	1.11

⋆ corresponds to DP

8.3.6 Turbine design

In this section, the number of turbine stages S_n and the turbine specific inlet radius $\overline{r_i}$ are selected for the Avgas and the Diesel powered TDR cycles, leading to the development of a turbine geometry and the determination of the concurring polytropic efficiency $\eta_{p,T}$. Using COP_M and relying on the parameters established previously, it is possible to determine the VLR-class TDR helicopter cycle design point. The turbine geometry is then shown for the selected design point and its losses expounded. Finally, the turbine off-design characteristics are retrieved, with and without endwall fences, and represented by means of a turbine map. Note that a detailed discussion of the calculation procedure was already conducted in Section 7.1.15, and will not be repeated here.

Turbine model input parameters

The most important input parameters used in the turbine model are summarised in Table 8.7. For both cycles, the rotational speed of the coaxial rotors is N_{DP} = 655 RPM, which is the design rotational speed. P_T^* was calculated using Eq.8.18, where the conventional

helicopter gross weight $W_{g,conv}$ in the calculations was selected such that $W_{g,TDR} = 500$ kg (as required).

Table 8.7. Turbine model input parameters.

LTIT [°C]	**Avgas/Diesel**
${}^1T_{ti}$ [K]	*LTIT* parametric [313 . . . 400]
${}^Lp_o$ [Pa]	101325 (no diffuser effect)
π_C [-]	$f(LTIT)$ parametric (Fig.8.7)
S_n [-]	parametric (Section 8.3.6)
P_T^* [kW]	83.7 (Eq.8.18)
v_{tip} [m/s]	215†
R_{tip} [m]	3.2 (Eq.8.30)
${}^M\alpha_i$ [°]	65 (Section 7.1.14)
c_{min} [mm]	20 (target value, Section 7.1.13)
$\hat{c}$ [-]	0.35 (Lowest high-cycle-fatigue, Eq.7.18)
t_s [mm]	5‡
w_{ss} [mm]	1‡
h_{ss} [mm]	1‡
Δ_{s_R} [mm]	0.1‡
Δ_{s_h}	0.016 R_o (Section 6.2.1)
N_{ss}	4 (Section 6.3.3)
ϵ_f [mm]	0.5⋆
e [μm]	1.2‡ (Section D.1.6)

† Section 2.2.2 – ‡ Antoine (2014)

⋆ Antoine & Buysschaert (2014b) : worst case scenario using Rohacell

Number of turbine stages and OED $\overline{r_i}$

The predesign procedure presented in Section 7.1.15 allows the determination of the number of turbine stages and the *optimum efficiency design* (OED) specific inlet radius $\overline{r}_{iopt}$, yielding the highest possible turbine efficiency. Recall that the Ljungström turbine is integrated in the rotor and the rotor tip speed and radius are already determined. This yields a fixed value for the angular velocity of the rotor but also of the turbine crowns (Ω_C), where :

$$ {}^1u_i = {}^1R_i\Omega_C = {}^1R_i\frac{2\pi N}{60} \quad \text{[N]=RPM} \tag{8.44} $$

or,

$$ {}^1u_i = \frac{{}^1R_i}{R_{tip}}\,(R_{tip}\Omega_C) = \overline{r_i}\,v_{tip} \tag{8.45} $$

It should be remembered that the above equation relates ${}^1u_i$ to $\overline{r_i}$ since $\Omega_C \propto v_{tip} = C^t$. The predesign procedure in Section 7.1.15 is now repeated for a set of stage numbers, and their impact on $\overline{r_{iopt}}$ examined. The results of the $\overline{r_{iopt}}$-study are summarised in Table 8.8.

The first observation is that $\overline{r_{iopt}}$ is more or less insensitive to the examined range of *LTIT* for a given turbine stage count, while it depends on the selected engine (Avgas/Diesel) and stage count. A plausible explanation for this behaviour is explained next. For this purpose, it is instructive to substitute Eq.8.43 in Eq.7.28, which yields :

$$\dot{m} = \frac{P_T^*}{{}^1h_{ti}\left\{1 - \left[\frac{1}{1+K_E\left(\frac{{}^1h_{ti}}{h_{ta}}-1\right)}\right]^{\eta_{p,C}\ \eta_{p,T}}\right\}} \tag{8.46}$$

where $h_{ta} = C_p\ T_{t1}$ and K_E a coefficient, which is mainly engine-type dependent :

$$K_E = \frac{\eta_m}{\eta_{CC}\ LHV\ SFC_{PE}} \tag{8.47}$$

For each engine cycle it is possible to calculate :

$$K_{E,Avgas} = 0.4844 \tag{8.48}$$

$$K_{E,Diesel} = 0.3646 \tag{8.49}$$

Fig.8.8 represents Eq.8.46 for the cycle parameters indicated in Table 8.5, but for two different turbine efficiencies. The figure shows that the combined effect of an increase in *LTIT* and concurring increase in cycle pressure ratio (Fig.8.7) for a given delivered turbine power P_T^*, results in a decrease in required mass flow $\dot{m}$. This is an interesting observation because it engenders a reduction in AR_a and Re/Re_{ref} (Section 7.1.14) and consequently impacts the turbine efficiency negatively. Fig.8.8 then also reveals that $\dot{m}$ should increase to compensate for the increased losses. However, in the event of a moderate drop in turbine efficiency, it is acceptable to state that the general tendency of $\dot{m}$ is to decrease with a temperature rise of *LTIT*.

In a second step, it is possible to prove the existence of an optimum ψ_T, i.e. $\psi_{T,opt}$, qualitatively, which is inversely proportional to $\dot{m}$. Fig.8.9 serves for this purpose. It reveals that $\overline{r_{iopt}}$ remains indeed more or less identical for other operating temperatures (*LTIT*). Increasing *LTIT* causes the operating line to move upward and to the right. If ${}^M\phi_{i_{,opt}}$ of the lower *LTIT* solution would be retained for the higher *LTIT* operating condition, there would be a significant increase in disk friction losses ζ_{FLT} due to the corresponding $\overline{r_i}$ increment (Section 7.1.14), which is already more pronounced due to the decreased mass flow (see Section 7.1.13). ${}^M\phi_{i_{opt}}$ of the higher *LTIT* should therefore be found at a larger value, while situated on the high-temperature operating line. A significant raise in ${}^M\phi_{i_{opt}}$ and thus decrease in $\overline{r_i}$, is not expected either. It would cause

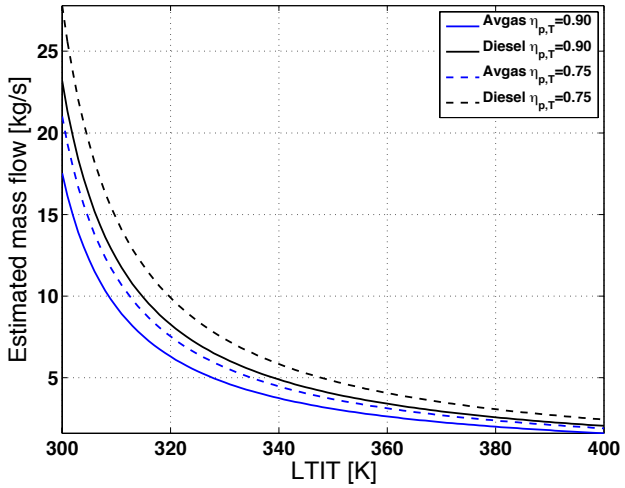

FIGURE 8.8. Impact of *LTIT* on required mass flow $\dot{m}$, $P_T^* = C^t$ (See Table 8.7).

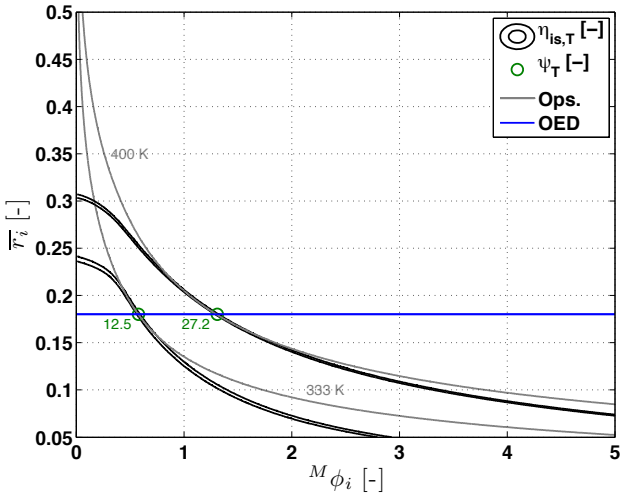

FIGURE 8.9. Impact of *LTIT* on $\overline{r}_{iopt}$.

a substantial growth of the aerodynamic losses ζ_{AT}, which are also already impacted negatively by the lower mass flow leading to a reduction in $Æ_a$ and Re/Re_{ref} (Section 7.1.14). Even though Fig.8.9 shows that some allowance is left to the designer to choose $\overline{r}_{iopt}$, it yet shows that $\overline{r}_{iopt}$ pinpoints a kind of *loss bucket*. Hence, it is reasonable to state that – the above aspects considered – there exists an optimum ψ_T, which is temperature independent, and obeys :

$$\dot{m} \propto \frac{1}{\psi_{T,opt}} \Rightarrow \overline{r}_{iopt} \cong C^t \tag{8.50}$$

since this is in line with the findings given by Eq.7.28 :

$$\dot{m}\, \overline{r}_{iopt}^2\, \psi_{T,opt} = \frac{P_T^*}{v_{tip}^2} = C^t \tag{8.51}$$

With regard to the amount of turbine stages, Table 8.8 uncovers that an increase in S_n results in a lower $\overline{r}_{iopt}$. The decrease in $\overline{r}_{iopt}$ can be attributed to the increased optimum turbine effective work coefficient ψ_T. If the change in isentropic efficiency is minor, Eq.8.46 then uncovers that – for a given *LTIT* – the mass flow is invariable, regardless of the selected amount of stages. Eq.7.28 can consequently be further reduced to :

$$\psi_T \, \overline{r}_i^2 = C^t \qquad \text{or} \qquad \overline{r}_i \propto \sqrt{\frac{1}{\psi_T}} \tag{8.52}$$

where, following Eq.7.164 :

$$\psi_T \cong 2(S_n - 1) \tan {}^M\alpha_i \, {}^M\phi_i \tag{8.53}$$

According to Figs. 7.3 and 7.4, increasing the number of stages only slightly decreases ${}^M\phi_{i_{opt}}$ – and thus ${}^M\psi_{opt}$ – for the selected ${}^M\alpha_i$ domain. As a conquence, $\psi_{T,opt}$ generally varies proportionally to the number of stages, i.e. (Eq.7.120) :

$$\psi_{T,opt} \cong (S_n - 1)^M\psi_{opt} \tag{8.54}$$

Hence, it is reasonable to expect that (Eq.8.52) :

$$\overline{r}_{iopt} \propto \sqrt{\frac{1}{\psi_{T,opt}}} \propto \sqrt{\frac{1}{(S_n - 1)^M\psi_{opt}}} \quad \Rightarrow \quad S_n \nearrow \quad \Rightarrow \quad \psi_{T,opt} \nearrow \quad \Rightarrow \quad \overline{r}_{iopt} \searrow \tag{8.55}$$

The more stages installed, the more dominant the loss characteristics of the middle stages will become, while the influence of $1/S_n$ weakens. Consequently, the effect of an increase in turbine stages on $\overline{r}_{iopt}$ should decrease, which is substantiated by the results adopted in Table 8.8.

Figs. 8.10-8.12 and Figs. 8.13-8.15 show the effect of the number of turbine stages on $\overline{r}_{iopt}$ for respectively the Avgas engine powered TDR cycle and the Diesel engine powered TDR cycle operating at their respective design point cycle conditions (Table 8.6). Because at the design point, the cycle pressure ratio and *LTIT* are almost identical for both cycles, and as a result $\dot{m}$ as well (Fig.8.8), it is not surprising that the iso-efficiency lines for a given number of turbine stages in the above reported Figs. 8.10-8.15, will be situated on comparable positions. $\psi_{T,opt}$ should then be very similar too. This is proven by use of Eq.8.51 and introduction of the values of $\overline{r}_{iopt}$ (Table 8.8) and $\dot{m}$ (Table 8.9) for each cycle. Indeed :

$$\dot{m} \, \overline{r}_{iopt}^2 \Big|_{Avgas} \cong \dot{m} \, \overline{r}_{iopt}^2 \Big|_{Diesel} \tag{8.56}$$

$$0.150 \cong 0.152 \quad \Rightarrow \quad \psi_{T,opt_{Avgas}} \cong \psi_{T,opt_{Diesel}} \tag{8.57}$$

For the design point of both cycles, selecting a six-stage turbine ($S_n = 6$) appears as a good compromise between high $\eta_{is,T}$ and low A_e (Table 8.8). This because an as low as reasonably possible value of $\overline{r}_{iopt}$ should be strived for, as it reduces the turbine flow-path area A_e. The latter coefficient will be used in this study as a yardstick for the RELT parasite drag. A_e will be defined and discussed in a subsequent section.

Table 8.8. Optimum turbine specific inlet radius $\overline{r}_{iopt}$.

			Avgas			**Diesel**		
$LTIT$	π_C	S_n	$\overline{r}_{iopt}$	$\eta_{is,T}/\eta^*_{is,T_{S_n=8}}$	$A_e/A_{e_{S_n=8}}$	$\overline{r}_{iopt}$	$\eta^*_{is,T_{S_n=8}}$	$A_e/A_{e_{S_n=8}}$
all	$f(LTIT)$	4	0.205	0.92	-	0.200	0.94	-
all	$f(LTIT)$	6*	0.180*	0.97	-	0.175*	0.98	-
all	$f(LTIT)$	8	0.170	1.00	-	0.170	1.00	-
$LTIT^\star$	$\pi_C^\star$	4	-	-	0.65	-	-	0.61
$LTIT^\star$	$\pi_C^\star$	6	-	-	0.83	-	-	0.80
$LTIT^\star$	$\pi_C^\star$	8	-	-	1.00	-	-	1.00

$*$ From predesign procedure, averaged. Serves as indicative value. * is DP.

Turbine efficiency and COP_M : Design point selection

Once $\overline{r}_{iopt}$ is selected, the detailed design model discussed in Section 7.1.15 allows calculating the geometry and thus the polytropic efficiency of the Ljungström turbine $\eta_{p,T}$ for each examined condition (OED). The results of the coupled cycle and turbine model are presented next.

Fig.8.16 shows the coefficient of performance margin COP_M for both the Avgas and Diesel powered TDR cycles. For the Diesel engine, a clear maximum exists near $LTIT = 69°C$, which concurs with a cycle pressure ratio of 1.24 (Fig.8.17). Note that the RELT polytropic efficiency drops when $LTIT$ increases (Fig.8.18), which is entirely due to the concurring rise in cycle pressure ratio (Fig.8.7) and decrease in $\dot{m}$ (Fig.8.8). The positive impact of an increased $LTIT$ on COP, as discussed in Chapter 4, is hereby nullified.
The Avgas engine powered TDR cycle does not exhibit such a maximum in the examined temperature range. Fig.8.16 indicates that a similar optimum for COP_M might be found near or below the minimum studied $LTIT$ of 40°C. However, pursuing lower turbine inlet temperatures appears unreasonable by the dramatic increase in frontal area of the Ljungström turbine (Fig.8.19), which is related to the parasite drag of the helicopter.
The parasite drag of a helicopter becomes important during forward flight, increases with the square of the flight speed (Newman (2003)) and should be minimised. Fig.8.19 uses the turbine relative frontal flow path area $A_{e,rel}$ as parasite drag metric, where the minimum turbine frontal area in the examined temperature range serves as parasite drag

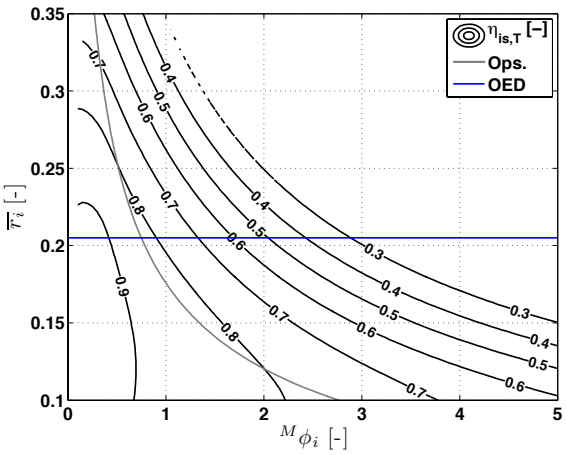

FIGURE 8.10. Avgas engine powered TDR cycle : $\overline{r}_{iopt}$ for $S_n = 4$.

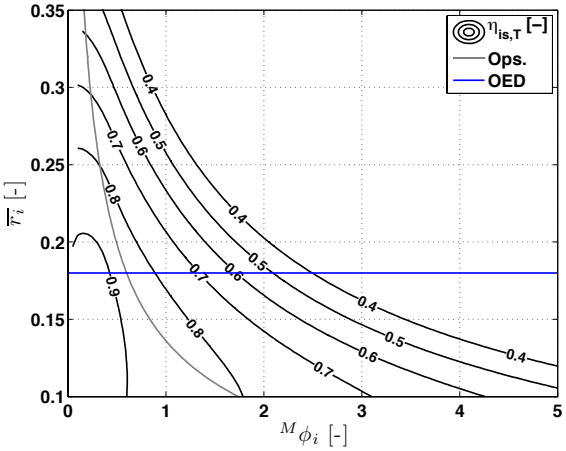

FIGURE 8.11. Avgas engine powered TDR cycle : $\overline{r}_{iopt}$ for $S_n = 6$.

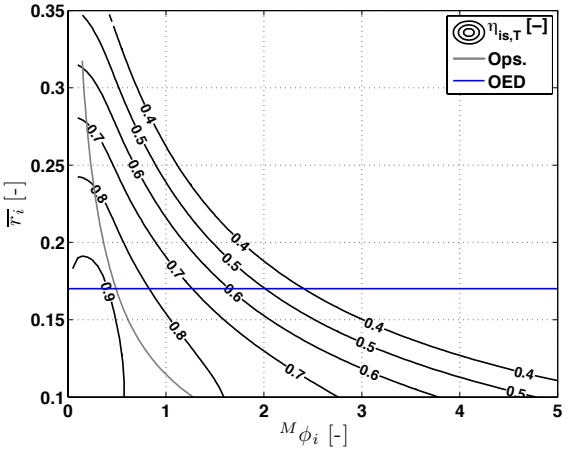

FIGURE 8.12. Avgas engine powered TDR cycle : $\overline{r}_{iopt}$ for $S_n = 8$.

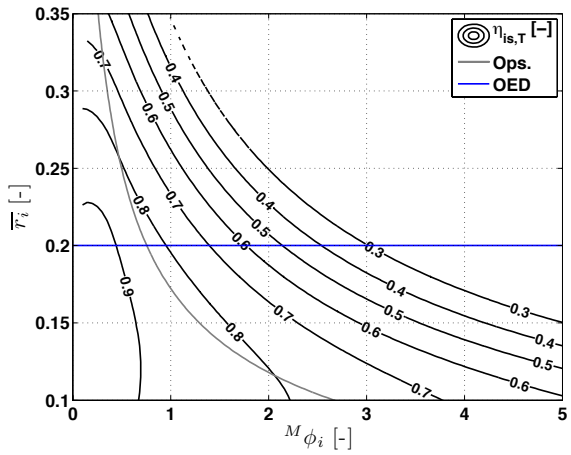

FIGURE 8.13. Diesel engine powered TDR cycle : $\overline{r}_{iopt}$ for $S_n = 4$.

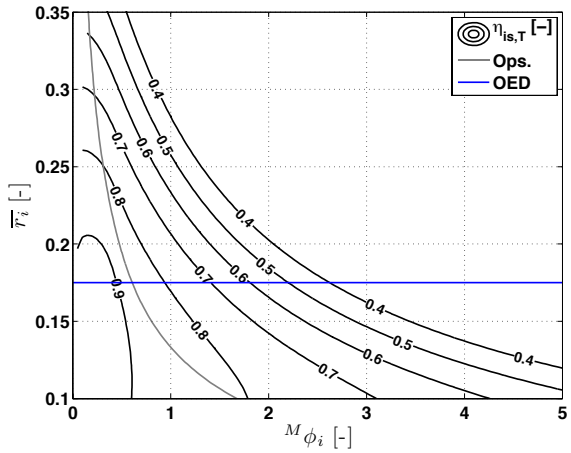

FIGURE 8.14. Diesel engine powered TDR cycle : $\overline{r}_{iopt}$ for $S_n = 6$.

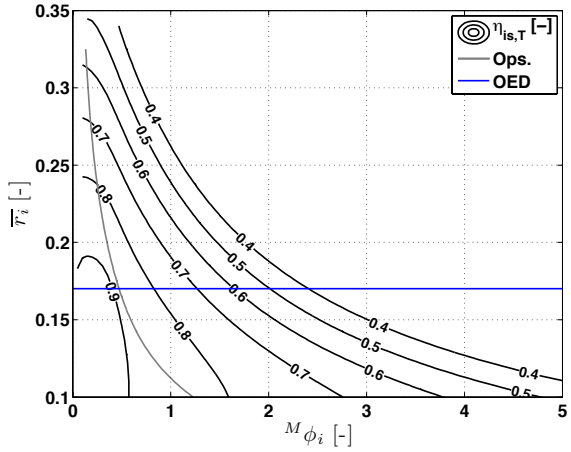

FIGURE 8.15. Diesel engine powered TDR cycle : $\overline{r}_{iopt}$ for $S_n = 8$.

datume, i.e. at a turbine inlet temperature of 400 K :

$$A_{e,rel} = \frac{A_e}{\min(A_{e,range})} = \frac{A_e}{A_{e,400K}} \tag{8.58}$$

A_e is the turbine frontal flow path area (Figs. 8.20 & 8.21), which is defined as :

$$A_e \triangleq 2\, {}^{L}H_{bo}\, {}^{L}R_o \tag{8.59}$$

where ${}^{L}H_{bo}$ and ${}^{L}R_o$ are respectively the outlet blade height and outlet radius of the last turbine stage. The helicopter community presents parasite drag commonly by an equivalent flat plate area f_e. It is defined as – Prouty (2002) :

$$f_e \triangleq \frac{D}{q} = C_D\, S_{ref} \tag{8.60}$$

D, C_D and S_{ref} in Eq.8.60 are respectively the drag, the drag coefficient and the concurring reference area of the examined object. q is the dynamic pressure of the flow passing over the object. For the free stream flow, the RELT is felt by the presence of a streamlined hub delimited between two cupolae (Fig.8.59). Since the shape of the hub will not change substantially as ${}^{L}R_o >> {}^{L}H_{bo}$, it is reasonable to expect that $C_D \cong C^t$. As a consequence :

$$f_e = \frac{D}{q} \propto S_{ref} \propto A_e \tag{8.61}$$

A_e may therefore be used as a parasite drag metric. The Avgas engine cycle design point is selected where $A_{e,rel}$ starts diverging substantially from the moderate slope it exhibits at the higher $LTIT$ (Fig.8.19), while limiting the negative impact on COP_M. This point is found at $LTIT$ = 60°C and is consequently adopted as the design point. The 2% COP_M-loss by selecting a higher operating temperature appears acceptable, while conserving a performance margin of 10% over the conventional equivalent.

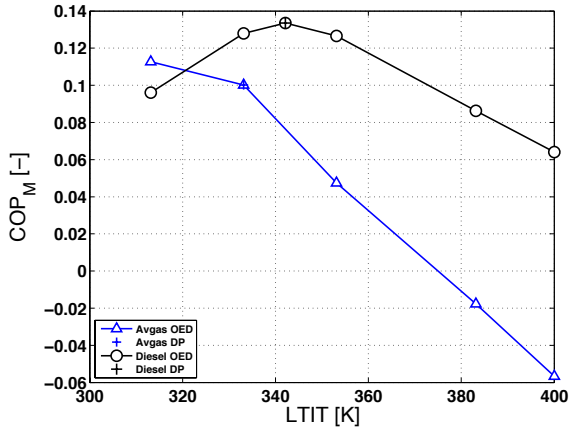

FIGURE 8.16. Cycle COP_M as a function of *LTIT* for the Avgas and Diesel engines, OED conditions.

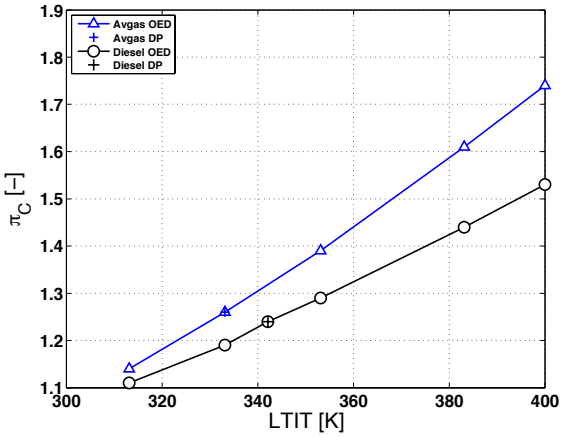

FIGURE 8.17. Cycle pressure ratio π_C as a function of *LTIT* for the Avgas and Diesel engines, OED conditions.

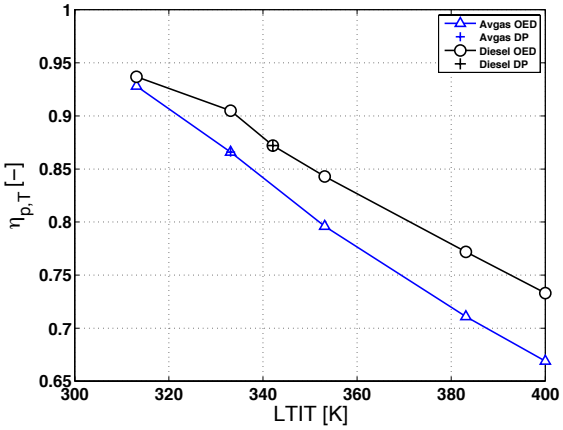

FIGURE 8.18. RELT polytropic efficiency as a function of *LTIT* for the Avgas and Diesel engines, OED conditions.

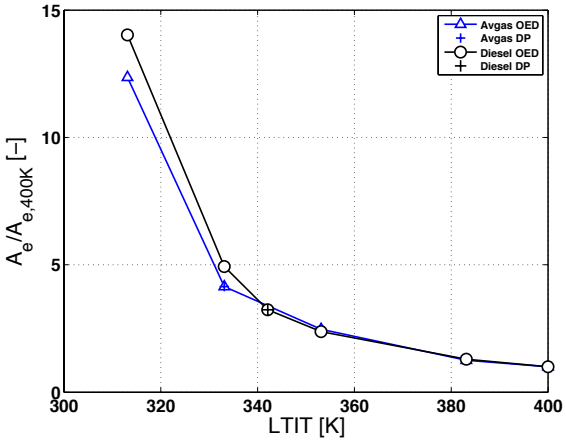

FIGURE 8.19. Turbine relative frontal flow path area $A_{e,rel}$ as a function of *LTIT* for the Avgas and Diesel engines, OED conditions.

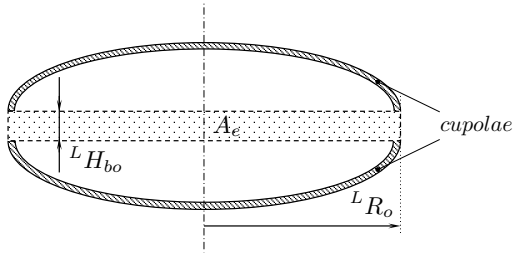

FIGURE 8.20. Definition of the frontal flow path area A_e.

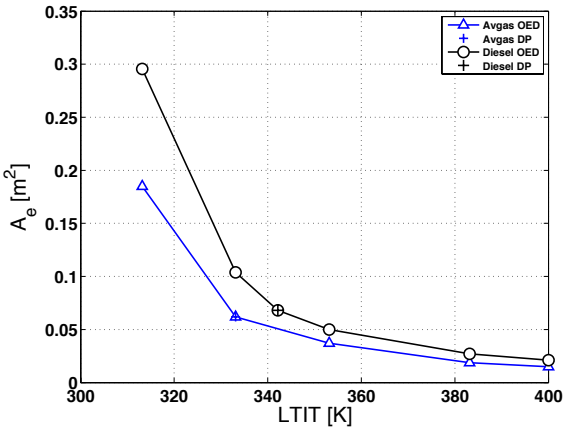

FIGURE 8.21. Turbine frontal flow path area A_e as a function of *LTIT* for the Avgas and Diesel engines, OED conditions.

From the conducted study, it is clear that the Diesel engine powered TDR cycle is the most efficient one, bearing the highest COP_M. The difference in turbine flow frontal area between both cycles at the design point is only marginally higher for the Diesel engine and will be largely offset by the higher COP_M (Fig.8.21).
Note that no distinction was made between the installation of either an Avgas or a Diesel engine when calculating ΔW_E. However, this issue can be waived, since the both cycles work at similar pressure ratios (pre-compression effect, Section 4.3.3) on the one hand, and the specific power outputs (SPP, Table 4.1) are of the same order of magnitude on the other.

Table 8.9 summarises the characteristics of the installed piston engines in the cycle and presents additional cycle data declared in Chapter 4. The turbine geometry is treated next.

Table 8.9. Design point cycle characteristics.

	Avgas	**Diesel**
P^*_M [kW]	106.0	102.5
SFC_{PE} [g/kWh]	250	230
π_C [-]	1.26	1.24
π_T [-]	1.25	1.23
$LTIT$ [°C]	60	69
PCF [-]	1.159	1.147
$\dot{m}$ [kg/s]	4.70	4.90
BPR [-]	63.6	35.5
FAR [-]	0.102	0.0483
COP [-]	0.793	0.817
COP_M [%]	10.0	13.4
$\eta_{p,T}$ [-]	0.866	0.872

Geometry

This section reports the important turbine design parameters and develops the turbine geometry. With the obtained geometry, the off-design performance of the turbine can be established. Tables 8.10 and 8.11 reflect the most important turbine parameters for respectively the Avgas and the Diesel powered TDR cycles. The value indicated by Horlock (1966) for the blade maximum thickness-to-camberline-length ratio of 0.2 is imposed (Section 7.1.12). The minimum chord target of 2 cm was approached within user imposed satisfactory margins of a few millimeters.

Studying Tables 8.10 and 8.11, the following is noted for all turbine stages ;
$Z > Z_{sl}$ allowing the use of the slip model discussed in Chapter 6. The blade aspect ratio AR is not excessive (≤ 3) and the leakage mass flow $\dot{m}_{LL}$ is negligibly small ($< 0.5\%$). The blade height decreases slightly with the turbine radius, which is necessary to compensate for the density decrease caused by the flow expansion on the one hand, and the increased flow area by the larger radius on the other. The relative Mach numbers near the inlet and outlet of the blade passages remain low.
The Reynolds number is about a third of the reference Reynolds number used in the model of Soderberg, except for the first stage, which benefits from a higher Reynolds number due to the larger blade chord. The consequence of this is a decreased turbine efficiency with respect to the reference.
The reaction degree $\hat{R}$ of the middle stages is around unity, as predicted by the conceptual performance model expounded in Section 7.1.11. An identical conclusion stands for the first and the last turbine stages, for which the reaction degree was predicted to be respectively higher and lower than unity.
A well balanced power production is established (ψ), where for each cycle both turbine halves deliver an equal amount of power $P_T^*/2$.
Finally it is important to highlight that the reason for needing a relatively larger blade chord for the first stage is entirely due to the high stagger angle λ (Eq.7.140), while keeping R_o/R_i constant throughout the turbine, as required by the fixed ${}^M\chi$ condition.
The geometry of the RELT for the Avgas engine powered TDR cycle is shown in Fig.8.22 and Fig.8.23, showing respectively the vertical and the horizontal cross-section of the Ljungström turbine. In Fig.8.22, the first crown is indicated in green and the second one in blue. The blades are plotted in black. Similar plots are also given for the Diesel engine powered TDR cycle in Fig.8.24 and Fig.8.25.

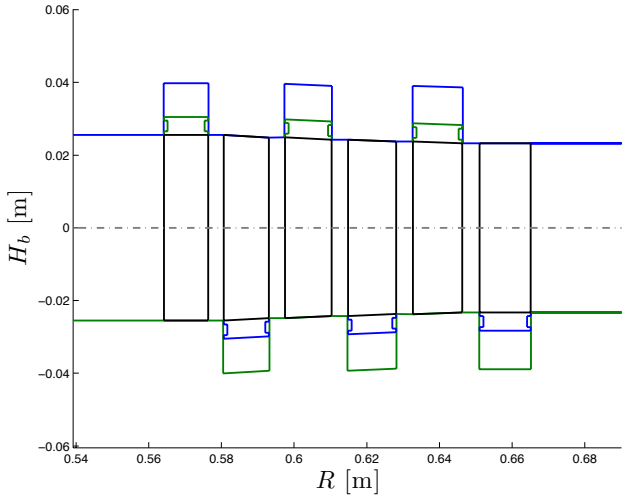

FIGURE 8.22. Avgas engine powered TDR cycle, vertical plane RELT cutaway (black : blades, green : first crown, blue : second crown).

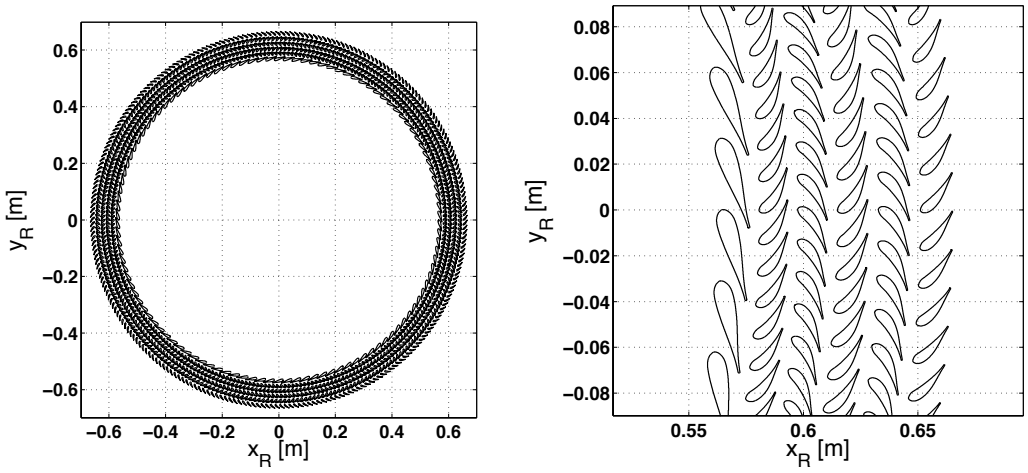

FIGURE 8.23. Avgas engine powered TDR cycle, horizontal plane RELT cutaway.

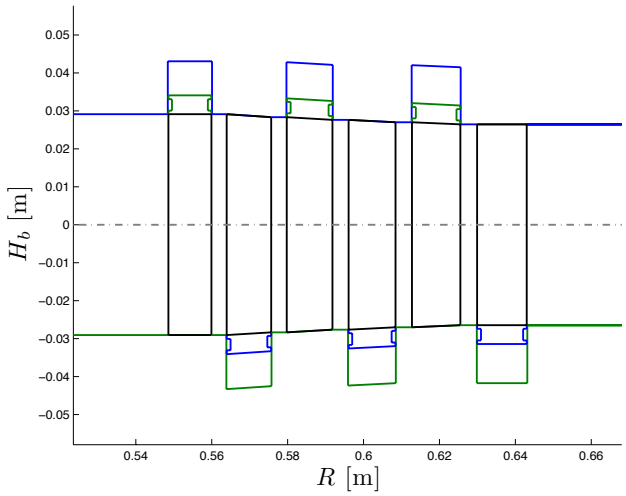

FIGURE 8.24. Diesel engine powered TDR cycle, vertical plane RELT cutaway (black : blades, green : first crown, blue : second crown).

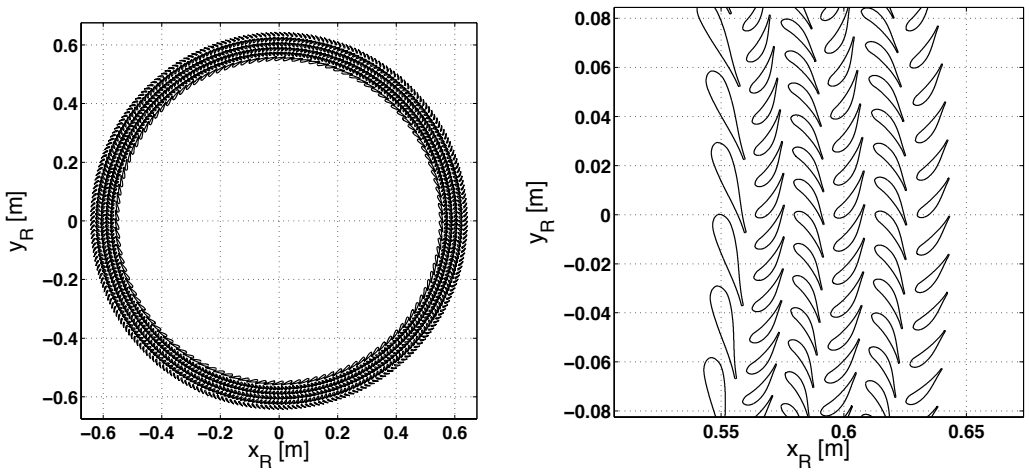

FIGURE 8.25. Diesel engine powered TDR cycle, horizontal plane RELT cutaway.

Table 8.10. Turbine characteristics – Avgas engine powered TDR cycle (DP, OED).
P_{C1}=42.1 kW – P_{C2}=42.0 kW – ISA SLS

Stage number →	S_1	S_2	S_3	S_4	S_5	S_6
${}^{M}\chi$ [-]			1.015			
$\hat{c}$ [-]			0.035			
R_i [m]	0.564	0.581	0.598	0.615	0.633	0.651
R_o [m]	0.576	0.593	0.610	0.628	0.646	0.665
ϕ_i [-]	0.508	0.490	0.490	0.490	0.490	0.490
ϕ_o [-]	0.497	0.497	0.497	0.497	0.497	0.474
ψ [-]	1.113	2.164	2.164	2.164	2.164	1.051
$\hat{\theta}$ [-]	223	210	196	183	171	160
$\hat{R}$ [-]	1.533	1.023	1.023	1.023	1.023	0.472
$\alpha_o - \alpha_{o,b}$ [deg]	0.4	0.5	0.5	0.5	0.5	2.6
ϵ [°]	13.4	82.4	82.4	82.4	82.4	70.6
λ [°]	74.8	56.3	56.3	56.3	56.3	49.6
β_{bi} [°]	-63.1	5.9	5.9	5.9	5.9	5.9
δ [°]	0.6	0.4	0.4	0.4	0.4	1.1
M_i [-]	0.05	0.13	0.13	0.14	0.14	0.15
M_o [-]	0.13	0.13	0.14	0.14	0.15	0.06
M_{ri} [-]	0.12	0.054	0.056	0.058	0.060	0.062
M_{ro} [-]	0.23	0.24	0.25	0.26	0.26	0.14
AR_a [-]	4.205	4.033	3.821	3.628	3.453	3.324
Re [10^5]	0.70	0.33	0.34	0.35	0.36	0.36
c [m]	0.041	0.022	0.023	0.023	0.024	0.021
H_{bi} [m]	0.051	0.051	0.050	0.049	0.047	0.047
$\overline{B}$ [-]	1	0.974	0.976	0.978	0.980	1
Z [-]	114	266	266	266	266	249
Z_{sl} [-]	86	88	88	88	88	158
$\eta_{p,T}$ [-]	0.86	0.87	0.87	0.87	0.86	0.87
$\dot{m}_{LL}/\dot{m}$ [-]	0.002	0.003	0.003	0.003	0.003	0.002
$(t/c)_{max}$ [-]	0.20	0.022	0.21	0.21	0.21	0.21
t_{TE} [mm]	0.8	0.5	0.5	0.5	0.5	0.4
o [mm]	5.0	3.6	3.7	3.8	3.9	7.1
R_c [m]	0.60	0.082	0.084	0.087	0.089	0.082
$e/c^{\dagger}$ [-]	$2.93{\cdot}10^{-5}$	$5.45{\cdot}10^{-5}$	$5.30{\cdot}10^{-5}$	$5.15{\cdot}10^{-5}$	$5.01{\cdot}10^{-5}$	$5.63{\cdot}10^{-5}$

† Relative blade roughness. See Appendix D, Section D.1.6

Table 8.11. Turbine characteristics – Diesel engine powered TDR cycle (DP, OED).
P_{C1}=41.9 kW – P_{C2}=41.9 kW – ISA SLS

Stage number →	S_1	S_2	S_3	S_4	S_5	S_6
${}^{M}\chi$ [-]				1.014		
$\hat{c}$ [-]				0.035		
R_i [m]	0.549	0.564	0.580	0.596	0.613	0.630
R_o [m]	0.560	0.576	0.592	0.608	0.626	0.643
ϕ_i [-]	0.513	0.495	0.495	0.495	0.495	0.495
ϕ_o [-]	0.502	0.502	0.502	0.502	0.502	0.479
ψ [-]	1.222	2.183	2.183	2.183	2.183	1.062
$\hat{\theta}$ [-]	243	229	214	201	188	176
$\hat{R}$ [-]	1.538	1.023	1.023	1.023	1.023	0.466
$\alpha_o - \alpha_{o,b}$ [deg]	0.3	0.4	0.4	0.5	0.5	2.2
ϵ [°]	13.6	83.5	83.5	83.5	83.5	71.5
λ [°]	74.7	55.7	55.7	55.7	55.7	49.1
β_{bi} [°]	-62.8	7.1	7.1	7.1	7.1	7.1
δ [°]	0.6	0.4	0.4	0.4	0.4	1.1
M_i [-]	0.05	0.12	0.13	0.13	0.13	0.14
M_o [-]	0.12	0.13	0.13	0.14	0.14	0.06
M_{ri} [-]	0.11	0.052	0.054	0.056	0.058	0.060
M_{ro} [-]	0.22	0.23	0.24	0.25	0.25	0.14
AR_a [-]	5.106	4.901	4.644	4.411	4.198	4.042
Re [10^5]	0.62	0.29	0.30	0.31	0.31	0.32
c [m]	0.038	0.020	0.021	0.022	0.022	0.020
H_{bi} [m]	0.058	0.058	0.057	0.055	0.054	0.053
$\overline{B}$ [-]	1	0.973	0.975	0.977	0.979	1
Z [-]	118	279	279	279	279	260
Z_{sl} [-]	89	91	91	91	91	165
$\eta_{p,T}$ [-]	0.88	0.87	0.87	0.87	0.87	0.88
$\dot{m}_{LL}/\dot{m}$ [-]	0.002	0.003	0.003	0.003	0.003	0.002
$(t/c)_{max}$ [-]	0.20	0.21	0.21	0.21	0.21	0.21
t_{TE} [mm]	0.8	0.4	0.4	0.5	0.5	0.4
o [mm]	4.7	3.3	3.4	3.5	3.6	6.6
R_c [m]	0.55	0.074	0.076	0.078	0.080	0.075
$e/c^{\dagger}$ [-]	$3.12{\cdot}10^{-5}$	$5.89{\cdot}10^{-5}$	$5.73{\cdot}10^{-5}$	$5.57{\cdot}10^{-5}$	$5.42{\cdot}10^{-5}$	$6.09{\cdot}10^{-5}$

† Relative blade roughness. See Appendix D, Section D.1.6

Off-design performance : the turbine map

The blade passage losses for the design point calculations are determined by means of the model of Soderberg, as highlighted in Section 6.1.4. When the turbine operates at other conditions than the design point, also called *off-design* operation, its performance must be calculated using another loss model, viz. the model of Ainley & Mathieson (1955), as mentioned in Section 7.2. The off-design performance of the Ljungström turbine is presented by a *turbine map*, which is shown in Fig.8.26 and Fig.8.27 for the Avgas and Diesel engine cycle respectively. Here, the maps are only calculated for $S_\Omega = 1$ (no slip, Section 5.3.5) and for the complete turbine system[v]. Note that several maps can be produced, for each stage and for various S_Ω, which can be implemented in a dynamic computer model of the TDR helicopter. Such a model would allow evaluating the performance of each component in the TDR helicopter and their interaction throughout the entire flight envelope. This work is not pursued here.

On the abscissa of the turbine map, the corrected mass flow $\dot{m}_{corr}$ is multiplied by a *stretch coefficient* $\sqrt{N_{ref}/N}$. This intervention is useful to present the data. Otherwise, the corrected speed lines (N_{corr}) would fall almost on top of eachother, which renders the readability difficult. Note that N_{ref} was set equal to the design rotational speed N_{DP} and that :

$$\frac{N_{ref}}{N} = \frac{N_{DP}}{\sqrt{{}^1\theta_{ti}}} \frac{\sqrt{{}^1\theta_{ti}}}{N} = \frac{N_{DP_{corr}}}{N_{corr}} \tag{8.62}$$

The ordinate represents the RELT total-to-total expansion ratio π_T (Eq.7.24). The corrected design point variables used to indicate the design point on the turbine maps by a red cross, are summarised in Table 8.12.

An interesting observation is that the calculated polytropic turbine efficiency $\eta_{p,T}$ using Soderberg's model with simplifications described in Section 7.1.1, predicts the obtained polytropic efficiency by the more sophisticated model of Ainley & Mathieson (1955) remarkably well.
The turbine polytropic efficiency $\eta_{p,T}$ remains fairly high for a large range of π_T and $\dot{m}$, which is encouraging when COP_M is to remain positive.

[v]The performance map for each turbine stage will not be discussed in this work.

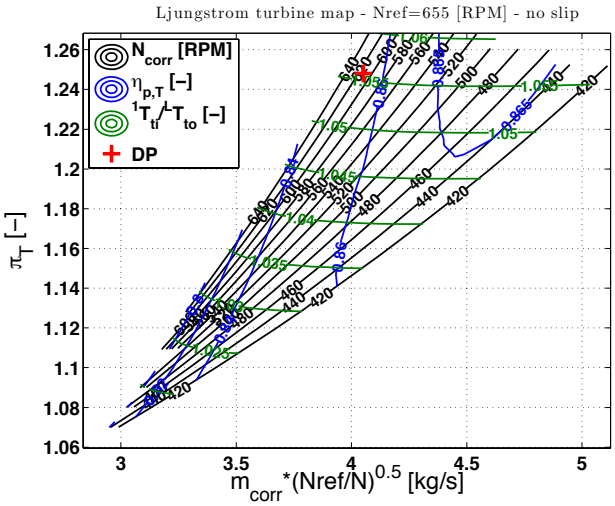

FIGURE 8.26. Avgas engine powered TDR cycle off-design turbine performance map.

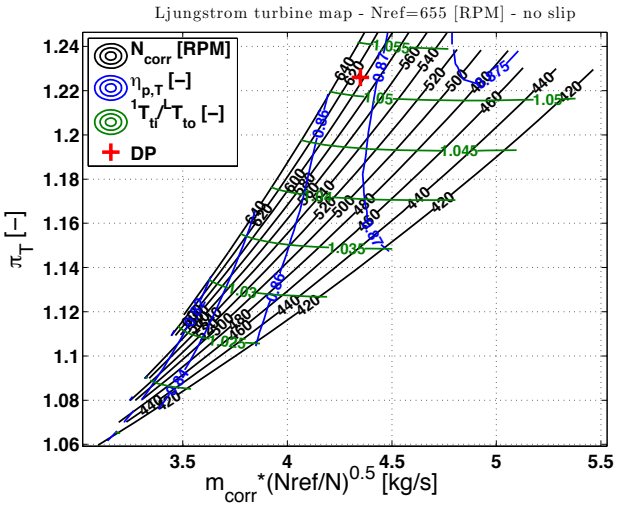

FIGURE 8.27. Diesel engine powered TDR cycle off-design turbine performance map.

Table 8.12. Turbine characteristics – corrected variables (DP, OED).

	Avgas	**Diesel**
$\dot{m}_{corr}$ [kg/s]	4.05	4.35
N_{corr} [RPM]	609	601
${}^{1}\delta_{ti}$ [-]	1.247	1.228
${}^{1}\theta_{ti}$ [-]	1.156	1.187

The impact of endwall fences discussed in Section 6.1.7, is represented in Fig.8.28 and Fig.8.29 for respectively the Avgas and the Diesel engine powered TDR cycles. Comparing the efficiency between the turbines with and without endwall fences does not reveal a noteworthy difference. This is a sensible consequence of having relatively normal blade aspect ratios $AR \cong 3$. Considering the added complexity to the design of the turbine blade, it appears wise not to install endwall fences for the examined cases.

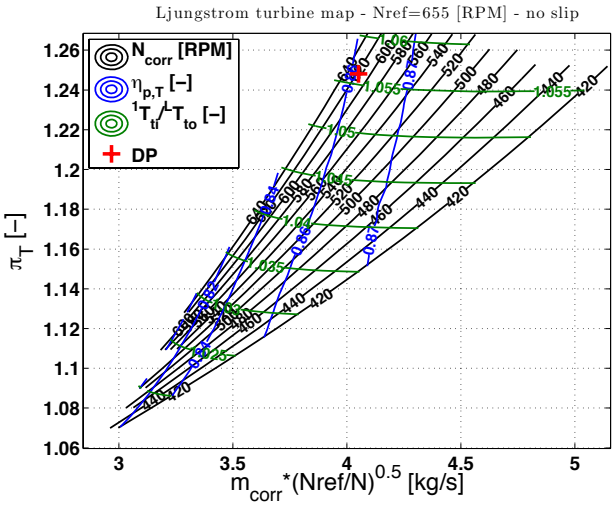

FIGURE 8.28. Avgas engine powered TDR cycle off-design turbine performance map with endwall fences.

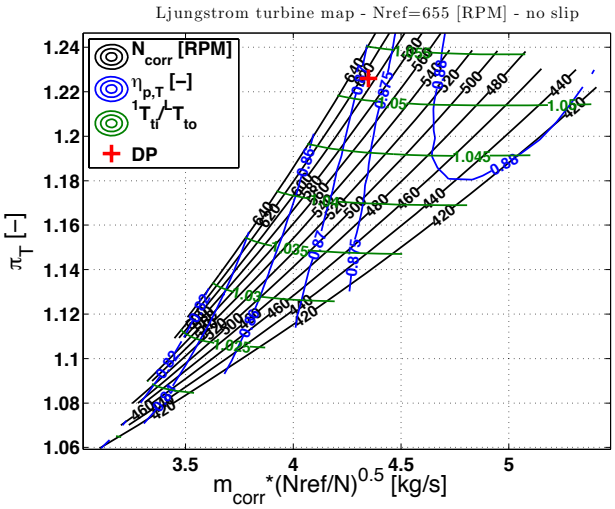

FIGURE 8.29. Diesel engine powered TDR cycle off-design turbine performance map with endwall fences.

8.4 TF-TDR cycle : NH90-class helicopter

In contrast to the VLR-helicopter for which $W_{g,TDR}$ was imposed, the maximum gross weight of the conventional helicopter $W_{g,conv}$ is the datum taken into consideration. The manufacturer documentation on the NH90 helicopter indicates that its gross weight is 10600 kg and as a consequence :

$$W_{g,conv} = 10600 \text{ kg} \tag{8.63}$$

8.4.1 Turbofan modelling

In the conventional helicopter of the considered weight category, the power is generally delivered by two turboshafts (Appendix A). In the TDR helicopter however, it will be sufficient to install a single mixed flow turbofan (Fig.8.31) of which the size and thus demanded (imaginary) thrust T_{Nt}[vi] will depend entirely on the required power P_T^* and the power gain PG.

Under T/O conditions, it is reasonable to adopt a turbofan *turbine inlet temperature TIT* of 1600 K – Cumpsty (2000). Additionally, the *overall pressure ratio* (*OPR*) of the turbofan may be found to be around 32 on average, as indicated in Fig.8.30, which was established using data collected by this author. Because the overall pressure ratio and *TIT* are imposed, the fan pressure ratio (π_F) will become a function of the turbofan bypass ratio (BPR_{TF}), whereas in Section 4.5, the latter was examined as an independent variable. The assumption of a fixed overall pressure ratio at T/O conditions is a reasonable design criterion. Consequently, the only cycle variable that remains to be evaluated parametrically is BPR_{TF}. The designer has now the liberty to select a convenient turbofan bypass ratio BPR_{TF} leading to the best possible COP_M. The bypass ratio will be evaluated in a range between 4 and 10, which is justifiable by observing the data in Fig.4.29.
Considering that the mixing process of the bypass and core flows is perfect, the mixed flow Mach number M_{64} (Fig.8.32) to be 0.2 (Hendrick & Buysschaert (2015)) and imposing the condition that $v_{163} \cong v_{63}$ to guarantee maximum flow uniformity in front of the RELT, enables the calculation of the turbofan cycle intensive properties. The mass flow can be selected in a second stage to match the required power.
The parametric cycle studies were performed using Joachim Kurzke's *GasTurb 11* software suite. Standard turbofan component efficiencies proposed in the software were adopted, which can be found in Appendix G.
For the above mentioned design conditions, correlations were established for the turbofan intensive variables of interest, which are summarised in Table 8.13. The correlations are third-order polynomials and based on five turbofan configurations, which were calculated in GasTurb 11 for a bypass ratio of 4, 6, 7.6[vii], 8 and 10. The used correlations will be

[vi] Note that $T_{Nt} = T_N$ since only one engine will be used.
[vii] This BPR_{TF} is the minimum allowable turbofan bypass ratio. It is explained in Section 8.4.4.

plotted when applied for the first time in the subsequent sections. For all configurations, the fuel-to-air ratio was observed to be reasonably constant, viz. :

$$FAR \cong 0.0228 \tag{8.64}$$

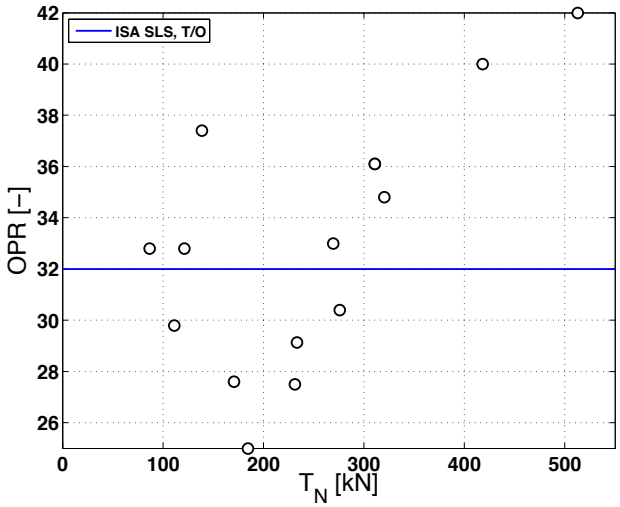

Figure 8.30. Survey on the turbofan *OPR* at T/O conditions ISA SLS, Appendix H.

Table 8.13. Turbofan intensive properties – TIT = 1600 K, OPR = 32, T/O ISA SLS, v_a = 0 [m/s].

$$a\ BPR_{TF}^3 + b\ BPR_{TF}^2 + c\ BPR_{TF} + d$$

	a	b	c	d
$EGT = LTIT$ [K]	$-2.7146 \cdot 10^{-1}$	7.8512	$-8.4802 \cdot 10^{1}$	$7.1054 \cdot 10^{2}$
π_F [-]	$-1.6812 \cdot 10^{-3}$	$4.8437 \cdot 10^{-2}$	$-5.1660 \cdot 10^{-1}$	3.4790
π_{HPC} [-]	$6.1667 \cdot 10^{-3}$	$-2.1050 \cdot 10^{-1}$	3.0363	6.2080
SPT [m/s]	$-2.7406 \cdot 10^{-1}$	8.2244	$-9.7307 \cdot 10^{1}$	$6.9140 \cdot 10^{2}$
$TSFC$ [kg/daNh]	$-1.4583 \cdot 10^{-4}$	$4.8750 \cdot 10^{-3}$	$-6.4667 \cdot 10^{-2}$	$5.8500 \cdot 10^{-1}$
C_{pg} [J/kgK]	$-4.1667 \cdot 10^{-2}$	1.3737	$-1.5936 \cdot 10^{1}$	$1.0978 \cdot 10^{3}$
p_{t64}/p_a [-]	$-1.5546 \cdot 10^{-3}$	$4.4940 \cdot 10^{-2}$	$-4.8134 \cdot 10^{-1}$	3.2848
v_8 [m/s]	$1.7396 \cdot 10^{-2}$	1.2094	$-4.2051 \cdot 10^{1}$	$5.4832 \cdot 10^{2}$

8.4.2 Rotor radius

The same procedure is followed as the one described for the VLR-class TDR helicopter. R_{tip} is calculated using Eq.8.30, based on $W_{g,conv}$. Consequently :

$$R_{tip} = 8.3 \text{ [m]} \tag{8.65}$$

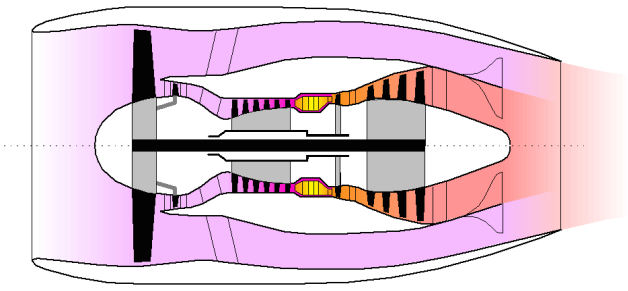

FIGURE 8.31. Mixed flow turbofan cross-section. Adopted from GasTurb 11, Joachim Kurzke.

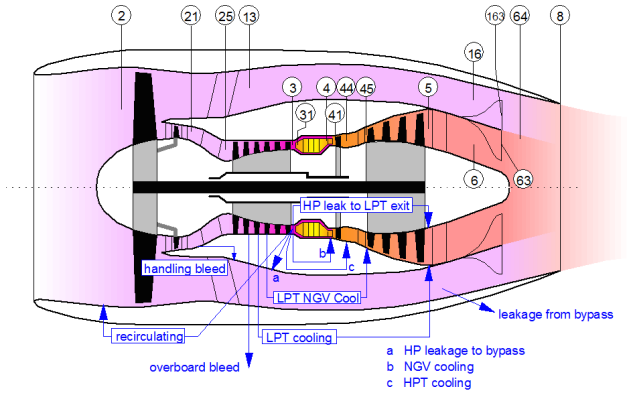

FIGURE 8.32. Mixed flow turbofan cross-section with engine stations. Adopted from GasTurb 11, Joachim Kurzke.

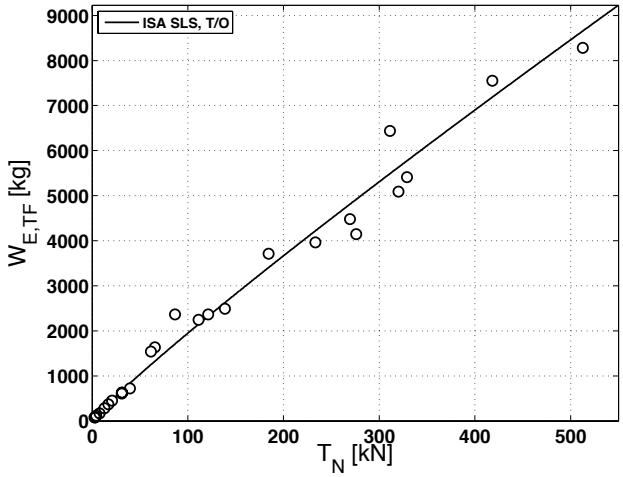

Figure 8.33. Turbofan weight $W_{E,TF}$ as a function of maximum T/O thrust at ISA SLS – Author survey, Appendix H.

8.4.3 Empty weight correction

The same methodology is followed as discussed in Section 8.3.3. Since the turbofan powered TDR cycle is considered, the weight of the turbofan needs to be added and the weight of the turboshaft $W_{E,7A}$ subtracted. Note that the fan takes over the function of the compressor in the piston engine powered TDR cycle. As a consequence, $W_{E,C}$ must not be considered. The above examination leads to the following relation for the empty weight correction :

$$\Delta W_E \cong W_{E,T} + W_{E,TF} + \Delta W_{E,2} - W_{E,3A} - W_{E,7A} - W_{E,7B} \tag{8.66}$$

$W_{E,TF}$ represents the weight of the turbofan and is a function of the maximum T/O thrust, as indicated in Fig.8.33. The trend-line resulting from the set of data found by a survey performed by this author yields :

$$W_{E,TF} = 29.141\left(\frac{T_N}{1000}\right)^{0.9125} \quad \text{[kg][N]} \quad \text{or} \quad W_{E,TF} = 29.141\left(\frac{P_T^*/PG}{1000}\right)^{0.9125} \quad \text{[kg][W][-]} \tag{8.67}$$

Eq.8.67 shows that $W_{E,TF} = f(T_N)$ and consequently, using the definition of the cycle power gain in this equation, it is clear that $W_{E,TF} = f(P_T^*, PG)$. Eq.8.10 and Eq.8.11 on the other hand, prove that $P_T^* = f(\Delta W_E)$. As a result, $W_{E,TF}$ and P_T^* depend on each other, and the solution has to be calculated iteratively by coupling the cycle model with the turbine model. Convergence is met quickly in case a good initial estimation is made for the power gain. This is possible since the power gain is mainly a function of the turbofan bypass ratio and the turbine polytropic efficiency, where the latter will be seen to be reasonably constant at the higher bypass ratios (Section 8.4.5 and Fig.8.42). Then, for a given bypass

ratio, the problem can then be further reduced to finding the required mass flow to meet the required turbine power, i.e. :

$$P_T^* = \dot{m}\, PG(BPR_{TF})\, SPT(BPR_{TF}) \cong \dot{m}\, C^t \tag{8.68}$$

Indeed, from the definitions of the specific thrust (Eq.4.146), turbine power (Eq.4.158) and power gain (Eq.4.168), it follows :

$$PG = \left(1 + \frac{FAR}{1+BPR}\right)\frac{C_{pg} LTIT}{SPT}\left[1 - \left(\frac{1}{\pi_T}\right)^{\frac{\gamma_g - 1}{\gamma_g}\eta_{p,T}}\right] \tag{8.69}$$

$LTIT$ (Fig.8.34), SPT (Fig.8.35), C_{pg} (Fig.8.36) and γ_g, are all functions of the turbofan bypass ratio, as shown in Table 8.13. What the turbine expansion ratio concerns, it is reasonable to state that :

$$\frac{p_{t64}}{p_a} = \frac{{}^1p_{t_i}}{p_a} \cong \pi_T \tag{8.70}$$

where the correlation for p_{t64}/p_a, which may be defined as the cycle pressure ratio in case of the turbofan powered TDR cycle, is given in Table 8.13 as a function of bypass ratio and presented in Fig.8.37. Note that with regard to the initialisation process, it is interesting to plot the generated power gain as a function of bypass ratio and turbine polytropic efficiency (Fig.8.38). By considering the polytropic efficiency as an independent variable in the plot, the cycle model is uncoupled from the turbine model, which yields valuable information to initiate the coupled-model iteration process. Making a good initial guess for $\eta_{p,T}$, which is calculated by the turbine model subsequently and typically around 90% for the larger Ljungström turbines, yields a power gain that will show to be reasonable constant throughout the iteration process.

Fig.8.38 reveals that the gross weight of the TDR helicopter will be about 5–10% lower than the gross weight of the conventional helicopter, which has a positive impact on the required rotor/turbine power P_T^*. This is mainly due to the removal of the transmission system. The impact of the installation of the turbofan on the helicopter gross weight is around 5%, which was verified to be in the same order of magnitude of $W_{E,7A}$ (6%). The figure also shows that the gross weight variations are sensitive to $W_{E,TF}$. This is to be expected. For all other components in Eq.8.66, Fig.8.6 already showed that the weight variation tends towards a constant for the heavier weights, leaving the turbofan as the dominant factor in the empty weight variation balance.

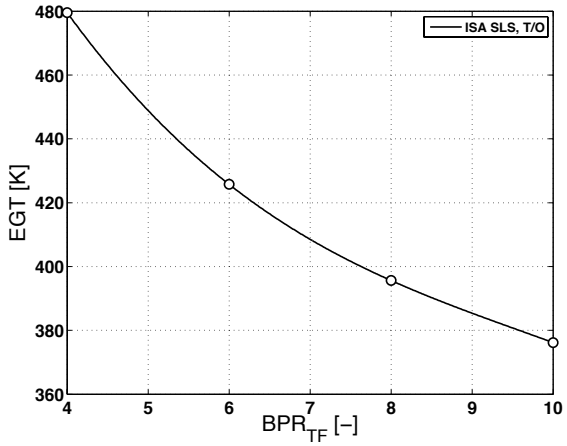

FIGURE 8.34. Turbofan EGT as a function of BPR_{TF}, ISA SLS maximum T/O setting.

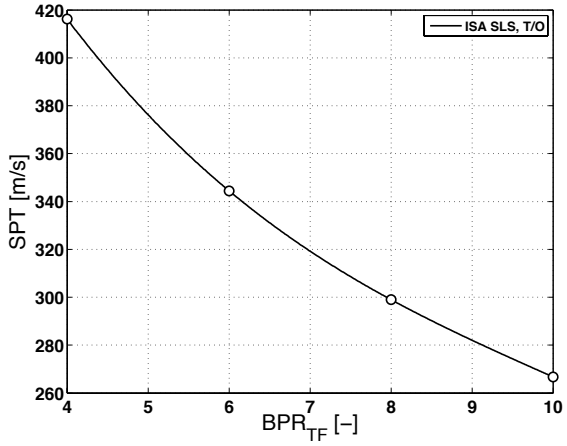

FIGURE 8.35. Turbofan SPT as a function of BPR_{TF}, ISA SLS maximum T/O setting.

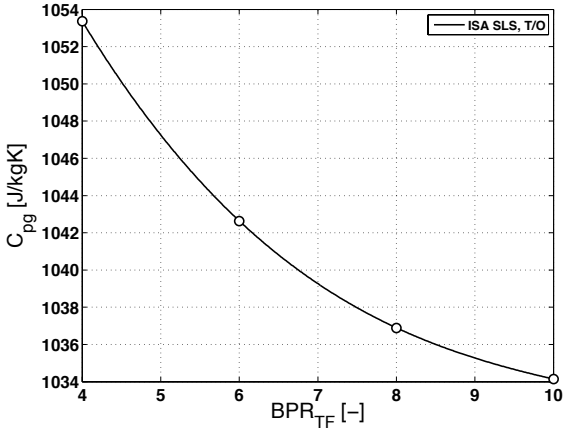

FIGURE 8.36. Turbofan exhaust gas C_{pg} as a function of BPR_{TF}, ISA SLS maximum T/O setting.

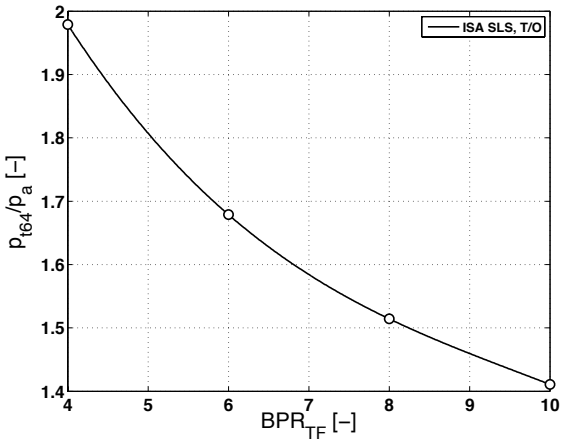

FIGURE 8.37. Turbofan p_{t64}/p_a pressure ratio as a function of BPR_{TF}, ISA SLS maximum T/O setting.

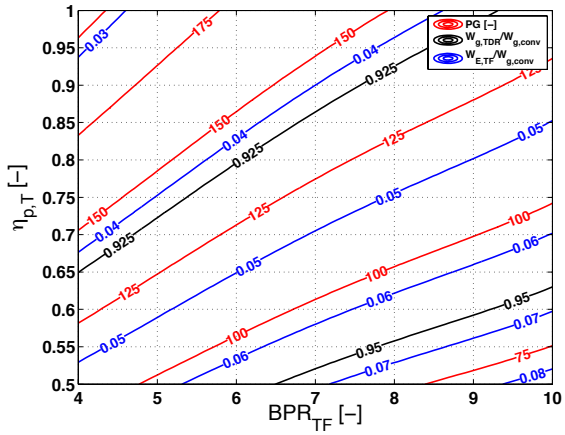

FIGURE 8.38. *PG* and weight variations as a function of BPR_{TF} and $\eta_{p,T}$.

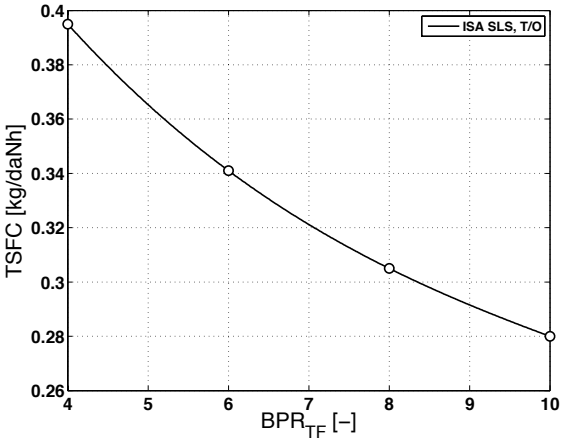

FIGURE 8.39. Turbofan *TSFC* as a function of BPR_{TF}, ISA SLS maximum T/O setting.

8.4.4 Determination of COP_{BE}

Recalling the break-even coefficient of performance for the turbofan powered TDR cycle (Eq.8.26) :

$$COP_{BE} = \frac{2}{SPT}\left(1 + \frac{FAR}{1 + BPR_{TF}}\right) PG_{BE}$$

as well as the function for the break-even power gain (Eq.8.21) :

$$PG_{BE} = \frac{TSFC}{SFC_{E,conv}}\left(1 + \frac{\Delta W_E}{W_{g,conv}}\right)^b (1 - k_{TX} - k_{TR})\, k_I$$

$TSFC$ is a function of the bypass ratio (Table 8.13) and is plotted in Fig.8.39. $SFC_{E,conv}$ is calculated using Eq.8.7 and Eq.8.27. Following a similar reasoning as conducted in Section 8.3.4, k_I is again assumed to be unity. The values of k_{TX} and k_{TR} are taken from Table 8.1.

The break-even power gain and break-even coefficient of performance are calculated in a similar way as the empty weight correction. Since the polytropic efficiency of the turbine is à priori unknown, it is interesting to introduce this variable as independent parameter, as done in the empty weight correction study (see previous section). For a given bypass ratio and adopting again the assumption that :

$$\pi_T \cong p_{t64}/p_a = f(BPR_{TF})$$

allows the presentation of the power gain, the coefficient of performance and the break-even parameters graphically, without the need of the turbine model. This is done in Fig.8.40, which is analysed next.

Remarkably, the coefficient of performance is almost entirely dependent on the turbine efficiency and the break-even condition is met for turbine polytropic efficiencies over 57% (green line). Providing good engineering practices are followed, $\eta_{p,T}$ will be much higher (90%), from which one may already conclude that the turbofan powered TDR cycle will outperform the conventional helicopter offering high COP_M, at least at low speeds (parasite drag).
Note that a minimum required bypass ratio is indicated in Fig.8.40 in red, i.e. $BPR_{lim} = 7.6$. The limitation arises from the maximum $LTIT$ of 400 K. The temperature constraint is violated when $BPR_{TF} < BPR_{lim}$ because then the turbofan EGT exceeds the limit. This cannot be accepted for reasons of RELT integrity. As a result, it is possible to state that :

$$PG_{BE} \cong 80 \tag{8.71}$$

$$COP_{BE} \cong 0.57 \tag{8.72}$$

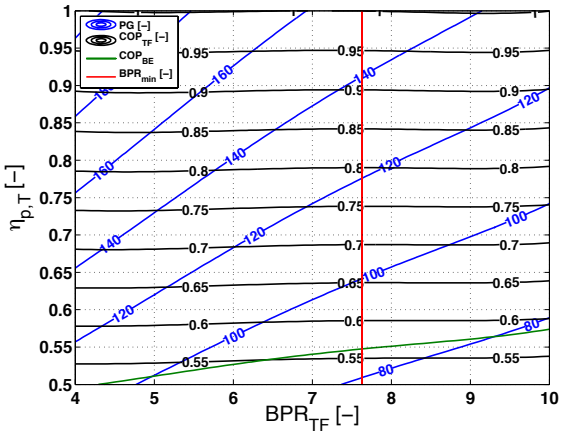

FIGURE 8.40. Turbofan powered TDR cycle, estimation of PG, COP_{TF} and break-even.

8.4.5 Turbine design

The design procedure is analogous to the one established for the VLR-class TDR helicopter. The analysis will therefore be restricted to the examination of the results. OED conditions are again adopted as a design basis.

Turbine model input parameters

The turbine model input variables are reflected in Table 8.14. In contrast to the VLR-class TDR helicopter, ${}^{M}\alpha_i$ is now also examined parametrically. The rotational speed of the coaxial rotors is N_{DP}=249 RPM.

Number of turbine stages, $\overline{r_i}$ and ${}^{M}\alpha_i$

Observe Table 8.15. The impact of the number of turbine stages S_n on the optimum turbine efficiency (OED) for the typical ${}^{M}\alpha_i$ of 65 ° shows again that the higher the stage count, the higher the isentropic efficiency becomes. However, an increase in stage number causes the turbine frontal flow path area A_e to grow drastically. Section 7.1.15 presented techniques to reduce the blade height by increasing the radial velocity of the flow passing through the turbine.

One possibility is reducing S_n as much as possible, but Table 8.15 then shows that $\overline{r_i}$ becomes rather high : the $k_I = 1$ assumption would possibly need to be reconsidered. The other possibility to reduce the blade height is by decreasing ${}^{M}\alpha_i$. Selecting ${}^{M}\alpha_i = 40°$ leads to satisfying results, where A_e is more than halved, while only a minor drop in turbine efficiency is induced.

Taking $S_n = 6$ and ${}^{M}\alpha_i = 40°$ therefore appears as the best compromise between size and efficiency. Fig.8.41 then shows that $\overline{r}_{iopt} = 0.27$. As a consequence, the parametric study on BPR_{TF} can now be conducted and the maximum COP_M retrieved.

TABLE 8.14. Turbine model input parameters.

BPR_{TF} [-]	parametric [4 . . . 10]
S_n [-]	parametric (Section 8.3.6)
v_{tip} [m/s]	215†
R_{tip} [m]	8.3 (Eq.8.30)
${}^M\alpha_i$ [°]	parametric (Section 7.1.14)
c_{min} [mm]	20 (target value, Section 7.1.13)
$\hat{c}$ [-]	0.35 (Lowest high-cycle-fatigue, Eq.7.18)
t_s [mm]	5‡
w_{ss} [mm]	1‡
h_{ss} [mm]	1‡
Δ_{s_R} [mm]	0.1‡
Δ_{s_h}	0.016 R_o (Section 6.2.1)
N_{ss}	4 (Section 6.3.3)
ϵ_f [mm]	0.5⋆
e [μm]	1.2‡ (Section D.1.6)

† Section 2.2.2 – ‡ Antoine (2014)

⋆ Antoine & Buysschaert (2014b) : worst case scenario using Rohacell

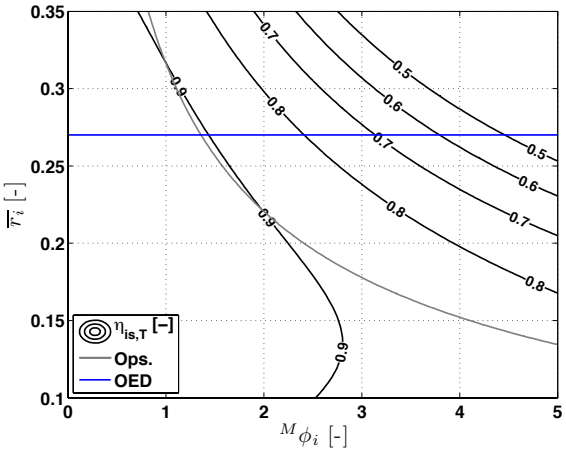

FIGURE 8.41. Turbofan powered TDR cycle : $\overline{r}_{iopt}$ for $S_n = 6$.

Note that the values in Table 8.15 are only mentioned for the bypass ratio $BPR_{TF} = 8$. This will be proven later in this section to be the design bypass ratio. Nevertheless, the same analysis and conclusions apply to other BPR_{TF}, which are not summarised in Table 8.15 because they contribute no additional value to the discussion.

Table 8.15. Selection of S_n, $\overline{r}_{iopt}$ and ${}^{M}\alpha_i$.

BPR	π_T	S_n	${}^{M}\alpha_i$ [°]	$\overline{r}_i$	$\eta_{is,T}$	$A_e/A_e^\star$	OED
8	1.502	4	65	0.32	0.89	1.98	yes
8	1.507	6	65	0.30	0.92	2.86	yes
8	1.510	8	65	0.29	0.94	3.67	yes
8	1.472	6	40	0.27	0.91	1.16	yes
8*	1.444*	6*	40*	0.20*	0.90	1	no

* is DP.

Turbine efficiency and COP_M : Design point selection

The coefficient of performance margin found for the NH90-class TDR helicopter is plotted in Fig.8.42. The plot confirms the high margin, which was already predicted in Fig.8.40. A maximum margin is observed near $BPR_{TF} = 8$, which is consequently selected as the design point. The optimum can be explained for an increasing bypass ratio by the interaction of a decreasing *LTIT* (Fig.8.34) and drop in inlet pressure ratio (Fig.8.37), which decrease COP_{TF} as explained in Section 4.5.3, and an increase in $\dot{m}$ (Fig.8.43), influencing $\eta_{p,T}$ positively by the increased blade aspect ratio and Reynolds number, from which COP_{TF} benefits.

Compared to Fig.8.42, the reader could notice an overestimation of the coefficient of performance margin when relying on the data in Fig.8.40. This is due to the approximation shown in Eq.8.70. Fig.8.44 reveals that $\pi_T < {}^{1}p_{t_i}/p_a$. As a result, the power gain in Eq.8.69 is overestimated, leading to optimistic coefficient of performance (margins) in Fig.8.40. However, the result is still within the previously estimated range.

The impact of the bypass ratio on the coefficient of performance margin remains fairly low, which would à priori permit the designer to use an average to fairly high bypass ratio. Nevertheless, it must be highlighted again that the *LTIT*-boundary needs to be respected (red dashed line in Figs. 8.42–8.45).

While the currently obtained coefficient of performance margin is high, it is worth considering the sacrifice of some of it to achieve a lower rotor parasite drag. This may be done by reducing $\overline{r}_i$ below $\overline{r}_{iopt}$, as shown in Table 8.15. Here, the parasite drag is again represented by A_e (Eq.8.59), and the relative frontal flow path area for the turbofan powered

TDR cycle is now defined as :

$$A_{e,rel} = \frac{A_e}{\min(A_{e,range})} = \frac{A_e}{A_{e,BPR_{TF}=4}} \tag{8.73}$$

$A_{e,rel}$ is shown in Fig.8.45. Taking $\overline{r}_{iDP} = 0.2$ causes A_e to decrease by about 15%, while the coefficient of performance margin is 5% lower ($\cong$ 47%). The turbine polytropic efficiency is only reduced by approximately 1%. This is a reasonable compromise and the presented configuration is therefore taken as the design point. The important cycle characteristics are now summarised in Table 8.16. The RELT geometry is discussed next.

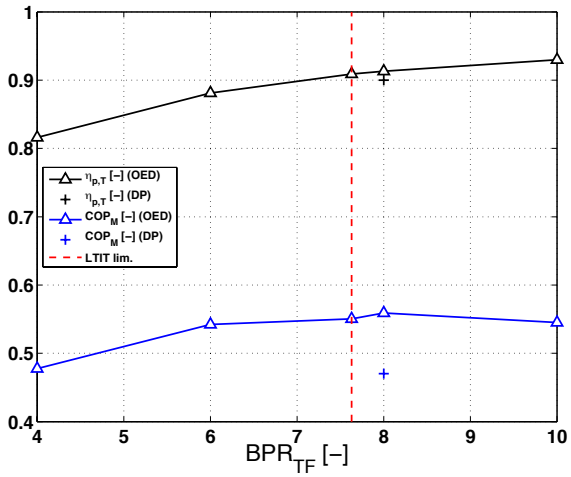

FIGURE 8.42. Cycle COP_M and turbine polytropic efficiency $\eta_{p,T}$ as a function of BPR_{TF}.

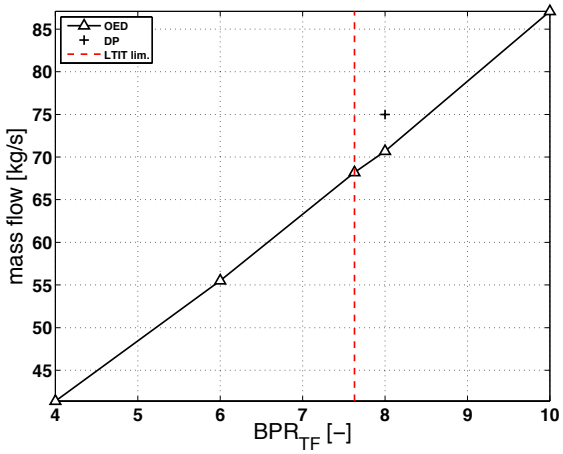

FIGURE 8.43. Required turbine mass flow $\dot{m}$ as a function of BPR_{TF}.

Geometry

Table 8.17, Fig.8.46 and Fig.8.47 report important geometric and performance characteristics of the Ljungström turbine developed for the previously discussed design point conditions.

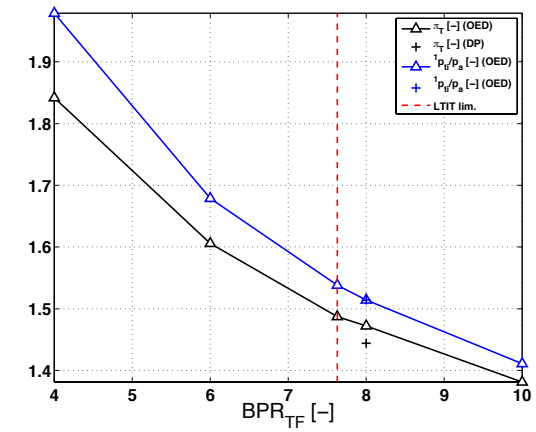

FIGURE 8.44. Cycle pressure ratio ${}^1p_{ti}/p_a$ and turbine expansion ratio π_T as a function of BPR_{TF}.

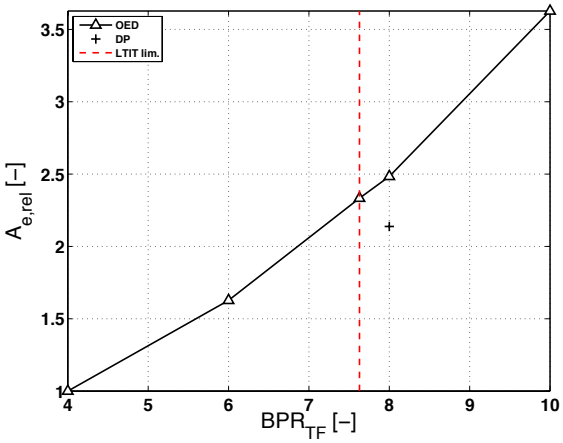

FIGURE 8.45. Relative frontal flow path area $A_{e,rel}$ as a function of BPR_{TF}.

Table 8.16. Design point cycle characteristics.

T_{Nt} [kN] (ISA SLS)	22.4
PG [-]	120.4
$\dot{m}$ [kg/s]	75
BPR_{TF} [-]	8
$TSFC$ [kg/daNh]	0.305
π_F [-]	1.59
π_{HPC} [-]	20.2
${}^1p_{ti}/p_a$ [-]	1.51
π_T	1.44
$LTIT$ [°]	123.5
FAR [-]	0.0228
COP_{TF} [-]	0.81
COP_M [%]	47
$\eta_{p,T}$ [-]	0.90

In general, similar conclusions may be drawn as found with the Avgas and Diesel engine powered TDR cycles. However, the first and the last stages have $Z < Z_{sl}$. Since for these stages $Z \cong 0.92\ Z_{sl}$, it is reasonable to assume that the slip model of Busemann-Wiesner (Eq.5.95) still predicts the slip angle with sufficient accuracy as it can be proven that $\epsilon \cong \epsilon_{lim}$ and as a consequence, Eq.5.97 reduces to Eq.5.96.

A well balanced power production is established, where both turbine halves deliver an equal amount of power $P_T^*/2$.

The Reynolds numbers are an order higher than the ones obtained for the piston engine powered TDR cycles. The main reason for this is the higher flow coefficient resulting from the selection of a lower ${}^M\alpha_i$. Note that the Reynolds number drops in the last stage, which is not that pronounced in case of the piston engine powered TDR cycles. The reason for this effect is found in Eq.7.170. The reduced flow deflection and the lower R_o/R_i conditions for the RELT in the turbofan configuration, may be considered as the reason behind this observation.

Also, due to the increased radial velocity component by having selected a lower ${}^M\alpha_i$, there is an increase in relative Mach numbers causing the compressibility effects to become more important and require slightly diverging blade heights, whereas for the piston engine powered TDR cycles, the opposite was observed.

Another consequence of selecting a lower ${}^M\alpha_i$ is that the first stage blade size is less affected by the typically higher first stage stagger angle setting. This is because the stagger angle is still below 60°, the angle above which one may prove that c/R_i increases substantially. The blade size is therefore similar to those of the subsequent stages. The flow deviation too increases due to a lower ${}^M\alpha_i$ setting. Indeed, β_g increases due to the lower required flow deflection ϵ, inducing higher δ (e.g. Fig.5.13).

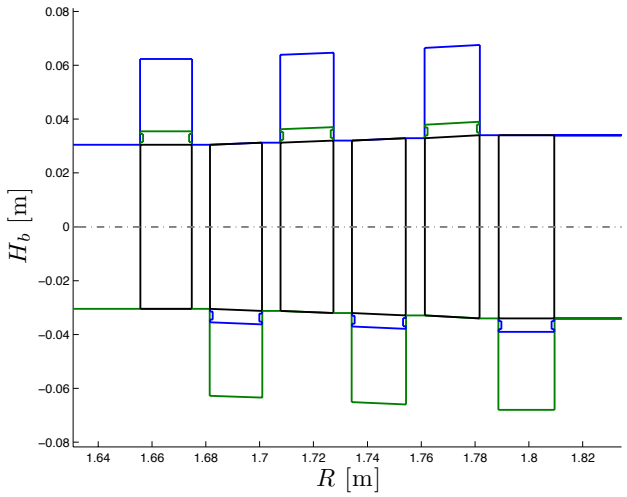

FIGURE 8.46. Turbofan powered TDR cycle, vertical plane RELT cutaway (black : blades, green : first crown, blue : second crown).

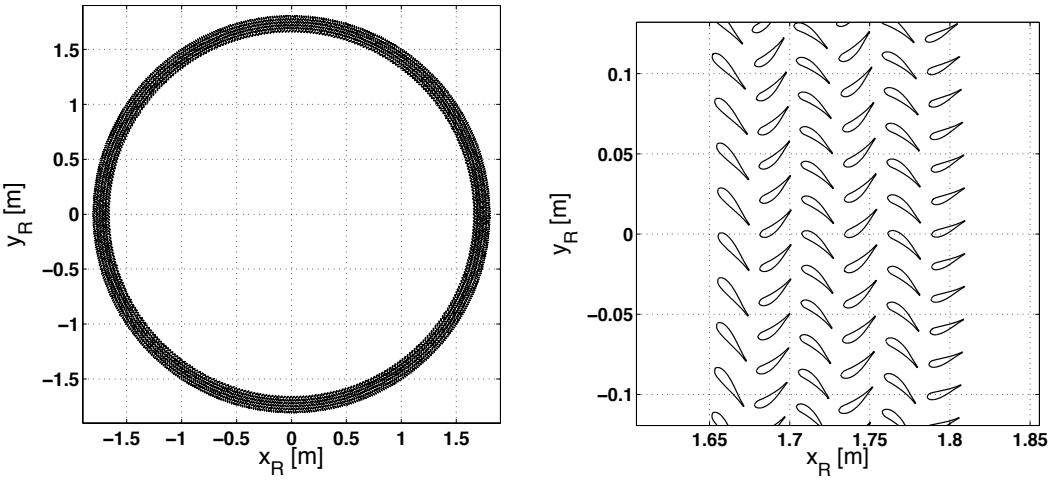

FIGURE 8.47. Turbofan powered TDR cycle, horizontal plane RELT cutaway.

Off-design performance : the turbine map

The same conditions apply as discussed in Section 8.3.6. The turbine map is again presented in Fig.8.48 and Fig.8.49, respectively with and without endwall fences. The corrected variables are presented in Table 8.18.

The model of Ainley & Mathieson (1955) correlates very well with the model of Soderberg. The use of endwall fences increases the turbine polytropic efficiency with approximately 1%.

The efficiencies on the turbine map remain quite high throughout the examined range of mass flow and expansion ratios. They are substantially higher than the break-even polytropic efficiency established in Fig.8.40, and which appear to be around 57%. This is an encouraging perspective when pursuing a positive *COP*-margin throughout the TDR helicopter flight envelope.

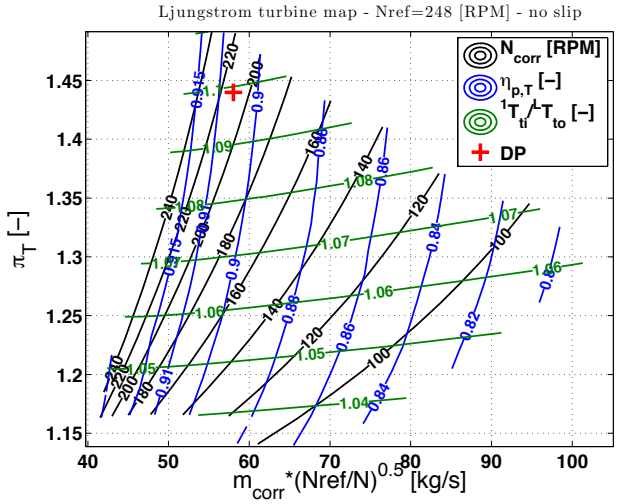

Figure 8.48. Turbofan powered TDR cycle off-design turbine performance map.

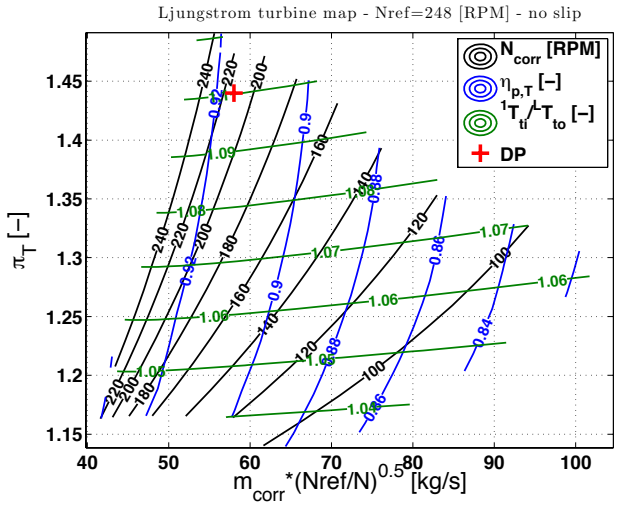

Figure 8.49. Turbofan powered TDR cycle off-design turbine performance map with endwall fences.

Table 8.17. Turbine characteristics – turbofan powered TDR cycle (DP).
P_{C1}=1.35 MW – P_{C2}=1.35 MW – ISA SLS

Stage number →	S_1	S_2	S_3	S_4	S_5	S_6
${}^{M}\chi$ [-]			1.008			
$\hat{c}$ [-]			0.35			
R_i [m]	1.656	1.682	1.708	1.734	1.761	1.789
R_o [m]	1.675	1.701	1.727	1.754	1.782	1.809
ϕ_i [-]	2.09	2.12	2.12	2.12	2.12	2.12
ϕ_o [-]	2.14	2.14	2.14	2.14	2.14	2.08
ψ [-]	1.835	3.614	3.614	3.614	3.614	1.779
$\hat{\theta}$ [-]	222	213	203	194	184	175
$\hat{R}$ [-]	1.985	1.042	1.042	1.042	1.042	0.0948
$\alpha_o - \alpha_{o,b}$ [deg]	0.1	0.1	0.1	0.1	0.1	0.1
ϵ [°]	27.0	72.8	72.8	72.8	72.8	45.8
λ [°]	50.1	37.7	37.7	37.7	37.7	21.8
β_{bi} [°]	-25.6	20.2	20.2	20.2	20.2	20.2
δ [°]	2.7	2.6	2.6	2.6	2.6	6.3
M_i [-]	0.23	0.31	0.32	0.32	0.33	0.34
M_o [-]	0.31	0.32	0.33	0.33	0.34	0.26
M_{ri} [-]	0.25	0.25	0.26	0.27	0.27	0.28
M_{ro} [-]	0.39	0.40	0.41	0.42	0.43	0.29
AR_a [-]	3.20	3.18	3.21	3.25	3.29	3.29
Re [10^5]	2.3	1.8	1.8	1.7	1.7	1.5
c [m]	0.030	0.024	0.025	0.025	0.026	0.022
H_{bi} [m]	0.061	0.061	0.062	0.064	0.066	0.068
$\overline{B}$ [-]	1	1.023	1.026	1.029	1.032	1
Z [-]	372	497	497	497	497	555
Z_{sl} [-]	406	406	406	406	406	604
$\eta_{p,Ts}$ [-]	0.88	0.90	0.90	0.90	0.90	0.93
$\dot{m}_{LL}/\dot{m}$ [-]	0.0006	0.0008	0.0007	0.0007	0.0007	0.0005
$(t/c)_{max}$ [-]	0.20	0.21	0.21	0.21	0.21	0.20
t_{TE} [mm]	0.6	0.5	0.5	0.5	0.5	0.4
o [mm]	15	12	13	13	13	17
R_c [m]	0.22	0.093	0.095	0.096	0.098	0.67
$e/c^{\dagger}$ [-]	$4.06{\cdot}10^{-5}$	$4.91{\cdot}10^{-5}$	$4.83{\cdot}10^{-5}$	$4.76{\cdot}10^{-5}$	$4.69{\cdot}10^{-5}$	$5.40{\cdot}10^{-5}$

† Relative blade roughness. See Appendix D, Section D.1.6

Table 8.18. Turbine characteristics – corrected variables (DP, OED).

$\dot{m}_{corr}$ [kg/s]	58.0
N_{corr} [RPM]	213
${}^{1}\delta_{ti}$ [-]	1.514
${}^{1}\theta_{ti}$ [-]	1.373

8.5 Conclusions

The TDR helicopter has been examined for a low (VLR) and a high (NH90) maximum gross weight under sea level conditions (ISA), considering the installed engine maximum power setting to be part of the cycle nominal operating regime, which prevents the RELT from exceeding the bearing temperature limitation. To compare the performance of the TDR helicopter with a conventional helicopter, the *COP*-margin was proposed and used (COP_M).

For the VLR-class TDR helicopter, an Avgas and a Diesel piston engine were considered separately. By linking their cycle characteristics to the Ljungström turbine model, it was possible to calculate COP_M.

For OED conditions, the VLR-class TDR helicopter powered by a Diesel piston engine showed a clear optimum COP_M at $LTIT = 69°C$, yielding a margin of approximately 14%. A similar optimum could not be retrieved for the Avgas engine in the studied temperature range, but it was found not necessary to examine the lower temperatures due to the concurring significant increase in RELT frontal area and thus parasite drag potential. A reasonable compromise was found between turbine size and COP_M by selecting $LTIT = 60°$ C, yielding a COP_M of 10% and a drag characteristic similar to the Diesel configuration.

The NH90-class TDR helicopter powered by a single turbofan engine was examined using a turbofan model established in GasTurb 11 for a $TIT = 1600$ K and $OPR = 32$.

The optimum BPR_{TF} was found to be around 8 for OED conditions, but in general, COP_M remained fairly constant and around 50% on average. However, selecting the optimum BPR_{TF} still allowed to reduce the turbine size resulting in a reduction in rotor hub parasite drag of 15%, while sacrificing COP_M minimally. This was possible by taking $\overline{r_i} = 0.20 < \overline{r}_{iopt}$.

For any studied case, a 6-stage RELT appeared as the best compromise between maximum efficiency and minimum size.

Off-design performance maps were established and the characteristics obtained by means of the model of Ainley and Mathieson. The retrieved efficiency at the design point corresponded well with the model of Soderberg, used to establish the turbine geometry.

The introduction of endwall fences results in a minor increase in turbine efficiency and the added performance value should be weighed against the increased development cost. However, the technique should not be left out of consideration, since no complete system

off-design calculations were made, where any slight increase in component efficiency may turn out to be indispensable.

8.6 Nomenclature

Please note that the units listed below apply unless stated otherwise.

Abbreviations and substance formulae

A	Flow area	[m^2]
A_e	Turbine frontal flow path area	[m^2]
A_R	Rotor disk area	[m^2]
AR	Blade aspect ratio	[-]
AR_a	Blade projected aspect ratio	[-]
$\overline{B}$	Blade height ratio	[-]
BPR	Cycle bypass ratio	[-]
BPR_{TF}	Turbofan bypass ratio	[-]
c	Blade chord	[m]
$\hat{c}$	Interstage space coefficient	[-]
c_b	Rotor blade chord	[m]
c_{min}	Minimum chord	[m]
C_D	Drag coefficient	[-]
C_p	Specific heat at constant pressure	[J/kgK]
C_T	Rotor thrust coefficient	[-]
COP	Coefficient of performance	[-]
COP_{BE}	Break-even coefficient of performance	[-]
COP_{TF}	Turbofan cycle coefficient of performance	[-]
COP_M	Coefficient of performance margin	[-]
D	Drag	[N]
DL	Rotor effective disk loading	[m^2]
DP	Design point	
$\dot{E}_k$	Turbofan exhaust gas kinetic energy rate	[W]
e	Blade peak-to-peak roughness	[m]
e/c	Relative blade roughness	[m]
EGT	Turbofan exhaust gas temperature	[K]
FAR	Fuel-to-air ratio	[-]
f_e	Equivalent flat plate area	[m^2]
$\overline{H}$	Interstage space height ratio	[-]
h_{ss}	Seal strip height	[m]
H_b	Blade height	[m]
l	Camberline length	[m]
ISA	International Standard Atmosphere	

k_I	Induced power correction coefficient	[-]
k_{TR}	Tail rotor power fraction	[-]
k_{TX}	Transmission loss power fraction	[-]
$L_{(j)}$	Labyrinth seal cavity length	[m]
LHV	Fuel lower heating value	[J/kg]
$LTIT$	Ljungström turbine inlet temperature	[K]
$\dot{m}$	Turbine mass flow rate	[kg/s]
$\dot{m}_{corr}$	Turbine corrected mass flow	[kg/s]
$\dot{m}_f$	Fuel mass flow	[kg/s]
$\dot{m}_{LL}$	Leakage mass flow rate	[kg/s]
M	Absolute Mach number	[-]
M_r	Relative Mach number	[-]
N	Rotational/Angular speed	[rad/s]
N_b	Number of rotor blades	[-]
N_e	Number of installed engines	[-]
N_{ss}	Number of seal strips	[-]
o	Blade passage throat	[m]
OED	Optimum efficiency design	
OPR	Turbofan overall pressure ratio	[-]
p	Static pressure	[Pa]
p_t	Total pressure	[Pa]
P	Power	[W]
P^*_M	Delivered internal combustion engine power	[W]
P_i	Rotor induced power	[W]
P^*_T	Delivered turbine power	[W]
PCF	Pre-compression factor	[-]
PE	Piston engine	
PG	Power gain	[-]
PG_{BE}	Break-even power gain	[-]
q	Dynamic pressure	[Pa]
R	Radius	[m]
$\hat{R}$	Reaction degree	[-]
$\overline{r_i}$	Turbine specific inlet radius	[-]
R_c	Blade suction side radius of curvature	[m]
R_g	Specific gas constant	[J/kgK]
R_i	Turbine (stage) inlet radius	[m]
R_o	Turbine (stage) outlet radius	[m]

R_{tip}	Rotor blade tip radius	[m]
Re	Reynolds number	[-]
RELT	Rotor-embedded Ljungström turbine	
RR	Ram recovery	[-]
S	Stage	
S_n	Turbine stage number	[-]
S_{pl}	Blade planform surface area	[m^2]
S_{ref}	Body reference area	[m^2]
S_Ω	Turbine slip factor	[-]
SFC	Specific fuel consumption	[kg/Ws]
SPT	Turbofan specific thrust	[Ns/kg]
SLS	Sea Level Static	
t	Blade thickness	[m]
t_s	Rim thickness	[m]
t_{TE}	Trailing edge thickness	[m]
T	Static temperature	[K]
T_N	Turbofan maximum take-off thrust	[N]
T_{Nt}	Installed maximum take-off thrust	[N]
T_t	Total temperature	[K]
TDR	Turbine driven rotor	
TF	Turbofan	
TIT	Turbofan turbine inlet temperature	[K]
T/O	Take-off	
$TSFC$	Thrust specific fuel consumption	[kg/Ns]
v	Absolute speed	[m/s]
$v_{j,av}$	Turbofan exhaust gas average speed (full expansion)	[m/s]
v_{tip}	Rotor blade tip speed	[m/s]
VLR	Very light rotorcraft	
w_{ss}	Seal strip width	[m]
W_E	Empty weight	[kg]
$W_{E,C}$	Compressor system weight	[kg]
$W_{E,T}$	RELT system weight	[kg]
$W_{E,TF}$	Turbofan system weight	[kg]
$W_{E,2}$	Main rotor system weight	[kg]
$W_{E,3}$	Tail rotor system weight	[kg]
$W_{E,7A}$	Powerplant system weight	[kg]
$W_{E,7B}$	Transmission system weight	[kg]

W_F	Fuel weight	[kg]
W_g	Maximum gross weight	[kg]
Z	Stage blade number	[-]
Z_{sl}	Slip model minimum blade number requirement	[-]
$2-s$	Two-stroke	
$4-s$	Four-stroke	
α	Absolute flow angle	[rad]
γ	Isentropic exponent	[-]
δ	Stage flow deviation angle	[rad]
${}^1\delta_t$	Non-dimensional turbine total inlet pressure	[-]
Δ_{s_h}	Axial gap clearance	[m]
Δ_{s_R}	Radial gap clearance	[m]
Δt_{flight}	Flying time	[s]
ΔW_E	Empty weight correction	[kg]
$\Delta W_{E,2}$	Coaxial rotor weight correction term	[kg]
ϵ	Flow deflection or R_i/R_o	[rad] or [-]
ϵ_f	Labyrinth peak-to-peak roughness	[m]
η_{CC}	Combustion efficiency	[-]
$\eta_{is,T}$	Turbine total-to-total isentropic efficiency	[-]
η_m	Mechanical transmission efficiency	[-]
$\eta_{p,C}$	Compressor polytropic efficiency	[-]
$\eta_{p,T}$	Turbine total-to-total polytropic efficiency	[-]
$\eta_{p,Ts}$	Stage total-to-total polytropic efficiency	[-]
$\hat{\theta}$	Non-dimensional inlet specific total enthalpy	[-]
${}^1\theta_t$	Non-dimensional turbine total inlet temperature	[-]
λ	Blade stagger angle	[rad]
π_C	Cycle pressure ratio	[-]
π_F	Turbofan fan pressure ratio	[-]
π_{HPC}	Turbofan high pressure compressor pressure ratio	[-]
π_T	Turbine total-to-total expansion ratio	[-]
σ_R	Rotor solidity	[-]
τ_f	Thrust factor	[-]
ϕ	Flow coefficient	[-]
${}^M\phi_{i_{opt}}$	Optimum middle stage flow coefficient	[-]
ψ	Stage work coefficient	[-]
${}^M\psi_{opt}$	Optimum middle stage blade passage work coefficient	[-]
$\psi_{T,opt}$	Optimum turbine work coefficient	[-]

${}^{M}\chi$	Interstage damping	[-]
Ω	Crown angular velocity	[rad/s]

Subscripts and superscripts

BE	Break-even
*C*1	First crown
*C*2	Second crown
coax	Coaxial rotor related
conv	Conventional helicopter
corr	Corrected
DP	Design point
E	Engine related
EWF	Endwall fence
g	Exhaust gas related
i	Inlet
j	Related to position *j*
L	Last stage
LL	Leakage loss
M	Middel stage
nh	No hub installed
o	Outlet
o, *b*	At outlet of a blade passage
Ops	Operating line
opt	Optimum
PE	Piston engine
ref	Reference
rel	Relative
ss	Seal strip
t	Total component
TDR	TDR helicopter
TE	Trailing edge
tip	Rotor tip related
1	First stage
163	Turbofan bypass pre-nozzle flow conditions
63	Turbofan core pre-nozzle flow conditions
64	Turbofan pre-nozzle mixed flow conditions
8	Turbofan (fictitious) nozzle flow conditions

Chapter 9

Conclusions and perspectives

"But Nature, on the other hand, is inexorable and immutable; she never transgresses the laws imposed upon her, or cares a whit whether her abstruse reasons and methods of operation are understandable to men"

Galileo Galilei – *Letter to Grand Duchess Cristina of Tuscany (1615)*[*]

9.1 Conclusions

9.1.1 First objective : identification of cost/safety/performance limitations in a conventional helicopter

Based on the production and direct operating cost, NTSB safety records and evaluation of component and conceptual limitations, the performance, safety/reliability and cost driving components inside a conventional helicopter were shown to be the mechanical transmission and the powerplant systems.

Alternative technologies were examined for implementation in a conventional helicopter, with the objective to tackle the previously mentioned issues. The following was observed :

→ The hydrostatic worm gear transmission appeared encouraging, but is believed not to be adopted by the industry for reasons of complexity.

→ Magnetic gearboxes, even though conceptually more reliable and robust, were currently found to be too heavy. The cycloid permanent magnet gear yielded the best performance, even though weighing at least twice as much as a conventional mechanical gearbox. The technology is considered not yet ripe for implementation in a helicopter environment.

[*] *Seeger & Haar (2013)*

→ Driving the *main rotor* by electric propulsion, the study of which also comprised batteries and a PEM fuel cell, showed to involve a too high weight penalty and the internal combustion engines remained the best available mechanical power source from a weight and fuel requirement (cost) viewpoint.

→ The partial removal of the transmission system and driving the *tail rotor* electrically was assessed, but no weight efficient configuration could be established. The best electric configuration is a switched reluctance motor fed by a cryocooler-refrigerated HTS generator, while the latter is driven by a turboshaft fuelled with kerosene. This results in a gross weight penalty of at least 5%. Hereby, the use of HTS technology is essential. The HTS generator operating temperature was 20 K. However, HTS devices need to be cooled. The cooling time required to attain the operating temperature using an onboard cryocooler is currently too high to be practically acceptable.

→ Liquid hydrogen as a future energy carrier is not recommendable, unless a considerable gross weight penalty of minimum 25% is accepted. It is also questionable whether FAR Part 135 aircraft will have continuous access to liquid hydrogen, which will depend entirely on the available infrastructure of the airport of departure and destination.

As a consequence, the examined novel technologies were – in the current timeframe – found impractical for implementation in a conventional helicopter.

With respect to the conceptual alternatives to the conventional helicopter, i.e. the compound, tilt-rotor and reaction-force-driven-rotor helicopters, no total improvement could be observed. It appeared that emphasising the improvement of one of the stated problem drivers such as performance, impacted the others, i.e. safety and cost, negatively. This behaviour is not expected for the TDR concept, which was further examined.

9.1.2 Second objective : Evaluation of the TDR concept as a viable alternative to the conventional helicopter in nominal operation

The Ljungström turbine needs to be fed with hot and pressurised air. In light of this, three conditioning cycles were examined theoretically :

→ the Avgas and Diesel piston engine powered RELT cycles ;

→ the turboshaft powered RELT cycle ;

→ the turbofan powered RELT cycle.

Because the Ljungström turbine is uncoupled from the mechanical power source in the cycle, the cycle coefficient of performance *COP* was defined as a performance metric,

which indicates how effectively the power delivered by the engine is transferred to the turbine.

The discussed cycles all have a coefficient of performance higher than 90%. For the low power class helicopter (< 300 kW), both the piston engine and turboshaft driven TDR cycles can be used to drive the Ljungström turbine. For the mid and high power class helicopters, the turbofan powered TDR cycle appeared as the best solution, thanks to its high coefficient of performance and simplicity. However, the use of the turboshaft powered TDR cycle was found to be not advisable because of the need of a heat exchanger, which renders the cycle more complex, while it increases the helicopter weight.

The potential of the piston engine and turbofan powered TDR cycles was examined by means of two case studies using respectively a VLR-class helicopter and a NH-90-class helicopter. For this purpose, the turbine geometry and performance model – developed under the third objective – had to be coupled with the cycle model. The performance characteristics of the test cases at nominal operation conditions were then compared to those of equivalent conventional helicopters and a noteworthy performance margin was observed, around 10% for the piston engine conditioned cycles and 50% for the turbofan conditioned cycle.

At the moment, the TDR helicopter appears to deal with the performance, cost and reliability concerns in the conventional helicopters, mainly by the removal of the transmission system and the reduction in gross weight, offering the possibility to increase the helicopter useful load or benefit from increased excess power. Also, compounding is feasible, which is an inherent capability of the turbofan powered TDR cycle. Note however, that the performance gain was observed for the stated nominal operating conditions only. As a result, the second objective was attained, but the performance gain should still be proven for the major part of the flight envelope (off-design conditions). This was not yet evaluated.

9.1.3 Third objective : the Ljungström performance and geometry model

A design protocol was developed for the rotor embedded Ljungström turbine, yielding :

→ the turbine blade and flow cavity dimensions/geometry ;

→ the aerodynamic, disk friction and leakage losses ;

→ the main performance characteristics ;

where :

→ proof was delivered that axial turbine loss models can be applied to a Ljungström turbine for as long as the blade chord is reasonably small with respect to the inlet radius of the turbine stage ;

→ a correction to the deviation angle for axial turbines was proposed due to the passage vortex existing in the radial plane and the increased divergence of the blade passage ;

→ the model of Soderberg was used to calculate the turbine passage losses at design conditions and was proven consistent by verification with the updated model of Ainley and Mathieson proposed by Aungier ;

→ the beneficial effect of endwall fences on the secondary losses was highlighted, but their installation à priori not found necessary ;

→ a leakage loss model was developed based on see-through labyrinth seals, which proved the leakage losses inside a rotor embedded Ljungström turbine to be minor due to the low stage expansion ratios ;

→ the friction losses were quantified, including their impact on the stage outlet angle and specific enthalpy ;

→ for nominal operating conditions (design –) the velocity triangles were kept constant over the turbine middle stages, which allowed the development of the design theory and the inlet & outlet geometry of the blades ;

→ the first and last stage blade height was considered to be constant (non-tapered blades), for constructional simplicity ;

→ a three-step turbine design methodology was formulated, where in a *predesign* phase, the major non-dimensional turbine characteristics are determined, such as the flow coefficient, the stage number and the optimum specific inlet radius ; in a subsequent *dimension and efficiency determination* phase a first estimation of the turbine geometry is developed based on the output of the predesign phase ; and in a *finetuning* phase, the required turbine power is matched and the total-to-total turbine expansion ratio found ;

→ for design point purposes, the typical rotor embedded Ljungström turbine middle stage absolute inlet flow angle was proven to be around 65 ° ;

→ minimising the blade chord improved the rotor embedded Ljungström turbine efficiency mainly due to the decreased impact of disk friction ; a minimum blade chord of 20 mm was imposed ;

→ the NACA A_3K_7 profile was used for the blade geometry, which is suitable for high reaction stages, a condition that appeared applicable over all but the last stage in the RELT.

The nominal operating point characteristics correlated well with those found on the turbine maps developed by the model of Ainley and Mathieson. Since experimental substantiation of the developed theory was not possible due to persistent technical problems,

the previously mentioned observation may still be regarded as encouraging.

9.2 Perspectives

The mechanical stresses in the rotor embedded Ljungström turbine were not considered in this work and should be examined in order to assess the stresses near the blade root and determine the size of the turbine disks.

Future work will have to focus on substantiating the developed theories, as well as the examination of off-design characteristics of the TDR helicopter. The viability of the concept will depend strongly on the outcome of that particular study as helicopters are not flying continuously in the nominal operating point. The mission profile and the component efficiencies, some of which are not highlighted in this work, will have to be assessed in more detail, notably :

→ the compressor off-design characteristics ;

→ the inlet, plenum and ducting pressure losses ;

→ the internal combustion engine off-design characteristics ;

→ the turbine and cycle operating characteristics throughout the flight envelope ;

→ the deviation angle correction model via CFD or experiments ;

→ the aerodynamic and disk friction losses via CFD or experiments ;

→ the directional control bleed air requirements and design ;

For nominal operating conditions, a slip factor of unity was imposed. In off-design conditions, it is possible that the turbine halves will no longer operate at the same rotational velocity. The impact of a fluctuating slip factor on the performance output should be examined and evaluated against several safety aspects of the helicopter (rotor underspeed & overspeed, autorotation).

A high turbine efficiency is important to enhance the break-even coefficient of performance. As a consequence, it is proposed to replace the currently used NACA A_3K_7 profile in the last turbine stage with a turbine profile specifically designed to work at a low reaction degree.

In the conditioning cycles, the air bled to the directional control system using the Coandă effect was not yet accounted for. Further analysis and dimensioning of the yaw-control system must be conducted to evaluate whether this simplification remains acceptable in

the cycle analysis.

The turbofan cycle offers the possibility to provide the TDR helicopter with a propulsive force. This effect should be further examined and compared with the flight envelope of competing configurations, such as the compound helicopter. It was indeed shown that a non-zero thrust factor decreases the coefficient of performance of the TDR cycle.

Improved weight correlations should be established for the TDR helicopter specific components in order to acquire a better platform gross weight estimation.

A cost model of the several components used in the TDR helicopter must be developed to assess the life cycle cost of the concept. However, it is the author's opinion that such a model can only be established appropriately when relying on experience-based data, which is currently unavailable.

Similarly, a risk assessment should be conducted to highlight reliability and safety concerns of the TDR concept. Even though the TDR helicopter does not have the technical reliability problems related to the use of a mechanical transmission system, the potential problems related to the use of a turbine in a vibrating environment (rotor head), should not be disregarded (for example blades detaching from disk).

Even though the TDR helicopter performance envelope was not entirely covered by this thesis, the concept holds the potential to improve the performance, cost and safety compared to contemporary vertical flight technologies without being revolutionary. The latter is particularly interesting from an industrial point of view, while the TDR helicopter concept offers new and exciting opportunities for academic research.

Appendix A

Weight and cost estimating relations

A.1 Introduction

The model of Beltramo & Morris (1980) is used to calculate the manufacturer recurring production and assembly costs of a helicopter. The total cost is calculated by the model by summing the individual component cost, which is generally calculated by empirical correlations based on component empty weight W_E. The major component groups used in the model are summarised in Table A.1. The use of W_E as cost evaluator is not unusual, even though better results are reported by Burns (1994) when using the airframe unit weight *AMPR*. However, he also mentions that *AMPR* and W_E correlate well, such that W_E is generally used.

The model of Beltramo & Morris (1980) unfortunately features rather old technology, but with the absence of other publicly affordable and available models, it was decided to continue the cost assessment with this model, while assuming that the impact of technological evolution on the relative cost scale has not been dramatic. If the absolute cost is required, the calculated year-1977 (*then-year*) cost by the model should then be corrected by the consumer price index *CPI*, as explained in Chapter 1, to obtain the *now-year* cost.

A practical issue with the model is that it requires the knowledge of some physical helicopter parameters which are not easily determined such as the helicopter body surface area. It would therefore be more interesting to determine the recurring costs just by helicopter *gross weight* W_g alone, a parameter extensively used in the model to derive $W_{E,i}$. Thanks to the data given in Beltramo & Morris (1980) and on the information acquired by a survey of contemporary rotorcraft performed by the author of this work, the model was modified where necessary in an attempt to expose the cost critical groups for various W_g and production volumes Q. Beltramo & Morris (1980) uses the helicopter *design gross weight DGW* in his model, while the survey of the author of this work considers *maximum gross weight MGW*. Although one could question the equality between both masses, it was necessary in order to complete the model. For the remainder of this section, *DGW*

and MGW will be set equal to W_g. A discussion of the model components with any concurring modifications follows next.

Table A.1. Helicopter mass and recurring cost group subdivision as used in the model of Beltramo & Morris (1980).

Group name	Group number
Production costs	
Wing system	1
Main rotor system	2
Tail system	3
Body system	4
Alighting gear system (undercarriage)	5
Nacelle system	6
Propulsion system	7
Flight controls system	8
Auxiliary power system	9
Instruments system	10
Hydraulic system	11
Pneumatic system	12
Electrical system	13
Avionics system	14
Furnishings & equipment system	15
Air conditioning system	16
Anti-icing system	17
Load & handling system	18
Assembly costs	
In-house assembly	19

A.2 Wing system

The wings are defined as the small extensions next to the fuselage wherein e.g. the retractable landing gear wheel wells are placed. The structure of the wings is rather simple and does not accommodate flight controls, hydraulic and/or fuel systems. For the cost evaluation, the wing system has been omitted since the total impact on mass and cost remains low (< 1%).

$$W_{E,1} = -99.418 + 0.0309 W_g \qquad \text{[lb][lb]} \qquad \text{(A.1)}$$

$$C_{RP,1} = 1019 W_{E,1}^{0.848} Q^{-0.286} \qquad \text{[\$Y77][lb][-]} \qquad \text{(A.2)}$$

A.3 Rotor system

Rotor blades, hub and hinge assembly constitute the rotor system. For a conventional helicopter, this is the main rotor system. For a tandem helicopter, two rotors must be taken into account. In Beltramo & Morris (1980), the blade planform surface area S_{pl} was found to be the most reliable parameter to determine the rotor system mass :

$$S_{pl} = \text{(Blade surface) x (Number of blades)} \tag{A.3}$$

$$S_{pl} = 0.0083\, W_g + 20.614 \qquad [\text{ft}^2][\text{lb}] \tag{A.4}$$

In view of using W_g as independent variable, a correlation between S_{pl} and W_g has to be established. This was done using the information given in Beltramo & Morris (1980). The result is presented in Fig.A.1 and correlates will with the data.

$$W_{E,2} = -194.685 + 12.164 S_{pl} \qquad [\text{lb}][\text{ft}^2] \tag{A.5}$$

$$C_{RP,2} = -12938 + 101 W_{E,2} Q^{-0.074} \qquad [\$Y77][\text{lb}][\text{-}] \tag{A.6}$$

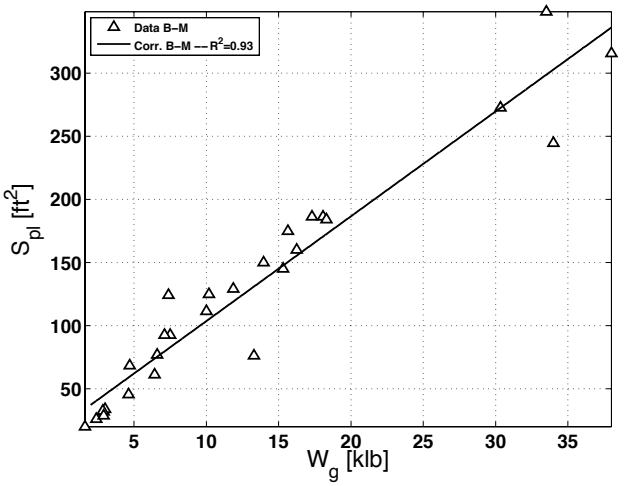

FIGURE A.1. S_{pl} as a function of W_g – Beltramo & Morris (1980).

A.4 Tail system

The tail system consists of the tail rotor and the tail structure, including the aerodynamic surfaces and mounts for the tail rotor. For the tail rotor the following is proposed :

$$\ln(W_{E,3A}) = -8.327 + 1.352 \ln(W_g) \qquad [\text{lb}][\text{lb}] \tag{A.7}$$

$$C_{RP,3A} = 102 W_{E,3A} Q^{-0.074} \qquad [\$Y77][\text{lb}] \tag{A.8}$$

And for the tail structure :

$$S_{tt} = 0.0030\ W_g + 8.1460 \qquad [\text{ft}^2][\text{lb}] \qquad \text{(A.9)}$$

$$W_{E,3B} = -17.872 + 2.829 S_{tt} + K_t \qquad [\text{lb}][\text{ft}^2] \qquad \text{(A.10)}$$

$$C_{RP,3B} = 759\ W_{E,3B}^{0.848}\ Q^{-0.286} \qquad [\$Y77][\text{lb}][-] \qquad \text{(A.11)}$$

where for a single rotor $K_t = 0$, while for a tandem rotor $K_t = -111.1$. S_{tt} is the sum of the horizontal and vertical tail plane areas. Again, a trend for this parameter as a function of W_g has been established by the author of this work relying on the data given by Beltramo & Morris (1980) and is shown in Fig.A.2. The correlation between W_g and S_{tt} proves to be mediocre, especially in the mid-range of W_g. It must be noted though that the cost impact of the tail system will be low with respect to the total cost of the helicopter. As a consequence, it is acceptable to use Eq.A.9. Finally note that the cost and empty weight relations are reported to be applicable to articulated, teetered and rigid rotors.

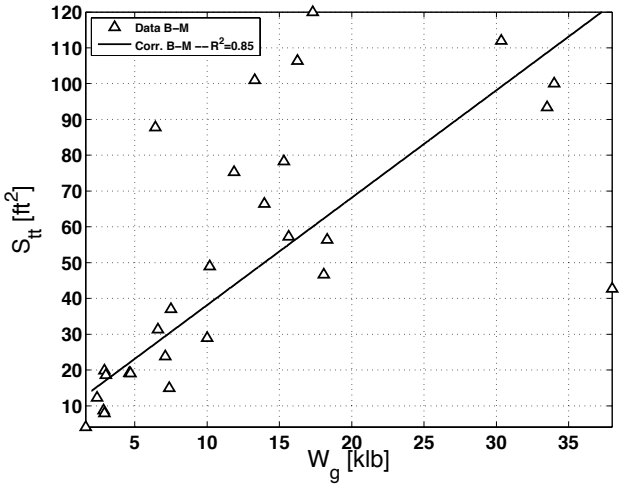

Figure A.2. Combined horizontal and vertical tail plane area S_{tt} – Beltramo & Morris (1980).

A.5 Body system

The system includes the fuselage shell structure, door and window frames, doors with corresponding actuation mechanisms, airstairs if installed, loading ramps, windows, cockpit windshield, floors, bulkheads and radome. S_{bo} is the body surface area (Fig.A.3), which was again related to W_g using the data in Beltramo & Morris (1980). The correlation between both parameters was found acceptable.

$$S_{bo} = 0.0574\ W_g + 63.716 \qquad [\text{ft}^2] \qquad \text{(A.12)}$$

$$W_{E,4} = -269.023 + 2.356\ S_{bo} \qquad [\text{lb}][\text{ft}^2] \qquad \text{(A.13)}$$

$$C_{RP,4} = 860\ W_{E,4}^{0.848} Q^{-0.286} \qquad [\$Y77][\text{lb}][\text{-}] \qquad \text{(A.14)}$$

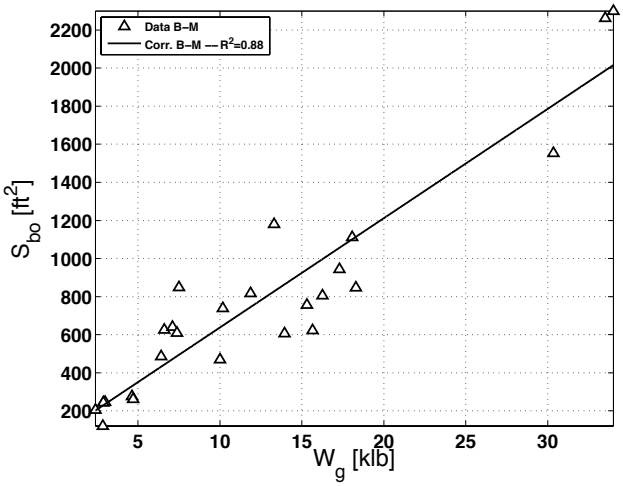

Figure A.3. Body surface area S_{bo} – Beltramo & Morris (1980).

A.6 Alighting gear system or undercarriage

There are mainly two types of landing gears : skids or wheels (see Chapter 1). The lighter helicopters (W_g <3000 kg[i]) normally have landing skids, while the heavier ones use the wheeled undercarriage (fixed or retractable). For both landing gear types, Beltramo & Morris (1980) gives a single mass trend that relates the helicopter gross weight to the alighting gear system empty weight, with sufficient accuracy ($R^2 = 0.935$). A generally applicable cost correlation for both landing gear types however, could not be established.

$$W_{E,5} = -5.489 + 0.0342\ W_g \qquad (\forall\ W_g) \qquad [\text{lb}][\text{lb}] \qquad \text{(A.15)}$$

$$C_{RP,5} = \frac{W_{E,5}}{W_{E,4}} C_{RP,4} \qquad (W_g < 3000\ \text{kg}) \qquad [\$Y77] \qquad \text{(A.16)}$$

$$C_{RP,5} = 84 W_{E,5}\ Q^{-0.2176} \qquad (W_g \geq 3000\ \text{kg}) \qquad [\$Y77][\text{lb}][\text{-}] \qquad \text{(A.17)}$$

Worthwhile mentioning are the system mass and cost reductions of respectively 20% and 15% proven by Thuis (2004) using composite materials fabricated via resin transfer

[i]This value was tacitly assumed after evaluation of the survey data.

moulding (RTM) in the alighting gear system of the NH-90. These figures are not adopted in the model.

A.7 Nacelle system

The nacelle incorporates the engine mount, firewall structure, cowl structure, engine air inlet, oil cooler scoop and other installation hardware. The mass of the nacelle system depends on the nacelle surface S_n. Correlating S_n with W_g gave poor results. Also, the data did not incorporate helicopters where the nacelles were located in the fuselage, which is generally the case for smaller helicopters. After evaluating the mass and cost impact of the nacelle on the final outcome, which was less of a few percent, the nacelle system was neglected. This is acceptable as the major cost drivers are sought in the analysis conducted in Chapter 1.

A.8 Propulsion system

The propulsion system is subdivided into three subsystems : the powerplant, the drive and the fuel system. The *powerplant subsystem* consists of the dry engine, residual fluids and installation hardware such as the starter, air inductor, exhaust and cooling components, engine lubrication systems and engine controls. The *drive subsystem* includes the speed reduction gearboxes, rotor brake and shaft and the lubrication system. The *fuel subsystem* is made of the fuel fill and drain system, the fuel distribution system, the fuel vent plumbing and fuel tanks. Each subsystem is studied separately. The current approach exclusively takes turboshaft engines into account as the reciprocating engines represent only a small fraction of the evaluated gross weight range.

A.8.1 Powerplant subsystem

Installed power H_{pe}

The powerplant weight $W_{E,7A}$ depends according to Beltramo & Morris (1980) on the total installed power H_{pe}. The correlations given for H_{pe} by these authors are linear equations with correlation coefficients R^2 around 90% for the turboshaft equipped helicopters, which now represent the largest helicopter population. Also, the dataset is somewhat dated and does not include European helicopters, which hold a significant share of the helicopter market at the moment. To cope with the previously mentioned issues, the author of this work established new H_{pe}-correlations. A correlation was made for both the maximum continuous power setting (MCP) and the maximum take-off power setting (MTOP) of the engines, exhibiting a slightly better correlation coefficient in addition (Fig.A.4). Note that

the correlations apply to standard day conditions at sea level.

$$MCP = 0.061\ W_g^{1.1705} \quad \text{[kW][kg]} \tag{A.18}$$

$$MTOP = 0.068\ W_g^{1.1693} \quad \text{[kW][kg]} \tag{A.19}$$

It was not clear whether Beltramo & Morris (1980) used maximum continuous power or maximum take-off power conditions in their database, used to calculate H_{pe}. Crosschecking with the data of the survey, a better agreement between MCP and the trend-line of Beltramo & Morris (1980) was found, as seen on Fig.A.5. Also, the decision to use MCP for the calculation of H_{pe}, supports a more conservative cost estimation of the subsystem, as it lowers the importance of the propulsion system in the total cost.

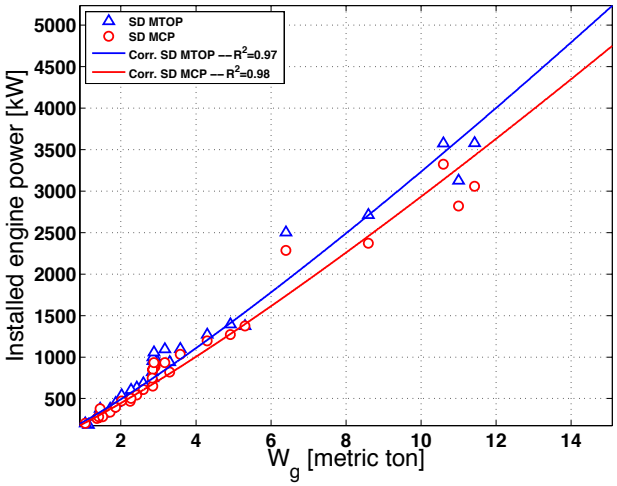

Figure A.4. Helicopter installed power, ISA SLS conditions – SD : survey data ; MCP : maximum continuous power setting ; MTOP : maximum take-off power setting.

Impact of installed amount of engines

The weight of the powerplant subsystem depends on the amount of engines installed in the conventional helicopter. Beltramo & Morris (1980) provide correlations to determine $W_{E,7A}$ for a single and twin-engine configuration, for both reciprocating and turboshaft engines. Investigation of the weight trend for the turboshaft configurations, showed an anomaly for the twin-engine configuration. Also, Beltramo & Morris (1980) do not provide a solution for helicopters with three engines installed, such as found on the AgustaWestland AW101. Hence, alternative powerplant weight estimation correlations will be proposed. The derivation of these formulae is performed next.

First, the single engine turboshaft configuration is examined. Beltramo & Morris (1980) subdivides $W_{E,7A}$ in an engine weight subclass $W_{E,7A'}$ and a engine peripheral subclass

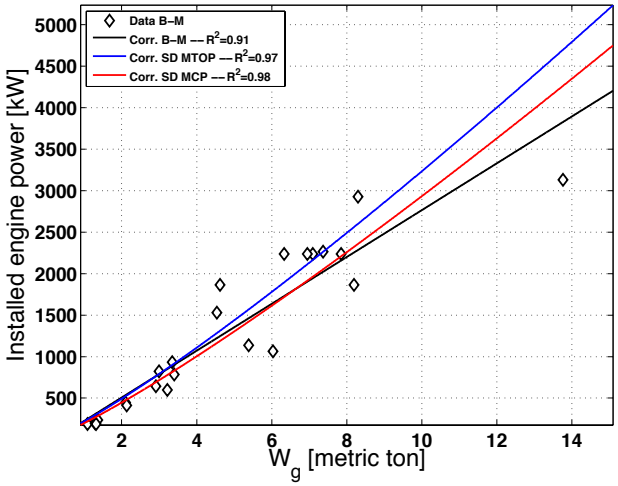

FIGURE A.5. Helicopter installed power, ISA SLS conditions – B-M : Beltramo & Morris (1980) ; SD : survey data ; MCP : maximum continuous power setting ; MTOP : maximum take-off power setting.

$W_{E,7A''}$, which contains components such as the air induction, exhaust, cooling and starter systems. The author of this work compared the weight of the engines alone ($W_{E,7A'}$) with $W_{E,7A}$ proposed by the correlation of Beltramo & Morris (1980) (Fig.A.6). Since the peripherals are not adopted in $W_{E,7A'}$, it is normal to observe that $W_{E,7A'} < W_{E,7A}$. To include the peripherals $W_{E,7A''}$, it is assumed that :

$$W_{E,7A''} \propto W_{E,7A'} \quad \Rightarrow \quad W_{E,7A'} = K_{f,ep}\, W_{E,7A} \tag{A.20}$$

For a single engine configuration, $K_{f,ep} \cong 0.8$ was found to be a reasonable value. Indeed, it is found sensible that the weight of the contemporary turboshaft-based powerplant systems is not higher than what is found for systems of two decades ago, on which the correlation of Beltramo & Morris (1980) is based (Fig.A.6). The new weight correlation can now be formulated as :

$$W_{E,7A} = \frac{3.6591\, MCP^{0.6733}}{K_{f,ep}} \quad \text{[lb][BHP]} \tag{A.21}$$

Note that the use of the foregoing equation predicts a lower powerplant subsystem weight at the higher installed power levels. This is not a concern as it results from the fact that the data of Beltramo & Morris (1980) is less populated in that region and thus less accurate.

In case of a twin-engine configuration, the powerplant subsystem weight correlation of Beltramo & Morris (1980) shows to be of concern (Fig.A.7). Indeed, $W_{E,7A}$ predicted by their model is similar or higher than $W_{E,7A'}$ for the majority of the examined H_{pe}-range, where $W_{E,7A''}$ has not yet been accounted for. The aberration is most likely due to the serious lack of data in the H_{pe}-range lower than 2500 BHP, possibly explaining the over-

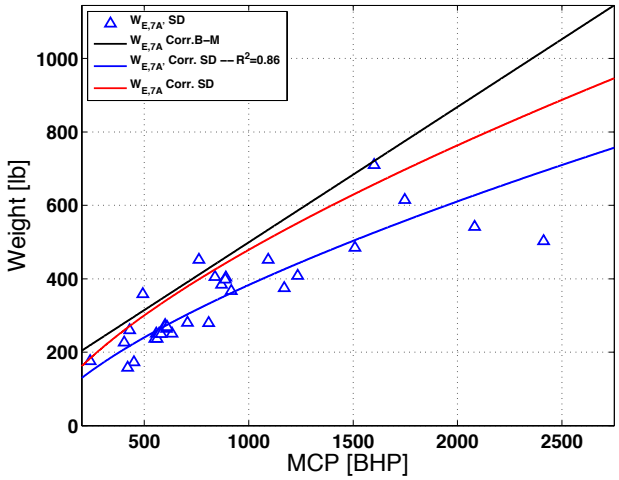

FIGURE A.6. Helicopter powerplant weight, single engine configuration, ISA SLS conditions – B-M : Beltramo & Morris (1980) ; SD : survey data.

estimation of the system weight in the low H_{pe}-range, and much less data in the mid H_{pe}-range, which were both well covered by the survey of the author of the work at hand. In order not to divert too much from the model of Beltramo & Morris (1980), $K_{f,ep}$ was

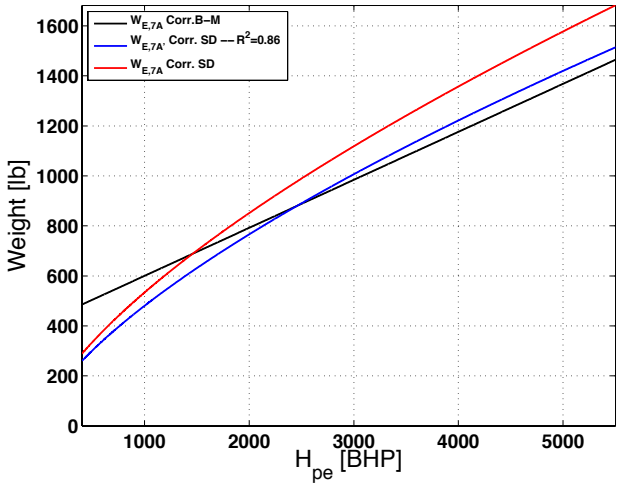

FIGURE A.7. Helicopter powerplant weight, twin-engine configuration, ISA SLS conditions – B-M : Beltramo & Morris (1980) ; SD : survey data.

taken to be 90% for all but the single engine configuration (Table.A.2). The model for calculating the powerplant subsystem weight can now be generalised as :

$$W_{E,7A} = 3.6591 \left(\frac{N_e}{K_{f,ep}}\right)\left(\frac{H_{pe}}{N_e}\right)^{0.6733} \qquad \text{[lb][BHP]} \tag{A.22}$$

and,

$$H_{pe} = 0.0286\ W_g^{1.1852} \qquad \text{[BHP][lb]} \qquad \text{(A.23)}$$

$$C_{RP,7A} = 83320 + 215\ H_{pe}\ Q^{-0.2345} \qquad \text{[\$Y77][BHP]} \qquad \text{(A.24)}$$

The number of engines N_e correlate relatively well with W_g, as is indicated in Fig.A.8.

Table A.2. Engine-to-Powerplant fudge factor $K_{f,ep}$.

Number of Turboshaft Engines N_e		$K_{f,ep}$
1	($W_g \leq 2500$ kg)	0.8
2	($2500kg < W_g \leq 15500$ kg)	0.9
3	($W_g >$15500 kg)	0.9

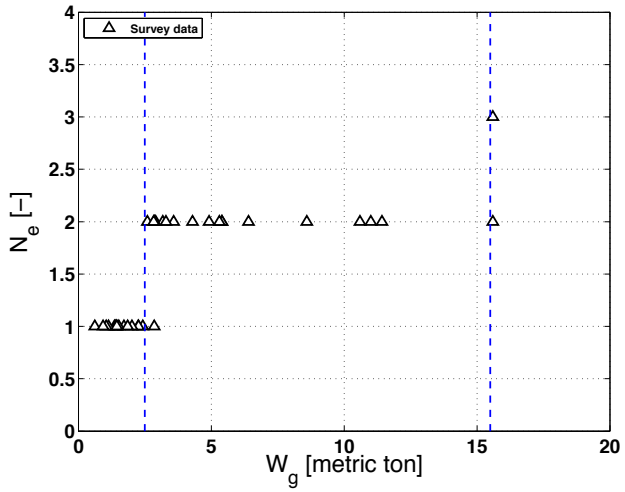

Figure A.8. Helicopter number of installed engines.

A.8.2 Drive subsystem

For the drive subsystem, the general mass correlation stated in Beltramo & Morris (1980) was adopted, though the cost model was moderately changed in order to avoid discontinuities in the $C_{RP,7B}$ cost estimation. The modified model keeps the cost constant for $W_{E,7B}$ ranging between 700 lb and $W_{E,7B^*}$ (see Eq.A.26). This avoids sudden and unrealistic price fluctuations. Table A.3 summarises the cost correlations for $C_{RP,7B}$.

$$W_{E,7B} = -35.551 + 0.101\ W_g \qquad [lb][lb] \qquad \text{(A.25)}$$

$$W_{E,7B^*} = 36\left(\frac{4025\ Q^{-0.074} + 323)}{83Q^{-0.074}}\right) \qquad [lb] \qquad \text{(A.26)}$$

Table A.3. Drive subsystem recurring production cost $C_{RP,7B}$.

Drive subsystem Empty Weight $W_{E,7B}$ **[lb]**	$C_{RP,7B}$ **[$Y77]**
$W_{E,7B} \leq 700$	$-4795 + 207\ W_{E,7B}\ Q^{-0.074}$
$700 < W_{E,7B} \leq W_{E,7B^*}$	$-4795 + 144900\ Q^{-0.074}$
$W_{E,7B} > W_{E,7B^*}$	$-16423 + 83\ W_{E,7B}\ Q^{-0.074}$

A.8.3 Fuel subsystem

The fuel subsystem mass $W_{E,7C}$ depends on the fuel storage capacity V_{ft}. The correlations given by Beltramo & Morris (1980) for V_{ft} as a function of W_g did not give an as high level of accuracy as the correlation established by the data of the survey performed by the author of the work at hand (Fig.A.9). Therefore, the latter was used to estimate $W_{E,7C}$. The effect of this action on weight and cost remained, however, minor.

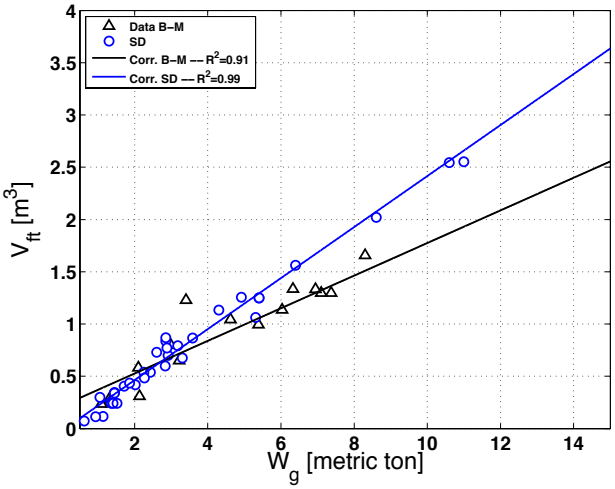

Figure A.9. Helicopter fuel tank volume V_{ft} trend comparison – Beltramo & Morris (1980) and survey data (SD).

$$V_{ft} = 0.0292\ W_g - 6.5348 \quad \text{[US Gal.][lb]} \tag{A.27}$$

$$W_{E,7C} = 10.974 + 0.790\ V_{ft} \quad \text{[lb][US Gal.]} \tag{A.28}$$

$$C_{RP,7C} = 56\ W_{7C}\ Q^{-0.0896} \quad \text{[$Y77][lb]} \tag{A.29}$$

A.9 Flight control system

Cabin controls (cyclic and collective yokes, pedals), mechanical operating system components (swash plate, bearings, levers, stabilizing bars, linkages, etc.) and hydraulic controls

(hardware and fluids) make up the flight control system. The mass and cost relations :

$$W_{E,8} = 62.025 + 0.0334 W_g \quad \text{[lb][lb]} \quad \text{(A.30)}$$

$$C_{RP,8} = 156 W_{E,8}\, Q^{-0.0896} \quad \text{[\$Y77][lb]} \quad \text{(A.31)}$$

A.10 Auxiliary power system

The auxiliary power system enables executing helicopter ground operations without needing an externally connected power unit. Amongst the ground operations we have the use of air conditioning, engine starting and electrical power supply (instruments, avionics, etc.). Not all helicopters have an auxiliary power system. Beltramo & Morris (1980) found such systems on helicopters having a Gross Weight of at least 13000 lb. However, the data used to establish this boundary consists mainly of military aircraft, where an auxiliary power system is installed in much smaller aircraft due to the logistical advantages. After removing the military attack versions, the boundary shifted to 15000 lb. In the survey data, the system was only mentioned for the first time on a Eurocopter AS332 Super Puma with a Gross Weight of about 19000 lb. Consequently, the more conservative value of 15000 lb was selected for the calculations. An average mass for the auxiliary power system was suggested.

$$W_{E,9} = 157 \quad (W_g \geq 15000 lb) \quad \text{[lb]} \quad \text{(A.32)}$$

$$C_{RP,9} = 234 W_{E,9}\, Q^{-0.0896} \quad \text{[\$Y77]} \quad \text{(A.33)}$$

A.11 Instruments system

The instruments system provides the basic monitoring and warning functions related to the electrical, hydraulic, pneumatic, fuel and engine system operations. Indicators, warning lights, circuitry and transducers are adopted in the mass calculations.

$$W_{E,10} = 42.106 + 0.00503\, W_g \quad \text{[lb][lb]} \quad \text{(A.34)}$$

$$C_{RP,10} = 125\, W_{E,10}\, Q^{-0.0896} \quad \text{[\$Y77][lb]} \quad \text{(A.35)}$$

A.12 Hydraulic system

Many rotorcraft require hydraulic flight controls and in some cases a hydraulic actuated landing gear is installed. The hydraulic systems includes pumps, filters, reservoirs, accumulators, pressure regulators, valves, hydraulic oil, plumbing and support/mounting hardware.

$$W_{E,11} = 15.890 + 0.00446\, W_g \quad \text{[lb][lb]} \quad \text{(A.36)}$$

$$C_{RP,11} = 91\, W_{E,11}\, Q^{-0.0896} \quad \text{[\$Y77][lb]} \quad \text{(A.37)}$$

A.13 Pneumatic system

The pneumatic system provides compressed air for cabin air conditioning and ventilation, engine starting, anti-icing and pneumatic emergency power systems. The system includes heat exchangers and air ducting leaving the engines (main and auxiliary). No mass correlations were found by Beltramo & Morris (1980). An attempt to estimate the pneumatic system mass via the combined hydraulic and pneumatic system mass given by Crabtree (1958) failed as the results were inconsistent for W_g up to 8000 lb. The pneumatic system was consequently left out of the model.

A.14 Electrical system

The electrical system generates and provides electrical power to multiple components in the helicopter such as avionics, instruments, lights, air conditioning etc. The system is composed of the AC and DC power generating equipment, converters, batteries, wiring and cables, fittings, supports and circuitry.

$$\ln(W_{E,13}) = -0.5385 + 0.6728\ \ln(W_g) \qquad \text{[lb][lb]} \qquad \text{(A.38)}$$

$$C_{RP,13} = 143\ W_{E,13}\ Q^{-0.0896} \qquad \text{[\$Y77][lb]} \qquad \text{(A.39)}$$

A.15 Avionics system

The avionics system can be subdivided in four major categories : *Integrated Flight Guidance and Controls subsystem* (flight director, gyrocompass, attitude and heading, IRU), *Communication subsystem* (internal and external communications), *Navigation subsystem* (VOR, DME, ADF, TCAS, Transponder, ILS) and *Miscellaneous Equipment subsystem* (Cockpit voice recorder, HUMS, mounting hardware). The mass of the avionics depends on the range of the aircraft R. The best R-W_g correlation was found using data of the survey (Eq.A.40 and Fig.A.10).

$$R = 27.252\ W_g^{0.2938} \qquad \text{[NM][lb]} \qquad \text{(A.40)}$$

$$W_{E,14} = -59.041 + 0.0175\ W_g + 0.348\ R \qquad \text{[lb][lb][NM]} \qquad \text{(A.41)}$$

$$C_{RP,14} = 6847 + 125\ W_{E,14}\ Q^{-0.0896} \qquad \text{[\$Y77][lb]} \qquad \text{(A.42)}$$

A.16 Furnishings and equipment system

This system considers multiple components in the cockpit, passenger and cargo compartments, going from seats, insulation, floor coverings, oxygen system and doors to hat-racks and baggage containers. Also included are lavatories, galleys, fire warning and

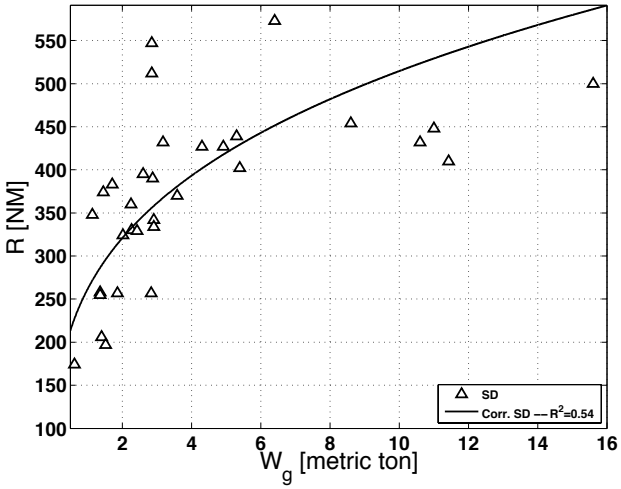

Figure A.10. Helicopter range R as a function of W_g – From survey data (SD).

extinguishing systems, first aid kits and exterior paint. An important parameter in determining mass and cost is the crew and passenger number N_{cp}. Again, the survey allowed establishing a reasonable relationship between N_{cp} and W_g (Eq.A.43 and Fig.fig:wgncp).

$$N_{cp} = \text{round}(0.000875\ W_g + 2.560) \qquad [\text{-}] \qquad (A.43)$$

$$W_{E,15} = -8.106 + 0.176\ S_{bo} + 20.456\ N_{cp} \qquad [\text{lb}][\text{ft}^2] \qquad (A.44)$$

$$C_{RP,15} = 69\ W_{E,15}\ Q^{-0.0896} \qquad [\$Y77][\text{lb}] \qquad (A.45)$$

A.17 Air conditioning system

The system provides the cabin with (acclimatised) air, warms the cargo compartment when necessary and supplies cooling air for the electronics and avionics bays.

$$W_{E,16} = 22.078 + 0.00414\ W_g \qquad [\text{lb}][\text{lb}] \qquad (A.46)$$

$$C_{RP,16} = 208\ W_{E,16}\ Q^{-0.0896} \qquad [\$Y77][\text{lb}] \qquad (A.47)$$

A.18 Anti-icing system

Both anti-icing system technologies are considered : via bleed air or via electrical blankets. The hot air system includes all ducting from the main pneumatic source and the inner skins that form the hot air cavities. The electric blanket system is made up by the blankets, wiring and controls. A general mass and cost relationship were derived and given below.

$$W_{E,17} = 19.938 + 0.000837\ W_g \qquad [\text{lb}][\text{lb}] \qquad (A.48)$$

$$C_{RP,17} = 213\ W_{E,17}\ Q^{-0.0896} \qquad [\$Y77] \qquad (A.49)$$

A.19 Load and handling system

The load and handling system takes the loading and handling gear into account, with the provisions for jacking, hoisting and mooring, and ballast. For the cost calculations, this system was left out of consideration. Observing Eq.A.50, the relatively low importance of $W_{E,18}$ with respect to W_g can be noted, but more importantly, for the lower W_g, the correlation predicts a negative mass due to the large negative intercept, which is unacceptable. Because it is the author's opinion that the model must be usable for all realistic W_g, negative masses and hence negative costs must be avoided.

$$W_{E,18} = -71.875 + 0.111\, S_{bo} + 3.489\, N_{cp} \qquad [\text{lb}][\text{ft}^2] \qquad (A.50)$$

$$C_{RP,18} = \left(\frac{W_{E,18}}{W_{E,4}}\right) C_{RP,4} \qquad [\$Y77] \qquad (A.51)$$

A.20 Assembly costs

The assembly costs account for all expenses made to assemble the helicopter in-house, i.e. those involved in joining components and subassemblies into a finished helicopter. Components such as the rolling assembly (part 5C), bare engine(s) (part 7A), instruments (part 10) and avionics (part 14) are normally fabricated by subcontractors and are therefore left out of the assembly cost calculations.

$$C_{RA} = 5.325 \left(\sum_{k=1}^{18} C_{RP,k} - \sum_{k=5C,7A,10,14} C_{RP,k}\right) Q^{-0.3959} \qquad [\$Y77] \qquad (A.52)$$

A.21 Manufacturer recurring production and assembly cost

The manufacturer recurring manufacturing costs C_{RM} can now be estimated for a given W_g and Q, viz. :

$$C_{RM} = k_{CPI} \left(\sum_{k=1}^{18} C_{RP,k} + C_{RA}\right) \qquad [\$] \qquad (A.53)$$

Appendix B

HTS device performance characteristics

B.1 HTS motor

A general model to estimate the mass and volume of a HTS motor requires significant knowledge and experience in the domain of electric motors. For the work at hand, a less involved approach was undertaken using the data given in Masson et al. (2005) and Masson & Luongo (2007). The former work graphically presents the minimum mass $W^{ref}_{HTS,m}$ and volume $V^{ref}_{HTS,m}$ of an air-gap HTS motor turning at 3000 RPM with four poles and a constant radius-to-length-ratio for various shaft powers. Based on this data, the following weight and volume correlations were established (Fig.B.1 & Fig.B.2) :

$$W^{ref}_{HTS,m} = 2.175\ P^{0.5825}_{HTS,m} \qquad \leq 500\text{ kW} \qquad [\text{kg}][\text{kW}] \qquad \text{(B.1)}$$

$$W^{ref}_{HTS,m} = 0.0975\ P_{HTS,m} + 32.490 \qquad > 500\text{ kW} \qquad [\text{kg}][\text{kW}] \qquad \text{(B.2)}$$

$$V^{ref}_{HTS,m} = 0.000340\ P^{0.6284}_{HTS,m} \qquad \leq 500\text{ kW} \qquad [\text{m}^3][\text{kW}] \qquad \text{(B.3)}$$

$$V^{ref}_{HTS,m} = 0.0000174\ P_{HTS,m} + 0.00822 \qquad > 500\text{ kW} \qquad [\text{m}^3][\text{kW}] \qquad \text{(B.4)}$$

This configuration is considered as the reference (ref) from which the performance characteristics of HTS motors working at other rotational velocities will be derived.
The operating temperature $T^{ref}_{OT,m}$ of the reference HTS motor was not mentioned in the work of Masson et al. (2005), but here it is assumed to be 20 K. Based on the previous reference correlations, it is possible to determine the mass and volume of a HTS motor turning at other design rotational velocities. Indeed, Masson et al. (2005) reports that for a given design shaft torque τ_m and rotational speed Ω_m the following equations apply :

$$P_{HTS,m} = \tau_m \Omega_m \qquad [\text{W}][\text{Nm}][\text{rad/s}] \qquad \text{(B.5)}$$

$$\tau_m = \sqrt{2} B^0_r K_{arm} \pi r^2_{arm} L \qquad [\text{Nm}] \qquad \text{(B.6)}$$

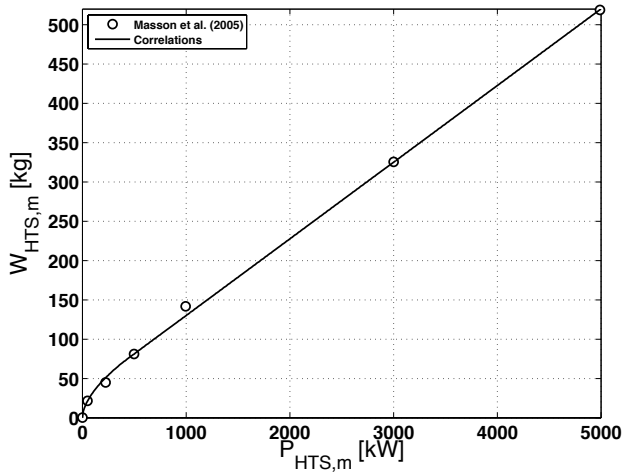

Figure B.1. HTS motor mass as a function of delivered power, 4 poles, 3000 RPM - Masson et al. (2005).

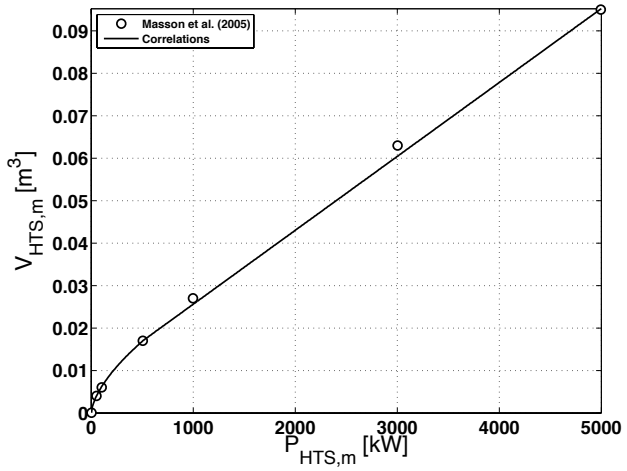

Figure B.2. HTS motor volume as a function of delivered power, 4 poles, 3000 RPM - Masson et al. (2005).

where B_r^0 and K_{arm} are machine constants, r_{arm} the armature radius and L the active machine length. Note that $\pi\, r_{arm}^2\, L$ represents the active machine volume and thus mass considering a constant machine density. Consequently, for a machine turning at Ω_m while generating a nominal power $P_{HTS,m}$ at an operating temperature $T_{OT,m}^{ref}$, the impact of rotational velocity on the design motor weight can be estimated by :

$$\left.\frac{W_{HTS,m}}{W_{HTS,m}^{ref}}\right|_{P_{HTS,m},\, T_{OT,m}^{ref}} = \frac{\Omega_m^{ref}}{\Omega_m} \tag{B.7}$$

If the motor operates at other temperatures than the reference of 20 K, another mass correction needs to be performed. Indeed, lower or higher operating temperatures require

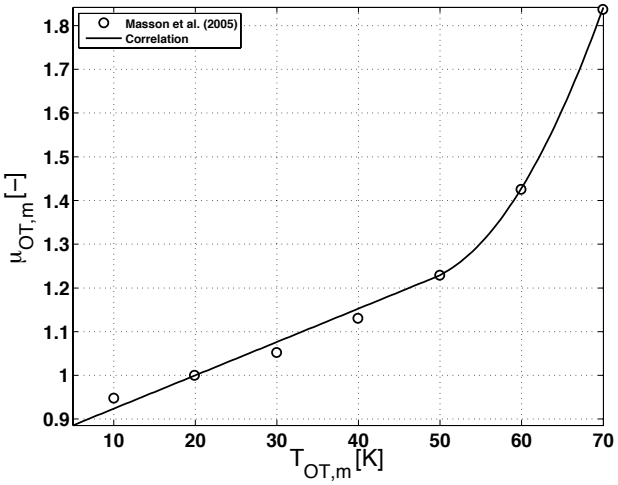

Figure B.3. Temperature related weight correction - Masson et al. (2005).

respectively less or more HTS material windings to maintain the design field strength[i], which will respectively decrease or increase the mass and volume of the motor. From graphical data given by Masson et al. (2005), the following mass-temperature trend was found (Fig.B.3) :

$$\left.\frac{W_{HTS,m}}{W^{ref}_{HTS,m}}\right|_{P_{HTS,m},\ \Omega^{ref}_{m}} = 0.00763\ T_{OT,m} + 0.84738 \qquad T_{OT,m} \leq 50\ \text{K} \qquad \text{(B.8)}$$

$$\left.\frac{W_{HTS,m}}{W^{ref}_{HTS,m}}\right|_{P_{HTS,m},\ \Omega^{ref}_{m}} = 0.00107\ T^2_{OT,m} - 0.0978\ T_{OT,m} + 3.445 \qquad T_{OT,m} > 50\ \text{K} \qquad \text{(B.9)}$$

The data was given for a HTS motor generating a shaft output power of 130 kW. Lack of additional information did not allow to verify the validity of the correlations at other power settings. However, it is tacitly assumed that the foregoing correlations are generally applicable. Table B.1 summarises all equations necessary to estimate the HTS motor mass and volume for a random rotational speed and operating temperature.

The power density calculated by the model was assessed using values given by Masson & Luongo (2007) for an air-gap motor turning at 10000 RPM (Fig.B.4). The model follows the data relatively well at the lower power settings, but breaks away from the curve for power settings above 1.5 MW. The reason for underestimating the power density is probably due to the implementation of flux-trapping in the newer design of Masson & Luongo (2007), a technology which was likely not to be included in the design released a few years earlier, and on which the model was based. However, for conceptual purposes, the model can be found to be reasonably adequate. A comparison of the performance between HTS motors and the turboshaft is conducted in Section 2.3.5, using the HTS

[i]The critical (maximum) current drops with an increasing operating temperature, thus requiring more windings.

Table B.1. HTS motor mass and volume estimation.

$\mu_{\Omega,m} = \left.\frac{W_{HTS,m}}{W^{ref}_{HTS,m}}\right\vert_{P_{HTS,m},\, T^{ref}_{OT,m}}$	Eq. B.7
$\mu_{OT,m} = \left.\frac{W_{HTS,m}}{W^{ref}_{HTS,m}}\right\vert_{P_{HTS,m},\, \Omega^{ref}_{m}}$	Eq. B.8 or B.9
$W_{HTS,m} = \mu_{\Omega,m}\, \mu_{OT,m}\, W^{ref}_{HTS,m}$	Eq. B.1 or B.2
$V^{\dagger}_{HTS,m} = \mu_{\Omega,m}\, \mu_{OT,m}\, V^{ref}_{HTS,m}$	Eq. B.3 or B.4

† Approximation considering a constant machine density.

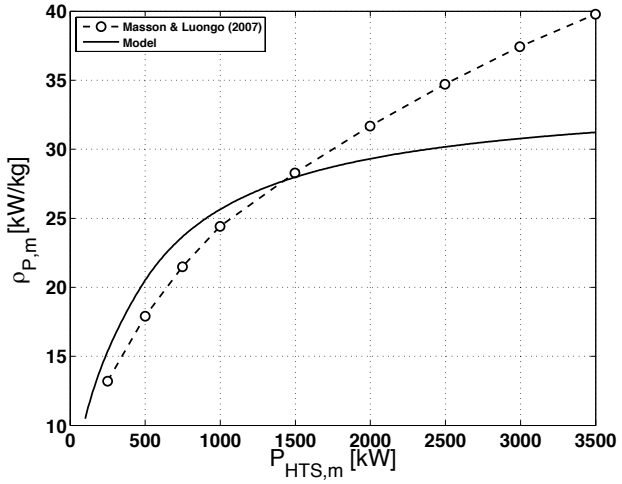

Figure B.4. Calculated power density compared with power density of a 10000 RPM HTS motor (no cryocooler) - Masson & Luongo (2007).

motor model described here. The results are reproduced in respectively Fig.B.5 & B.6 and reveal that HTS motors can allow a significant improvement in mass and volume-weighed power densities respectively $\rho_{P,m}$ and $\rho_{P,V}$ with respect to those of turboshaft engines. Note however, that a free cold source is required to operate the HTS motor, such as liquid hydrogen, and that no consideration is made of the mechanical stresses acting on the motor at the imposed design rotational velocities, which can be very high.

If a cryocooler must work as the cold source, the mass and mechanical power penalty it involves, must still be quantified. Masson et al. (2005) supply graphical data to retrieve cryocooler mass W_{Cryo} and volume V_{Cryo} for several cold source temperatures $T_{CS,Cryo}$ (Figs.B.7&B.8) :

$$W_{Cryo} = 210.01\, e^{-0.0326\, T_{CS,Cryo}} \quad \text{[kg][K]} \tag{B.10}$$

$$V_{Cryo} = 0.2630\, e^{-0.0329\, T_{CS,Cryo}} \quad \text{[m}^3\text{][K]} \tag{B.11}$$

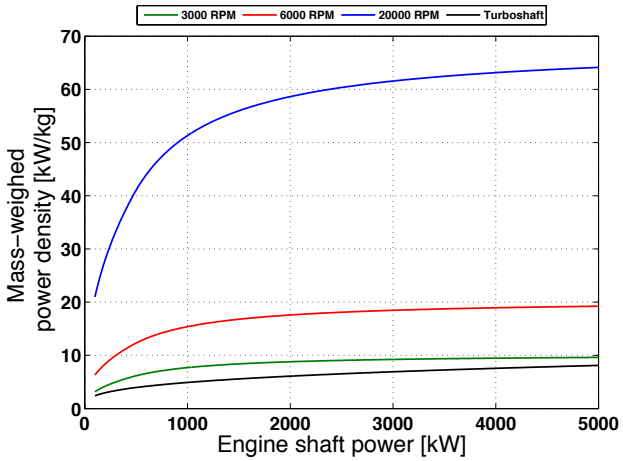

FIGURE B.5. Mass weighed power density, free cold source.

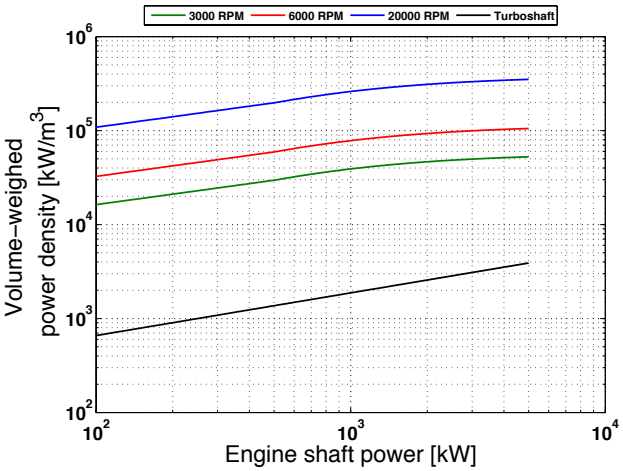

FIGURE B.6. Volume weighed power density, free cold source.

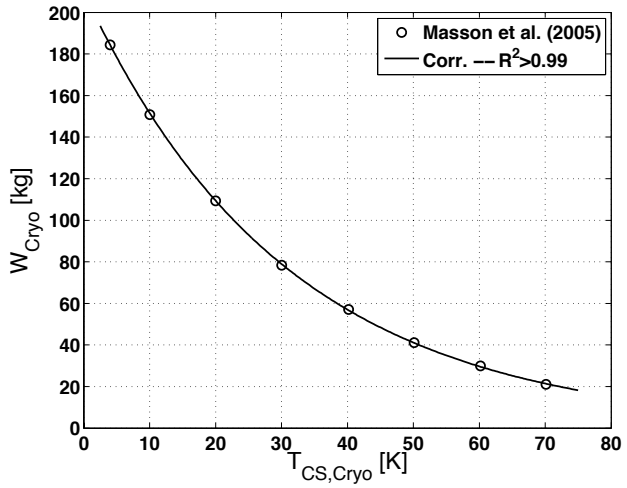

Figure B.7. Cryocooler mass as a function of operating temperature - Masson et al. (2005).

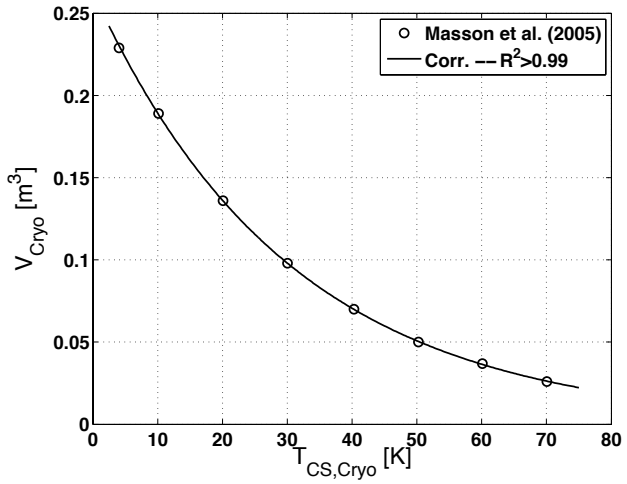

Figure B.8. Cryocooler volume as a function of operating temperature - Masson et al. (2005).

The equations are valid for cryocoolers with a heat absorption capability of 20 W, which is according to Masson et al. (2005) a good average for the heat losses produced inside a HTS motor and valid for a large range of output shaft powers. The efficiency of the cryocooler is examined next.

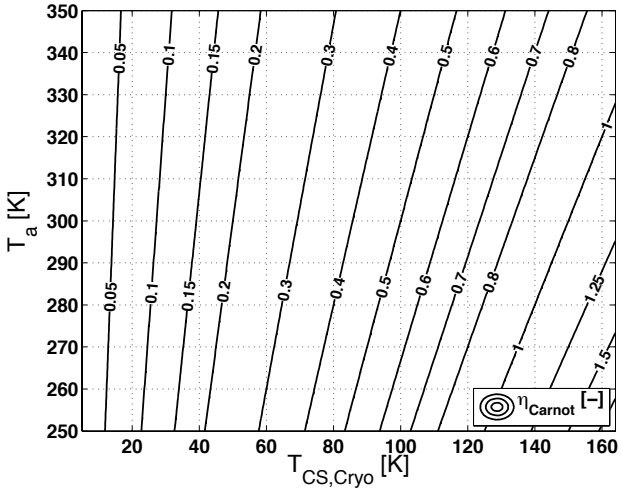

FIGURE B.9. Refrigerator Carnot efficiency (η_{Carnot}).

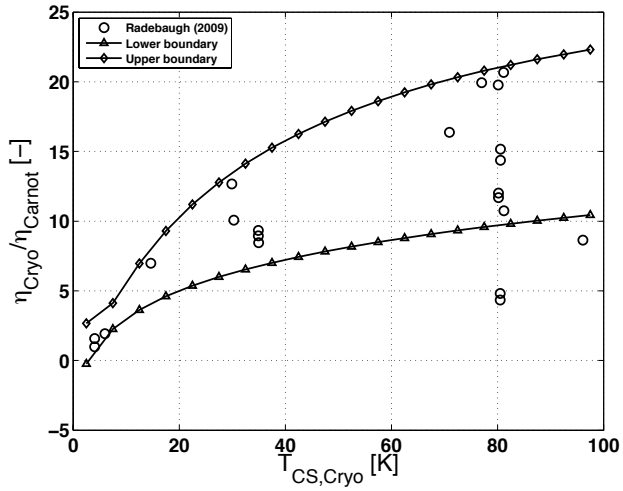

FIGURE B.10. Cryocooler relative efficiency range – Radebaugh (2009).

Since the cryocooler is a refrigerating system, the Carnot efficiency is defined as – Moran & Shapiro (2004) :

$$COP_{Carnot} = \eta_{Carnot} \triangleq \frac{T_L}{T_H - T_L} \tag{B.12}$$

The high temperature of the cycle T_H is related to the atmosphere, which works as the free heat source. For a range of ambient and cold source temperatures, respectively T_a and $T_{CS,Cryo}$ (=T_L), the cryocooler Carnot efficiency[ii] can be established. This is done in Fig.B.9. For a cooling temperature of 20 K, the Carnot efficiency drops below 10%.

[ii]The Carnot efficiency or also effectiveness is the maximum possible coefficient of performance (*COP*) of a refrigerating cycle, where *COP* is the ratio of cooling heat flux and delivered power.

Radebaugh (2009) examined several cryocoolers and their thermal efficiency. For cryocoolers demanding less than 10 kW to be driven, he estimated an efficiency range typical of contemporary state-of-the-art cryocoolers (Fig.B.10). The upper and lower efficiency boundaries in the work of Radebaugh (2009) were consequently transformed into equations by the author of the work at hand, which allows the efficiency of a cryocooler to be adopted in the HTS motor performance model. The established correlations for these efficiency boundaries are :

$$\left.\frac{\eta_{Cryo}}{\eta_{Carnot}}\right|_{Upper} = -0.517\ \ln(T_{CS,Cryo})^3 + 5.457\ \ln(T_{CS,Cryo})^2 - 11.188\ \ln(T_{CS,Cryo}) + 8.739 \quad [-] \tag{B.13}$$

$$\left.\frac{\eta_{Cryo}}{\eta_{Carnot}}\right|_{Lower} = 0.248\ \ln(T_{CS,Cryo})^2 + 1.555\ \ln(T_{CS,Cryo}) - 1.882 \quad [-] \tag{B.14}$$

As a result, the efficiency of the cryocooler operated at several ambient and cold source temperatures is now determinable :

$$\eta_{Cryo} = \frac{T_{CS,Cryo}}{T_{ambient} - T_{CS,Cryo}} \frac{\eta_{Cryo}}{\eta_{Carnot}} \tag{B.15}$$

Fig.B.11 shows that efficiencies can range between a few tenths of a percent to a few tens. Note that with 20 W of heat losses found in HTS devices, some heat source temperature conditions lead to a required mechanical input power of more than 10 kW, which exceeds the power domain in which the efficiency boundaries were validated. Nevertheless, this issue appears not to be a major concern. Indeed, in the work of Radebaugh (2009) it is shown that an increase of heat-load and thus required mechanical power results in an improvement of the cryocooler thermal efficiency. As a consequence, it is reasonable to expect that the stated efficiency boundaries reflect in general a conservative estimation of the efficiency. Figs.B.12 & B.13 show respectively the mass and volume-weighed power densities of a HTS motor with cryocooler. Clearly, the power densities dropped with respect to those of the motor refrigerated with a free cold source (Figs.B.5 & B.6). However, in all examined cases, the mass- and volume-weighed power density remained mostly superior to the one of the turboshaft. Note that the additional power dissipated to drive the cryocooler has to be included. In the performance model explained in Section 2.3.6, the average of upper and lower boundaries is taken to determine the involved power penalty. A constant cooling heat flux of 20 W was adopted in the calculations, as reported by Masson et al. (2005), but this simplification should not be generalised in case a more detailed study is pursued. Finally, some important notes. The HTS motors considered above are all synchronous motors. This motor type is characterised by a rotor turning exactly at the the same frequency of the current in the armature. As all helicopter rotors turn at a constant speed, this motor could assure a more stable rotor frequency if, for example, the frequency is electronically determined. Also, the efficiency of the HTS

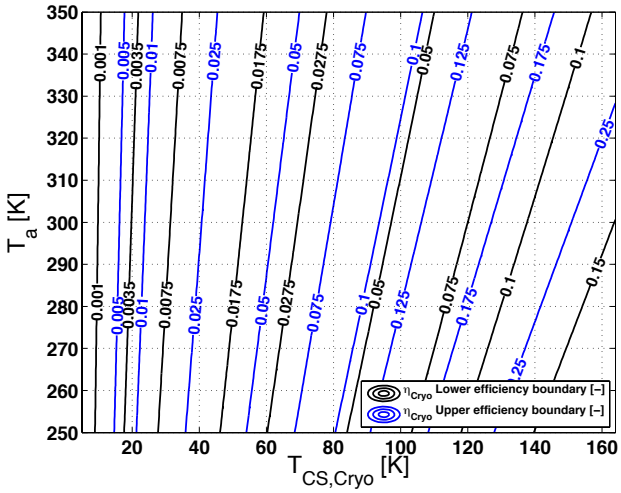

FIGURE B.11. Cryocooler efficiency range.

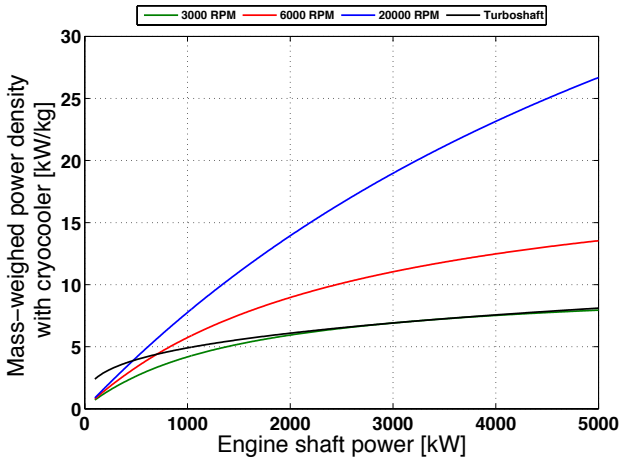

FIGURE B.12. Mass weighed power density with cryocooler.

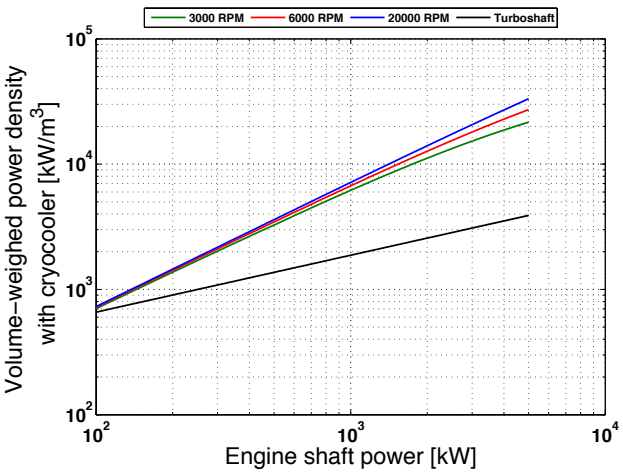

FIGURE B.13. Volume weighed power density with cryocooler.

motor deserves some attention. Unfortunately, this topic is poorly documented in the literature. Only Kwon et al. (2007) mentions nominal efficiencies ranging from 94-98%. For the calculations, a fixed average efficiency of 96% will be taken.

B.2 HTS Generators

Still remains the issue of producing the electricity to feed the motor. This could be done by a conventional generator, but this would involve a too high weight penalty. The discussion of the different types of HTS generators will not be conducted here, and the reader is therefore referred to the works of, for example Edkin et al. (1968), Singh et al. (1999), Kalsi (2001), Nanao & Maki (2006), Lewis & Müller (2007), Zhang et al. (2007), Bailey et al. (2009), Sivasubramaniam et al. (2009) and Wen et al. (2009).

For this work, it is important to establish relations that determine the HTS generator mass- and volume-weighed power densities. This purpose is served well by the work of Masson & Luongo (2007). They describe several HTS machines and compare the power densities of motors and generators without making any distinction. Indeed, in first approximation, one could imagine reversing the modus operandi of the HTS motor becoming a generator and vice versa. As a result, using the same model established for HTS motors appears a sensible option, though some modifications need to be implemented[iii]. Applying a constant average HTS generator efficiency $\eta_{HTS,g}$, for example 98% – Nanao & Maki (2006), then the delivered electric power by the HTS generator may be estimated by :

$$P_{HTS,g} = \eta_{HTS,g}\, P_{HTS,m} \qquad \text{[kW]} \qquad \text{(B.16)}$$

The electrical power densities are consequently defined as :

$$\rho_{P_e,m} \triangleq \frac{P_{HTS,g}}{W_{HTS,g}} \qquad \text{[kW/kg]} \qquad \text{(B.17)}$$

$$\rho_{P_e,V} \triangleq \frac{P_{HTS,g}}{V_{HTS,g}} \qquad \text{[kW/m}^3\text{]} \qquad \text{(B.18)}$$

where (using Eq.B.2 and Eq.B.4) :

$$W_{HTS,g} = W_{HTS,m}\Big|_{\frac{P_{HTS,g}}{\eta_{HTS,g}}} \qquad \text{[kg]} \qquad \text{(B.19)}$$

$$V_{HTS,g} = V_{HTS,m}\Big|_{\frac{P_{HTS,g}}{\eta_{HTS,g}}} \qquad \text{[m}^3\text{]} \qquad \text{(B.20)}$$

[iii] None of the cases studied involving HTS generators gave sufficient information to evaluate the impact of cooling temperature and shaft power on the power densities, necessary to establish a separate HTS generator model.

Appendix C

Outlet relative flow angle modelling

Based on the deviation angle δ discussion, it is interesting to examine the impact of gauging angle β_g and non-dimensional mass flow Θ_r on the relative outlet flow angle $\beta_{o,b}$ parametrically. Recall that (Eq.5.89) :

$$\beta_{o,b} = \beta_g + \delta - \frac{\pi}{2} \tag{C.1}$$

If the turbine total temperature and pressure are known, it is possible to establish Θ_r, which will be seen to have an important impact on δ. Starting from the conservation of mass and applied on the relative flow conditions :

$$\dot{m} = \rho A_R w \cos\beta \tag{C.2}$$

A_R is the flow area perpendicular to the radial plane. Applying the perfect gas law on the static density and replacing the static components of temperature and pressure by their respective total components :

$$\dot{m} = \frac{p_{tr}}{\sqrt{T_{tr}}} \sqrt{\frac{\gamma}{R_g}} A_R \Theta_r \cos\beta \tag{C.3}$$

where,

$$\Theta_r = M_r \left(1 + \frac{\gamma - 1}{2} M_r^2\right)^{-\frac{1}{2}\frac{(\gamma+1)}{(\gamma-1)}} \tag{C.4}$$

Note that the relative total components must be used. Rewriting Eq.C.3 proves that Θ_r may be seen as the non-dimensional mass flow in the relative frame of motion, which is a function of the relative Mach number M_r (Eq.C.4) :

$$\Theta_r = \frac{\sqrt{T_{tr}}}{p_{tr}} \sqrt{\frac{R_g}{\gamma}} \left(\frac{1}{A_R \cos\beta}\right) \dot{m} \tag{C.5}$$

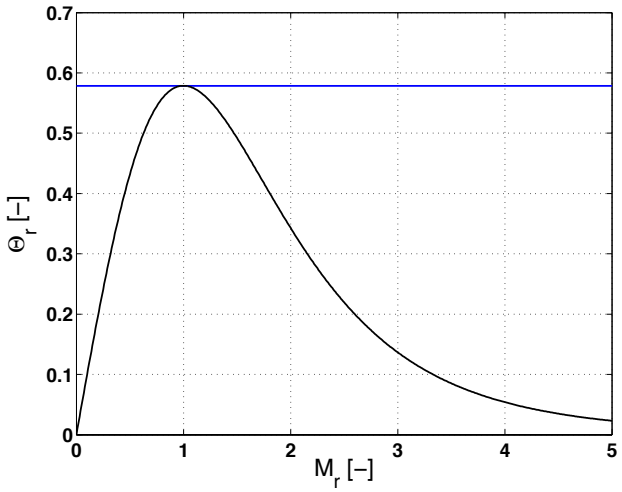

FIGURE C.1. Θ as a function of M_r.

At this time, it is instructive to examine Eq.C.4. The function peaks at $M_r = 1$ (Fig.C.1). For this condition, the flow through A_R is choked. In both subsonic and supersonic flow regimes, Θ_r must always be lower than this maximum Θ^*, which is :

$$\Theta_r \leq \Theta^* = \left(\frac{\gamma+1}{2}\right)^{-\frac{1}{2}\frac{(\gamma+1)}{(\gamma-1)}} \tag{C.6}$$

In case $\Theta_r > \Theta^*$ the result is non-physical and the mass flow $\dot{m}$ will have to be reduced. This criterion is very useful when performing a parametric performance study on the turbine stage. When $\Theta_r > \Theta^*$, one will have to reduce Θ_r (the mass flow) through the stage and reiterate. Continuing this discussion on subsonic flows, it is consequently obvious that :

$$\dot{m} \leq \dot{m}^* \tag{C.7}$$

where $\dot{m}^*$ the maximum mass flow that can pass through the blade passages. Consequently for sonic/supersonic flows :

$$\dot{m} = \dot{m}^* \tag{C.8}$$

Applying the above theory to the Ljungström turbine gives for the non-dimensional mass flow at the outlet section :

$$\Theta_{ro,b} = \frac{T_{tro,b}}{\sqrt{p_{tro,b}}}\sqrt{\frac{R_g}{\gamma}}\left(\frac{1}{A_o \cos\beta_{o,b}}\right)\dot{m} \tag{C.9}$$

In case of choked flow in the throat of the blade passage, which concurs with section o, it is found that (Fig.5.4) :

$$\Theta^* = \frac{T^*_{tr}}{\sqrt{p^*_{tr}}} \sqrt{\frac{R_g}{\gamma}} \left(\frac{1}{A_o \cos \beta^*} \right) \dot{m}^* \tag{C.10}$$

Since the throat o is the smallest section in the blade passage, M^*_r will consequently be unity when choked. Under these conditions, the flow will pass perpendicularly through section o. As a result :

$$A_o \cos \beta^* = A_o \sin \beta_g = A^* \tag{C.11}$$

and,

$$\sin \beta_g = \frac{A^*}{A_o} \tag{C.12}$$

By approximation, the throat of the blade passage is near the outlet of the turbine. Conservation of rothalpy then yields :

$$T^*_{tr} \approxeq T_{tro,b} \tag{C.13}$$

At this time, it is necessary to distinguish the subsonic and choked throat flow regimes and discuss the influence on $\beta_{o,b}$ separately.

Subsonic throat

In case of subsonic flow, the work of Ainley & Mathieson (1955) points out that the total relative pressure losses between throat and outlet section are negligible :

$$p^*_{tr} \approxeq p_{tro,b} \tag{C.14}$$

Substitution of Eq.C.9, Eq.C.6, Eq.C.13 and Eq.C.14 in Eq.C.7 gives after simplification :

$$\Theta_{ro,b} \cos \beta_{o,b} \leq \Theta^* \sin \beta_g \tag{C.15}$$

with the additional boundaries that :

$$\cos \beta_{o,b} \in]0, 1] \quad \Rightarrow \quad \beta_{o,b} \in]-\pi/2, \pi/2] \tag{C.16}$$

$$\Theta_{ro,b} \leq \Theta^* \tag{C.17}$$

For subsonic flow, a closer examination of Eq.5.93, Eq.5.100 and Eq.5.102 shows that δ is only depending on geometric variables such as β_g, the relative outlet Mach number $M_{ro,b}$ and the non-dimensional rotational velocity $M_{u,o}$. Indeed, only additional proof is required for Eq.5.100 demanding a relationship between ϕ_o, $M_{ro,b}$ and $M_{u,o}$. Defining $M_{u,o}$

as :

$$M_{u,o} = \frac{u_o}{\sqrt{(\gamma R_g T_{o,b})}} \tag{C.18}$$

it is found that :

$$\phi_o = \frac{v_{R_o}}{u_o} = \frac{w_o \cos\beta_{o,b}}{u_o} = \frac{w_o}{\sqrt{\gamma R_g T_{o,b}}} \frac{\sqrt{\gamma R_g T_{o,b}}}{u_o} \cos\beta_{o,b} = \frac{M_{ro,b}}{M_{u,o}} \cos\beta_{o,b} \tag{C.19}$$

where the static temperature $T_{o,b}$ follows immediately via the total-to-static relationship between $T_{tro,b}$ and $M_{ro,b}$ – Çengel & Cimbala (2010) :

$$T_{tro,b} = T_{o,b}\left(1 + \frac{\gamma - 1}{2} M_{ro,b}^2\right) \tag{C.20}$$

Sometimes, it is more convenient to use total rotational speed Mach number,

$$M_{tu,o} = \frac{u}{\sqrt{\gamma R_g T_{tro,b}}} \tag{C.21}$$

especially in cases where $T_{tro,b}$ is given and $M_{ro,b}$ is a variable (Fig.C.2). Even though $\beta_{o,b}$ is required to find $\Delta\delta_{sl}$ and thus δ, which demands an iterative approach to find the solution, there is only one solution for $\Theta_{ro,b}\cos\beta_{o,b}$ (Eq.C.15) and thus $\beta_{o,b}$, as illustrated by Fig.C.2. Indeed, considering a given geometry (β_g, Π_p, Z, $\beta_{b,o}$), total relative pressure $p_{tro,b}$, total relative temperature $T_{tro,b}$ and $M_{tu,o}$, Eq.5.89, Eq.5.100, Eq.5.102 and Eq.C.19 yield :

$$\delta = f(M_{ro,b}, \beta_{o,b}) \quad \Rightarrow \quad \beta_{o,b} = f(\delta) = f(M_{ro,b}, \beta_{o,b}) \quad \Rightarrow \quad \beta_{o,b} = f(M_{ro,b}) \tag{C.22}$$

and consequently for the subsonic regime with Eq.C.4,

$$M_{ro,b} = f(\Theta_{ro,b}) \quad \Rightarrow \quad \beta_{o,b} = f(\Theta_{ro,b}) \tag{C.23}$$

Fig.C.2 shows that $\Theta_{ro,b}\cos\beta_{o,b}$ is not a constant value, from which one may deduce that $\dot{m}$ is not constant (Eq.C.3) and $\dot{m} < \dot{m}^*$ (Fig.C.3).

Sonic throat – supersonic outlet

The Ljungström turbine is an outflow turbine with $A_o \geq A^*$. Under saturated conditions, the outlet will then become supersonic $M_{ro,b} \geq 1$. This will imply supersonic expansion losses, as explained by the loss model of Ainley & Mathieson (1955) ($Y_{EX} \neq 0$). Because of this, the conservation of total relative pressure $p_{tro,b}$ between throat and outlet does not stand :

$$p_{tr}^* \geq p_{tro,b} \tag{C.24}$$

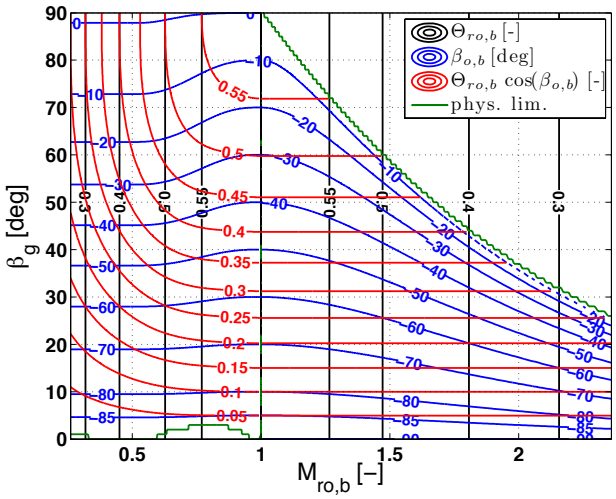

FIGURE C.2. Relative outflow angle $\beta_{o,b}$: example of a single Ljungström turbine stage – $M_{tu,o} = 0.085$. The ragged physical limit indicated on the figure is due to the discretisation of the evaluated domain.

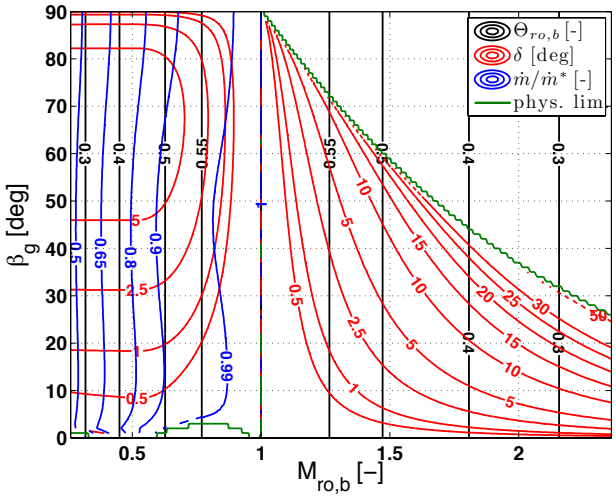

FIGURE C.3. Deviation angle δ : example of a single Ljungström turbine stage – $M_{tu,o} = 0.085$. The ragged physical limit indicated on the figure is due to the discretisation of the evaluated domain.

Since now a choked turbine stage is considered, Eq.C.8 holds and substituting Eq.C.9, Eq. C.10 and Eq.C.11 in the former give :

$$\Theta_{ro,b} \cos \beta_{o,b} = \frac{p^*_{tr}}{p_{tro,b}} \Theta^* \sin \beta_g \tag{C.25}$$

This equation shows that for a given β_g and total pressure ratio $p^*_{tr}/p_{tro,b}$, $\Theta_{ro,b} \cos \beta_{o,b}$ appears to be a constant (Fig.C.2). Unlike the subsonic case, there is no deviation model available relating $\beta_{o,b}$ to $\Theta_{ro,b}$. Therefore a closing equation must be provided in order to find the relative outflow angle. $M_{ro,b}$ is most suitable for this purpose (Eq.C.4), but this requires the knowledge of the static pressure of the flow in the outlet. From a numerical point of view, solving this problem is not an easy task, especially in multi-stage turbines, as the Ljungström turbine – Aungier (2006). However, it can be shown that the efficiency of the Ljungström turbine becomes quite low near the choking point. Because it is important to have a high cycle efficiency, a choked turbine is therefore not desirable. Consequently, the supersonic outflow regime will not be considered. Finally note that the supersonic part of Fig.C.2 and Fig.C.3 were obtained for $p^*_{tr}/p_{tro,b} = 1$ and where it was assumed that $M_{ro,b}$ is known.

Appendix D

Blade passage loss model of Ainley and Mathieson in the Ljungström turbine

This appendix incorporates the formulae used by Aungier (2006), which represent the model of Ainley & Mathieson (1955) and corrected by the former. It includes also the correction proposed by this author to the secondary losses due to the installation of endwall fences. The non-dimensional pressure loss Y defined by Ainley & Mathieson (1955) is :

$$Y = \frac{p_{tro,b_{ID}} - p_{tro,b}}{p_{tro,b} - p_{o,b}} = \sum_j Y_j = Y_p + Y_s + Y_{TE} + Y_{EX} \tag{D.1}$$

where $p_{o,b}$ the static pressure, $p_{tro,b}$ the relative total pressure and $p_{tro,b_{ID}}$ the relative total pressure without losses at the outlet of the turbine, i.e. :

$$p_{tro,b_{ID}} = p_{tri}\left(\frac{T_{tro,b}}{T_{tri}}\right)^{\frac{\gamma}{\gamma-1}} \tag{D.2}$$

The approach of Aungier (2006) was followed to formulate the loss model components Y_j of Ainley & Mathieson (1955). Since the model uses a different blade angle convention, the following conversion rules needs to be taken into account :

$$\hat{\alpha}_1 \triangleq \frac{\pi}{2} - \beta_i \tag{D.3}$$

$$\hat{\alpha}_2 \triangleq \frac{\pi}{2} + \beta_o \tag{D.4}$$

$$\hat{\beta}_1 \triangleq \frac{\pi}{2} - \beta_{b,i} \tag{D.5}$$

D.1 Profile loss coefficient Y_p

The blade profile loss coefficient is written as :

$$Y_p = K_{mod}K_{inc}K_M K_p K_{RE}\left\{[Y_{p1} + \xi^2(Y_{p2} - Y_{p1})]\left[5\left(\frac{t}{c}\right)_{max}\right]^{\xi} - \Delta Y_{TE}\right\} \tag{D.6}$$

D.1.1 Nozzle blade configuration loss Y_{p1}

The nozzle blade configuration loss is (note angles in *degrees*) :

$$Y_{p1} = A + BX^2 + CX^3 \qquad \hat{\alpha}_2 \leq 30^\circ \tag{D.7}$$

$$Y_{p1} = A + B|X|^n \qquad \hat{\alpha}_2 > 30^\circ \tag{D.8}$$

$$A = 0.025 + \frac{(27^\circ - \hat{\alpha}_2)}{530^\circ} \qquad \hat{\alpha}_2 \leq 27^\circ \tag{D.9}$$

$$A = 0.025 + \frac{(27^\circ - \hat{\alpha}_2)}{3085^\circ} \qquad \hat{\alpha}_2 > 27^\circ \tag{D.10}$$

$$B = 0.1583 - \frac{\hat{\alpha}_2}{1640^\circ} \tag{D.11}$$

$$C = 0.08\left[\left(\frac{\hat{\alpha}_2}{30^\circ}\right)^2 - 1\right] \tag{D.12}$$

$$n = 1 + \frac{\hat{\alpha}_2}{30^\circ} \tag{D.13}$$

$$X = \frac{s}{c} - \left(\frac{s}{c}\right)_{opt} \tag{D.14}$$

$$\left(\frac{s}{c}\right)_{opt} = 0.46 + \frac{\hat{\alpha}_2}{77^\circ} \qquad \hat{\alpha}_2 \leq 30^\circ \tag{D.15}$$

$$\left(\frac{s}{c}\right)_{opt} = 0.614 + \frac{\hat{\alpha}_2}{130^\circ} \qquad \hat{\alpha}_2 > 30^\circ \tag{D.16}$$

$(s/c)_{opt}$ is (s/c) where Y_{p1} is minimum.

D.1.2 The impulse blade configuration loss Y_{p2}

The impulse blade configuration loss is :

$$Y_{p2} = A + BX^2 - CX^3 \tag{D.17}$$

$$A = 0.242 - \frac{\hat{\alpha}_2}{151^\circ} + \left(\frac{\hat{\alpha}_2}{127^\circ}\right)^2 \tag{D.18}$$

$$B = 0.3 + \frac{30 - \hat{\alpha}_2}{50^\circ} \qquad \hat{\alpha}_2 \leq 30^\circ \tag{D.19}$$

$$B = 0.3 + \frac{30 - \hat{\alpha}_2}{275^\circ} \qquad \hat{\alpha}_2 > 30^\circ \tag{D.20}$$

$$C = 0.88 - \frac{\hat{\alpha}_2}{42.4^\circ} + \left(\frac{\hat{\alpha}_2}{72.8^\circ}\right)^2 \tag{D.21}$$

$$X = \frac{s}{c} - \left(\frac{s}{c}\right)_{opt} \tag{D.22}$$

$$\left(\frac{s}{c}\right)_{opt} = 0.224 + 1.575\left(\frac{\hat{\alpha}_2}{90^\circ}\right) - \left(\frac{\hat{\alpha}_2}{90^\circ}\right)^2 \tag{D.23}$$

with again, $(s/c)_{opt}$ delivering the minimum Y_{p2}.

D.1.3 Incidence correction factor K_{inc}

The off-design incidence correction factor K_{inc} accounts for the non-shock-free flow. Defining the incidence angle to be :

$$i = \hat{\beta}_1 - \hat{\alpha}_1 \tag{D.24}$$

and introducing the stalling incidence i_s :

$$K_{inc} = -1.39214 - 1.90738\left(\frac{i}{i_s}\right) \qquad \frac{i}{i_s} < -3 \tag{D.25}$$

$$K_{inc} = 1 + 0.52\left|\frac{i}{i_s}\right|^{1.7} \qquad -3 \leq \frac{i}{i_s} < 0 \tag{D.26}$$

$$K_{inc} = 1 + \left(\frac{i}{i_s}\right)^{2.3+0.5\ i/i_s} \qquad 0 \leq \frac{i}{i_s} < 1.7 \tag{D.27}$$

$$K_{inc} = 6.23 + 9.8577\left(\frac{i}{i_s} - 1.7\right) \qquad \frac{i}{i_s} \geq 1.7 \tag{D.28}$$

where it must be assured that $K_{inc} \leq 20$. The stalling incidence may be estimated by :

$$i_s = i_{sr} + \Delta i_s \tag{D.29}$$

The stalling incidence is calculated based on the stalling incidence i_{sr} of the reference cascades used by Ainley & Mathieson (1955) having $(s/c) = 0.75$, and to which a correction term is added to cope with other (s/c) values :

$$i_{sr} = i_{s0} + A - B\xi^2 + C\xi^3 + D\xi^4 \qquad \hat{\alpha}_2 \leq 40^\circ \qquad \text{(D.30)}$$

$$i_{sr} = i_{s0} + \left| i_{sr=40^\circ} - i_{s0} \right| \left| \frac{55^\circ - \hat{\alpha}_2}{15^\circ} \right| \qquad \hat{\alpha}_2 > 40^\circ \qquad \text{(D.31)}$$

and,

$$\xi = \frac{90^\circ - \hat{\beta}_1}{90^\circ - \hat{\alpha}_2} \qquad \text{(D.32)}$$

$$i_{s0} = 20 - \left(\frac{\xi + 1}{0.11} \right) \qquad \text{(D.33)}$$

$$A = 61.8 - \hat{\alpha}_2 \left(1.6 - \frac{\hat{\alpha}_2}{165^\circ} \right) \qquad \text{(D.34)}$$

$$B = 71.9 - 1.69\ \hat{\alpha}_2 \qquad \text{(D.35)}$$

$$C = 7.8 - \hat{\alpha}_2 \left(0.28 - \frac{\hat{\alpha}_2}{320^\circ} \right) \qquad \text{(D.36)}$$

$$D = 14.2 - \hat{\alpha}_2 \left(0.16 + \frac{\hat{\alpha}_2}{160^\circ} \right) \qquad \text{(D.37)}$$

The stalling incidence correction was given to be :

$$\Delta i_s = -38X - 53.5X^2 - 29X^3 \qquad \frac{s}{c} \leq 0.8 \qquad \text{(D.38)}$$

$$\Delta i_s = 2.0374 - \left[\left(\frac{s}{c} \right) - 0.8 \right] \left[69.58 - \left(\frac{\hat{\alpha}_2}{14.48^\circ} \right)^{3.1} \right] \qquad \frac{s}{c} > 0.8 \qquad \text{(D.39)}$$

$$X = \left(\frac{s}{c} - 0.86 \right) \qquad \text{(D.40)}$$

D.1.4 Mach number correction

The tests performed by Ainley & Mathieson (1955) were at low Mach numbers. K_M corrects for the profile losses when $M_{r,o} > 0.6$. If $M_{r,o} > 1$, the supersonic expansion loss Y_{EX} takes over and is added separately. Defining (s/R_c) as the ratio of blade pitch and blade suction curvature radius :

$$K_M = 1 \qquad M_{r,o} \leq 0.6 \qquad \text{(D.41)}$$

$$K_M = 1 + [1.65(M_{r,o} - 0.6) + 240(M_{r,o} - 0.6)^3]\ 0.43 \left(\frac{s}{R_c} \right)^{(3M_{r,o} - 0.6)} \qquad 0.6 < M_{r,o} \leq 1 \qquad \text{(D.42)}$$

$$K_M = 1 + 6.8886 \left(\frac{s}{R_c} \right)^{2.4} \qquad M_{r,o} > 1 \qquad \text{(D.43)}$$

D.1.5 Compressibility effects

Aungier (2006) mentions the work of Kacker & Okapuu (1982) who propose an additional correction coefficient to the profile losses in the model of Ainley & Mathieson (1955) to cope with the effect that compressible flows in accelerating flows tend to postpone the boundary layer separation. This effect is reflected by K_p. Aungier (2006) extended their model for hub-to-shroud analysis and proposes a slightly modified model assuring that $K_p > 0.5$:

$$K_p = 1 - (1 - K_1)X^2 \tag{D.44}$$

$$K_1 = 1 - 0.625(\tilde{M}_{r,o} - 0.2 + |\tilde{M}_{r,o} - 0.2|) \tag{D.45}$$

$$X = \frac{2\tilde{M}_{r,i}}{\tilde{M}_{r,i} + \tilde{M}_{r,o} + |\tilde{M}_{r,o} - \tilde{M}_{r,i}|} \tag{D.46}$$

$$\tilde{M}_{r,i} = \frac{M_{r,i} + 0.566 - |0.566 - M_{r,i}|}{2} \tag{D.47}$$

$$\tilde{M}_{r,o} = \frac{M_{r,o} + 1 - |M_{r,o} - 1|}{2} \tag{D.48}$$

D.1.6 Surface roughness

The effect of surface roughness and Reynolds number on the profile loss is captured by K_{RE}. The Reynolds number based on chord length Re_c is defined as:

$$Re_c = \frac{\rho_o w_o c}{\mu_o} \tag{D.49}$$

For $Re_c \leq 10^5$ the flow is said to be laminar. In case $Re_c \geq Re_{tr} = 5 \cdot 10^5$, the flow is turbulent. In between, the flow is in transition for which K_{RE} is assumed to be unity. Aungier (2006) also proposes a blade-chord-based critical roughness Reynolds number above which the blade roughness becomes important :

$$Re_{c,r} = 100\frac{c}{e} \tag{D.50}$$

where e is the roughness peak height. The formula for K_{RE} is then given by :

$$K_{RE} = \sqrt{\frac{10^5}{Re_c}} \qquad Re_c < 10^5 \tag{D.51}$$

$$K_{RE} = 1 \qquad 10^5 \leq Re_c < Re_{tr} \tag{D.52}$$

$$K_{RE} = \left[\frac{\log_{10}(Re_{tr})}{\log_{10}(Re_c)}\right]^{2.58} \qquad Re_c \geq Re_{tr} \quad \text{and} \quad Re_{c,r} > Re_c \tag{D.53}$$

$$K_{RE} = \left[\frac{\log_{10}(Re_{tr})}{\log_{10}(Re_{c,r})}\right]^{2.58} \qquad Re_{c,r} \geq Re_{tr} \quad \text{and} \quad Re_{c,r} \leq Re_c \tag{D.54}$$

$$K_{RE} = 1 + \left\{\left[\frac{\log_{10}(Re_{tr})}{\log_{10}(Re_{c,r})}\right]^{2.58} - 1\right\}\left[1 - \left(\frac{Re_{tr}}{Re_c}\right)\right] \qquad Re_{c,r} < Re_{tr} \quad \text{and} \quad Re_{c,r} \leq Re_c \tag{D.55}$$

D.1.7 Experience factor

Finally, Kacker & Okapuu (1982) suggest the use of an *experience* correction factor K_{mod} to the profile losses to account for the use of improved technology levels. For highly optimised designs, they suggest $K_{mod} = 0.67$. Otherwise $K_{mod} = 1$ should be used.

D.2 Secondary losses Y_s

$$Y_s = K_{EWF} K_{RE} K_s \sqrt{\frac{\tilde{Y}_s^2}{1 + 7.5\tilde{Y}_s^2}} \tag{D.56}$$

$$\tilde{Y}_s = 0.0334\, F_{AR} Z\, \frac{\sin(\hat{\alpha}_2)}{\sin(\hat{\beta}_1)} \tag{D.57}$$

$$K_s = 1 - (1 - K_p)\left[\frac{(c_a/h)^2}{1 + (c_a/h)^2}\right] \tag{D.58}$$

$$Z = \left(C_L \frac{c}{s}\right)^2 \frac{\sin^2(\hat{\alpha}_2)}{\sin^3(\hat{\alpha}_m)} \tag{D.59}$$

$$C_L \frac{c}{s} = 2\, \sin(\hat{\alpha}_m)(cot(\hat{\alpha}_1) + cot(\hat{\alpha}_2)) \tag{D.60}$$

$$\hat{\alpha}_m = \frac{\pi}{2} - \text{atan}\left(\frac{cot(\hat{\alpha}_1) - cot(\hat{\alpha}_2)}{2}\right) \tag{D.61}$$

$$F_{AR} = 0.5\left(\frac{2}{h/c}\right)^{0.7} \qquad \frac{h}{c} < 2 \tag{D.62}$$

$$F_{AR} = \frac{1}{(h/c)} \qquad \frac{h}{c} \geq 2 \tag{D.63}$$

where h is the blade height, c_a the axial projection of the chord length c [i], and K_{RE} and K_p as defined previously in respectively Eqs.D.51-D.55 and Eq.D.44.
K_{EWF} is a new factor proposed by this author to allow for quantifying the use of endwall fences, which are reported to drastically reduce the secondary losses. Indeed, Moon & Koh (2001) mention an extensive list of experimental work, amongst which Kawai et al. (1989), Chung et al. (1991) and Lee (1997), and highlight that an endwall fence positioned at the centre of the blade passage and aligned with the blades with a height of one third of the inlet boundary thickness, has the potential to reduce the secondary losses by 20%. Indeed, the endwall fence hinders the crossflow and the migration of the pressure leg of the horseshoe vortex to the suction side of the subsequent blade. This reduces the vortex strength and hence, the secondary losses. The author of this work therefore proposes, in case endwall fences are installed, the reduce Y_s accordingly using :

$$K_{EWF} = 0.8 \quad \text{(with endwall fences)} \tag{D.64}$$

Otherwise,

$$K_{EWF} = 1 \quad \text{(without endwall fences)} \tag{D.65}$$

D.3 Trailing edge losses Y_{TE}

The trailing edge loss coefficient proposed by Aungier (2006) is based on the abrupt expansion of the flow in the outlet due to finite blade trailing edge. He proposes :

$$Y_{TE} = \left(\frac{t_{TE,o}}{s\ \sin(\beta_g) - t_{TE,o}}\right)^2 \tag{D.66}$$

where $t_{TE,o}$ is the blade trailing edge thickness.

[i] Note that c_a is the radial projection of the chord length in case of the Ljungström turbine.

D.4 Supersonic expansion losses Y_{EX}

When the flow leaves the blade at supersonic speeds, the effect of shock losses must be accounted for. Aungier (2006) proposes the following loss factor Y_{EX} :

$$Y_{EX} = 0 \qquad M_{r,o} < 1 \tag{D.67}$$

$$Y_{EX} = \left(\frac{M_{r,o} - 1}{M_{r,o}}\right)^2 \qquad M_{r,o} \geq 1 \tag{D.68}$$

Appendix E

$\zeta_A - \zeta_{FL}$ sensitivity study graphical results

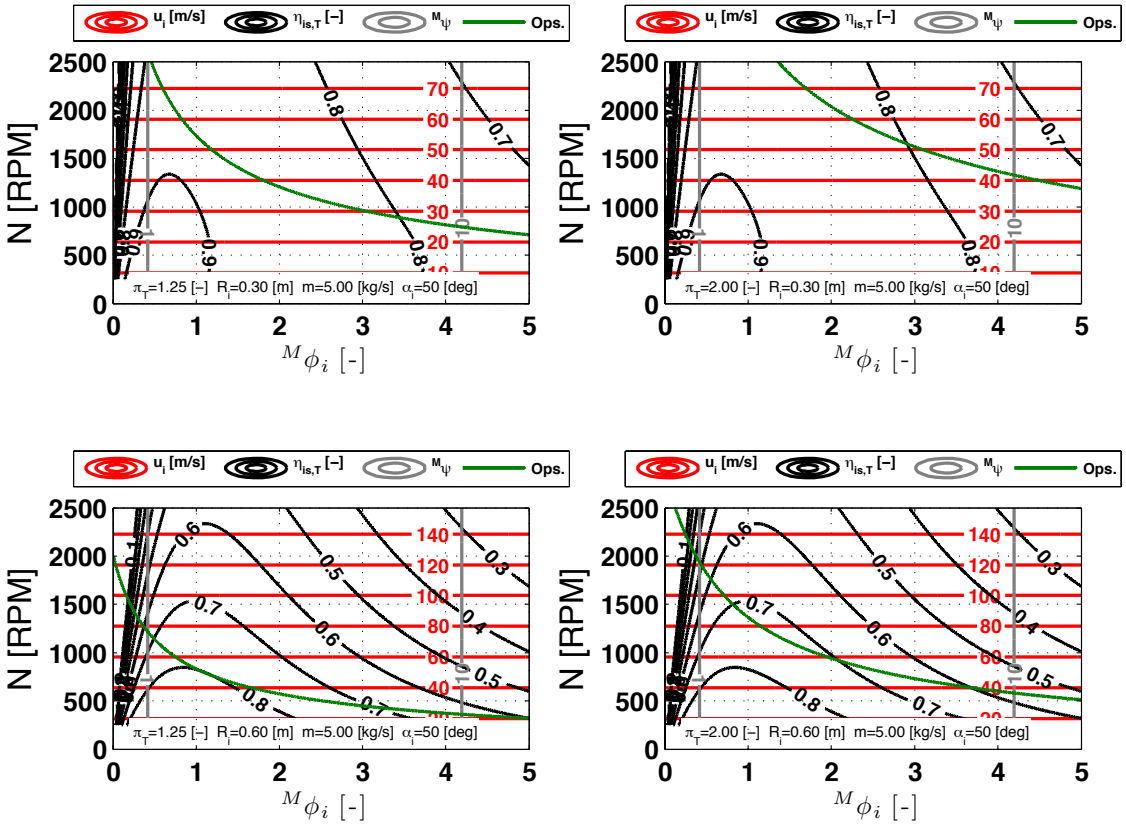

Figure E.1. Sensitivity study on π_T and $R_i - \dot{m} = 5$ kg/s.

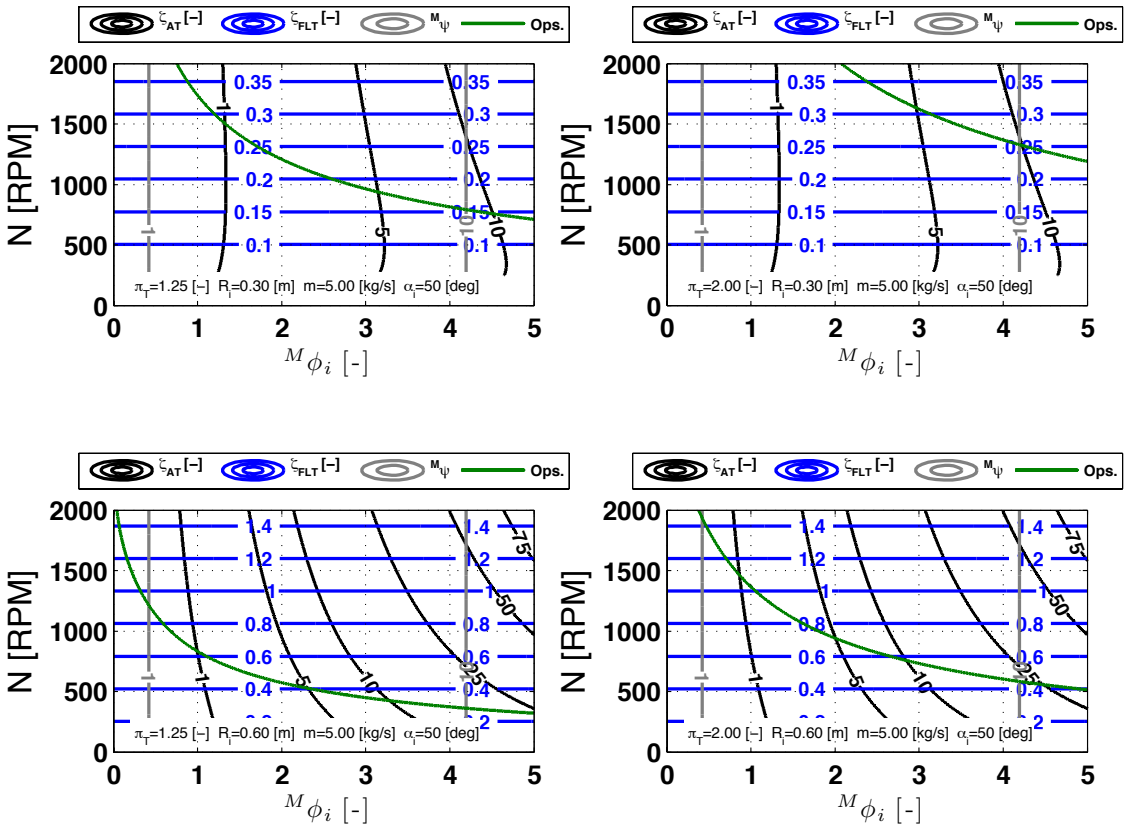

Figure E.2. Sensitivity study on π_T and $R_i - \dot{m} = 5$ kg/s.

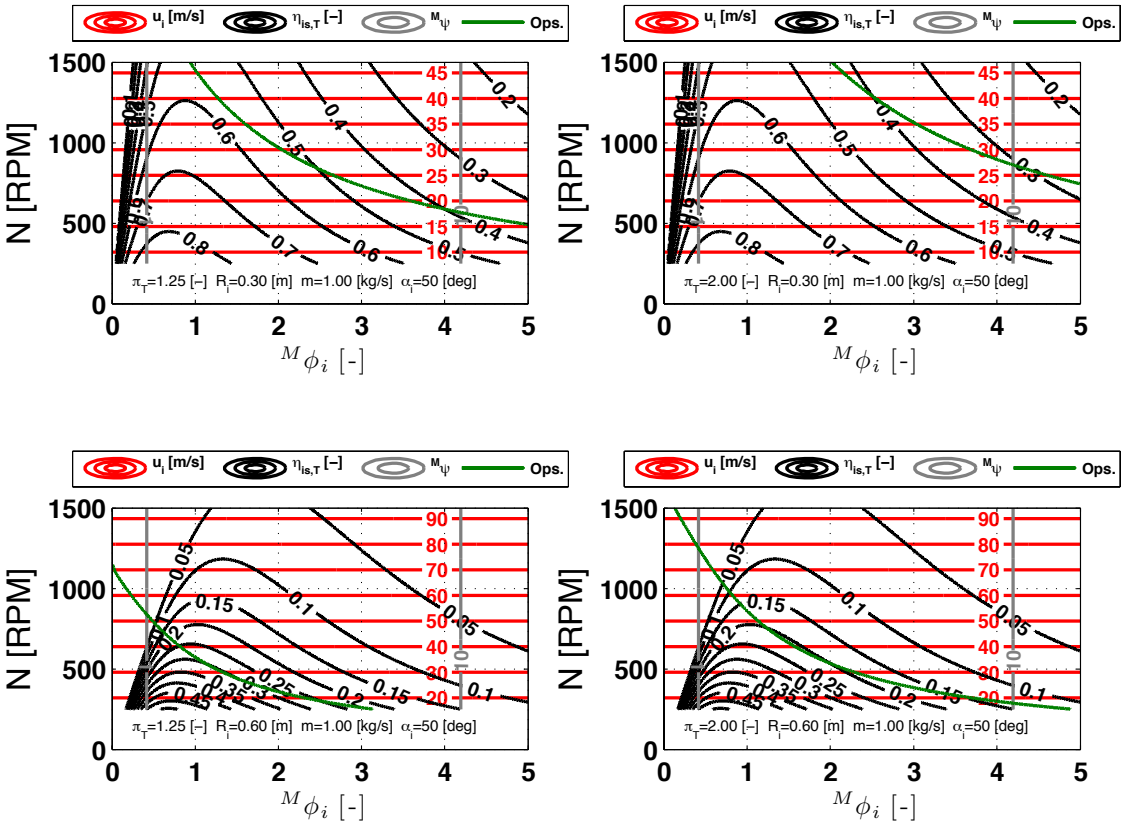

Figure E.3. Sensitivity study on π_T and $R_i - R_o/R_i = 1.10$.

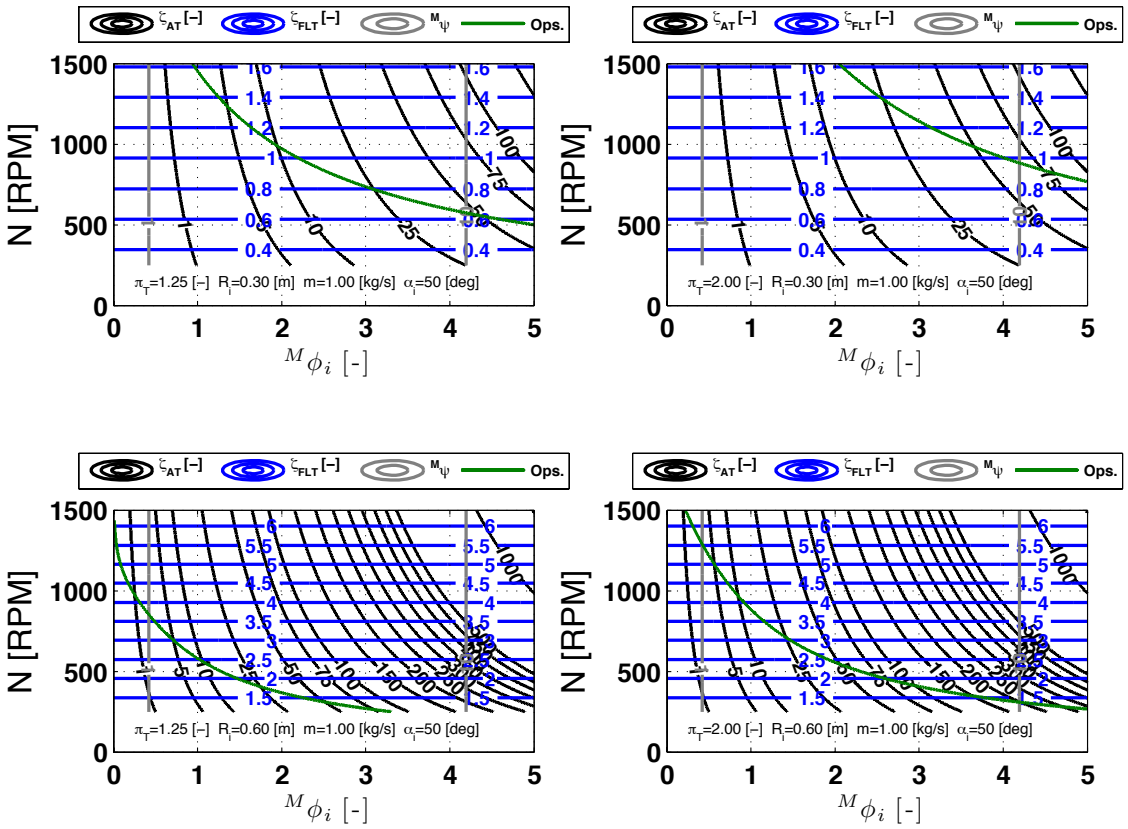

FIGURE E.4. Sensitivity study on π_T and $R_i - R_o/R_i = 1.10$.

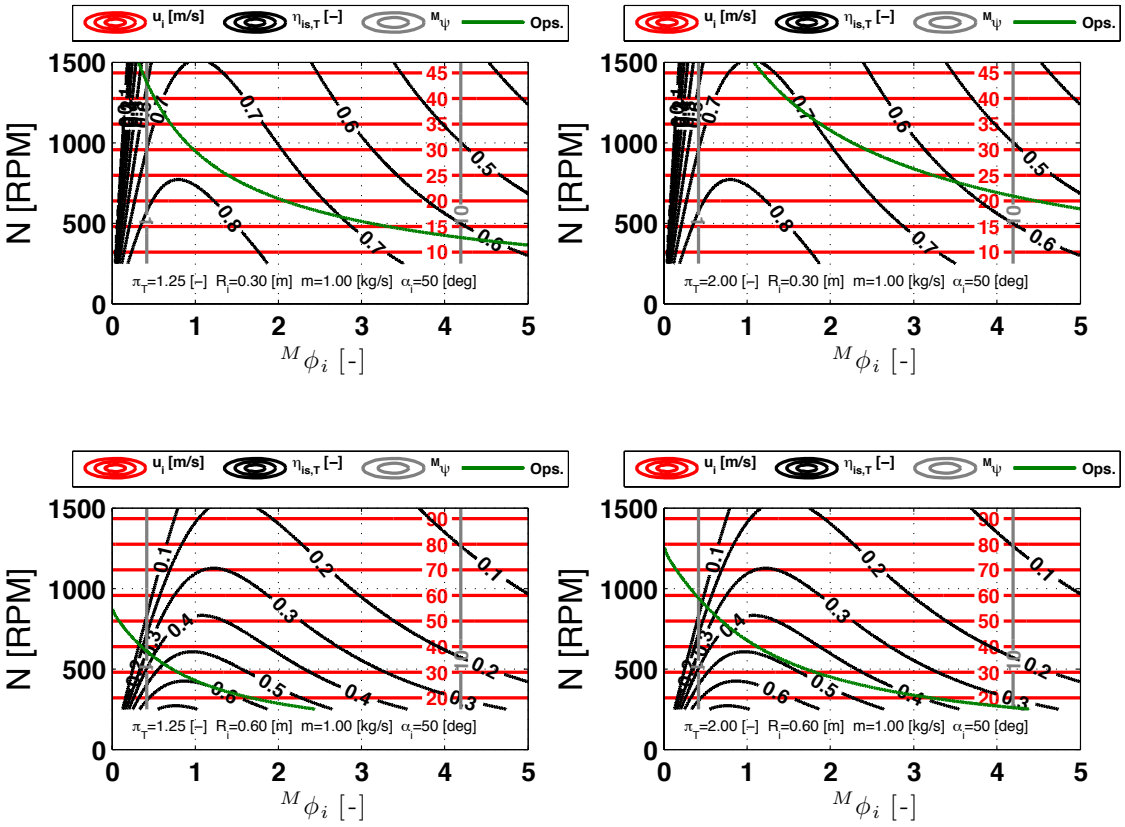

FIGURE E.5. Sensitivity study on π_T and $R_i - S_n = 10$.

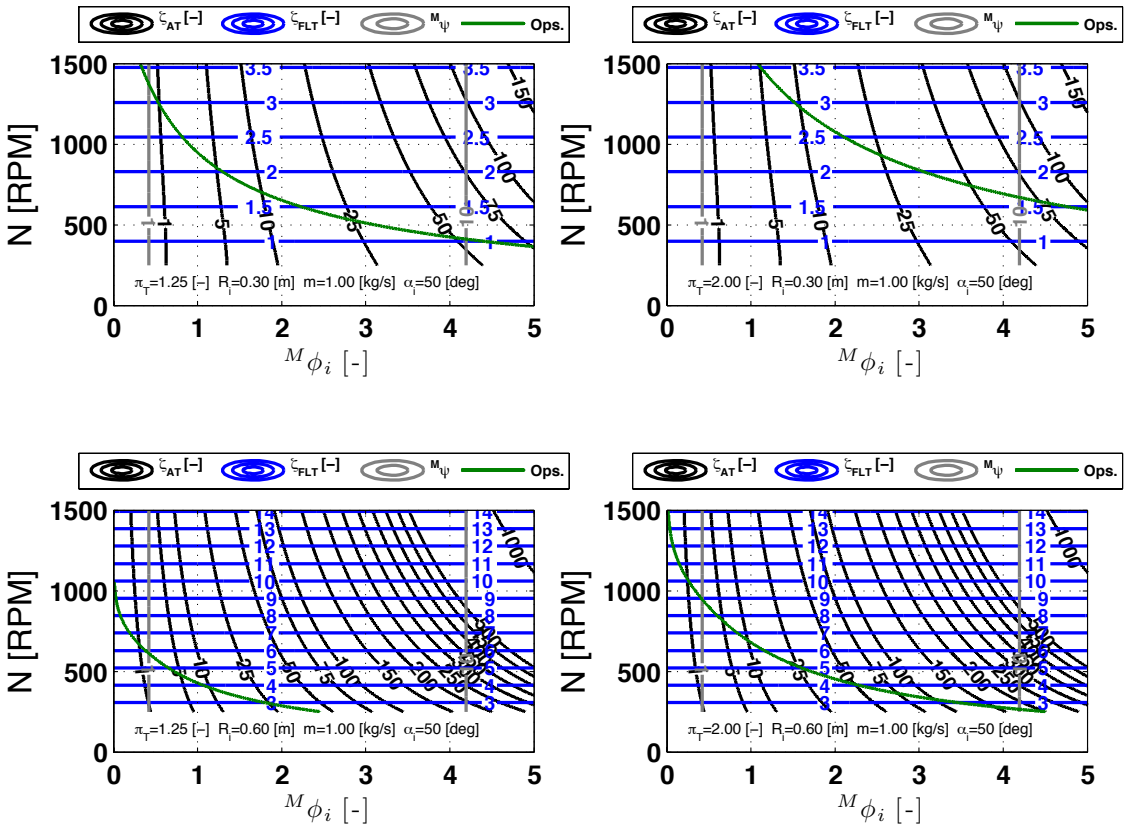

FIGURE E.6. Sensitivity study on π_T and $R_i - S_n = 10$.

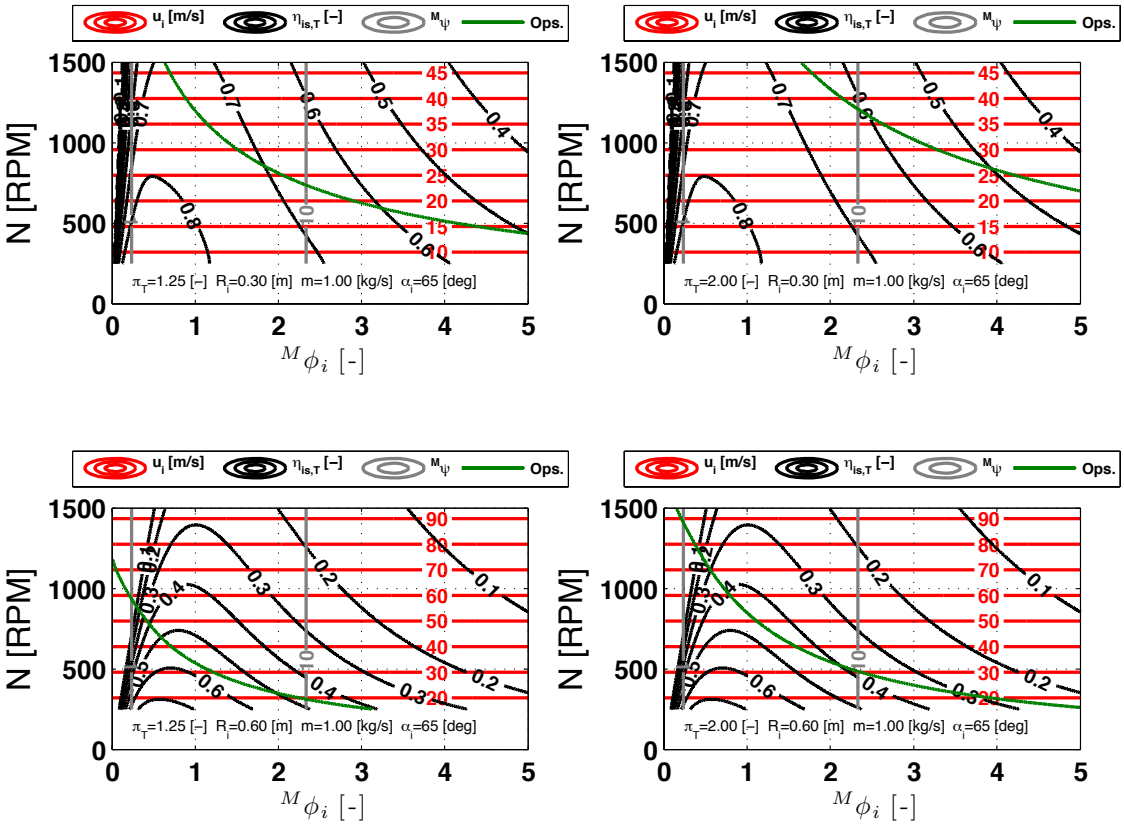

FIGURE E.7. Sensitivity study on π_T and R_i – ${}^M\alpha_i = 65°$.

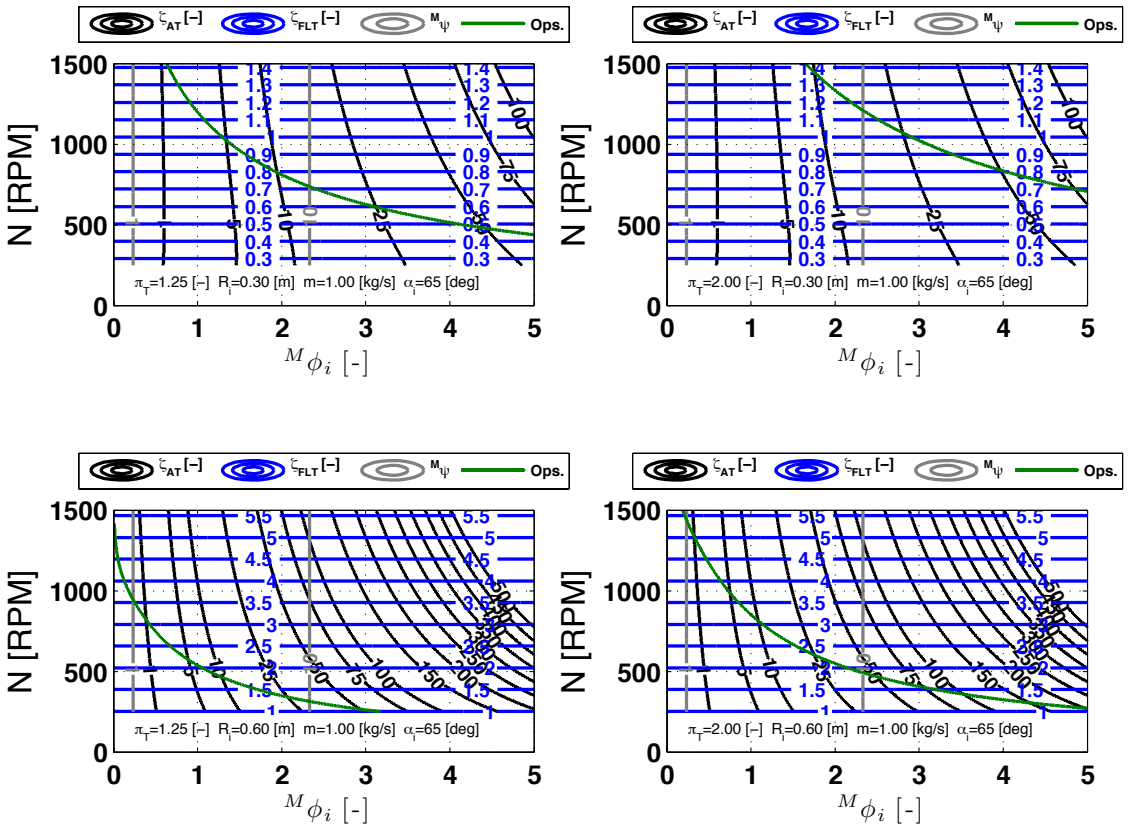

Figure E.8. Sensitivity study on π_T and $R_i - {}^{M}\alpha_i = 65°$.

Appendix F

Optimum blade pitch-to-chord ratio according to Ainley and Mathieson

Here, the empirical optimum blade spacing model of Ainley & Mathieson (1955) is given here, as mentioned by Aungier (2006). Aungier uses the $\vec{u}$-flow angle reference system (Section 5.1.4). The following conversions are consequently defined :

$$\hat{\alpha}_1 \triangleq \frac{\pi}{2} - \beta_i \tag{F.1}$$

$$\hat{\alpha}_2 \triangleq \frac{\pi}{2} + \beta_o \tag{F.2}$$

$$\hat{\beta}_1 \triangleq \frac{\pi}{2} - \beta_{b,i} \tag{F.3}$$

The model of Ainley & Mathieson (1955) retrieves the optimum blade pitch by interpolating between the optima, i.e. minimum losses, found for impulse ($\beta_i = \beta_o$) and nozzle ($\beta_i = 0°$) turbine cascades.

Nozzle cascades

$$\left(\frac{s}{c}\right)_0 = 0.427 + \frac{\hat{\alpha}_2\,[°]}{58} - \left(\frac{\hat{\alpha}_2\,[°]}{93}\right)^2 \tag{F.4}$$

Impulse cascades

$$\left(\frac{s}{c}\right)_1 = 0.224 + \left(1.575 - \frac{\hat{\alpha}_2\,[°]}{90}\right)\left(\frac{\hat{\alpha}_2\,[°]}{90}\right) \tag{F.5}$$

Optimum blade pitch-to-chord ratio

$$\xi = \frac{90 - \hat{\beta}_1\,[^\circ]}{90 - \hat{\alpha}_2\,[^\circ]} \tag{F.6}$$

$$\left(\frac{s}{c}\right)_{opt} = \left(\frac{s}{c}\right)_0 + \left[\left(\frac{s}{c}\right)_1 - \left(\frac{s}{c}\right)_0\right] |\xi|\,\xi \tag{F.7}$$

Additional governing equation

In case $\hat{\alpha}_2 > \hat{\beta}_1$, the optimum blade pitch-to-chord ratio of the impulse nozzles will be used :

$$\left(\frac{s}{c}\right)_{opt} = \left(\frac{s}{c}\right)_1 \tag{F.8}$$

Appendix G

GasTurb

This appendix provides additional information on the two-spool mixed flow turbofan cycle calculations of which the results were used in the discussion conducted in Section 8.4. The cycle calculations were undertaken in GasTurb 11, a commercial software program developed by Joachim Kurzke (MTU). The methodology used by the program to determine the turbofan performance will not be expounded here, and is extensively elaborated in Kurzke (2004a) and Kurzke (2004b).

The performance characteristics of the mixed flow turbofan, of which the configuration is recalled in Fig.G.1, are determined for an overall pressure ratio OPR of 32, turbine inlet temperature of 1600 K and over a range of engine bypass ratios BPR_{TF} (4 . . . 10). The component characteristics used are standard values proposed by GasTurb 11, which may be considered as commonly applicable. The most import parameters are summarised in Table G.1.

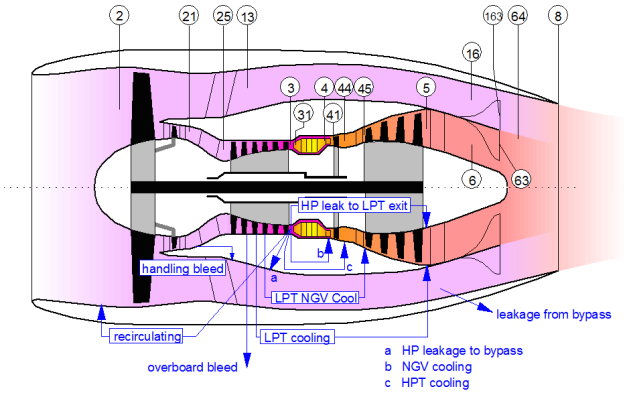

Figure G.1. Mixed flow turbofan cross-section with engine stations. Adopted from GasTurb 11, Joachim Kurzke.

For each BPR_{TF}, a mixed flow Mach number M_{64} of 0.2 is selected – Hendrick & Buysschaert (2015). Since the flow speed profile in front of the RELT should be as uniform as possible, it is reasonable to impose that the flow velocities of bypass (163) and core (63)

prior to mixing are identical, i.e. :

$$v_{163} \cong v_{63} \tag{G.1}$$

or, using the definition of Mach number and speed of sound :

$$M_{163}\sqrt{\gamma_{163}R_g T_{163}} = M_{63}\sqrt{\gamma_{63}R_g T_{63}} \tag{G.2}$$

$$\frac{M_{163}}{M_{63}} \cong \sqrt{\frac{T_{63}}{T_{163}}} \tag{G.3}$$

where T the static temperature, R_g the specific gas constant and γ the specific heat ratio. Since the Mach numbers are low when entering the mixing chamber (< 0.3) and the total temperatures calculated by the program, Eq.G.4 can be modified to, without major loss in accuracy :

$$\frac{M_{163}}{M_{63}} \cong \sqrt{\frac{T_{t,63}}{T_{t,163}}} \tag{G.4}$$

Unfortunately, it is not possible to introduce this design condition in GasTurb 11 and the solution has to be traced by trial and error. Indeed, for a given BPR_{TF} and TIT, the total temperatures depend on the fan and high-pressure compressor pressure ratios, respectively π_F and π_{HPC}, which are input parameters. In GasTurb 11, the pressure ratio of the inner and outer part of the fan is treated separately. However, for the calculations at hand, the pressure ratio of both sections is considered to be identical. Since the inner and outer fan pressure ratios cannot be coupled in GasTurb 11, it is not possible to execute a sensitivity study that would yield an immediate result, by means of, for example, a carpet plot, as the input problem remains three dimensional ($\pi_{F,inner}$, $\pi_{F,outer}$, π_{HPC}). Consequently, the coupling of the fan pressure ratios must be done manually and thus a stepwise approach to find the solution is unavoidable.

Once converged, the turbofan cycle is fully determined, from which follow the turbofan performance characteristics used in the TDR cycle characteristics.

Table G.1. Turbofan component characteristics TIT = 1600 K, OPR = 32, T/O ISA SLS, v_a = 0 [m/s].

Inlet	
Ram recovery [-]	0.99
Fan	
Polytropic efficiency [-]	0.89
High pressure compressor	
Polytropic efficiency [-]	0.90
Combustion chamber	
Combustion efficiency [-]	0.999
Burner pressure ratio [-]	0.97
LHV [MJ/kg]	43.124
High pressure turbine	
Polytropic efficiency [-]	0.89
Low pressure turbine	
Polytropic efficiency [-]	0.90
Nozzle	
Standard converging	
Nozzle petal angle [°]	25

Appendix H

Survey data

In this thesis, several discussions are substantiated by means of data obtained by a survey conducted by its author. The survey data is mainly extracted from documentation made available by manufactures of helicopters and engines. It was decided not to adopt the data in tabular form, but to present it graphically in the context wherein it is used. The reader is referred to the manufactures of the examined components, in case more information is required.

What helicopters concern, the survey included data made available by :

→ AgustaWestland

→ Airbus Helicopters (former Eurocopter)

→ Bell Helicopter

→ Kazan Helicopters

→ NHIndustries

→ MIL helicopters

→ Robinson Helicopter Company

→ Schweizer Aircraft Corporation

→ Sikorsky Aircraft Corporation

→ The Boeing Company

Also, data was taken from the vast documentation provided by Jackson et al. (2004-2005) and Ripley (1998).

Engine data is based on the documentation released by :

→ CFM International

→ Continental Motors, Inc.

→ DeltaHawk Diesel engines

→ Engine Alliance

→ General Electric Aviation

→ Hirth Motoren

→ Honeywell

→ International Aero Engines

→ LHTEC

→ Lycoming Engines

→ Microturbo

→ MTU Aero Engines

→ Pratt & Whitney

→ Pratt & Whitney Canada

→ Price Induction

→ Rolls-Royce PLC

→ Thielert aircraft engines

→ Turbomeca

→ Zoche aero-diesels

Bibliography

Abramowitz, M., & Stegun, I. (Eds.) (1972). *Handbook of mathematical functions*, (9th ed.). Dover publications, inc.

Acharya, S., Mahmood, G., & Dennis, R. (2006). *The Gas Turbine Handbook*. U.S. Department of Energy. National Energy Technology Laboratory.

AgustaWestland (2015). Media gallery.
URL `www.agustawestland.com/media/gallery`

AIAA (2003). AIAA Aerospace Design Engineers Guide. American Institute of Aeronautics and Astronautics, Inc.

Ainley, D., & Mathieson, G. (1955). An examination of the flow and pressure losses in blade rows of axial-flow turbines. Tech. Rep. 2891, Ministry of supply : Aeronautical research council reports and memoranda.

Akridge, J., & Mikhaylik, Y. (2005). Lithium-sulfur secondary battery : Chemistry and practical system performance. In *International Conference on Polymer Batteries and Fuel Cells*. Las Vegas, Nevada, USA.

Alvarez, M. (1974). Economics of air transport. NASA TT F-15249.

Anderson, Jr., J. D. (2001). *Fundamentals of Aerodynamics*, (3rd ed.). McGraw-Hill, Inc.

Antoine, H. (2014). Documentation, Sagita S.A.

Antoine, H., & Buysschaert, F. (2014a). Meeting minutes.

Antoine, H., & Buysschaert, F. (2014b). Meeting minutes.

Antoine, H., Dimitriadis, G., Hendrick, P., Kagambage, E., & Rayee, T. (2009). A novel concept for helicopter rotor drives. In *3rd European Conference for Aero-Space Sciences*. Versailles, Paris, France.

Atallah, K. (2004). Design, analysis and realisation of a high-performance magnetic gear. *IEEE Proceedings-Electric Power Applications*, *151*(2), 135–143.

Aungier, R. H. (2000). *Centrifugal compressors. A strategy for aerodynamic design and analysis*. ASME press.

Aungier, R. H. (2006). *Turbine Aerodynamics. Axial-flow and radial-inflow turbine design and analysis*. ASME press.

Bailey, W. O., Al-Mosawi, M., Yang, Y., Goddard, K., & Beduz, C. (2009). The design of a lightweight HTS synchronous generator cooled by subcooled liquid nitrogen. *IEEE Transactions on Applied Superconductivity*, *19*(3), 1674–1677.

Barron, R. F. (1985). *Cryogenic systems*, (2nd ed.). Oxford University Press, Inc.

Bastien, J., & Handler, C. (2006). Hydrogen production from renewable energy sources. IEEE 1-4244-0218-2/06.

Beck, D. D., & Wilson, D. G. (1996). *Gas-Turbine Regenerators*. Chapman & Hall.

Beltramo, M. N., & Morris, M. A. (1980). Parametric study of helicopter aircraft systems, costs and weights. NASA CR-152315.

Bennett, J., & Jack, A. (2004). Fault-tolerant control architecture for an electrical actuator. In *35th Annual IEEE Power Electronics Specialists Conference*, Aachen, Germany: IEEE.

Berrittella, M., Franca, L. L., & Zito, P. (2009). An analytic hierarchy process for ranking operating costs of low cost and full service airlines. *Journal of Air Transport Management*, *15*, 249–255.

Berton, J. J., Freeh, J. E., & Wickenheiser, T. J. (2003). An analytical performance assessment of a fuel cell-powered small electric plane. NASA/TM-2003-212393.

Boeing (2014). 2014 environment report.
URL `http://www.boeing.com/aboutus/environment/environment_report_14/sb_4_2_1_green_diesel.html`

Boirum, C. G. (2009). Review of historic and modern cyclogyro design. No. AIAA 2009-5023 in 45th AIAA/ASME/SAE/ASEE Joint Propulsion Conference & Exhibit. American Institute of Aeronautics and Astronautics.

Bosch (2007). *Automotive Handbook*, (7th ed.). Robert Bosch GmbH.

Bossel, U. (2005). On the way to a sustainable energy future. Invited Paper, Intelec '05.

Bossel, U. (2006). Does a hydrogen economy make sense ? In *proceedings of the IEEE*, vol. 94, (pp. 1826–1837).

Brewer, G., Morris, R., Davis, G., Versaw, E., Cunningston, G., Riple, J., Baerst, C., & Garmong, G. (1978). Study of fuel systems for LH_2-fueled subsonic transport aircraft. NASA CR-145369.

Brown, G. V., Kascak, A. F., Ebihara, B., Joghnson, D., Choi, B., Siebert, M., & Buccieri, C. (2005). NASA Glenn research center program in high power density motors for aeropropulsion. NASA/TM-2005-213800.

Burns, J. W. (1994). Aircraft cost estimation methodology and value of a pound derivation for preliminary design development applications. No. 2228 in 53th Annual Conference of Society of Allied Weight Engineers, Inc., (pp. 1–44). Long Beach, CA, USA.

Bushmarin, L., Dementyev, P., Ioffe, G., & Kestelmana, V. (1983). *Mechanical transmission of helicopters*. Moscow.

Buysschaert, F., & Hendrick, P. (2004). Research on inlet precooling for mini-turbojet engines. In *40th AIAA/ASME/SAE/ASEE Joint Propulsion Conference and Exhibit*. American Institute of Aeronautics and Astronautics.

Buysschaert, F., Newman, S., Walker, S., Antoine, H., & Hendrick, P. (2013). The Ljungström turbine for aeronautical applications. In *5th European Conference for Aeronautics and Space Sciences*. München: EUCASS.

Cabrera, N., Meza, E., Romero, A., & Cintli Rodríguez, R. (2013). "if there is no struggle, there is no progress": Transformative youth activism and the school of ethnic studies. *The Urban Review*, *45*(1), 7–22.

Cale, D. B. (1979). Contributions of the engine R&D community to reduce cost of ownership of army helicopters. No. AIAA 79-1360 in 15th AIAA/SAE/ASME Joint Propulsion Conference, (pp. 1–7). American Institute of Aeronautics and Astronautics.

Çengel, Y., & Boles, M. A. (2006). *Thermodynamics. An Engineering Approach*, (5th ed.). Boston, MA, USA: McGraw-Hill, Inc.

Çengel, Y., & Cimbala, J. (2010). *Fluid Mechanics : Fundamentals and Applications*, (2nd ed.). New York, USA: McGraw-Hill, Inc.

Chaiko, L. (1990). Assessment of worm gearing for helicopter transmissions. NASA Technical Memorandum 102441.

Chan, C., & Chau, K. (1996). An advanced permanent magnet motor drive system for battery-powered electric vehicles. *IEEE Transactions on Vehicular Technology*, *45*(1), 180–188.

Choi, B. B., & Siebert, M. (2006). A bearingless switched-reluctance motor for high specific power applications. NASA/TM-2006-214486.

Chung, J., Simon, T., & Buddhavarapu, T. (1991). Three-dimensional flow near the blade/endwall junction of a gas turbine: application of a boundary layer fence. In *International Gas Turbine and Aeroengine Congress and Exposition*, 91-GT-45. ASME.

Coleman, C. P. (1997). A survey of theoretical and experimental coaxial rotor aerodynamic research. Technical paper 3675, National Aeronautics and Space Administration.

Crabtree, J. A. (1958). Weight estimation for helicopter design analysis. No. 177 in 17th Annual Conference of Society of Allied Weight Engineers, Inc. New York, USA.

Craig, H., & Cox, H. (1970-1971). Performance estimation of axial flow turbines. In *Proceedings of the Institution of Mechanical Engineers*, vol. 185, (pp. 407–424).

Cumpsty, N. (2000). *Jet Propulsion : a simple guide to the aerodynamic and thermodynamic design and performance of jet engines*. Cambridge University Press.

Daily, J., & Nece, R. (1960). Chamber dimension effects on induced flow and frictional resistance of enclosed rotating disks. *Journal of Basic Engineering*, *82*(1), 217–230.

DARPA (2008). DARPA/Army A160T Hummingbird unmanned rotorcraft completes phase I flight tests. DARPA News Release.

Demir, Ö., Claus, M., & Kilic, F. (2014). *Quotes for the Elite of the World: The best quotes from around the world*. Books on Demand.
URL `https://books.google.be/books?id=vHUZBQAAQBAJ`

Denton, J. (1993). Loss mechanisms in turbomachines. *Journal of Turbomachinery*, *115*, 621–656.

Dixon, S. (2005). *Fluid mechanics and thermodynamics of turbomachinery*, (5th ed.). Elsevier Butterworth-Heineman.

Dou, H.-S., Khoo, B. C., & Yeo, K. S. (2008). Instability of Taylor-Couette flow between concentric rotating cylinders. *International Journal of Thermal Sciences*, (47), 1422–1435.

Dunavant, J. D., & Erwin, J. R. (1956). Investigation of a related series of turbine-blade profiles in cascade. Tech. Rep. 3802, National Advisory Committee for Aeronautics, Washington.

Dunham, J., & Came, P. (1970). Improvements to the Ainley-Mathieson method of turbine performance prediction. *Journal of Engineering for Gas Turbines and Power*, *92*(3), 252–256.

Dyess, S. B. (1991). Drive system weight optimization. No. 2034 in 50th Annual Conference of the Society of Allied Weight Engineers, San Diego, California. Society of Allied Weight Engineers.

Edkin, R. A., Valgora, M. E., & Perz, D. A. (1968). Performance characteristics of 15k*VA* homopolar inductor alternator for 400 *Hz* brayton-cycle space-power system. NASA TN D-4698.

Einstein, A., Calaprice, A., & Dyson, F. (2010). *The Ultimate Quotable Einstein*. Princeton University Press.
URL `https://books.google.be/books?id=G_iziBAPXtEC`

Eser, D., & Dereli, Y. (2007). Comparisons of rotordynamic coefficients in stepped labyrinth seals by using Colebrook-White friction factor model. *Meccanica*, *42*, 177–186.

Eser, D., & Kazakia, J. Y. (1995). Air flow in cavities of labyrinth seals. *International Journal for Engineering Sciences*, *33*(15), 2309–2325.

Ferguson, T. (1968). Centrifugal compressors for gas turbines. In *Proceedings of the Institution of Mechanical Engineers, Conference Proceedings*, vol. 183. Institute of Mechanical Engineers.

FlightGlobal (2015). Cutaways.
URL `www.flightglobal.com`

Folenta, D. (1983). Design study of self-aligning bearingless planetary gear (sabp). NASA Contract NAS3-21604.

Folenta, D., & Lebo, W. (1988). Design, manufacture, and spin test of high contact ratio helicopter transmission utilizing self-aligning bearingless planetary (sabp). NASA CR 4155.

Frankel, D. J. (1979). Model for flux trapping and shielding by tubular superconducting samples in transverse fields. Stanford University, Stanford, California 94305, USA.

Gaugler, R. E., & Russell, L. M. (1982). Flow visualisation study of the horseshoe vortex in a turbine stator cascade. TP1884, National Aeronautics and Space Administration.

Gibbings, D. (2009). *Fairey Rotodyne*. The History Press, Great Britain.

Goulburn, J., & Wilson, J. (1975). High speed disk friction losses in a gaseous medium. *International Journal of Mechanical Sciences*, *17*(6), 379–382.

Haddadi, S., & Poncet, S. (2008). Turbulence modeling of torsional Couette flows. *International Journal of Rotating Machinery*, *2008*, 27.

Hendrick, P., & Buysschaert, F. (2015). Meeting minutes.

Henry, Z. S. (1995). Bell helicopter advanced rotorcraft transmission (art) program. NASA CR 195479.

Hileman, J. I., Ortiz, D. S., Bartis, J. T., Wong, H. M., Donohoo, P. E., Weiss, M. A., & Waitz, I. A. (2009). Near-term feasibility of alternative jet fuels. Tech. rep., Rand corporation, 1776 Main Street, P.O. Box 2138, Santa Monica, CA 90407-2138.

Hodkinson, B. (1939). Estimation of the leakage through a labyrinth gland. *Proceedings of the Institution of Mechanical Engineers*, *141*, 283–288.

Horlock, J. (1966). *Axial Flow Turbines : Fluid mechanics and thermodynamics*. London, United Kingdom: Butterworths.

Horlock, J., & Denton, J. (2005). A review on some early design practice using computational fluid dynamics and a current perspecive. *Journal of Turbomachinery*, *127*, 5–13.

Houberechts, A. (1972). *les Turbines*. Vander.

Huang, C.-C., Tsai, M.-C., Dorrell, D. G., & Lin, B.-J. (2008). Development of a magnetic planetary gearbox. *IEEE Transactions on Magnetics*, *44*(3), 403–412.

Jack, A. G., Mecrow, B. C., & Haylock, J. A. (1996). A comparative study of permanent magnet and switched reluctance motors for high performance fault tolerant applications. *IEEE Transactions on Industry Applications*, *32*(4), 889–895.

Jackson, P., Munson, K., & Peacock, L. (Eds.) (2004-2005). *Jane's all the world's aircraft*, (95th ed.).

Jacques, R. (2004a). *Energetische studie der propulsieturbomotoren. Deel 2 : figuren*. Vrije Universiteit Brussel.

Jacques, R. (2004b). *Energetische studie der propulsieturbomotoren. Deel I : theorie*. Vrije Universiteit Brussel.

Jenkinson, L. R., Rhodes, D., & Simpkin, P. (1999). *Civil Jet Aircraft Design*. AIAA Education Series.

Jia, W., & Liu, H. (2013). Computational study of the effects of a shroud geometric variation on turbine performance in a 1.5-stage high-loaded turbine. *Journal of Thermal Science*, *22*(5), 439–446.

Joergensen, F., Andersen, T., & Rasmussen, P. (2006). The cycloid permanent magnet gear. IEEE 1-4244-0365-0/06.

Johnson, W. (1994). *Helicopter theory*. Dover publications, inc.

Jørgensen, F., Andersen, T., & Rasmussen, P. (2008). The cycloid permanent magnet gear. *IEEE Transactions on Industry Applications*, *44*(6), 1659–1665.

Kachapornkul, S., Jitkreeyarn, P., Somsiri, P., & Tungpimolrut, K. (2007). A design of 15 kW switched reluctance motor for electric vehicle applications. In *Proceeding of International Conference on Electrical Machines and Systems*, (pp. 1690–1693). Seoul, Korea.

Kacker, S. C., & Okapuu, U. (1982). A mean line prediction method for axial flow turbine efficiency. *J. Eng. Gas Turbines Power*, *104*(1), 111–119.

Kalsi, S. (2001). A small-size superconducting generator concept. In *International Machines and Drives Conference*, (pp. 998–1003). Cambridge, MA, USA.

Kawai, T., Adachi, T., & Shinoki, S. (1989). Secondary flow control and loss reduction in a turbine cascade using endwall fences. *Japan Society of Mechanical Engineers Int. J. Ser.II*, *32*(3), 375–387.

Klung, R., & Griggs, M. (2004). Reliability and availability of megawatt drive concepts. 2004 International Conference on Power System Technology - POWERCON 2004, Singapore.

Knothe, G. (2008). "designer biodiesel" : Optimizing fatty ester composition to improve fuel properties. *Energy & Fuels, American Chemical Society*, *22*, 1358–1364.

Krantz, T. (1994). Nasa/army rotorcraft transmission research, a review of recent significant accomplishments. NASA TM-106508.

Krantz, T. L., & Handschuh, R. F. (1990). Efficiency study comparing two helicopter planetary reduction stages. NASA TM-103106.

Krishnan, R., Blanding, D., Bhanot, A., Staley, A., & Lobo, N. (2003). High reliability SRM drive system for aerospace applications. 0-7803-7906-3/03 IEEE.

Kumar, K. N., & Govardhan, M. (2011). Secondary flow loss reduction in a turbine cascade with a linearly varied height streamwise endwall fence. *International Journal of Rotating Machinery*, *2011*, 16.

Kurzke, J. (2004a). *GasTurb 10 Technical Reference*. Germany.

Kurzke, J. (2004b). *GasTurb 10 User's Manual*. Germany.

Kwon, Y., Baik, S., Lee, E., Lee, J., Kim, Y., Moon, T., Park, H., Kwon, W., Lee, S., Hong, J., Jo, Y., & Ryu, K. (2007). Status of HTS motor development in Korea. IEEE 1-4244-1298-6/07.

Landers, C. L., Lucero, L., & Henthorn, K. D. (2001). Helicopter preliminary design. No. 3165 in 60th Annual Conference of Society of Allied Weight Engineers, Inc., (pp. 1–53). Arlington, Texas, USA.

Large, J. P., Campbell, H. G., & Cates, D. (1976). Parametric equations for estimating aircraft airframe costs. Report R-1693-A-PA&E, Rand corporation, Santa Monica, CA. 90406.

Lee, Y. (1997). *Experimental study on effects of the boundary layer fence on the three-dimensional flow in gas turbines*. Master of science thesis, Department of Mechanical Engineering, Korea University.

Leishman, J. (2002). *Principles of Helicopter Aerodynamics*. Cambridge University Press.

Leishman, J. (2007). *The Helicopter. Thinking Forward Looking Back*. College Park Press.

Lewis, C., & Müller, J. (2007). A direct drive wind turbine HTS generator. IEEE 1-4244-1298-6/07.

Lewis, R. (1996). *Turbomachinery performance analysis*. Oxford: Elsevier Ltd.

Licht, S. (2008). Renewable highest capacity VB_2/air energy storage. *Chemical Communications*, *28*, 3257–3259.

Liebeck, R. H., Andrastek, D. A., Chau, J., Girvin, R., Lyon, R., Rawdon, B. K., Scott, P. W., & Wright, R. A. (1995). Advanced subsonic airplane design and economic studies. NASA CR-195443.

Lozza, G. (1982). A comparison between the craig-cox and the kacker-okapuu methods of turbine performance prediction. In *Meccanica*, vol. 17, (pp. 211–221).

Majumdar, A., Mak, K., Lettington, C., & Nalder, P. (2009). A causal factors analysis of helicopter accidents in new zealand 1996-2005 and the united kingdom 1986-2005. *The Aeronautical Journal*, *113*(1148), 647–660.

Malvano, R., Vatta, F., & Vigliani, A. (2001). Rotordynamic coefficients for labyrinth gas seals: single control volume model. *Meccanica*, *36*, 731–744.

Masson, P. J., & Luongo, C. A. (2007). HTS Machines for applications in All-Electric Aircraft. IEEE 1-4244-1298-6/07.

Masson, P. J., Pienkos, J., & Luongo, C. A. (2007). Scaling up of HTS motor based on trapped flux and flux concentration for large aircraft propulsion. *IEEE Transactions on Applied Superconductivity*, *17*(2), 1579–1582.

Masson, P. J., Soban, D. S., Upton, E., Pienkos, J. E., & Luongo, C. A. (2005). HTS motors in aircraft propulsion : Design considerations. *IEEE Transactions on Applied Superconductivity*, *15*(2), 2218–2221.

AIR BP (2000). Handbook of products. Hertfordshire, United Kingdom.

Horizon Energy Systems (2009). AEROPAK^{TM} brochure. Singapore.

Michael Zoche Antriebstechnik (2007). Zoche aero-diesels brochure, München, Germany.

Optimal Aircraft Design Software (2008). OAD. Namur, Belgium.

Mecrow, B., Atkinson, D., Jack, A., Green, S., & Haylock, J. (1999). The need for fault tolerance in an aeroengine electric fuel control system. IEE.

Memardezfouli, M., & Nourbakhsh, A. (2009). Experimental investigation of slip factors in centrifugal pumps. *Experimental Thermal and Fluid Science*, *33*, 938–945.

Million, D. J. (1978). Research requirements to reduce maintenance cost of civil helicopters. NASA CR-145288.

MMPA (2009). Standard specifications for permanent magnet materials. MMPA Standard No. 0100-00, Magnetic Materials Producers Association, Chicago, Illinois, USA.

Moon, Y. J., & Koh, S.-R. (2001). Counter-rotating streamwise vortex formation in the turbine cascade with endwall fence. *Computers & fluids*, (30), 473–490.

Moore, M. D. (2010). NASA puffin electric tailsitter vtol concept. In *10th* AIAA *Aviation Technology, Integration, and Operations Conference*. American Institute of Aeronautics and Astronautics.

Moran, M., & Shapiro, H. (2004). *Fundamentals of Engineering Thermodynamics*, (5th ed.). John Wiley and Sons, Inc.

Moustapha, H., Zelesky, M. F., Baines, N. C., & Japikse, D. (2003). *Axial and radial turbines*. Concepts NREC.

Nagrial, M., Rizk, J., & Hellany, A. (2007). Design and development of magnetic torque couplers and magnetic gears. IEEE.

Nanao, Y., & Maki, N. (2006). Fundamental design and parameter optimization study of HTS Generators for co-generation systems. *IEEE Transactions on Applied Superconductivity*, *16*(2), 1485–1488.

Nelms, D. (2012). Speed streak. *Aviation Week & space technology*, (pp. 64–66).

Nerowski, G., Frauenhofer, J., Ries, G., Nick, W., & Neumüller, H.-W. (2004). Advances and prospects of HTS Rotating machine development at Siemens. *Power Engineering Society General Meeting*, *2*, 2052–2055.

Neumann, K. (1964). Zur frage der verwendung von durchblickdichtungen im dampfturbinenbau. *Maschinentechnik*, *13*(4).

Newman, S. (2003). *The foundations of helicopter flight*. Butterworth-Heinemann.

Nichols, J. (1964). Tip-mounted turbojets for helicopter propulsion - A progress report. Technical paper 640345, SAE International.

Nicolai, L. M., & Carichner, G. E. (2010). *Fundamentals of aircraft and airship design*. vol. 1. AIAA Education Series.

Peng, W. W. (2008). *Fundamentals of Turbomachinery*. New Jersey, United States: John Wiley and Sons, Inc.

Polte, H.-J. (2006). *Hubschrauber. Geschiche, Technik und Einsatz*, (4th ed.). Hamburg, Berlin, Bonn. Deutschland: Verlag E.S. Mittler & Sohn.

Privoznik, E. J. (1968). Allison t63 regenerative engine program. In *24th Annual National Forum of the American Helicopter Society*.

Prouty, R. (2002). *Helicopter Performance, Stability and Control*. Krieger.

Prouty, R. (2007). *Helicopter Aerodynamics*. P.O. Box 46885, Cincinnati, OH, 54246, United States of America: Eagle Eye Solutions.

Radebaugh, R. (2009). Cryocoolers : the state of the art and recent developments. *Journal of Physics: Condensed Matter*, *21*, 9pp.

Ramme, M. (1968). Helicopter rotor and turbine assembly, patent 3417825. United States Patent Office.

Rashidi, M., & Krantz, T. L. (1992). Dynamics of a split torque helicopter transmission. NASA TM-105681.

Rasmussen, P., Andersen, T., Joergensen, F., & Nielsen, O. (2005). Development of a high-performance magnetic gear. *IEEE Transactions on Industry Applications*, *41*(3), 764–770.

Raymer, D. P. (1992). *Aircraft Design: A conceptual approach*, (2nd ed.). AIAA Education Series.

Rekik, M., Besbes, M., Marchand, C., Multon, B., Loudot, S., & Lhotellier, D. (2008). High-speed-range enhancement of switched reluctance motor with continuous mode for automotive applications. *European Transactions on Electrical Power*, *18*, 674–693.

Rens, J., Atallah, K., Calverley, S., & Howe, D. (2007). A novel magnetic harmonic gear. IEEE 1-4244-0743-5/07.

Ripley, T. (1998). *Jane's pocket guide : Modern military helicopters*. HarperCollins.

Runge, W., Buysschaert, F., Hayez, J., Carlier, F., Antoine, H., Hendrick, P., Dimitriadis, G., & Degrez, G. (2013). Numerical and experimental investigation of slot-blowing air over a cylinder. In *5th European Conference for Aeronautics and Space Sciences*. München: EUCASS.

Samet, J. (2008). The historical controversies surrounding innateness. In E. N. Zalta (Ed.) *The Stanford Encyclopedia of Philosophy*. Fall 2008 ed.

Sampatacos, E., Morger, K., & Logan, A. (1983). NOTAR : the viable alternative to a tail rotor. AIAA Aircraft Design, Systems and Technology Meeting.

Scharrer, J. K. (1987). Theory versus experiment for the rotordynamic coefficients of labyrinth gas seals : Part I - A two control volume model. In *Rotating Machinery Dynamics, ASME 11th Biannial Conference on Mechanical Vibration and Noise*, vol. 2, (pp. 411–426).

Schobeiri, M. (2005). *Turbomachinery flow physics and dynamic performance*. Springer-Verlag Berlin Heidelberg.

Schroijen, M. (2009). Mav propulsion system using the Coanda effect. No. AIAA 2009-4809 in 45th AIAA/ASME/SAE/ASEE Joint Propulsion Conference & Exhibit. American Institute of Aeronautics and Astronautics.

Schubring, G. (2006). *Conflicts between generalization, rigor and intuition : Number concepts underlying the development of analysis in the 17th-19th century France and Germany*. Springer Science & Business Media.

Seeger, R., & Haar, D. (2013). *Men of Physics: Galileo Galilei, His Life and His Works*. Commonwealth and international library: Selected readings in physics. Elsevier Science. URL `https://books.google.be/books?id=pq83BQAAQBAJ`

Semple, R. D. (1976). Research requirements for development of regenerative engines for helicopters. NASA CR-145112.

Serenus (2009). Serenus fuel cell evaluation kit, high temperature pem fuel cell system brochure.

Shapiro, J. (1958). *The helicopter*. New York, USA: The MacMillan Company.

Shaw, R. (1966). Efficiency predictions for axial-flow turbines. *International Journal of Mechanical Sciences*, *8*(3), 171 – 192.

Sheahen, T. P., McConnell, B. W., & Mulholland, J. W. (2002). Method for estimating future markets for high-temperature superconducting power devices. *IEEE Transactions on Applied Superconductivity*, *12*(2), 1784–1789.

Singh, S. K., Scherbarth, D. W., Ortoli, E. S., Repp, J. R., Christianson, O. R., Parker, J. H., & Carr, J. W. (1999). Conceptual design of a high temperature superconducting generator. *IEEE Transactions on Applied Superconductivity*, *9*(2), 1237–1240.

Sivasubramaniam, K., Zhang, T., Lokhandwalla, M., Laskaris, E., Bray, J., Gerstler, B., Shah, M., & Alexander, J. (2009). Development of a high speed HTS generator for airborne applications. *IEEE Transactions on Applied Superconductivity*, *19*(3), 1656–1661.

Soderberg, C. R. (1949). Unpublished notes, Gas Turbine Laboratory, Massachusetts Institute of Technology.

Sostilio, N. (1997). Weight control overview S-92 medium lift helicopter program. 2375, (pp. 1–31). Society of Allied Weight Engineers, Inc., Bellevue, Washington: Society of Allied Weight Engineers, Inc.

Stepniewski, W., & Keys, C. (1984). *Rotary-Wing Aerodynamics*. vol. I & II. New York, USA: Dover publications, inc.

Stewart, R., & Roder, H. (1964). *Properties of Normal and Parahydrogen*. Pergamon Press.

Stodola, A. (1922). *Dampf- und Gas-Turbinen*. Springer.

Sun, D. C., & Yuan, Q. (1995). Wormgear geometry adopted for implementing hydrostatic lubrication and formulation of the lubrication problem. NASA contractor report 195416, State University of New York at Binghamton.

Taylor, C. F. (1985a). *The Internal-Combustion Engine in Theory and Practice*. vol. 2 : Combustion, Fuels, Materials, Design. The M.I.T. Press.

Taylor, C. F. (1985b). *The Internal-Combustion Engine in Theory and Practice*. vol. 1 : Thermodynamics, Fluid Flow, Performance. The M.I.T. Press.

STAL (1927). 10,000-14,000 kW. Ljungström steam turbine, constructed by Svenska Turbinfabriks Aktiebolaget Ljungström, Finspong, Sweden. Reprinted from "ENGINEERING".

STAL (1939). STAL Steam-turbine generators. Svenska Turbinfabriks Aktiebolaget Ljungström, Finspong, Sweden.

Thuis, B. G. (2004). The development of composite landing gear components for aerospace applications. 3333, (pp. 1–21). Society of Allied Weight Engineers, Inc., Newport, California: Society of Allied Weight Engineers, Inc.

Torenbeek, E., & Wittenberg, H. (2009). *Flight Physics. Essentials of Aeronautical Disciplines and Technology, with Historical Notes*. Springer.

Turner, J. W. (1986). Interrelationship of weight and cost reduction. 1748, (pp. 1–10). Society of Allied Weight Engineers, Inc., Williamsburg, Virginia: Society of Allied Weight Engineers, Inc.

Uematsu, T., & Wallace, R. S. (1995). Design of a 100 kW switched reluctance motor for electric vehicle propulsion. In *APEC '95 conference proceedings*, vol. 1, (pp. 411–415).

Van den Braembussche, R. (2013). *Centrifugal compressors analysis and design*. Von Karman Institute.

Van Loenen Martinet, F. P. G. (1915). Mededeelingen betreffende de Ljungström turbine, vervaardigd door de Svenska Turbinfabriks Aktiebolaget Ljungström te Finspong, Zweden. *De Ingenieur*, *30*(30), 601–617.

Van Zoest, W. H. (1935). Twee "werkspoor-stal" turbogeneratoren van 17000/22500 kW voor de P.E.N.-Centrale te Velsen. *De Ingenieur*, *51*(34), 113–118.

Verstraete, D. (2009). *The potential of liquid hydrogen for long range aircraft propulsion*. Phd dissertation, Cranfield University, Cranfield, United Kingdom.

Verstraete, D., & Hendrick, P. (2008). Parametric sizing of more-electric regional jet aircraft with hydrogen fuel : Addendum A : Sizing of the fuel tank. Deliverable D2/6 Add.A.

Verstraete, D., Hendrick, P., Pilidis, P., & Ramsden, K. (2010). Hydrogen fuel tanks for subsonic transport aircraft. *International Journal of Hydrogen Energy*, *35*(20), 11085–11098.

Walsh, P., & Fletcher, P. (2004). *Gas turbine performance*, (2nd ed.). Blackwell Publishing.

Watkinson, J. (2004). *The art of the helicopter*. Oxford, United Kingdom.: Elsevier Butterworth-Heineman.

Welborn, B. (1967). Propeller and rotor driven v/stol power transmission weight estimation method. No. 595 in 26th Annual Conference of the Society of Allied Weight Engineers, Boston, Massachusets. Society of Allied Weight Engineers.

Wen, H., Bailey, W., Goddard, K., Al-Mosawi, M., Beduz, C., & Yang, Y. (2009). Performance test of a 100 kw HTS generator operating at 67 K - 77 K. *IEEE Transactions on Applied Superconductivity*, *19*(3), 1652–1655.

White, G. (1985). 3600 hp split torque helicopter transmission. NASA CR 174932.

Wilson, D. G. (1987). New guidelines for the preliminary design and performance prediction of axial-flow turbines. vol. 201, (pp. 279–290). Institute of Mechanical Engineers.

Woo, J. W. (2011). *Analysis of compressible and incompressible flows through see-through labyrinth seals*. Master's thesis, Texas A&M University.

Woodruff, S., Boenig, H., Bogdan, F., Fikse, T., Petersen, L., Sloderbeck, M., Snitchler, G., & Steurer, M. (2005). Testing a 5 MW high-temperature superconducting propulsion motor. *IEEE Electric Ship Technologies Symposium*, (pp. 206–216).

Zhang, G., Chen, B., Song, F., Dai, S., Guo, H., Wang, H., & Yu, S. (2007). Optimal design of an innovative high temperature superconducting generator with the evaporative cooling stator and the magnetic flux oriented rotor. *IEEE Transactions on Applied Superconductivity*, *17*(2), 1545–1548.

Zweifel, O. (1945). The spacing of turbomachine blading, especially with large angular deflection. *Brown Boveri Review*, *32*(12), 436.